The University of Sheffield



Investigation on Vibration of Interior Permanent Magnet Synchronous Machines for Electric Vehicles

Iain MacLennan Urquhart

A thesis submitted for the degree of Doctor of Philosophy

Department of Electronic and Electrical Engineering

The University of Sheffield

Mappin Street, Sheffield, S1 3JD, UK

Abstract

The growing popularity of electric vehicles is being driven by a combination of an increased awareness of global climate change and improvements in batteries and driveline efficiencies. Whilst more efficient and less noisy than a combustion engine, a poorly designed electric machine can still generate damaging vibrations into the vehicle drivetrain and produce nuisance noise. The concern is that for all the apparent mechanical simplicity of an electric machine, modelling the vibration is a notoriously difficult task owing to the multi-physics nature of the problem. This thesis attempts to tackle this issue by carefully measuring and characterising the electromagnetic and mechanical characteristics of a baseline 20kW liquid cooled interior permanent magnet synchronous machine.

Based on mechanical finite element (FE) modelling techniques, methods of best representing the non-homogenous laminated stator core and complex windings structures are explored. It is found that stator laminations and windings can be represented by equivalent composite materials. Although the full winding model has good alignment to the measured results, it takes excessive calculation time. The best compromised solution is to apply the derived composite material to the slots only. To ease the modelling process of complex machine structure, the modal frequencies are obtained experimentally at different stages of assembly so that the model can be fine-tuned step by step as it is assembled, while the structure shape is also simplified by removing complex features and the mesh is optimised to reduce the calculation time. For the end plates, using the spot weld method within the FE tool is found to be an effective method of replacing the bolts. A novel method of linking the coolant shell by optimising the co-efficient of friction is implemented. Overall, the final simplified model shows good alignment with the experimental results.

An electromagnetic FE model is established to calculate the tooth forces acting on the stator from the air gap field harmonics. The derived tooth forces are exported from the electromagnetic FE model and applied to the developed 3D mechanical FE model to allow the dynamic vibration responses to be calculated and compared with the measured results on the baseline machine. The final FE model is then used to comparatively investigate the effects of four different rotor designs which exhibit almost the same torque-speed characteristics, losses, and efficiency, as the baseline machine.

Dynamic experiments of the baseline machine show that the key vibratory frequencies are directly linked to the slot frequency owing to the high torque pulsations of the machine. A PWM component equal to the switching frequency plus the 3rd harmonic of the electrical frequency, identified as a side effect of using the SVPWM technique, is highlighted as a concern and can be mitigated by avoiding mechanical resonances. In addition, it is shown experimentally the amplitudes of the major electromagnetically induced vibration frequency components drop as current angle shifts towards the maximum torque per Ampere point before rapidly rising once the optimal point has passed.

Acknowledgements

First and foremost, I would like to thank my supervisor, Professor Zi-Qiang Zhu, for his strong support and guidance throughout my PhD study. His enthusiasm and expertise on the topic of electric machines was one of the main drivers for me embarking on my PhD study from working in industry. On a personal note, I would also like to sincerely thank him for his support during a personal crisis that occurred during my studies, and I will always be grateful for his help during such a challenging period.

I would like to thank members of the Electric Machines and Drives group, in particular Dr Srivinas Mallampalli for his help in setting up the machine control system on the test rig, as well as Dr James Dexter and Dr Jaime Maravi Nieto for their advice and numerous discussions during the course of this PhD study. I would also like to thank the technical support staff and in particular give my heartfelt thanks to Mr Laurence Obodo who sadly passed away from a long-term illness during the period of study. Laurence helped me out of numerous sticky situations during my testing both in this PhD study and on previous projects, and I will miss our chats. I give my condolences to his family.

I would like to thank my colleagues from the Nissan Technical Centre Europe, in particular Mr Bob Bateman and Mr Jim Greenough for their help and support. I would like to give special thanks to Takashi Kato from the Nissan Research Centre Japan for his input, especially in the early period of the study.

I would like to thank my family and friends for their support and patience during my studies. I would also like to give special thanks to my daughter Amelia and wife Elizabeth who is the strongest and bravest person I know. I love you both dearly.

Contents

Abstract *2*

Acknowledgements *3*

Abbreviations *11*

Symbols *13*

1 General Introduction *17*

1.1 Thesis overview **17**

1.2 Project motivation **20**

1.2.1 A brief history of the electric vehicle 20

1.2.2 The EV market and risks 21

1.2.3 Impact of noise and vibration in electric vehicles 22

1.2.4 Utilisation of CAE tools in development 24

1.3 Introduction to the interior permanent magnet synchronous machine **26**

1.3.1 Permanent magnet machine commutation, AC vs. DC. 28

1.3.2 Machine configurations 29

1.3.3 Permanent magnet rotor topologies 30

1.3.4 Features of IPM rotor machines 31

1.3.5 Winding configurations 34

1.4 The fundamentals of noise and vibration **36**

1.4.1 The source of noise and vibration in electric machines 36

1.4.2 Introduction to natural modes 38

1.4.3 Simple harmonic oscillation 39

1.4.4 The damping ratio 41

1.4.5 Complex system mode shapes 42

1.4.6 Frequency response function 46

1.5 A review of noise and vibration sources in electric machines **48**

1.5.1 Electromagnetic sources 50

1.5.2 Power electronic and control sources 62
1.5.3 Mechanical sources 66
1.5.4 Load induced and structural sources 76
1.5.5 Aerodynamic sources 77
1.6 Noise and vibration mitigation techniques 80
1.6.1 Slot pole number combination & windings 80
1.6.2 Skewing 81
1.6.3 Stator tooth and slot gap designs 83
1.6.4 IPM rotor topology designs 84
1.6.5 PWM noise reduction techniques 86
1.6.6 Control techniques 87
1.6.7 Mechanical noise and vibration mitigation techniques 88
1.7 Summary and Contributions of the Thesis 91
1.7.1 Thesis contributions 92
1.7.2 Published papers 92
2 Experimental investigation of the electromagnetic performance of the baseline machine 93
2.1 Introduction 93
2.2 Baseline machine - specifications 93
2.3 Measuring the machine 96
2.3.1 LCR measurement 97
2.3.2 Cogging torque measurement 99
2.3.3 No load testing 101
2.3.4 Load testing – Measuring the T-N curve 104
2.3.5 Mapping the machine efficiency 114
2.4 Chapter summary 120
3 Finite element modelling of the electromagnetic performance of the baseline machine 122
3.1 Introduction 122

3.2 Establishing the model 123

3.2.1 Applying the materials 123

3.2.2 Establishing the geometry 125

3.3 FE model electromagnetic analysis 130

3.3.1 Radial flux distribution 130

3.3.2 Cogging torque 132

3.3.3 No load calculation 135

3.3.4 Load testing 137

3.3.5 Efficiency and loss maps 147

3.4 Tooth Forces 155

3.4.1 Establishing the force curve position 155

3.4.2 No load tooth force analysis 159

3.4.3 On load tooth forces 164

3.4.4 Summary of tooth force study 178

3.5 Summary 180

4 Experimental modal analysis of the baseline machine 181

4.1 Introduction 181

4.2 Overview of the baseline machine structure, experimental setup, and procedure 182

4.2.1 The baseline machine structure 182

4.2.2 Baseline machine measurement test sequence 184

4.2.3 Overview of hammer, test bench and test equipment 185

4.2.4 Measurement procedure 196

4.3 Impact hammer test results 200

4.3.1 Coolant shell 200

4.3.2 The Stator 203

4.3.3 Wound stator in frame. 207

4.3.4 Rear end plate attached 211

4.3.5 Front and rear end plates attached, no coolant shell 214
4.3.6 Full machine, no rotor 218
4.3.7 Full machine assembly with rotor installed. 222
4.3.8 Machine mounted on dynamometer rig 227
4.3.9 Fully dressed machine 231
4.4 Summary 235
5 Development of mechanical finite element model of baseline machine 237
5.1 Introducing the 3D machine model 237
5.1.1 Defining the materials 238
5.1.2 Modelling the stator laminations 242
5.1.3 Modelling the windings 246
5.2 Modelling the full machine assembly 256
5.2.1 Simplifying the geometry and optimising the mesh 256
5.2.2 Representing the fixtures – attaching the rear plate 260
5.2.3 Representing the fixtures – attaching the front plate 267
5.2.4 Modelling the coolant shell linkage 272
5.2.5 Representing the rotor 280
5.2.6 Mounting the machine 284
5.2.7 The fully dressed machine 286
5.3 Tuning the final model 289
5.3.1 Tuning the complete machine assembly 292
5.4 Summary 294
6 Measurement and Simulation of the vibratory performance of the baseline machine 296
6.1 Introduction 296
6.2 Baseline machine vibration measurement results 297
6.2.1 Overview of measurement setup 297
6.3 Results of vibration measurement 303

6.3.1 No load testing 304
6.3.2 On load vibration measurement: Constant speed, variable torque 307
6.3.3 Influence of the PWM switching on the machine 316
6.3.4 Current angle sweep 326
6.3.5 T-N curve 342
6.3.6 Maximum Torque Per Ampere (MTPA) measurement 345
6.4 Simulating the vibratory performance of the baseline machine 351
6.4.1 The integrated FE models 351
6.4.2 Comparison of the model and measured data 354
6.5 Chapter summary 360
6.5.1 Summary of measured data analysis 360
6.5.2 Summary of dynamic model 361
7 Investigation into the influence of IPM topologies on the vibratory performance of a machine 362
7.1 Introduction 362
7.1.1 Common IPM designs for automotive powertrains 363
7.2 Generating the IPM topologies 368
7.2.1 Establishing the constraints and procedure for the topology comparison 368
7.2.2 Development of the delta topology 372
7.2.3 Development of single layer topology 374
7.2.4 Development of dual layer bar topology 377
7.3 Comparison of the IPM topologies performance 382
7.3.1 Comparison of T-N curves 382
7.3.2 Static air gap flux distribution 383
7.3.3 Magnet volumes 386
7.3.4 No load flux linkage and EMF comparison 387
7.3.5 Machine inductance and torque composition 390
7.3.6 Comparison of efficiency and loss 393

7.3.7 Comparison of torque pulsations 401

7.4 Tooth force comparison 407

7.4.1 Tooth force comparison setup 407

7.4.2 No load tooth force comparison 410

7.4.3 On load tooth force comparison – I_{rms} = 26.7A, β=0° 415

7.4.4 On load tooth forces comparison – I_{rms} = 26.7A, β=45° 424

7.4.5 Conclusion of tooth force investigation 433

7.5 Comparison of vibratory and ERP performance 435

7.5.1 Vibratory performance comparison 436

7.5.2 Comparison using ERP level waterfall diagrams 438

7.6 Summary of topology study 441

8 General conclusions 442

8.1 Effect of control and switching strategy on vibratory performance 442

8.1.1 Influence of switching strategy and frequency 442

8.1.2 Influence of flux weakening control. 443

8.2 Modelling the machine structure 444

8.2.1 Impact hammer test results 445

8.2.2 Modelling the lamination materials 445

8.2.3 Modelling the windings 447

8.2.4 Building the full assembly model 448

8.3 Linking the electromagnetic FE model to the mechanical model 452

8.3.1 Hybrid method 452

8.3.2 Full FE method 453

8.3.3 Results of full FE method 454

8.4 Influence of rotor topology on vibratory behaviour 455

8.4.1 Selecting and matching the different rotor topologies 455

8.4.2 Performance comparison of the 4 topologies 456

8.4.3 Torque pulsations - cogging and ripple torques 458

8.4.4 Tooth forces 459

8.4.5 Vibratory and ERP performance 462

8.5 Next steps and future work 464

8.5.1 Acoustic measurement and modelling 464

8.5.2 Scalability and modelling the skew 464

8.5.3 Rotor model and expand the scope of the system model 465

8.5.4 Influence of coolant and supply on dynamic vibratory performance 465

8.5.5 Shape optimisation of the stator and rotor air gap faces and flux barriers 466

Bibliography 467

Abbreviations

Abbreviation	Full term
2D	2 dimensional
3D	3 dimensional
AC	Alternating current
BEV	Battery electric vehicle
BH	Flux density vs. magnetizing force
BLAC	Brushless AC motor
BLDC	Brushless DC motor
BNC	Bayonet Neill-Concelman (co-axial connector)
CAA	Californian Clean Air Act
CAD	Computer aided design
CAE	Computer aided engineering
CCLD	Constant current line driver
CCW	Counter-clockwise
CFD	Computational fluid dynamics
CO_2	Carbon dioxide
CPSR	Constant power speed range
cRIO	National instruments compact RIO embedded controller
CW	Clockwise
D2A	Digital to analogue conversion
DAQ	Data acquisition
d-axis	Direct axis
DC	Direct current
DSA	Digital signal analyser
EM	Electromagnetic
EMD	Electric machines and drives group
EMF	Electromotive force
ERP	Equivalent radiated power
ERPL	Equivalent radiated power level
EV	Electric vehicle
FE	Finite element
FFT	Fast Fourier transform
FRF	Frequency response function
GCD	Greatest common divisor
GM	General Motors
GPIB	General purpose interface bus
HEV	Hybrid electric vehicle
ICE	Internal combustion engine
ID	Inner diameter
IGBT	Insulated gate bi-polar transistor
IM	Induction machine
IP	Intellectual property
IPM	Interior permanent magnet
IPMSM	Interior permanent magnet synchronous machine
ISO	International organisation for standardisation

iUK	Innovate UK
km/kWh	Kilometres per kilowatt hour (distance per unit energy)
LCM	Lowest common multiple
LCR	Inductance, capacitance, resistance meter
LEAF	Leading environmentally friendly affordable, family car (Nissan)
MEPA	Maximum efficiency per ampere
MMF	Magnetomotive force
MTPA	Maximum torque per ampere
MYxx	Vehicle model year, xx = year
NDT	Non-destructive testing
NLPQL	Nonlinear programming by quadratic lagrangian (optimisation)
NI	National instruments
NOx	Nitrous oxide
OD	Outer diameter
OPEC	Organization of the petroleum exporting countries
PC	Personal computer
PF	Power factor
PLC	Product life cycle
PM	Permanent magnet
PM2.5	Particulate matter, 2.5µm
PMaSynRM	Permanent magnet assisted synchronous reluctance machines
PMSM	Permanent magnet synchronous machine
PWM	Pulse width modulation
q-axis	Quadrature axis
rad	Radian
RPM	Revolutions per minute
SM	Synchronous machines
SPM	Surface permanent magnet
SRM	Switched reluctance machines
SVPWM	Space vector pulse width modulation
T-N Curve	Torque vs. speed curve
TSB	Technology strategy board
UMF	Unbalanced magnetic force
UMP	Unbalanced magnetic pull
USB	Universal serial bus
USP	Unique selling point
VA	Volt-Amperes - apparent power of motor and drive
VW	Volkswagen motor group

Symbols

Symbol	Meaning	Unit
a_m	Modulation coefficient	
A_{slot}	Slot area	m^2
A_{str}	Area of 1 winding strand	m^2
B	Flux density	T
B_m	Peak magnetic flux density	T
B_{pk}	Peak flux density	T
B_{rad}	Radial flux density	T
B_r	Remanent flux density	T
B_{tan}	Tangential flux density	T
C	Damping coefficient	
C_c	Critical damping factor	
C_e	Material constant	
C_T	Goodness factor for cogging torque	
D	Diameter	m
dT	Time step	s
E	Young's modulus	Pa
E_0	EMF fundamental	V
E_f	Epoxy Young's modulus	Pa
E_m	Steel Young's modulus	Pa
E_{slot}	Winding slot Young's modulus	Pa
E_{xy}	Composite X-Y plane Young's modulus	Pa
E_z	Composite Z plane Young's modulus	Pa
F	Force	N
F(ω)	Input spectrum	N
F_0	Fundamental force	N
f_c	PWM switching frequency	Hz
f_d	Dominant vibration frequency	Hz
f_e	Electrical frequency	Hz
F_f	Frictional force	N
f_m	Mechanical (rotor) frequency	Hz
f_{max}	Maximum frequency	Hz
F_n	Normal force	N
f_o	Natural frequency	Hz
f_r	Natural frequency of order r	Hz
F_{rad}	Radial force	N
$F_{reading}$	Force reading from cogging torque measurement	N
f_{rip}	Ripple frequency	Hz
F_{ru}	Unbalanced force	N
F_{tan}	Tangential force	N
g	Air gap length	m
g'	Effective air gap length	m
G_f	Epoxy shear modulus	Pa
G_m	Steel shear modulus	Pa
G_{xy}	Composite x-y plane shear modulus	Pa

G_z	Composite Z plane shear modulus	Pa
H	Magnetic field strength	A/m
H(ω)	Frequency response function	ms^{-2}/N
I_c	Characteristic current	
I_d	d-axis current	A
I_{dq}	Current vector on d-q plane	A
$I_{dq(max)}$	Maximum current on d-q plane	A
I_{max}	Maximum supply current	A
I_q	q-axis current	A
I_{rms}	Root mean square current	A
I_{sc}	Short circuit current	A
j	√-1, 90° complex rotation operator	
K	Lumped stiffness	N/m
k	General counter, number, integer, or index	
K_c	Carter's coefficient	
K_d	Distribution factor	
k_{fr}	Offset for α_p to account for fringing	
K_{hys}	Steinmetiz's hysteresis coefficient	J/m^3
K	Flux leakage factor	
$K_{m1,2}$	Rotor mechanical loss coefficients	
K_{sf}	Slot fill factor	
K_{sp}	Coil span factor	
k_w	Winding factor	
l_{arc}	Total length of air gap arc	m
L_b	Beam length	m
L_d	d-axis inductance	H
L_m	Magnet length along direction of magnetisation	m
L_q	q-axis inductance	H
L_{stk}	Stack length	m
M	Mass	kg
m	Circumferential mode	
M_f	Modulation factor	
$M_{preload}$	Preload mass used in cogging torque measurement	kg
M_{water}	Mass of water	kg
n	Axial mode	
N	Rotor speed	RPM
N_c	Cogging fundamental, LCM between slot and pole number	
n_{divs}	Number of divisions in curve	
N_g	Number of bearing axial grooves	
n_h	Harmonic order	
N_p	Number of poles	
N_{ph}	Number of phases	
N_{pp}	Number of pole pairs	
N_s	Number of slots	
N_{spp}	Number of slots per pole per phase	
N_{str}	Number of strands of winding in the slot	
N_α	N_c/N_p	
P_m	Amplitude of magnetic pressure	N/m^2 or Pa

P_{out}	Output power	W
q	Vector	
r	Magnetic force order	
R_{coils}	Coil resistance	Ω
r_i	Inner radius of bearing cage	m
RippleRate	Ripple rate of torque	-
r_o	Outer radius of bearing cage	m
R_{ph}	Phase resistance	Ω
t	Time	s
T_{avg}	Average torque	Nm
T_c	Cogging torque	Nm
TC_{br}	Magnet thermal coefficient	
T_{lam}	Lamination plate thickness	m
T_m	Magnet temperature	°C
T_{max}	Maximum torque	Nm
T_{min}	Minimum torque	Nm
T_{mutual}	Mutual torque component	Nm
T_{out}	Rotor torque	Nm
$T_{reluctance}$	Reluctance torque component	Nm
T_{total}	Total machine torque	Nm
u	Rotor harmonic number	
V	Velocity	m/s
w	Stator harmonic number	
v	Poisson's ratio	
V_n	Normal velocity of vibrating structural surface	
$V_{channel}$	Volume of water in coolant channel	mm^3
V_d	d-axis voltage	V
V_{dc}	DC supply from power supply	V
V_{dq}	Voltage vector on d-q plane	V
$V_{dq(max)}$	Maximum voltage on d-q plane	V
v_f	Epoxy Poisson’s ratio	
v_m	Steel Poisson’s ratio	
V_{max}	Maximum voltage	V
V_q	q-axis voltage	V
v_{xy}	Composite Poisson's ratio	
W_{cop}	Total copper loss	W
W_e	Eddy current loss	W
W_h	Hysteresis loss	W
W_{iron}	Total iron loss	W
W_{mech}	Total mechanical loss	W
X	Displacement	m
X(ω)	Output spectrum	ms^{-2}
X_d	d-axis reactance	Ω
X_q	q-axis reactance	Ω
Z_b	Number of ball bearings	
Z_m	Mechanical impedance	Ns/m

Greek symbols

Symbol	Meaning	Unit
α_{cp}	Coil pitch	
α_d	Angular distance from origin	
α_p	Optimal pole pitch to pole arc ratio	
α_{sk}	Ratio of skew distance to slot pitch	
α_{st}	Steinmetiz's exponent (frequency)	
β	Current angle	Radians
β_{st}	Steinmetiz's exponent (maximum flux density)	
Δd	Stator core deflection	m
ζ	Damping ratio	
η	Efficiency	%
η_m	Mechanical loss factor	
θ_e	Rotor position in electrical degrees	°
λ_a	A-phase flux linkage	Wb
λ_b	B-phase flux linkage	Wb
λ_c	C-phase flux linkage	Wb
λ_d	d-axis flux linkage	Wb
λ_{fund}	Fundamental flux linkage	Wb
λ_q	q-axis flux linkage	Wb
μ_0	Permeability of free space	H/m
μ_r	Relative permeability	
μ_{rec}	Relative recoil permeability	H/m
μ_s	Coefficient of friction	
ξ_{hsf}	Scaling factor between harmonic and fundamental	
ξ_s	Saliency ratio	
ρ	Mass density	kg/m^3
ρ_0	Mass density of air	kg/m^3
ρ_f	Epoxy density	kg/m^3
ρ_m	Steel density	kg/m^3
ρ_{water}	Density of water	kg/m^3
σ	Conductivity	S/m
σ_{rf}	Radiation factor	
τ_s	Air gap arc section length	m
φ	Phase angle	radians
ϕ_s	Stack factor	
ψ_m	PM flux linkage	Wb
ω	Angular frequency	rad/s
ω_0	Angular natural frequency	rad/s
ω_b	Base speed	rad/s
ω_e	Electrical speed	rad/s
ω_m	Mechanical (rotor) speed	rad/s
ω_{mod}	Modulation angular speed	rad/s
ω_r	Angular frequency at radial force order, r	rad/s

1 General Introduction

1.1 Thesis overview

Interior permanent magnet synchronous machines (IPMSMs) are a popular choice of electric machine topology for electric vehicles (EVs) and hybrid electric vehicles (HEVs) owing to high torque density, wide speed range, and most importantly, high efficiencies. The importance of high efficiency is underlined by the fact that despite great advances in battery chemistry and management techniques over the past few decades the energy density of modern batteries is still very low compared to fossil fuel alternatives such as gasoline or diesel so having a highly efficient powertrain is essential in maximising the drive range of the vehicle. The more km/kWh a vehicle can achieve under a given drive cycle, the better the battery can be utilised with all the cost and convenience advantages this incurs.

The mechanisms behind the high efficiency capabilities of the IPMSMs will be discussed later in this chapter. It will be seen that the advantages gained in efficiency come a cost of complexity both the machine design and control requirements, as well as issues such as torque pulsations, losses, and vibrations.

Whilst electric machines are structurally simple, especially compared to an internal combustion engine, this apparent simplicity masks a complex multi-physics system where the world of control, power electronics, magnetics and mechanics are required to synergise in order to generate the required output power to the road wheel. This requires a multi-disciplinary approach to fully optimise and realise the potential of the machines. A poorly designed machine can generate damaging vibrations and high levels of audible noise into the surrounding environment leading to discomfort for people surrounding or operating the machine and accelerated fatigue or damage of both the machine components and the larger system into which it operates. Understanding these mechanisms and methods of counter measuring them is therefore of high importance to increase the performance and reliability of both the electric machine and the system, which in the case of this thesis is an electric vehicle.

The aforementioned multi-physics nature means that whilst the problems associated with vibration is well understood the methods of tackling the problem and in particular modelling electric machines such that potential concerns are captured and solved as early in the design phase of the electric machine as possible is notoriously difficult.

This thesis will study this issue by careful measurement of both the electromagnetic and mechanical attributes of a prototype IPMSM. The machine utilised was designed as a 1/4 scale representation of the 80kW IPMSM used as the traction machine in the 2010 Nissan LEAF. Using the empiric data from the measurement and state of the art methodologies in finite element (FE) modelling a 3D baseline model of the machine is developed, which attempts to balance the need for high fidelity but also minimise the processing time required in order to reduce the development times of modern vehicles and powertrains.

The structure of the thesis is shown in Fig. 1.1.1.

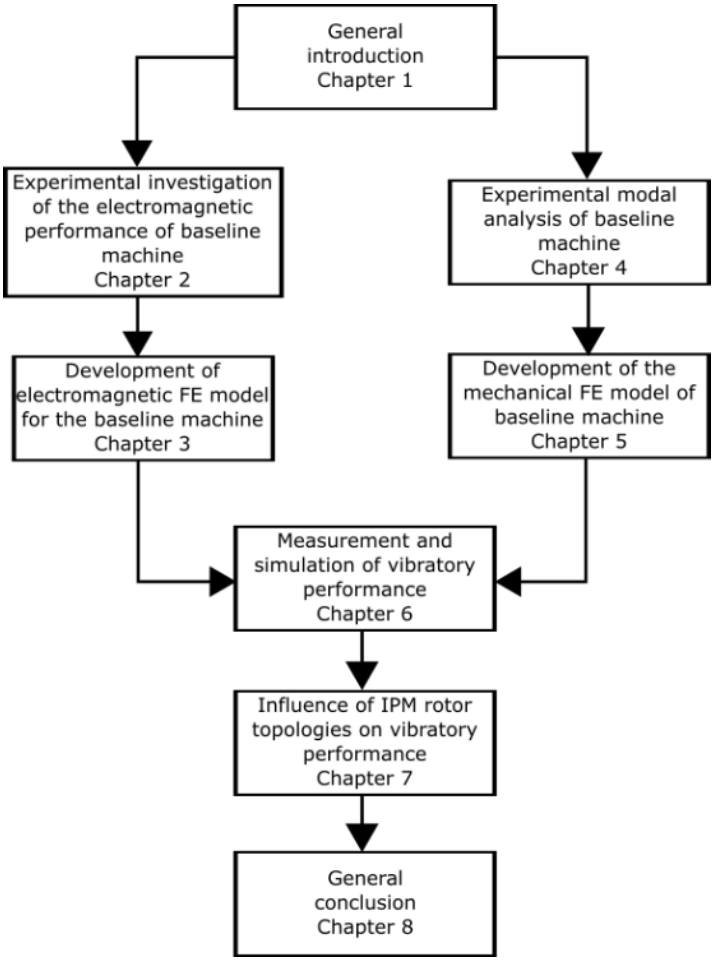

Fig 1.1.1 Flow diagram of the thesis.

The thesis has 8 chapters which flow in sequence to show the build-up in complexity of the model leading to the final vibratory model then utilisation of the model in a study on the impact of different IPM topologies on the machine performance. Table 1.1.1 provides a detailed overview of the chapters shown in Fig. 1.1.1.

Table 1.1.1 Detailed overview of thesis contents.

Chapter	Title	Content	Output	Leads to
1	General introduction	Project motivation, introduction to vibration & measurement review of research area: - Electric machine topologies. - Sources of vibration in electric machines - Methodologies of mitigating vibration	Project motivation and state of the art review	CH2 CH4
2	Experimental investigation of EM performance of baseline machine	Measurement of the electromagnetic and performance aspects of the prototype machine including cogging torque, no-load Back EMF, T-N curve, mapping the MTPA and hence efficiency of the machine.	Empiric results of electromagnetic performance of physical machine	CH3

3	Development of EM FE model of baseline machine	Creation of electromagnetic model of prototype machine utilising the empiric data from CH2 to align the model to the physical machine. Once aligned tooth forces are calculated and studied in depth.	Electromagnetic FE model and tooth forces	CH6
4	Experimental modal analysis of baseline machine	Measurement of the baseline machine using an impact hammer. Machine is stripped to base parts and measured. Assembly is slowly built back up with testing at each stage from base rotor to machine mounted on the test rig, fluid filled machine and ready to run.	Empiric results of impact hammer test for prototype machine.	CH5
5	Development of mechanical FE model of baseline machine	Similar process as chapter 3 where the measured results are used to allow the mechanical FE model to be built up. Given 3D nature of model the emphasis is on creating a model that balances the need for accuracy and simplicity to reduce processing times.	3D mechanical model of the baseline machine	CH6
6	Measurement and simulation of vibratory performance	Analysis of acceleration data captured during dynamic testing. Resultant data is used to align final model which uses the tooth forces from the EM model in chapter 3 as the excitation source for the mechanical model developed in CH5	Full vibratory model of the baseline machine	CH7
7	Influence of IPM topologies on vibratory performance of machine	Identify the most common IPM topologies used in EV applications. Create FE models of selected topologies and match T-N curves to the baseline. Undertake comparison in terms of general performance (loss etc.) and vibratory performance and any difference investigated. Further comparisons into the influence of features such as magnet shaping, and flux barriers is explored	Comparison of vibratory performance of IPM machines.	CH8
8	General conclusion	Summarise the thesis and detail key findings.	-	CH9

The first step is to give some background into why this topic is important from an automotive engineering perspective before moving on a state-of-the-art review of IPM machine topologies, sources of noise and vibrations in electric machines and some of the methods developed to mitigate the vibration.

1.2 Project motivation

1.2.1 A brief history of the electric vehicle

Whilst appearing an ultra-modern product of the 21st century the electric vehicle (EV) is by no means a new concept. The original generation of practical EVs date back to the 1880's When Gustave Trouvé of France first demonstrated an electric tricycle [JC12], [MG12]. Fig 1.2.1 gives a summary of the key points in the history of electric vehicles [MG12], [JC12]. [LPW20], [KC17], [TM11], [NMG10], [AC19] as well as the general trend in EV sales [IEA20].

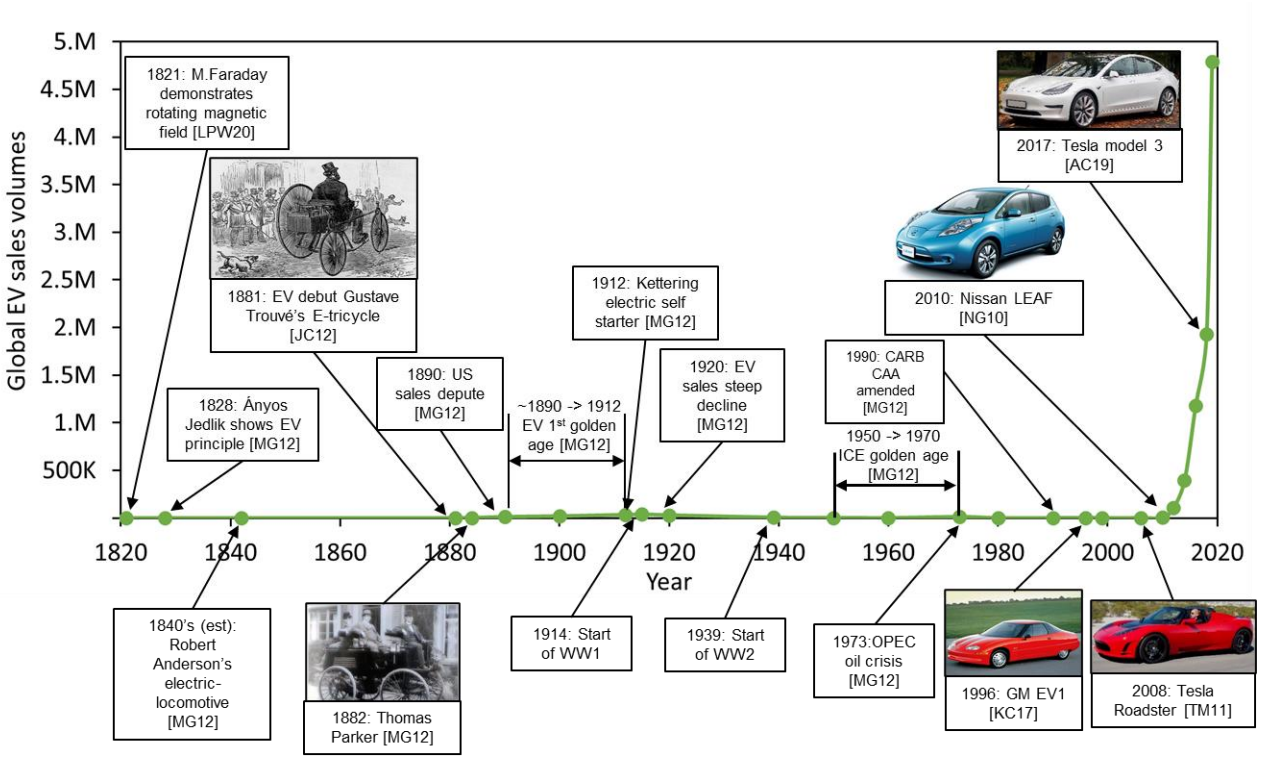

Fig 1.2.1 Key points in the history of battery electric vehicles and sales volume, [MG12], [JC12]. [LPW20], [KC17], [TM11], [NMG10], [AC19], [IEA20]

It can be seen in Fig 1.2.1 that the history of the electric vehicles is very long, covering almost 200 years from Faraday's demonstration of a simple rotating magnetic structure to the modern era. Key historical points are:

- 1880's – French engineer Gustave Trouvé demonstrates the first EV, a tricycle [JC12] in 1881 followed closely by British engineer Thomas Parker with a 4-wheel carriage in 1882.
- 1900 - ~1910: EV's accounted for 38% of the US auto market (vs. 22% for gasoline cars) [MG12].
- 1912: The invention of the electric starter motor by C. F. Kettering [MG12] and cost reductions due to mass production of Ford Model T mark EVs decline, fading from production in 1920.
- 1973, 1979: Renewed interest due to global oil price shocks (OPEC oil embargo in 1973, Iranian oil crisis 1979 to 1980), interest wanes following recovery of oil price.
- 1996: GM EV1 developed as an advanced prototype in reaction to Californian Clean Air Act (CAA) to mitigate hazardous smog in cities such as Los Angeles.

- 1996 -2003: GM along with other major US car manufacturers successfully fought CAA in courts and won, EV1 project terminated and infamously all cars crushed [KC17]
- 1997: Toyota releases the 1st Prius [CC20] which goes on to dominate the hybrid vehicle market.
- 2008: Tesla, formed by some of the engineers on the EV1 project and the billionaire founder of PayPal (Elon Musk) launches the Roadster, an EV sports car, high cost means volumes limited.
- 2010: Nissan Launches the LEAF, first affordable and practical mass produced EV of the new era.
- 2015: "Diesel gate" scandal, VW caught using specialist software to circumvent US emissions tests [AC15], as more OEMs get embroiled in the crisis Diesel vehicle volumes begin to drop.
- 2017: Tesla Model 3 releases to high praise in automotive world, proves to be a sales success.
- 2019: Most OEMs have released or are in the process of releasing EVs, improvements in battery density see vehicle ranges exceed 200 miles.

In many ways the internal combustion engine (ICE) is a victim of its own success. The availability of low-cost fuel and mass production saw the world's cities and highways fill with tens of millions of vehicles, each producing large quantities of $C0_2$, strongly linked to climate change, and localised pollutants such as NOx, unburnt hydrocarbons, and particulate matter (PM2.5 etc.). These factors combined with scandals such as "Diesel gate" have created the perfect conditions for a resurgence of the electric vehicle.

1.2.2 The EV market and risks

Fig 1.2.1 shows the exponential growth of the EV market from ~10,000 units in 2010 to an estimate 4.8 million units in 2019 [IEA20]. By automotive standards, these volumes are quite low (Toyota alone made 10.7 million cars in 2019), however the rise of the EV seems to be accelerating. This places EVs as a product very much in the growth stage of the standard product life cycle (PLC) profile (Fig 1.2.2).

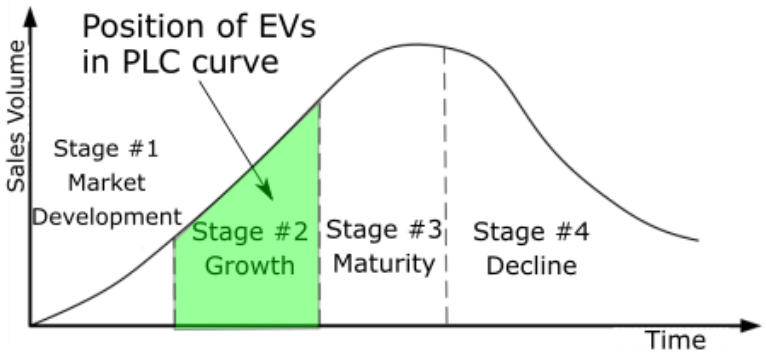

Fig. 1.2.2 Standard product life cycle showing location of EV, based on [RV79].

As a product matures the customer base shifts away from the early adopters to a more mainstream customer. Mainstream customers are more interested in value for money and reliability than the distinctiveness and novelties that satisfy early adopters. As such a manufacturer faces the age-old problem of trying to balance the need for a reliable product with the need for a low-cost product to attract the customer. A second aspect to consider with increased volumes is the cost to a manufacturer to fix a problem once it is in the market,

both in financial costs and less tangible costs such as damage to the brand reputation or even the reputation of the technology as a whole. Fig 1.2.3 gives an indication of the cost impact of a given concern or design error [BH04] at different stages of the design cycle.

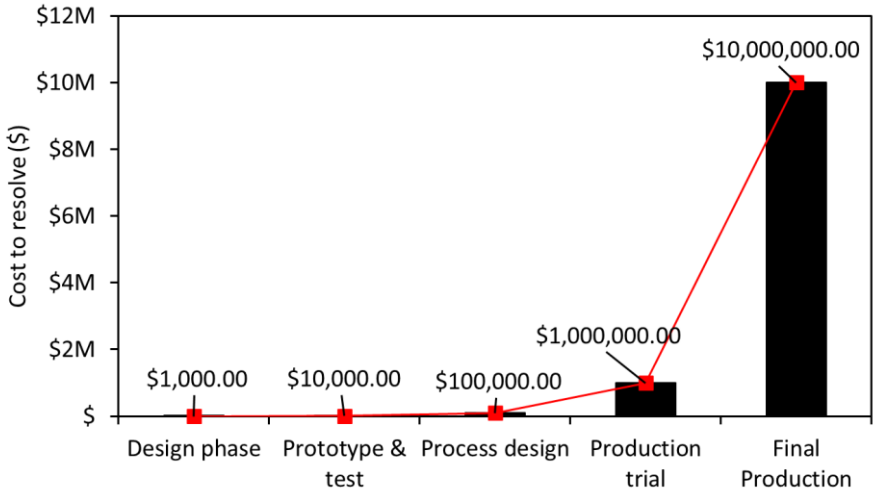

Fig. 1.2.3 Error cost escalation at different phases of the design cycle [BH04].

It is very clear that catching a problem at the earliest possible stage of a design is highly desirable, ideally before any prototype tooling or fabrication takes place. This is where having a good understanding of aspects detrimental to the life of the vehicle, such as the vibratory performance of the machine as well as effective use of modern computer aided engineer (CAE) techniques early in the design phase becomes very important.

1.2.3 Impact of noise and vibration in electric vehicles

Some applications such as loudspeakers positively gain from the system vibrating. However, the majority of applications would look to minimise the phenomena as far as possible. The primary reasons for this are:

- **Component fatigue:** the action of rapidly moving causes the component to fatigue and wear creating early life failures of a part if not carefully controlled. In an automotive application this can generate warranty and/or aftermarket concerns with both cost and brand reputation implications.
- **User discomfort:** noise and vibration can cause discomfort in humans which can, in extreme cases, lead to injuries or disease in humans; studies have shown that high levels of noise and vibration on a vehicle can significantly contribute to driver fatigue [KJ04] [JFM09] and discomfort.

These aspects can have a detrimental impact on two of the key unique selling points (USPs) of an EV, that is:

- A silent and smooth driving experience.
    - Driving an EV should be a simple, quiet, and relaxing experience.
- High reliability and low maintenance costs.
    - There is no need for oil changes and regular servicing that is common on ICE vehicles.
    - Regenerative braking means that even brake pads and discs wear significantly less (despite increased vehicle mass).

Fig. 1.2.4 shows a typical EV front wheel drive driveline setup.

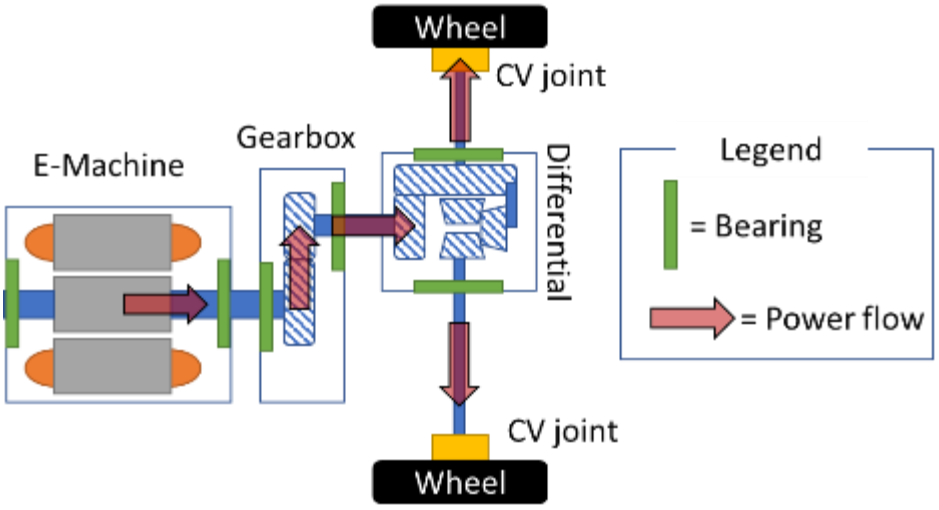

(a) Typical layout of EV powertrain from eMachine to road wheel

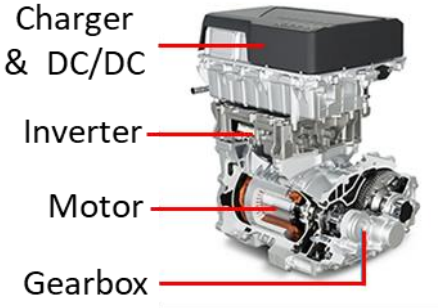

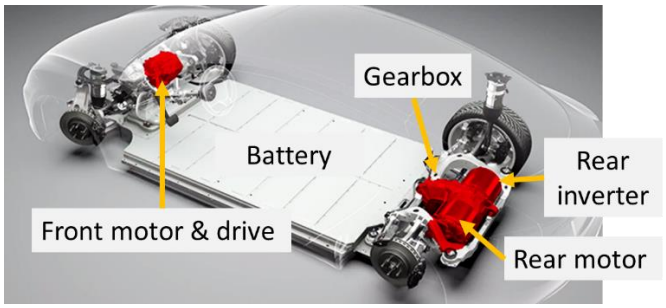

(b) "Stack" drive train assembly [NG19] (c) "Skateboard" layout [CM14]

Fig. 1.2.4 Simplified diagram of typical EV driveline setup and example vehicle layouts.

How the system depicted in Fig 1.2.4(a) is packaged in the vehicle can vary according to manufacturer or even from vehicle to vehicle. Legacy manufacturers such as Nissan, GM and Renault tend to stack the components such that it resembles an ICE (fig 1.2.4(b)) as this allows the vehicles to use the same vehicle production lines and engine insertion tools as standard ICE cars. New manufacturers such as Tesla have no legacy process to deal with so can implement EV specific platforms such the "skateboard" in Fig. 1.2.4(c) where the motors are brought into line with the wheel axles and the battery, giving a solid platform onto which different body designs can be applied, saving cost longer term.

With the advantages and mechanical simplicity of an electric driveline it would be a mistake to assume there are no problems associated with its utilisation. Three key characteristics of electric vehicles have been the source of a number of concerns in the early production EVs.

- High vehicle mass
    - Battery stacks are very heavy (>300kg), significantly increasing the net vehicle mass.
    - Mass does not change as energy is consumed (unlike gasoline or diesel).
    - High mass = high driveline load.
- Reaction speed of the machine

  - Rated torque of the machine may be similar or even lower than an equivalent ICE. However, the *rate* at which it can be applied is significantly higher.
  - High rate of change + high vehicle mass = large impulse forces on gearbox, drive shafts and differentials risking accelerated fatigue and early life failure.
  - In addition, high torque from start and low rolling resistance tyres mean wheel spin on pull-off is a problem with high tyre wear and loss of performance.
- Vibratory characteristics of the machine
  - Vibration and vibratory harmonics frequencies generated by a machine can be significantly higher than an ICE.
  - This can cause accelerated wear in gear boxes, bearings, and the drive line, in particular parts which were carried over from ICE vehicles to reduce development costs.
  - Higher vibratory frequencies may also mean excitations align with natural frequencies of downstream components leading to discomfort and audible noise in the best-case scenario and parts failure in the worst case.

With the above aspects to consider and the cost impacts of market issues highlighted in Fig. 1.2.3 the development of good CAE model of the machine and drive is very important.

1.2.4 Utilisation of CAE tools in development

The flux bridging the air gap between the stator and rotor in an electrical machine is one of the few places where the world of mechanics, electromagnetics and indeed the software controlling the system can be physically observed. Modelling the vibratory performance in electric machines is therefore very challenging as it is a requires a multi-physics approach to tackle the problem typically requiring the integration of electromagnetic and mechanical FE models to yield any accuracy. Digging deeper into the structure of the electric machine shows the apparent simplicity masks a complex non-homogenous structure, highlighted in Fig. 1.2.5.

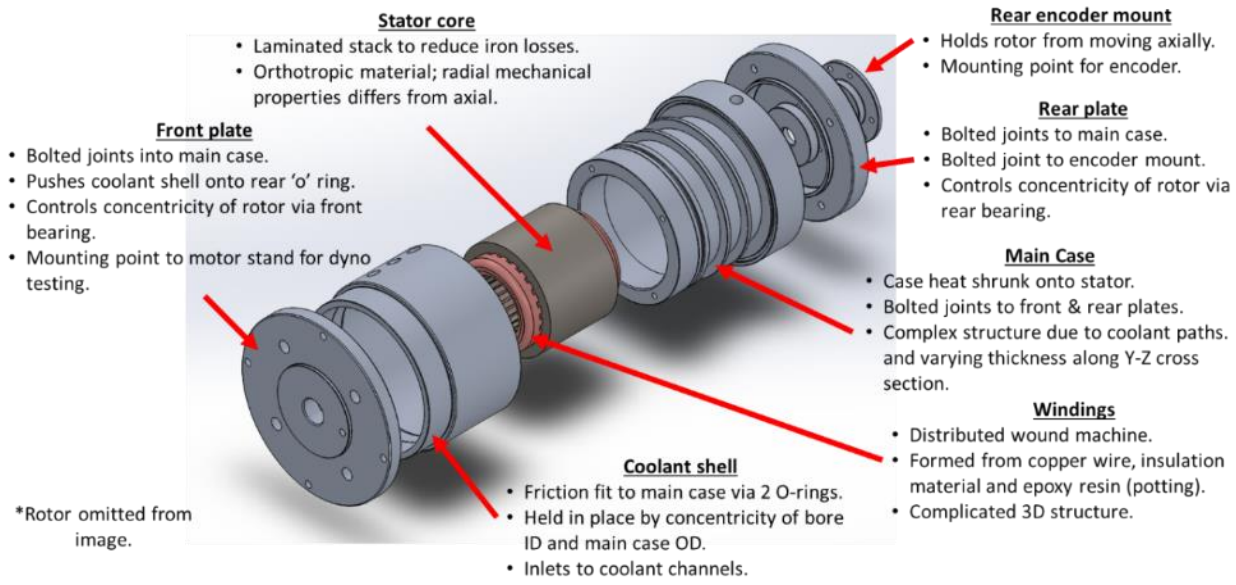

Fig. 1.2.5 Overview of water-cooled electric machine structure.

In Fig 1.2.5 the main concerns unique to the electric machine are the laminated nature of the rotor and stator cores and the complex shape and structure of the windings. These aspects combined with the structural complexity of casing, cooling systems etc. conspire to make accurate modelling very challenging. Further complexities lie in processing the model itself; finite element methods offer an excellent way of calculating the performance of a machine. However, they are computationally intense and generate very large volumes of data requiring very powerful and expensive computers to handle effectively, and complex structures can still have computation times that can be many hours long.

Despite these challenges the life cycle cost impact in Fig. 1.2.3 highlights that the reward for creating a high-fidelity CAE model is enormous; with accurate simulations a large number of different designs and operating conditions can be evaluated, and any concerns quickly highlighted and changed with a few clicks of the mouse before a physical part is ever machined.

This is the motivation for this thesis. By carefully measuring a physical machine the electromagnetic and mechanical characteristics can be captured. Using this analysis, a CAE model of the machine can be made, and the key attributes adjusted such that a good balance between model complexity and alignment to the real machine can be achieved. This model then forms a baseline from which different rotor designs can be compared, giving good confidence in the simulation results, and mitigating the risk of concerns further down the development process and into the marketplace.

1.3 Introduction to the interior permanent magnet synchronous machine

"Electric machines" is a term that covers a vast array of different topologies than have developed and evolved since the earliest days of machine design dating back to the 1820's when scientists and engineers such as Michael Faraday and William Sturgeon began applying the newly discovered properties of electromagnetism to real world solutions. Fig 1.3.1 provides a high-level overview of the different machine topologies available, though this list is not exhaustive.

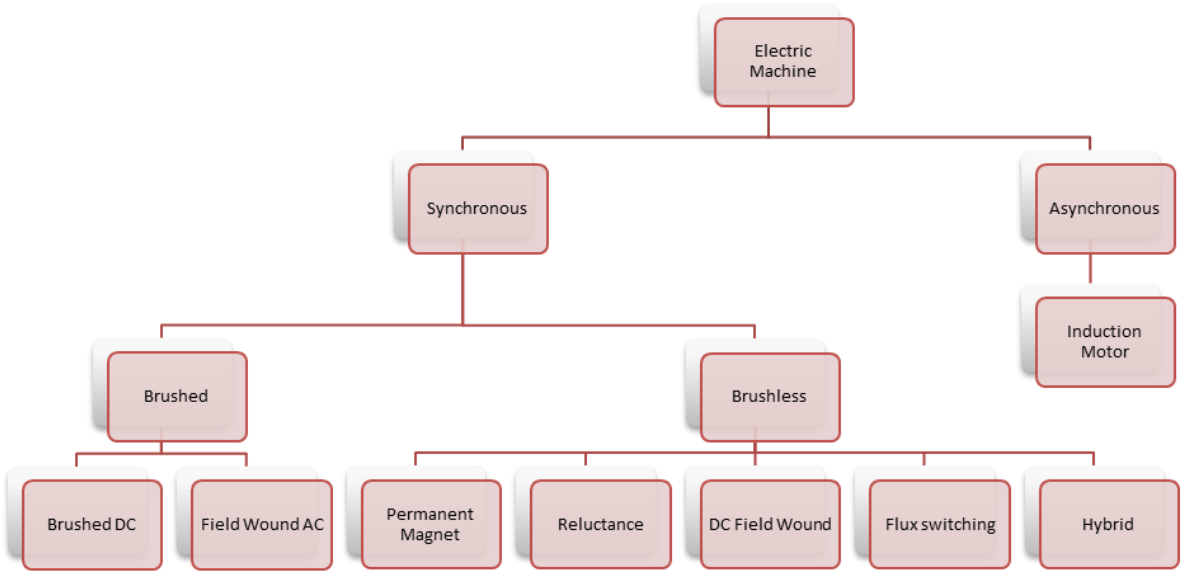

Fig. 1.3.1 High level overview of electric machine topologies.

From Fig. 1.3.1 it can be seen that electric machines broadly fall into two major categories:

- Asynchronous or induction machine (IM): the field rotating within the stator rotates at a higher speed than the rotor creating a so-called slip velocity; this slip induces current on windings in the rotor, generating a magnetic field that couples to the field generated by the armature coils in the stator and forces the rotor to move.
- Synchronous machines (SM): The rotor rotates at the same speed as the field rotating within the stator coils; this is typically achieved through a fixed DC magnetic field from coils in the rotor or permanent magnets (PMSM) which link directly to the stator field or using shaped rotors which allow the machine to utilise the reluctance effect to generate torque.

From the machines highlighted in Fig. 1.3.1 there is no "best" topology, the suitability of each topology is very much application specific. Thus, to determine which topologies are best suited to EVs the basic requirements must first be determined, which is well described in [ZQZ07b]:

- High torque and power density
    - High torque for starting from rest (city driving) and hill climbing.
    - High power for high-speed operation (highway cruising).

- Wide speed range
    - Constant power operation range of 3-4 times base speed is considered the best balance between the peak torque requirement of the machine and the VA rating of the inverter [ZQZ07b], [YH97].
- High efficiency over a wide range of the speed-torque range of the vehicle to maximise range
- Intermediate overload capability for very high torque demands (e.g., kerb mounting)
    - Twice rated torque for short durations is typical [ZQZ07b], [CCC02].
- High reliability
- Acceptable cost
- Low acoustic noise and vibration

From the above requirements the permanent magnet synchronous machine (PMSM) and the induction machine (IM) meet the bulk of the requirements. The lack of brushes mean reliability is high, losses are lower due to lack of friction, there is no electrical arcing and there are little maintenance requirements. Both are also capable of wide speed operation, in particular when control techniques such as flux weakening is applied and suffer less from noise and vibratory problems that is the Achille's heal of lower cost alternative brushless designs such as Switched Reluctance Machines. Table 1.3.1 compares high-level advantages and disadvantages of the PMSM and IM topologies.

Table 1.3.1 High-level advantages and disadvantages of asynchronous and synchronous machines.

	Advantages	Disadvantages
Induction machines (IM) (Asynchronous)	✓ Simple design ✓ Highly robust ✓ Low-cost materials and manufacture ✓ Self-starting	X Low power factor X Low efficiency vs. IPMSM X Difficult to control in variable speed applications
Permanent magnet synchronous machines (PMSMs)	✓ Very high efficiency (>96%) ✓ High power factor ✓ High torque density ✓ Easy to control in multispeed applications	X High cost, especially if rare earth magnets used X PMSM susceptible to demagnetisation under high load conditions X Complex rotor design to package magnets or supply power to coils X Requires special control to start

Given that both technologies are capable of achieving the requirements previously laid out the choice of topology with the automotive industry tends to boil down to cost and efficiency.

- Induction machines are highly robust and relatively cheap in terms of both material cost and manufacturing but suffer from lower efficiency vs. PMSM and poor power factor. The low power factor means the VA rating for the inverter has to be higher, leading to a larger and more expensive inverter.

- PMSM machines are sensitive to demagnetisation at high loads and temperatures so require much more care and monitoring when operating. To maximise efficiency, they utilise rare-earth materials for the permanent magnets, which are expensive and subject to volatile supply conditions. These issues are compensated for by the very high torque densities and efficiencies the machines are capable of plus the high-power factor (>0.9) mean the VA requirement and therefore cost of the inverter is lower.

When selecting the topology, the automotive designer must consider the system cost; a motor needs a drive to operate so the increased VA rating of the inverter for an IM means higher costs which may outweigh the low cost of the machine. Also, the requirement of high efficiency to maximise the range of vehicle means a PMSM typically has a higher MTPA than an IM meaning less battery charge is required to achieve a given distance over a common drive cycle allowing for a greater range. This can mean that the overall kilometres per Watt-hour (km/Wh) is higher giving the vehicle with a PMSM motor a longer driving range for a given battery pack.

1.3.1 Permanent magnet machine commutation, AC vs. DC.

Generally, PMSM machines can be split into 2 categories according to the shape of the back EMF waveforms shown in Fig. 1.3.2 [TMJ96]:

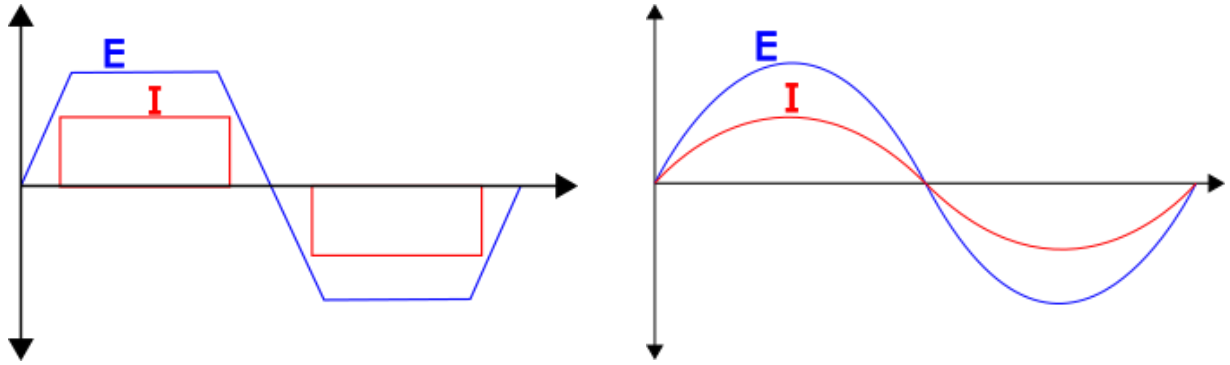

(a) BLDC trapezoidal EMF (b) BLAC Sinusoidal EMF

Fig 1.3.2 Ideal BLDC versus ideal BLAC EMF waveforms [TMJ96].

The construction of both machines is very similar as are the key external components such a position sensor and inverter. However, the method of commutation is quite different; in a BLDC machine the phase currents need only be turned on and off whilst a BLAC needs shaped, sinusoidal waveforms requiring much more sophisticated control methods and careful design of the stator windings and rotor.

At a system level BLDC machines tend to be lower cost than BLAC owing to the lower cost of the position sensor required, simpler commutation method and the fact the method favours SPM rotor topologies and concentrated windings [ZQZ07b] which allow for low cost and high-volume manufacture. Despite the disadvantage in cost and increased controller complexity, the smoother, less harmonic rich BLAC machine are preferred for automotive traction applications due to the lower iron loss which is important in maximising vehicle range in high-speed highway drive cycles where the iron loss dominates. BLAC machines also have

improved performance above the base speed versus BLDC machines [ZQZ06], [YFS06] and utilisation of aspects such as the reluctance torque component on certain designs (see later in this section) means the BLAC meets a large number of the traction motor requirements hence its popularity among EV power trains.

Table 1.3.2 Advantages and disadvantages of brushless AC and DC commutation.

Commutation method	Advantages	Disadvantages
Brushless DC	✓ Low-cost construction. ✓ Simple commutation. ✓ Easy to control.	X High levels of flux harmonics. X Increased machine loss (copper and iron).
Brushless AC	✓ Smooth sinusoidal back EMF. ✓ Lower iron loss. ✓ Utilise established manufacturing process for IM machines.	X Distributed windings, difficult to wind and end windings add parasitic loss. X Expensive position sensors to control. X Complex control system, requires powerful processor to fully utilise.

1.3.2 Machine configurations

Within the realm of PMSMs the topologies can be further broken down into how the rotor and stator are positioned relative to each other. Illustrations of the major types are shown in Fig. 1.3.3:

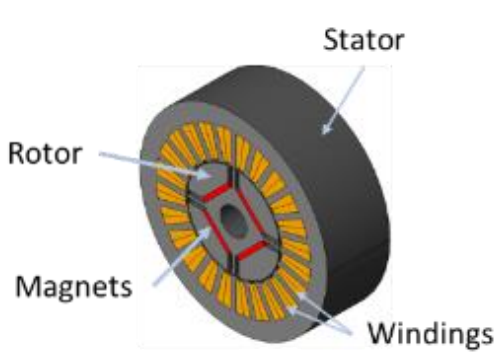

(a) Interior rotor, radial flux machine

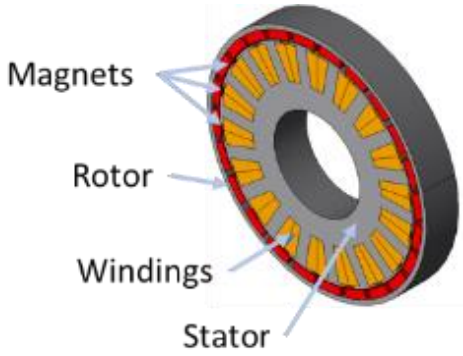

(b) Exterior rotor, radial flux machine

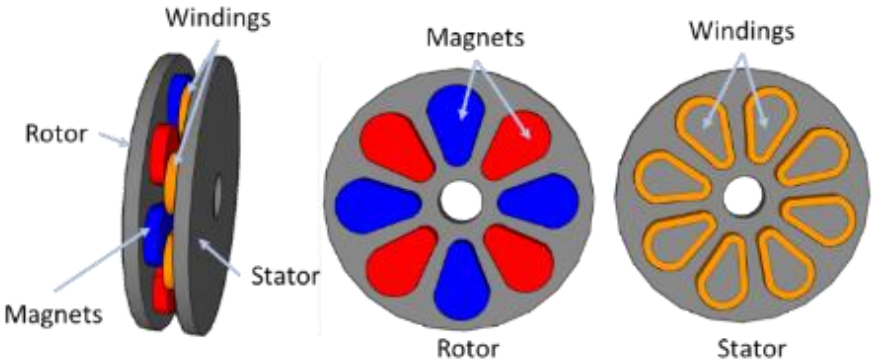

(c) Axial flux machine

Fig 1.3.3 Major machine configurations for brushless machines.

Table 1.3.3 details some of the advantages and disadvantages of each configuration.

Table 1.3.3 Advantages and disadvantages of the main stator/rotor configurations [JRH10], [DH12].

Arrangement	Advantages	Disadvantages
Interior rotor radial flux	✓ Low-cost design ✓ High speed capability. ✓ low Inertia = less effort to accelerate/decelerate.	X Stator winding process complicated X Higher effort vs exterior rotor to maintain steady speed X Difficult to cool magnets. X High centrifugal forces in rotor core.
Exterior rotor radial flux	✓ High torque density ✓ High inertia = less effort to maintain target speed ✓ Good packaging capabilities e.g., in-wheel applications etc.	X High inertia – increased effort to accelerate/decelerate X Low torque/inertia ratio VS interior rotor X Rotor balancing difficult -> increased risk of mechanical vibration.
Axial flux	✓ Very high torque density. ✓ Smooth rotation – no cogging. ✓ Compact shape – easy to package. ✓ Relatively low-cost design.	X Difficult to utilise traditional manufacturing techniques. X Relatively large axial gap – increased flux leakage. X Imbalanced magnetic forces can cause axial wobbling of the rotor. X Susceptible to large eddy current losses at high speed

Within each of the configurations highlighted in Fig. 1.3.3 are a large array of different possible arrangements with multiple rotors or stators etc. Within the automotive sector the preferred arrangement is the interior rotor, radial flux machine; the low inertia and well-established manufacturing processes mean it aligns well to the performance and cost requirements of an automotive component.

1.3.3 Permanent magnet rotor topologies

Within the sub-category of PM rotor designs there is a large variety of different topologies depending on where the magnets are located; some have the magnets bonded to the outer diameter of rotor the core (Surface Permanent Magnet (SPM)), some embedded within the rotor (Interior Permanent Magnet (IPM)) and some in between (inset). Fig. 1.3.4 [ZQZ07b] shows some of the different types of machines with the PM on the rotor.

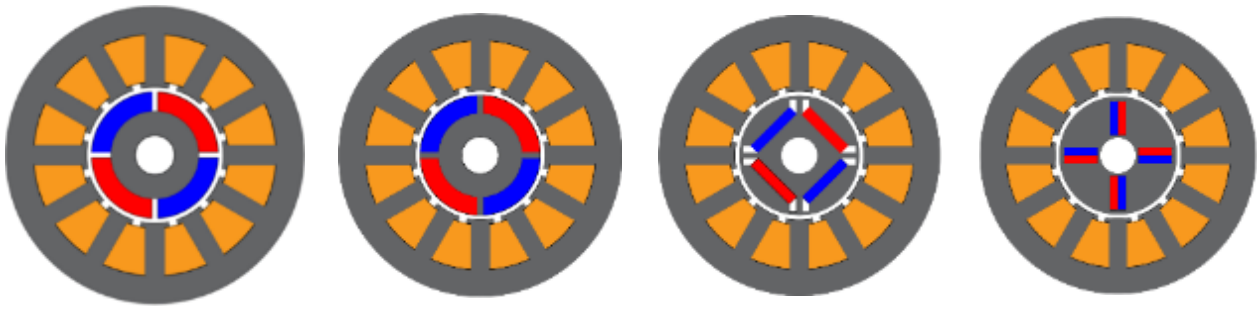

(a) Surface-mounted (b) Surface-inset (c) Interior-radial (d) Interior-circumferential

Fig. 1.3.4 Example PMSM rotor topologies.

As with all applications each method has advantages and disadvantages. IPMs tend to have the following advantages and disadvantages over SPM Machines highlighted in Table 1.3.4 [JRH10], [DH12].

Table 1.3.4 Advantages and disadvantages of IPM machines versus SPM machines

Advantages	Disadvantages
✓ High speed operation (no need for banding)	X High rotor core flux leakage
✓ Improved thermal performance	X Torque ripple due to variations in inductance
✓ Simple bar magnets can be used.	X Rotor complexity and manufacturing costs
✓ Reluctance torque component	

The advantages of IPM machines in terms of better thermal performance of the magnets, less PM usage (utilisation of reluctance torque), simpler bar magnets, higher MTPA and high-speed operation without the need for additional processes such as banding give IPM machines the edge over SPM for traction applications.

1.3.4 Features of IPM rotor machines

The torque equation for a 3-phase IPM PMSM is given as [ZQZ07b], [GQ09]:

$$T = \frac{3}{2} N_{pp} \left[\psi_m I_q - \left(L_q - L_d \right) I_d I_q \right] \tag{1.1}$$

Where N_{pp} = number of pole pairs, Ψ_m = flux linkage due to the PM, L_d, L_q and I_d, I_q are the d and q axis inductances and currents, respectively. This equation is very important as it shows that an IPM has two sources of torque.

- The first part in the brackets ($\Psi_m I_q$) is referred to as the mutual or PM torque.
- The second part ((L_q-L_d)$I_d I_q$) is referred to as the reluctance torque component and relies on the saliency of the machine, that is the difference between the L_q and L_d components.

With two torque sources a well-designed IPM machine can achieve a higher maximum torque per ampere (MTPA) rating than a similar surface PM machine which relies entirely on the mutual (PM) torque pointing towards a higher efficiency. The key advantage of the IPM is therefore the saliency of the machine.

A machine has said to have saliency if the winding inductances vary as a function or rotor position [JRH10], that is $L_q \neq L_d$. The level to which a machine can utilise this effect is given by the saliency ratio (ξ_s) [WLS93], [JRH10]:

$$\xi_s = \frac{L_q}{L_d} \tag{1.2}$$

For the SPM machine in the example above $L_q = L_d$ and therefore $\xi_s = 1$, whereas in the IPM machine $\xi_s > 1$. To improve the saliency the q-axis path can be enhanced by adding multiple layers of magnets or flux barrier or even axially laminate the core such that q-axis inductance is boosted. These are highlighted in Fig. 1.3.5 [ZQZ07b], [LF10], [WLS93], [YHJ12].

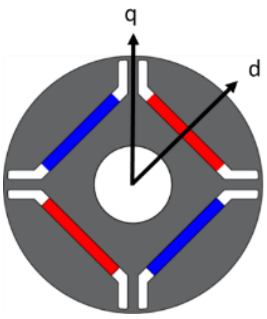

(a) Reduced reluctance q-axis armature path

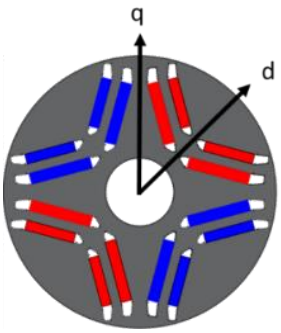

(b) Multilayer magnets

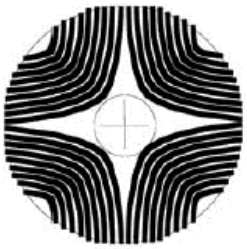

(c) Axially laminated core [WLS93]

Fig. 1.3.5 Methods to increase rotor saliency [ZQZ07b], [WLS93].

These designs offer different methods of boosting the reluctance torque by enhancing the L_q component and/or reducing the L_d component such that the saliency ratio can be quite high. Shaping of the magnets in a 'V' shape in 1.3.5(b) allows so called flux-focussing to be used to boost the Ψ_m component, increasing the mutual and reluctance torque component [LG09]. Utilisation of multi-layer magnets in Fig. 1.3.5 (b) has the additional benefit of improving the flux distribution across a pole arc [YH98], rendering the flux density across the more sinusoidal and therefore less full of parasitic harmonics that contribute to increased iron loss and torque pulsations.

Techniques to mitigate the flux leakage with the rotor core can also be used to both boost Ψ_m by ensuring more flux links with the stator coils and increase the machine saliency by enhancing the q-axis flux path. Adding features such as flux barriers or elongating the magnet slots cut into the core forces more of the flux across the air gap giving higher utilisation of the PM flux as well as enhancing the saliency effect. Some examples of this techniques can be observed in Fig. 1.3.6 [ZQZ07b], [LSH09].

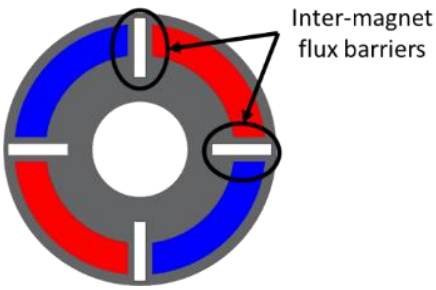

(a) Flux barriers on arc-type IPM rotor

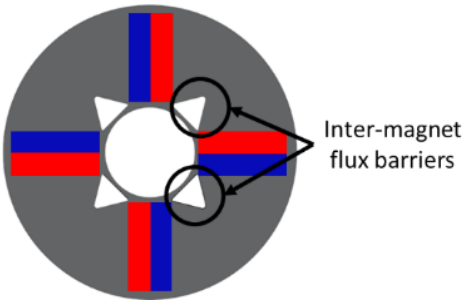

(b) Flux barriers on interior circumferential rotor

Fig. 1.3.6 Methods of reducing flux leakage in the rotor core.

Utilisation of these different methods can mitigate flux leakage and boost the saliency of the machine, but they come with some cost:

- Addition of extra magnet layers and features such as flux barriers to enhance the q-axis flux path comes at the cost of mechanical strength, which is of high concern in particular for high-speed applications.
    - To boost the mechanical strength ribbing and shape optimisation of the different shapes are required at the cost of increased leakage flux in the core.
    - A delicate balance is therefore required between the electromagnetic and mechanical design requirements [ELC04].
- High shape complexity means tooling and assembly is more challenging and therefore more expensive.

Further concerns arise when trying to utilise the reluctance torque component in practical machines:

- Inductance is a function of changing flux linkages (Faradays' law), meaning the effect changes not only with rotor position but also with the MMF of the stator coils leading to complexities in control.
- To produce reluctance torque, the current has to be in advance of the back EMF, achieved by injecting current ($-I_d$) into the d-axis of the d-q plane [WLS94].
    - Applying current into the d-axis will lower the PM flux leakage, Ψ_m, acting to both reduce the back EMF (flux weaken) but also the mutual torque component.
    - A trade-off is therefore required to find a current angle that best balances the mutual and reluctance components.
    - Care must also be taken as aggressive use of this technique can lead to irreversible demagnetisation of the PMs [YY17].
- As a machine comes under higher and higher loads the magnetic steel in the lamination cores begin to saturate, in particular the q-axis [JRH10] and stator teeth leading to reductions in inductances with knock on effects to the overall torque that can be achieved.

The variations in inductance due to aspects such as rotor position, current, as well as non-linear aspects such as flux saturation, both due to the loading of the machine and d-q axis cross coupling [ZQZ07b] mean prediction of the reluctance torque is challenging. Analytical methods are difficult due to the non-linear aspects so numerical techniques such as FE analysis is required along with more advanced analysis techniques such as the frozen permeability method [JKT09], [WQC13a], [GTP14a], [GTP14b], [GTP14c] to improve accuracy. It also means that finding the MTPA of a machine can be a laborious exercise as the change in optimal current angle according to load conditions means a large number of simulations or tests have to be run in order to map each speed and torque point.

From a noise and vibration standpoint these variations in inductance indicate a variation on the flux density across the air gap, which as will be seen has a direct impact on the forces induced on the machine structure.

1.3.5 Winding configurations

The method by which the armature coils are distributed within the stator is a core design aspect of the machine as it dictates the flux distribution on no-load due to the tooth design and during load due to the flux generated by the coil MMF. There are numerous different methods of winding a machine; however, the methodologies can generally be split into two major categories [JRH10]:

- Distributed (overlapping) windings
    - Coils are distributed over a number of slots such that the coils span aligns as closely as possible the pole arc of the rotor allowing for a more uniform flux distribution.
- Concentrated (non-overlapped) windings
    - Coils are wound directly onto each tooth and the different poles and phases interconnected externally.

Fig. 1.3.7 illustrates the two major winding types.



(a) Concentrated (non-overlapped) winding. (b) Distributed (overlapping) winding.

Fig. 1.3.7 Basic winding types for a 4-pole PM machine (A-phase only).

As with all things, each method has a number of advantages and disadvantages, as listed in Table 1.3.5.

Table 1.3.5 Comparison of different winding configurations.

	Advantages	Disadvantages
Concentrated winding	✓ Short end windings ✓ Good thermal conductivity ✓ High copper fill factor ✓ Low cogging torque (fractional slot) ✓ Easy to automate manufacturing	X High MMF harmonics resulting in increased iron loss in the core materials [LC11] and also rotor PM eddy current loss X Low winding factor versus distributed winding X Difficult to utilise the reluctance torque component
Distributed winding	✓ High winding factor, less MMF harmonics, reducing iron loss ✓ Good flux weakening performance and of reluctance torque component ✓ Uses same winding process as induction machines (low cost)	X Large end windings; increased copper loss (I^2R) X Lower copper utilisation X Increased cogging and ripple versus concentrated winding X Lower copper fill factor X Complex manufacturing process; can be labour intensive

Concentrated windings are on typically found on such as those used in domestic appliances or similar applications owing to their relatively low cost and low cogging torque. Large machines such as the traction machine in the Nissan LEAF tend to use distributed windings due to the reduced iron losses from the lower MMF harmonics [YH97] and the ability to utilise flux weakening techniques to increase the constant power band of the machine and the aforementioned reluctance torque component of the machine to boost the MTPA performance [YH98]. The key aspects in determining the winding layout is [DH12]:

- Coil span
    - The number of slots each coil must span or "jump" to form a pole
    - Coil span is also referred to as winding pitch
- Number of turns per/coil and diameter of wire
    - Number of turns dictates the MMF of the coil
    - Diameter of each conductor in the coil dictates the current carrying capacity of a coil
    - Both these factors influence the inductance and therefore maximum back-EMF of a coil
    - Both factors are also influenced by the size of the slot and how much space can be utilised
- Manufacturing
    - Cost and complexity of fabricating and inserting coils

1.4 The fundamentals of noise and vibration

1.4.1 The source of noise and vibration in electric machines

Vibration is defined as a "limited reciprocating motion of a particle of an elastic body or medium in alternately opposite directions from its position of equilibrium" [JFG06, p. 1]. For a body or system to vibrate it must have two key characteristics: elasticity and mass. The vibration which a system undergoes can be defined as either:

- **Forced vibration:** the structure or system is forced to vibrate at a frequency dictated by an external periodic source of force.
- **Natural or free vibration:** Specific frequency at which the total energy stays the same over time so given a single input to start the system the amplitudes remain constant.

For a system to vibrate there must be some form of energy inputted into the system in order to generate the forces required to move the system. In an electric machine the sources are the electrical power suppling the MMF in the stator coils, as well as the PMs on the rotor. The energy conversion process is summarised in Fig. 1.4.1(a) [JFG06].

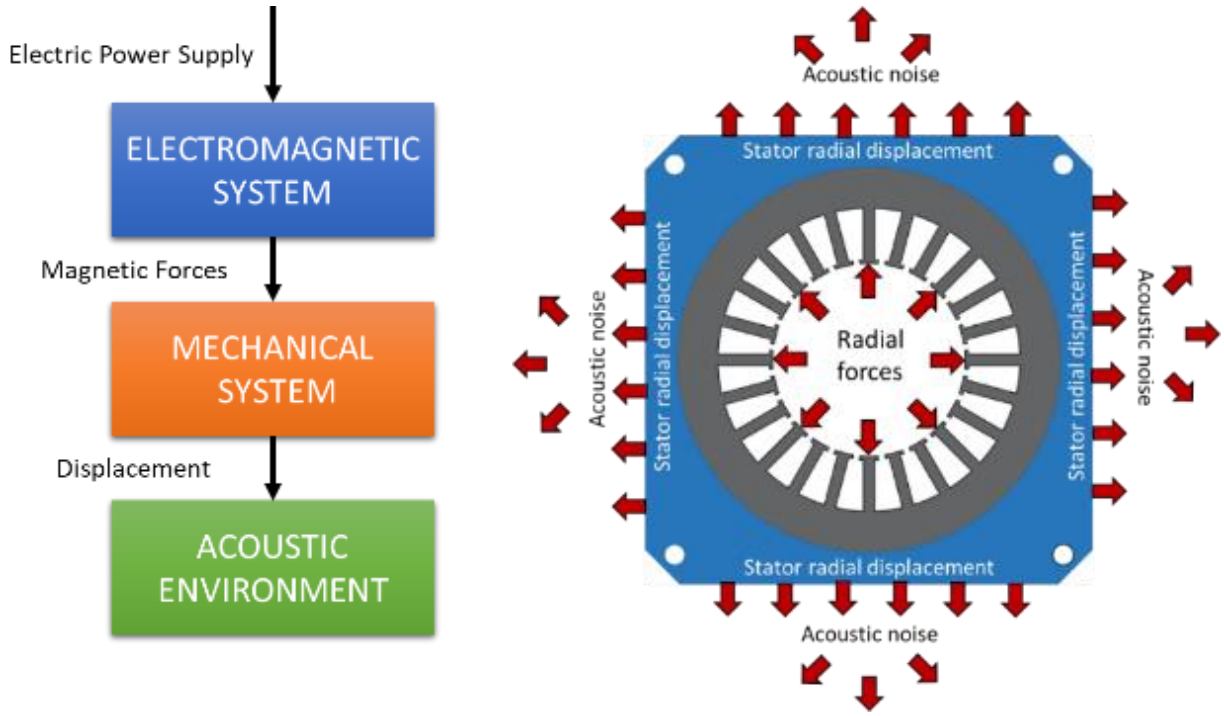

(a) Conversion of electrical energy into acoustic environment

(b) Mechanism of generation of noise and vibration in electrical machines

Fig. 1.4.1 System flow of noise generation in an electric machine [JFG06].

It can be seen that in an IPM rotor machine the air gap magnetic flux density imparts a force on the tooth faces that form the inner bore of the machine. These forces propagate through the stator and into the casing causing displacement which is a function of the force distribution and the material and geometric properties of the core. Given a machine surrounded in air the displacement of the outer body forces the air around the

casing to move creating shock waves (sound) that propagate outwards into the wider environment. The frequency and amplitude of these shock waves dictate the noise level and therefore the potential level of discomfort on any persons close to the machine [JFM09]. Furthermore, as was highlighted in Fig. 1.2.5(a) the vibrations generated by the machine will propagate via conduction through the driveshaft and machine mounting points into the wider driveline and indeed vehicle body, meaning that whilst the vibratory characteristics may have limited effect on the machine, it may have more serious implications further down the driveline generating accelerated fatigue on key components such as gear boxes which has all the negative consequences on reliability and ultimately cost previously discussed.

The source of both the torque and parasitic aspects such as vibration lies in the interaction between the magnetic flux between the stator and the rotor. The rotor is separated from the stator by an air gap and how the magnetic flux interacts with the rotor and stator surfaces that form the air gap boundaries dictates the force distribution within the machine. When discussing the forces in a radial system, it is good practice to define the forces in terms of radial and tangential forces, illustrated in Fig. 1.4.2.

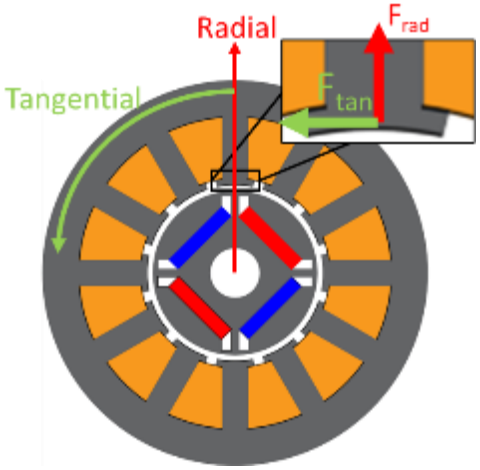

Fig. 1.4.2 The definition of the tangential and radial directions.

The forces induced in the tangential and radial directions are defined by the Maxwell stress tensor which is defined in (1.3) and (1.4) respectively [JFG06], [YH09], [RI09], [MSI14], [CL19].

$$F_{tan} = \frac{L_{stk}}{\mu_0} \oint B_{rad} B_{tan} dl \tag{1.3}$$

$$F_{rad} = \frac{L_{stk}}{2\mu_0} \oint \left(B_{rad}^2 - B_{tan}^2\right) dl \tag{1.4}$$

where

- F_{tan} and F_{rad} are the tangential and radial forces respectively (N).
- L_{stk} is the stack length of the machine (m).
- l is the unit length of the surface on which the force is acting (m).
- B_{rad} and B_{tan} are the radial and tangential flux density components (T).
- μ_0 is the permeability of free space ($4\pi x10^{-7}$ H/m).

From Fig. 1.4.2 it can be seen that a tangential force acting on the rotor will cause it to spin on its rotational axis which is the desired effect. A radial flux density caused by the field in the magnetic circuit trying to find the shortest route across the air gap is also present which tends to act against the stator teeth that form the inner bore of the stator, applying a radial force to the structure. This radial force is less useful, with the tangential flux density the bulk of the energy is utilised in generating a torque in the output shaft to provide mechanical power to an external load, for the radial flux density the energy has nowhere else to go but into the wider machine structure, generating an excitation.

Furthermore, if $B_{rad} >> B_{tan}$ then the square function in (1.4) means that the radial force can be orders of magnitude higher than the tangential force creating significant problems in the machine, in particular if there are any unbalanced magnetic forces (UMF) due to design or structural issues (see the later in this chapter).

As previously discussed, the flux density distribution around the air gap is not uniform, as will be seen slotting effects as well as variations in inductance due to saliency and core material saturation mean that as the rotor spins the forces generated changes, inputting an excitation frequency proportional to this change in force. As the rotor increases or decreases speed and load, this excitation frequency changes accordingly and if it aligns to a natural frequency of the same mode order, either of the stator or the wider machine or driveline structure through propagation of the forces then the part can begin to move violently creating high levels of fatigue or even component failure. An understanding of these natural frequencies and modes is therefore required.

1.4.2 Introduction to natural modes

If the forced vibration applied to a system matches the natural frequency of the system, defined by (1.5), then the system becomes resonant [TZ04].

$$f_0 \propto \sqrt{\frac{E}{\rho}} \tag{1.5}$$

where f_0 is the resonant frequency, E is the modulus of elasticity (Young's modulus) in Pascals (Pa) and ρ is the mass density of the structure in kg/m^3. When the resonant frequency of the system is encountered the amplitude of the displacement of the system greatly increases over that of a non-resonant frequency given the same excitation. Fig. 1.4.3 illustrates the effect.

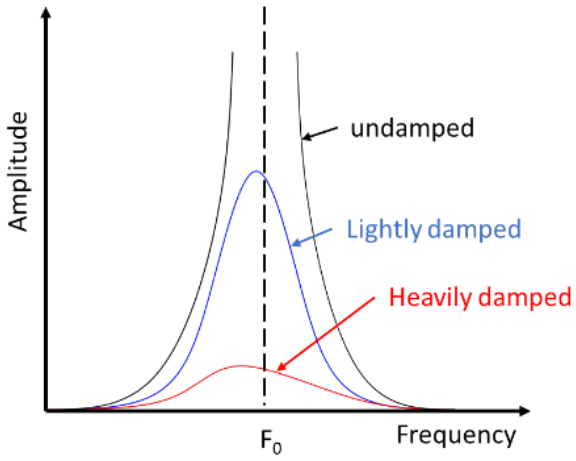

Fig. 1.4.3 Illustration of the resonance effect with different levels of damping.

The undamped condition in Fig. 1.4.3 is a theoretical case, all systems have some form of loss that will dissipate the energy e.g. friction or viscosity in a mechanical system or resistive losses in an electrical system. Therefore, in the real world the natural frequency of an unoptimized system would resemble the lightly damped curve in Fig. 1.4.3 where the amplitude is high but finite. For some systems such as oscillators or resonant converters in power electronics this natural amplification is much sought after as it allows for designers to utilise smaller reactive (lighter, lower cost) components. In a mechanical system such as the electric machines that are the focus of this thesis the resonant frequency is to be avoided owing to the potential for fatigue and damage to the system and the surrounding components. If the natural frequency of a system can be established, then from (1.5) the material properties or structure of the system can be adjusted to shift the natural frequency above or below the operating frequency bandwidth of the system. To understand this a short overview of simple harmonic oscillation is required.

1.4.3 Simple harmonic oscillation

A simple mass-spring damper system forms a basic harmonic oscillator which can be used to illustrate an example which is shown in Fig. 1.4.4 [JG06].

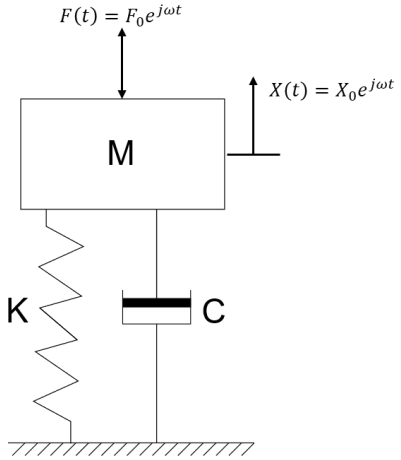

Fig. 1.4.4 Simple mass-spring damper system [JG06].

The motion equation for the system in Fig. 1.4.4 can be shown as (1.6) [JG06].

$$M\frac{d^2X(t)}{dt^2} + C\frac{dX(t)}{dt} + KX(t) = F(t) \tag{1.6}$$

where X(t) is the displacement, M is the mass, C is the damping coefficient, K is the stiffness of the spring and F(t) is the force applied at time, t. If the system is subject to a sinusoidal force F_0e^{jwt}, shown in Fig. 1.4.4, then for a steady state solution the displacement of the mass would be of the form X_0e^{jwt}. (1.6) now becomes [JFG06].

$$X_0(-\omega^2M + jC + K)e^{j\omega t} = F_0e^{j\omega t} \tag{1.7}$$

Rearranging gives the displacement of the mass [JFG06]

$$X_0 = \frac{F_0}{K - \omega^2M + j\omega C} = \frac{F_0e^{j\varphi}}{\omega\sqrt{(K/\omega - \omega M)^2 + C^2}} \tag{1.8}$$

Where φ is the phase angle:

$$\tan\varphi = \frac{K/\omega - \omega M}{C} \tag{1.9}$$

From (1.5) the system response is related to the system parameters (damping, mass, stiffness) and the frequency of the input. This is an important point as this shows the excitation frequency has a large contribution to the displacement of the system. Given that the velocity, V, of the mass is related to the displacement as (1.10) [JFG06]:

$$V(t) = j\omega X_0e^{j\omega t} \tag{1.10}$$

The impedance of the spring-damper system can be obtained as (1.11) [JG06].

$$Z_m(\omega) = \frac{F(t)}{V(t)} = C + j\left(\frac{K}{\omega} - \omega M\right) \tag{1.11}$$

Setting the imaginary side to of the impedance to zero yields the resonance or natural frequency of the system [JG06].

$$\omega_0 = \sqrt{\frac{K}{M}} \tag{1.12}$$

Given this (1.6) can be rewritten as (1.13) [JG06]:

$$X(t) = \frac{F_0}{M}\frac{e^{jwt}}{(\omega_0^2 - \omega^2) + j\eta_l\omega_0\omega} \tag{1.13}$$

where η_m is the mechanical loss factor of the system (1.14) [JG06]

$$\eta_m = \frac{C}{(\omega_0M)} \tag{1.14}$$

From (1.13) if the system is at the natural frequency (i.e., $\omega = \omega_0$) the displacement is greatly amplified as the (ω_0^2-ω^2) term cancels. Thus, if the excitation frequency aligns with a natural frequency the displacement of the mass within the system would be much higher. This is where the damping aspect of the system becomes important.

1.4.4 The damping ratio

For any given system, the damping can be classified as:

- Underdamped: The system reaches the zero point rapidly but overshoots it and keeps oscillating over time with the amplitude at each cycle reducing until the oscillation decays to zero.
- Critically damped: The "sweet spot" where the damping is enough to prevent oscillation and the time taken to reach the zero point is minimised.
- Overdamped: The system does not oscillate but takes a long time to reach the zero point, at the extreme it can get "stuck" in one position before ever reaching the zero point.

Fig. 1.4.5 illustrates the different terminologies listed above.

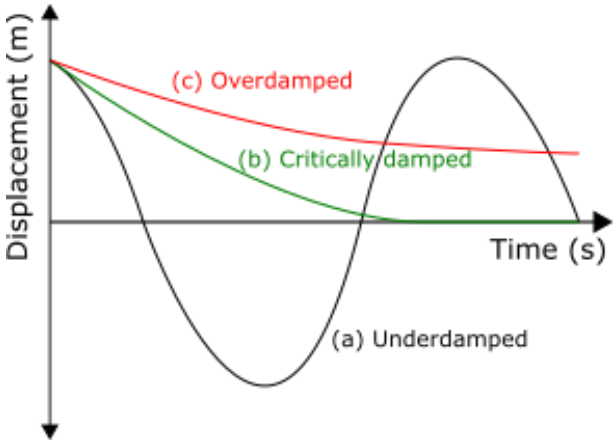

Fig. 1.4.5 Illustration of the 3 main damping definitions.

A method of simplify the damping performance of a system is the damping ratio, denoted by ζ which is defined as (1.15).

$$\zeta = \frac{C}{C_c} \tag{1.15}$$

where C is the actual damping, defined in (1.6), and C_c is the critical damping defined as (1.16).

$$C_c = 2M\omega_0 \tag{1.16}$$

M is the mass and ω_0 is the natural frequency defined in (1.12). The variations of ζ are:

- ζ=0, system is undamped.
- 0 < ζ < 1, system is underdamped, represented by (a) in Fig. 1.4.5.
- ζ = 1, system is critically damped, represented by (b) in Fig. 1.4.5.
- ζ > 1, system is overdamped, represented by (c) in Fig. 1.4.5.

For a simple system such as the mass-spring damper in Fig. 1.4.4 achieving a critically damped system involves tuning the system stiffness and mass density such that ζ = 1. This becomes more difficult as a system becomes more complex and non-homogeneous as more than one natural frequency can be exhibited.

1.4.5 Complex system mode shapes

As a system becomes more and more complex the vibration displacement at each natural frequency begin to form a pattern which is known as the mode shapes or eigenmodes. These shapes are a function of not only the material properties and the frequency, as discussed with the simple mass-spring damper system, but also the geometry of the system. For a cylindrical system, such as the stator, things get even more complicated as the curvature of the structure means that the 3 orthogonal directions (radial, axial, and tangential) are all coupled [JG06]. This means that for a complex system there could be an unlimited number of different modes across a wide frequency range. For this study, the interest is frequencies below 20kHz; this is the upper range of human hearing. Thus, vibrations in this band may create undesirable audible noise that can be clearly heard. Also, the higher the mode number the more complex the shape. Hence, the lower the deflection, the lower modes are of greater interest as the higher deflections are more likely to induce damaging forces into the rest of the system [SJY81].

There are 2 basic types of mode: rigid body and flexible modes.

- **Rigid body modes**: Translation or rotation of a structure without undergoing any significant deformation
- **Flexible modes**: The structure deforms into a series of patterns (modes) dependant on the natural frequencies of the structure. For cylindrical structures, the modes can split into 2 categories:
    - Circumferential modes (m): these are deflections in the X-Y plane of the shape
    - Axial modes (n): deflections in the axial (X-Z or Y-Z) plane of the shape

Each of these will be explored briefly in the following sub-sections.

1.4.5.1 Rigid body modes

A structure in free space (i.e., unconstrained) will have 6 degrees of freedom or rigid body modes at 0Hz. These are:

- Translation modes in the X, Y and Z directions (TX, TY, TZ).
- Rotational modes around the X, Y and Z axis (RX, RY, RZ).

When a force is applied to any of these modes an object would move or rotate according to Newton's 1st law with no deformation. Applying a constraint to the structure reduces the number of degrees of freedom accordingly. Depending on the type of constraint it is possible to have rigid body features that are above zero frequency. Fig. 1.4.6 gives an example of how an impulse force on a very stiff structure will cause the object to rock over a central position before coming to rest. This is assuming the force is not high enough to simply knock the structure over.

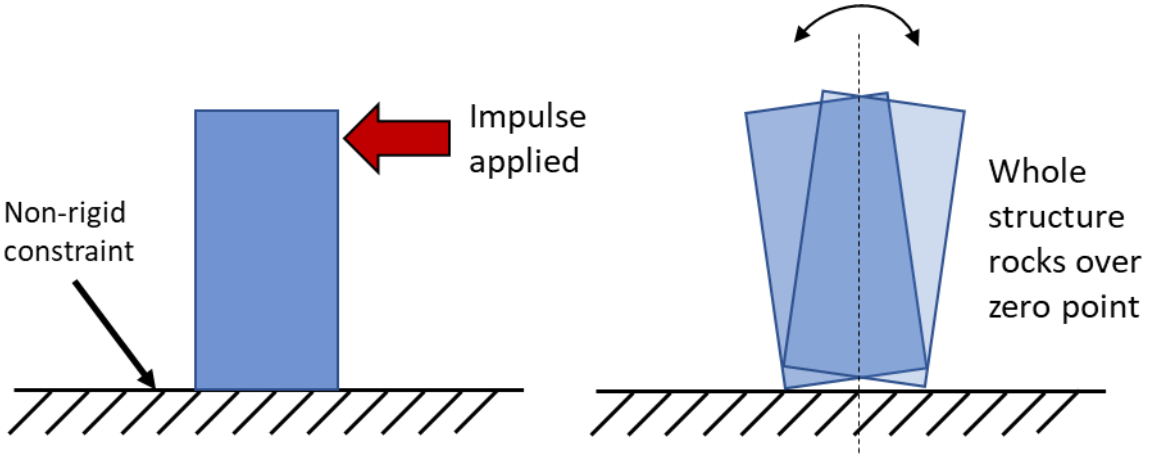

Fig. 1.4.6 Example of non-zero frequency rigid body mode.

In this case, whilst the structure may have experienced some small deformation there would be a very low frequency rigid mode reflecting the motion of the entire structure as it rocks over the zero point before coming to rest. Generally, rigid body modes are undesirable for modal testing as they introduce complexities and noise to the analysis [AT00], [OD88a]. A general rule of thumb is the highest rigid body frequency should be 1/10th that of the first flexible modes [AT00]. If this is found not to be the case, then the methodology of constraining the structure must be re-evaluated to attenuate the rigid body mode frequencies.

1.4.5.2 Flexible body modes: Circumferential modes

In an electric machine the magnetic forces per unit area can be generalised as (1.17) [JFG06]:

$$p_r(\alpha_d, t) = P_{mr}\cos(r\alpha_d - \omega_r t) \tag{1.17}$$

P_{mr} is the amplitude of magnetic pressure, t is the time, α_d is the angular distance from the origin of the coordinate system ω_r is the angular frequency and r = 1, 2, 3… and is the order of radial forces.

The amplitude of P_{mr} is dependent on the harmonics of the magnetic flux density that are participating in the generation of the pressure. These are [JG06]:

Excited by stator harmonics of the same number, w:

$$P_{mr} = \frac{B_{mw}^2}{4\mu_0} \tag{1.18}$$

Excited by the stator, w, and rotor, v, harmonics:

$$P_{mr} = \frac{B_{mv}B_{mw}}{4\mu_0} \tag{1.19}$$

Excited by the rotor, v, harmonics of the same number:

$$P_{mr} = \frac{B_{mv}^2}{4\mu_0} \tag{1.20}$$

Where w is the stator harmonic number, v is the rotor harmonics number, B_m is the peak magnetic flux density and μ_0 is the permeance of free space.

To obtain the amplitude of the radial force, F_{rad}, at a given order the calculated P_{mr} can be multiplied by the stator inner diameter and stack length (1.21) [JG06]:

$$F_{rad} = P_{mr}\pi D_{sb} L_{stk} \tag{1.21}$$

where F_{rad} is the radial force (N), D_{sb} is the inner diameter of the stator (m) and L_{stk} is the stack length (m).

Considering the circumferential deformation of the stator core the deflection, Δd, is an inverse function of the fourth power of the force order, r (1.22) [JFG06]

$$\Delta d \propto \frac{1}{r^4} \tag{1.22}$$

The mode shapes for circumferential modes m = 0 to m = 4 are described in Table 1.4.1 [SJY81], [JFG06]. For modes 5 onwards the shapes should be self-explanatory given the explanations of the first 4 modes.

Table 1.4.1. Description of circumferential modes 0 to 4.

Mode no	Image	Description
m = 0	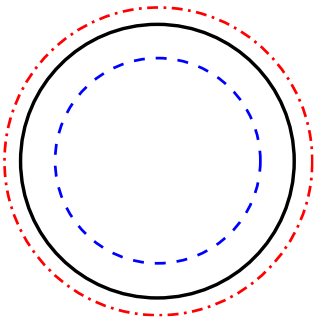	• Shape of part remains the same. • Diameter expands and retracts from a maximum (red) to a minimum (blue). • Sometimes called “breathing” or “pulsating” as the part moves between the maximum and minimum points.
m= 1	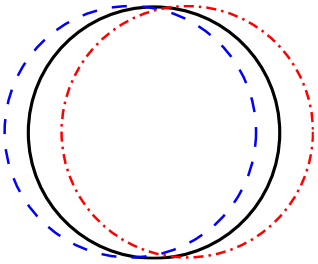	• Unity vibration mode. • Diameter remains constant. • Part “rocks” over a single point on the outer diameter. • Moves between a maximum (red) and a minimum (blue).
m=2	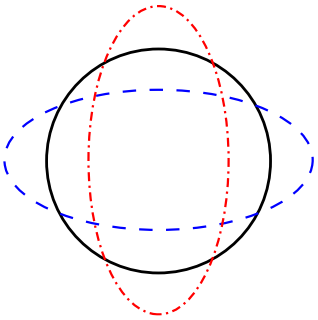	• Outer diameter distorts into oval shape with 2 maxima and 2 minima. • Cycles from the starting position (solid black line) to the 1st oval (blue line), back through starting position (black line), to the red line and back. • High level of deflection in this mode means it tends to dominate the spectrum [JFG06].
m=3	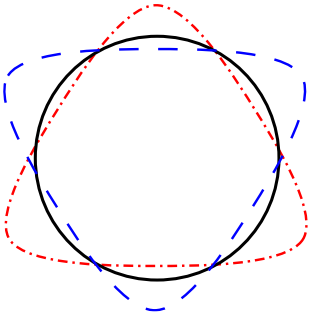	• OD distorts into a rounded triangular shape. • Like Mode 2 the part cycles from start (back) to blue to black to red and back to black. • Occurs at higher frequencies than the mode 2 but deflection is lower.

m=4	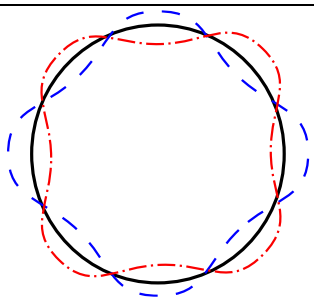	• OD distorts into quadrangle shape. • Again, occurs at higher frequencies (energy levels) than mode 3.

From the relationship between the force order in (1.22) shows that the lower modes should be avoided as much as possible with mode 2 being attributed with high levels of acoustic noise [SJY81].

1.4.5.3 Flexible body modes: axial modes

The axial modes can be described in a similar manner. Here, the cylindrical shape is shown as a section in the Y-Z (or X-Z) plane. In the examples in the following sections, we can consider this using 2D or 3D models. Like the circumferential modes the red dashed lines represent the maxima of the displacement and the blue line represents the minima.

Table 1.4.2 Description of axial modes 0 to 4.

Mode.	Image	Description
n = 0		• Top and bottom edges remain parallel. • Edges move apart and towards each other. • "Pulsating" or "Breathing" mode, like circumferential mode.
n = 1	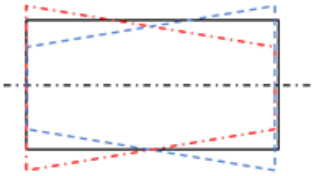	• Shape becomes trapezoidal. • Diameters of the cylinder ends shrink whilst opposite end grows. • Shape oscillates between a maximum (red) and a minimum (blue).
n = 2	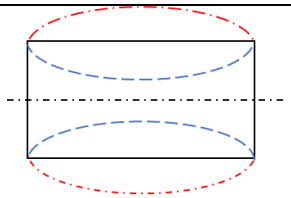	• Upper and lower edges curve outwards and inwards. • Shape resembles ½ wave or a single peak. • High levels of deflection.
n = 3	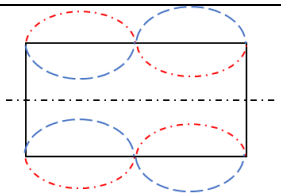	• Full wave now shown on upper and lower edges.
n =4	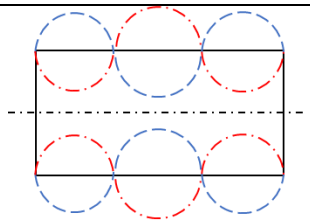	• Pattern repeats 3 times.

Mode 0 provides a uniform displacement along the axial length creating the largest surface area with which to displace the surrounding materials [SJY81], [JG06]. In terms of high noise, the literature indicates axial mode 0 and circumferential modes 0 to 4 are the modes with the highest influence on the noise and vibratory performance of the machine.

1.4.6 Frequency response function

An efficient means of the modelling the response of a system is a frequency domain model where the output spectrum measured by the chosen transducer is proportional to the input spectrum multiplied by a system descriptor [OD88a] called the Frequency Response Function (FRF). The functionality is highlighted in Fig. 1.4.5 [OD88a].

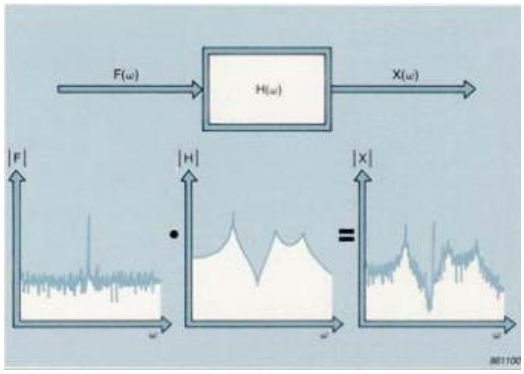

Fig. 1.4.5 Illustration of the frequency response function [OD88a].

The relationship shown in Fig. 1.4.5 can be shown as (1.27) [OD88a].

$$H(\omega) \equiv \frac{X(\omega)}{F(\omega)} \tag{1.23}$$

where H(ω) is the frequency response function (FRF) and is the complex ratio between the output spectrum X(ω) the input spectrum F(ω). F(ω) is the input excitation force whereas X(ω) is the motion of the structure and can represent the displacement, velocity or acceleration, dependant on what transducer is being used during measurement. The fact that the FRF is a complex function indicates it has a magnitude |H(ω)| and phase ∡H(ω) = ϕ(ω). What this implies is that given a sinusoidal input force at frequency ω, an output will occur at the same frequency with an amplitude dictated by |H(ω)| and a phase offset of ∡H(ω) between the output and input. When dealing with linear systems the input/output spectrum can be considered as a summation of sinusoids [OD88a], [AT00].

Given the definition of the FRF above a system can be measured by exciting the structure at specific frequencies or simultaneously at a wide bandwidth. Unless the natural frequencies are known at the start the most useful method is to excite the structure with a wide band of frequencies and identify the modes presented. The wide band excitation technique is utilised in this section of the study.

The defined frequency response is a function of the chosen output parameter. The frequency response function therefore tends to fall into one of 3 categories [OD88a]:

- Compliance, how far the part deflects with a given input excitation.
    - X(ω) = displacement, typically in meters (m).
    - Resultant function, H(ω), units are meters per Newton (m/N).
- Mobility, how fast the structure moves with a given input excitation.
    - X(ω) = Velocity, typically in meters per second (ms^{-1}).
    - Resultant function, H(ω), units are ms^{-1}/N.
- Accelerance, how rapidly the structure accelerates with a given input excitation.
    - X(ω) = Acceleration, given in g or meters per second per second (ms^{-2}).
    - Resultant function, H(ω), units are typically g/N or ms^{-2}/N.

All three categories are algebraically related. Thus, measuring any one of the above categories allows any of the others to be calculated [OD88a].

1.5 A review of noise and vibration sources in electric machines

The mechanisms described thus far in the generation of vibration by an electric machine and the wider impact on the surrounding environment are by no means new. These factors have existed in machine design since the earliest days of the technology emerging in the mid-1800's. It is of little surprise therefore to find there is very large amount of literature on the subject with a large number of different studies on the root cause of noise and vibration; some provide a high-level review such as [PV98] or [TMJ96] but a larger number of the papers found look into the different sources as a means of optimising a given machine design [LSH09], [MC14], [MB14]. From all the gathered data the general consensus is that there are 4 primary sources for the generation of noise and vibration in electric machines [PV98]:

- **Magnetic sources**: vibration sources due to the interaction of the magnetic field generated by the coils/PMs with the structure of the machine, in particular due to the geometry of the air gap.
- **Mechanical sources**: vibration sources due to the physical structure and materials of the machine.
- **Aerodynamic sources:** vibration sources generated by the rotating parts disturbing the air surrounding the components.
- **Electronic sources**: vibration sources due to the switching of the power electronics or non-linear nature of the drive signal.

Using the literature, a summary of the key sources can be derived and expanded upon to understand the lower-level mechanisms beneath each source. A mind map of the key sources is shown in Fig. 1.5.1. Using the map of the different sources will be looked at in turn to allow an understanding of what the different mechanisms are and what influence they have on the noise and vibration generated within a machine.

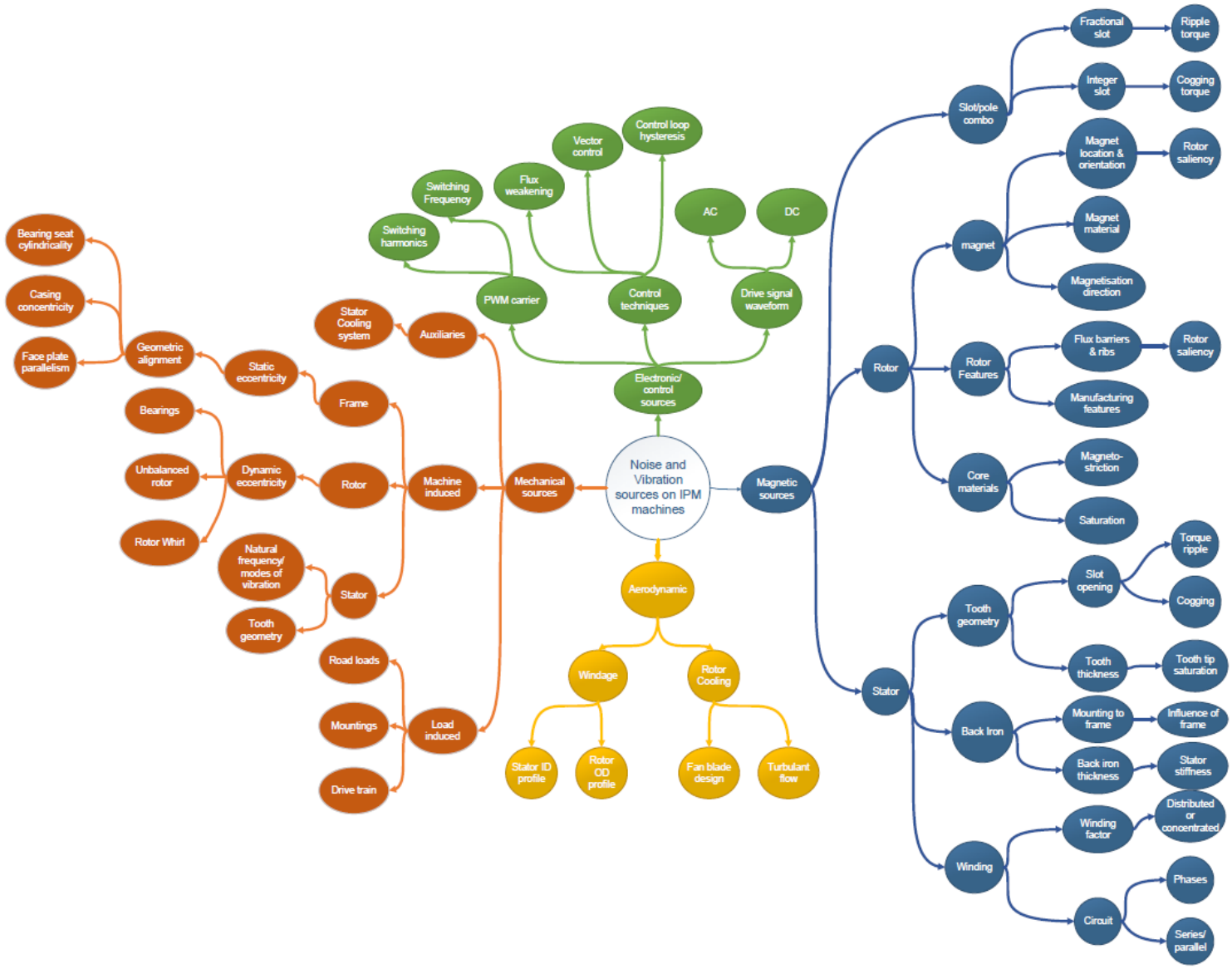

Fig. 1.5.1 Overview of key sources of noise and vibration in electric machines.

Some of the literature goes a little deeper and looks to understand where in the noise bandwidth the different mechanisms lie allowing both optimisation of the design of specific areas or fault diagnosis to occur. Fig. 1.5.2 below highlights one such approach [LSH09], [MC14].

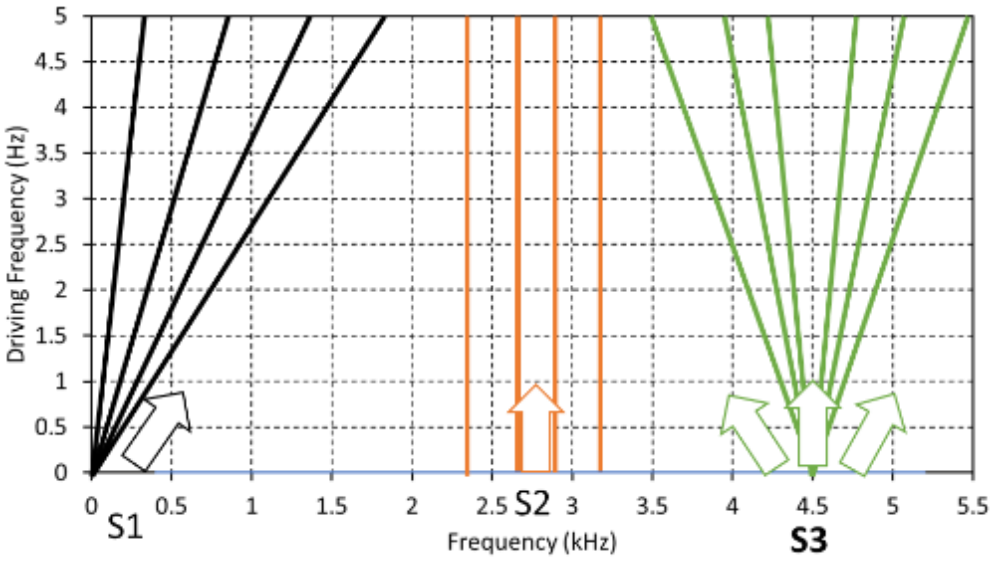

Fig. 1.5.2 Noise spectra of different vibration mechanisms.

From Fig. 1.5.2, 3 noise bands can be seen [LSH09, [MC14]]:

- S1: This moves **proportionally** to the driving frequency and as such is an effect of commutation (phase current switching). This is the **MAGNETIC** response.
- S2: This is **fixed** and is an effect of **structural resonance**. This is the **MECHANICAL** response.
    - Exceptions to this rule are bearing noise and dynamic eccentricities which increase proportionally to the rotor frequency [PV98], [MC14].
- S3: This spreads as the drive frequency increases and is the result of the PWM frequency. This is the **ELECTRONIC** response.

Having built a high-level image of how each source contributes to the overall noise spectra a more detailed study of each source can be undertaken, starting with the electromagnetic sources.

1.5.1 Electromagnetic sources

Fig. 1.5.3 gives a high-level overview of the different magnetic sources of noise.

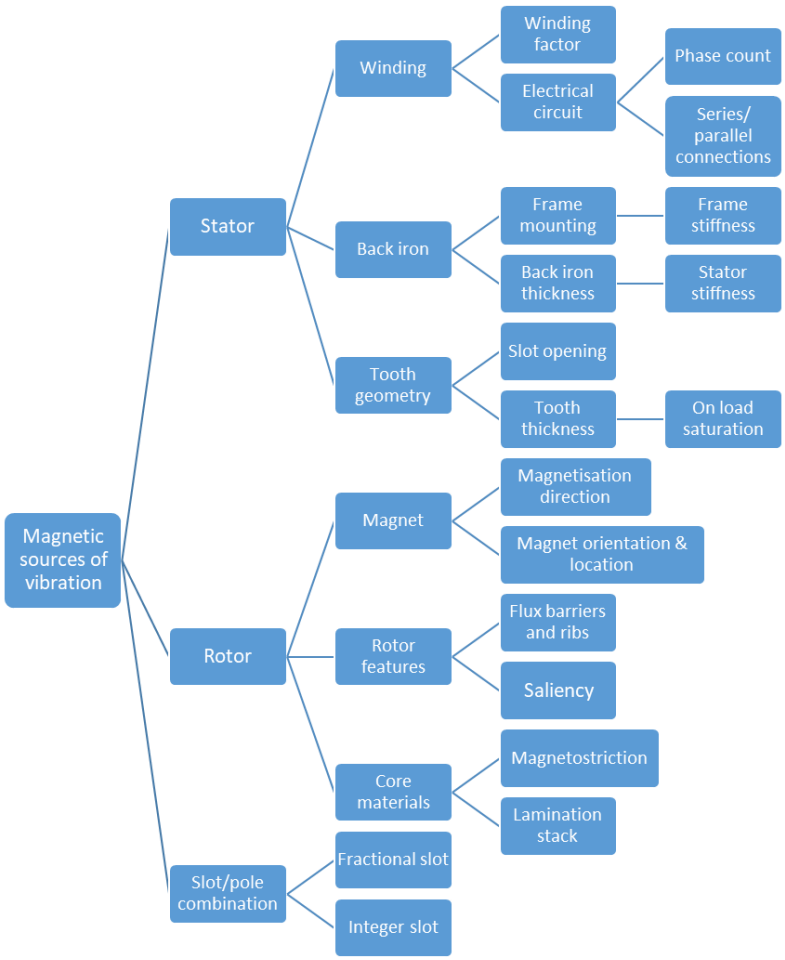

Fig. 1.5.3 Overview of magnetic sources of noise in electric machines

Fundamentally the noise and vibration from electromagnetic sources is caused by the magnetic flux density waves in the air gap interacting with the rotor and the stator. How these waves are established varies for a number of reasons. However, machine designers tend to combine the different processes into specific categories. [TMJ96] provides a good definition for torque pulsations:

1) **Cogging Torque**: Pulsating torque components generated by the interaction of the rotor magnetic flux and angular variations in the stator magnetic reluctance. By definition, no stator excitation is involved in cogging torque production.
2) **Ripple Torque**: Pulsating torque components generated by the interaction of stator current magnetomotive forces (MMFs) and rotor electromagnetic properties, which can take two forms:
    a. Mutual or Alignment Torque: resulting from the interaction of the current MMFs with the rotor magnet flux distribution.
    b. Reluctance Torque: resulting from the interaction of the current MMFs with the angular variation in the rotor magnetic reluctance.
3) **Pulsating Torque**: the sum of the cogging and ripple torque components.

There is a further component called unbalanced magnetic force (UMF), sometimes called unbalanced magnetic pull (UMP). This is where the magnetic forces acting diametrically across the rotor are not balanced. There are two primary sources of UMF:

- Rotor eccentricity: [ZQZ14] static or dynamic eccentricity means that the air gap is non-uniform so one part of the rotor is closer to the stator teeth than another, given it is a square law that dictates the force the influence of the eccentricity can greatly multiply the radial forces acting on the rotor and stator resulting in high levels of vibration.
- Diametric asymmetric poles/windings: [DI05] fractional slot machines where the slot number, N_s, and the pole number 2p differ by one, i.e., 2p = ± 1, may have asymmetry across the rotor resulting in UMP and the associated concerns.

1.5.1.1 Slot/pole number combination

The discussions into electric machine designs thus far has highlighted that there are a bewildering number of different machine topologies available in all manner of possible arrangements. How to choose which arrangement is the best is one of the big challenges of machine design.

One of the fundamental aspects of any electric machine aspect is the relationship between the slot/pole numbers, defined as (1.24) [DH12]:

$$N_{spp} = \frac{N_s}{N_p N_{ph}} \tag{1.24}$$

where Nspp = number of slots per pole per phase, Ns = number of slots, Np = number of poles, Nph = number of phases.

If N_{spp} is an integer, then the machine is described as an integer slot. If N_{spp} is a non-integer, then the machine is described as a fractional slot. Care should be taken with the definitions as it can be easy to confuse fractional slot and fractional pitch windings, the former characterises the stator slots whilst the later characterises the windings. Fig. 1.5.4 shows 2 SPM machines, a 12S4P (N_{spp} = 1) and a 15S4P (N_{spp} = 1.25) to illustrate the differences.

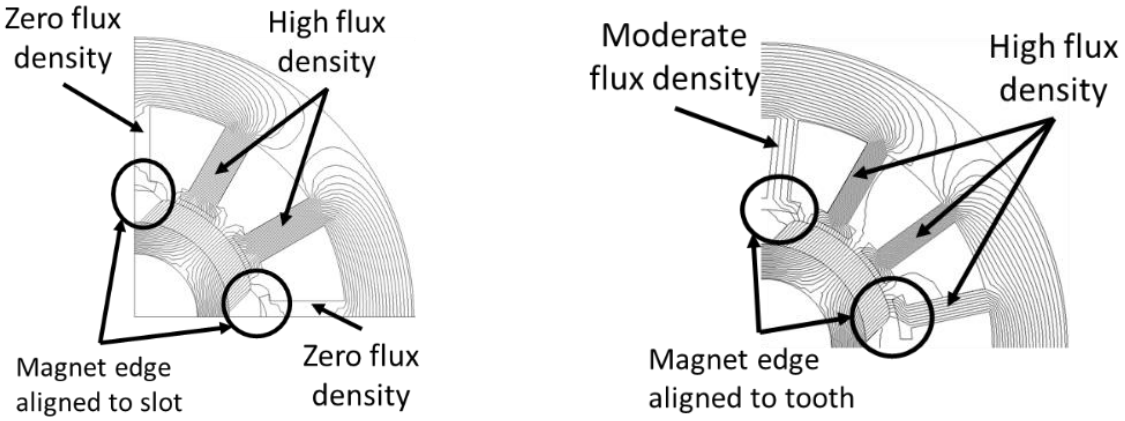

(a) 12S4P integer slot PM flux distribution (b)15S4P, Fractional slot PM flux distribution

Fig 1.5.4 Comparison of static PM flux distributions in an integer and fractional slot SPM machine.

It can be seen in Fig. 1.5.4(a) that there is symmetry between the teeth and the poles in the stator as each magnet has the same relative position with respect the stator slots giving an additive effect to the cogging [CB00], [JRH10]. For the fractional slot, the relationship is less symmetrical as the teeth and the magnet poles align differently according to the rotor pole, meaning the additive effect is reduced. The cost of this advantage in cogging torque is increased air gap harmonics and a lower winding factor which means a lower maximum torque than an integer slot machine which can obtain winding factors of 1 [JRH10], [RI09].

A more detailed analysis of different slot/pole number combinations is found in [RI09] which introduces a classification system for different slot/pole combinations which can be expanded upon using [JRH10], [DH12], [GJL16], [YSC06], and [ZQZ00] to understand the effect each slot/pole combination has on the UMF and cogging torque. The summary is shown in Table 1.5.1. Note ripple torques are omitted from this as these are strongly influenced by the winding arrangement which can vary between machines of the same slot/pole number.

Table 1.5.1 Classifications of slot/pole number combination and influence on UMF and cogging torque [RI09]

Classification	Definition	Example (Slot/Pole)	UMF	Cogging
Type I	Diametric asymmetric disposition of slot and pole number combinations	3S2P, 3S4P, 9S8P, 9S10P, 15S14P, 15S16P	HIGH	LOW
Type II	Modular machines, same phase windings in diametrically opposite slots	6S8P, 12S10P, 12S14P	LOW	HIGH
Type III	Non-modular machines, symmetrical windings	9S6P, 12S8P, 15S10P, 27S6P, 18S12P	LOW	LOW

In the ideal case, motor types in type II and type III should not have any unbalanced radial force on the stator [RI09].

[HYID13] provides a general rule of thumb for deriving the slot/pole number combination:

- **Fundamental winding factor** – Higher winding factor results in higher torque.
- **Lowest Common Multiple (LCM)** - between number of stator slots and number of rotor poles. A larger LCM value implies lower cogging torque.
- **Greatest Common Divisor (GCD)** - between number of stator slots and number of rotor poles. GCD is an indicator of the forcing function shape of tooth force corresponding to the fundamental order.
    - A high GCD leads to a shape favourable to be excited at higher frequencies, thus the greater the GCD the lower the noise and vibration due to the modal frequency being pushed outside the bandwidth of the machine [HYID13].

[ZQZ00] developed a useful formula (1.25) to assist in choosing the slot/pole number combination that provides the designer with a "goodness" value, C_T, for minimising the cogging torque.

$$C_T = \frac{N_p N_s}{N_C} \tag{1.25}$$

where N_p = number of poles, N_s is the slot number and N_c is the lowest common multiple between the slot number (N_s) and the pole count (N_p).

The higher the "goodness" value (1.29), the higher the cogging torque [ZQZ00]. It is important to note that C_T does not denote a torque value, rather indicates which slot/pole number selection will have the highest-level cogging torque. Although this gives a good method of predicting the severity of the cogging torque in machine it does not account for the other key vibration sources such as ripple or UMP.

[YSC06] developed a method of calculating the vibration frequency in a 12S10P fractional slot machine. The paper determined the dominant vibration frequency is of these machines is (1.26).

$$f_d = N_p f_m \tag{1.26}$$

Where f_d is the dominant vibration frequency, N_p is the number of poles and f_m is the mechanical frequency of the rotor. The paper also concludes that the most important vibration order is dependent on the slot/pole number combination, e.g. [YSC06]:

1. In three phase motors having 3 slots per pole, the vibration mode order is equal to the pole number
2. In motors having 1.5 slots per pole, the vibration mode order is equal to the pole-pair number.
3. In motors in which the slot number and the pole number differ by 2, the vibration mode order is 2.
4. In motors in which the slot number and the pole number differ by 1, the vibration mode order is 1.

The conclusions in [YSC06] and [RI09] are reinforced in [DI05] where the force components for the UMP are analytically derived using the Maxwell stress tensor and compared using finite element results. The results of the 9S8P machine can be seen in Fig. 1.5.5 [DI05].

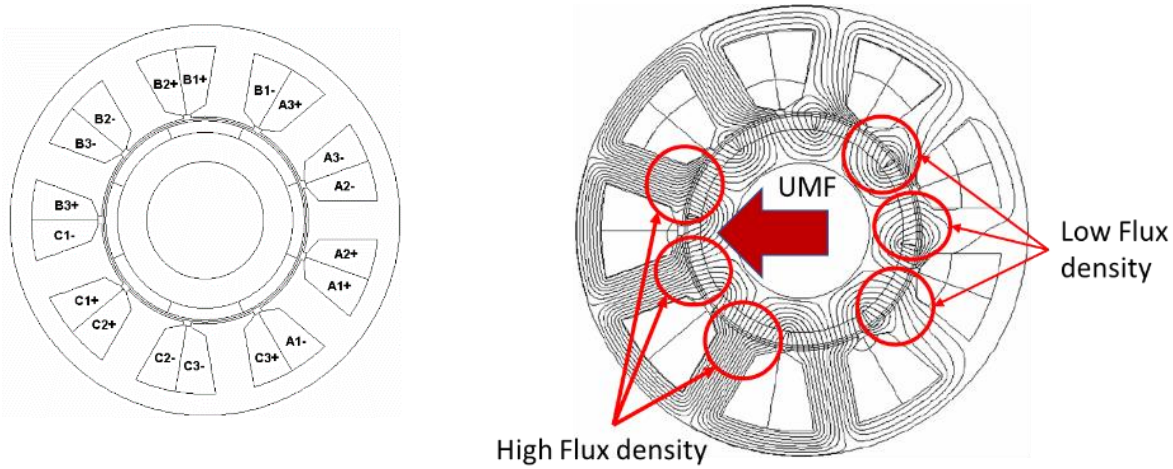

(a) 9S8P winding arrangement (b) 9S8P resultant field distribution (on load)

Fig. 1.5.5 Flux distribution of 9S8P under load [DI05].

It can be seen from Fig. 1.5.5 that the on-load flux distribution in the 9S8P machine is non-uniform meaning there is an asymmetry of flux density in the air gap. Given the Maxwell stress tensor for radial forces (1.4) this flux imbalance means a high unbalanced magnetic force will be experienced. [DI05] shows the amplitude of the UMF is linearly proportional to the input current to the armature windings, which is logical given the higher current means higher MMF and consequently higher flux densities. This linearity is only observed to a point; at higher loads, the core materials begin to saturate changing the magnetic circuit reluctance and therefore the flux distribution.

[HSK04] provides a detailed investigation into the different torque pulsation components of a 12S4P IPM and SPM BLDC machine. The paper draws the following important conclusions to the frequency characteristics of the electromagnetic sources in IPM motors [HSK04].

1. **Cogging torque**: lowest common multiple of numbers of slots and poles times the rotor frequency (f_m) and its higher harmonics.
2. **Ripples of mutual and reluctance torque**: $6f_m$ and higher harmonics.
3. **Fluctuations of radial attractive force**: number of poles times f_m and its higher harmonics.

These rules of thumb are key to characterising the vibratory performance and as can be seen, the slot/pole number combination lies at the heart of it.

1.5.1.2 Stator slot openings

The stator slot opening is the gap that separates the tooth tips from each other and allow access to the main slot region from the inner bore of the stator structure (assuming interior rotor). These slots serve 2 important purposes:

1. Allow insertion of the windings into the stator slots during assembly.
2. Prevent flux short circuiting between the stator teeth, either from the stator armature or flux from the rotor.

The concern with the slot opening is the relative permeance of the slot, μ_r, is 1. Thus, any flux aligned with the slot trying to bridge the air gap will deflect and bend to try and reach the high relative permeance of the laminated magnetic steel that forms the tooth, the flux deflecting in this manner is collectively called fringing [JRH10]. This variation in permeance is a prime contributor towards:

- **Cogging torque**: The rotor PM flux bridging the air gap will tend to prefer the relatively low reluctance of the tooth tip to rotor air gap than the much higher reluctance of the slot region and resist being moved away from the resting point.
- **Ripple torque**: as the rotor spins in the changes in permeance create high frequency pulses, at the frequency determined in (1.27) [HSK04].

$$f_{rip} = n_h N_s f_m \quad (1.27)$$

where f_{rip} is the ripple frequency, N_s is the slot number, f_m is the rotor frequency and n_h is the harmonic order.

Fig. 1.5.6 illustrates the flux lines around a tooth in (a) stationary no load and (b) maximum load.

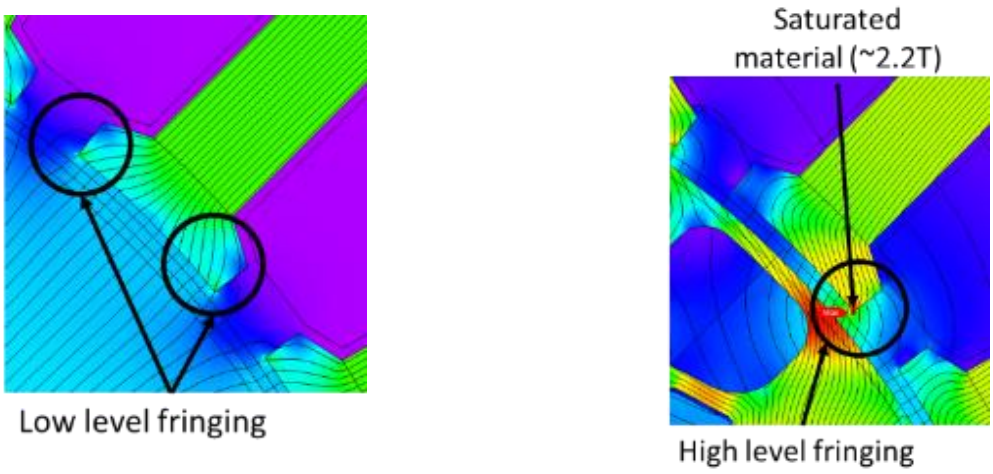

(a) No load (b) Full load

Fig 1.5.6 Influence of fringing on tooth due to slot gap under no load and full load conditions.

The tooth under full load (Fig. 1.5.6b)) has to handle both the flux on the main flux path and the flux density on the edge of the tooth from the fringing which saturates the tooth material. In terms of the magnetic circuit this effectively expands the slot opening distance, exacerbating the concerns with variations in permeance.

Accounting for the slotting effect is a challenging task due to the non-linearities involved. Traditionally machine designers attempt to simplify these challenges by calculating the effective air gap in an attempt to compensate for the slotting effect, for example (1.28) for an SPM machine [JRH10].

$$g' = K_c g + \frac{L_m}{\mu_{rec}} \quad (1.28)$$

where g' is the effective air gap, g is the mechanical air gap length (stator bore to rotor OD), L_m is the magnet length (in direction of magnetisation), and μ_{rec} is the relative recoil permeability. K_c in (1.28) is the Carter's coefficient, which in its most basic form is a function of the ratio of the slot opening width and the air gap width. It has numerous derivations [DH12], [JRH10], [JFG06], [CGV70] according to the machine type (e.g. induction or PM [JFG06]), position of the rotor to the stator (axial, radial interior or exterior) as well as the stator tooth designs. Other work such as Freeman's method [EMF62] or Zhu [ZQZ93] provide more accurate methods by expanding the variables attributed to the phenomena. These analytical methods are very useful for the initial calculations required to establish the magnetic circuit but the non-linearities created by the tooth saturation and the fact that the system permeance is affected by aspects such as core temperature and the B-H properties of the material means that finite element methods tend offer the more accurate means of predicting the performance. Using the FE tool of course comes at a price; expensive and complex FE software and powerful computers to handle the volume of computation required.

The effect of the slot opening distance on the cogging torque is investigated for different slot/pole combinations of IPM machines by [ZQZ00], the results are in fig 1.5.7.

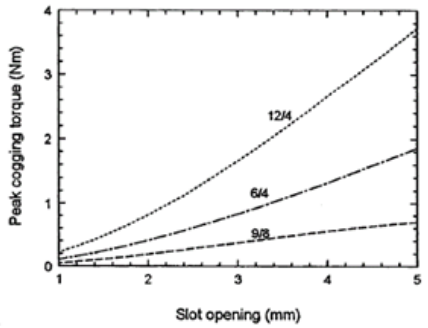

Fig. 1.5.7 Influence of slot opening distance on cogging torque with different slot/pole number combinations [ZQZ00]

It can be seen, perhaps unsurprisingly, that there is a direct correlation between the size of the slot openings and the cogging torque. The role of the slot/pole number combination is again highlighted with the integer slot machine (12/4) having a much higher cogging torque than the fractional slot machines. Compensating for the slotting effect in the design is difficult to countermeasure as that there still needs to be some slot opening in order to allow the windings to be inserted and prevent short circuit flux paths. However, some methodologies are covered later in this chapter.

1.5.1.3 Winding distribution

The winding distribution is intrinsically linked to the slot/pole number combination of the machine as well as the number of phases, which for this study is assumed to be 3 [JRH10], [DH12]. [YH97], [TN14]. These aspects dictate the basic requirements for the winding. However, machine designers over time have developed a large variety of different winding methods to maximise the performance of the machine beyond the simple distributed and concentrated definitions provided earlier. The measure of the flux linkage between a coil and the magnet is known as the winding factor and is the product of the coil span factor and the distribution factor of the stator [JRH10].

- Coil span factor (K_{sp}): electrical angle of the arc covered by each coil. The fundamental coil span factor can be calculated as follows (1.29) [JRH10]:

$$K_{sp} = sin\left(\frac{\alpha_{cp}}{2}\right) \tag{1.29}$$

where α_{cp} is the coil pitch in electrical degrees, defined as:

$$\alpha_{cp} = \frac{N_p 180^{\circ}}{N_s} \tag{1.30}$$

where N_p = number of poles and N_s = number of slots

- Distribution factor (k_d): dictates the spread of the flux from the coil. On a distributed wound machine this should be unity as the coil span = pole span. Can be calculated as (1.31) [DH12]:

$$K_d = \frac{sin\left[\frac{N_{spp}\alpha_{cp}}{2}\right]}{N_{spp} \cdot sin\left(\frac{\alpha_{cp}}{2}\right)} \quad (1.31)$$

where N_{spp} = number of slots per pole per phase.

The final winding factor (K_w) is then (1.36) [DH12]:

$$K_w = K_{sp}K_d \quad (1.32)$$

A winding factor of 1 means 100% linkage of all the flux between the coil and magnets, less than one means the flux linkage is lower and therefore the torque is lower [JRH10], [DH12], [FM03]. Using eqns. (1.29) to (1.32) the maximum winding factor for a number of different slot pole combinations with dual layer windings can be calculated [FM03], [EM20].

Table 1.5.2 Maximum winding factor for dual layer wound machines with different slot pole number combinations [EM20]

Slots \ Poles	2	4	6	8	10	12	14
3	0.866			0.866	0.866		0.866
6	1	0.866		0.866	0.5		0.5
9	0.945	0.617	0.866	0.945	0.945	0.866	0.617
12	0.966	1		0.866	0.966		0.966
15	0.951	0.951		0.711	0.866		0.951
18	0.96	0.945	1	0.617	0.735	0.866	0.902
21	0.953	0.953		0.538	0.65		0.866

From Table 1.5.2 it can be seen there is a colour coding system which indicates the winding type according to the slot/pole number combination:

- **Black**: Unbalanced winding, winding arrangement is unable to produce a balanced rotating field.
- **Orange**: Integer slot winding, number of slots/pole/phase is an integer.
- **Blue**: Fractional slot winding, number of slots/pole/phase is fractional and greater than 1.
- **Green**: Concentrated winding, number of slots/pole/phase is fractional and strictly less than 1.

The difference between fractional slot wound and concentrated wound is tricky as technically both are fractional slot.

- Concentrated winding typically referred to distributed winding.
- Fractional slot refers to integer slot.
- Both concentrated and distributed windings can be employed in fractional slot machines, but it is more common to employ concentrated winding, particularly tooth wound coils for fractional slot PM machines.

As previously highlighted the integer slot, distributed wound machine is the method favoured for traction applications [YH97], the high winding factor means average torque is high and it allows for good utilisation of the reluctance torque component. The draw backs due to copper loss, packaging and winding insertion issues with the end windings as well as high cogging torque inherent in the integer slot winding mean effort

is being placed into fractional slot windings [DI05], [DI06], [ZQZ07a], [YH97]. [FM07], [FM03]. With a high enough slot/pole number combination it is possible for a fractional slot machine to show similar performance [ZQZ07b]. However, there are knock on effects at a system level; more poles mean the number of electrical cycles per mechanical cycle has to increase which means the inverter has to switch at a higher frequency to achieve a given speeds and of course the impact on iron losses due to higher electrical frequency.

The primary concern with fractional slot wound machines from a vibratory standpoint is, aside from the risk of UMF on certain slot/pole number arrangements [DI05], [ZQZ07a], is the rich MMF harmonics which the winding arrangement can produce. A good illustration of the difference is shown in Fig. 1.5.8 [JZ18] where a 72 slot, 12 pole distributed wound machine is compared with an 18 slot 12 pole single layer concentrated wound machine of the same key specifications (torque, speed, power, stack length and stator outer diameter).

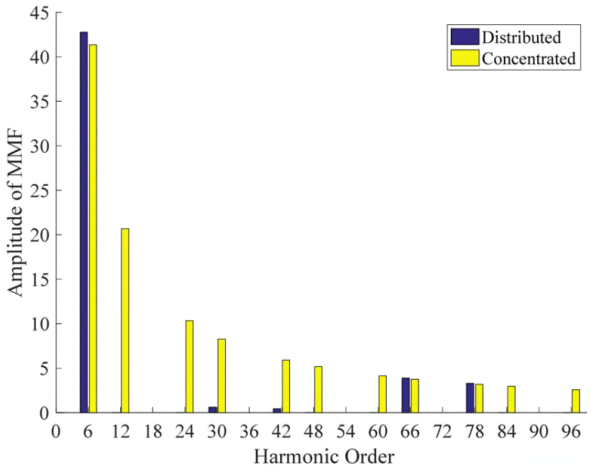

Fig 1.5.8 Comparison of the MMF harmonics in the distributed wound and concentrated wound machines [JZ18]

The contrast in spectral content of the MMF is stark between the distributed wound machine, shown as blue bars in Fig 1.5.8, and the single layer concentrated wound machine (yellow bars in Fig 1.5.8). These harmonics increase iron losses and contribute to the ripple torque having implications on the vibratory tooth forces. Within each of these categories lies a large variety of different winding methods, a detailed list of which is covered in the vibration mitigation section of this chapter.

1.5.1.4 Influence of rotor topology

The layout of the magnets in the rotor core dictates the flux density distribution across the air gap and the linkage with the coils in the stator, much like the winding layouts detailed previously. The key differences are:

- The layout of the magnets is only constrained by the pole arc (dictated by the selected number of poles) and not constrained by the slot geometry like the armature coils.
- The PM flux is DC and constant, it cannot vary like the armature coils.

- The PM material is typically sintered and mechanically weak requiring a careful balance between adding strengthening features and the level of flux leakage [ECL04], especially for high-speed design.

One metric for describing the PM distribution in the rotor is the pole arc to pole pitch ratio which is illustrated in Fig. 1.5.10 (a). [ZQZ00], [ZQZ03] detail how the pole-arc to pole pitch ratio can influence the cogging torque with the resultant cogging torque vs. pole-arc to pole pitch ratio shown in Fig. 1.5.10(b).

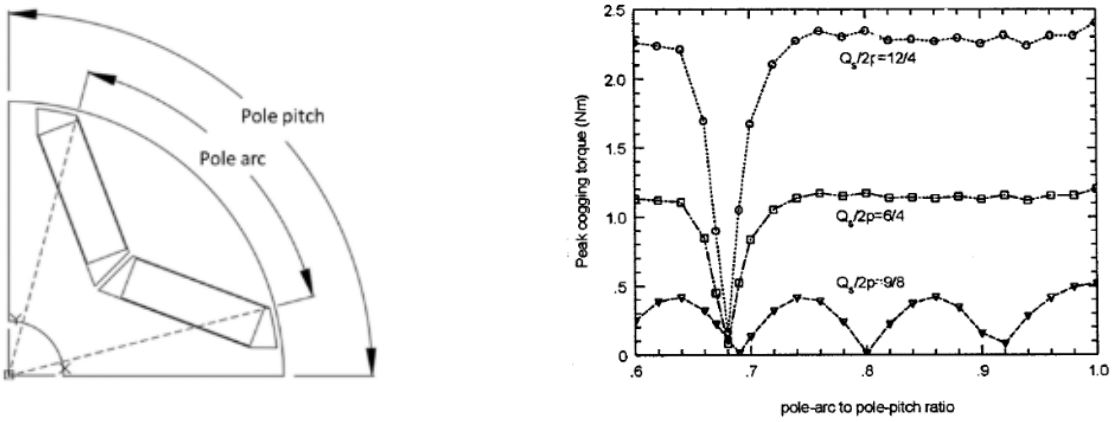

(a) Definition of pole pitch and pole arc

(b) Influence of pole pitch to pole arc ratio on cogging [ZQZ00]

Fig. 1.5.10 Effect of pole-arc to pole-pitch ratio with different slot/pole number combinations on cogging waveforms [ZQZ00].

Using the trends set out in Fig. 1.5.10(b) [ZQZ00] provides a formula that obtains the optimal pole arc to pole pitch ratio to minimise the fundamental component of the cogging torque (1.33) [ZQZ00].

$$\alpha_p = \frac{(N_\alpha - 1)}{N_\alpha} + k_{fr} \tag{1.33}$$

where: k_{fr} is an offset to account for fringing and ranges from 0.01 to 0.03 depending on the air gap and N_α is given in (1.34)

$$N_\alpha = \frac{N_c}{N_p} \tag{1.34}$$

where N_c is the LCM between the slot number and the pole number, N_p.

k_2 in (1.34) is used to account for the fringing effect on the stator tooth and is dependent on the airgap length [ZQZ00].

Earlier in the chapter it was explained that the primary difference between an IPM machine and an SPM machine is the saliency of the IPM machine allows for the use of the reluctance torque component. The influence of the saliency on the radial force distribution of the machine is well illustrated in Fig. 1.5.11 [TJK10] which compares an SPM and IPM machines of the same dimensions and slot/pole number combination (24S4P).

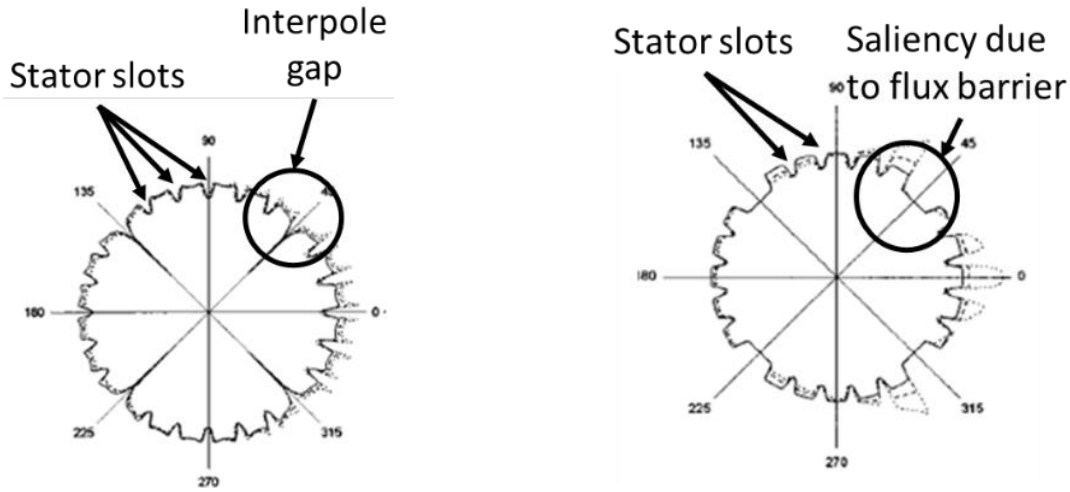

(a) SPM radial force profile (b) IPM force profile

Fig. 1.5.11 Radial force density comparison between IPM and SPM machines [TJK01].

The force density plot in Fig. 1.5.11 clearly illustrates some of the key differences between the two magnet arrangements:

- Common to both arrangements is the effect of slotting; both the pole count and slot count can be observed from the radial force profiles in Fig. 1.5.11 (a) and (b).
- The effects of saliency on the IPM machine can be clearly seen by the “notches” on the pole q-axis, starting at 45°from the x-axis and repeating in 45° steps, lining up with the flux barriers of the IPM machine in (a).
- The SPM is much smoother, and however, the effect of the inter-pole magnet can be observed on the q-axis of each pole (again these are in 45° steps starting at 45° from the x-axis)

In addition to the concerns with ripple torque IPM machines have also been shown to suffer higher unbalanced forces when subject to eccentricities [TJK01], [KTK01]. Fig 1.5.12 highlights this factor.

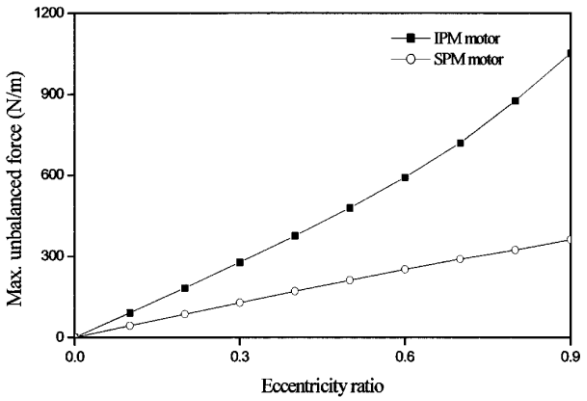

Fig 1.5.12 Effects of rotor eccentricity on UMF of IPM vs. SPM [TKJ01].

[TKJ01] notes that not only are the unbalance forces on the IPM machine significantly higher, but the effect is non-linear as the eccentricity increases, reflecting the fact high levels of saturation on the teeth due to the reduced air gap which acts to further amplify the UMF. The conclusion is therefore that IPM machines are significantly more sensitive to UMF due to eccentricities than a similar SPM machine [TKJ01], [KTK01].

In a similar manner to the windings, the rotor can have multiple layers of magnets in a variety of different arrangements. These multi-layered machines offer a boost to the reluctance component due to the increased saliency as well as the ability to achieve a more sinusoidal air gap flux density. The price of this, aside from the obvious structural complexities, is increased cogging torque [YH98]. The larger saliency means higher risk of torque ripple due to variations in d- and q-axis inductances [YH97], [EA15]. Analysis by [YH97] shows that the 2 layers provides the most effective boost for the q-axis inductance; 3 or more does increase the saliency but the gains are much lower than the step from single layer to 2 layers. Increased numbers of layers and careful shaping of the magnet slots means the machine begins to resemble a synchronous reluctance machine instead of an IPM machine. Indeed, there is much research into so-called permanent magnet assisted synchronous reluctance machines (PMaSynRM) that look to utilise this feature using low-cost magnets to counter the poor power factor that limits the application of synchronous reluctance machines [FC15], [YHJ12], [KR13].

1.5.2 Power electronic and control sources

The power electronics provide the critical role of converting the DC voltage from the battery in the vehicle into an AC waveform.

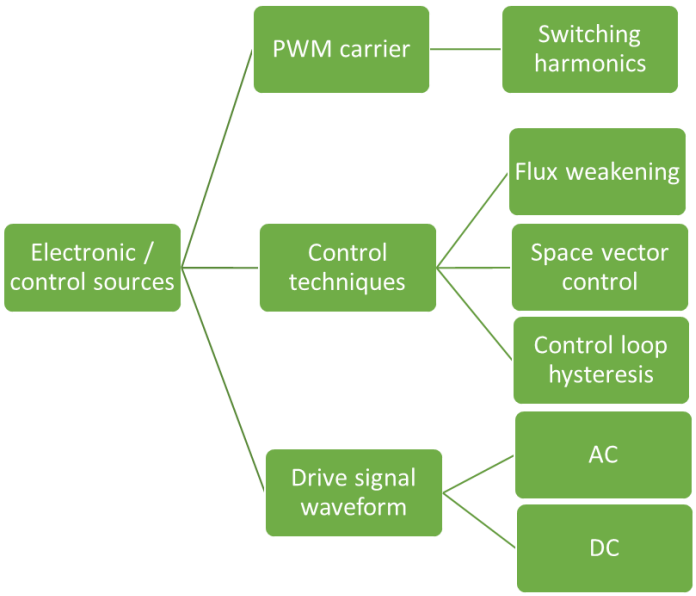

Fig. 1.5.13 Electronic and control sources of noise in electric machines.

1.5.2.1 Drive signal waveform, AC vs DC

As previously discussed, the drive waveforms tend to fall into AC (sinusoidal) or DC (trapezoidal). The effect is studied in much of the literature [TMJ96], [JRH10], [DH12], [ZQZ06], [YFS06] and the differences are best summarised in Fig. 1.5.14 [YH09].

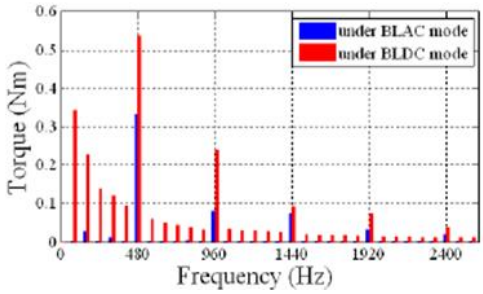

Fig. 1.5.14 Torque harmonics of 8-pole 12-slot machine at 1200rpm (480Hz electrical) [YH09].

The rich harmonic content is of course a well understood phenomenon, but as has previously been seen the difference in operating in AC and DC mode becomes complicated by the slot/pole number combination and winding methodology [JRH10], [DI06], [DH12], [ZQZ07a].

1.5.2.2 PWM carrier signal

The concern with the PWM signal lies with the carrier signal switching frequency [TGH91], [SLC03]. The switching frequency typically sits within the audio range of humans, typically between 3 kHz and 20 kHz. Whilst it would be desirable to move these frequencies to beyond the human spectrum of hearing this is not realistic, for two key reasons [BD09], [JD15]:

1. Increased switching loss. IGBTs suffer highest loss when moving from “on” to “off”; the more the IGBT has to move between the two states, the higher the net-switching loss, in particular at the high currents experienced with an electric vehicle at high speed.
2. Increased part fatigue: Whilst solid state IGBTs still suffer from fatigue, the higher amplitudes of thermal cycling caused by the increased switching loss puts strain on the bond wires between the semiconductor material and the power supply copper.

The harmonics generated as the switch flips from “on” to “off” interact with the fundamental flux wave in the air gap [TGH91], [AB12], [PV98], [MC14], [AS16], [CL19], [SLC03]. Generally, for a PWM source the tones generated are of the order $k*f_c$, where k is the order number and f_c is the carrier frequency [SLC03], [AS16]. Thus, for a machine utilising a carrier switching frequency of 10kHz, tones could be excepted at 10kHz, 20kHz etc. This is well illustrated in Fig. 1.5.15 with measured results [TGH91], [AS16].

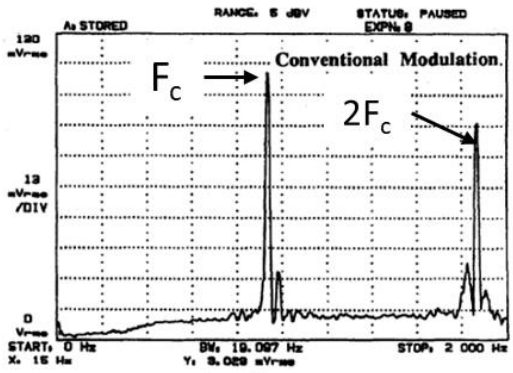

Fig. 1.5.15 Measured PWM tones on induction machine, 1000rpm, F_c = 1kHz [TGH91].

Much of the work around this phenomenon is more focussed on the electromagnetic interference the machine generates [AB12], [SLC03], as the tones observed in the vibration in Fig. 1.5.15 can extend far into the electromagnetic spectrum which can become a big issue for electromagnetic compatibility (EMC), an area that is strictly regulated within the automotive industry due to the potential disruption to the increasing array of microcontrollers on-board, and is set to become even stricter with the advent of self-driving vehicles.

1.5.2.3 SVPWM Control.

The PWM frequency and duty cycle dictate the voltage output of the inverter. However, a higher level of control is required to ensure the correct switch on the inverter is activated at the correct time to create the rotating field in the stator.

One of the most popular methods is the so-called space vector PWM (SVPWM) technique [JTB90], [JAH84]. The switching sequence is shown in Fig. 1.5.16.

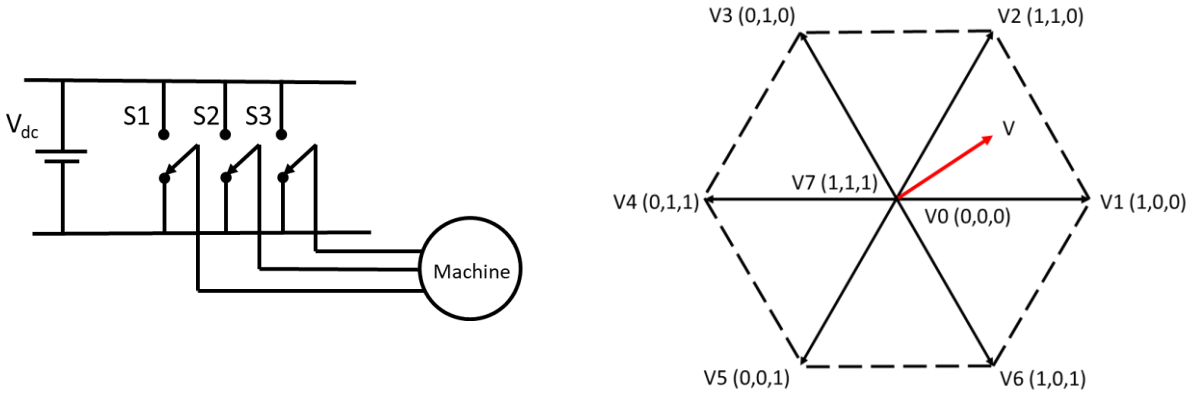

(a) Simple 3 phase Inverter

(b) Inverter output with inverter leg switching states required to generate rotating voltage vector, V

Fig. 1.5.16 SVPWM switching method based on [JTB90].

A core advantage of the SVPWM technique is it has a 3rd harmonic deliberately added into the pseudo-sinusoidal output voltage of the inverter [JTB90], the purpose of which is “flatten” the peaks of the voltage waveform, effectively boosting the voltage of the inverter [JAH84] and providing the machine with more voltage overhead. Increased voltage overhead means the machine can operate at higher speeds before the voltage control saturates and flux weakening is required. This is clearly beneficial in applications such as battery electric vehicles where offsetting the need to flux weaken is a useful feature to reduce current consumption, in particular when driving at highway speeds, allowing the vehicle range to be maximised. With this benefit comes some cost however as deliberately injecting harmonics into the machine will have the price of increased iron loss due to the additional high frequency flux components and additional vibratory components. Liang et al. goes into some depth exploring this subject [WL14], [WL18], deriving an

approximation for the modulation wave, *y(t)* for the output pulse width from the inverter, eqn. (1.35), based on the fundamental and the third harmonics [WL14].

$$y(t) \approx M_f(\sin(\omega_{\mathrm{mod}}t)) + \xi \sin(3\omega_{\mathrm{mod}}t) \quad (1.35)$$

$$\text{where: } M_f = \frac{2a_m}{\sqrt{3}} \quad (1.36)$$

$$\text{and: } \xi_{hsf} = \frac{3\sqrt{3}}{8\pi} \quad (1.37)$$

where a_m is the modulation coefficient, $0 \leq a_m \leq 1$, ω_{mod} is the modulation angular speed and M is the modulation ratio and ξ_{hsf} is the scaling factor between the 3rd harmonic and the fundamental.

1.5.2.4 Flux weakening control

Utilising field weakening control [SM89], [TMJ87] current can be injected into the d-axis in order to advance the stator field angle relative to the rotor field, encouraging more flux along the q-axis path generating the reluctance component. As was discussed previously this requires some care as the injection of $-I_d$ current suppresses the flux linkage from the PMs (ψ_m) reducing the mutual torque component meaning that a careful balance of the two torque components is required. Fig. 1.5.17 shows the flux distribution of an IPM machine at full load with a current angle (β) of 0° and 45°.

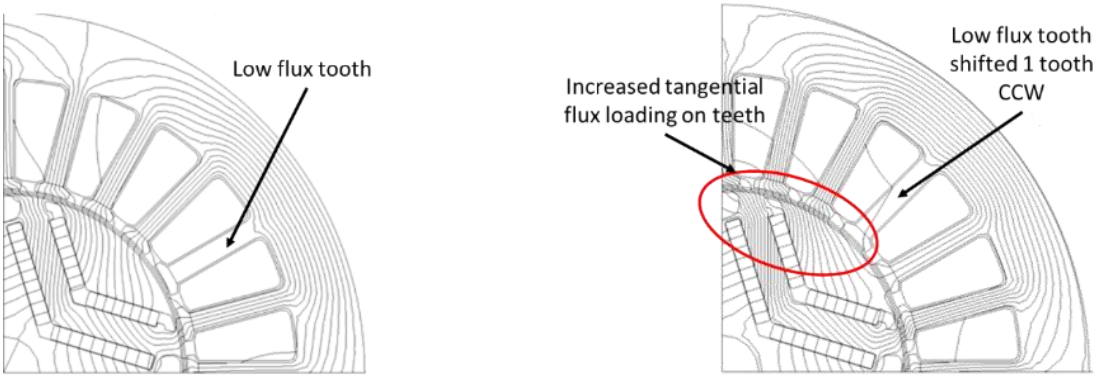

(a) I = 26.7Arms, β = 0° (b) I = 26.7Arms, β = 45°

Fig. 1.5.17 Comparison of flux distributions in an IPM machine with β =0° and β = 45°.

The change in flux distribution from Fig. 1.5.17 (a) and Fig. 1.5.17(b) due to the change in relative position of the stator field can clearly be seen to influence the tooth forces. Using an 8-pole 12 slot spoke-type IPM machine [DYK13a] did an in-depth FE investigation on the forces experienced across the air gap at different current (β°) angles, Using the resultant radial and tangential forces can be seen in Fig. 1.5.18.

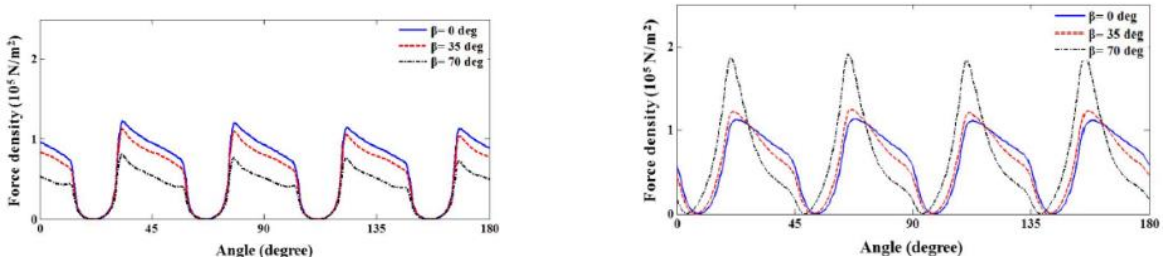

(a) Calculated radial force on tooth at different β° (b) Calculated tangential force on tooth at different β°

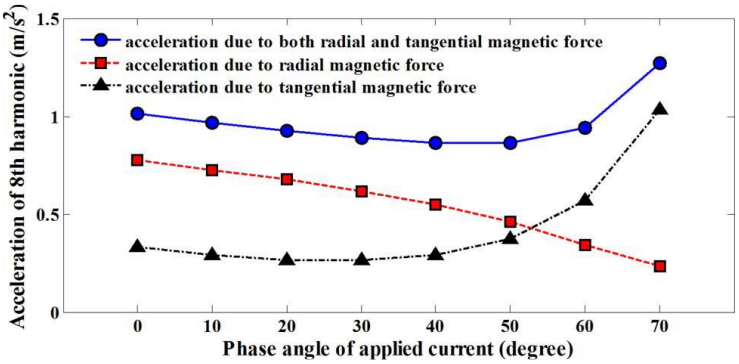

(c) Acceleration of the 8th harmonic due change of phase angle

Fig. 1.5.18 Calculated influence of incrementing the current angle on the air gap forces and ripple [DYK13a].

From Fig. 1.5.18(a) there is a marked decrease in the radial forces whilst in (b) there is increase in the tangential magnetic force and the torque ripple with increasing phase angle. However, the effect is non-linear, as highlighted in analysis of the 8th harmonic (EMF harmonic). This reflects the fact that the change in position of the stator field relative to the rotor is encouraging a higher tangential flux component. The high uneven nature of the force profiles indicates a potential concern with vibratory forces being applied to the machine [DKY13a]. Similar results are shown in [GO11] where it was shown torque ripple becomes excessive at higher current angles, primarily due to the high variation in inductance at high loads and speeds.

1.5.3 Mechanical sources

Mechanical sources of noise and vibration are those that arise from the structure of the machine and passive components such as the bearings or air being disrupted as the machine operates. Some aspects are can be described as static, these are items such as poor tolerance of the machine structure leading to misalignment of the rotor within the air and the concerns this induces. Other aspects are dynamic and are related to the rotating speed of the rotor and load the machine is driving.

Fig. 1.5.19 gives an overview of some of the different mechanical sources.

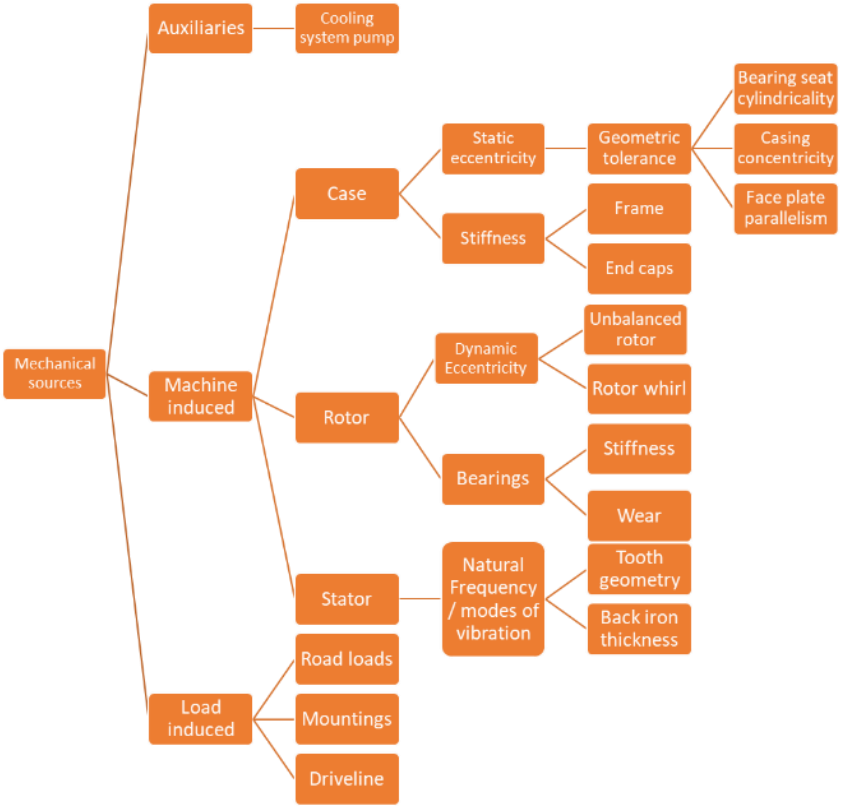

Fig. 1.5.19 Overview of mechanical noise sources in electrical machines.

From Fig. 1.5.19, it can be seen that there are a large number of potential noise sources from a mechanical perspective the key aspects will be summarised in this section.

1.5.3.1 Stator structure

Given the size and bulk of the stator it is typically viewed as being the prime source of mechanical noise [LSH09], [JFG07], [YSC06], [KTK01], [MEHB93]. If the stator is driven into a natural mode, then this has serious implications on the wider machine structure and therefore tends to be the primary focus in the literature. Table 1.5.3 highlights the effect key features have on the vibratory performance.

Table 1.5.3 Effect of stator features on vibratory performance

Feature	Effect	Ref
Slot/pole number combination	Pole count dictates back iron thickness ○ Higher pole number = thinner back iron ○ Thinner iron = reduced stiffness Slot geometry strongly contributes to mode shape ○ Thin back iron with thick tooth means high risk of encountering low order mode ○ Low order mode = higher displacement & induced vibration	[JRH10], [DH12], [MSI14], [RI09], [EC15], [PV98], [SAL01], [WC01]
Tooth width and tooth tip	Tooth tip design – large tooth tip with tight slot opening on thin tooth represents poorly constrained mass that can have multiple low frequency modes Tooth modes can have limited influence when back iron is thick. ○ Main concern is rapid motion due to tooth mode can accelerate fatigue of tooth, especially at yoke interface	[MEHB93], [SAL01], [EC15]

Windings (active length)	Contribution of overall system winding mass and stiffness due to potting strongly contributes to frequency performance ○ Mass due to windings tends to lower natural frequencies ○ Stiffness due to copper and potting material increases natural frequency [MEHB93 Acts to constrain tooth modes, dampening motion	[SAL01], [KI02], [SN87], [WC02], [JS14]
Winding (end windings)	Large mass with stiff structure Influence of end winding strongly linked to winding method ○ Balance of mass and stiffness act to attenuate effect of end winding on concentrated wound machine [SAL01]. ○ Influence found to vary widely between distributed wound machines [SN87], [KI02]	[KI02], [SN87]. [SAL01]

[RI09], [MSI14] and [EC15] show that low order modes which are characterised by high displacement have a much higher influence on the vibratory performance than just the radial forces and excitation frequency. The likely mode orders are directly correlated to the slot/pole number combination. Fractional slot machines with low tooth counts and high pole counts are more susceptible to low order modes at lower frequency as the ratio between the thin yoke and the relatively thick teeth mean the shape is more likely to deflect on the mid-slot point where the structure weakest. For given stator inner and outer diameters the higher the number of slots, the less significant the difference in thickness so the natural mode shape will increase as highlighted in Fig. 1.5.20 [EC15].



(a) 12S10P showing mode 2,0 (b) 18S14P showing mode 4,0

Fig 1.5.20 Comparison of mode order @ rated torque and 1000rpm on 12S10P and 18S14P stators of same inner and outer diameter [EC15]

[PV98] and [SJY81] highlights that given the geometric complexity of the stator, the equations describing the mode shape changes as the mode number increases, making predicting the noise and vibration analytically beyond the first 2 or 3 modes computationally intense and time consuming. This lends the design process to utilising FE analysis methods and is indeed the primary methodology use in much of the literature [MEHB93], [SAL01], [HYID13], [KD14]. [RP16] etc.

1.5.3.2 Influence of materials

The resonant natural frequency (1.5) is proportional to the Young's modulus, E, and the mass density of the component. These aspects are dictated by both the geometry of the part and the material(s) utilised. For the magnetic steel cores of the rotor and stator structure this becomes a difficult problem:

- The cores are formed by thin magnetic steel laminations of thickness T_{fe} which are separated by very thin layers isolation material. Many layers are stacked to form the active length, L_t.
- These isolation materials act to electrically isolate the plates to mitigate eddy currents in the core and can act as an epoxy to bond the stack together.

A simplified lamination structure is illustrated in Fig. 1.5.21.

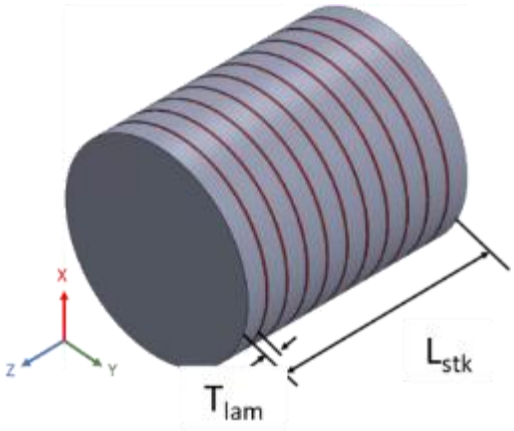

Fig. 1.5.21 Simple illustration of the laminated stacks and key measurements, T_{lam} = plate thickness, L_{stk} = active length of stack.

This means that the full active length of the core is formed of the sum of the steel and the inter-plate material. The ratio of magnetic steel to epoxy is called the stack factor, ϕ_s, and is defined in (1.38).

$$\phi_s = \frac{\sum T_{lam}}{L_{stk}} \times 100\% \qquad (1.38)$$

The implications of this from a structural standpoint is that the material is orthotropic; that is the material properties in the X-Y plane (radial) differs from the Z-X plane (axial). The concern is that a typical material specification for core material typically does not account for this, an example is shown in Table 1.5.4 [CP08].

Table 1.5.4 Lamination stack material properties [CP08]

Property	Stator core	Epoxy	Units
Material	M250-35	Epoxy (E645)	
Density	7600	1186	Kg/m^3
Young's modulus	200	3.44	GPa
Poisson's ratio	0.3	0.3	
Shear modulus	80.8	1.32	GPa

As can be seen from the data provided only isotropic information is provided which does not represent the orthotropic nature of the core. Fortunately, there been a lot of work on this area. Some of the literature use

stress and strain measurements on samples of the materials to obtain the characteristics of the measured data using more traditional stress testing methods [MVDG12] or ultrasonic NDT methods [ZT04]. Others attempt to use FE tools to calculate the properties given some known input forces [RP16] which reduces costs in terms of equipment but risks problems with accuracy.

A more attractive method utilises the fundamental rules of mixture that material engineers apply to simplify the modelling of fibre reinforced materials and apply this to the stator stack, effectively treating the stack as a composite material. The theory [RP16] [MVDG12] [PPB96] is to combine the key characteristics of the component parts of the stator structure (steel plates, epoxy) to form a single material that can be applied to the existing 3D shape of the part. An important point here is that there is a separate value for the moduli on the X-Y (radial) plane and the Z-(axial) plane. This is due to the fact that the strength of the magnetic steel will dominate for the radial plane, but the epoxy will have a tangible influence on the axial strength of the stack, in particular under tensile load. The equations used to define the characteristics of the "composite" stator material [MVD12], [RP16] are listed in Table 1.5.5.

Table 1.5.5 Equations to combine material properties [RP16], [MVDG12].

Property	Equation	Unit	Eq#
Density	$\rho = \rho_f \phi_s + \rho_m (1 - \phi_s)$	kg/m³	(1.39)
Young's Modulus	$E_{xy} = E_f \phi_s + E_m (1 - \phi_s)$	Pa	(1.40)
	$E_z = \left(\frac{\phi_s}{E_f} + \frac{1 - \phi_s}{E_m} \right)^{-1}$		(1.41)
Shear modulus	$G_f = \frac{E_f}{2(1 + v_f)}$	Pa	(1.42)
	$G_m = \frac{E_m}{2(1 + v_m)}$		(1.43)
	$G_{xy} = \frac{E_{xy}}{2(1 + v_{xy})}$		(1.44)
	$G_z = \frac{G_m G_f}{G_m \phi_s + G_f (1 - \phi_s)}$		(1.45)
Poisson's ratio	$v_{xy} = v_f \phi_s + v_m (1 - \phi_s)$	-	(1.46)
	$v_z = v_{xy} \frac{E_z}{E_{xy}}$		(1.47)
Symbols	ρ = density, *E* = Young's modulus, *G* = shear modulus, v = Poisson's ratio, ϕ_s = stack factor X_f = steel property, X_m = Epoxy property X_{xy} = XY –plane, X_z = Z-plane (axial)		

What is important in each of the above equations is that the stack factor (1.38) is key to deriving the properties of the material. By using the formulae in Table 1.5.5 and varying the stack factor from 0.5 to 1 the influence on the mechanical properties of the stator can be analytically calculated. The results are shown in Fig. 1.5.22.

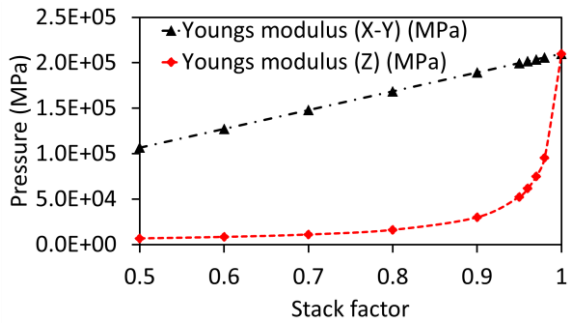

(a) Influence of stack factor on Young's modulus on the XY plane and the Z-axis in the composite material

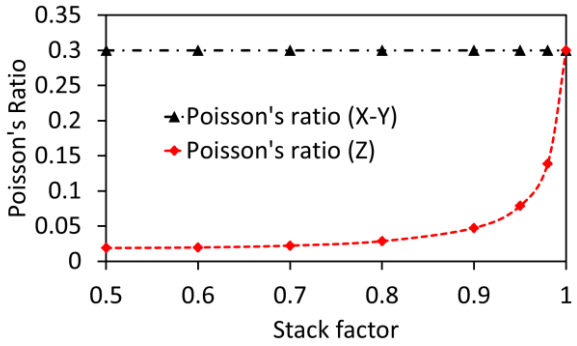

(b) Influence of Poisson's ratio on the XY plane and the Z-axis in the composite material

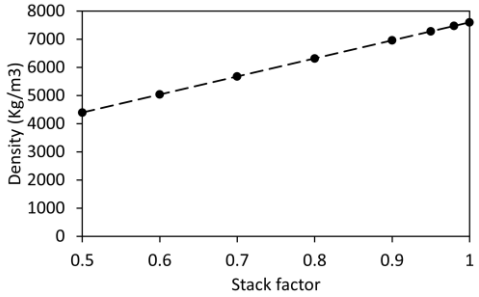

(c) Composite density vs. stack factor

Fig. 1.5.22 Characteristics of the composite with varying stack factor (0.5-> 1) [RP16].

From Fig 1.5.22, it can be seen that:

- Density changes linearly with stack factor
- X-Y plane Young's modulus and Poisson ratio change linearly with stack factor
- Z-Y plane Young's modulus and Poisson ratio show non-linear relationship with very sharp rise in between stack factors of 0.9 and 1

The practical effect of this is that in the case of bonded stator cores the axial stiffness can vary enormously for small changes in stack factor and of course the epoxy chosen.

A similar concern exists for the representing the windings which are again non-homogenous structures formed of:

- Strand of copper wire forming the turns of the winding
- Enamel coating to electrical insulate the wire strands
- Epoxy resin to boost the mechanical strength of the windings and improve thermal conductivity of the winding to the stator core (potting).

[KI02] provides an empirically derived chart of the Young's modulus of the winding in-slot. Within the paper many distributed wound machines for induction machines of all shapes and sizes were measured and an empirical equation derived based on a best fit curve through the collated data (1.48) [KI02].

$$E_{slot} = 0.0004S^2 - 0.0212S + 0.694 \quad (1.48)$$

E_{slot} is the Young's modulus of the slot (in GPa) and S is the slot fill factor (as a %). Using (1.48) a general trend of the slot's modulus can be generated and is illustrated in Fig. 1.5.23(a).

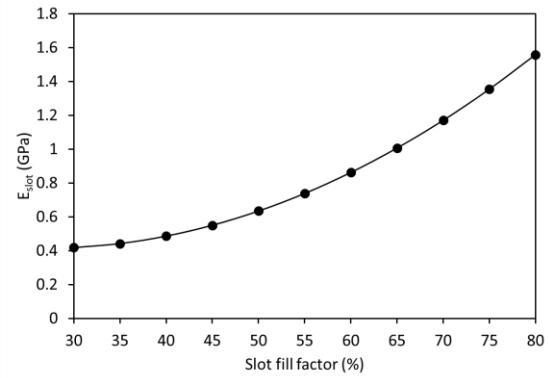

(a) Young's modulus of winding in slot versus slot factor (30% -> 80%)

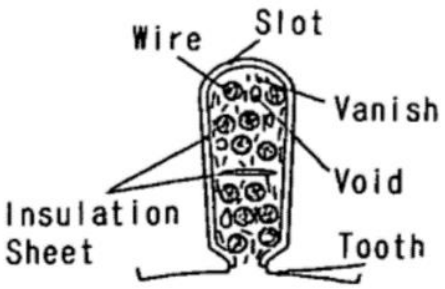

(b) Example section of slot measured in [KI02]

Fig. 1.5.23 Results of empirical measurement by [KI02] and example slot cross section.

The machines measured in [KI02] utilise windings which are both distributed wound and potted (Fig. 1.5.23 (b)), aligning well with the winding arrangement on the baseline machine. The work also gives the assumption that the calculated composite material is isotropic i.e., $E_x = E_y = E_z$.

Key to (1.52) is the slot fill factor, that is the proportion of the total slot area that is occupied by the winding (1.49) [JRH10].

$$K_{sf} = \frac{N_{str} A_{str}}{A_{slot}} \tag{1.49}$$

where K_{sf} is the slot fill factor, N_{str} is the number of strands in the slot, A_{str} is the area of one strand (including coating) and A_{slot} is the total area of the slot.

1.5.3.3 Machine induced sources

In an ideal machine the housing, rotor, stator, bearings etc. would all have perfect concentricity and cylindricality, and everything would rotate across the required speed range perfectly smooth. Unfortunately, in the real world there are manufacturing and material tolerances which can stack up meaning that if not carefully controlled can lead to misalignments in the machine. The two types of eccentricity are [DGD94], [IPB12], [ZQZ14]:

- **Static eccentricity:** this is where the rotor spins on a different axis than the centre axis of the stator. These axes are fixed and are caused by issues in the machine structure
- **Dynamic eccentricity**: this is where the rotor spins on the central axis of the stator but rotates in an eccentric manner (whirls) due to an unbalance in the rotor, where this is mass, the bearings or deflection of the rotor shaft

Fig. 1.5.24 below illustrates the concept of static eccentricity [ZQZ14].

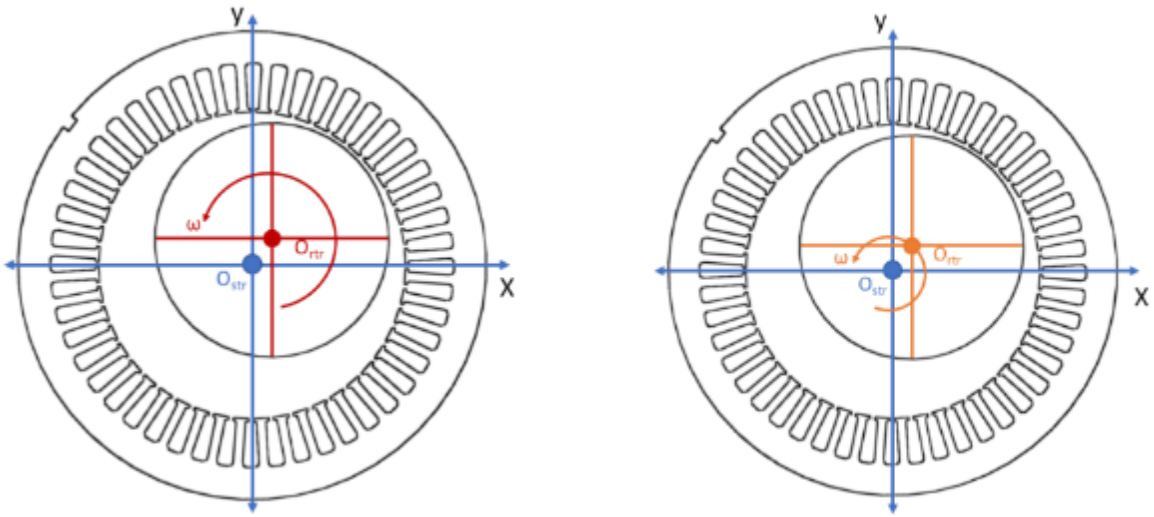

(a) Static eccentricity, rotor spins on own axis, O_{rtr}, offset from stator axis, O_{str}

(b) Dynamic eccentricity, rotor axis, O_{rtr}, rotates **around** the stator axis, O_{str}.

Fig. 1.5.24 Illustration of static and dynamic rotor eccentricities with the rotor centre of rotation, O_{rtr}, offset from the stator central axis (O_{str}) based on [ZQZ14].

Static eccentricity can be thought of as a structural problem with the machine, either from poor design methodologies or fatigue and wear within the bearings or casing that result in the rotor centre of rotation falling out of alignment with the stator bore centre line ("ideal axis"). Fig. 1.5.25 gives some examples of where the geometric tolerances [XI05], [DGD09] within the machine can lead to static eccentricities.

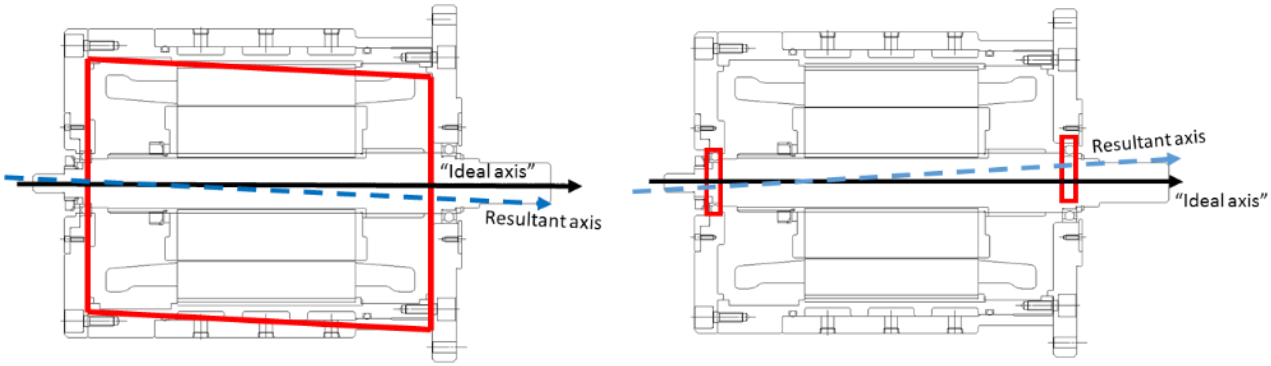

(a) Casing bore, cylindrical misalignment

(b) Bearing seat, concentric misalignment

Fig. 1.5.25 Examples of geometric tolerance on static eccentricity.

A key point of the above is that the eccentricity is driven by the overall geometric tolerances of the structure.

- Each component in an assembly has its own geometric tolerances according to the materials and process of manufacture.
- These tolerances combine in the assembled structure, a phenomenon called stack-up. This is very important in the formation of static eccentricities as different components can be within their individual tolerances but when combined (stacked up) the final system can be misaligned giving the machine a static eccentricity.

Dynamic eccentricity is more complex and harder to characterise than static owing to the fact it is dictated by a number of factors such as poor dynamic balancing of the rotor [PD14], misalignment in the driven load or more fundamental issues like poor specification of the rotor shaft material means it flexes/bends at high speeds [RM14], high bearing deflection [RM14] or the speed of rotor exciting a natural mode of the rotor causing large deflections [RM14]. Fig. 1.5.26 below illustrates some examples of dynamic eccentricity:

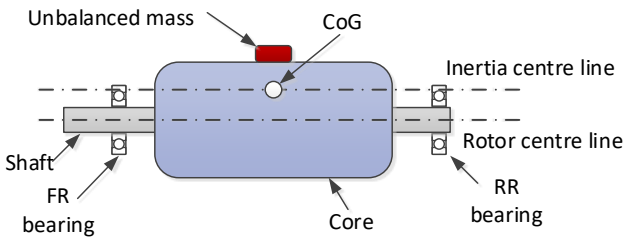

(a) Effect on rotor centre of gravity due to mass imbalance

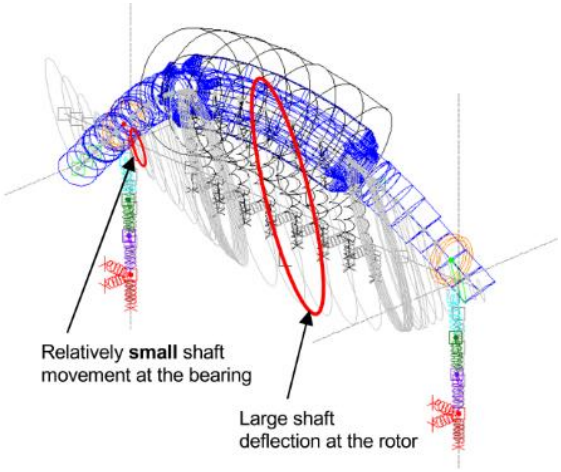

(b) Rigid body mode due to bearing deflection [RM14]

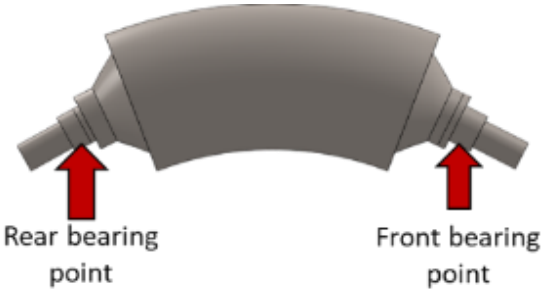

(c) Shaft deflection, due to bending mode

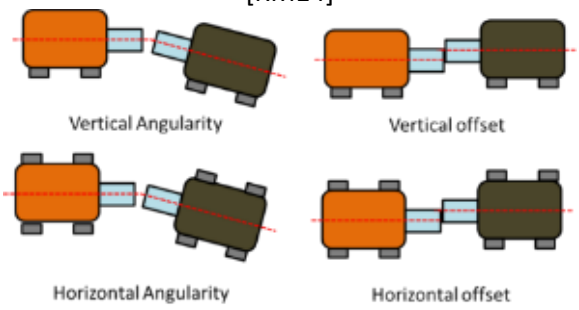

(d) Coupling/linkage misalignment

Fig. 1.5.26 Example sources of dynamic eccentricity, [PD14], [RM14].

Table 1.5.6 summarises the influence of different factors of the rotor on the modal performance of the rotor [RM14].

Tables 1.5.6 Degree of influence on critical speed for different mode shapes [RM14]

	Bearing stiffness	Support stiffness	Rotor stiffness	Rotor mass
Bending mode	LIGHT	MODERATE	HEAVY	MODERATE
Rigid body mode	HEAVY	HEAVY	LIGHT	MODERATE

It can be seen that both the rotor support and bearings have the largest influence on the rigid body mode (i.e. dynamic eccentricities) whilst the rotor stiffness has the highest influence on bending mode.

The exciting force due to the rotor imbalance has the following frequency (1.50) [PV98]:

$$F_{ru} = \frac{kN}{60} \tag{1.50}$$

where F_{ru} is the unbalanced force N = rotor speed (rpm) and k is a positive integer.

To avoid dynamic eccentricity due to rotor modes Campbell diagrams [FCN07] are used which allows the speed and frequency of the rotor to be plotted against the calculated modal frequencies. If the frequency of the rotor intersects with a modal frequency, then the machine has hit a so-called critical speed where high deflection can be expected, in particular for lower modes. The designer can then attempt to avoid or mitigate these modes, either by limiting the operating speed to avoid the critical speed or adjusting the rotor design such that the modal frequencies are moved away from the operating speed range.

1.5.3.4 Influence of bearings

The bearings within a machine are a critical component as they suspend the rotor in the correct position within the stator in order to avoid the aforementioned issues with eccentricity. Bearings are a non-stiff component within the drive system giving the rotor some flexibility, in particular in the axial direction. There are many types of bearings rated to a variety of loads and speeds. However, from a general perspective an electric machine manufacturer will tend to choose between sleeve bearings and rolling bearings [PV98].

The causes of noise due to sleeve bearings are [PV98]:

- The roughness of sliding surfaces.
- Lubrication: type, and age.
- Stability of oil film in the bearing, in particular at high speeds and loads.
- Manufacturing faults.

Roller bearings offer a lower cost solution but the ball bearings moving within the larger bearing assembly can be the source of some noise, in particular if the bearing is poorly specified or fitted incorrectly to the rotor. Noise from rolling bearings is produced due to [PV98]:

- The accuracy of bearing elements track geometry and sphericity of the ball bearings.
- Ingress of dirt and other foreign material.
- lubrication conditions.
- The natural frequencies of the outer ring and covers etc.
- Running speed and load, in particular where phenomena such as lubrication starvation occurs.
- Operating temperature relative to bearing spec.
- Installation of bearing, in particular damage due to misaligned press tool or overheating when using heat shrink techniques to mechanically bond bearing to rotor shaft.
- Bearing alignment.

The exciting forces are summarised in Table 1.5.7 [PV98].

Table 1.5.7 Bearing excitation forces [PV98]

Source	Equation	Eq.no
Rotor imbalance/eccentricity	$f_{unbalance} = \frac{N}{60}$	(1.51)
Axial grooves	$f_{groove} = \frac{N_g N}{60}$	(1.52)
Irregularities in ball cage	$f_{ball_cage} = \frac{N}{60}\frac{r_i}{r_i + r_o}$	(1.53)
Defects in bearing outer ring	$f_{outer_ring} = Z_b \frac{N}{60}\frac{r_i}{r_i + r_o}$	(1.54)
Variation of bearing stiffness	$f_{B_stiffness} = k \cdot Z_b \frac{N}{60}\frac{r_i}{r_i + r_o}$	(1.55)
Symbol meaning:	N = rotor speed (rpm), N_g = number of grooves, r_i = inner radius of cage, r_o = outer radius of cage, Z_b = number of ball bearing, k = positive integer.	

Bearings act as the primary mechanical loss mechanism. Failure of the bearings can result in increasing levels of acoustic noise as the bearing wear or in the extreme case complete failure of the machine (rotor impacting stator). A primary objective of reducing vibration within a machine is to minimise wear on the bearing given the implications on the life of the motor.

[KHY12] and [RM14] provide additional analysis and showing how bearing compliance strongly influences rigid body modes, creating rotor eccentricities and all the concerns discussed previously.

1.5.4 Load induced and structural sources

The electric machine on an EV does not run-in isolation, it is mounted within a casing and linked to a drive train that is in turn linked to the road wheel and the road surface below it. The casing into which the motor sits will change the fundamental stiffness of the machine, changing the modes of the stator compared to a "free body" example. Within the literature the focus tends to be on the stator structure [SAL01], [DI05], [WL18], where casing is included [RP16], [ZT04], [WC01] it tends to be simple cylindrical structures to avoid model complexity. [WC02] study the effects of end-bells and windings on an air cooled SRM machine by taking developing 3D models of the machine comparing modal performance with and without the end bells and windings, the trends of which were verified using shaker rig tests. An addition to reinforcing the conclusions from [SAL01] and [SN87] with regards to the influence of the windings [WC02] also concluded:

- End-bells must be included in model to determine accurate resonant frequencies, errors of up to 25% can be found if neglected.

This is entirely logical as the end bells of the machine must be stiff structures to avoid the aforementioned eccentricities in the machine structure. [ZQZ99] implemented a more practical study by measuring a test induction machine in different conditions (off rig, mounted to rig, no coupling, fully coupled to load dynamometer) and drew the following conclusions:

- The mounting and shaft-coupling can significantly affect the natural frequency and consequently the radiated acoustic noise.
- The mounting will introduce additional natural frequencies, and also restricts the vibration of the stator, changing the dynamics of the vibration modes.
- Shaft-coupling of the rotor to the load constrains the rotor movement, and, therefore, both increase the stiffness of the motor and hence can reduce the emitted acoustic noise.
- In contrast, the operating conditions, whether the motor is stationary or rotating, are found to have negligible effect on the natural frequencies.

[RM14] details a similar study on a much larger machine and considers the impact of factors such as coupling misalignment and even ambient temperature heat. It is shown that coupling misalignment place high forces on the bearings, effectively inducing noise and eccentricity into the machine. Furthermore, differences in temperature can cause different aspects of the driveline to expand or contract at different rates potentially inducing a misalignment within the driveline.

1.5.5 Aerodynamic sources

Aerodynamic sources of vibration are those created by air being disturbed by the action of the rotor rotating. Some machines, in particular machines used in industrial processes, have fan blades attached to the rear portion of the rotor shaft forcing air into the stator/rotor assemblies to cool the machine. IPM machines utilised within EV/HEV tend to have high current densities which mean at full load they can get very hot very quickly without sufficient cooling typically requires fluid cooled to maintain performance under load conditions.

The rotor does not rotate in a vacuum so air disturbed within the air gap will interact with surrounding air and structures creating some loss and potentially generating noise. Fig. 1.5.27 highlights the mechanisms that can create aerodynamic noise.

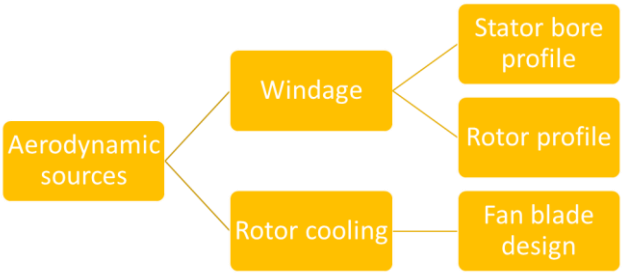

Fig. 1.5.27 Aerodynamic sources of noise in electric machines.

Windage noise refers to the noise and associated losses generated by the interaction of the air within the air gap and the rotating parts. Windage noise is airborne and will not generate vibrations on the yoke like the structural and magnetically generated aspects previously discussed [WRF91].

Most papers dealing with windage discuss the influence of the noise on induction machines [WRF91] and SRM machine [KK14a] where saliency on the rotor bore exists, either due to the rotor teeth (SRM) or due to extension of the rotor bars (IM) or external fan added to the rotor for cooling. Examples of the kind of saliency on the rotors can be seen in Fig. 1.5.28 where the complexity goes from a non-salient smooth bore in (a) to the extreme of an SRM rotor in (d).

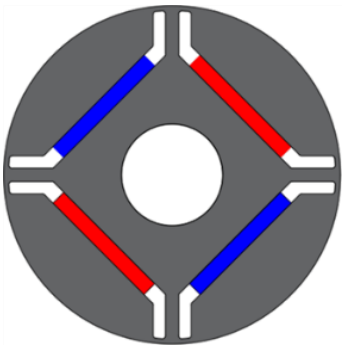

(a) Smooth Circumference IPM machine

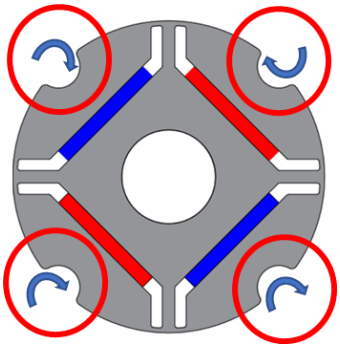

(b) Notch applied to d-axis, increased disruptions to air.

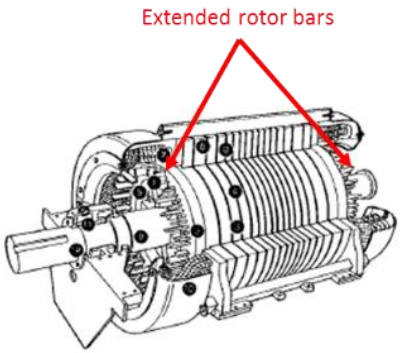

(c) Open frame induction machine with extended bars for cooling [WRF91]

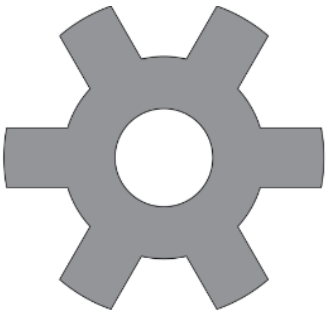

(d) SRM for hybrid vehicle traction system showing salient poles

Fig. 1.5.28 Examples of machine saliency from smooth bore IPM to highly salient SRM rotor.

For an IPM machine the rotor bore is typically smooth (often cited as the best method to reduce windage [KK14b], [WRF91], [TMJ96], [PV98]). However, some windage will occur due to laminar flow of the air surrounding the rotor [JEV68] as well as inconsistencies in surface of the cylindrical shape of the rotor due to slight misalignment of the plates during the stacking of the lamination core etc. It is of particular relevance when the rotor is profiled (Fig 1.5.28 (b)) in order to tune the air gap flux harmonics (see later in this chapter); in this case the added saliency will disturb more of the air in the air gap and introduce additional windage loss which must be accounted for in case the benefits from adding the feature is negated by the additional windage losses induced.

Fig. 1.5.29 shows the difference in loss between a cylindrical rotor such that shown in Fig. 1.5.28(a) and an SRM rotor with high saliency of the type shown in Fig. 1.5.28(d) and rotor.

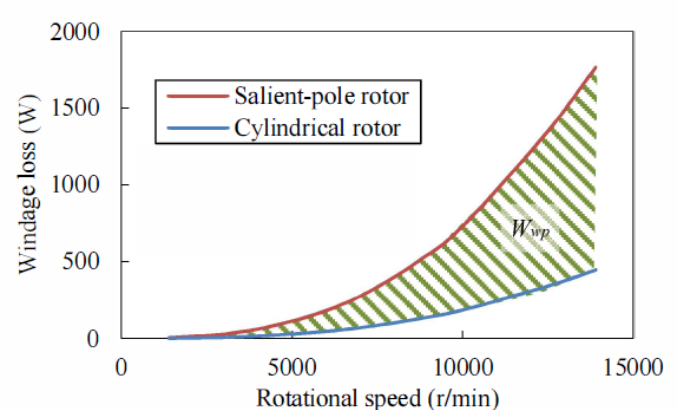

Fig. 1.5.28 Influence of rotor tooth saliency on windage loss [KK14a].

As can be seen the addition of saliency greatly increases the loss component of windage. It effectively moves it from being “background” loss of a few 100W to a primary loss component of > 1kW. This should be kept in mind when adding salient features to the outer bore of the rotor geometry.

1.6 Noise and vibration mitigation techniques

The discussion thus far has looked at the various sources of vibration within electric machines from the fundamental aspect of the slot pole number combination, through the stator winding and rotor magnet arrangement to eccentricity and windage. This section provides an overview of some of the methods implemented in the literature to counter measure the issues associated with the generation of vibration. The order of this section follows the same process as the sources, starting with the electromagnetic aspects, then the control and power electronics, followed by the mechanical and aero dynamic.

1.6.1 Slot pole number combination & windings

It is difficult in much of the literature to separate the slot/pole number combination and the windings as they are inherently linked. [RI09], [MSI14] and [EC15] do some effort to focus solely the slot/pole number combination and highlight the issues with the mode shapes for different slot/pole number combinations can encounter under similar load conditions. Much of the rules established on the fundamental winding factor, LCM and GCD of slot/pole number combinations are applied across the literature.

In terms of how the windings are arranged there is a very large variation in winding methodologies. The aim ultimately is to obtain as smooth an air gap flux as possible without compromising the average torque by lowering the winding factor or impacting the efficiency by having a large end winding and associated losses and parasitic end-effects. The concern with the windings is the layout is constrained by the slots which means a pure sinusoidal distribution is impossible. Typically, the technique is a compromise and looks to target the more troublesome lower harmonics such as the 5th or 7th harmonic [BN91], [JRH10] with the assumption the balanced nature of the 3-phase winding will reject the 3rd harmonic. Table 1.6.1 highlights some of the key methodologies.

Table 1.6.1 Examples of winding distribution techniques to mitigate vibration

Method	Description	Refs	Advantages	Disadvantages
Number of phases	Increase number of phases	[JRH10], [TMJ96], [EF93]	✓ Reduce torque ripple ✓ Improved winding utilisation	X Increased number of inverter switches X Limited influence on cogging torque X Limited gains vs. cost beyond 3 phases
Lap winding	Distributed winding, 2 coils per pole, one coil overlaps the other	[JRH10], [DH12], [TI15]	✓ High torque ✓ Good reluctance torque capabilities ✓ Very high slot fill factors. ✓ Low MMF harmonics	X Difficult to wind, typically manual installation X Very long end windings X Integer slot – high cogging torque
Concentric winding	Distributed winding, 2 coils per pole, one wound concentrically over the over	[JRH10], [TMJ96] [WO05]	✓ Suited for automated coil insertion ✓ Good slot fill factor ✓ Adjustment of coil-turns enables limited tuning of air gap harmonics	X Lower average torque vs. lap wound X Long end windings X Integer slot – high cogging torque

Short (fractional) pitch winding	Coil is deliberately inserted such that it spans < 180° electrical	[TMJ96], [BN91], [JS16]	✓ Better freedom to shape back EMF ✓ Improved THD ✓ Improved iron loss due to reduced harmonics ✓ Can be designed to reject specific harmonics (5th, 7th etc.) ✓ Reduced end winding length	X Lower winding factor = less flux linkage X Less flux linkage = Lower average torque X Only practical to target low order harmonics, higher frequency harmonics still exist
Dual layer concentrated winding	Two coil ends per slot rather than one coil end per slot in single layer in fractional slot machine	[FM03], [FM07], [ZQZ09], [LC11]	✓ Reduced end winding length vs. single layer ✓ Significant reduction in MMF harmonics VS single layer ✓ Maintains advantage of low cogging torque with single layer machine ✓ Good field weakening capabilities	X Lower winding factor vs. single layer [FM03]. X Harmonics still higher than distributed X More difficult to wind vs. single layer.
Alternative tooth concentrated wound	Armature coils wound on every 2nd tooth	[DI06], [AGJ96], [JDE02]	✓ Improved winding factor over all-tooth wound ✓ Higher torque ✓ Low cogging torque	X Longer end windings vs. all tooth wound X Higher ripple in BLAC mode X Winding factor sensitive to slot/pole number X Poor reluctance torque capabilities
Air gap winding	Coils are located directly in the air gap, either bonded or attached with nonmagnetic structure eliminating the stator teeth	[JRH10], [DW10], [NB12], [KSI06]	✓ No teeth mean no cogging torque ✓ No tooth saturation ✓ Lower iron loss (less iron) ✓ Excellent packaging potential ✓ Less constraints on winding layout	X Retention challenging X Larger air gap vs. slotted machine X Larger magnets required to compensate for large air gap – higher cost X Challenging thermal management
Parallel paths.	Dampen UMF from eccentricity using the “equal flux” [ELR65] property of parallel stator windings.	[DGD94], [AB07], [IPB12]	✓ Mitigate UMF generated by rotor eccentricity ✓ Uses the stator windings – no additional components	X More effective on induction machines than PM machines [IPB12] X Requires high number of parallel paths to be effective (3 or more) X Constrains winding layout options

1.6.2 Skewing

Skewing is a very popular method of reducing torque pulsation [JRH10], [ZQZ00], [TMJ96], in particular the cogging torque. It works by deliberately misaligning the pole arc and the slot pitch such that the net variation of permeance “seen” by the rotor magnets along the active length is reduced and hence the cogging torque is reduced. The cogging torque varies approximately linearly from its peak with an un-skewed rotor and stator to ideally zero. Highly cited papers such as [TMJ96] or [PV98] indicate that the best method is to skew by one

slot pitch. However, [ZQZ00] shows that this value can change depending on the slot/pole number combination and developed a characteristic equation (1.56).

$$\alpha_{sk} = \frac{kN_s}{N_c} \tag{1.56}$$

where N_s = slot number, N_c = LCM between the slot number and pole number and k = 1,2,…, N_c/N_s

There are various methods of skewing which have been developed over time. Fig 1.6.1 highlights two of the major methods with Table 1.6.1 giving a more detailed summary.

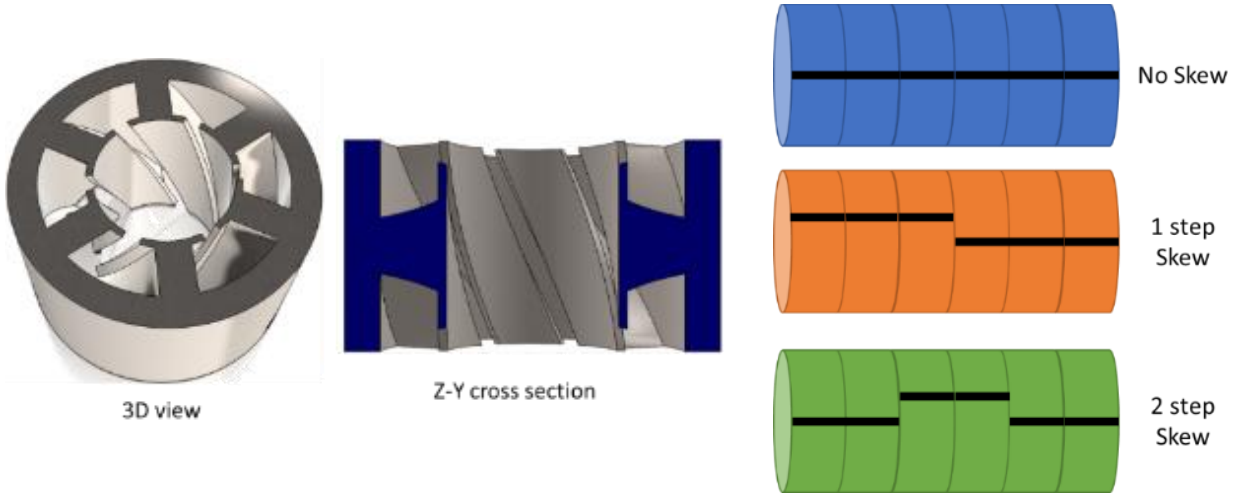

(a) Continuous skewing (stator) (b) Basic stepped skew types (rotor)

Fig. 1.6.1 Illustration of the two basic skew types.

Table 1.6.2 Overview of skewing techniques

Method	Description	Refs	Advantages	Disadvantages
Continuous skew	Skew is one continuous axial "twist" of the stator core starting from alignment to the required skew angle at the other end	[TMJ96], [JFG06] [JRH10], [PV98], [SW95]	✓ Large reduction in cogging torque. ✓ Acts as low pass filter for air gap flux harmonics, smoother EMF	X Reduction in average torque X Increased leakage inductance X Stator only for PM rotors due to magnet shape and insertion complexity X Specialist winding insertion tools required
Single step	Skew is applied in one step, typically at the mid-point of the stack length	[GO11], [TMJ96], [SW95]	✓ Reduce cogging torque ✓ Easy to implement when applied to rotor	X Reduced average torque X Increased part complexity (2 different laminations required) X 3D flux leakage paths between skewed sections X Axial force generated on rotor

Multi-step	Similar to single step but happens at multiple, regular intervals along the stack by splitting core into multiple segments	[JFE97], [HYID13], [JB14], [JWJ16], [WF13], [XG17]	✓ Greater reduction in cogging vs. single step ✓ Additional degree of freedom on design ✓ Careful selection of skew pattern can mitigate axial forces	X Increase complexity & cost X Requires 3D FE analysis to account for inter-step leakage and axial forces X Effectiveness of step pattern varies by machine [JB14], [JWJ15]

1.6.3 Stator tooth and slot gap designs

Whilst skewing has been clearly shown to be effective in reducing torque pulsations the reduction in average torque plus complexities the process places on the air gap harmonics means many designers target the tooth and slot geometry to mitigate the torque pulsations. Fig. 1.6.2 highlights some of the major design types whilst Table 1.6.3 provides a summary and references.

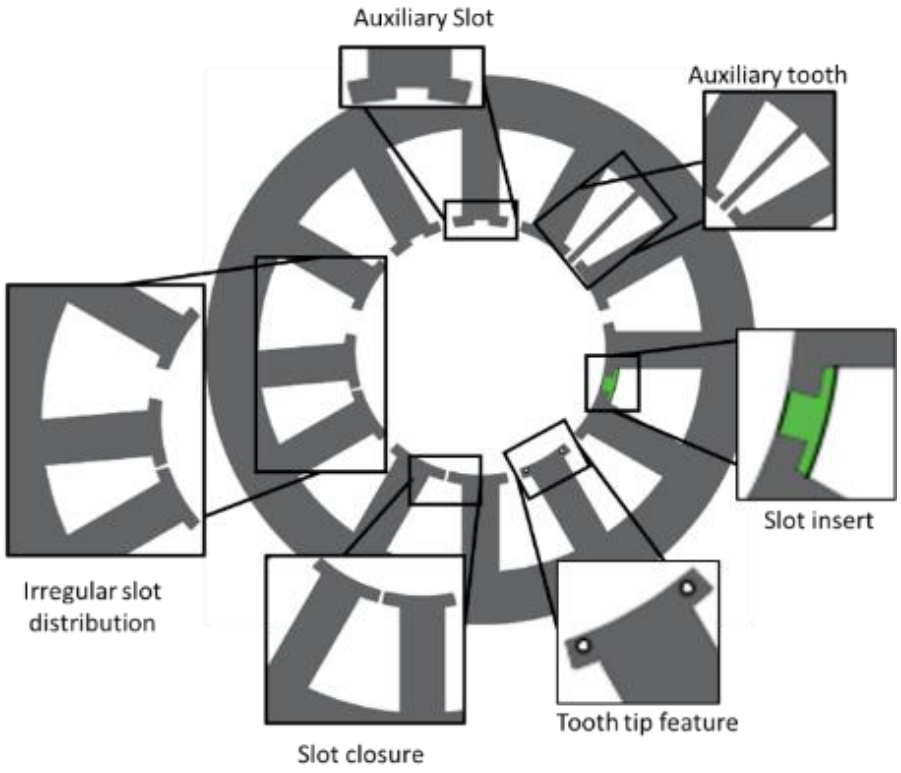

Fig. 1.6.2 Example stator showing different tooth and slot gap design techniques.

Table 1.6.3 Examples of stator tooth and tooth tip design methodologies to mitigate vibration

Method	Description	Refs	Advantages	Disadvantages
Auxiliary slots	Additional slots added to tooth tip	[TMJ96], [ZQZ00], [LSH09], [JFG06]	✓ Increase cogging frequency ✓ Decrease cogging amplitude ✓ Simple to implement	X Less iron in tooth, lower flux linkage and therefore torque X Increased risk of tooth tip saturation X High frequency components risk increased iron loss

Auxiliary teeth	Additional, unwound, teeth added to slot	[TMJ96], [ZQZ00], [JRH10], [DI06]	✓ Similar effects to cogging as above ✓ Better flux linkage vs. slot method ✓ Enhanced winding factor for single layer CW machines	X Similar risk to iron loss due to higher frequencies X Tooth occupies winding space – reduced fill factor X Reduced slot width means winding insertion difficult
Irregular slot distribution	Tooth width varied by a factor of the slot pitch +/- a given factor	[JRH10], [TMJ96], [ZQZ92], [ZQZ05], [DI05], [YF16]	✓ Increased torque ✓ Reduce torque ripple ✓ Reduce magnetic force fundamental	X Risk of increased winding complexity X Different slots have different fill factors leading to winding issues
Slot closing shape optimisation	Adjust slot opening to reduce permeance variation	[LSH09], [JFG06], [ZQZ00], [JRH10]	✓ Closed/ limited gap improves cogging ✓ Reduce fringing on tooth edge ✓ Reduce MMF harmonics	X Closing slot gap increases risk of leakage X Difficult to wind, more suited to needle winding
Tooth tip features	Addition of features such as holes to tooth tip	[GO11], [LS11], [KJ10], [JJ10].	✓ Reduce ripple at higher current angles ✓ Mitigate fringing on tooth edge	X Increased tooth saturation on load X Lower average torques X Tolerancing difficult, especially on small machines
Slot inserts	Low reluctance material added to slots or slot opening	[TMJ96], [JMP01], [REF]	✓ Similar to slot closing but winding easier ✓ Increase tooth stiffness ✓ Mitigate slot harmonics	X Risk of increase flux leakage in teeth X Reduced average torque X Potentially lower fill factor to package inserts in slot

1.6.4 IPM rotor topology designs

As previously discussed, there is more design freedom with the rotor than the windings as the magnet design and layout is less constrained than the windings. This freedom is not unlimited however as packaging issues such as flux leakage and mechanical strength requirements act to eliminate some of the wilder proposals. Some of the major design aspects put forwards in the literature is shown in Fig. 1.6.3 and a summary containing giving a brief description and references is provided in Table 1.6.4. Given the large number of studies in this area the summary is limited to IPM topologies.

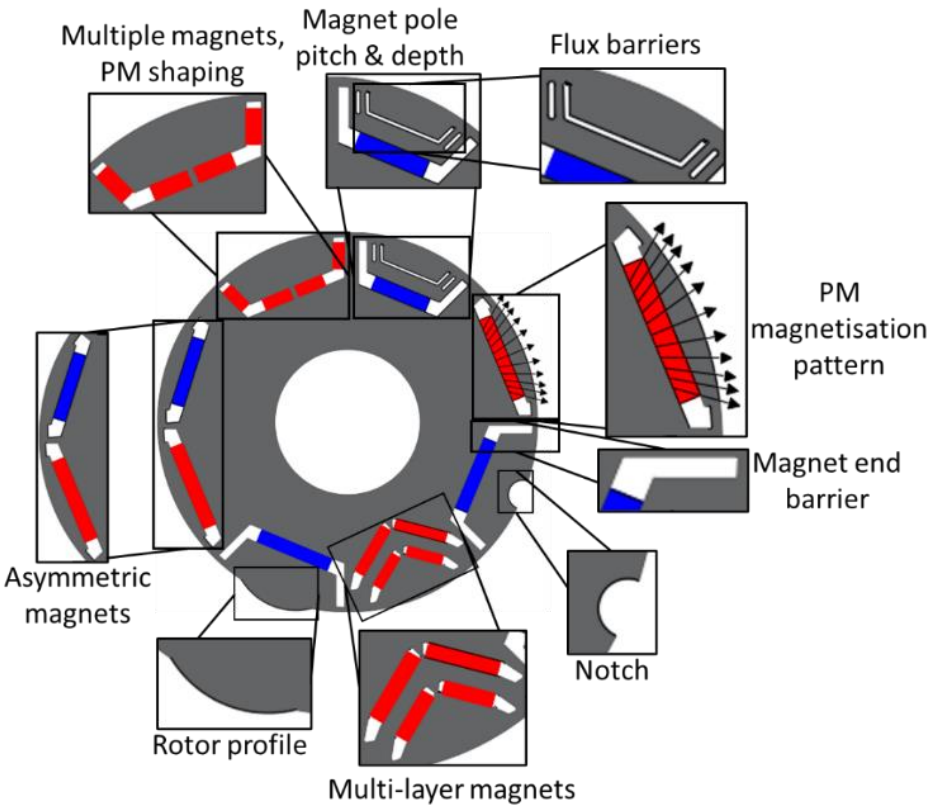

Fig. 1.6.3 Example IPM rotor showing different features to mitigate vibration.

Table 1.6.4 Examples of rotor design methodologies to mitigate vibration

Method	Description	Refs	Advantages	Disadvantages
PM magnetisation pattern	Field distribution from PM shaped during initial magnetisation process	[TMJ96], [JRH10], [YL03], [PV98], [HSK13]	✓ Improved air gap distribution ✓ Can use simple bar magnets ✓ Simple to package in rotor	X Higher manufacturing costs X Highly sensitive to manufacturing tolerances
PM shaping & multiple PMs (single layer)	Use of arc magnets or arrange bar magnets into different arrangements, e.g. 'V' shape to shape air gap flux distribution and reduce harmonics	[TMJ96], [YH97], [MFH05], [ZQZ12], [KW12], [SKL12], [GDL15], [AD15], [KSI05], [SHH07], [HSK13], [PU13]	✓ Improve PM flux distribution ✓ Tune Ld/Lq to boost reluctance component ✓ Utilise flux focussing -> reduce PM volume ✓ Utilise harmonic injection to boost torque ✓ Alternatively, harmonic rejection to eliminate troublesome harmonics	X Increased saliency risks increased torque pulsations and iron loss X Harmonic injection risks increased iron loss X Multiple magnets present packaging & strength concerns X Tolerances very difficult in high pole count machines
Magnet pole pitch and depth	Adjust magnet(s) width and depth in core	[KSI05], [ZQZ00], [CHZ05], [ZQZ03]	✓ Improved cogging performance ✓ Improve flux distribution ✓ Improved demagnetisation resistance ✓ Tune saliency	X Increase flux leakage risk X Increased 'V' angles mean higher stress concentration in magnet slots

Rotor shaping/notches	Shaping of outer circumference of rotor by adding material or removing notches	[JWR10a], [TN14], [DIK05], [SAE10], [JJ10], [KW12], [MC15], [DIK05], [SC10], [AD15]	✓ Similar advantages as magnet shaping for harmonic rejection/injection ✓ Easy to implement in lamination tooling ✓ Can utilise simple bar magnets	X Non-smooth rotor bore means increased aero losses (high speed issue) X Sensitive to manufacturing tolerances
Increased number of PM layers	Boost L_q by adding more magnet layers per pole	[YH97], [SM00], [YHJ12], [JQZ15], [AKP16], [YY17], [LF08]	✓ Higher reluctance component ✓ Good MTPA – high efficiencies possible ✓ Can reduce PM content for same torque	X Limited gain past 2 layers X Careful design required to balance mechanical and magnetic requirements X Increased ripple due to higher saliency
Magnet end barrier design	Optimisation of flux barriers at magnet end	[LSH09], [LF10], [UJS11] [SMH06], [KSI05]	✓ Reduce interpole leakage. ✓ Increase saliency ✓ Can target specific concern harmonics	X Increase saturation on core at high load X Increased core complexity X May compromise mechanical strength
Asymmetric magnet distribution	Magnet position adjusted at each pole, or within a pole (multi magnet topologies)	[CB00], [MS03], [KPP18], [WR15], [FM16]	✓ Mitigate cogging torque harmonics ✓ Reduce magnet force fundamental	X Risk of asymmetric mass in rotor – difficult to balance X Lower torque
Addition of Flux barriers/guides	Addition of regions of high reluctances to improve control of flux path in rotor	[BYY06], [MS03], [AK06], [DY17]	✓ Improve q-axis path through core ✓ Reduce core flux leakage ✓ Mitigate d-q axis cross coupling ✓ Mitigate vibration	X Rotor shape complexity X Compromise mechanical strength X Increase ripple through increased saliency X Increased core saturation

1.6.5 PWM noise reduction techniques

As previously discussed, the PWM frequency and the tones induced into the air gap flux MMF via the windings are a side effect of using discrete devices (IGBTs etc.) to switch the DC voltage from the battery source into an AC voltage required to generate the rotating field in the stator. To countermeasure this a number of different methods have been developed which again have their own benefits and costs. This is summarised in Table 1.6.5.

Table 1.6.5 Methodologies to reduce PWM carrier frequency tone.

Method	Description	Refs	Advantages	Disadvantages
Signal filter	Addition of capacitive and inductive components to filter high frequency components	[TMJ96], [PV98]	✓ Filters high frequency components ✓ Simple to implement	X Increased impedance loss X Increased component cost X Lower system power factor

Random carrier frequency modulation (RCFM)	Randomise the carrier frequency such that tones are spread across wide bandwidth	[TGH91], [TMJ96], [AMT04]	✓ Eliminates high tones from PWM carrier ✓ Simple implementation ✓ Reduces EMI of machine	X Increases noise amplitude across bandwidth X Coupled with duty cycle, high duty cycle means random factor drops, so tones can return X Open loop control, no method of compensating for drop in random factor
Random Pulse Position modulation (RPPM)	Similar to RCFM but uses signal fall time, β, to provide random factor for modulation	[SES07], [AB12]	✓ Similar results as RCFM ✓ Closed loop control ✓ Decoupled from duty cycle	X Additional control loop in PWM controller X Requires current sensor
Dual Random PWM	Combines elements of RCFM and RPPM	[KEKD03], [AB12]	✓ Two degrees of freedom on randomisation ✓ Allows systems to condition switch between modes ✓ Integrated into main control loop	X High processing overheads, especially for high speed. X More effective at EMI suppression than vibration mitigation

1.6.6 Control techniques

The above techniques highlighted how to reduce the PWM carrier signal. However, modern controllers have allowed for an explosion in techniques for mitigating the noise of a machine. The main advantage of utilising the controller is that machines produced at the edge of tolerances, or those that develop faults can made to be less noisy by the real-time sampling of the controller. A combination of a good, balanced, machine design and control leads to much higher overall system performance. Table 1.6.6 highlights some of the methods.

Table 1.6.6 Selected control methodologies to reduce torque pulsations [TMJ96], [BG06], [DHL12], [KK15].

Technique	Overview	Advantages	Disadvantages
Selected harmonic injection [TMJ96]	Injects pre-programmed harmonics into the drive to reduce torque pulsations. Harmonics and frequencies chosen during development.	✓ Can have similar effect as rotor shaping using simple rotor shape ✓ Can target specific problematic harmonics	X Increased I^2R loss from injected components X Increased iron loss due to high frequency harmonics X Pre-programmed means issues due to part wear etc. difficult to compensate for
Speed-loop disturbance rejection filter [TMJ96]	Sensors feed motor parameter to pass filter in controller which acts to attenuate speed variations caused by the motor pulsating torque	✓ Closed loop control – can compensate for machine wear and tolerances ✓ Effective at low speeds	X Difficult to control at high speeds – high bandwidth controller required X Limited by transducer and controller capabilities
Overmodulation [TMJ96]	Allows operation of motor operation at saturation point of current transducers	✓ Mitigates large torque pulsations that occur at machine limit ✓ Ensures machine stability at limit ✓ Prevents effective short circuiting of phases that can damage machine and drive	X Not as effective as other techniques such as flux weakening control X Injects high frequency harmonics into machine – increased loss X Should be utilised as a safety net only to protect machine and drive

Active harmonic control [BG06]	Actively controls the 5th, 7th, and 11th harmonics by placing each on a separate d-q axis frame and controlling accordingly	✓ Significant torque ripple reduction ✓ Can use off-the-shelf standard controller	X Machine specific X Requires high quality current transducer to pick up high frequency harmonics X High speed DSP required
Adaptive notch filter [DHL12]	Uses a notch filter tuned to the natural frequency of the machine to control the target current in the d-q axis frame such that resonance in the drive train is minimised	✓ Reasonable reduction in vibration versus non-filtered control ✓ Can be tuned to mitigate torque ripple	X Hysteresis high

The key finding in the study of the control system is best summarised by [TMJ96] and [JFG07] who state that whilst control techniques do have a positive impact on the vibratory performance of the machine it is highly reliant on the addition of high-quality transducers and high-speed controllers and in some cases the additional expense and complexity is not justified given the level of improvement provided, especially compared to having a machine with sound fundamentals.

1.6.7 Mechanical noise and vibration mitigation techniques

As discussed, the stator represents the key component in a radial flux machine given its relative size and mass compared to the rest of the machine and it was also shown that the radial forces acting on the teeth and the modal performance of the stator are key performance indicators. Thus, optimising the mechanical characteristics in tandem with the methods of mitigating the electromagnetic aspects as described above is important in the overall system optimisation. Fig. 1.6.5 illustrates some of the key areas of focus and Table 1.6.7 summarises some of the key aspects explored in the literature.

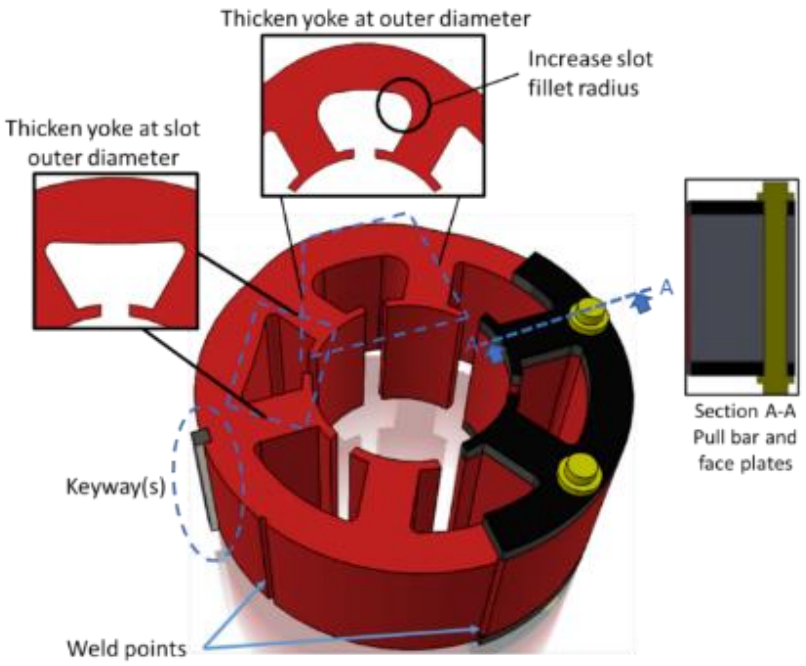

Fig. 1.6.5 Illustration of mechanical strengthening features applies to the stator core.

Table 1.6.7 Mechanical vibratory mitigation methodologies.

Method	Description	Refs	Advantages	Disadvantages
Adjust lamination material	Choose stiffer/thicker laminate plate material	[TMJ96], [JRH10], [ZG18]	✓ Increase radial stiffness ✓ Minimal impact on machine geometry	X Care to avoid increase losses due to material change (iron loss) X Increased tool wear for manufacture X Higher material cost
Stator stack welding	Welding of stator core to increase stiffness	[JRH10], [FC19]. [ZG18]	✓ Boosts axial strength & stiffness ✓ Improve longitudinal modal performance ✓ Limited design change requirements to stator ✓ Different weld patterns can be applied	X Risk of short-circuiting lamination plates – increased eddy currents X Only suitable for exterior diameter of yoke X Risk of splaying lamination plates at air gap
Pulling bars and stator end plates	Use of long bars with bolt or welded ends to retain and strengthen the lamination stack	[SC16], [JRH10], [CM20], [ZG18]	✓ High strength & increased stiffness ✓ End plates allow for uniform clamp force ✓ Reduce splay	X Plates, bolts, and bars add to mass and machine axial length X Increases stator volume X Risk of circulating currents in end plates X Care must be taken that bar material does not interact with field in back iron (eddy currents etc) X Tight control of fixing points required to ensure clamp force is correct and uniform
Increase back iron thickness.	Add material to the back iron	[TMJ96], [JRH10], [DH12], [LSH09], [KSI06]	✓ Effective method of increasing stiffness ✓ Simple to implement ✓ Does not impact core magnetic design (improves)	X Increased stator mass X If added to OD, increased machine volume X If added to slot, reduced slot area X Increased material utilisation

Optimisation of chamfer or fillet feature to tooth/yoke interface	Add strengthening features to tooth/yoke interface	[LSH09], [KSI06], [MB98].	✓ Increased strength with minimal material ✓ Maintain stator OD ✓ Mitigate stress concentrations at yoke interface ✓ Shift tooth mode frequencies higher	X Reduced slot area (less copper) X Less copper means increased copper loss
Increase bond strength between case and stator	Increase bonding with stator (e.g. shrink fit) or addition of keyways	[YH09], [DM09], [KY15]	✓ Increase stator stiffness ✓ Limited changes to stator design ✓ Strong bond between core and case	X Special process required to insert X Shrink fit requires careful design of tolerances– error means either bond too loose or too tight leading to distortion of case X Once inserted it cannot be removed X High core stress can lead to increased core losses
Casing strengthening	Optimisation of the case design &materials.to stiffen and strengthen the machine	[YH09], [IY99], [DP97], [HJC13]	✓ Independent of stator ✓ Can mitigate/supress low order mode shapes	X Can mask poor machine design X Can only really target X Limited effect against high frequency components such as PWM

From the sources section of this chapter the eccentricity was highlighted as a concern. This is a little more difficult to define as manufacturing practices towards aspects such as geometric tolerancing and manufacturing standards are less well published due to the highly sensitive nature of the topic. Manufacturers typically link to the ISO standards such as ISO 8015 for geometric dimensioning and tolerancing or ISO 1940-1 for rotor balancing but these standards serve more as a guide than hard rules. Table 1.6.8 denotes some good practise in eliminating many of the eccentricity concerns highlighted previously.

Table 1.6.8 Methods of mitigating eccentricity

Static eccentricity	Dynamic eccentricity
• Tight control of rotor outer diameter and stator inner diameter concentricity and cylindricity of both parts. • Strict control of the parallelism and concentricity of the bearing seats and bearings to ensure uniform air gap. • High strength and good locating features on casing end caps to mitigate assembly errors.	• Careful modelling of rotor in design phase to identify critical speeds and countermeasure as required. (stiffen rotor, optimise geometry etc.) • Balancing of rotor prior to installation into machine assembly. • Ensure bearing specification is matched to motor application with good safety factor (>2).

The bearings are of course a critical part of the machine, being both responsible for supporting the rotor such that it can freely rotate whilst maintaining a uniform air gap across the required speed and load range. Aspects such as bearing wear and the impact the degradation has on the performance is a large topic in itself which will not be covered here, the author recommends [NTN12] from bearing supplier NTN for a good guide to bearings.

1.7 Summary and Contributions of the Thesis

Given the breadth of topics this chapter has covered it can be seen that the reputation of noise and vibration as being one of the more challenging topics within machine design is well founded. The primary source of the vibration lies at the very heart of the electric machine, the interaction of the magnetic flux and its harmonics traversing the air gap between the rotor and stator. It has been seen that the air gap flux density and its numerous harmonics are affected by a large number of factors from the fundamental slot/pole number combination of the machine, through variations in the machine inductance due to the magnet arrangement on the rotor and winding layout on the stator to the commutation switching strategy and even the high-level control strategy. Issues such as eccentricity due to geometric problems in the machine design offsetting the rotor spin axis (static) or rotor whirl (dynamic) exacerbate the issue with IPM machines being particularly sensitive to any eccentricities due to the variations in inductance due to the rotor saliency being amplified by the variation in air gap due to the eccentric rotation.

Modelling the vibratory behaviour necessitates a multi-physics approach which in terms of FE software means utilising different solvers to gain an insight into the vibratory response. This is a complex and time-consuming method and perhaps explains why much of the literature concentrates on the tooth forces or torque pulsations such as cogging torque and on-load torque ripple rather than the more macro scale vibratory response. Those that do study the vibratory response tend to focus only on the stator or, where there is casing it tends to be very simple shapes. This is entirely logical given the computational efforts required however as EV manufacturers explore increasingly higher power densities the high current densities necessitate liquid cooled systems which forces the structural complexity high. Detailed studies into the mechanics of these structures are less apparent in the academic literature, partly because the focus tends to be on the thermal performance but also due to the fact that the casing and cooling are largely application specific. More interest can be found within industrial or patent literature, but methodologies and techniques are less detailed than the academic literature, reflecting the commercial sensitivity of these aspects. At the start of the chapter, it was shown that the cost benefits of eliminating potential market concerns as early as possible in the design phase are very high, so manufacturers are less keen to share any advantages they have in this area, especially in the highly competitive automotive market.

The main concern with this is that given the complexity of an electric machine it is difficult to have confidence in a model without some real-world performance data to compare the model to; FE packages will blissfully output inaccurate results if given inaccurate input data. Measuring both the electromagnetic and mechanical characteristics of a real-world machine allows the performance to be captured empirically and used as benchmarks for the FE model. Further benefits lie in knowing precisely what materials were used and what fabrication processes went into the fabrication of the machine providing vital information for the model, minimising the need for error-inducing assumptions.

Utilising this baseline, the effect of different machine design variations on the overall vibratory performance can be studied. As this chapter has shown there is a near very large number of different machine design variations so the focus will primarily be on the interior permanent magnet rotor topologies used within EV and HEV powertrains to understand their comparative performance both in terms of aspects such as efficiency and torque but also the full machine vibratory performance. This apparently straight forward task requires care, however, as has been seen differences in fundamental aspects such as the slot/pole number combination can lead to very large changes in vibratory performance, even for the same machine volume and rotor design so the challenge is to fix as many key aspects of the machine design as possible such that the only variation lies in the rotor design.

1.7.1 Thesis contributions

The contributions of the thesis can be summarised as follows.

1. Development of novel methods for 3D mechanical finite element modelling to greatly simplify the model, improve the prediction accuracy, and save the computation time:
    - Representation of the non-homogenous laminated stator core and windings by employing equivalent composite materials and applying the derived composite material for windings to the slots only.
    - Identification of material mechanical properties of various components and fittings/mountings by detailed experimental impact modal tests and 3D FE models systematically, which should provide useful information for designers and researchers.
    - Simplification of fastening front and rear face plates by using equivalent spot weld and frictional contact methods, and simplification of coolant shell by optimising the co-efficient of friction.
2. Identification of the influence of four IPM rotor topologies, which have been designed in this thesis with similar electromagnetic performance, including torque-speed characteristics, losses, and efficiency, on the stator vibratory force behaviour.
3. Detailed dynamic analysis of vibratory behaviour of the prototype machine, highlighting the influence of torque ripples, PWM switching frequency, in particular the influence of the SVPWM control technique, on the vibratory behaviour.

1.7.2 Published papers

- I.M. Urquhart and Z.Q. Zhu “Development of mechanical model for vibratory simulation of water cooled interior permanent magnet synchronous machine”, IET 10th International Conference on Power Electronics, Machines, and Drives, (PEMD), Online, 2020.

2 Experimental investigation of the electromagnetic performance of the baseline machine

2.1 Introduction

The baseline machine acts as the datum to which all the electromagnetic and mechanical models required for the simulation of the vibratory performance of the machine are aligned. As the literature review in chapter 1 alluded to, full FE models are notoriously difficult to develop owing to the complexity of the machine structure and the sheer number of variables that can influence the vibratory performance. Having a pre-fabricated machine that can be utilised as a benchmark for the model provides a boon in terms of both judging the reliability of the model and gives increased confidence that any applied design change is reflective of a real machine.

In this chapter the specifications and structure of the baseline machine is introduced and then the machine is run through a number of experiments to establish the performance of the machine, starting with very basic aspects such as measuring the phase resistance and inductances. Complexity is increased initially by cogging measurement and then mounting the machine to a dynamometer to enable no-load testing. Following this a full control and data acquisition system is applied to map maximum performance envelope of the machine (T-N curve) and then the efficiency of the machine at a number of points on the T-N curve. The tools and methodologies used to operate and capture the machine parameters are described at each stage.

2.2 Baseline machine - specifications

The baseline machine is a 24-slot 4-pole interior permanent magnet machine that utilises a dual layer 'V' shape rotor magnet topology. The machine was originally designed as a ¼ scale proof of concept machine for Nissan LEAF sized Battery Electric Vehicle (BEV) as part of a TSB (now iUK) funded joint project between the Nissan Technical Centre Europe and The University of Sheffield Electric Machines and Drives (EMD) group. The machine was designed to allow analysis of a novel mechanically actuated variable flux function to adjust the peak efficiency region of an EV traction motor depending on load conditions. For this study, the novel variable flux mechanism is omitted to minimise unnecessary complexity and to allow utilisation of the full air gap flux. The specifications of the motor are provided in table 2.2.1.:

Table 2.2.1 Specifications of the baseline motor

General specification	Small scale	Unit	Notes
Outer diameter (OD)	100	mm	
Stack length	75	mm	
Number of slots	24		

Number of poles	4		
Slot per pole per phase	2		
Max line voltage	600	V	at 11000rpm
Phase current	26.7	A_{rms}	
Number of turns	24		Per coil
Winding circuit	4S1P		S = series, P = parallel
Current density	17	A/mm^2	
Skew	NONE		
Max speed	11,000	rpm	
Max torque	16.5	Nm	Target

A cross section and key dimensional information are detailed in figure 2.2.1.

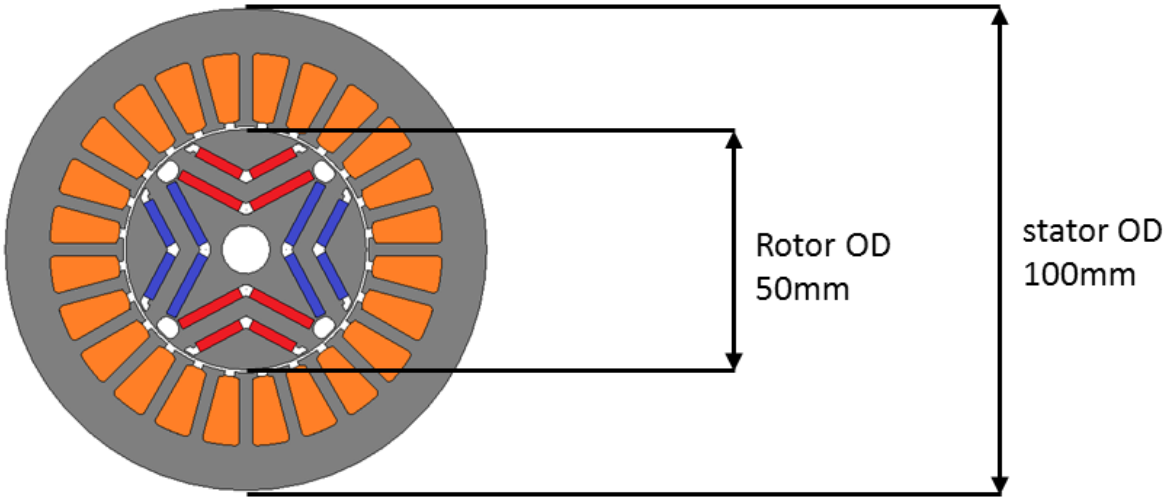

(a) Rotor and stator cross-section showing the outer diameter (OD) of each core respectively

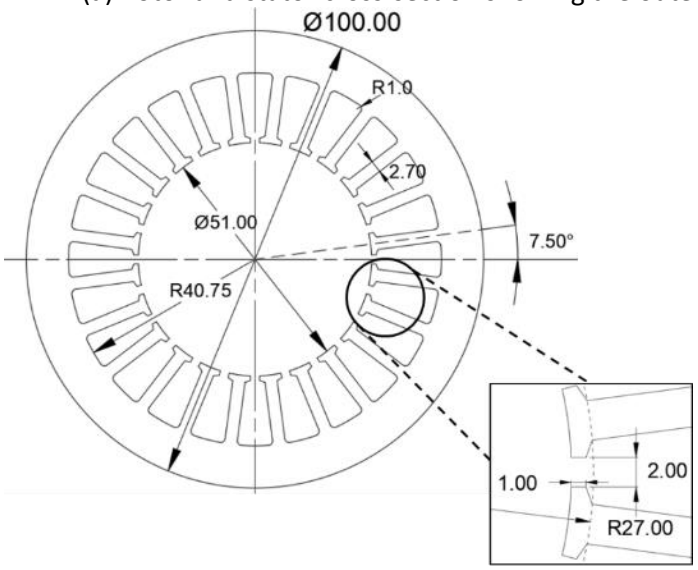

(b) Stator tooth key dimensions



(c) Fabricated stator core

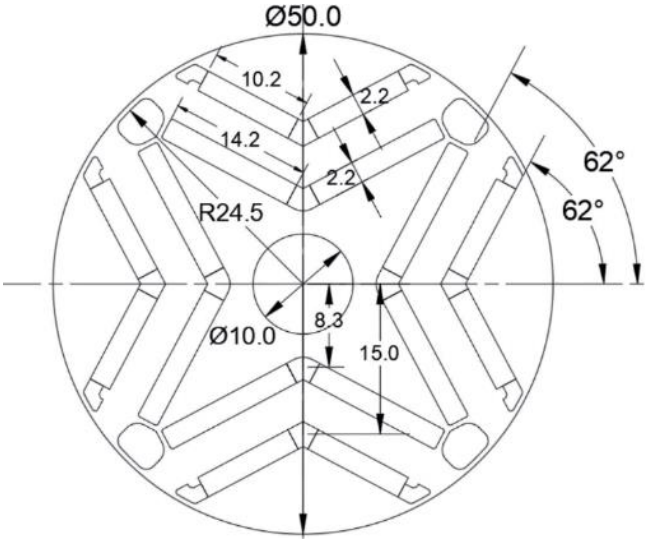

(d) Key rotor core & magnet dimensions



(e) Fabricated rotor core (during magnet insertion)

Fig. 2.2.1 Small scale machine cross-section

The dual 'V' topology is clearly seen in Fig. 2.2.1 (a), (d) and (e). This was implemented primarily to enhance the variable flux mechanism, which required an axial (3D) flux path but also to provide a back EMF profile that was analogous to the Nissan LEAF traction motor. The LEAF utilises a Delta type topology, as will be seen in chapter 7, but at the time the machine was designed this was commercially sensitive information, so the project had to implement an alternative, less IP sensitive topology. Another key differential between this machine and the LEAF is the rotor and stator are unskewed whereas the LEAF has a single step skew on the rotor.

The machine utilises a 3-phase single layer distributed wound winding. The winding layout and circuit is shown in Fig. 2.2.2.

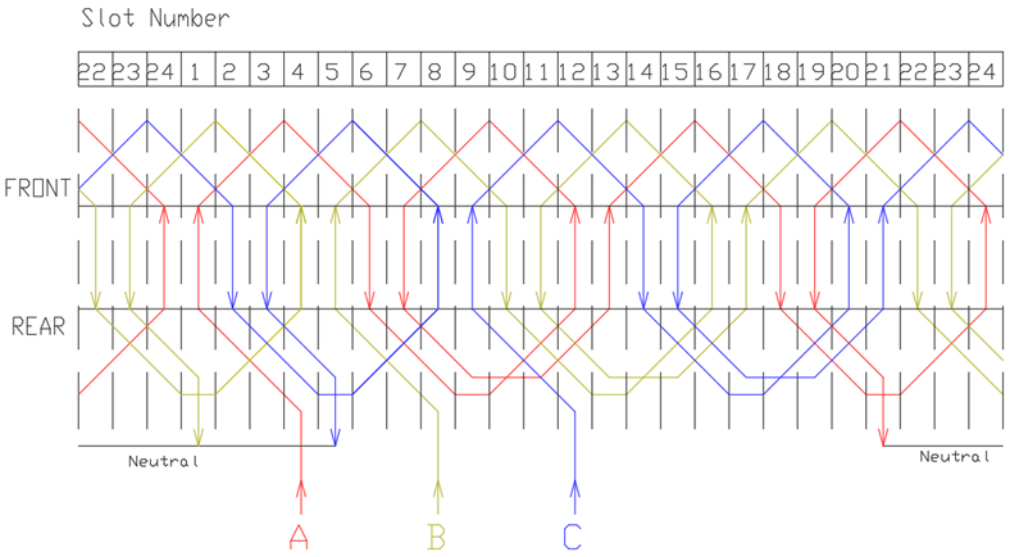

(a) Winding layout

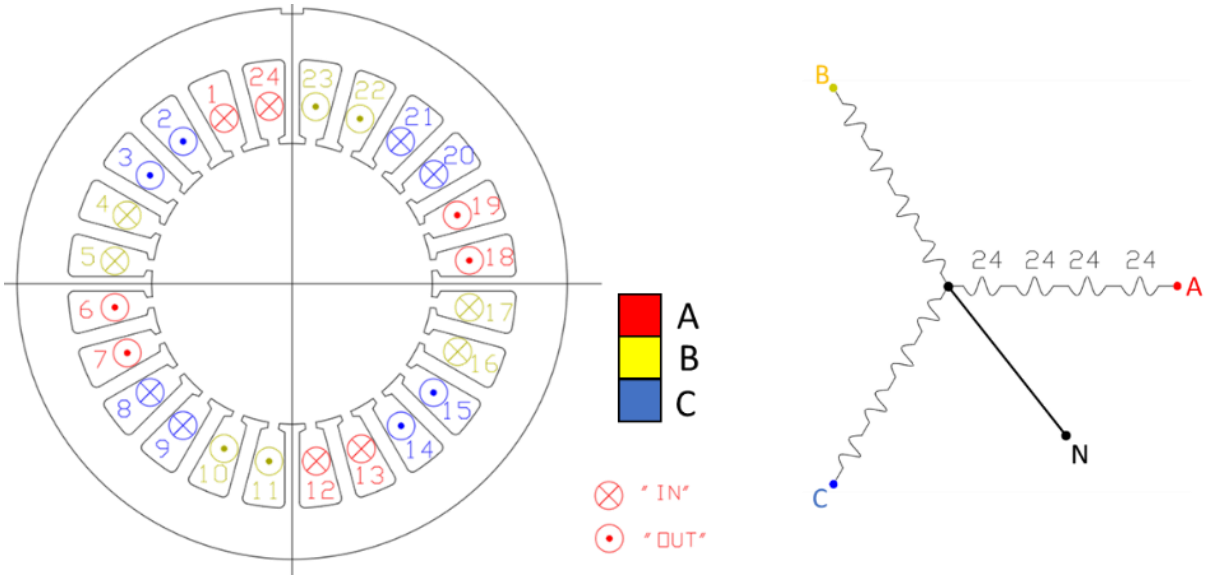

(b) Coil locations in stator teeth (c) Winding circuit

Fig. 2.2.2 Machine winding layout.

From fig 2.2.2 (a) and (b) the coils can be seen to have a span of 4 slots. Each phase is formed of 4 coils, each with 2 wires in parallel and 24 turns per coil. For this chapter, the details of the casing will be omitted as it will be discussed in great depth in chapter 3 when the 3D mechanical model is generated. However, it is important to note that given the high current density of the windings in the stator core a water coolant system is required to prevent the machine overheating at high loads and as such increases the complexity of the machine.

2.3 Measuring the machine

Having established the key specifications of the machine the next step is to measure the motor. This is a standard process to capture the key characteristics of the motor ensuring the fabricated machine performs as expected, and in this case allows the FE model to be validated. The measurement occurs in several distinct phases, detailed in Table 2.3.1.

Table 2.3.1 Summary of machine performance measurement

Test type	Test#	Machine state	Process	Output
Static	1	Off rig	LCR measurement	• Phase resistance • Line to line resistance • Phase inductance VS. rotor position • Line to line inductance VS. rotor position
	2		Cogging measurement	• Cogging torque over 1 mechanical cycle
No Load	3	Motor mounted to rig. Linked to dynamometer via couplings and inline torque transducer. Inverter & control offline	Machine rotated at 1200rpm	• Back EMF waveform (Phase & Line to line) • Identify any concerns across speed range

Load	4	Dynamometer setup same as no load, coolant system connected, phase lines linked to inverter via power analyser and all control and DAQ systems engaged	T-N curve, Spin motor at set speeds, sweep current angle to find maximum torque @ current limit	• Speed • Torque • Electrical power, mechanical power, efficiency • Phase currents, voltages, PF • Id, Iq • Temperatures
	5		Efficiency map Utilise MTPA control method to map maximum efficiency at a number of speed and torques	• Speed • Torque • Electrical power, mechanical power, efficiency • Phase currents, voltages, PF • Id, Iq • Temperatures

Each of these steps will be repeated with the FE model and the results compared in order to ensure good parity between the measured and the model; any significant errors will mean the force data outputted by the model is erroneous making the vibratory simulation less representative of the real machine.

2.3.1 LCR measurement

The first step in characterising the machine is to measure the basic electrical characteristics of the windings using an LCR meter. One advantage of the prototype machine is that during the winding process a low-gauge wire was linked to the neutral point was installed allowing the phase and line to line characteristics to be measured directly. The measurement process is shown in Fig. 2.3.1.

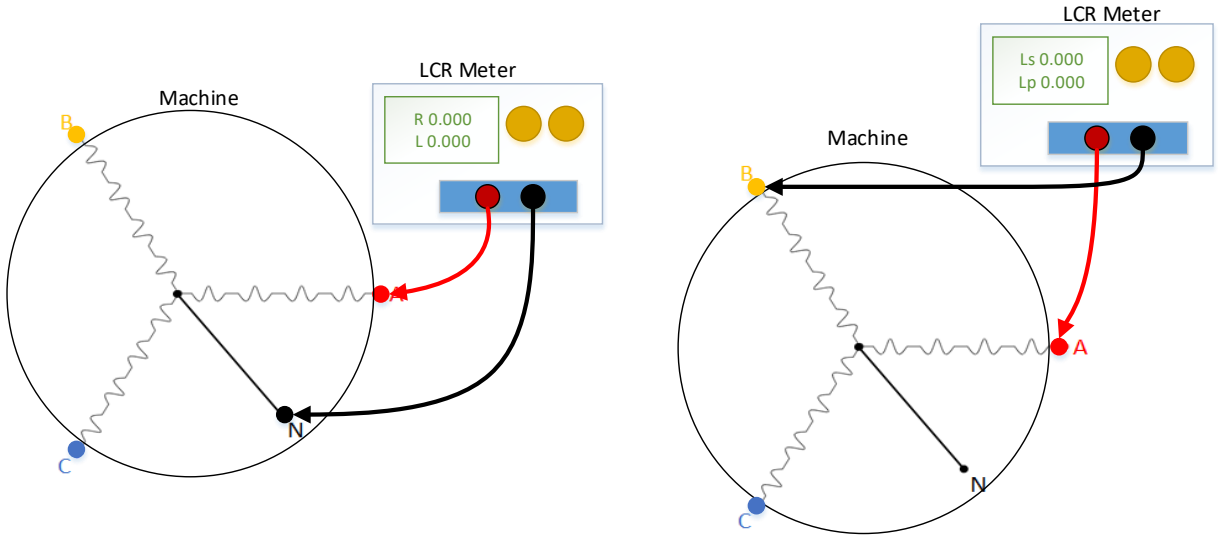

(a) Phase line measurement. (b) Line to Line measurement.

Fig. 2.3.1 Measurement of winding electrical characteristics.

The full table of results is provided.

The winding resistances are the simplest to measure and the results can be seen in Table 2.3.2.

Table 2.3.2 Measured phase and line to line resistances.

Phase resistance (Ω)		Line to line resistance (Ω)	
A	0.413	A-B	0.735
B	0.414	B-C	0.734
C	0.413	C-A	0.734
Average	0.413	Average	0.734

The average phase resistance can be seen to be 0.413 Ω. Given the winding circuit is 4 coils in series (fig 2.3.1 (c)) the coil resistance can be approximated to 0.413/4 = 0.103Ω.

Following on from the resistance measurement the inductances are measured. As previously explained the inductance is a 1st order phenomenon therefore needs an AC signal to be measured. In addition, the saliency of the IPM rotor means the inductance will vary depending on the rotor position. An initial sweep of each phase is undertaken, rotating the rotor in 15° (30° electrical) steps with the LCR meter set to input a 5kHz sinusoidal waveform.

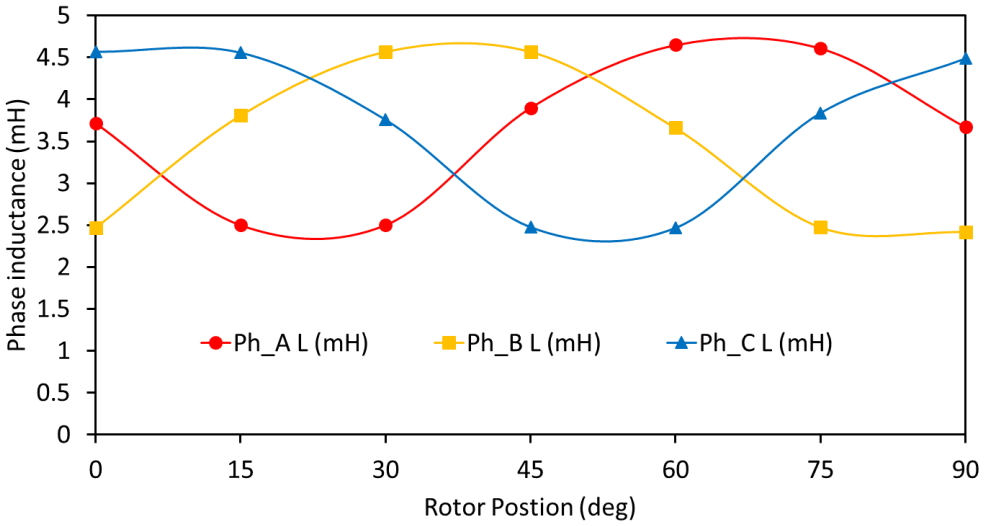

(a) Phase inductances.

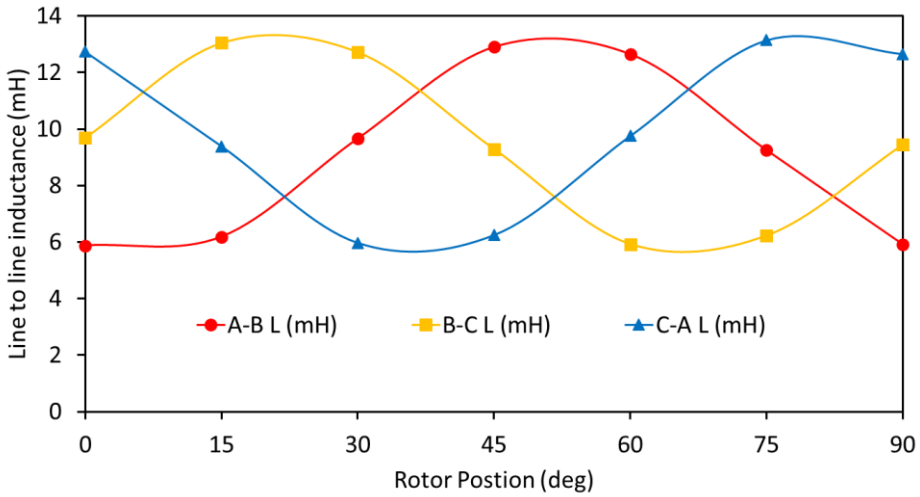

(b) Line to line inductance.

Fig. 2.3.2 Phase and line to line inductances in the machine versus different rotor position.

The data from the charts in fig 2.3.2 can be seen in Table 2.3.3.

Table 2.3.3 Measured inductance values for phase and line to line.

Angle (mech)	Angle (elec)	Phase			Line to Line		
		Ph_A L (mH)	Ph_B L (mH)	Ph_C L (mH)	A-B L (mH)	B-C L (mH)	C-A L (mH)
0	0	3.719	2.47	4.57	5.875	9.69	12.73
15	30	2.5	3.81	4.56	6.19	13.05	9.38
30	60	2.5	4.57	3.76	9.67	12.72	5.96
45	90	3.9	4.57	2.479	12.91	9.29	6.24
60	120	4.65	3.66	2.47	12.65	5.925	9.75
75	150	4.61	2.476	3.84	9.25	6.23	13.14
90	180	3.67	2.42	4.49	5.91	9.45	12.65

Given the low resolution of the sample (15 deg. mechanical = 30 deg. electrical) and the low currents utilised by the LCR meter mean that these measurements are only useful to check the windings and magnet circuit for any major concerns. From the results the 3 phases are well balanced reaching the same maxima and minima comfortably within the error bands expected during measurement.

2.3.2 Cogging torque measurement

The measurement of the cogging torque on machine is deceptively difficult; the rotor has to be rotated and held in precise angular steps and the steps must be small enough to give a good picture of the torque waveform. For this machine, the cogging must be measured off rig; linking the machine to the much larger dynamometer complicates the measurement process even more as the much larger inertia acts as a mass damper and makes it difficult to control the position of the rotor over one or more cogging cycles. Other methods use specialised torque sensors which are good in terms of precision but are expensive. The technique used is much simpler and utilises a method detailed in [ZQZ09b]. The stator is fixed into a lathe (or similar precision device) which can be rotated and held in precise angular steps. The rotor shaft has a balance beam attached which has one end resting on a set of digital scale. A weight is placed on the beam over the scale to act as a preload and prevent the bar from coming away from the scales. The stator is then rotated in precise steps causing the relative position of the stator to move from that of the rotor and the variation in force is recorded using the scales. The torque is obtained simply using the following equation [ZQZ09b]:

$$T_c = L_b\left(F_{reading} - M_{pre_load}\right) \quad (2.1)$$

where T_c is the resultant torque, L_b is the beam length, $F_{reading}$ is the reading from the scales and M_{pre_load} is the pre-load mass. Fig 2.7 illustrates the method and the machine setup.

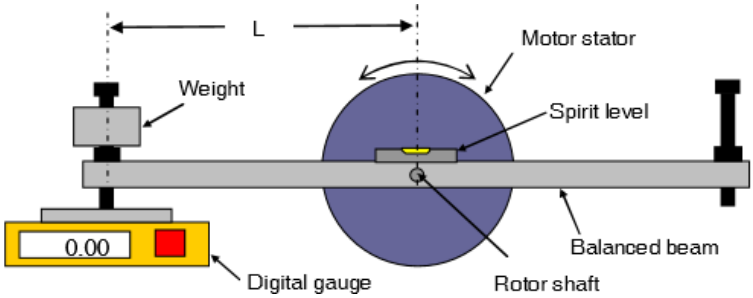

(a) Schematic diagram of the cogging torque measurement from literature [ZQZ09b].



(b) Photograph of the baseline machine under measurement.

Fig. 2.3.4 Illustration of cogging torque measurement.

The machine is measured in 1-degree (mechanical) steps for 1 electrical cycle and is shown in Fig. 2.3.5.

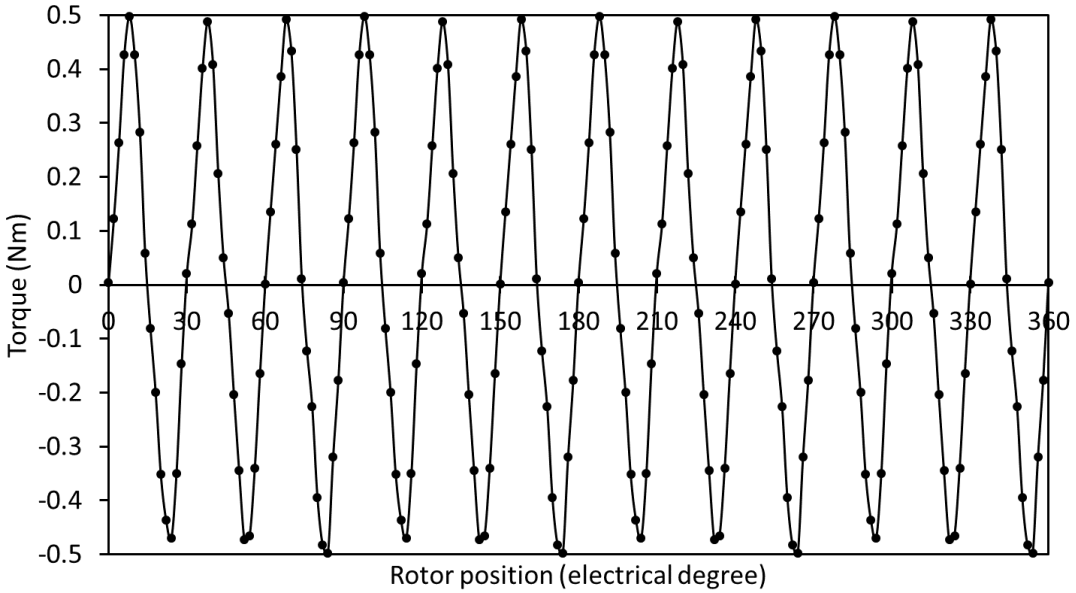

(a) Measured cogging waveform

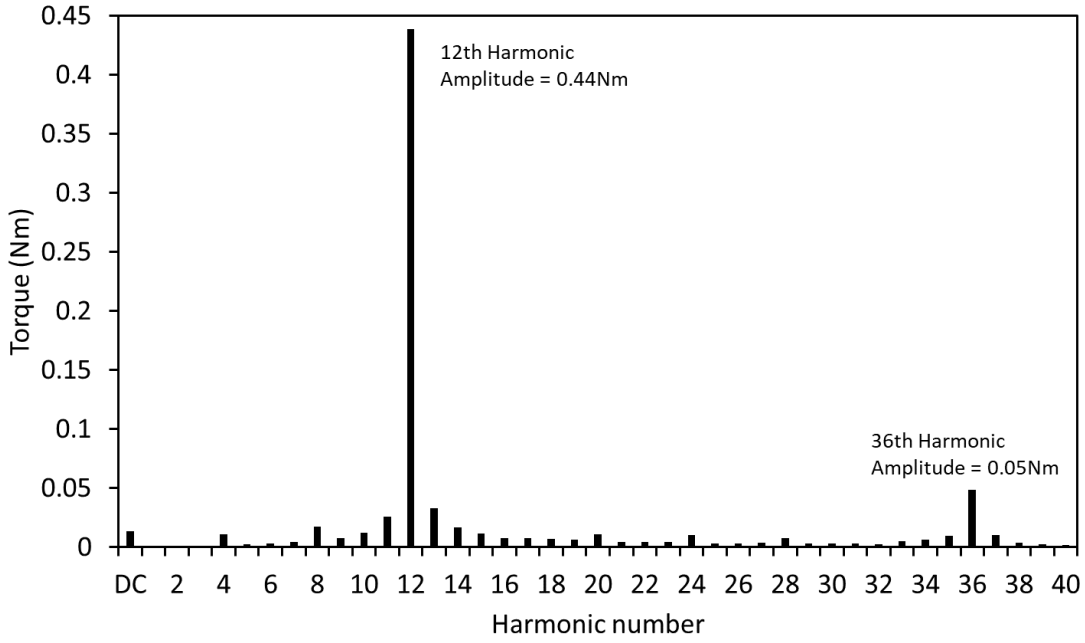

(b) Measured cogging FFT.

Fig. 2.3.5 Measured cogging torque over 1 mechanical cycle.

Table 2.3.5 Cogging measurement key results.

Item	Torque (Nm)
Max	0.50
Min	-0.50
Peak to Peak	1
Fundamental	0.44

From the results the waveform is relatively well balanced. Like the inductance measurement the main concern is the low resolution of measurement; 1 cogging cycle is 15 degrees mechanical, so 1 mechanical degree is 360/15 = 24 degrees of a cogging cycle. From the FFT the fundamental is very clear at the 12th harmonic which is correct (1 electrical cycle = 12 cogging cycles) as well as the 36th harmonic but the low sampling rate means the waveform is non-sinusoidal, introducing a large number of low amplitude harmonics across the frequency domain.

2.3.3 No load testing.

The machine is mounted to the test rig and is coupled to the dynamometer. Using the dynamometer, the rotor is spun to 1200rpm (40Hz electrical) and the back EMF is measured using 3 differential probes (1 per phase) linked to an oscilloscope. The differential probes are utilised primarily as a safety mechanism to protect the oscilloscope from high voltages in the case the rotor is rotated too quickly such that the induced EMF exceeds the voltage rating of the oscilloscope either through user error or some issue with the dynamometer. The system diagram is shown in fig. 2.3.6.

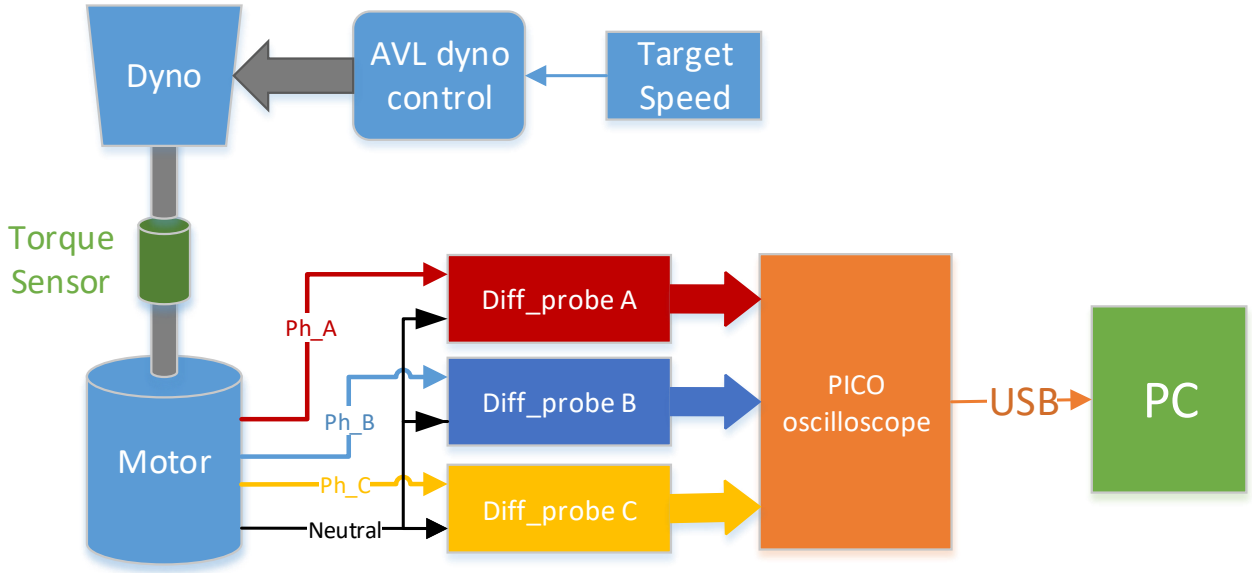

Fig. 2.3.6 System diagram back EMF measurement.

Temperature data is also captured using one of the thermocouples embedded in the stator core and showed the machine temperature averaged 19.9°C during the no-load measurement. The results of the phase and line to line measurements are shown in Fig. 2.3.7.

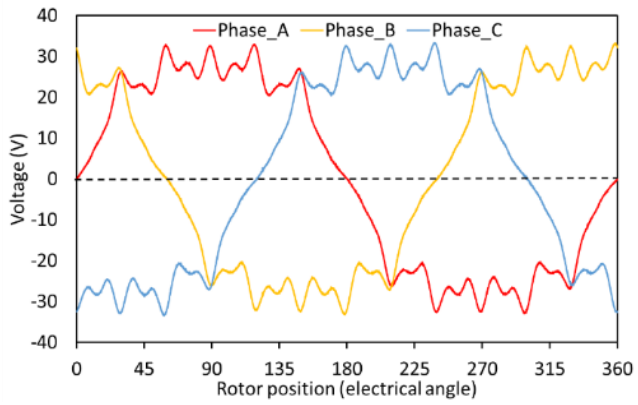

(a) Phase line EMF.

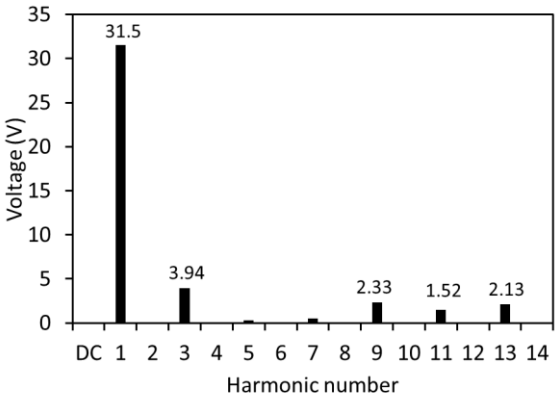

(b) Phase line FFT (phase A).

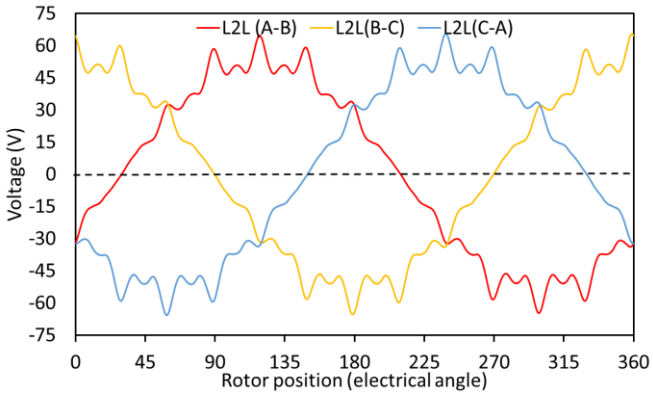

(c) Line to line voltage.

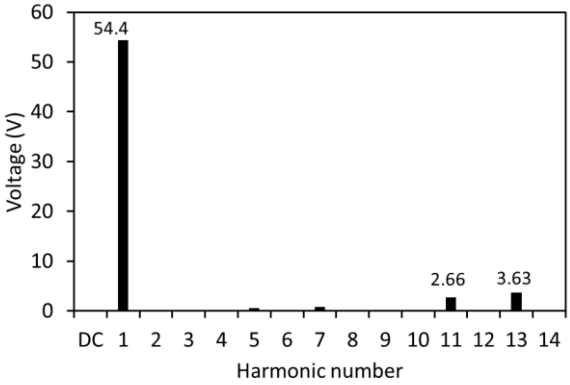

(d) Line to line FFT (A-B)

Fig. 2.3.7 Back EMF phase and line to line measurement @ 1200rpm.

The key resultant waveform data are shown in Table 2.3.5 and the harmonic amplitudes are shown in Table 2.3.6.

Table 2.3.6 Summary of back EMF results (speed = 1200rpm).

	Phase			Line to Line		
	A	B	C	A-B	B-C	C-A
Max (V)	33.02	33.22	33.34	64.78	65.43	65.59
Min (V)	-32.99	-33.25	-33.45	-64.78	-65.38	-65.80
RMS (V)	23.35	23.49	23.58	45.81	46.27	46.38
PP (V)	66.01	66.46	66.80	129.57	130.81	131.39

Table 2.3.7 Back EMF results FFT key harmonic amplitudes.

Harmonic	Phase A	Line to Line (A-B)
Fundamental	31.51	54.43
3rd	3.94	N/A
9th	2.33	N/A
11th	1.52	2.66
13th	2.13	3.63

The results show good balancing between the phases with the profiles matching closely and very small differences between the peak values of each. The waveform is sinusoidal in nature but is by no means smooth, as is shown in the FFT of phase A which shows the 3rd, 9th, 11th and 13th harmonics to be the main contributors to the non-sinusoidal nature of the waveform. The line-to-line results by their nature filter out the 3rd and 9th harmonics. However, the 11th and 13th are still present.

2.3.3.1 High speed resonance concern

As is anticipated with testing any complex system several concerns were encountered during the setup and measurement of this machine which had to overcome in order to run the machine. One concern, however, could not be overcome in the limited time on the test rig. As the rotor was accelerated past 7500rpm a distinct roaring noise began to be heard from the test chamber that became very loud at ~8000rpm. The test chamber can only be run with the door closed due to the safety interlock system and has a high level of sound insulation in the walls and doors so to be clearly audible outside indicates a serious problem with the driveline. Fig. 2.3.8 highlights the concern as measured on the torque sensor.

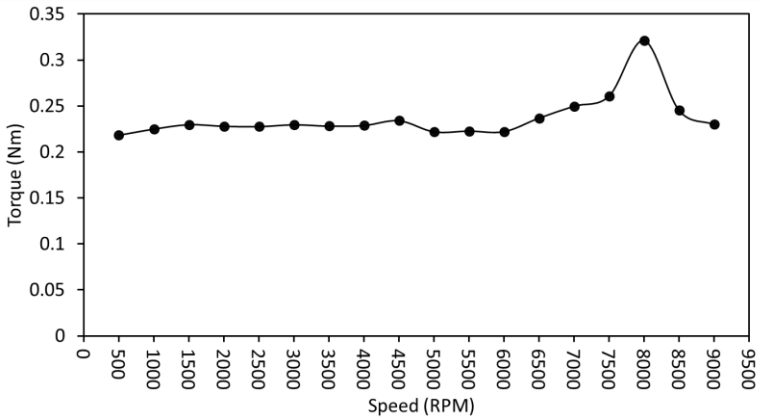

Fig. 2.3.8 No load torque measurement highlighting resonance concern.

The rotor had been balanced and certified to 11,000 rpm so the concern had to be some imbalance in the driveline or some component hitting a natural frequency at this speed. Unfortunately, during the investigation the rear stub-shaft onto which the encoder is mounted sheared just after the rear bearing, the damage is shown in Fig. 2.3.9.



(a) Photo of the sheared shaft end

(b) Location of the shear on the assembly

Fig. 2.3.9 Image of failed rear encoder shaft mount.

This was a serious concern which could have ended the load testing before it could even start. With no means to mount the encoder load testing would be very difficult and vector control impossible without a position sensor. Fortunately, a spare rotor shaft had been fabricated and balanced during the original fabrication of the machine to mitigate any such concern. The broken shaft was carefully swapped out and the machine carefully re-assembled and mounted back on the rig. To prevent recurrence of the failure the following steps were undertaken:

- Deflection tolerances of the drive line components tightened and strictly adhered to (reduce deflection forces).
- Speed limit of 7500rpm imposed.

There was no 3rd rotor shaft and the limited time on the rig meant there was no time to fabricate a new shaft, so the imposition of a speed limit was necessary to protect the machine and prevent any further delays to the testing.

2.3.4 Load testing – Measuring the T-N curve

2.3.4.1 Introducing the test rig

Measuring the T-N curve requires a full drive, control and data acquisition system to operate the machine such that the performance of the machine can be maximised and, of equal importance, captured in as much detail as possible for post-process analysis.

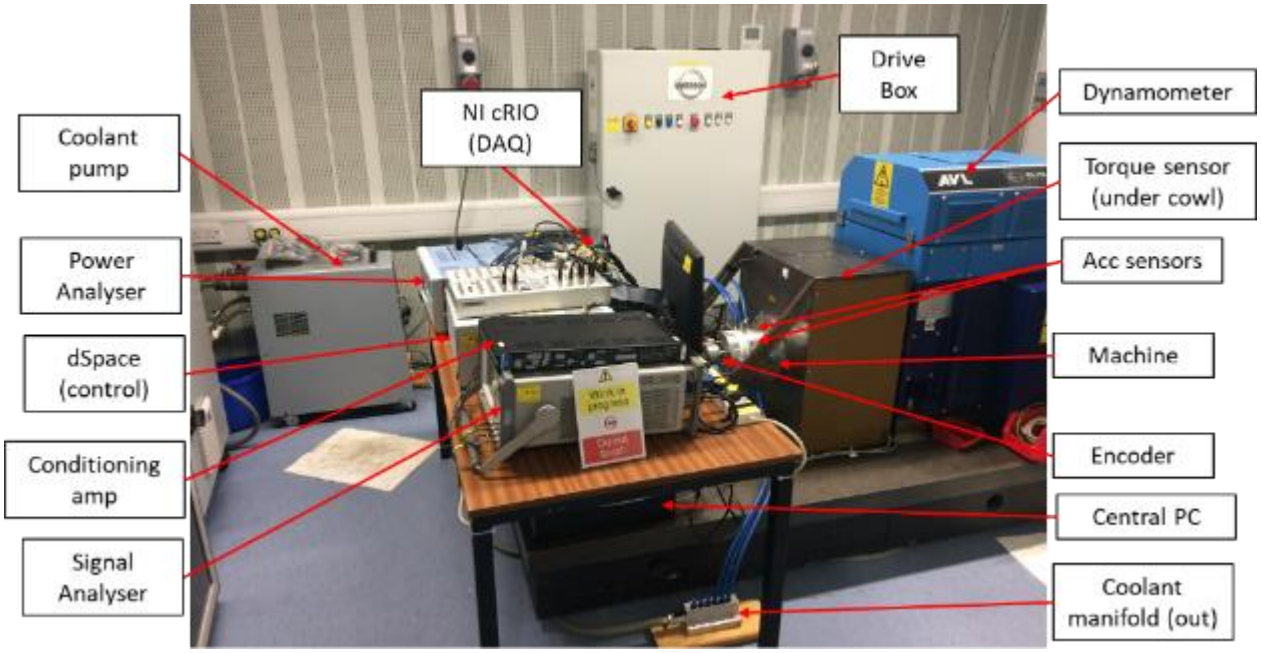

(a) Photo of the full test rig setup and ready to run.

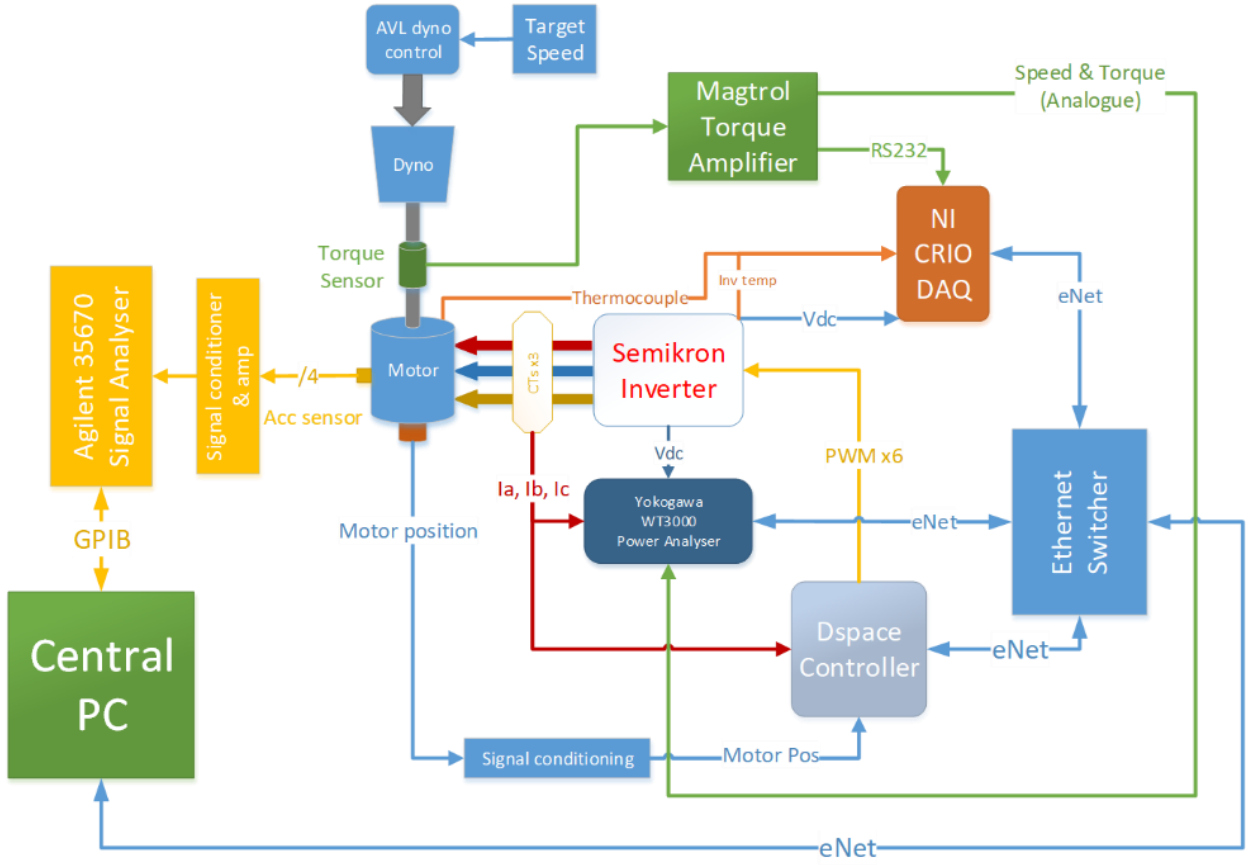

(b) Block diagram of the test rig.

Fig. 2.3.10 Block diagram of the full dynamic test rig.

A short description of each component is detailed in Table 2.3.8 for convenience.

Table 2.3.8 Functionality of each block of the machine test rig

Block	Function
Motor	Machine under test
Torque sensor	Inline torque sensor located between the dyno and motor that measures the rotational speed and torque output of the machine
Torque amplifier	Provides power to the torque sensor and acts as a signal conditioner to output the speed and torque in analogue and digital (RS232) formats.
Dynamometer	Load machine for the motor to act against. The dyno is operated in speed mode whilst the machine is operated in torque mode
Encoder	Optical encoder uses engraved disk to give precise angular position of the rotor to the dSPACE controller to allow for vector control of the machine.
Inverter	100kW 3 Phase inverter by Semikron switching the current from the DC link into the 3 phase AC signals required to generate the rotating field in the machine windings as dictated by the controller
Controller	Real time control system using dSPACE platform that takes in the positional data of the motor and generates the switching signals to the inverter in order to control the machine to the target torque
Power Analyser	Yokogawa WT3000 Power analyser sits between the inverter and the machine to monitor the electrical power into the machine as well as the mechanical power of the system (from the torque sensor) in order to calculate the efficiency of the system as well as key parameters such as the power factor
Data Acquisition (DAQ)	National Instruments Compact RIO data acquisition (DAQ) system, interfaces with all the different measurement systems (RS2323/Ethernet/analogue/ thermal) synchronising the data and then transmitting the collated data to the central PC for monitoring and data logging
Acceleration sensors	Sensitive piezo-electric sensors attached to the casing of the motor to capture the vibrations on the machine outer casing
Signal conditioner and amp	Removes common mode noise and boosts (if required) the signal from the acceleration sensor to improve the accuracy of the readings.
Signal analyser	Generates FFT for each of the acceleration channels recorded by the system, The unit is trigger and data is captured via a GPIB comms link to the central PC
Central PC	Monitoring & datalogging hub for the whole system. Utilises a Labview system developed by the author to capture all the data generated within system

Both the block diagram in fig 2.3.10(b) and table 2.3.8 show the acceleration sensors and the associated amplifier and signal analyser used to measure the vibratory behaviour of the machine under various loads. This will be explored in much greater depth in chapter 6 of this thesis where the final dynamic model is developed. For this section the only real comment to make is every measurement of the machine generates a trigger to the signal analyser to capture the output of the acceleration sensors meaning each test point and each current angle sweep has a corresponding set of acceleration data recorded.

2.3.4.2 Controlling the machine

All testing at this point have had the machine in a passive state being measured off the rig or rotated by the dynamometer. For operating the machine at load some form of control is required. This is achieved using vector control developed using Simulink and dSPACE to operate the machine. A summary block diagram can be seen in fig. 2.3.11.

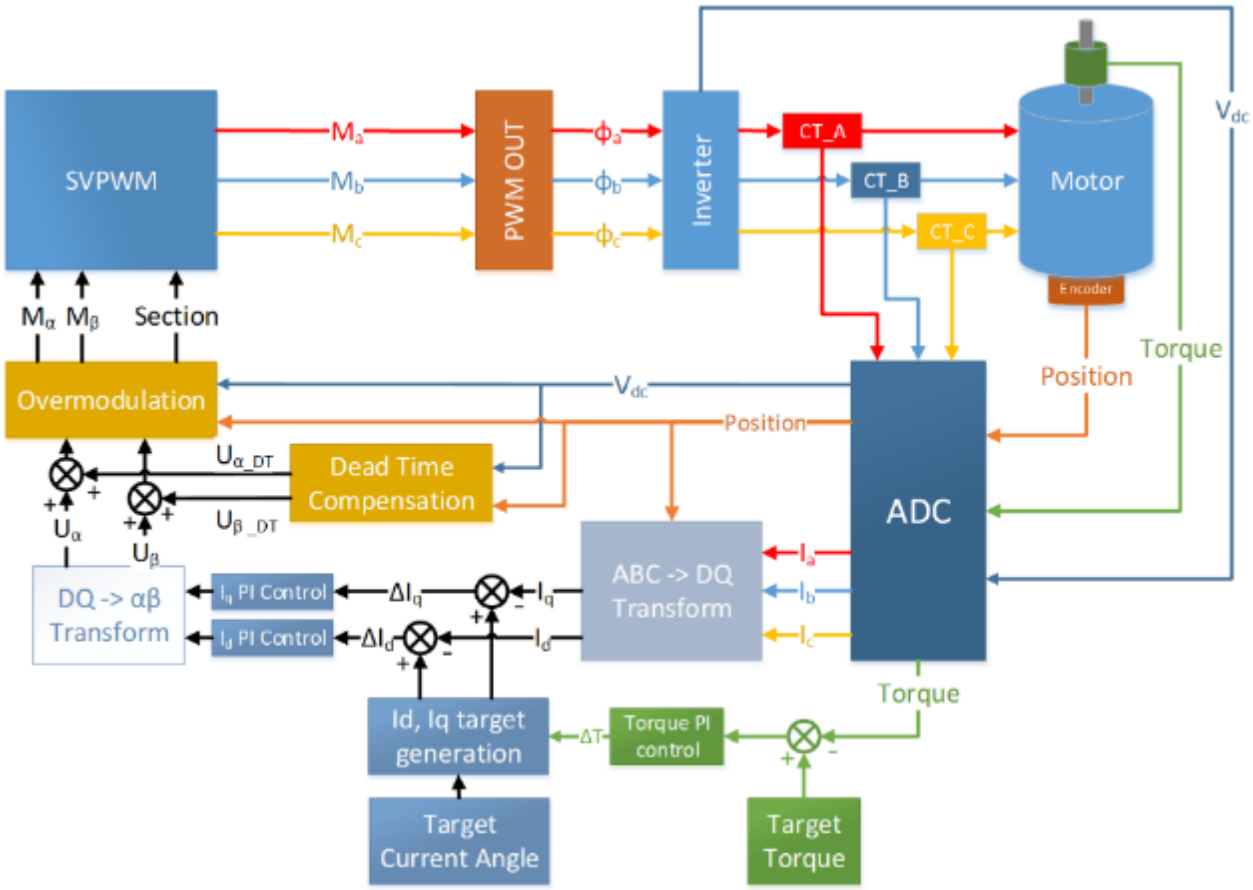

Fig. 2.3.11 – Block diagram of the controller.

From fig 2.3.11 it can be seen that the system runs a continuous loop of the following tasks:

1. Sample the instantaneous torque, phase currents, voltage, and rotor position.
2. Transform the 3-phase current into a stationary frame co-ordinate system (dq-axis frame).
3. Generate error signal based on current torque VS demand torque.
4. Use PI controller(s) to adjust I_d and I_q currents according to the error from (3).
5. Generate voltage vector based on new current values.
6. Transform voltage vector into αβ-axis frame.
7. Add Compensation for inverter and control dead time.
8. Determine if modulation index = 1 and implement overmodulation strategy if required.
9. Transform final voltage into 3 phase space vector PWM signal.
10. Output signal to hardware.

This is a fairly standard control methodology for this type of machine, the only care that must be taken is tuning of the I_d and I_q PI gains; maintaining control of the machine is very important in particular at high speeds to prevent damage to the inverter, dynamometer or power supplies.

2.3.4.3 Mapping the T-N curve

The T-N curve describes the maximum torque and power boundary of the machine on a speed-torque graph. The limits of the machine are dictated by the maximum voltage (V_{max}) and maximum current (I_{max}). These

limits are typically set by the VA rating of the power electronics and power supply; these parts tend to be higher cost and more sensitive to failure if overloaded than the machine, so it is best practice to consider the full system when setting the limits. In this case the limits are:

- V_{max} = 300V_{dc}
- I_{max} = 26.7 A_{rms}

Given the chosen control strategy it is convenient to convert these values into vectors on the dq-axis plane, $V_{dq(max)}$ and $I_{dq(max)}$. (2.2) and (2.3) show the conversion formula.

$$V_{dq(\mathrm{MAX})} = \frac{V_{max}}{2} \tag{2.2}$$

$$I_{dq(MAX)} = \sqrt{2} I_{max} \tag{2.3}$$

where $V_{dq(Max)}$ (Volts) is the net voltage vector on the dq-axis plane, V_{dc} is the DC bus voltage, I_{dq} (Amps) is the net current vector on the dq-axis plane. This establishes the maximum voltage and current that can be fed into the machine and ultimately dictates what torque can be generated at what speed.

The next point is to understand the EMF generated by the machine as it rotates at different speeds. The formula for calculating the q- and d-axis voltages can be seen in (2.4) and (2.5) and the resultant voltage vector is given in (2.6).

$$V_d = -\omega_e \lambda_q + R_{coils} I_d \tag{2.4}$$

$$V_q = \omega_e \lambda_d + R_{coils} I_q \tag{2.5}$$

$$V_{dq} = \sqrt{\left(V_d^2 + V_q^2\right)} \tag{2.6}$$

where ω_e is the electrical speed in rad/s, R_{coils} is the coil resistance (Ω), λ_x is the flux (Wb), I_x is the current (A), V_x is the voltage (V), d and q are the d-axis and q-axis references, respectively.

A simple method of working out whether the machine has reached the set voltage limit is the ratio of V_{dq} to $V_{dq(max)}$, this is sometimes to referred to as the modulation factor (M_f). (2.7) highlights this.

$$M_f = \frac{V_{dq}}{V_{dq(MAX)}} \tag{2.7}$$

From (2.7) it can be seen that as the EMF in the machine approaches the maximum, the modulation factor, M_f, will approach 1. At this point the current controller will begin to saturate leading to loss of control of the machine. To avoid this, flux weakening control is implemented [TMJ87], [SM89].

Flux weakening control is in essence a method of applying a demagnetisation current onto the d-axis of the machine in an attempt to temporarily drop the flux linkage between the permanent magnets and the armature coils. Lowering the flux linkage means the EMF generated at a given speed is reduced and consequently the modulation factor drops allowing the machine to speed up. For an IPM machine, the shifting of the current angle has the added benefit of allowing the reluctance torque to be utilised, which will be discussed in the efficiency mapping process.

Flux weakening comes at a cost, however, dropping the ψ_m component from the magnet reduces the mutual torque and the technique comes with the very real risk of the d-axis armature reaction irreversibly demagnetising the permanent magnets if not managed correctly.

To understand the operation of flux weakening, the favoured method [TMJ87], [SM89], [WLS94] is to plot the voltage and current limits of the machine on the d-q axis plane. Fig 2.3.12 shows the current and voltage limits [SM89], [JRH10].

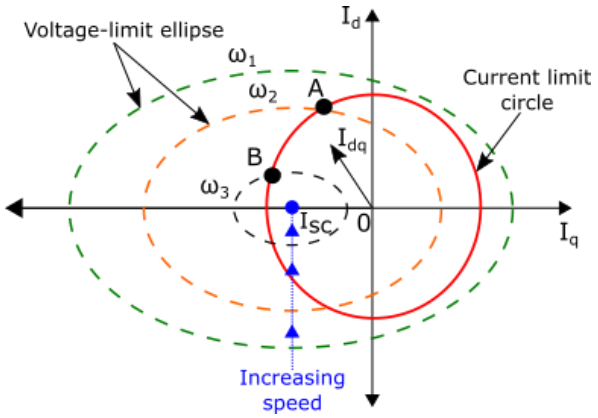

Fig. 2.3.12 Illustration of voltage and current limits in an IPM machine [SM89].

It can be seen that the current limit forms a circle centred on the origin, 0, the circle is dictated by

$$I_{dq(max)}^2 = I_d^2 + I_q^2 \tag{2.8}$$

The current limit, $I_{dq(max)}$, is typically determined by the current rating of the inverter as it represents the maximum current the system can inject into the machine. In the case of the tested baseline machine the inverter VA rating greatly exceeds that of the machine as the drive box was designed to accommodate the full size EV machine with some minor modifications (different current sensors) to allow the smaller baseline machine in this thesis to be driven. Therefore, $I_{dq(mx)}$ is dictated by the machine to prevent damage. Within the control software there is safety logic to prevent the current exceeding the maximum current of the machine (26.7A_{rms}).

The voltage limit is very different in its form. The limit is an ellipse, (2.9) [SM89], [JRH10], which is a function of the difference in L_d and L_q inductances that is a key attribute of IPM machines.

$$(E_0 + X_d I_d)^2 + \left(X_q I_q\right)^2 = V_{dq(\max)}^2 \tag{2.9}$$

where E_0 is the EMF fundamental (V), X_d is the d-axis reactance, and X_q is the q-axis reactance.

It is important to note that the ellipses ω_1 and ω_2 in Fig. 2.3.12 is a *current* ellipse and describes the maximum current the machine can operate to with a given voltage limit, $V_{dq(max)}$. The ellipse is centred on the point (I_{sc},0) on the x-axis where I_{sc} is the short circuit current and is defined by.

$$I_{sc} = \frac{-E_0}{X_d} \tag{2.10}$$

From (2.9) it can also be seen that if $X_d = X_q$ (i.e. an SPM machine) then the voltage limit will be a circle. However, it forms an ellipse if $X_q > X_d$ as is the case for an IPM machine which is why the voltage limits depicted are elliptical in form. Setting the shape of the ellipse aside the key point about the voltage limit is that as the rotor speed increases the limit decreases. In Fig. 2.3.12 three different ellipses can be seen representing 3 different speeds:

- Green line (ω_1): Low speed operation, limit due to voltage greatly exceeds the current limit meaning the current limit (red line) acts as the limiting factor.
- Orange line (ω_2): Base speed, limit due to the voltage has dropped such that it intersects the current limit, the machine is now limited by both the current limit and the voltage limit.
- Black line (ω_3): High speed operation, $-I_d$ current has to be very high in order to clamp the EMF from the rotor sufficiently to keep the current vector within the voltage limit ellipses.

What this means in terms of mapping the T-N curve is that when the base speed is struck the machine must balance the maximum current and voltage limits to maintain control and prevent damage to the machine or inverter. Fig 2.3.13 shows a more practical example of the limits [SM89], [WLS94].

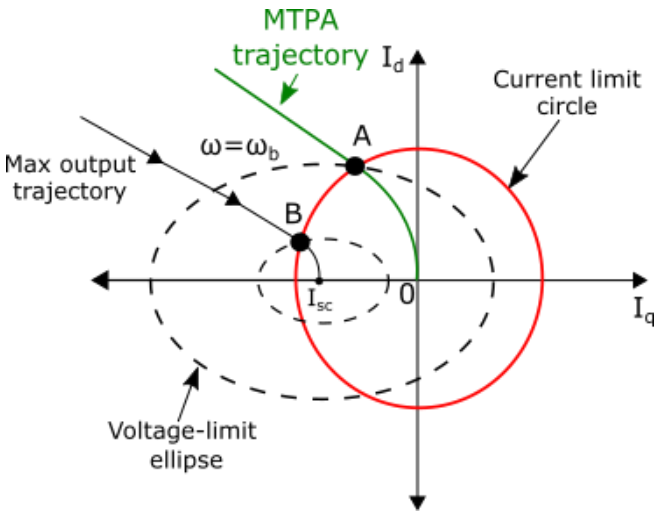

Fig. 2.3.13 Operating at the current and voltage limits.

Utilisation of the reluctance torque component gives the MTPA trajectory shown in Fig. 2.3.13 with point 'A' being the location of maximum torque. It should be noted that the location of I_{sc} is within the current limit circle, reflecting the oversized inverter used. The effect of the torque due to the voltage limit at higher speed is as follows [WLS94]:

- At low speeds maximum torque is achieved by placing the current at point 'A' on the MTPA trajectory, representing the maximum torque of the machine at the current limit.
    - This is region I or the constant torque region.

- When the rotor speed increases to a certain point, the current and voltage limits (line $\omega=\omega_b$ in Fig 2.3.13) intersect, attempting to drop the current angle (e.g. -Id = 0) will breach the voltage limit causing the modulation index to rise above 1 and induce the aforementioned loss of control.
    - This is the base or corner speed of the machine.
- As the speed increases above ω_b the maximum torque drops as the voltage limit drops proportionally to the speed forcing the maximum current vector to follow the path "A" to "B" in Fig 2.3.13.
    - This is region II or the constant power region as the drop in torque is proportional to the gain in speed.
- When point 'B' is reached the minimum speed of the maximum-output current vector due to the dominance of the back EMF of the machine at such high speeds, the current vector will follow the path from "B" to I_{sc}.
    - This is region III or the reduced power region.

It should be noted that region III operation can only occur if the inverter is oversized, i.e. the current limit of the inverter exceeds the short circuit current of the machine. An interesting side effect of region III operation is that when the current controller reaches I_{sc} from point 'B' the machine can theoretically be driven to infinite speed [JRH10], [ZQZ07b]. Practically of course this is not feasible, switching limitations of the inverter plus the mechanical limits of the machine mean the speed has to be limited. An illustration of the 3-regions on a T-N curve can be seen in Fig. 2.3.14 [ZQZ07b].

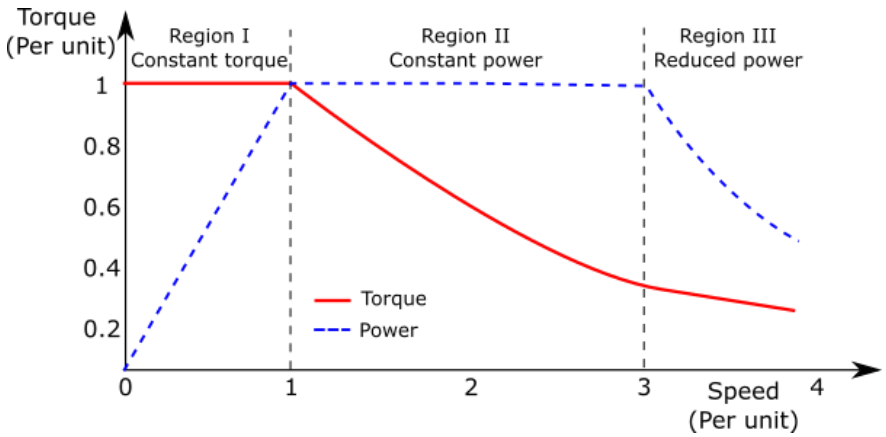

Fig 2.3.14 Idealised T-N curve highlighting regions I, II, and III.

In this application the imposed maximum speed limit of 7500rpm due to the resonance concern means during the testing the current vector will sit somewhere between 'A' and 'B' in the constant power region shown in Fig. 2.3.13.

Using the circle diagram in Fig. 2.3.13 as a guide the methodology of mapping the T-N is defined as:

- At low speed, increase current towards the limit and increment the current angle until the crossover point between the MTPA trajectory and the current limit is met.

- Increase the speed in regular steps, paying attention to the calculated modulation index, M_f.
    - When M_f approaches 1 then the voltage limit is close so increase the current angle by injecting higher $-I_d$ current.
    - Creep the target torque higher until maximum is found, taking care not to breach the current or voltage limits.
- At high speeds beyond the base speed the machine is sped up to a known speed, typically 5000rpm to allow a small amount of torque to be applied and current angle increased to drop M_f before the machine is carefully accelerated to the target speed.
    - This keeps the current vector within the voltage limit, some increments to the current angle may be required to maintain controller stability as the speed increases.
    - Once at the target speed the target torque is increased, and the current angle adjusted to find until the maximum stable torque at the voltage and current limits.
- Care must be taken to monitor the temperature of the machine at each stage.
    - The DAQ system has an alarm system in place to warn the user the temperature of the machine or inverter is reaching critical levels.

The control software is very much prototype in nature and thus does not contain any derate systems that would be found in a production drive. Thus, running a machine with such a high current density at maximum current at increasing speeds whilst giving the DAQ system time to capture the acceleration and performance data of the machine means great care must be taken not to overheat the machine. The DAQ system records the thermal channels and contains logic in it to warn the user when the machine is overheating. However, it is still up to the user to safely control the machine to a stop. This is of particular concern when the machine is running at high speed as the controller can be very sensitive; small adjustments to the current angle can lead to the machine breaching the current or voltage limits. In this situation high levels of concentration are required, and it can be easy to neglect the rising temperature in the machine at full load making an alarm system very useful.

The final point is the speeds chosen to sample. The ultimate aim is to develop a vibratory model of the machine which is time consuming to run; the more points there are to run, the longer the analysis period. Thus, a balance is required to ensure the performance envelope is characterised well but does not provide a data overload for later analysis. It was decided that 1000rpm steps was sufficient fidelity with additional points at 1500, 4500 and 7500 rpm due to the integer values of the different machine frequencies at these speeds. Integer values make it much easier to both operate the machine and quickly identify any concern both during measurement and post processing. This is illustrated in Table 2.3.9.

Table 2.3.9 Frequency components at each speed

Speed (rpm)	Mechanical Frequency (Hz)	Electrical frequency (Hz)	EM force frequency (Hz)	Cogging frequency (Hz)
1000	16.67	33.33	66.67	400
1500	25	50	100	600
2000	33.33	66.67	133.33	800
3000	50	100	200	1200
4000	66.67	133.33	266.67	1600
4500	75	150	300	1800
5000	83.33	166.67	333.33	2000
6000	100	200	400	2400
7000	116.67	233.33	466.67	2800
7500	125	250	500	3000

7500rpm is the maximum speed for the reasons stated in section 2.3.3.1 of this chapter.

Fig. 2.3.15 shows the results of the mapping process.

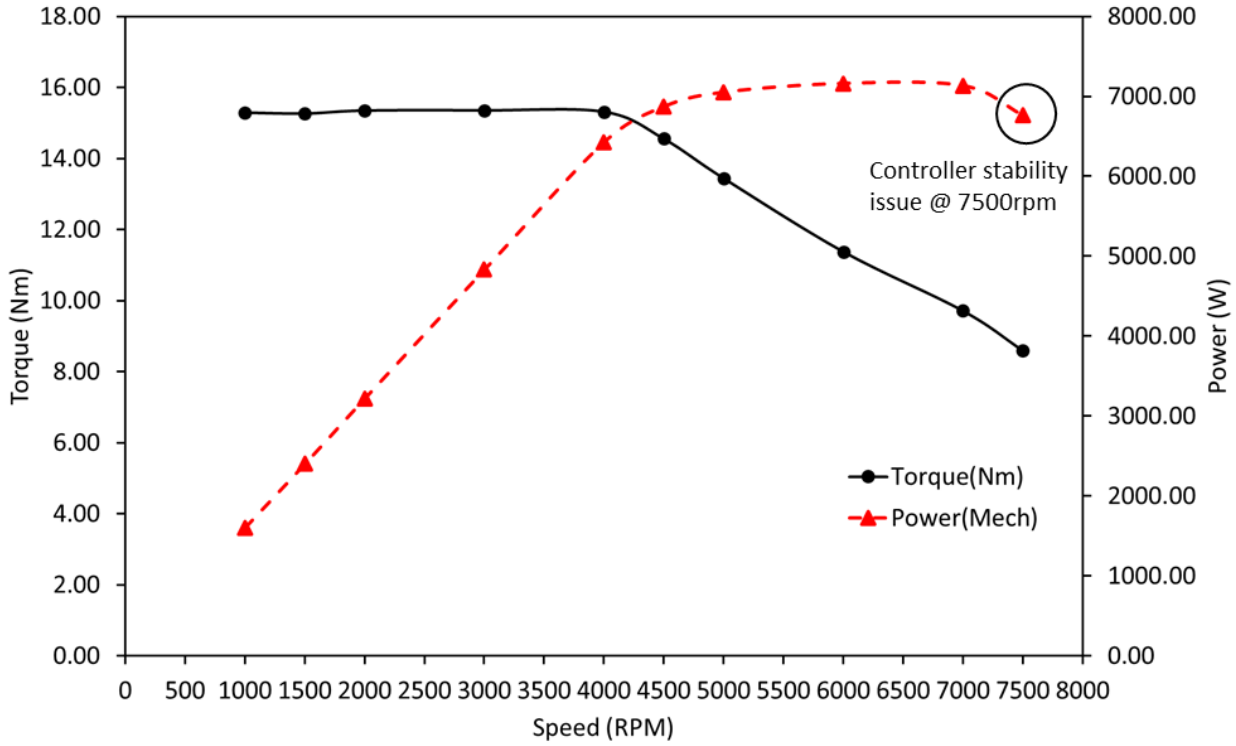

Fig. 2.3.15 – Measured T-N curve of the machine

The measured values are shown in Table 2.3.10, including the average measured temperature from both a thermal couple embedded in one of the slots of the stator core and one located on the outer shell of the machine to highlight the temperature of the machine at each point.

Table 2.3.10 Measured results of T-N curve

Speed (RPM)	Power IN (Electrical) (W)	Power OUT (Mechanical) (W)	Efficiency (%)	Torque (Nm)	I_{dq} (A)	β (°)	Avg core Temp (°C)	Avg Surface temp (°C)
1000	2652.48	1604.19	60.48	15.29	37.69	43.92	61.51	13.54
1500	3448.55	2402.03	69.65	15.26	37.52	44.00	60.50	12.49
2000	4376.24	3218.70	73.55	15.35	37.80	44.02	78.95	13.57
3000	5942.51	4830.20	81.28	15.35	37.74	44.02	62.52	13.25
4000	7590.69	6423.63	84.63	15.31	37.62	44.41	71.97	13.13
4500	8112.10	6869.29	84.68	14.56	37.58	59.01	88.02	14.47
5000	8302.62	7049.39	84.91	13.44	37.51	64.82	87.82	15.31
6000	8361.51	7159.94	85.63	11.38	36.36	70.03	82.48	14.22
7000	8440.71	7131.66	84.49	9.71	37.39	75.01	78.45	14.37
7500	7783.55	6761.39	86.90	8.6	32.74	74.02	66.46	15.08

Maximum average torque is observed to be 15.3Nm with a current angle of 44° up to 4500rpm where the voltage limit is approached, and controller has to apply a much larger current angle to maintain control. This means the base speed lies between 4000 and 4500 rpm.

The odd drop in the power at 7500rpm is due to a controller stability concern. This speed is around the point where the resonance concern began to make its appearance on the no-load measurements. The current shown for 7500rpm in Table 2.3.9 represents the maximum current that could be injected; all attempts to push towards the current limit and therefore the maximum torque ended with the controller becoming very unstable and losing control resulting in the system requiring immediate shutdown to prevent damage to the inverter. Thus, the point shown in Fig. 2.3.15 is the highest torque that could be maintained without de-stabilising the controller. There were no concerns when measuring torque points up to 8Nm at 7500rpm, and therefore, the efficiency and vibration were measured for all points up to 8Nm.

2.3.5 Mapping the machine efficiency

With the performance limits of the machine established the machine efficiency can now be mapped. The mapped points can be seen in Fig. 2.3.16.

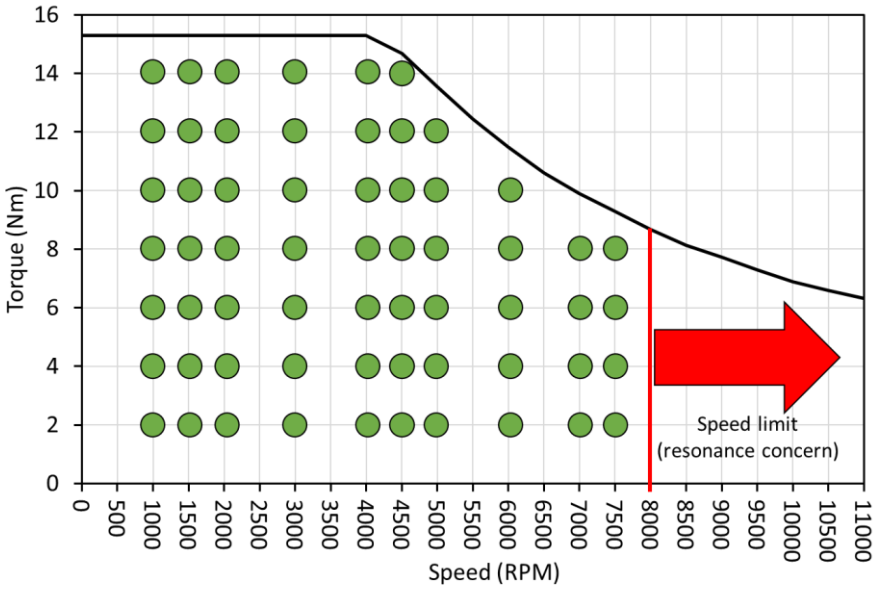

Fig. 2.3.16 Speed and torque points for mapping the efficiency.

The speeds and torque values used in fig 2.3.14 are shown in Table2.3.11

Table 2.3.11 Speed and torque values used in MEPA/MTPA mapping

Torque (Nm)	Speed (rpm)									
	1000	1500	2000	3000	4000	4500	5000	6000	7000	7500
2	✓	✓	✓	✓	✓	✓	✓	✓	✓	✓
4	✓	✓	✓	✓	✓	✓	✓	✓	✓	✓
6	✓	✓	✓	✓	✓	✓	✓	✓	✓	✓
8	✓	✓	✓	✓	✓	✓	✓	✓	✓	✓
10	✓	✓	✓	✓	✓	✓	✓	✓	X	X
12	✓	✓	✓	✓	✓	✓	✓	X	X	X
14	✓	✓	✓	✓	✓	✓	X	X	X	X

From table 2.3.11 it can be seen that the highest target torque at each speed point is held below the maximum torque as these were established in the previous section.

Two methodologies are investigated [ATDA11]:

- Maximum Torque Per Ampere (MTPA): Torque is fixed and minimum current for each torque point is established by sweeping the current angle.
- Maximum Efficiency per Ampere (MEPA). Similar to the MTPA method however the priority lies in finding the best balance between the copper and iron loss of the machine for every given point on the machine.

The two methods were both measured primarily to see if changing the target parameter of the sweep would yield any differences in the vibratory performance, in particular at the extreme edges of the machine performance where some differences in current angle would be observed due to the different priorities.

The procedure for measuring both the MTPA and MEPA is similar, the difference is the target variable being hunted. Fig 2.3.17 illustrates the process on the dq-axis plane for a target torque below the current limit.

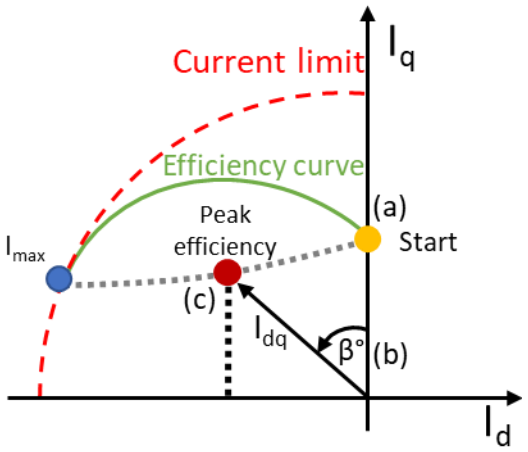

Fig. 2.3.17 Finding the peak efficiency point at a set torque point below the current limit on the dq- axis plane.

From Fig. 2.3.17, the procedure is:

1. Set the target speed using the dynamometer.
2. Increase the target torque on the controller causing the I_q current to rise to point (a) on Fig. 2.3.17.
    - If the target torque is greater than the maximum mutual torque, then some current angle (β) is applied to utilise reluctance torque to meet the target.
3. With the target torque fixed, slowly increase the current angle (β), shown at point (b) in Fig. 2.3.17, as the reluctance torque component increases the net current (I_{dq}) should begin to drop up to a certain point (c) in Fig. 2.3.17. Past this point, I_{dq} will start to rise again as the flux weakening reduces the PM flux linkage too far, dropping the mutual torque component which means more current is required to achieve the target torque.
4. The current angle is typically allowed to overshoot the point (c) in Fig. 2.3.17 by a few degrees to confirm the MTPA point has been located and then some fine tuning around (c) occurs to fix the optimum value.
5. All monitored variables at this point are captured and recorded for post-process analysis.

The procedure above is followed for both MTPA and MEPA methodologies, and the resultant efficiency maps can be seen in Fig.2.3.18.

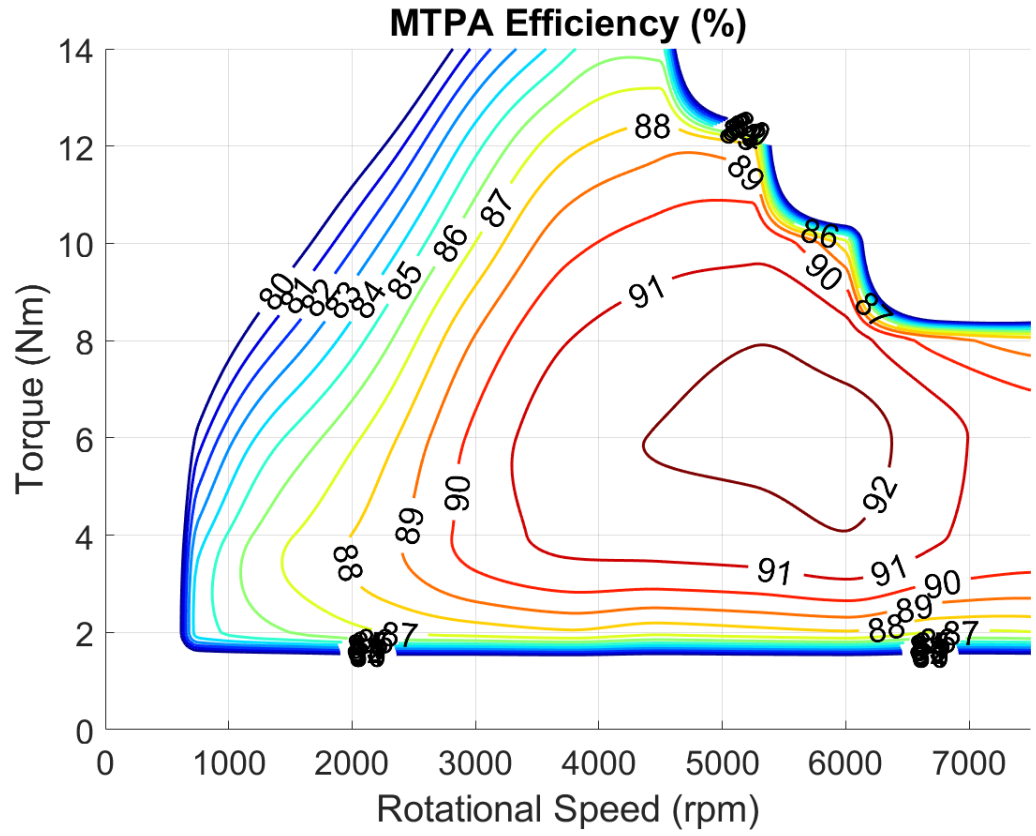

(a) MTPA measured map

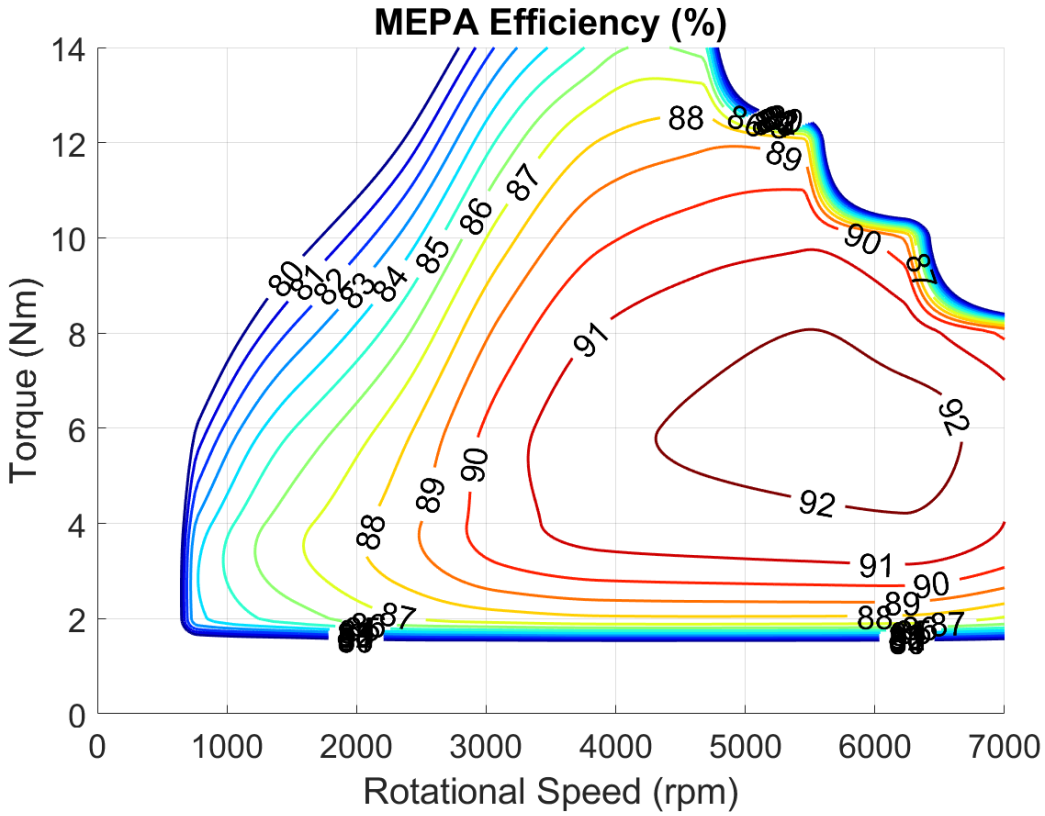

(b) MEPA measured map

Fig. 2.3.18 Measured efficiency maps using MTPA and MEPA methods.

The recorded efficiency values for the two maps are shown in Tables 2.3.12 and 2.3.13 respectively.

Table 2.3.12 MTPA Measurement efficiency results (%)

Torque (Nm)	Speed (RPM)									
	1000	1500	2000	3000	4000	4500	5000	6000	7000	7500
2	84.75	86.33	87.28	87.65	88.01	87.58	87.84	88.07	87.11	87.37
4	83.71	87.30	88.76	90.54	91.37	91.65	91.82	92.07	91.20	90.72
6	80.65	85.44	87.74	90.32	91.69	92.16	92.32	92.55	91.40	90.61
8	76.96	82.46	85.78	89.19	91.08	91.70	92.02	91.51	89.62	88.53
10	72.73	79.24	83.26	87.08	89.76	90.54	90.77	87.46	0.00	0.00
12	67.98	75.65	80.09	84.77	87.78	88.80	88.20	0.00	0.00	0.00
14	62.36	69.17	75.48	81.35	84.85	85.58	0.00	0.00	0.00	0.00

Table 2.3.13 MEPA Measurement efficiency results (%)

Torque (Nm)	Speed (RPM)									
	1000	1500	2000	3000	4000	4500	5000	6000	7000	7500
2	84.09	85.84	87.31	87.71	88.03	88.05	88.06	87.95	87.02	0.00
4	83.55	86.98	88.80	90.64	91.50	91.73	91.93	92.00	91.11	0.00
6	80.51	85.36	87.76	90.57	91.80	92.24	92.53	92.56	91.46	0.00
8	76.58	82.62	85.77	89.35	91.12	91.73	92.09	91.53	89.85	0.00
10	72.17	79.43	83.25	87.57	89.89	90.59	90.90	88.99	0.00	0.00
12	67.25	75.30	80.01	85.30	88.14	88.87	88.52	0.00	0.00	0.00
14	61.56	70.00	76.33	82.39	85.55	85.69	0.00	0.00	0.00	0.00

The results show little difference between the two methodologies. The key advantage to MEPA over the MTPA method relies on being able to balance the iron loss and copper loss. However, from the results it can be seen that the copper loss is dominant for this machine making MTPA the optimal control methodology, not least because it is easier for the controller to monitor the currents directly from the current sensors than calculating the efficiency. The current angles utilised to achieve the maximum MTPA and MEPA are shown in Figs.2.3.19 (a) and (b) respectively.

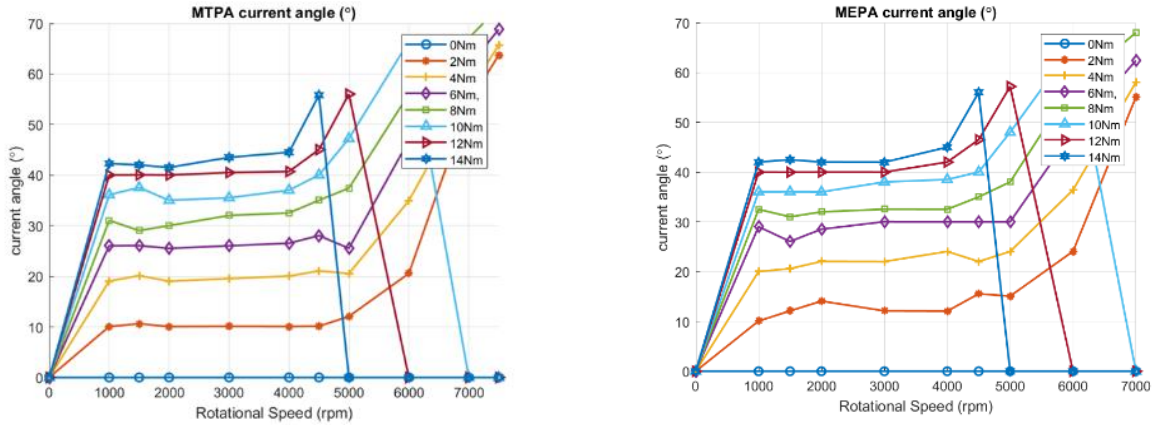

(a) MTPA Current angles (b) MEPA Current angles

Fig. 2.3.19 Current angles for each speed/torque point on MTPA and MEPA maps.

The raw data can be seen in Tables 2.3.14 and 2.3.15.

Table 2.3.14 MTPA Measurement current angle (°)

Torque (Nm)	Speed (RPM)									
	1000	1500	2000	3000	4000	4500	5000	6000	7000	7500
2	10.1	10.6	10.1	10.1	10.1	10.1	12.1	20.6	54.2	63.7
4	19.1	20.1	19.0	19.5	20.0	21.1	20.6	34.9	56.3	65.7
6	26.0	26.1	25.5	26.0	26.5	28.0	25.5	46.8	61.5	68.8
8	31.0	29.0	30.0	32.0	32.5	35.0	37.4	56.0	67.1	73.1
10	36.1	37.5	35.0	35.5	37.0	40.0	47.2	66.4	0.0	0.0
12	40.0	40.0	40.0	40.5	40.7	45.0	56.0	0.0	0.0	0.0
14	42.3	42.0	41.5	43.5	44.5	55.8	0.0	0.0	0.0	0.0

Table 2.3.15 MEPA Measurement current angle (°)

Torque (Nm)	Speed (RPM)									
	1000	1500	2000	3000	4000	4500	5000	6000	7000	7500
2	10.1	12.1	14.1	12.1	12.1	15.6	15.1	24.1	55.1	0.0
4	20.0	20.6	22.1	22.0	24.1	22.0	24.1	36.4	58.1	0.0
6	29.0	26.1	28.5	30.0	30.0	30.0	30.0	48.1	62.4	0.0
8	32.5	31.0	32.0	32.6	32.5	35.0	38.0	57.5	68.0	0.0
10	36.0	36.0	36.0	38.0	38.5	40.0	48.0	65.4	0.0	0.0
12	40.0	40.0	40.0	40.0	42.0	46.5	57.2	0.0	0.0	0.0
14	42.0	42.5	42.0	42.0	45.0	56.0	0.0	0.0	0.0	0.0

From the values seen Tables 2.3.14 and 2.3.15 it can be seen that there is very little difference between the current angle utilised meaning that the relative position of the winding and PM fields within the machine are basically identical so there would be very little difference in vibratory performance; the forces and angles are the same. A similar comparison can be drawn looking at the thermal performance of the machine under the different control methods, provided in Table 2.3.16 and Table 2.3.17.

Table 2.3.16 Average case and stator core temperatures during MTPA measurement

Speed	1000rpm		1500rpm		2000rpm		3000rpm		4000rpm	
Torque (Nm)	Case surface (°C)	Stator Core (°C)	Case surface (°C)	Stator Core (°C)	Case surface (°C)	Stator Core (°C)	Case surface (°C)	Stator Core (°C)	Case surface (°C)	Stator Core (°C)
2	13.8	18.6	11.2	17.0	11.6	17.4	11.6	18.3	11.5	18.8
4	13.0	19.8	11.2	19.4	11.5	19.5	11.2	20.1	11.6	20.8
6	12.9	24.4	11.3	23.7	11.6	23.8	11.0	25.3	11.7	26.2
8	13.0	29.9	11.6	32.8	11.9	31.1	11.4	34.4	12.0	33.3
10	12.9	40.7	12.1	44.5	12.3	40.3	12.3	50.3	12.6	44.9
12	13.0	53.3	12.4	53.3	12.8	55.5	12.9	64.2	13.5	63.2
14	13.4	72.7	14.3	91.1	14.1	80.6	14.0	87.4	15.3	92.8
Speed	4500rpm		5000rpm		6000rpm		7000rpm		7500rpm	
Torque (Nm)	Case surface (°C)	Stator Core (°C)	Case surface (°C)	Stator Core (°C)	Case surface (°C)	Stator Core (°C)	Case surface (°C)	Stator Core (°C)	Case surface (°C)	Stator Core (°C)
2	11.6	17.7	11.2	18.1	11.7	22.6	12.0	18.6	12.0	23.1
4	10.4	18.1	11.4	21.2	11.6	22.5	12.1	23.4	12.1	30.4
6	10.7	23.8	11.9	27.2	11.7	28.4	12.5	32.4	12.5	40.0
8	10.9	31.3	12.2	33.6	11.9	37.1	13.0	48.2	13.0	60.6

10	11.4	44.0	12.7	47.0	12.7	68.0	0.0	0.0	0.0	0.0
12	12.3	61.3	13.7	68.4	0.0	0.0	0.0	0.0	0.0	0.0
14	13.2	87.3	0.0	0.0	0.0	0.0	0.0	0.0	0.0	0.0

Table 2.3.17 Average case and stator core temperatures during MEPA measurement

Speed	**1000rpm**		**1500rpm**		**2000rpm**		**3000rpm**		**4000rpm**	
Torque (Nm)	**Case surface (°C)**	**Stator Core (°C)**	**Case surface (°C)**	**Stator Core (°C)**	**Case surface (°C)**	**Stator Core (°C)**	**Case surface (°C)**	**Stator Core (°C)**	**Case surface (°C)**	**Stator Core (°C)**
2	11.1	14.5	10.1	15.3	11.1	15.7	12.5	16.5	11.1	16.6
4	11.0	17.2	10.1	17.6	11.5	19.9	12.5	19.9	11.6	20.4
6	11.2	24.0	10.3	22.3	11.6	24.5	12.7	25.1	11.6	26.2
8	11.5	32.2	10.6	30.5	11.8	31.5	12.8	32.8	11.8	32.4
10	12.0	44.4	11.2	42.1	12.2	41.4	13.3	43.6	12.4	42.7
12	12.6	58.9	12.1	58.9	12.8	55.2	13.7	56.2	12.9	55.7
14	13.4	79.8	13.2	81.9	13.3	69.6	14.4	72.4	13.9	78.6
Speed	**4500rpm**		**5000rpm**		**6000rpm**		**7000rpm**		**7500rpm**	
Torque (Nm)	**Case surface (°C)**	**Stator Core (°C)**	**Case surface (°C)**	**Stator Core (°C)**	**Case surface (°C)**	**Stator Core (°C)**	**Case surface (°C)**	**Stator Core (°C)**	**Case surface (°C)**	**Stator Core (°C)**
2	12.1	16.3	11.9	16.3	12.0	18.2	13.1	20.7	0.0	0.0
4	12.1	19.1	12.2	19.7	12.1	21.5	13.2	25.6	0.0	0.0
6	12.5	25.6	12.5	25.7	12.6	27.6	13.7	34.3	0.0	0.0
8	12.8	33.8	13.2	35.3	12.9	39.5	14.2	48.7	0.0	0.0
10	13.5	45.1	13.8	46.8	13.8	58.5	0.0	0.0	0.0	0.0
12	14.1	60.2	14.4	65.6	0.0	0.0	0.0	0.0	0.0	0.0
14	14.8	86.9	0.0	0.0	0.0	0.0	0.0	0.0	0.0	0.0

The results in Tables 2.3.16 and 2.3.17 follow much the same trends established in the efficiency map and current angle results which is to say there is little to differentiate the methods. What differences there are, in particular the higher temperatures at the 12Nm and 14Nm points at 3000rpm and 4000rpm on the MTPA, are more attributed to the manual nature of the control indicating it took a little longer to establish the optimum current angle and operating at the limits of the machine meant the core got hotter at these points. Thus, the MTPA method will be utilised as it is much easier to track the current entering the machine than monitor the net efficiency.

2.4 Chapter summary

A 24 slot 4-pole IPM machine was introduced which will be used as the baseline for the development of the mechanical model and for investigations into the influence different rotor and stator designs which has on the vibratory behaviour of the machine.

This chapter focussed on the electromagnetic performance of the machine with the key machine characteristics measured using a dynamometer and control and data acquisition systems developed in-house. The machine was measured under no-load conditions to capture the back EMF characteristics and

then at full load in order to capture the maximum performance envelope. The efficiency of the machine was then mapped at a number of speed-torque values under the previously derived T-N curve. Both MTPA (Maximum Torque Per Ampere) and MEPA (Maximum Efficiency Per Ampere) methods were used, and it was found that given the high electrical loading of the machine the two methods yielded the same currents and current angles so the MTPA method was judged as being the most suitable for this machine.

3 Finite element modelling of the electromagnetic performance of the baseline machine.

3.1 Introduction

Chapter 2 introduced the specifications of the baseline machine and provided the experimental results of the key machine characteristics. This chapter uses the data captured during the experimental phase to allow development of the electromagnetic finite element (FE) model of the machine which ultimately provides the tooth force profile of a given speed/load of the machine by modelling the air gap flux density. It acts as a key component in the overall vibration model which is shown in Fig 3.1.1.

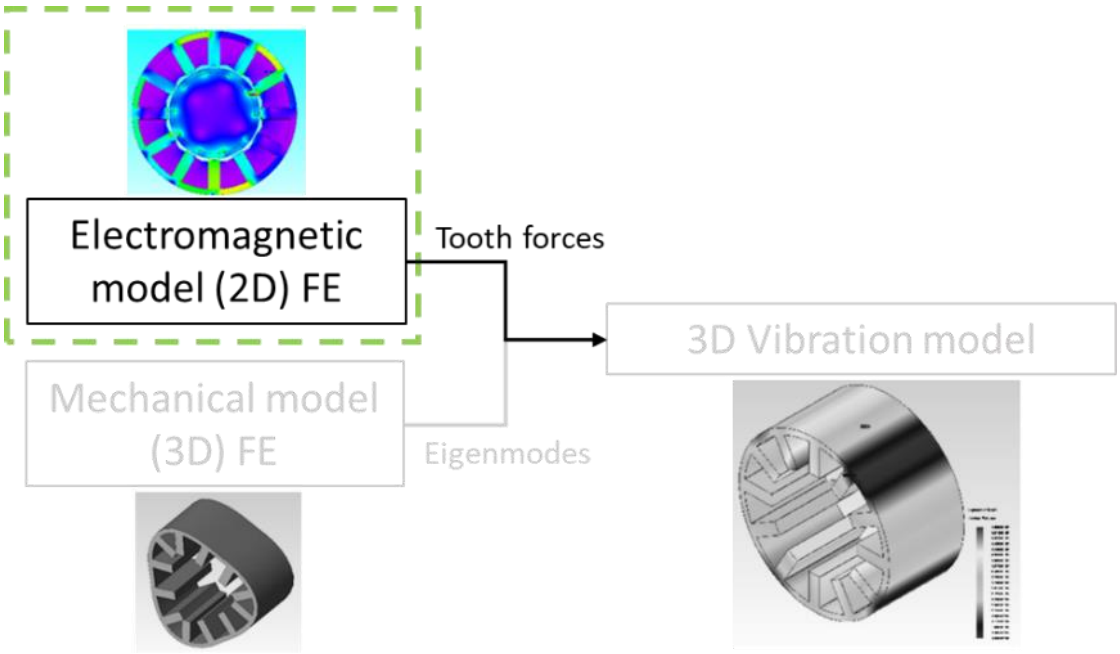

Fig. 3.1.1 Flow diagram of the vibratory modelling of an electrical machine.

For the development of the FE model both JMAG (V18 at time of writing) and later ANSYS® electronics desktop (previously MAXWELL) is utilised. JMAG is used as this is the FE tool used by Nissan allowing effective model sharing. ANSYS® is used later in the development as the Electronics desktop tool is integrated into the much larger ANSYS® workbench suite which includes the mechanical simulators into which the 3D mechanical model of the machine is developed.

3.2 Establishing the model

3.2.1 Applying the materials

Before the model can be built the materials must be firstly established. A model is only as good as the information it contains. Thus, accurate information on the materials utilised is very important. The following figures and tables provide the key electromagnetic data as provided by the magnet [SE16] and lamination steel [CP08] suppliers.

Table 3.2.1 Key EM specifications for PM magnets [SE16]

Item	Value	Unit
Supplier	Shin Etsu	
Grade	N36Z	
Remanence (B_r) @20°C	1.16	T
Coercivity @ 20°C	875000	kA/m
Thermal coefficient of B_r	-0.09	%/K
Permeability (μ_r)	1.05	

The datasheet by any good magnet supplier also contains a chart highlighting the demagnetisation curves for the material at a range of temperatures. The data provided by Shin-Etsu is shown in Fig. 3.2.1 [SE16].

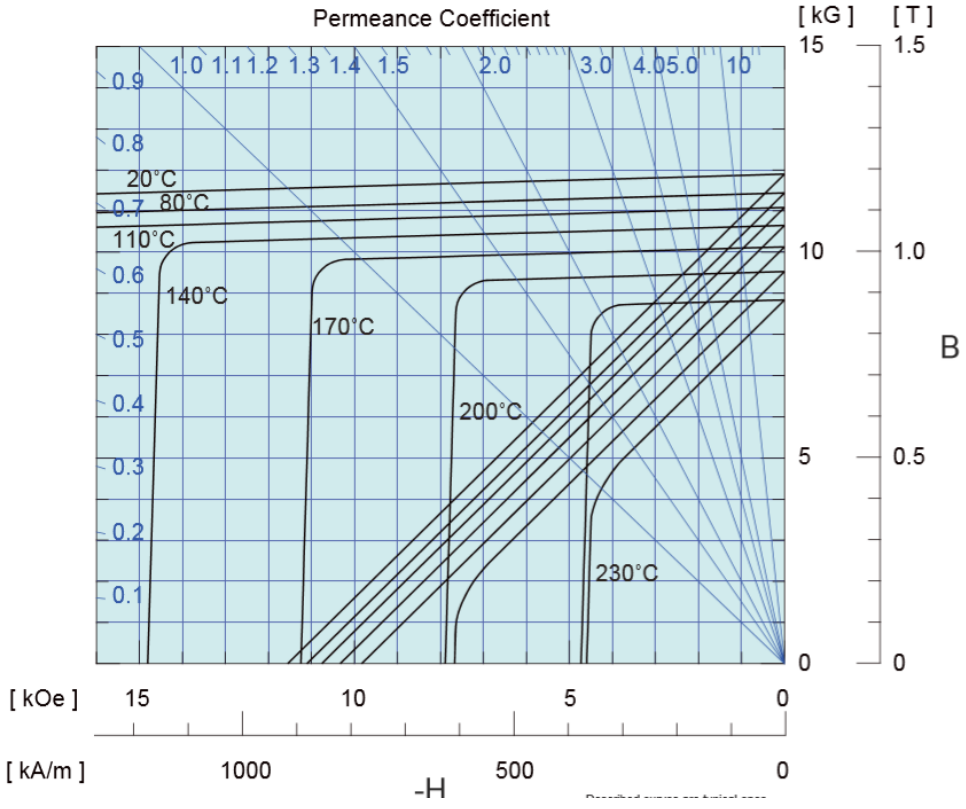

Fig 3.2.1 Shin-Etsu N36Z Demagnetization curves at elevated temperatures [SE16].

It should be noted that the values both in Table 3.2.1 and the demagnetisation curves in Fig. 3.2.1 represent typical values of the magnets as derived by the supplier. Aspects such as manufacturing tolerances of the magnets, both in terms of the formation of the sintered shape and the magnetisation process mean the actual values will deviate from the quoted values from the supplier. In addition, the machine underwent a large number of high load cycles in the original project for which it was designed so there is some risk the magnets degraded a little due to the thermal cycling endured during these tests.

The stator laminations key specifications are detailed in Table 3.2.2.

Table 3.2.2 Key EM specifications for magnetic steel [CP08]

Item	Value	Unit
Supplier	Cogent Power Ltd.	
Steel grade	M250-35A (35H250)	
Thickness	0.35	mm
Maximum stack factor	0.98	
Resistivity	$5.5x10^{-7}$	Ωm
Loss @ 1.5T, 50Hz	2.5	W/kg
relative permeability (μ_r) @ 1.5T	660	

For the stator lamination the supplier provides the data for the B-H curve and the core loss curves at different frequencies which need to be inputted into the FEA tool to ensure the model operates as close to the real machine as possible. The values are shown in Fig. 3.2.2 [CP08].

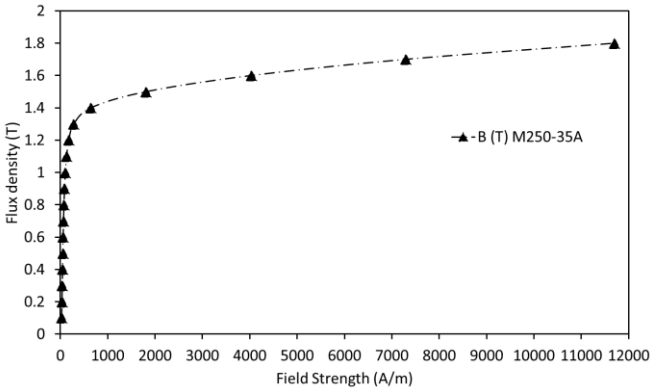

(a) B-H curve of the M250-35A lamination steel

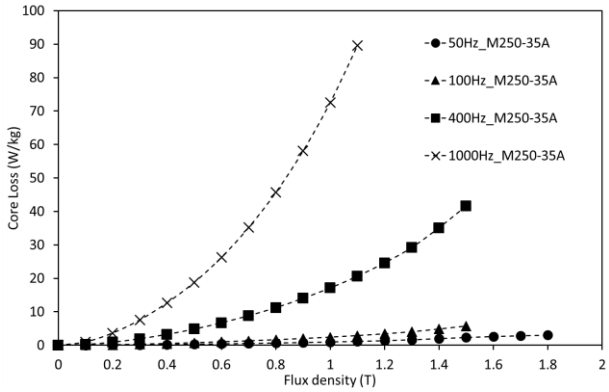

(b) Core loss curves

Fig. 3.2.2 M250-35A B-H curve and core loss curves [CP08].

With the materials established the geometry can be generated.

3.2.2 Establishing the geometry

The initial geometry for the FE model is shown in Fig. 3.2.3.

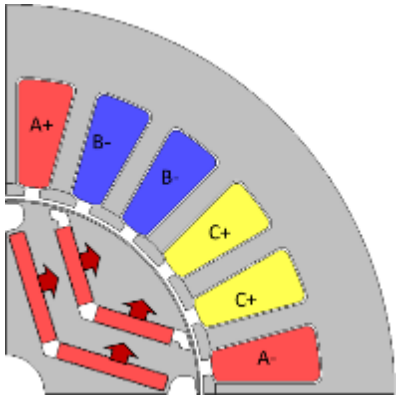

Fig. 3.2.3 Initial drawing of machine ¼ model.

Setting the FE simulation up and running a no-load simulation for 1 electrical cycle at 1200rpm allows the calculated EMF and the measured to be compared. The resultant comparison is shown in Fig. 3.2.4.

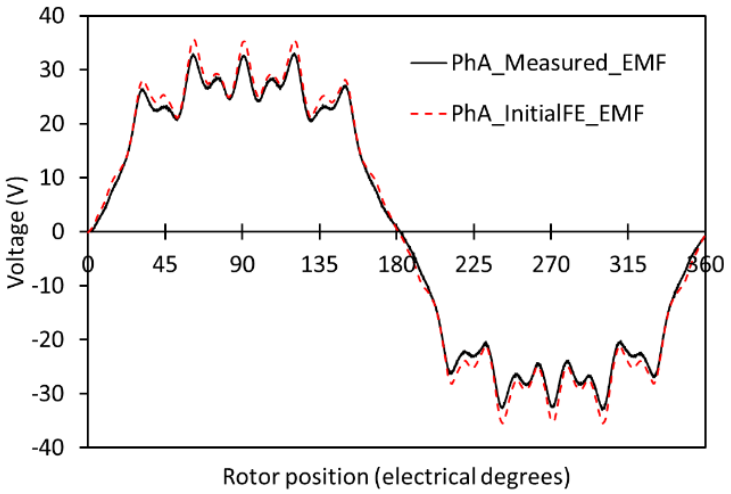

(a) Waveforms

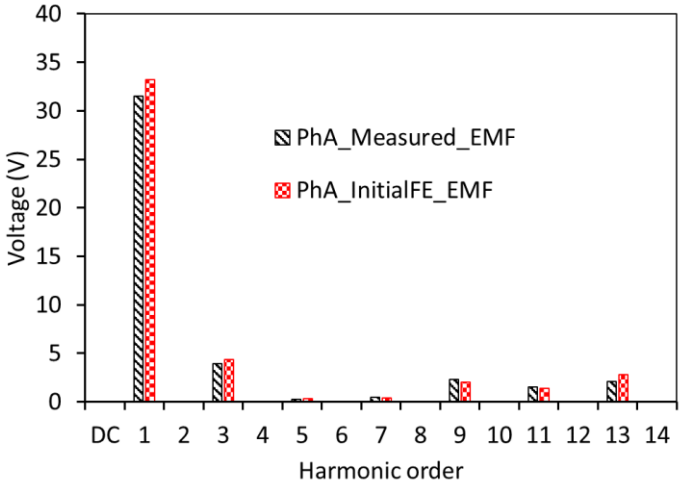

(b) Harmonics

Fig. 3.2.4 Comparison of calculated and measured EMFs @ 1200rpm.

The values in Fig.3.2.4 can be seen in Table 3.2.3.

Table 3.2.3 Comparison of FE and measured harmonics of A-phase EMF @ 1200rpm

Item	Measured (V)	FEA (V)	Diff(V) (measured – FE)	Diff (%)
Max	33.02	35.55	-2.53	-7.67%
Min	-32.99	-35.47	-2.48	-7.53%
Peak to Peak	66.01	71.02	-5.01	-7.6%
Fundamental	31.51	33.23	-1.72	-5%
3rd	3.93	4.36	-0.43	-11%
9th	2.33	2.01	0.31	14%
11th	1.52	1.39	0.13	9%
13th	2.13	2.79	-0.67	-32%

The results show the calculated EMF has a much higher voltage. Given the only source of flux under no-load conditions is the PM, the results suggest the flux linkage between the PMs and the stator coils is too high. It is important to get these values as close as possible as the flux crossing the air gap determines the tooth forces so if the calculated flux from the FE tool is too high compared to the measured results then by extension the calculated tooth forces and therefore the calculated vibratory performance of the mechanical model will be erroneous, negating much of the careful work in chapter 4 and 5 to align the mechanical model to the actual machine. It is therefore a priority to ensure that this fundamental aspect of the machine performance is aligned as closely as possible.

The drawing in Fig. 3.2.3 is a simplified version of the full mechanical drawing but its simplicity shows a number of concerns.

1. The magnets perfectly fit the magnet slot width in the rotor core.
2. The coils perfectly fit the stator slots.

The concern here is that even discounting effects such as tolerance stack-up between all the different components, this model is not reflective of the actual machine. The slots cut into the rotor must be wider than the magnets to allow both insertion of the magnets and to give some space for the epoxy bonding agent used to hold the magnets axially in the core to occupy. The windings need some form of high resistance slot liner in order to mitigate the risk that one or more coils shorts with the iron core creating a serious situation for the machine. What difference this makes can be seen when the magnetic circuit is considered in Fig. 3.2.4.

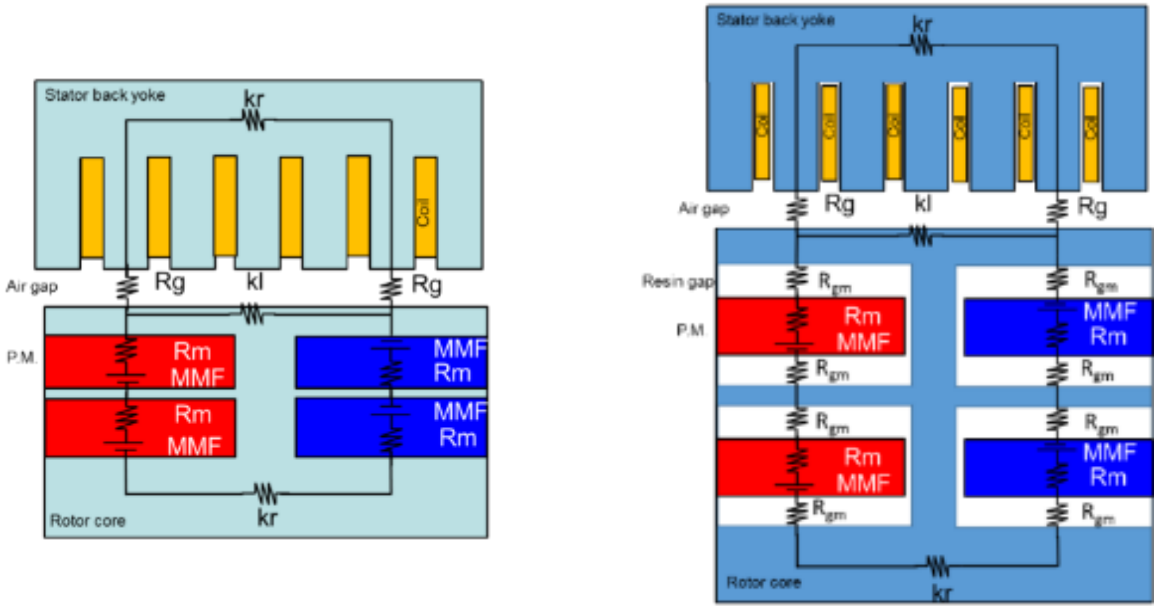

(a) 'ideal' model magnetic circuit

(b) 'complex' model magnetic circuit with influence of added air gaps shown

Fig. 3.2.4 Magnetic circuits of the initial, simple FE model and the more accurate complex model.

The 'ideal' magnetic circuit in Fig.3.2.4(a) reflects the simple model where the only real reluctances in the circuit are those of the air gap (R_g) and losses due to leakage (Kl) within the rotor core steel. A better approximation of the circuit is shown in Fig. 3.2.4(b) [DH12], which highlights the differences:

- The slots for the PMs have additional air gaps, each of which adds a small reluctance (R_{gm}) to the magnetic circuit. These reluctances are in series meaning the net circuit reluctance will increase, lowering the net flux density crossing the air gap.
- In addition to the above the magnets are thinner in the actual model by an amount equal to the sum of the resin gaps added above and in the slot. The thinner magnets lower the magnet MMF reducing the flux that the magnet can produce.

The reduced flux density due to the more complex magnetic circuit means that there are less flux linkages and therefore the EMF produced by the FE model will be lower than the initial, simple design should prove to be a closer match to the measured data. It is important at this point to highlight that given the model is 2 dimensional there are some aspects the model detailed cannot fully capture, namely the end effect i.e. the 3D effects that occur and the axial ends of the machine. These require a 3D FEA model (ideally including end windings) to full represent which greatly increases the complexity of the model and the processing time for each run. Thus, on balance using the proposed 2D model with the more complex magnetic circuit offers an acceptable compromise between the need for speed and the need for accuracy.

One method to achieve this is to adjust the magnet B_r using an equivalent circuit, as shown in [JRH10]. Whilst this is a perfectly valid solution the concern is that adjusting the fundamental material properties of the

magnet is time consuming in the FE package (at the time of writing) meaning parametric sweeps and optimisations are difficult. Using the actual mechanical drawings allows the different dimensions to be easily parameterised and better represents the machine. With this in mind the following adaptions are applied to the model:

- Magnet thickness reduced by 0.2mm, introducing a 0.1mm gap above and the magnet. This is left as air giving a permeability of μ_0 ($4\pi x10^{-7}$H/m)
- 0.25mm air gap around the coils. This is based on the Nomex 414-10 slot liner specified for the machine.
- The magnet temperature is set to 80°C, rather than the default 20°C. This is a standard automotive requirement to ensure the machine is simulated under the upper temperature region of the expected normal operation of the machine.

The elevated temperature means the remanence must drop, as shown in Fig. 3.2.1. The B_r at 80°C can be gleaned from the chart in Fig. 3.2.1, but the chart is of a low resolution making it difficult to get an accurate read. Instead, the B_r at the elevated temperature can be calculated (3.1) [AMT15].

$$B_r(T_m) = B_{r(20)}\left(1 + \frac{TC_{Br}(T_m - 20)}{100}\right) \quad (3.1)$$

where $B_r(T_m)$ is the required B_r at a magnet temperature, T_m (°C). $B_{r(20)}$ is the remanence at 20°C, TC_{Br} is the thermal coefficient of the magnet. In this case, T_m = 80°C and using the appropriate data from Table 3.2.1 it can be seen that $B_r(T_m)$ = 1.16T and TC_{br} = -0.09. Putting these values into (3.1) yields a B_r of 1.10 T, a ~5% reduction in the PM remanence.

The resultant drawing is shown in Fig.3.2.5

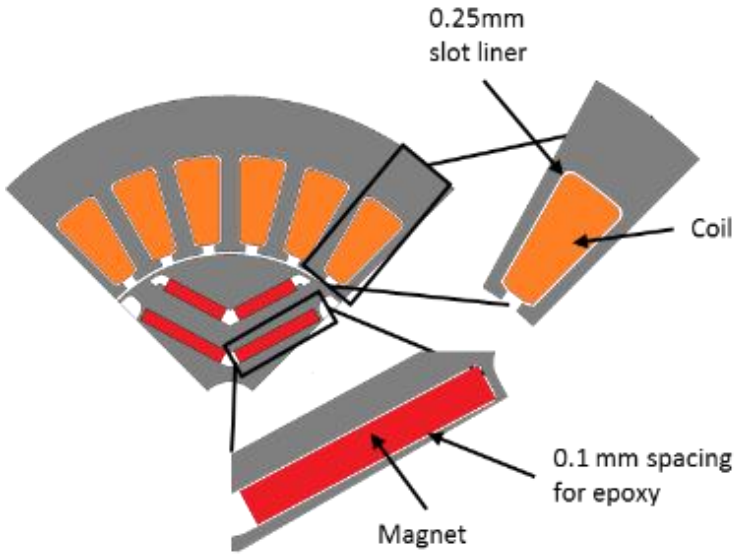

Fig. 3.2.5 Modified geometry to include magnet gaps and slot line.

With the new model in place the no-load simulation is re-run and the results shown in Fig.3.2.6 and Table 3.2.4.

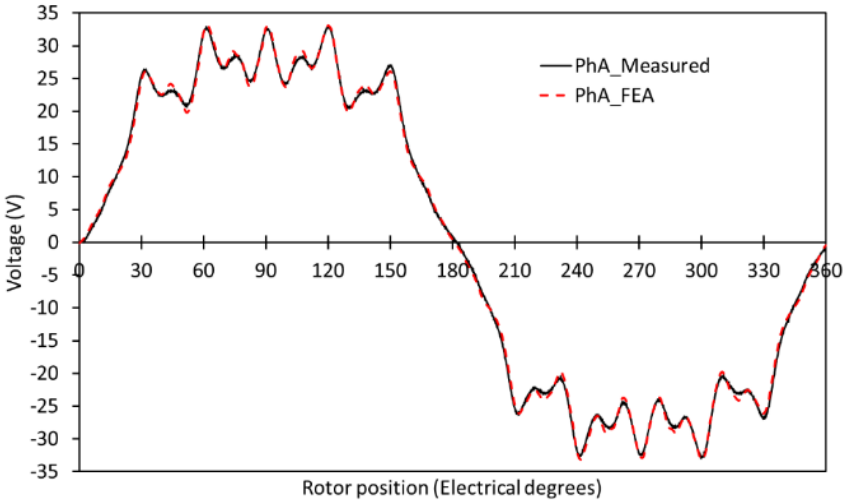

(a) Waveforms

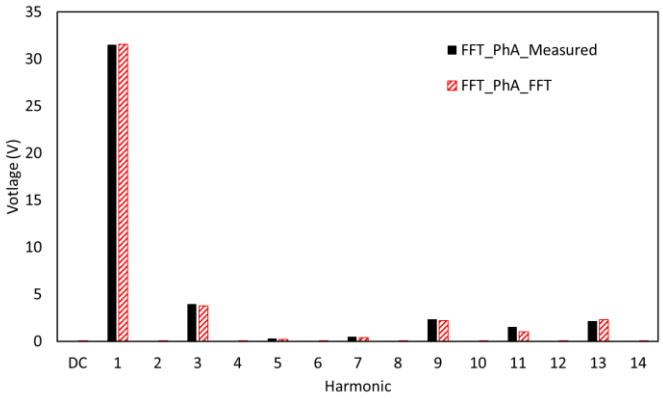

(b) Harmonics

Fig. 3.2.6 Comparison of FEA and measured A-phase back EMF @ 1200rpm.

Table 3.2.4 Comparison of FE and measured harmonics of A-phase EMF @ 1200rpm

Item	Measured (V)	FEA (V)	Diff(V)	Diff (%)
Max	33.02	33.16	-0.14	-0.43
Min	-32.99	-33.16	-0.17	-0.51
Peak to Peak	66.01	66.32	-0.31	-0.47
Fundamental	31.51	31.56	-0.05	-0.16
3rd	3.93	3.75	0.18	4.61
9th	2.33	2.2	0.13	5.54
11th	1.52	1.1	0.54	35.14
13th	2.13	2.28	-0.16	-7.67

The adjustment to the magnetic circuit brought the EMF neatly into line with the measured data, the only slight concern being a large difference on the 11th harmonic, though the actual difference is only around 0.5V. The final meshed model is shown in Fig.3.2.7.

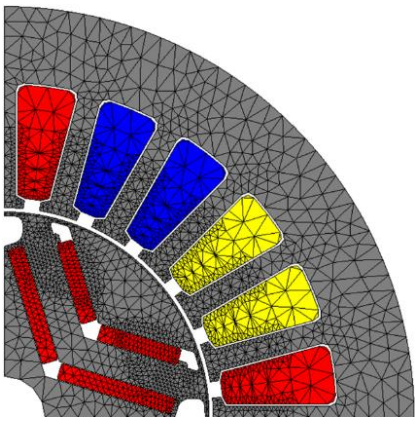

Fig. 3.2.7 Final 2D FE model of rotor and stator with mesh applied.

With the geometry established and the material data applied the analysis can begin. The FE analysis follows the same steps as the measurement, with some additional steps afforded by the ability of FE to allow analysis and visualisation of aspects such as the flux lines and saturation that are very difficult to obtain from the physical machine.

3.3 FE model electromagnetic analysis

3.3.1 Radial flux distribution

The flux distribution is obtained by running the machine in a magnetostatic simulation. This provides 2 key pieces of information:

- Flux lines and distribution of the PM magnetic flux density within the rotor and stator cores
- Distribution of the PM flux across the air gap

It is the simplest and quickest of all the FE simulations to run and provides a good initial check that the PMs have been setup correctly and allows aspects such as rotor core flux leakage to be observed which are very difficult to achieve on the physical machine. The results can be seen in Fig.2.4.8.

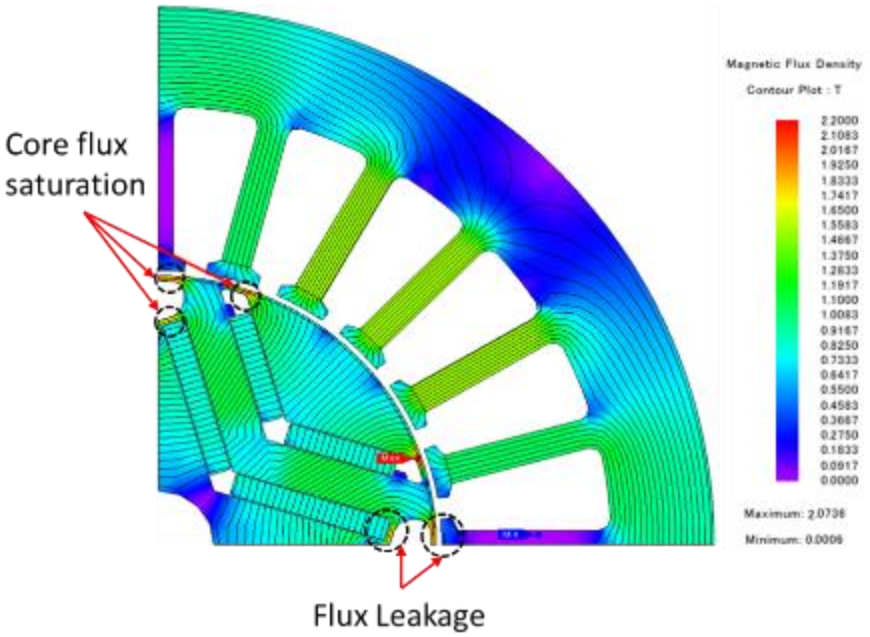

Fig. 3.3.1 Flux distribution in rotor and stator.

The distribution is nice and symmetrical indicating that the magnet orientation and magnetization direction are good, and the mesh is OK. Areas of flux saturation can be seen at the magnet ends; this is a standard technique within the IPM machine order to limit the leakage flux. That being said some leakage can be observed at the magnet ends, in particular on the larger, lower layered magnets.

Drawing an arc in the middle of the air gap allows the FE tool to measure the PM flux crossing the air gap to/from the rotor core. Fig. 3.3.2 shows the air gap flux distribution.

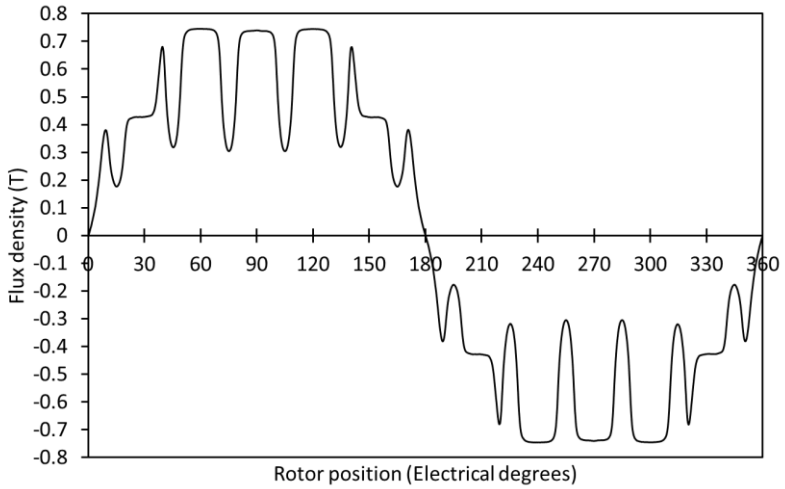

(a) Radial air gap flux distribution. Measurement point = mid-line of airgap (r = 25.25mm)

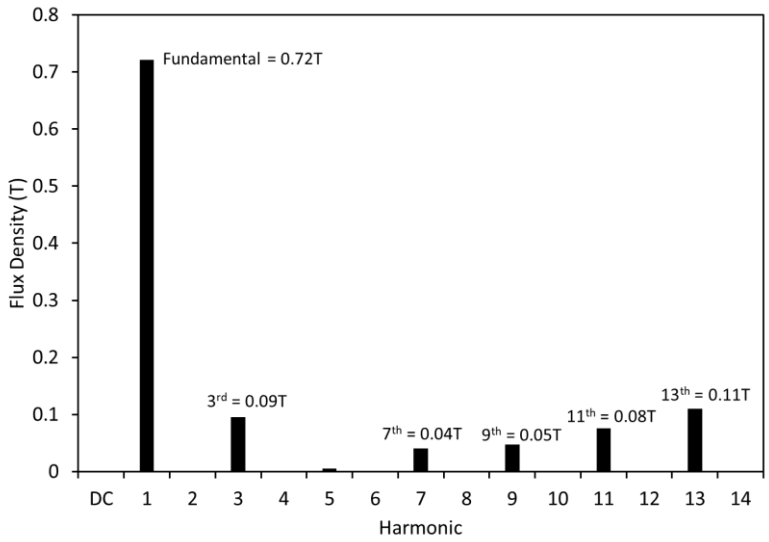

(b) Radial air gap flux harmonic content

Fig. 3.3.2 Radial air gap Flux distribution of baseline motor.

The waveform in Fig.3.3.2(a) shows good symmetry confirming that the flux distribution is symmetrical over one pole pair.

The influence of the stator slots can be clearly seen with the regular drops in the flux density in the waveform in Fig.3.3.2(a) and the profile of the dual 'V' shape can also be observed with a 2 step to the positive and negative halves of the waveform, giving a slightly more sinusoidal profile. The non-sinusoidal nature of the wave is reflected in the rich harmonics of the waveform which can be observed in the FFT in Fig 3.3.2(b). The 3rd, 7th, 9th, 11th and in particular the 13th harmonics are clearly visible in the frequency domain. Table 3.3.1 summarises the amplitudes of the flux densities of each harmonic.

Table 3.3.1 Summary of air gap flux density harmonics

Harmonic	Fund	3rd	7th	9th	11th	13th
Amplitude (T)	0.721	0.095	0.040	0.047	0.075	0.109

3.3.2 Cogging torque

Similar to the physical measurement the cogging torque simulation is highly sensitive to the calculation procedure. An additional complexity for the FEA lies in the mesh. To accurately calculate the cogging torque a very dense, symmetrical mesh is utilised with particular focus on the air gap interfaces at the rotor outer circumference and the stator inner circumference. There is no need for coils, so these are disabled for the cogging simulation to reduce processor load. Fig. 3.3.3 shows the meshed model.

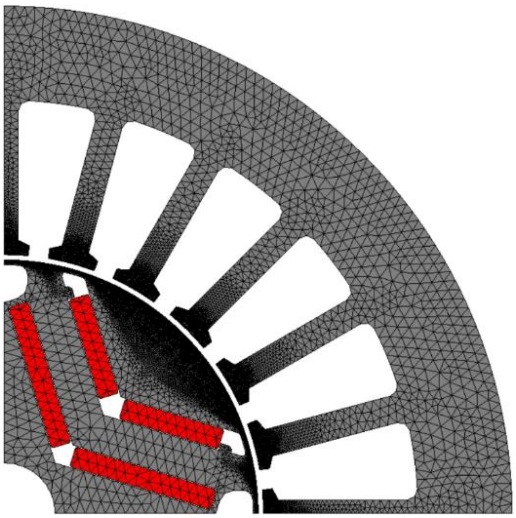

Fig 3.3.3 Cogging measurement – meshed model.

Cogging is also very sensitive to position. To achieve a high-resolution profile the simulation is reset to rotate at 1 degree/second for 1 electrical cycle (180 degrees mechanical). Given the simulation is run for 721 steps giving a resolution of 0.25° per mechanical step (0.5 per electrical step).

Fig.3.3.4 shows the results of the FE calculation and a comparison with the measured cogging waveform and harmonics.

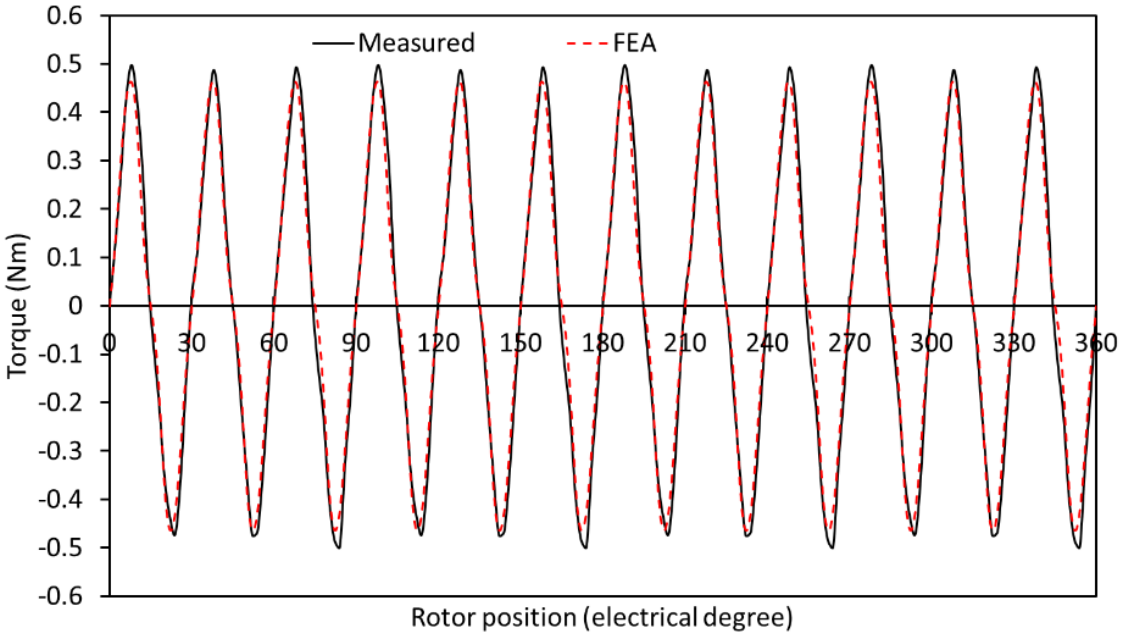

(a) Waveforms

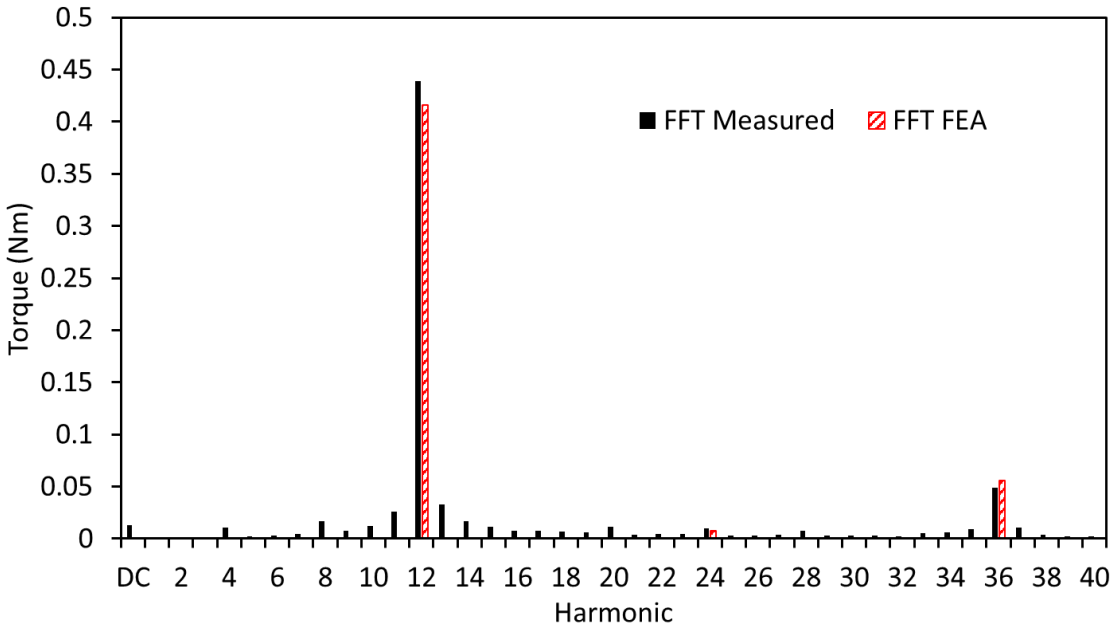

(b) Harmonics

Fig. 3.3.4 Comparison of measured and FEA cogging torques.

The FE calculated cogging profile is reasonably smooth, with good symmetry for each cogging period. The calculated waveform is much smoother than the measured owing to the much higher resolution the FE tool offers. The machine is a 4-pole 24 slot machine, so the rotor has to pass 12 slot openings to complete one electrical cycle, reflected in the high 12th harmonic in Fig.3.3.4(b). The smoothness of the FE is further reflected in the lack of harmonics in the frequency domain, a slight peak can be seen on the 24th harmonic and further spike at the 36th.

Table 3.3.2 shows the difference between the measured and the FE calculation.

Table 3.3.2 Comparison of FE calculated, and measured cogging torques

Harmonic	Measured (Nm)	FEA (Nm)	Diff (Nm)	Diff (%)
Max	0.50	0.46	0.04	6.86%
Min	-0.50	0.46	0.04	6.87%
PP	1	0.93	0.07	6.86%
Fund (12th)	0.44	0.42	0.02	5.21%
36th	0.05	0.06	0.01	-14.9%

Overall, the results are very reasonable for this kind of test. Given the difficulty of measuring the cogging and the high mesh and step control resolution required on the simulation an error of ~7% is acceptable, especially when the overall cogging amplitude is so small.

3.3.3 No load calculation

3.3.3.1 Coil flux linkage profile

No load calculation is achieved in an identical manner to the measured. The model is returned to a moderate mesh density (see Fig.3.2.7) and the coils and winding circuit are re-enabled. The machine is then "rotated" at 1200rpm to allow comparison of the EMF with the measured values of the machine. Similar to the magnetostatic calculation the FE tool offers the ability to directly calculate the change in flux linkages across the air gap as the rotor spins allowing the resultant waveform to be directly analysed. Fig. 3.3.5 shows the resultant data for A phase only.

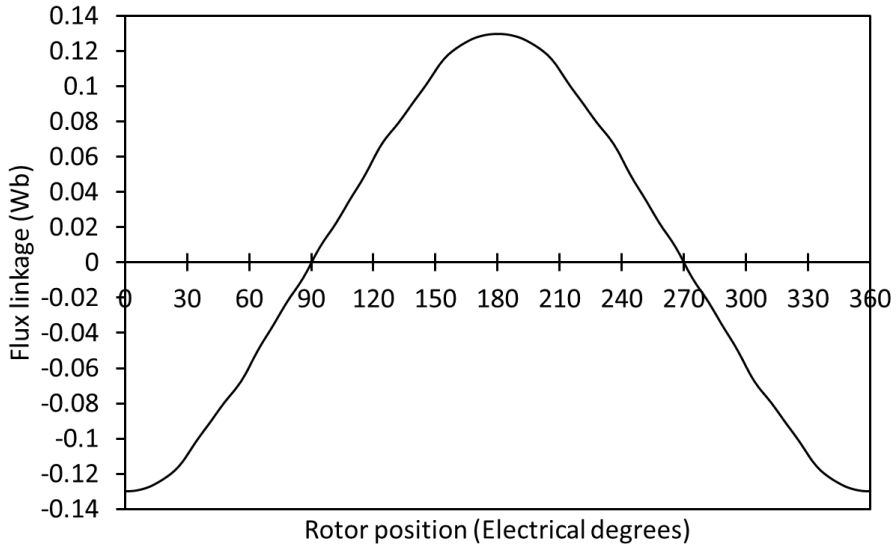

(a) Waveform

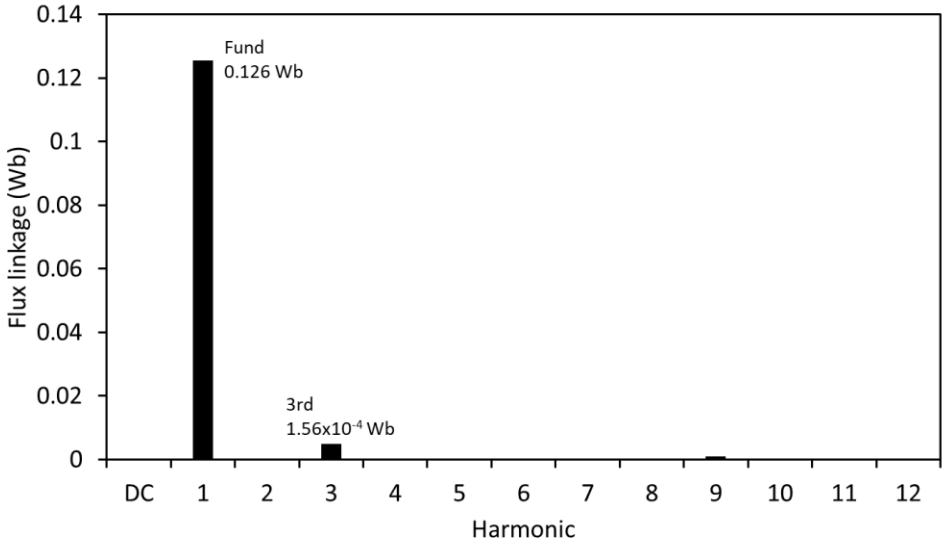

(b) Harmonics

Fig. 3.3.5 A-phase flux linkage @ 1200rpm.

The results show a reasonable sinusoidal waveform with a minor amplitude on the 3rd harmonic. Calculation of the flux linkage can be performed using (3.2).

$$\Psi_m = \sqrt{\frac{3}{2}}\lambda_{fund} \tag{3.2}$$

where Ψ_m = flux linkage and λ_{fund} = a-phase fundamental from FFT.

Given a fundamental of 0.126 Wb the flux linkage can therefore be shown to be **0.154 Wb**.

3.3.3.2 Back EMF

The predicted and measured phase EMF were shown in Fig. 3.2.6 during the geometry discussion. The line-to-line EMF results also need to be compared. Fig.3.3.6 shows the comparison, as before both the waveform and harmonic content are shown.

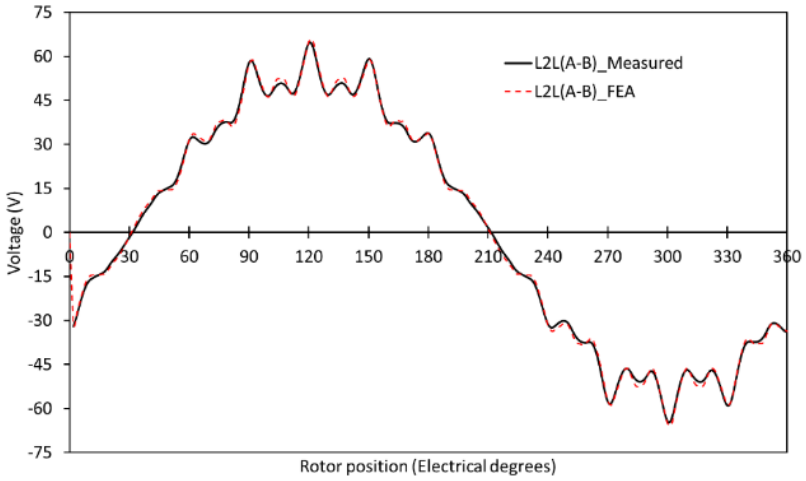

(a) Waveforms

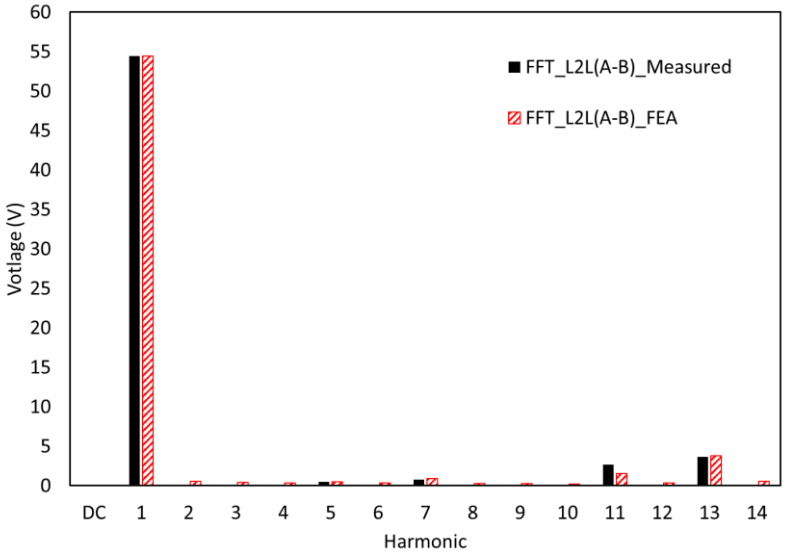

(b) Harmonics

Fig. 3.3.6 Comparison of FEA and measured line to line EMFs (1200rpm).

The comparison draws much the same conclusions as the phase EMF. The only real difference is again the 11th harmonic and the lower resolution of the FE waveform means several very low amplitudes can be seen across the frequency domain. Similar to the phase EMF results the key data for the line to line EMF can be seen in Table 3.3.3.

Table 3.3.3 Comparison of FE and measured harmonics of line to line (A-B) EMF @ 1200rpm

Harmonic	Measured(V)	FEA (V)	Diff (V)	Diff (%)
Max	64.78	65.54	-0.75	-1.2%
Min	-64.78	-65.53	0.74	-1.1%
PP	129.57	131.07	-1.50	-1.2%
Fundamental	54.43	54.44	-0.01	-0.01%
11th	2.66	1.53	1.13	42.49%
13th	3.63	3.77	-0.14	-3.9%

3.3.4 Load testing

3.3.4.1 Mapping T-N curve

Obtaining the T-N curve in FE is not too different to the measurement in that the goal is to find the maximum available torque at a given speed whilst keeping within the current and voltage limits. For the FE tool this could be a very time-consuming process giving the sheer number of simulations that would need to be run to hunt for the value; each little "tweak" of current angle that takes milliseconds on the test rig requires a full run of the FE simulation. A more time-efficient process involves generating a map of the machine flux by running the machine on coarse step setting to gain a snapshot of the flux and run the machine on load for a broad sweep of I_d and I_q values. The resultant flux is then exported to a post-process tool which uses a Matlab script to calculate the torque and voltage limits analytically. I_d and I_q are defined in (3.3) and (3.4) respectively and generate the net current vector I_{dq}, (3.5) which is used by the simulation tool to generate the coil current.

$$I_d = -\sqrt{3} I_{rms} \sin(\beta) \quad (3.3)$$

$$I_q = \sqrt{3} I_{rms} \cos(\beta) \quad (3.4)$$

$$I_{dq} = \sqrt{I_d^2 + I_q^2} \quad (3.5)$$

Table 3.3.4 highlights the settings used.

Table 3.3.4 FE settings for T-N curve mapping

Item	Value	Units/notes
Rotor speed	1500	rpm
Sweep arc: mech. (elec.)	60° (120°)	
Step* resolution: Mech. (elec.)	5° (10°)	Degrees/step
Step* number per run	13	12 steps @ 10deg/step*
Id values	0, -1, -3.78, -7.55, -11.33, -15.1, -18.88, -22.66,-26.43, -30.21, -33.96, -37.76	Amps
Iq values	1, 3.78, 7.55, 11.33, 15.1, 18.88, 22.66, 26.43, 30.21, 33.98, 37.76	Amps

Total number of runs	132	

*Step = 1 calculation point of the transient analyser; the sweep arc (total rotor angle rotated for a run) is divided into steps, each representing one step of motion for the rotor and hence the resolution of the simulation results.

The settings make for a coarse analysis, but at this stage a picture of the flux at differing loads is required so high fidelity is not as important as speed, given the high number of runs required. A high fidelity run showing the ripple torque is detailed later in this chapter.

Once the simulation has been completed the 3-phase flux values are transformed onto the dq-axis plane using (3.6) and (3.7):

$$\lambda_d = \frac{2}{3}\left(\lambda_a \cos(\theta_e) + \lambda_b \cos\left(\theta_e - \frac{2\pi}{3}\right) + \lambda_c \cos\left(\theta_c + \frac{2\pi}{3}\right)\right) \quad (3.6)$$

$$\lambda_q = \frac{2}{3}\left(-\lambda_a \sin(\theta_e) - \lambda_b \sin\left(\theta_e - \frac{2\pi}{3}\right) - \lambda_c \sin\left(\theta_e + \frac{2\pi}{3}\right)\right) \quad (3.7)$$

where λ_a, λ_b and λ_c are the A, B and C phase fluxes and θ_e is the rotor angle in electrical degrees. The mapped flux values can be seen on the surface maps in Figs.3.3.7 (a) and (b).

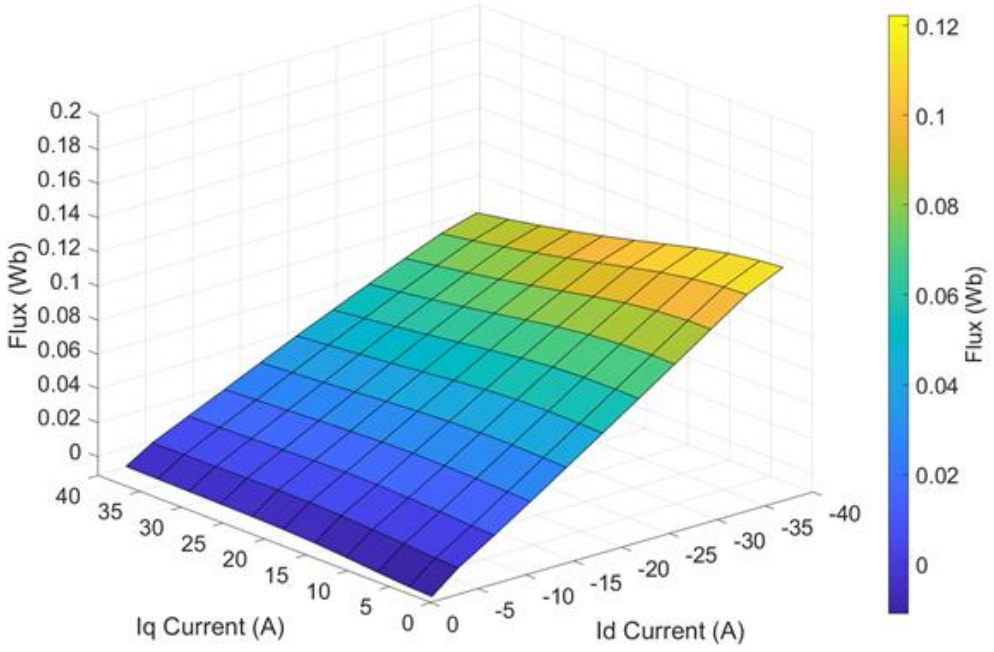

(a) d-axis flux (λ_d) with varying Id and Iq values

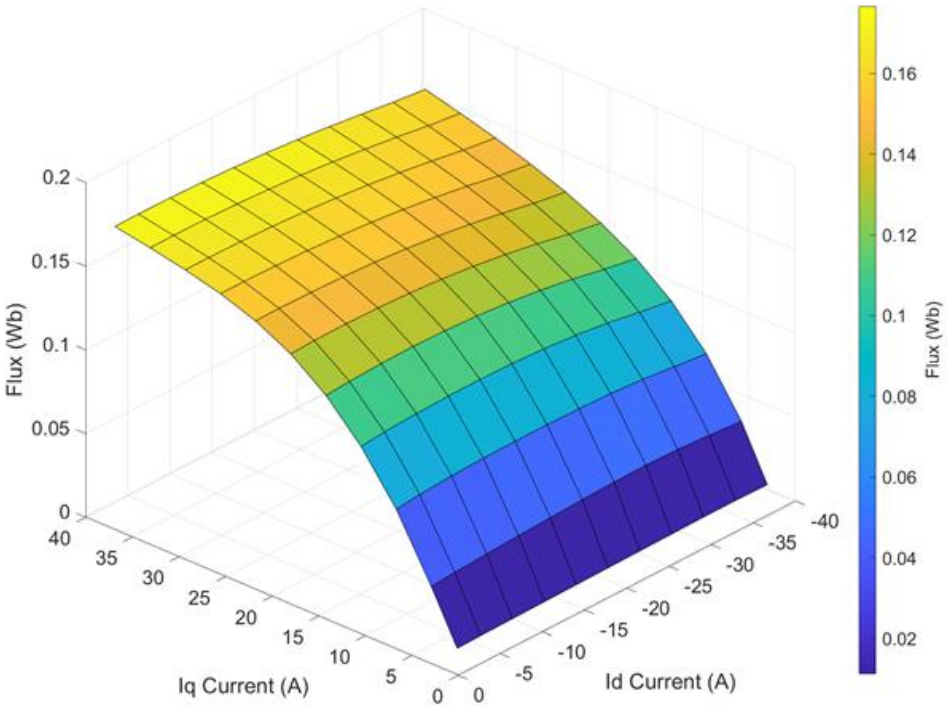

(b) d-axis flux (λ_q) with varying Id and Iq values

Fig. 3.3.7 Mapped flux as a function of Id and Iq currents.

Given the flux values and the number of pole pairs (N_{pp} = 2) the torque at any point can be calculated using (3.8).

$$T_{total} = \sqrt{\frac{3}{2}} N_{pp}\left(\lambda_d I_q - \lambda_q I_d\right) \tag{3.8}$$

In addition, using the d- and q-axis flux values in addition to the PM flux linkage, ψ_m, the L_d and L_q inductances can be mapped in a similar method as Fig.3.3.7 using (3.9) and (3.10).

$$L_d = \frac{\lambda_d - \psi_m}{I_d} \tag{3.9}$$

$$L_q = \frac{\lambda_q}{I_q} \tag{3.10}$$

The resultant maps can be seen in Fig.3.3.8.

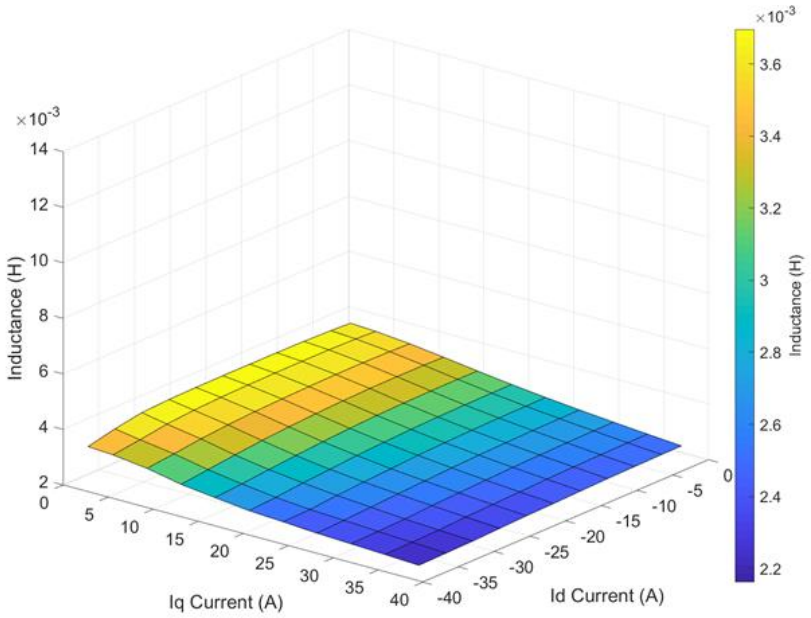

(a) d-axis inductance (L_d) with varying I_d and I_q values

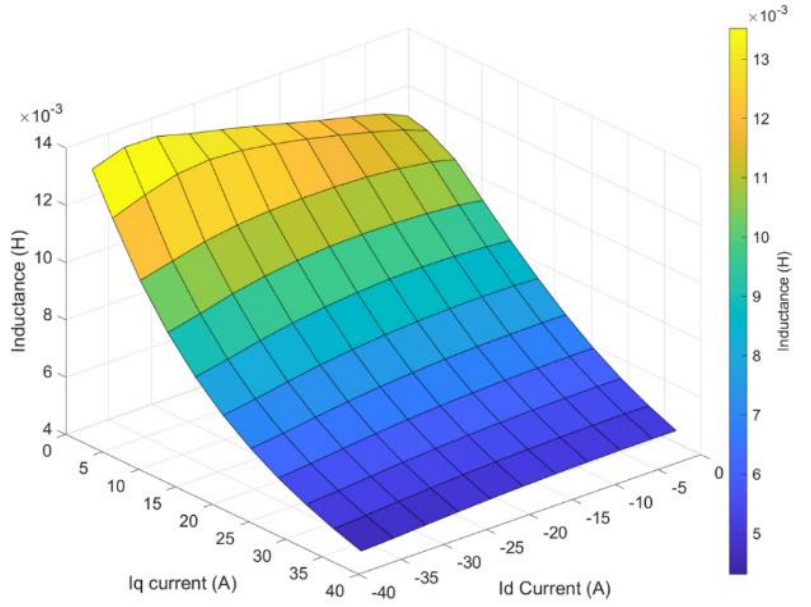

(b) q-axis Inductance (L_q) with varying I_d and I_q values

Fig. 3.3.8 Mapped inductance as a function of I_d and I_q currents.

Armed with the flux data the T-N curve can now be calculated.

The tool was developed based on the method described in [QI09] within the EMD group and uses the flux data as well as information on the system parameters (V_{dc}, I_{max}, coil resistance) to hunt for the peak torque value. A simplified flow diagram of the tool is shown in Fig.3.3.9.

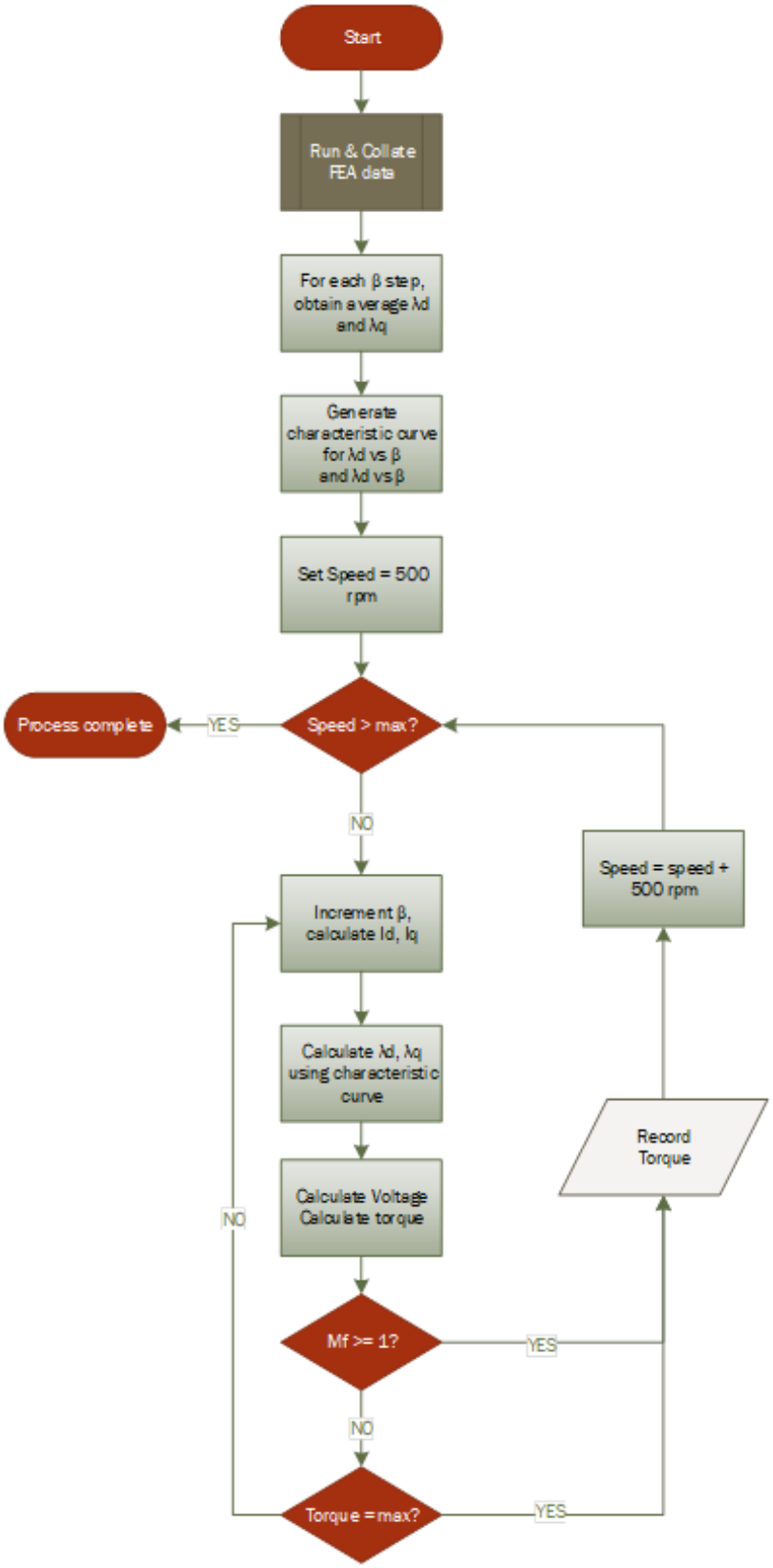

Fig. 3.3.9 Flow diagram of T-N curve mapping tool.

The process is not too different from the measurement methodology, the optimal torque point is hunted for by sweeping the current angle whilst ensuring the voltage limit is not breached. Using this method, the T-N curve is mapped in seconds rather than hours. The resultant T-N curve is shown in Fig.3.3.10.

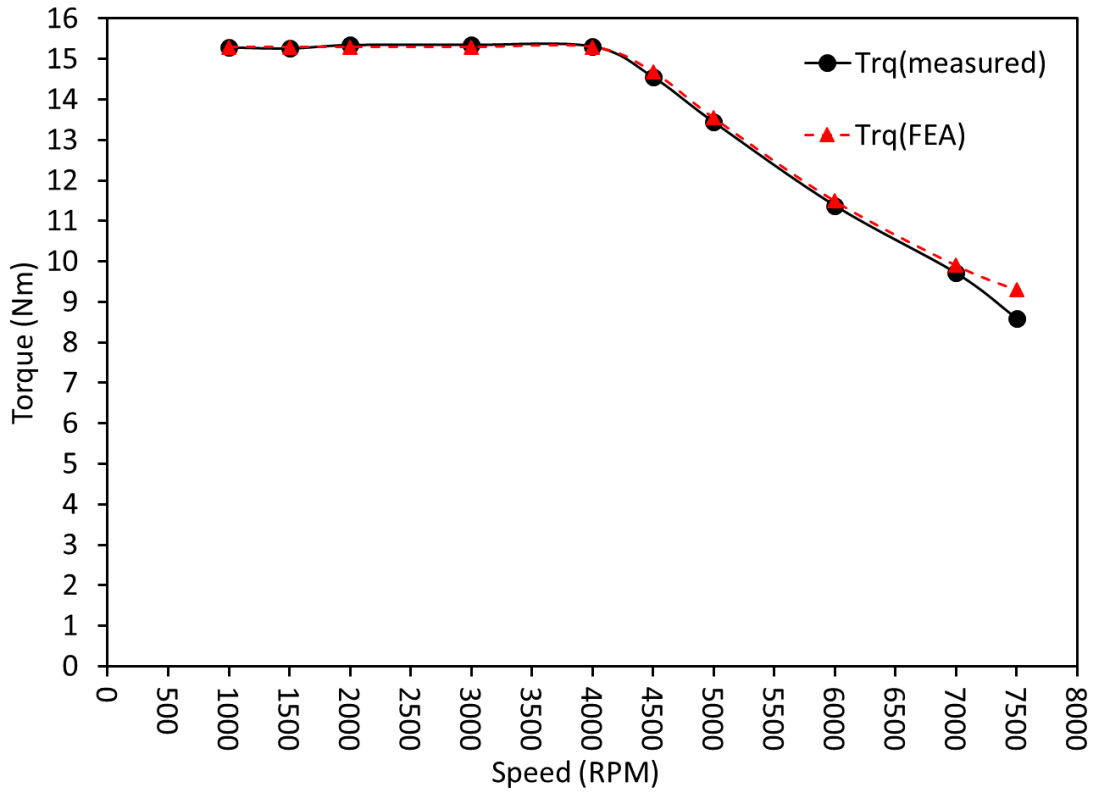

Fig. 3.3.10 Comparison of measured and simulated torque speed curves.

A comparison of the raw speed-torque values is shown in Table 3.3.5.

Table 3.3.5 – Comparison of measured and simulated maximum torques VS speed

Speed	Trq(measured)	Trq(FE)	Diff(%)
1000	15.29	15.30	-0.05%
1500	15.26	15.30	-0.23%
2000	15.35	15.30	0.32%
3000	15.35	15.30	0.36%
4000	15.31	15.30	0.10%
4500	14.56	14.68	-0.84%
5000	13.44	13.55	-0.76%
6000	11.38	11.49	-0.99%
7000	9.71	9.91	-1.96%
7500	8.60	9.29	-8.12%

The simulated values show very good correlation with the measured data. The only point to note is the 7500rpm point where the measured value is ~8% lower due to the previously highlighted controller stability issue that occur while trying to measure the maximum torque at this speed.

3.3.4.2 Simulating the torque ripple

The FE tool is reset to a much finer step setting, the current is set to maximum (26.7Arms) and the simulations run for 1 electrical cycle 10 times, for each run the current angle (β°) incremented in 10° steps from 0° to 90°. This allows the torque ripple at the different current angles to be simulated and characterised as well as the flux at each current angle point to be captured. The torque ripple profiles, and harmonic content can be observed in Fig.3.3.11.

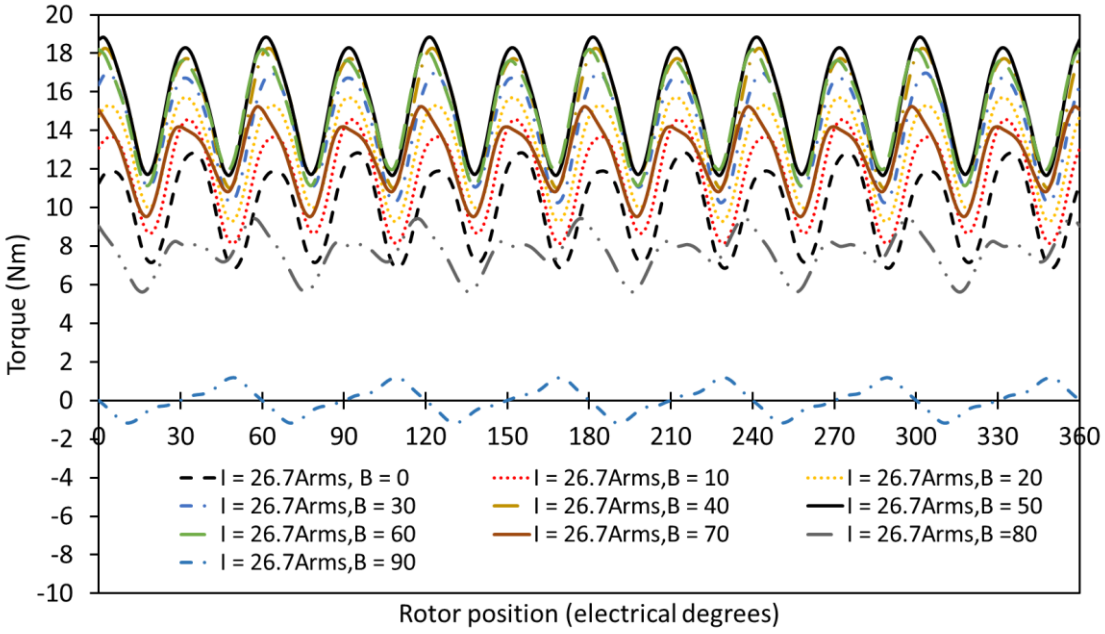

(a) Torque waveforms at max current and incrementing current angles

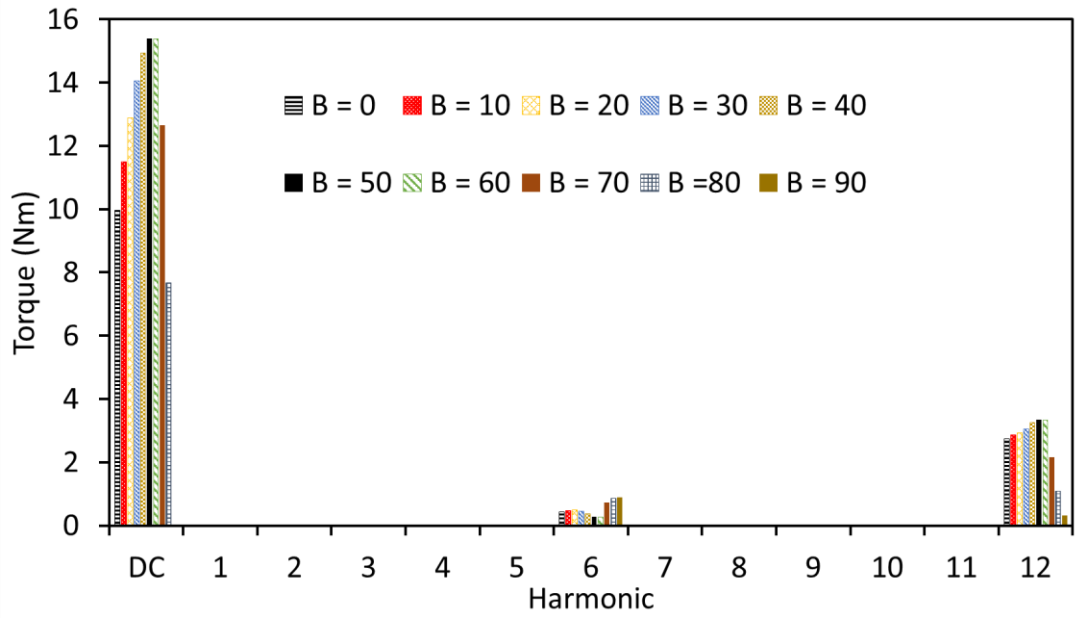

(b) Harmonics

Fig. 3.3.11 Torque waveforms at maximum current (26.7A_{rms}) and incrementing current angle.

A summary of the key attributes is in Table 3.3.6. Note the ripple rate in the table is calculated using (3.11):

$$RippleRate = \frac{(T_{max} - T_{min})}{T_{avg}} \quad (3.11)$$

where the RippleRate is a ratio (Nm/Nm) which is dimensionless, T_{max} is the maximum torque of the waveform, T_{min} is the minimum torque and T_{avg} is the arithmetic average torque of the waveform, all in Nm.

Table 3.3.6 Torque waveform characteristics at maximum current with increasing current angle (Nm)

	β = 0°	β = 10°	β = 20°	β = 30°	β = 40°	β = 50°	β = 60°	β = 70°	β = 80°
Max	12.82	14.52	15.71	16.96	18.24	18.84	18.19	15.25	9.40
Min	6.87	8.18	9.33	10.26	11.03	11.69	11.13	9.54	5.62
Average	9.96	11.50	12.89	14.07	14.96	15.41	15.00	12.67	7.68
RippleRate	0.60	0.55	0.49	0.48	0.48	0.46	0.47	0.45	0.49
Harmonic summary									
DC	9.96	11.49	12.88	14.06	14.94	15.39	15.39	12.66	7.671
6th	0.43	0.472	0.486	0.457	0.364	0.268	0.268	0.736	0.86
12th	2.75	2.872	2.921	3.049	3.244	3.343	3.343	2.155	1.094
24th	0.27	0.276	0.365	0.367	0.342	0.37	0.37	0.454	0.262

From the results a number of observations can be made about the torque waveforms:

- The machine has a high ripple rate, especially at low current angles.
- As the current angle increases the influence of the reluctance net torque increases to maximum average torque of 15.4 Nm between β = 40° and β = 50°, this is very close to the measured maximum of 15.35 Nm and the current angle where this occurred (β = 44.4°).
- The 6th harmonic drops and reaches a minimum at 50° where the reluctance torque reaches its maximum whilst simultaneously the 12th harmonic increases to a maximum at the same angle.
    - Maximum torque in this series is at 50° and the machine is operating over 1 electrical cycle which means 12 teeth. Maximum torque means the maximum reaction force from the stator which is reflected in the 12th harmonic being at its peak at this angle.
    - The mitigation of the ripple rate is reflected in the 6th harmonic reduction.
- As the current angle progresses past 50° the stator field begins to clamp the PM flux more and more, initially reducing the mutual torque and then the reluctance component drops off as the field alignment shifts until at β=90°when the average torque is effectively 0Nm.

3.3.4.3 Torque composition

The measurement of the ripple torque allows the flux to be captured for each run at full load. Using this data, the inductance at full load and the torque composition (ratio of reluctance torque to mutual torque) for each current angle can be analytically determined, giving an insight to the torque characteristics of the machine. To achieve this the flux data at each current angle is captured and converted to the dq-axis plane, in much the same manner as the T-N curve previously. Using the 3-phase flux data from the FE and (3.6) and (3.7) d- and q-axis fluxes can be plotted against current angle.

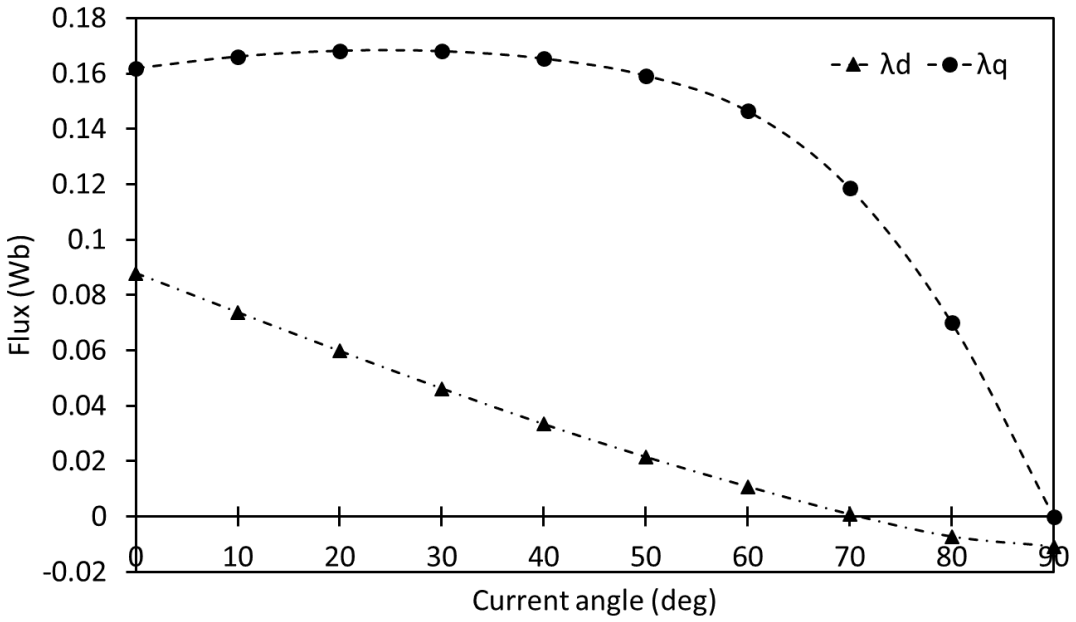

Fig. 3.3.12 Calculated d- and q-axis flux linkages of machine at maximum current (26.7Arms) and sweeping the current angle from 0° to 90°.

Fig. 3.3.12 shows that as the current angle passes 70° the d-axis flux goes negative, indicating the magnet flux is being overwhelmed by the flux from the coil. This situation would risk permanently demagnetising the magnet and thus under normal operation would not be utilised.

Armed with the machine parameters the torque total torque, T_{total} is calculated using (3.8) and the components can be calculated using (3.12) and (3.13).

$$T_{mutual} = \frac{3}{2} N_{pp} \psi_m I_q \tag{3.12}$$

$$T_{reluctance} = \frac{3}{2} N_{pp} (L_q - L_d) I_d I_q \tag{3.13}$$

where N_{pp} is the number of pole pairs, T_{mutual} and $T_{reluctance}$ are the mutual and reluctance torque components in (Nm).

(3.12) and (3.13) are the standard analytical formulae but the concern is that when the machine is on-load phenomena such as saturation of the iron in high-load areas of the rotor and stator cores mean that the reluctance of the magnetic circuit is non-linear, this is further complicated by the fact that these aspects are very sensitive to temperature. These factors conspire to reduce the accuracy of the analytical methods which tend to predict much higher torques than reality and require quite unwieldy non-linear mathematics to try to compensate for the saturation. A popular methodology to resolve this is the frozen permeability method [JAW05], [JKT09], [WQC13a] which uses the FE tool to isolate each torque component by firstly calculating the non-linear solution at full load, freezing the calculated permeability of the magnetic circuit then turning "off" either the magnet or the field coils to obtain the torque contribution of each. This is quite a processor intensive procedure, and thus for this chapter a simpler if less accurate method is applied.

The torque equation (3.8) is used to calculate the torque at each current angle based on the flux data, I_d and I_q values and compared with the FE results. At β = 0 the only torque component is the mutual torque so we can re-arrange (3.12) to obtain the on-load ψ_m. (3.12) is applied to each current step in order to determine the mutual torque at each point. The reluctance torque is then estimated using (3.14).

$$T_{reluctance} = T_{Total} - T_{mutual} \tag{3.14}$$

The calculated values are shown in Table 3.3.7.

Table 3.3.7 Calculated torque composition at full load (I_{rms} = 26.7A) and increasing current angle (Nm)

	β = 0°	β= 10°	β= 20°	β= 30°	β= 40°	β = 50°	β = 60°	β = 70°	β = 80°	β = 90°
AvgTrq (FEA)	9.96	11.50	12.89	14.07	14.96	15.41	15.00	12.67	7.68	0.00
Avg Trq (calc)	9.95	11.49	12.88	14.05	14.94	15.38	14.97	12.65	7.67	0.00
Mutual Tq	9.95	9.80	9.35	8.62	7.62	6.40	4.98	3.40	1.73	0.00
Reluctance tq	0.00	1.69	3.52	5.43	7.31	8.98	10.00	9.25	5.94	0.00

The final torque composition can be observed in Fig.3.3.13.

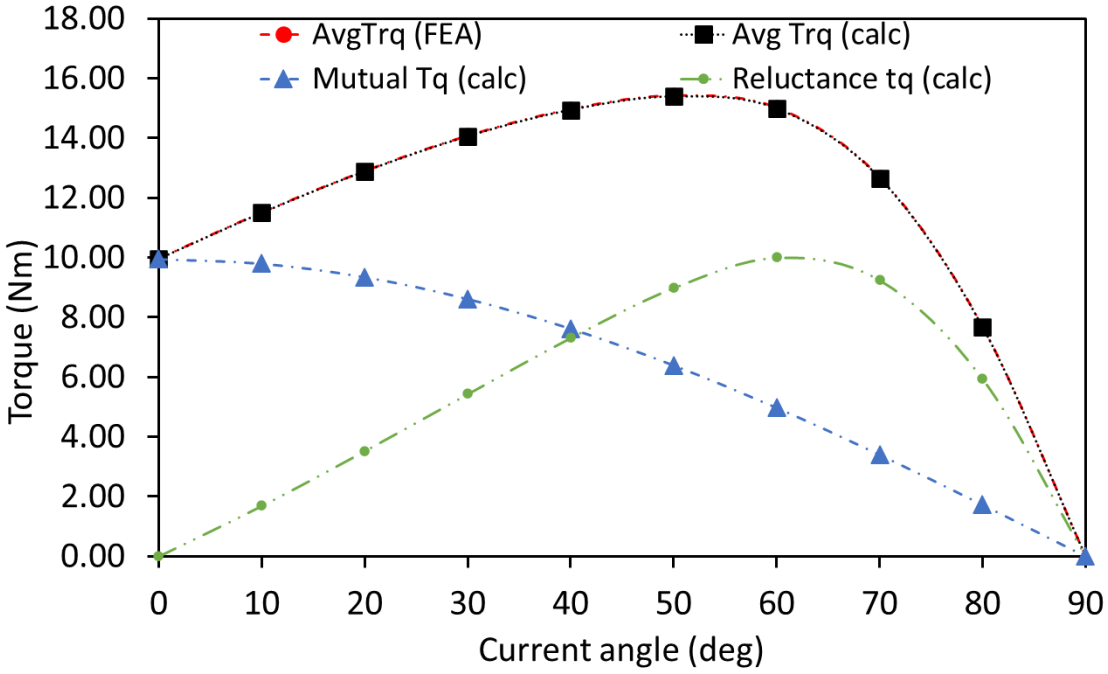

Fig. 3.3.13 Calculated torque composition of the machine.

From Fig.3.3.13 the influence of the reluctance torque is much clearer. As I_d current is added the current angle shifts and the reluctance torque contribution increases until around 50° where the MTPA point is reached where the mutual torque and reluctance torque meet their optimum value. Beyond this point the drop in ψ_m due to the flux weakening effect and the fact that with I_{dq} at maximum and given (3.5) the q-axis current has to drop to allow current angle to be increased therefore the drop in mutual torque exceeds the

rise in reluctance torque bringing the net torque down. Fig. 3.3.14 illustrates each torque component as a percentage of the net torque for each current angle, up to 80°.

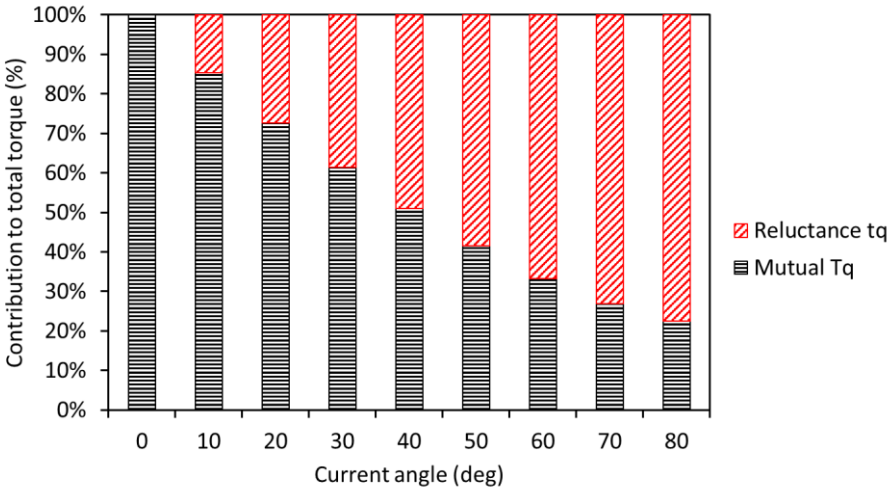

Fig. 3.3.14 Contribution of torque components as a percentage of the net torque at each current angle, $I_{rms} = 26.7A_{rms}$.

These values give a good a general guide to the torque composition, as mentioned previously the non-linear effects at high loads mean much more detailed analysis is required to gain precise values but the general trend matches the observations during test.

3.3.5 Efficiency and loss maps

3.3.5.1 Efficiency map tool

The efficiency mapping process utilises a more complex version of the T-N tool show in Fig. 3.3.9. The major difference is there is an additional program loop after the establishment of the maximum torque at a given speed to generate a number of torque values between 0Nm and the established maximum. For each torque point it interpolates loss data to find maximum efficiency for that speed and torque. For this process to happen the tool needs to know what the losses of the machine are for each point to calculate the efficiency. This means that in addition to the matrices of d and q axis flux values captured from the FE tool that is required to calculate the torque (as detailed in the T-N process) the tool also needs to know the loss at each point. The loss aspects it needs are:

- Iron loss: loss due to the varying magnetic field in the core materials.
- Copper loss: loss due to resistance in the windings.
- Mechanical loss: loss due to the bearings and windage.

The efficiency at each torque speed point is calculated using

$$\eta = \frac{P_{out}}{\left(P_{out} + W_{iron} + W_{cop} + W_{mech}\right)} \times 100 \tag{3.15}$$

where η is the efficiency (%), W_{Iron} is the iron loss (W), W_{cop} is the copper loss (W) and W_{mech} is the mechanical loss) (W), P_{out} is defined as:

$$P_{out} = \omega_m T_{out} \quad (3.16)$$

where ω_m is the rotor speed (rad/s) and T_{out} is the torque (Nm).

The resultant matrix of maximum efficiency values and the loss components of each point can be plotted on a contour map and compared with the measured data. The methodology of calculating each of the different loss mechanisms is summarised in the following sub-sections.

3.3.5.2 Iron loss calculation

Iron loss, or core loss is due to the interaction of the varying magnetic flux-density within the ferromagnetic materials that form the core and can be split into two components:

- Hysteresis loss.
- Eddy current loss.

The relationship between the hysteresis and eddy current losses in terms of loss/frequency is illustrated in Fig. 3.3.15.

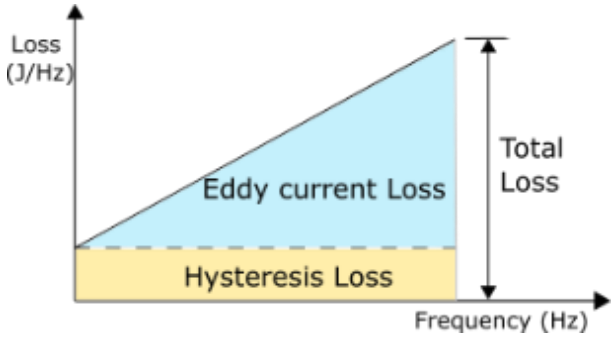

Fig. 3.3.15 Relationship of hysteresis and eddy current iron losses.

It can be seen that as the motor frequency increases the loss per frequency becomes substantial, typically the iron loss dominates in the high speed, low torque region of the T-N curve. Iron loss is a very large and complex subject matter as it is non-linear in nature and sensitive to aspects such as the material selection, magnetic saturation due to load and core temperature. Thus, for this thesis a short overview of each of the above will be provided.

Hysteresis loss

Magnetic hysteresis is the tendency for ferromagnetic materials to "retain" magnetism following the application of a field which results in a non-linear decay in magnetism when the applied field is reduced to zero or the switched to the opposite polarity. Hysteresis loss is commonly calculated using the empirically derived Steinmetiz's equation (3.17).

$$W_h = K_{hys} f^{\alpha_{st}} B_{pk}^{\beta_{st}} \quad (3.17)$$

where W_h is the loss in W/kg, f is the frequency (Hz), B_{pk} is the peak magnetic flux density (T), and K_{hys} is the hysteresis coefficient (J/m^3), α_{st} and β_{st} are Steinmetiz's constants.

The Steinmetiz's constants (k, α and β) are related to the materials, typically α is set to 1 and β ranges from 1.6 to 2.2 [JRH10] depending on the material.

Eddy current loss

Eddy current loss is a result of the varying magnetic field on the core materials inducing an EMF in the core. This EMF, if unbalanced, will generate a circulating current within the material due to Ohms law. These currents are called eddy currents due to their resemblance to eddies produced in fluid flow. The eddy currents produce heat and, due to Lenz's law, they act to oppose the magnetic flux that induced them creating a drag effect, which again creates loss. A simplistic calculation of the loss due to eddy currents is given in (3.18) [JRH10].

$$W_e = C_e B_{pk}^2 f^2 \tag{3.18}$$

where W_e is the eddy current loss (W/kg), B_{pk} is the peak flux density (T), f is the frequency of the flux and C_e is the material constant calculated in (3.19):

$$C_e = \frac{\pi^2 T_{lam}^2 \sigma}{6\rho_m} \tag{3.19}$$

where t_{lam} is the lamination thickness (m), σ is the conductivity (S/m) and ρ_m is the density (kg/m^3).

It can be seen that the eddy current losses are a function of the frequency and flux density squared and as such the eddy current loss can quickly become the dominant loss component as the rotor speed and therefore the machine frequency increases. In terms of mitigating the loss, the terms in (3.19) gives some clues. By making the material as thin and dense as possible the loss can be mitigated. Reducing the conductivity will also provide some benefit. However, this may come at the cost of magnetic performance. This is why the rotor and stator cores tend to be laminated, by splitting the active length into thin plates with an interpolate material of very high electrical resistance (low conductance) the eddy currents can be greatly mitigate. Which of course comes at the cost of mechanical and manufacturing complexities.

The total iron loss is simply the summation of the hysteresis and the eddy current loss (3.20):

$$W_{iron} = W_h + W_e \tag{3.20}$$

The above calculations and trends work reasonably well for along the linear parts of the B-H curve. However, the accuracy reduces once aspects such as saturation and temperature begin to factor in, requiring models of increasing complexity to account for the non-linearities. The best method is to measure a sample of the material using methods such as Epstein frame [IEC08], which is a standard process of measuring the loss, typically in W/kg plotted against frequency. Suppliers do provide a sample of this data (Fig. 3.2.2 is an example). However, the frequencies plotted tend to be too low to meet the requirements of calculating the loss due to high harmonics from slotting or the PWM switching frequency. Some FE tools such as JMAG and ANSYS® Maxwell come pre-installed with large material libraries that contain loss data up to 10kHz, much higher than the supplier data. These tools also use proprietary loss calculations which are modified versions of (3.17) and (3.18) to better compensate for aspects such as the influence of temperature. The precise nature of these models is commercially sensitive and thus any published information tends to be vague at

best. For this machine, JMAG is used in the calculation of the iron loss, primarily due to the extensive supplier data pre-installed having the correct material data available. The iron loss tool is a post-processing tool that requires the machine to operate over a minimum of 1 electrical cycle to calculate the flux variation in an element in the machine and then the hysteresis and eddy current components calculated and stored. This is repeated for each current step the FE tool is run for and results in two matrices of eddy current and hysteresis loss that the MATLAB tool mapping tool can interpolate to establish the iron loss for a given speed/torque point.

3.3.5.3 Copper loss

The copper loss is the resistive losses in the windings. For high current density machines such as the baseline machine managing the copper loss is a big concern and is why the machine requires the liquid cooling system which, as will be seen in later chapters, creates much of the challenges in modelling the mechanical aspects of the machine. Copper loss dominates in the low speed/high torque region. The MATLAB tool uses (3.21) to calculate the copper loss without considering the AC copper loss [QG16].

$$W_{cop} = \frac{3}{2}\left(I_d^2 + I_q^2\right)R_{ph} \tag{3.21}$$

where R_{ph} is the phase resistance.

Where the iron loss calculation was performed using the FE tool, the copper loss calculation is performed by the MATLAB tool using the I_d and I_q current matrices. The resultant copper loss at each speed and torque point is then calculated in the same manner as the iron loss with the loss data interpolated from the loss matrix.

3.3.5.4 Mechanical loss

Mechanical loss is a more challenging aspect to calculate. With the iron loss and the copper loss there is enough data from the FE to make reasonable approximations. Bearing losses can be approximated supplier data but similar to the iron loss these results must be regarded with caution as best case data is likely to be provided in data sheets. Also, windage loss is a complex problem to solve. The methodology in the MATLAB tool is to use a best fit curve from empiric data (3.22).

$$W_{mech} = k_{m1}f_m + k_{m2}f_0^2 \tag{3.22}$$

where k_{m1} and k_{m2} are loss coefficients and f_m is the rotor frequency.

The key to the loss is obtaining the coefficients k_{m1} and k_{m2}. Fortunately, previous testing on the machine provides an empiric means to gain this. During the initial development of the machine a 2nd rotor, called the dummy rotor, was used as shown in Fig. 3.3.16.

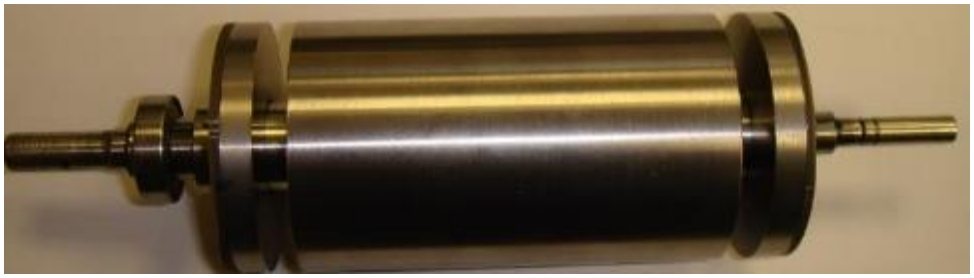

Fig. 3.3.16 Dummy rotor used to measure mechanical losses.

The dummy rotor is so-called because it is a solid cylinder of iron that has the same dimensions as the active rotor but does not have any magnets to interact with the rotor. The purpose of the dummy rotor is to measure the bearing and windage loss up to the maximum rotor speed. The rotor is inserted into the machine which is then linked to a dynamometer and accelerated up to the maximum speed in 500rpm steps, with the torque at each step measured using an inline torque sensor. The power measured is the loss which can be plotted. Using this plot k_{m1} and k_{m2} can be determined, the measured data and the resultant best fit curve are shown in Fig. 3.3.17.

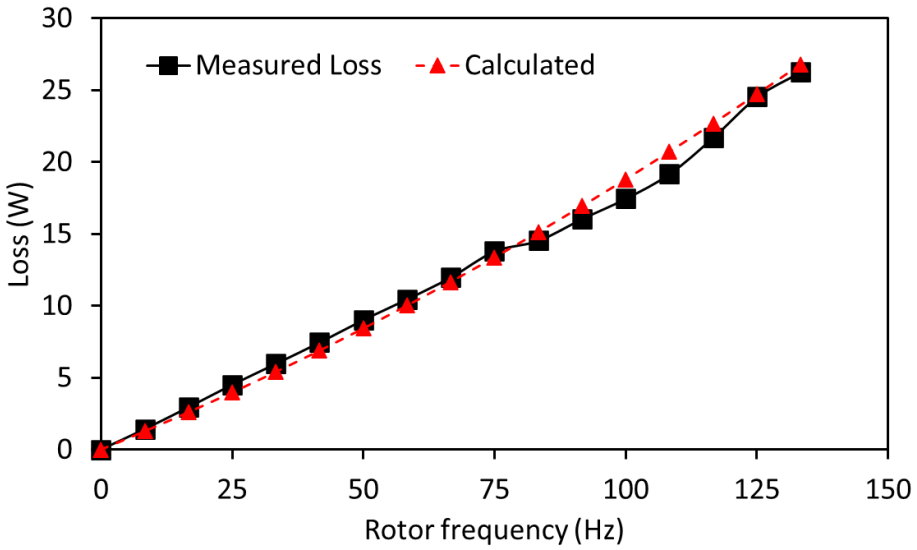

Fig 3.3.17 Measured loss and best fit curve.

From Fig. 3.3.17 the constants were derived as:

- k_{m1} = 0.15.
- k_{m2} = 0.0004.

The curve fits well to the measured, considering slight drift on the measured data. This was due to the torque sensor utilised being on the low end of its sensor range. It can be seen that the loss even at 7500rpm is around 25W which is very small compared to the copper and iron losses. Armed with the loss coefficients the MATLAB loss tool can calculate the loss at each speed step and use it the final efficiency calculation.

3.3.5.5 Resultant calculated efficiency plot

The output of the tool is a series of contour plots showing the calculated efficiency and loss maps of the machine. The MTPA method is used following the conclusion from the measured phase which showed no benefit in utilising the MEPA method for this machine.

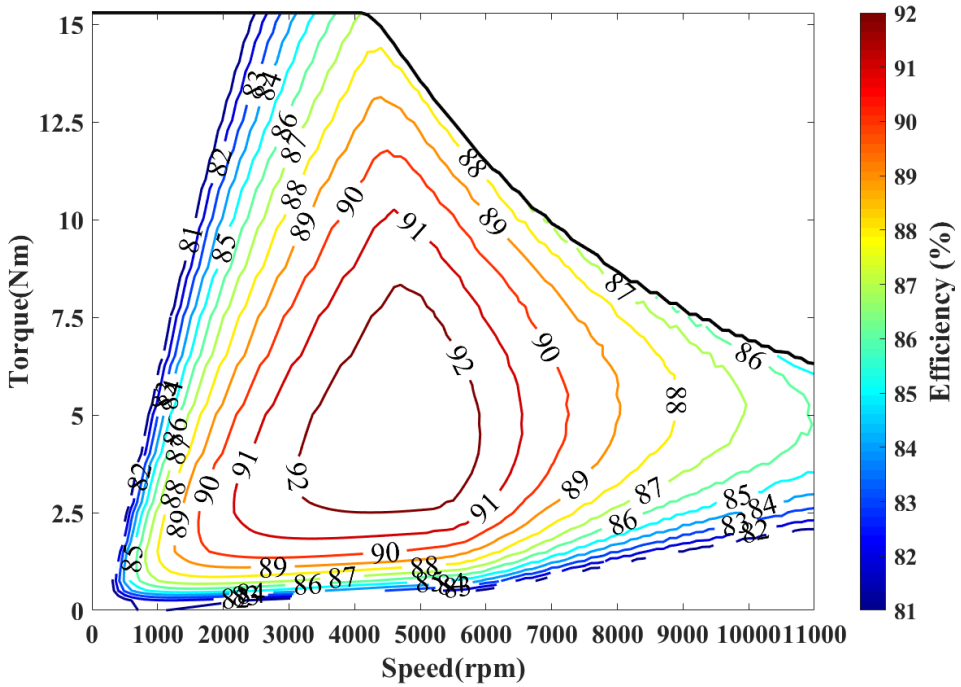

(a) Efficiency map (values in %)

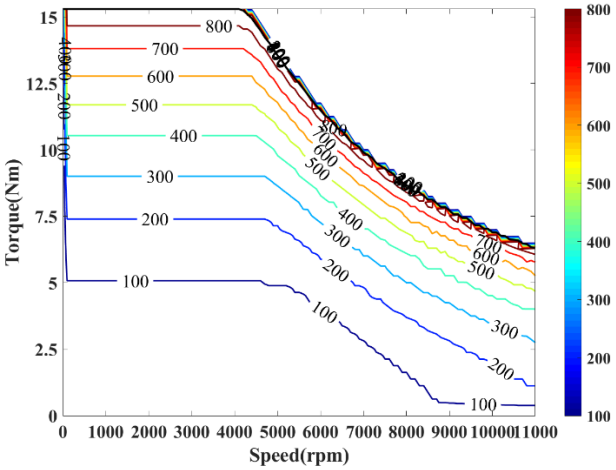

(b) Copper loss (values in Watts)

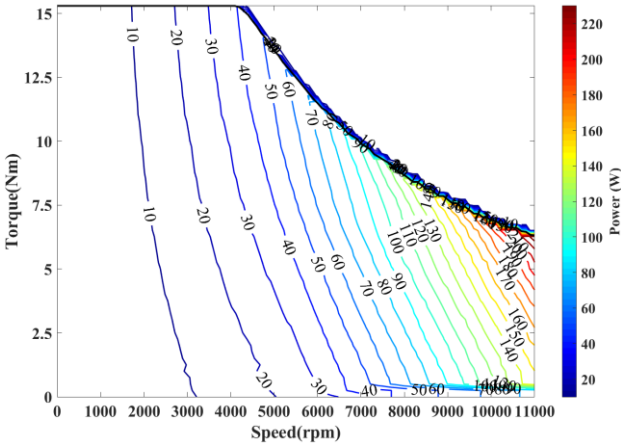

(c) Iron Loss (values in Watts)

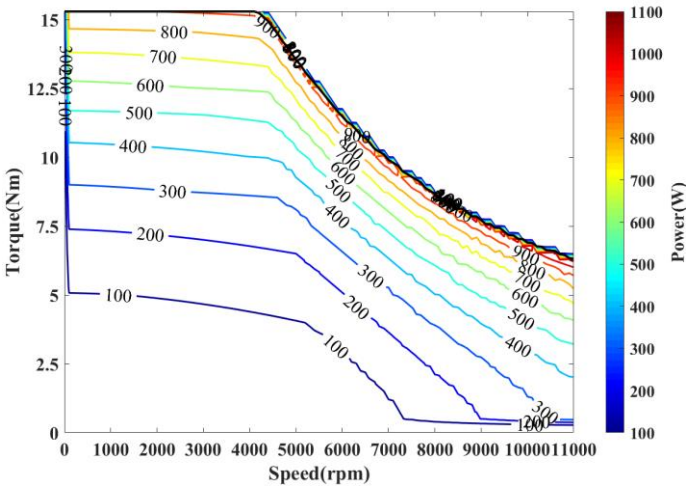

(d) Total loss (values in Watts)

Fig. 3.3.18 FE efficiency map and loss maps.

The simulation allows area under the T-N curve to be explored in higher fidelity than the test allowing both the maximum speed to be reached and much smoother contours. The loss contours in Figs.3.3.19 (b) to (d) show that the loss leader in the machine is copper loss (I^2R). Analysis of the percentage of the total loss is shown in Fig.3.3.19.

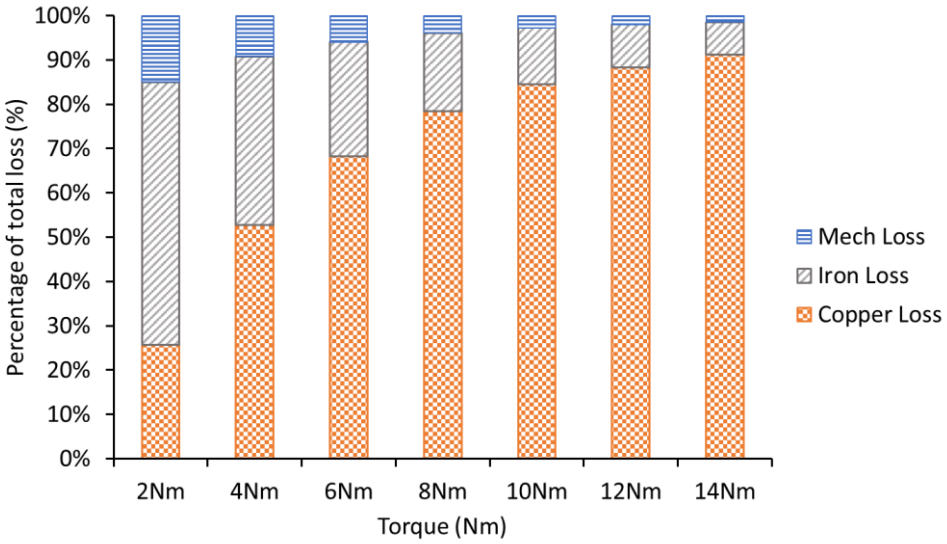

Fig. 3.3.19 Copper Loss vs. mechanical and iron losses at different torques with the machine running @ 3000rpm (100Hz electrical).

The data in Fig.3.3.19 shows that as the torque demand increases the copper loss quickly dominates the machine loss.

The efficiency of the machine can be compared with the measured data (fig 2.3.18(a)). The simulation results are adjusted so that the same speed and torque values from the measurement process are used and plotted onto a contour graph, as shown in Fig.3.3.20.

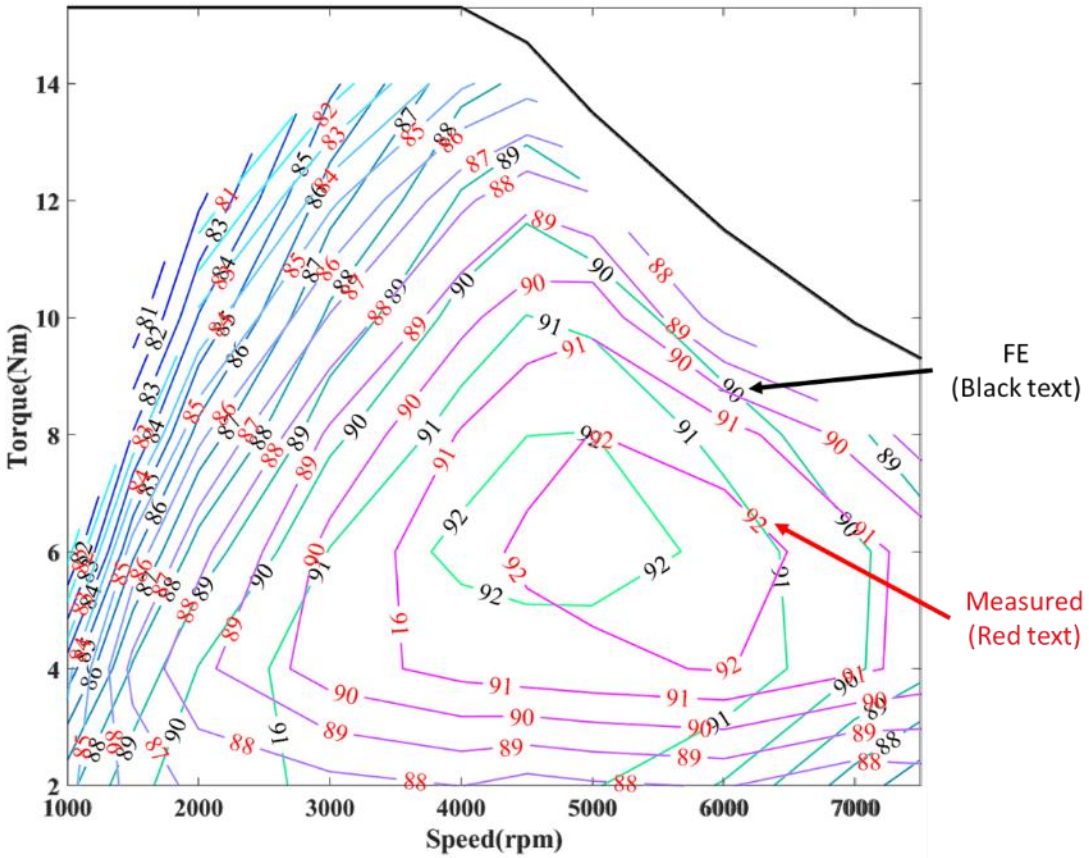

Fig. 3.3.20 Comparison of FE and measured efficiency maps.

The FE matches the efficiency of the measured data reasonably well. This is primarily due to the fact the machine is copper loss led, which suffers far less from the non-linearities that gives iron loss its previously discussed notoriety. As the copper loss drops away in the low torque, high speed region differences in efficiency are observed. For example, at 5000 rpm, 2Nm the measured efficiency sits between 88% and 89% whilst the FEA model is at 91% indicating some mismatch between the actual machine and the simulation, all be it minor. If the measurement had been able to go into the very high-speed region beyond 9000 rpm these differences may have been more apparent. However, the data captured shows good alignment.

Overall, the FE model matches well with the measured data indicating that the model is a good baseline for this PhD project.

3.4 Tooth Forces

The primary aim of developing the FEA model in this thesis is to generate the tooth forces that will be inputted into the mechanical model (developed in chapter 5). The work so far has ensured that the model matches the measured performance as close as possible has given good confidence that the electromagnetic performance shown by the FE model can be judged as representative of the real machine. This is very important as the accuracy of the tooth forces is heavily dependent on the accuracy of the airgap flux density. The Maxwell stress tensor method used to calculate the radial and tangential forces acting on the stator teeth was discussed in Chapter 1 using equations (1.3) and (1.4). Whilst these key equations dictate the force there have been many different methodologies developed to calculate the tooth forces as efficiently as possible for the entire machine, these methods can be broadly split into 3 different types:

1. Analytical: Air gap flux is calculated by analytical means then forces derived using the Maxwell stress tensor ((1.3) and (1.4)).
2. Hybrid FE method [KW14]: FEA package such as MAXWELL or JMAG used to provide more accurate derivation of the airgap flux density components then Maxwell stress tensor used to derive the tangential and radial forces across the air gap.
3. Full FEA method: Electromagnetic FE package calculates airgap flux components which then links to mechanical FE package to map the forces acting on the system.

Ultimately method (3) will be utilised to output the forces as it eliminates the need for special scripts or software to extract the flux, calculate the forces and import them to the mechanical tool with all the risk of error each step adds.

For this final section of the development of the electromagnetic model the hybrid methodology will be used to allow a close examination of the distribution of the magnetic flux as it crosses the air gap under different load conditions and different rotor positions. The FE tool is used to calculate to the radial and tangential forces at different points of interest then the forces calculated post process.

3.4.1 Establishing the force curve position

Within the hybrid method there has to be some object or region onto which the forces can be calculated. Typically, this is achieved by drawing a curve at or near the tooth surface. The nature of computer graphics mean there is no such thing as a curve, rather they are many-sided polygons creating a phenomena called aisling where the “circle” has rough edges; modern graphics hardware uses sheer processor power and some clever tricks such as anti-aisling to fool the eye into seeing a smooth circle. Thus, the arc is a series of sections splitting the shape up and the radial and tangential flux densities acting on each section is captured from the FE tool. Given an arc length L_{arc} split into a number of divisions, n_{divs}, the length of each divisiton, τ_s, can be determined using (3.23):

$$\tau_s = \frac{l_{arc}}{n_{divs}} \tag{3.23}$$

Given the stack length, L_{stk}, the force acting over the area of each section can be determined by applying (3.22) to (1.3) and (1.4) to give the tangential force (3.24) and the radial force (3.25):

$$F_{tan} = \frac{B_r B_t}{\mu_0} \tau_s L_{stk} \tag{3.24}$$

$$F_{rad} = \frac{B_r^2 - B_t^2}{2\mu_0} \tau_s L_{stk} \tag{3.25}$$

The total force over the curve is a summation of the forces.

With the method of calculating the forces established the next key questions are:

1. How long should the arc be?
2. Where should the arc be located radially?

The answer to the first question is reasonably straight forwards. Whilst the tooth tip width seems the most obvious length this tends to miss the slot gap flux that interacts with the edges of the tooth. As was seen in Chapter 1 the fringing effect due to the slot gap flux is a significant source of torque pulsation due to the variation in permanence caused by the contrast between the air in the slot gap and the very low reluctance of the tooth material. To capture as much of the fringing flux in the slot gap as possible the curve should cover one slot pitch, starting and ending at the mid-slot points between the tooth being measured. For this machine this means the curve covers and angle of 15°.

The second question is much more complicated. The most logical place for the curve is on the tooth surface. However, in the literature [JM88], [ZR94], [RP20], and [YX14], it is highlighted that the Maxwell stress tensor methodology as depicted in (3.24) and (3.25) is too simplistic due to:

- Slotting effect, i.e. the variations in permeance between the air gap, where $\mu_r = \mu_0$ and the ferromagnetic tooth material where $\mu_r >> \mu_0$ is difficult to compensate for [ZR94], [JM88].
- The mesh along the tooth edge is less uniform meaning τ_s varies along the length of the curve, again complicating the calculation.
- Discretization of the air/steel interface due to the meshing can make placing the curve very difficult with some sections crossing into the air gap leading to irregular spikes in the flux density trace as the permeance suddenly changes [JM88].
- Non-linearities due to aspects such as flux saturation on the tooth, in particular the tooth tips, reducing the accuracy.

Whilst there are methods to compensate for this such as the virtual work principle [JM88], [ZR94], these are much more computationally intense and more suited to the full FEA method than the hybrid methodology.

Where the Maxwell stress tensor is utilised, the preference is to locate the curve in the air gap as the flux density is much higher and in regular intervals, the permeance is constant and the material does not saturate [JM88], [ECTS93], [ZR94], [RF20].

To best utilise the Maxwell stress tensor as has been defined the curve must be located in the air gap, but the question still remains, which is the best radial position? Typically the mid-air gap is the chosen location but there is some risk this interacts with neighbouring teeth and aspects of the rotor core such as leakage flux which may loop into the air gap but does not interact with the stator tooth. Alternatively, the curve could sit as close as possible to the tooth surface as possible without encountering the previously discussed risks. Fig. 3.4.1 shows the curves compared.

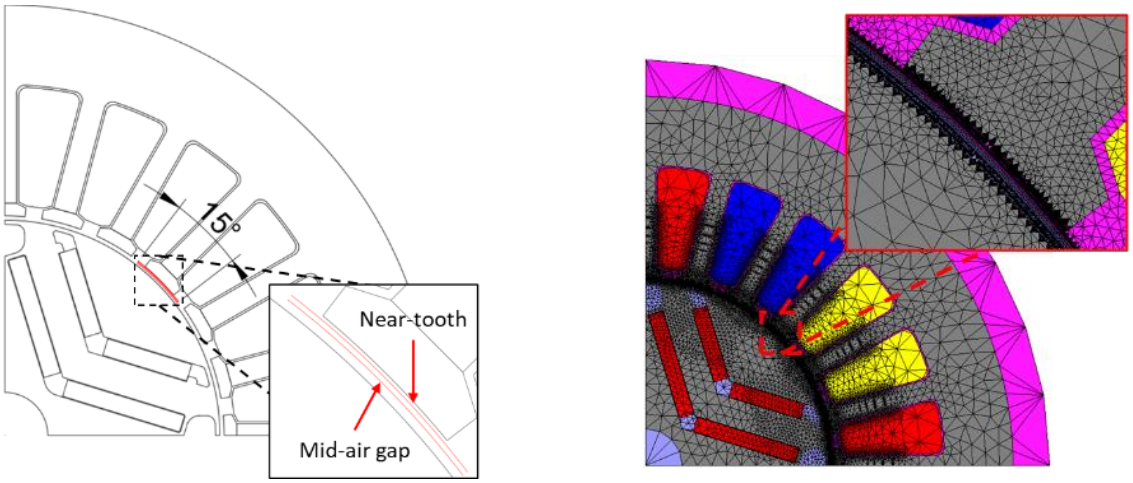

(a) ¼ model and flux sampling curves locations (b) High density mesh FE model

Fig. 3.4.1 FEA model and air gap curve locations for deriving forces.

From Fig.3.4.1(a) it can be that two air-gap curves have been added that sweep a 15° arc from mid-slot to mid-slot across a single tooth pitch.

- Two curves have been added at the following locations
  - Mid-air gap (radius = 25.25mm)
  - Near tooth (radius 25.4 mm)
  - For reference the stator inner diameter is 25.5mm
- The direction of the curves is set by the FE tool and is COUNTERCLOCK WISE (CCW) from the start (0mm) to the maximum length of the curve, l_{arc}, sweeping right to left on the model in Fig. 3.4.1(a).
  - This point is very important when interpreting the flux and force distribution graphs shown later in this section.

As highlighted previously the force calculations are highly sensitive to the mesh, so a very high mesh density is created within the air gap, shown in Fig 3.4.1(b).

To compare the different arcs the FE simulation is run under no load conditions at 1500rpm for a single force cycle, that is 90° mechanical, reflecting one magnet pole arc passing the tooth, starting at the 0° position

illustrated in Fig. 3.4.1(b). Fig 3.4.2 shows the calculated radial and tangential forces over one cycle as well as the radial and tangential flux at 0°, 30° and 45°. Under no load conditions, the magnetic loading is purely from the PM and is symmetrical so 45° to 90° will be a mirror image of 0° to 45°.

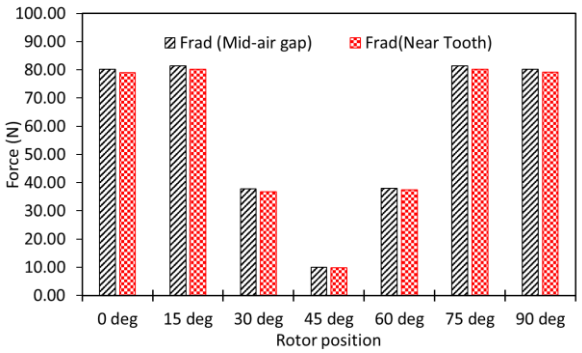

(a) Radial forces.

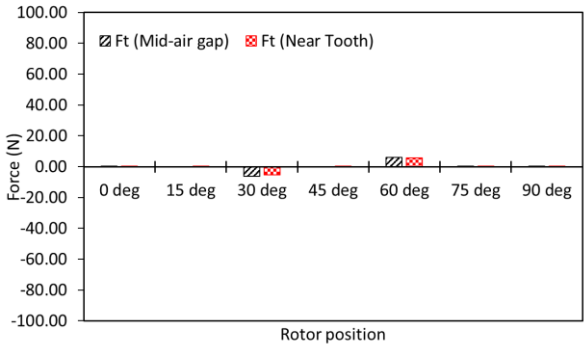

(b) Tangential forces.

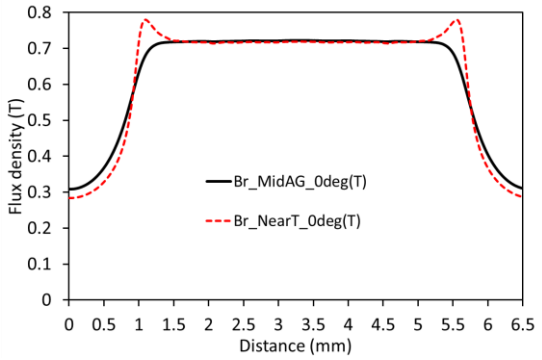

(c) Radial flux density, rotor @ 0 deg.

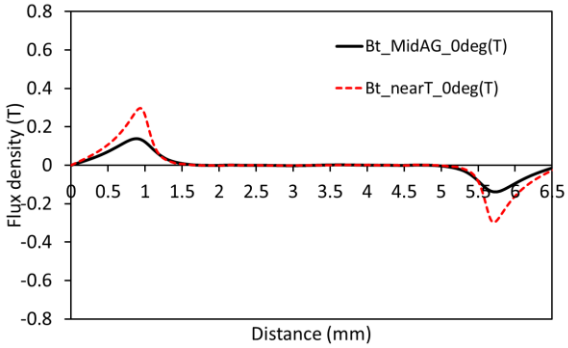

(d) Tangential flux, rotor 0 deg.

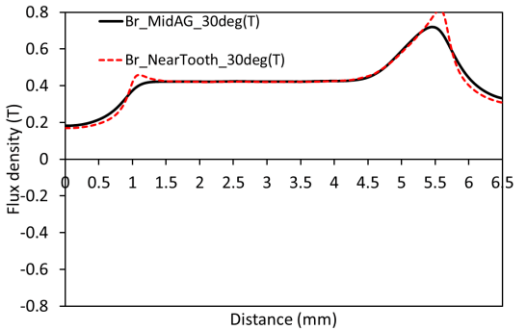

(e) Radial flux density, rotor @ 30deg.

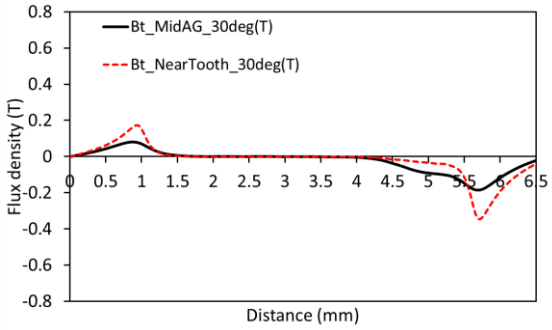

(f) Tangential flux, rotor @ 30 deg.

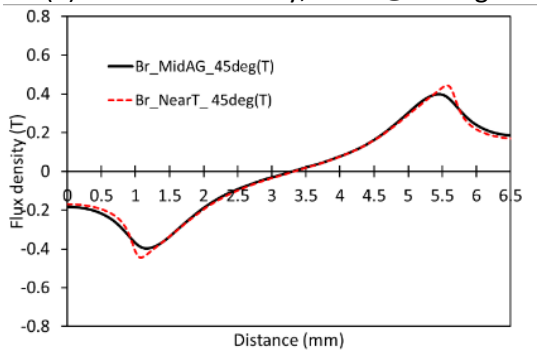

(g) Radial flux density, rotor @ 45deg.

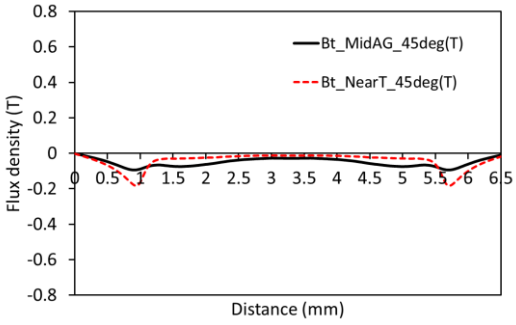

(h) Radial flux density, rotor @ 45 deg.

Fig. 3.4.2 Comparison of force and flux density on near tooth and mid-air gap curve positions at different rotor positions and no-load conditions.

The calculated forces in Fig. 3.4.2 (a) and (b) are summarised in Table 3.4.1.

Table 3.4.1 Comparison of near tooth and mid-air gap forces

Rotor position	Near tooth		Mid-air gap	
	Fr (N)	Ft (N)	Fr (N)	Ft (N)
0°	79.08	0.22	80.20	0.01
15°	80.23	0.06	81.39	-0.15
30°	36.76	-5.39	37.75	-6.12
45°	9.74	0.09	10.03	0.00
60°	37.48	5.80	37.91	6.14
75°	80.15	0.34	81.36	0.15
90°	79.09	0.22	80.21	0.00

Comparing the forces in the near-tooth and mid-air gap positions in Fig. 3.4.2 (a) and (b) and Table 3.4.1 shows very little difference in the forces, and between the two minor differences of ~1N can be seen at the maximum force positions on both the radial and tangential forces. Comparing the radial and tangential flux densities on the curves at the different rotor positions (Fig. 3.4.2 (c) to (h)) shows some differences:

- The biggest difference lies at the tooth edges, the near tooth shows raised “horns” for both radial and tangential flux densities showing the curve is passing through a region of higher flux density due to the fringing effect on the tooth tip than the mid-air gap.
- Minor differences between tangential flux densities along the tooth edge at 30° and 45°, the mid-air gap appears to pick up a slightly higher flux density at 45° due to the leakage flux from the rotor bridging into the air gap but the density is balanced and hence the net force is zero.

Given the minor differences between the two curves the mid-air gap curve is chosen as the smoother trace makes calculations and comparisons at different load conditions a little more straight-forward.

3.4.2 No load tooth force analysis

With the force calculation curve established a more detailed investigation of the force characteristics of the machine can now be undertaken. Fig. 3.4.2 shows the forces and flux density on the calculated curves. However, the reasoning for the distribution being the way it was is less clear from simply looking at the waveforms. Using the FE tool, the flux density in relation to the rotor and stator geometry can be studied at each rotor step point to understand why the curves are the way they are and what effect this has on the resultant forces. Fig. 3.4.3 shows the flux density distribution on the tooth and rotor geometry at different rotor positions as well as the flux lines and vectors illustrating the flux bridging the air gap.

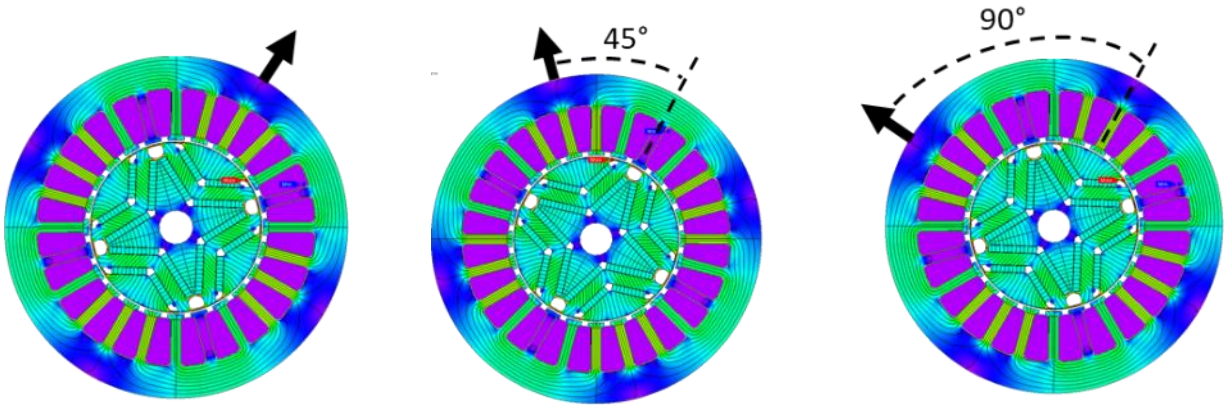

(a) Rotor at 0° (b) Rotor at 45° (c) Rotor at 90°

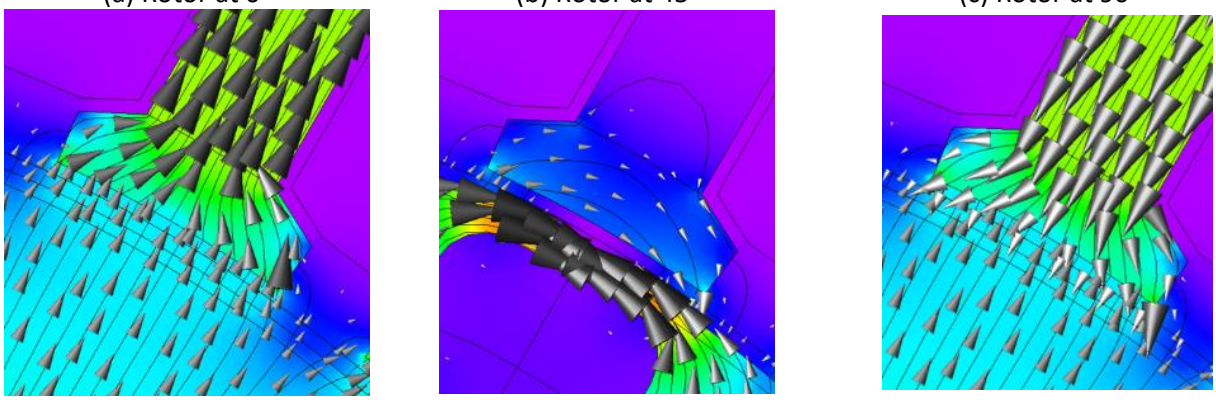

(d) Tooth flux lines & density @ 0° (e) Tooth flux lines & density @ 45° (f) Tooth flux lines & density @ 90°

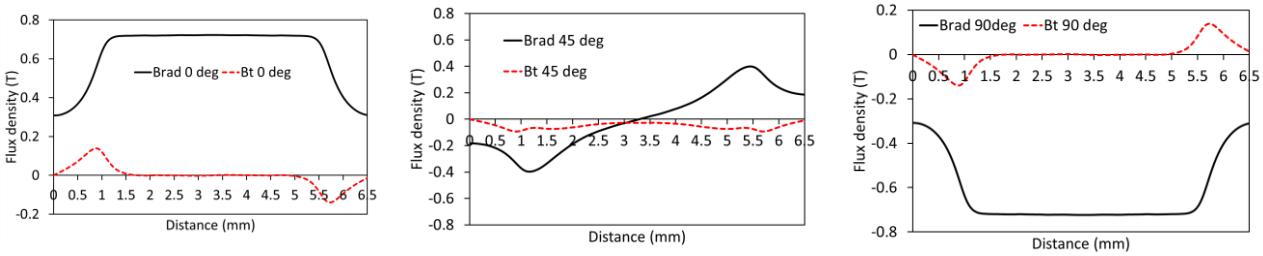

(g) Radial and tangential flux density @ 0° (h) Radial and tangential flux density @ 45° (i) Radial and tangential flux density @ 90°

Fig. 3.4.3 Flux densities and tooth loading across one pole pitch with rotor positions of 0°, 45° and 90°.

From Fig 3.4.3 some observations can be made:

- 0° and 90° for both tangential and radial flux densities are mirror images of each other; along the x-axis on the radial flux and y-axis on the tangential. This is logical as the rotor has moved half an electrical cycle (4 pole machine) so the geometry is identical, but the magnet polarity has changed therefore the flux is flowing in the opposite direction
- Some peaks are observed on the tangential traces at 0° and 90° reflecting the fringing effect due to the slots.
- At 45° the picture changes, from the image on Fig.3.4.2 (e) it can be seen that the tooth is aligned to the q-axis flux barrier which creates a fairly saturated region of flux at the rotor edge and has high flux density in the rotor. The leakage in the rotor core means the flux density in the tooth at this point

is low and what little flux is bridging the gap tends to be fringing, and hence the higher tangential flux density component at the tooth. At this state, some radial force would be expected as the function (B_r^2-B_t^2) would produce a net radial force.

The tangential force data in Fig. 3.4.2 (b) shows a distinct difference at 30° and 60° compared to the other rotor positions which warrants further investigation. Fig. 3.4.4 shows the flux lines in the teeth and the flux density traces for 30° and 60°.

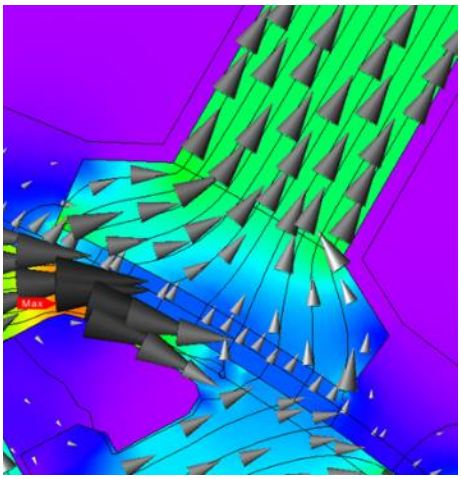

(a) Flux lines and density at 30°

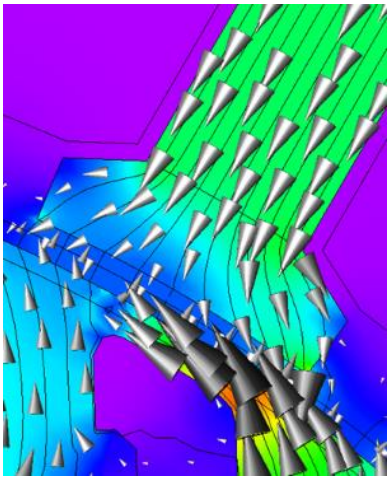

(b) Flux lines and density at 60°

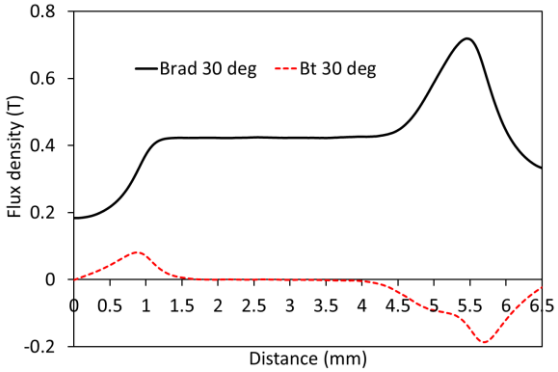

(c) Radial and tangential flux density @ 30°

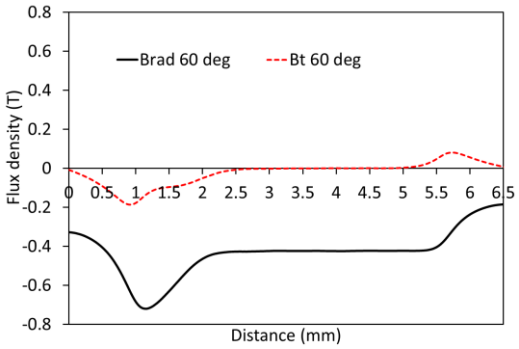

(d) Radial and tangential flux density @ 60°

Fig. 3.4.4 Radial and tangential flux densities with rotor positions 30° and 60°.

It can be seen in the flux density images (Figs.3.4.4 (a) and (b)) that at these positions the upper layer magnet flux barrier on the rotor is aligned with the mid-air gap curve used to calculated the flux density.

- The small area of rotor steel present is quite saturated at the edge of the upper layer of magnets (to the left at 30° (Fig. 3.4.4 (a))and to the right at 60° (Fig. 3.4.4 (b))) at this point which means the flux passing through the curve is asymmetrical and therefore unbalanced.
- The tangential flux density highlights this best the flux density observed on the curve located on the stator tooth is unbalanced.
    - At 30° at a position of ~1mm on the curve the flux density hits a small peak at the tooth edge of around 0.09T, whereas the opposite end of the tooth, moving along the curve CCW to the 4mm the gap aligns with the region of high flux density on the leading edge of the flux barrier

leading to the flux density climbing to hit a maximum at the 5.5mm mark where the flux density sits around 0.19T.

- From the Maxwell stress tensor, the tangential forces are proportional to the product of the B_r and B_t flux density components (3.24); if there is an asymmetry of flux density across the air gap curve then there must be an unbalanced force.
- At 60° the trend and amplitudes are the same, but polarities reversed.

3.4.2.1 Nodal force probe – no load

FE tools enable the use of the nodal force method [JLC84], [YK05], [JM18]. Where the Maxwell stress tensor method covered so far gives the integral force acting over curve spanning a full slot pitch, the nodal force method calculates the force on the nodes linking elements of a mesh and is used in electromagnetic and mechanical FE packages giving a more microscopic view of the forces. Whilst the method has some draw backs such as high sensitivity to mesh density and concerns with effects such as saturation the advantage is that it allows for the force acting on a node to be traced over one period of the simulation. JMAG offers a "probe" tool that allows the force and flux densities acting on a node at each step of the simulation to be traced giving a force profile. Placing a probe at the tooth edge allows the effect of the rotor passing below the probe over a given cycle to be visualised. Fig. 3.4.5 shows the setup and results of applying the probe to the no-load force cycle detailed in the previous section.

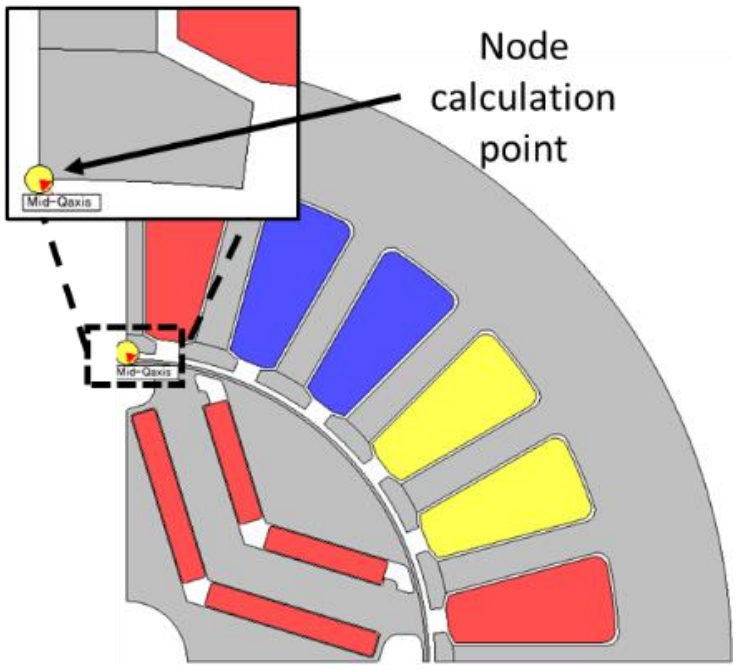

(a) Nodal force calculation point.

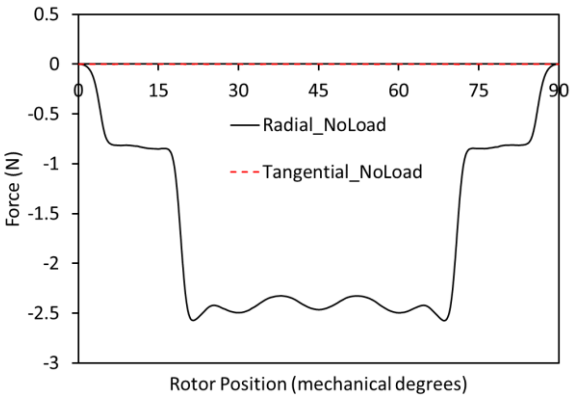

(b) Radial and tangential nodal force waveform

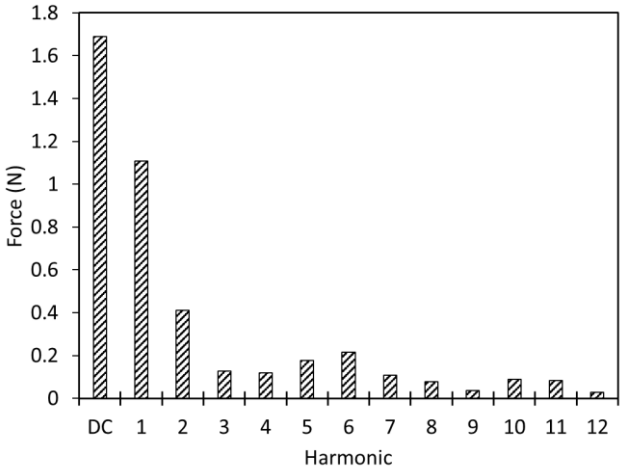

(c) Tooth force (radial) FFT

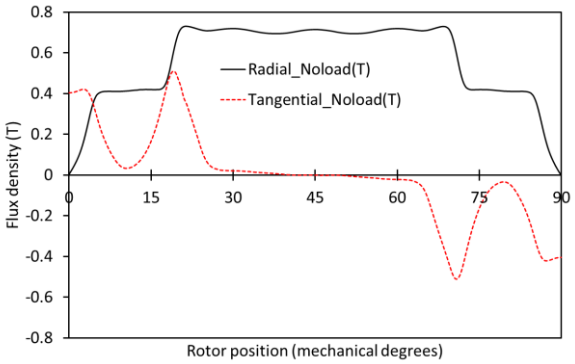

(d) Probe calculated Radial and tangential flux densities

Fig. 3.4.5 Nodal force and flux density profile over 1 force cycle

Given the starting position of the rotor the probe is aligned to the q-axis and located in the centre position based on the applications notes from JMAG [JM13]. This avoids effects such as saturation due to fringing. The influence of the 2-layer magnet design and flux guides can be clearly observed by the force profile in Fig.3.4.5 (a). Fig. 3.4.6 shows the rotor with an angle guide superimposed on top, with each angle showing what rotor geometry the node is aligned to as the rotor moves beneath the “probe”.

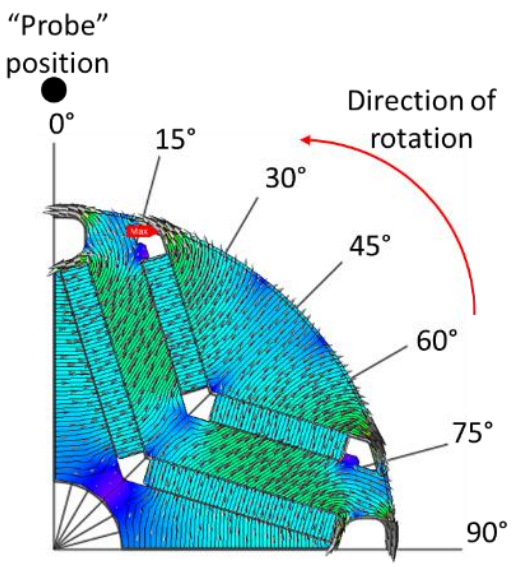

Fig 3.4.6 Position of node above rotor in 15° intervals during one force cycle

- As the rotor moves from 0° the probe is aligned to the q-axis flux barrier so the net flux bridging the air gap is low and tangential in nature.
- As the q-axis barrier passes the probe aligns with the main rotor magnetic circuit from the lower layer of magnets causing a sharp rise in the radial flux density and force.
- Between the edge of the of the q-axis barrier as the rotor continues to move counter-clockwise the probe is aligned with the inter magnet layer iron which has a pretty constant radial component.
- At ~15°the probe comes into alignment with upper layer magnet flux barrier. The high reluctance of this region causes the rotor PM flux to cross the air gap creating a spike in the tangential flux component.
- Past ~20° the upper layer comes into alignment and the force raises to maximum caused by both radial and tangential components (Fig. 3.4.5(d)).
- By around 30° the flux is purely radial and begins to drop with a distinct ripple from the slot-effect of the stator as it algins with the rotor d-axis at 45°.
- From 45° the process reverses, rising back to the maximum before dropping off as the upper then lower layers pass the virtual probe.

It can be seen that given the only flux source is the PM flux the bulk of the flux calculated at the node is radial, the only time the tangential component appears is at the edges of the q-axis and upper layer magnet flux barriers.

3.4.3 On load tooth forces

Following the no-load forces calculations, the established process is repeated with on load. The major difference here is that in addition to the PM flux the flux generated by the coils come into play which are influenced both by the current magnitude and the current angle, which affect the field position relative to

the PM flux. The high mesh density required to gain good fidelity on the curves applied to the mid-air gap mean that the simulation run time is very high so 2 scenarios will be run:

1. Current is set to maximum (I_{max} = 26.7A_{rms}) and the current angle is set to zero (β = 0°)
2. Current is set to maximum (Imax = 26.7Arms) and current angle is set to 45°

In scenario 1 the machine is being studied with the current angle at zero which means the only torque available to the machine is the mutual torque. In scenario 2 the current angle is shifted such that the maximum reluctance torque is applied so the machine is producing maximum torque. The same mesh as the no load study is applied.

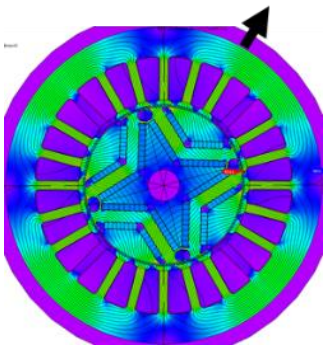

(a) Rotor at 0°

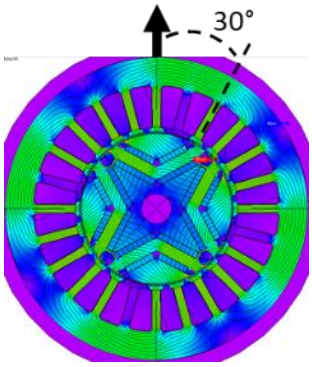

(b) Rotor at 30°

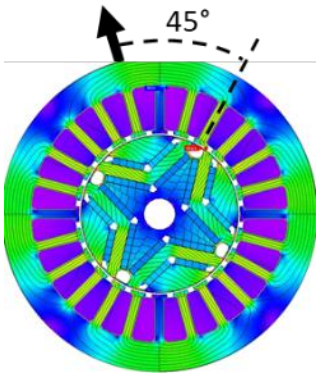

(c) Rotor at 45°

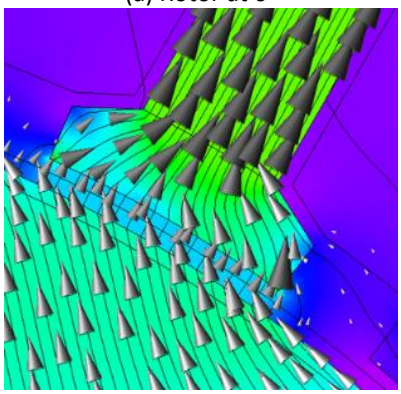

(d) Tooth flux lines & density @ 0°

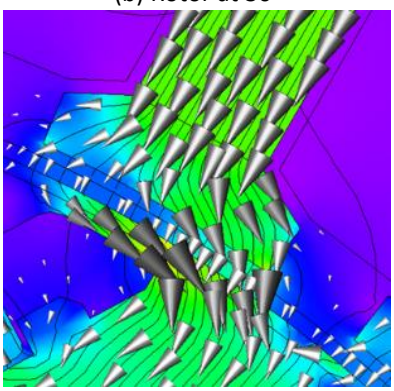

(e) Tooth flux lines & density @ 30°

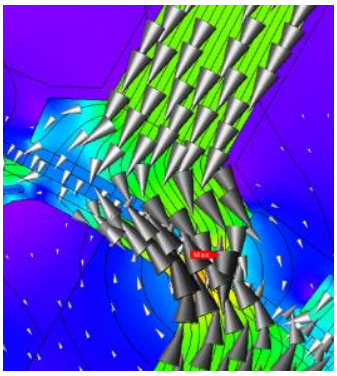

(f) Tooth flux lines & density @ 45°

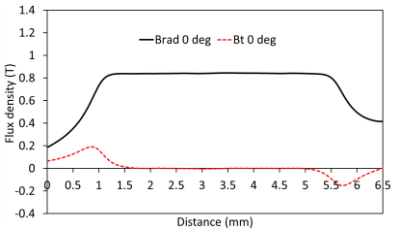

(g) Radial and tangential flux density @ 0°

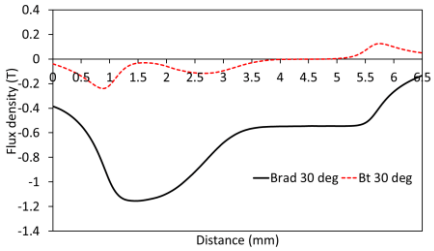

(h) Radial and tangential flux density @ 30°

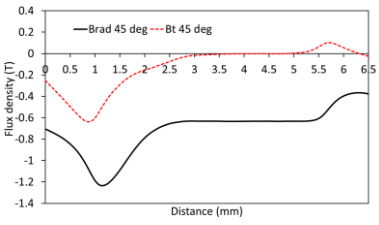

(i) Radial and tangential flux density @ 45°

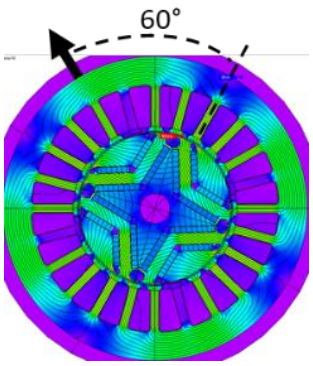

(j) Rotor at 60°

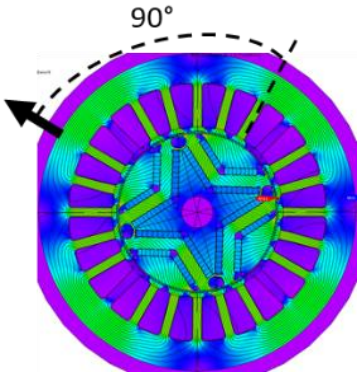

(k) Rotor at 90°

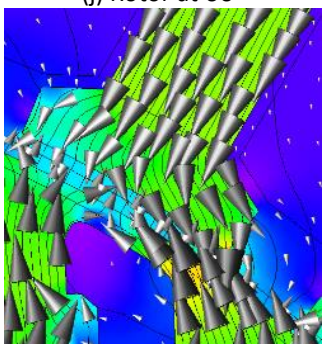

(l) Tooth flux lines & density @ 60°

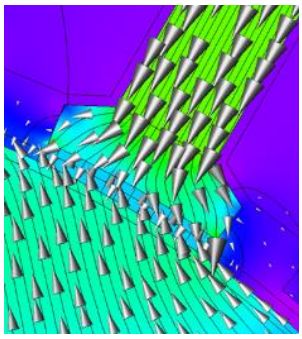

(m) Tooth flux lines & density @ 90°

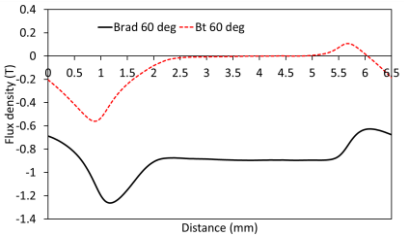

(0) Radial and tangential flux density @ 60°

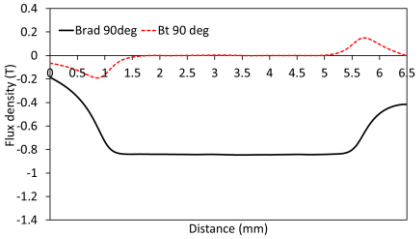

(p) Radial and tangential flux density @ 90°

Fig. 3.4.7 Rotor flux density across one pole pitch at maximum torque (I_{rms} = 26.7, B = 0°) with rotor positions of 0°, 30°, 45°, 60° and 90°.

The stator field has acted to change the flux densities calculated on the air gap curve considerably compared to the no load.

- At the 0° and 90° positions the flux in the rotor is being pulled tangentially within the core giving an asymmetric waveform for both the radial and tangential components along the length of the curve, with considerably less tangential flux at the upper edge of the curve, which is illustrated in Fig. 3.4.7(d).
- At the 30°, 45° and 60° the flux barriers block the main flux path such that the flux is heavily biased on the lower edge of the curve, showing high imbalance in the tangential direction.
    - More of the curve is covered by the flux barrier at the 45° and 60° positions amplifying the effect vs. the distribution at the 30° position.

Using the radial and tangential forces shown in Fig 3.4.7 the forces of the machine can be generated and can be seen in fig3.4.8.

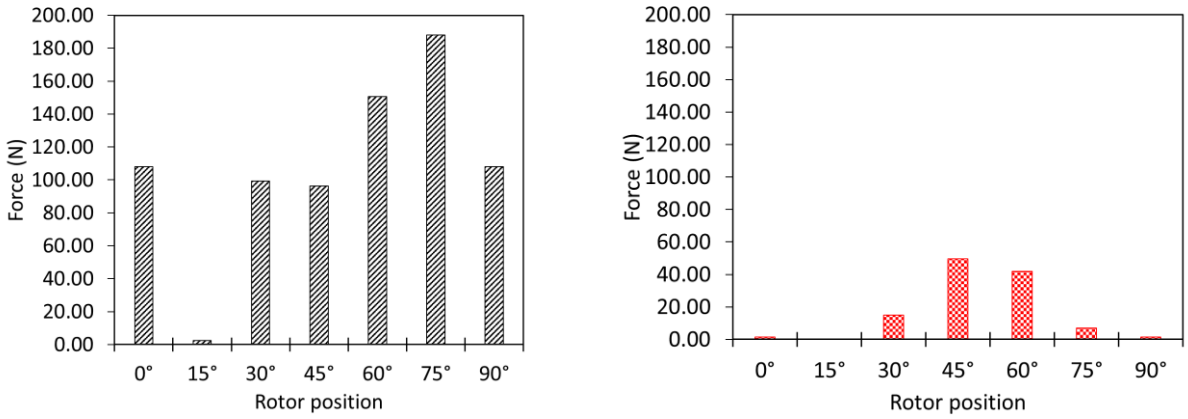

(a) Radial forces (b) Tangential forces

Fig. 3.4.8 Calculated forces on air gap curve with machine at I = 26.7Arms, β = 0° at different rotor angles.

Table 3.4.2 provides the force values for the charts in Fig. 3.4.7.

Table 3.4.2 Calculated forces on air gap curve using B_r and B_t data from FE at I = 26.7Arms and β = 0°

Rotor position	Radial Force (N)	Tangential force (N)
0°	108.11	1.36
15°	2.48	-0.03
30°	99.24	14.90
45°	96.27	49.44
60°	150.52	41.79
75°	188.00	7.14
90°	108.11	1.36

It can be seen from Fig.3.4.8 that the additional flux from the coils has not only greatly increased the forces acting on the curve but the symmetry seen at no load is no longer present.

- At the 0° position where the curve is aligned to the d-axis there is a large radial force but very small tangential force, reflecting the fact the bulk of the flux is moving radially across the air gap.
- At 30°, 45° (rotor q-axis) and 60° the imbalance of flux density across the curve has resulted in significant tangential forces, the peak of which is at 45°, reflecting the fact that the bulk of the flux flowing through the machine is moving tangentially towards the q-axis, attracted by the armature field.

From Fig. 3.4.8 (a) and Table 3.4.2, it can be seen that the radial forces at 15° and 75° contrast starkly, and 15° shows almost no radial or tangential forces whilst 75° generates the maximum radial force. It is worth analysing a little further to understand why.

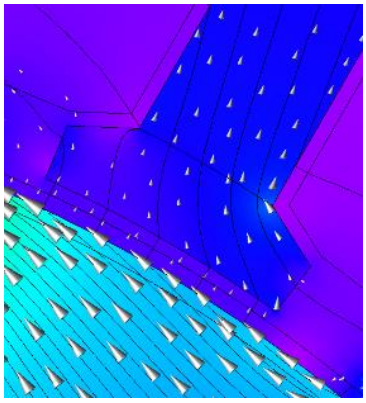

(a) Flux lines and flux density of tooth and rotor surface with rotor @ 15°.

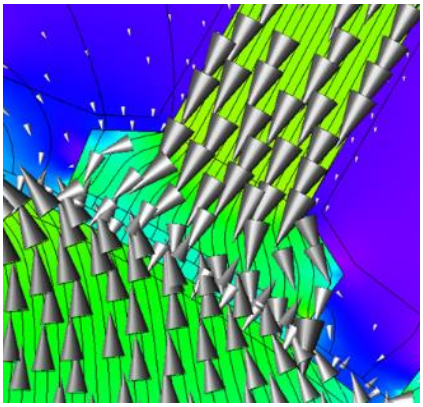

(b) Flux lines and flux density of tooth and rotor surface @ 75°.

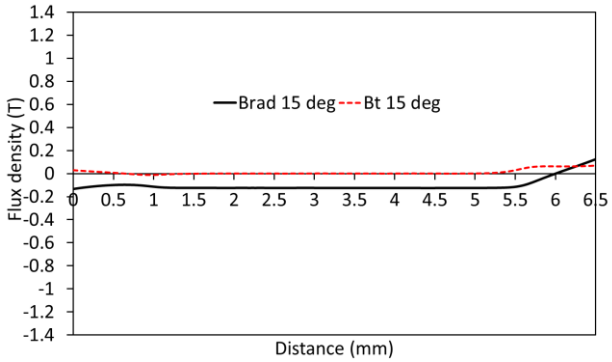

(c) Radial and tangential flux densities on mid-air gap curve @ 15°.

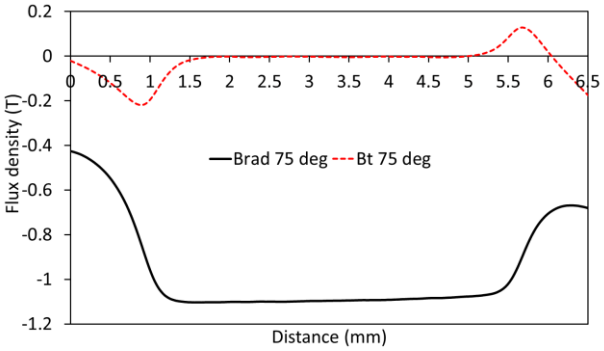

(d) Radial and tangential flux densities on mid-air gap curve @ 75°.

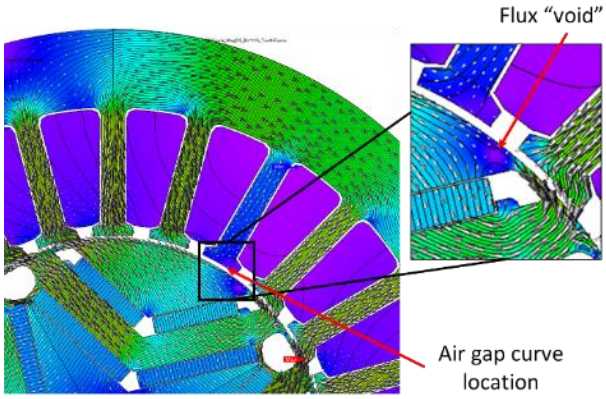

(e) View of back iron and rotor flux paths with rotor position = 15°.

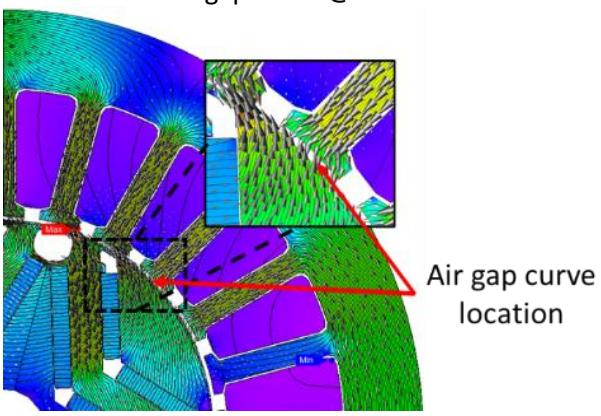

(f) View of back iron and rotor flux paths with rotor position = 75°.

Fig. 3.4.9 Radial and tangential flux densities with rotor positions 15° and 75°.

It can be seen that the flux density of the tooth at 15° (Fig. 3.4.9(a)) is much lower than at 75° (Fig. 3.4.9(b)) which is reflected in the flux density on the air gap curves (Fig. 3.4.9 (c) and Fig 3.4.9(d)).

- At 75 the tooth is aligned to a region of high flux density on the rotor (Fig. 3.4.9(f)).
    - Flux traversing the rotor is encountering a region of saturation around the upper layer flux barrier.
    - Faced with this high reluctance region and the slot gap, a large amount of flux moves radially across the air gap to the tooth, reflected in the very high and constant radial flux density along the region of the curve aligned with the tooth surface in Fig. 3.4.9(d).

- The loading resembles that of tooth aligned to the d-axis under no-load conditions, but the increased flux loading due to the coil MMF mean the forces are considerably higher.

- Moving the rotor 15° places the tooth in alignment with a region of very low flux density in the rotor (fig 3.4.9(e)).
  - Flux from the upper magnet is passing tangentially through the low reluctance region of the rotor above the upper 'V' as it is drawn to link with the field from the stator coil.
  - The flux in the stator back iron has very little to attract it down the tooth, with only a small leakage flux appearing.

How much this effect has on the vibration behaviour is of interest; the effect occurs every 15° affecting 4 teeth (1 per pole) which are diametrically opposite to each other, indicating that the forces are the same at opposing sides of the rotor. This means there is no UMF but there is a saliency in the force profile which may be of interest. Fig. 3.4.10 shows the pattern repeats every 15° from 0° to 75° (90° is the same as 0°).

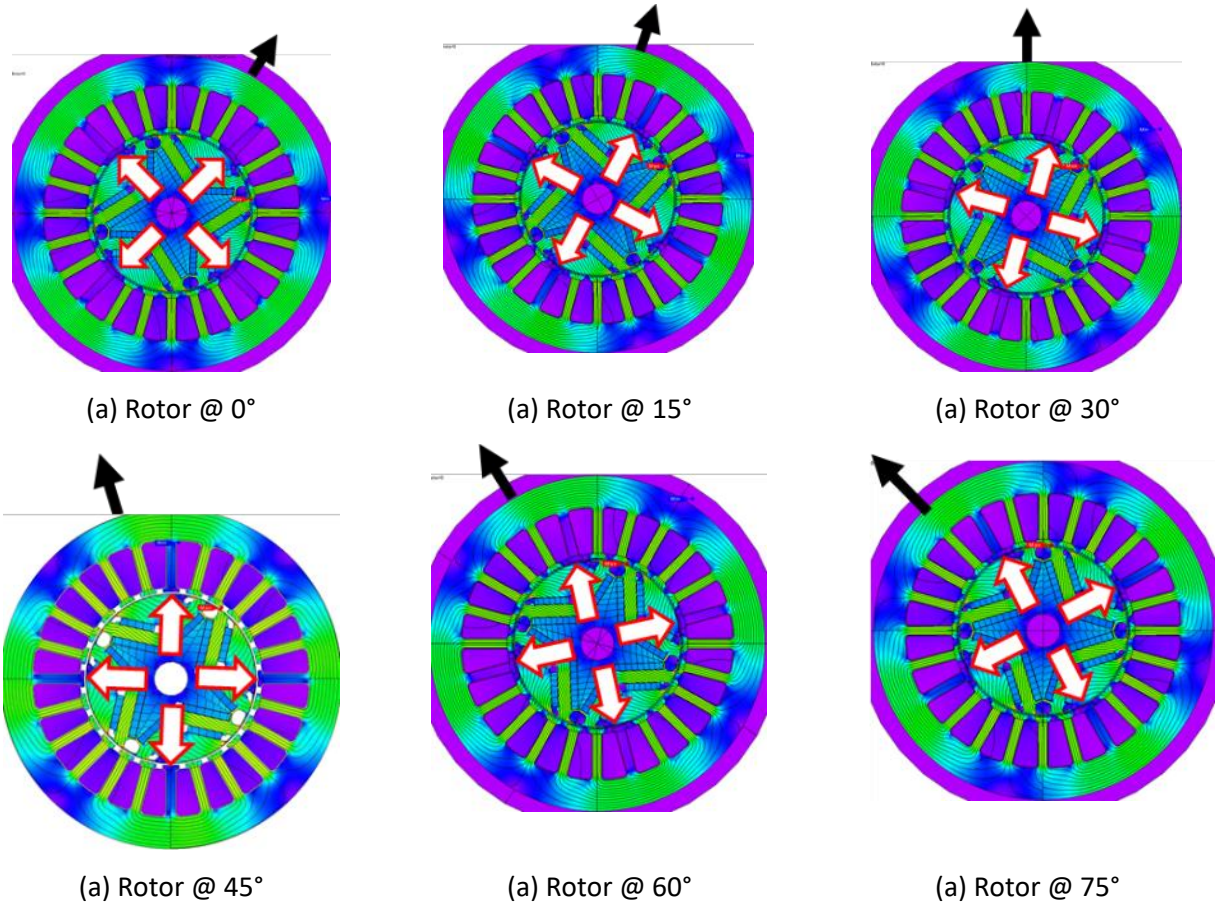

(a) Rotor @ 0° (a) Rotor @ 15° (a) Rotor @ 30°

(a) Rotor @ 45° (a) Rotor @ 60° (a) Rotor @ 75°

Fig. 3.4.10 Snap shots of full rotor flux highlighting the "dead" tooth follows the same point as the rotor spins.

Fig. 3.4.11 shows positions at 10°, 20° and 50°. It is clear from these images that all the teeth in the machine are being utilised.

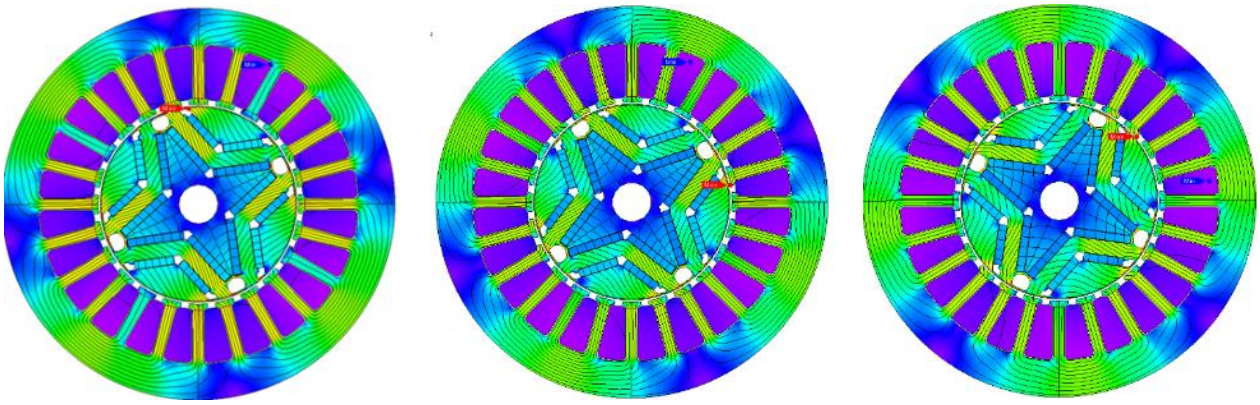

(a) Rotor position = 10° (a) Rotor position = 20° (a) Rotor position = 50°

Fig. 3.4.11 Comparison of stator and iron magnetic loading at different rotor positions with I = 26.7Arms and β = 0°.

Clearly there is some stack up with rotor/stator geometry and the coil field position relative to d-axis that conspire to create the "dead" teeth. To understand if this phenomenon has any impact on the vibratory performance of the machine the mechanical model is required which is the subject of subsequent chapters.

3.4.3.1 Nodal force probe –load, I = 26.7A_{rms}, β=0°

Similar to the no load the tooth force waveform over one magnetic force cycle can be captured from a tooth force probe, the location of which is identical to that shown in Fig3.4.5(a). The nodal force calculated by the FE tool is shown in Fig.3.4.12.

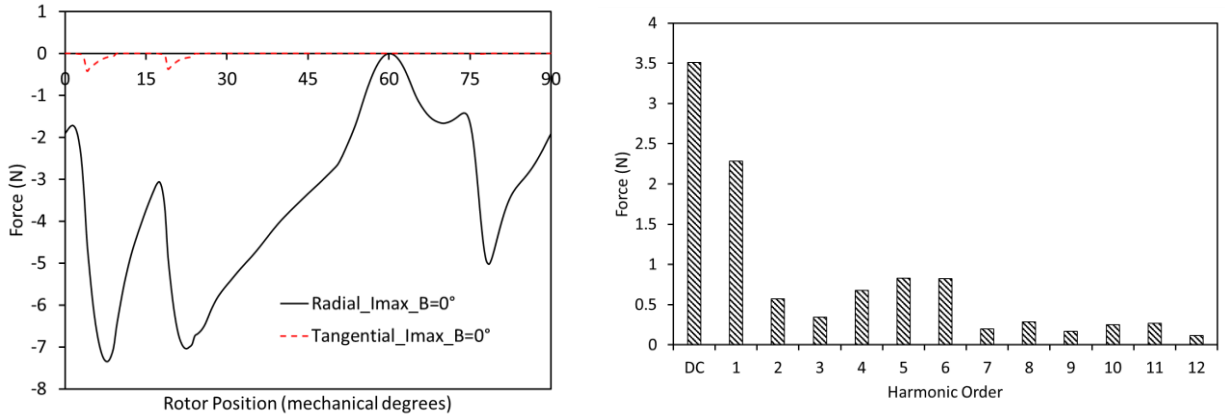

(a) Radial and tangential Force waveforms (b) Harmonics (radial)

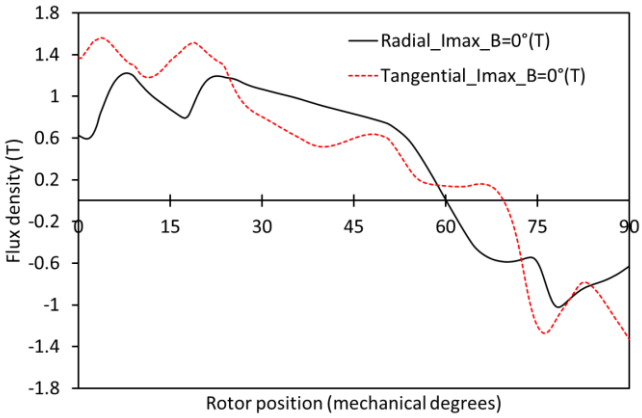

(c) Radial and tangent flux densities calculated at node

Fig. 3.4.12 Nodal force profile with current at Imax and β = 0°.

Compared to the symmetrical shape of the no-load waveform the force profile is heavily distorted. Much of this relates to the contribution of the coil MMF greatly changing the flux vector. Similar to the no-load the flux density and distribution of the rotor can be added to illustrate the reasoning for the nodal force profile. In addition, it's clear that once again the radial force component is dominant, due to the mid-tooth position of the probe, although some tangential force is seen around the edges of the q-axis flux barrier and the upper layer PM flux barrier.

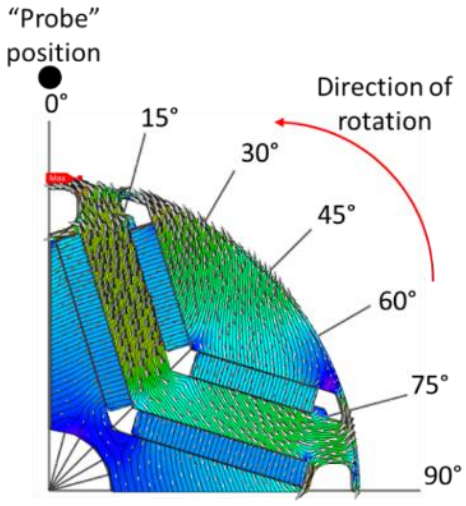

Fig. 3.4.13 Rotor flux distribution at I = 26.7Arms and β = 0°.

- The probe begins aligned to the q-axis flux barrier where the bulk of the flux density is towards the right side of the tooth
- As the rotor moves away from the q-axis flux barrier the lower layer starts to align with the probe creating a substantial increase in the flux density and the highest radial force point at around 10° rotor position.
- The upper magnet outer flux barrier then comes into alignment creating the drop between 15° and ~20°. The high level of leakage around this region means the force is still relatively high.
- Passing 25° the flux reaches its 2nd maxima as the upper layer magnet aligns with the probe.

- As the rotor passes the large region of iron above the upper 'V' the force drops towards zero The coils have the effect of attracting flux in the rotor tangentially towards the stator field in the q-axis so the further away the probe moves from that point the less the flux is inclined to bridge the air gap so the net force must fall, reaching a minimum at 60°.
- As the rotor approaches the right upper flux barrier it begins to pick up leakage flux from the tip of the upper layer magnet so the force builds.
- Past 80° the probe comes into alignment with the lower layer PM where the flux returning to the magnet is crossing the air gap increasing the force until the next q-axis flux barrier is reached at 90° and the cycle starts once more.

Thus, with careful analysis the distortion is quite logical and follows the flux densities depicted in Fig. 3.4.12 quite nicely.

3.4.3.2 Maximum torque point, I_{rms} = 26.7 β= 45°

The final analysis is of the machine at maximum torque. In this condition, the current angle is shifted to 45° to allow the machine to utilise the optimal balance of mutual and reluctance torque components. The effect of shifting the current angle on the armature field can be clearly seen in Fig. 3.4.14.

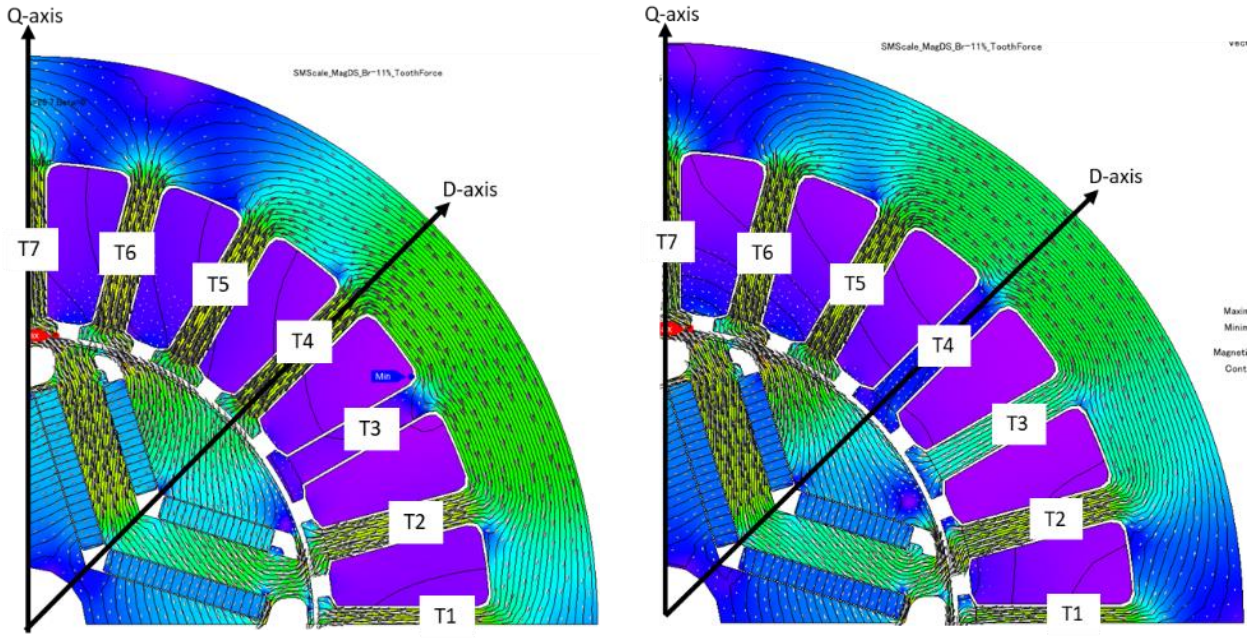

(a) β = 0°. (b) β = 45°.

Fig 3.4.14 Comparison of stator field distributions at initial position (rotor = 0°) with maximum current (I= 26.7A_{rms}), β = 0° and β = 45°.

Comparing Fig. 3.4.14(a) and (b) it can be seen that region of highest flux density in the back iron has shifted counter-clockwise. The effect on the rotor flux path is also clear and the bulk of the flux is now moving tangentially along the q-axis path formed by the magnet slot geometry concentrating high flux densities on T7 and T6 in Fig. 3.4.14(b) and leaving T4 as the tooth with the lowest flux density, a shift of 15 from the β = 0° shown in Fig. 3.4.14(a) and T3 having a relatively lighter loading. With the field in this position the machine

is fully utilising the reluctance torque component meaning the machine is achieving maximum torque. The effect on the tooth forces can be once again analysed using the same procedures as before and the flux distribution at different rotor positions can be seen in Fig. 3.4.15.

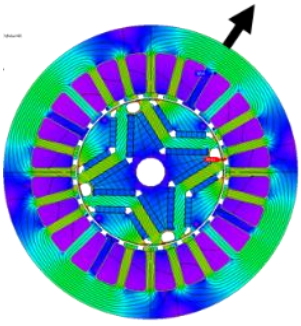

(a) Rotor at 0°

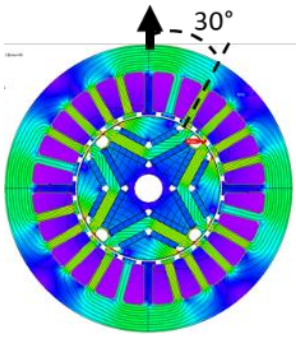

(b) Rotor at 30°

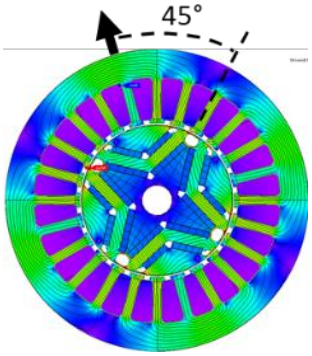

(c) Rotor at 45°

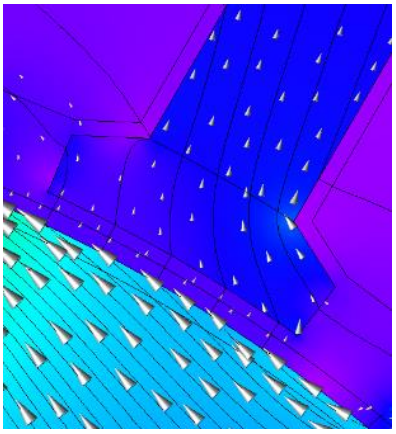

(d) Tooth flux lines & density @ 0°

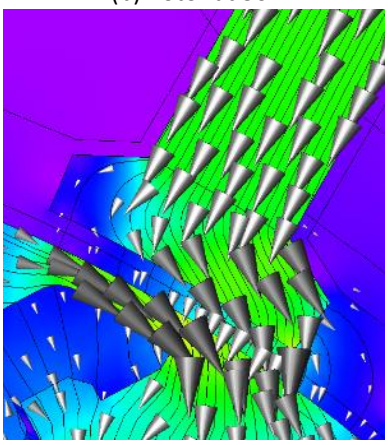

(e) Tooth flux lines & density @ 30°

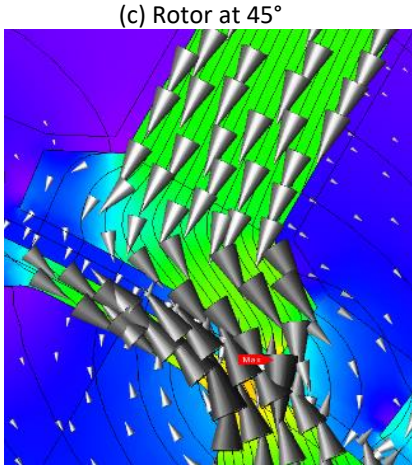

(f) Tooth flux lines & density @ 45°

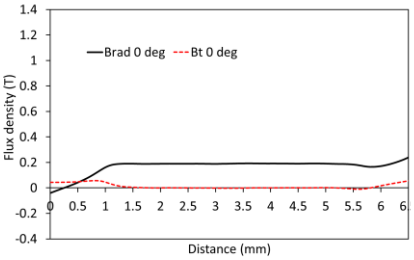

(g) Radial and tangential flux density @ 0°

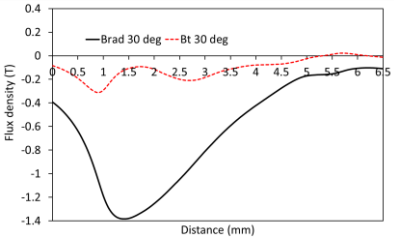

(h) Radial and tangential flux density @ 30°

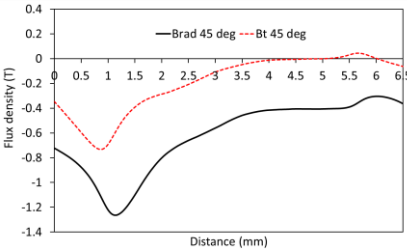

(i) Radial and tangential flux density @ 45°

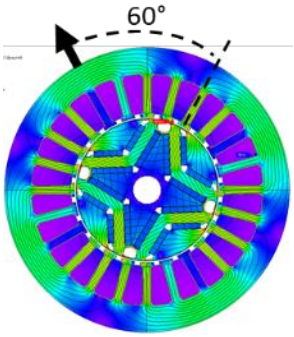

(j) Rotor at 60°

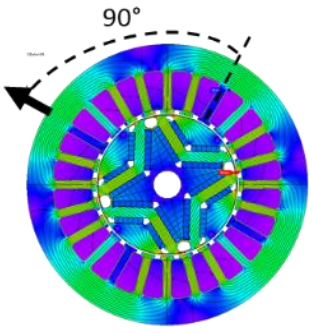

(k) Rotor at 90°

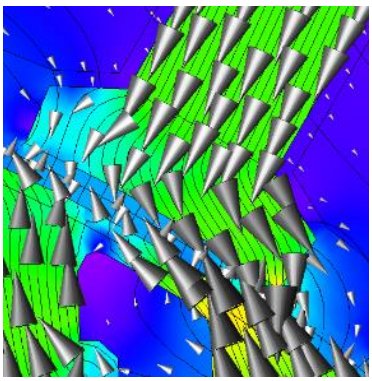

(l) Tooth flux lines & density @ 60°

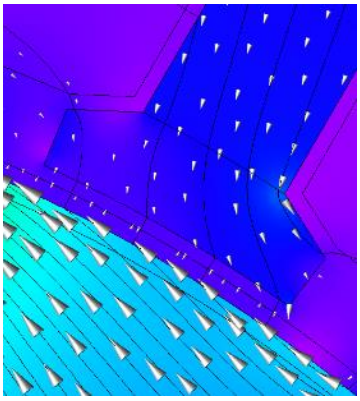

(m) Tooth flux lines & density @ 90°

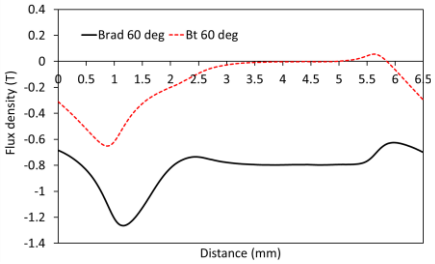

(0) Radial and tangential flux density @ 60°

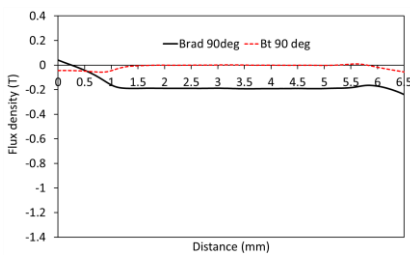

(p) Radial and tangential flux density @ 90°

Fig. 3.4.15 Rotor flux density across one pole pitch at maximum torque (I_{rms} = 26.7, B = 45°) with rotor positions of 0°, 30°, 45°, 60° and 90°.

The major difference between the β = 0° and β = 45° conditions is that shift in relative field position in the armature has meant the "dead" tooth phenomenon is observed at 0° and 90°, rather than 15° as before. Interestingly, the frequency has also changed with the "dead tooth" phenomenon occurring once every 30° rather than every 15° as previously observed. This is highlighted in Fig.3.4.16.

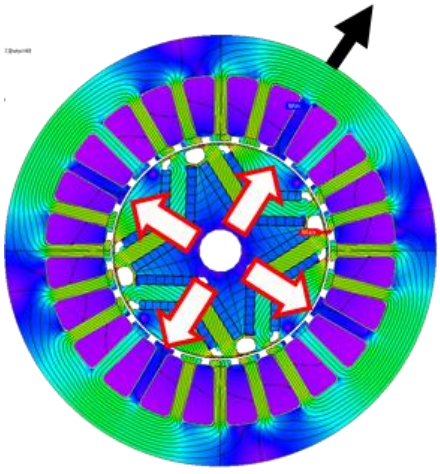

(a) Rotor position = 0°

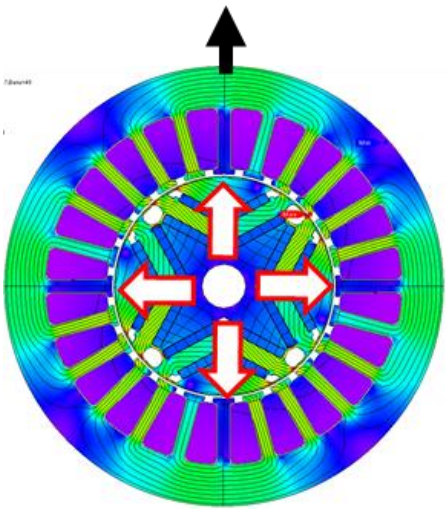

(b) Rotor position = 30°

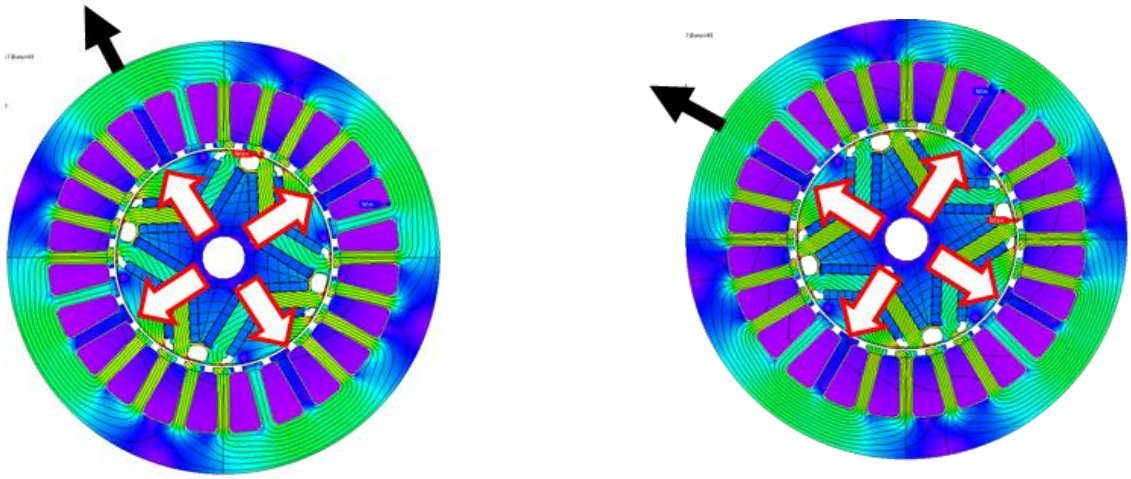

(c) Rotor position = 60° (d) Rotor position = 90°

Fig. 3.4.16 Occurrences of the “dead” tooth phenomena at I = 26.7Arms and β= 45°.

The mechanism is much the same as before, the key difference being the change in field angle means the flux is flowing in tangentially than previously, with more magnetic flux following the low reluctance path offered by the dual ‘V’ shaped topology. The tooth lies over a region which has no attraction to the flux in either the rotor core or the back iron. This does mean the phenomenon is half the frequency of the previous case, occurring 12 times per full revolution versus 24 times for the case where the current angle is at 0°.

The forces on the curve are once again calculated using the Maxwell stress tensor. However, to better highlight the influence of the shift in current angle the radial and tangential forces can be compared, which is shown in Fig. 3.4.17.

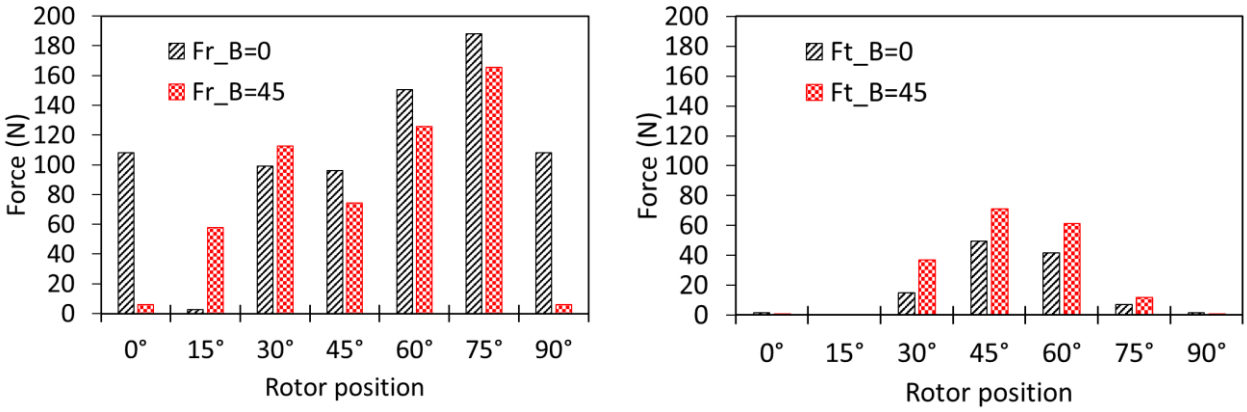

(a) Radial forces (b) Tangential forces

Fig. 3.4.17 Comparison of calculated radial and tangential forces on mid-air gap curve for I = 26.7Arms and β = 0° and β = 45°.

The resultant values are summarised in Table 3.4.3.

Table 3.4.3 Calculated forces on air gap curve using B_r and B_t data from FE at I = 26.7Arms and β = 45°

Rotor position	Radial force (N) β = 0°	Radial Force (N) β = 45°	Tangential force (N) β = 0°	Tangential force (N) β = 45°
0°	108.11	6.11	1.36	0.60
15°	2.48	57.91	-0.03	-0.31
30°	99.24	112.48	14.90	36.97
45°	96.27	74.43	49.44	71.12
60°	150.52	125.68	41.79	61.19
75°	188.00	165.46	7.14	11.64
90°	108.11	6.10	1.36	0.59

From the results in Fig. 3.4.17 and Table 3.4.3 the key observations of the effect of the shift in current are:

- The "dead" tooth at 0°and 90° is reflected in a stark drop in radial force at this position, tangential forces were negligible in both cases.
- The higher flux density at 15° has led to a greater increase in radial force only, however the amplitude is relatively low compared to the other rotor positions studied.
- Tangential forces at 30°, 45° and 60° are considerably higher at the advanced current angle, a reflection of the higher torque the machine is producing with the reluctance component engaged.
- Conversely the radial forces are lower for all angles with the exception of 30° which sees a 13N increase in force.

The increase in forces at the 30° position reflects fact one edge of the tooth is aligned with the inter-magnet layer of iron and the other is aligned with the upper layer flux barrier, illustrated in Fig 3.16(e) and the radial and tangential flux densities in 3.4.16(h). A very high radial flux can be seen at the lower edge of the curve, which is aligned with the inter-layer flux path made even more attractive by the shift in the armature field location, whereas the density drops markedly towards the upper edge of the curve. The result is a high radial and tangential force component. When the rotor is at 15° there appears to be no tangential force and only a small radial force. A closer analysis of the rotor at 15° is in Fig.3.4.18.

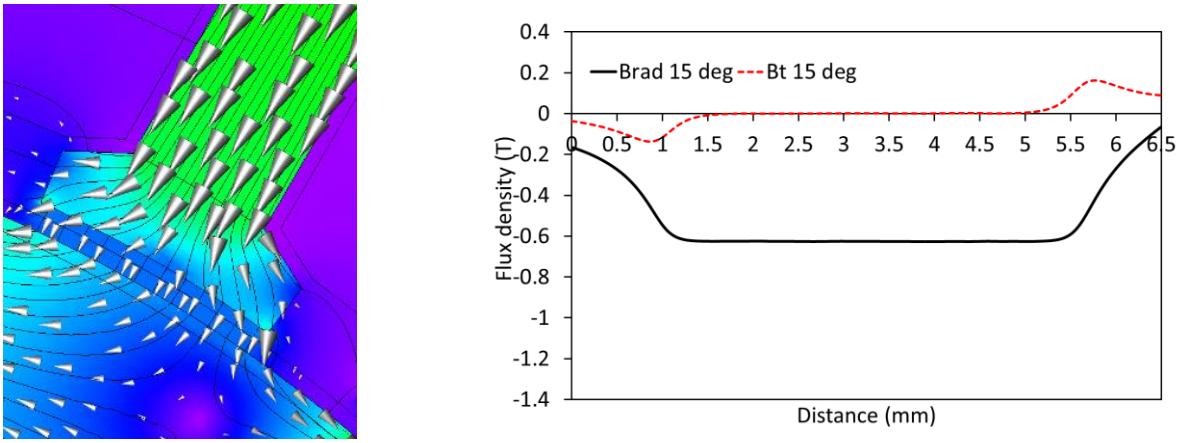

(a) Flux in tooth @ 15° (b) radial and tangential flux density on curve

Fig. 3.4.18 Tooth fluxes and calculated tooth pitch flux densities with rotor at 15°, I = 26.7A_{rms} and β=45°.

The flux densities in Fig. 3.4.18(a) are very low on the tooth tip and rotor edge which are shown in the radial and tangential Flux in Figs. 3.4.18 (b). The flux profiles suggest a reasonable balance of flux across the tooth pitch similar to the no-load condition. A slight asymmetry on the tangential flux density on the stator tooth surface gives rise to a small force but it is very small compared to the forces seen at 30°, 45° and 60° positions.

1. Nodal force probe –load, I = 26.7A_{rms}, β=0°

The final aspect is the influence of the shift in current angle on the nodal force probe, located in the same position as shown in Fig 3.4.5(a). Similar to the previous force calculation the force at β = 45° is compared to β = 0° to better understand the influence, shown Fig. 3.4.19.

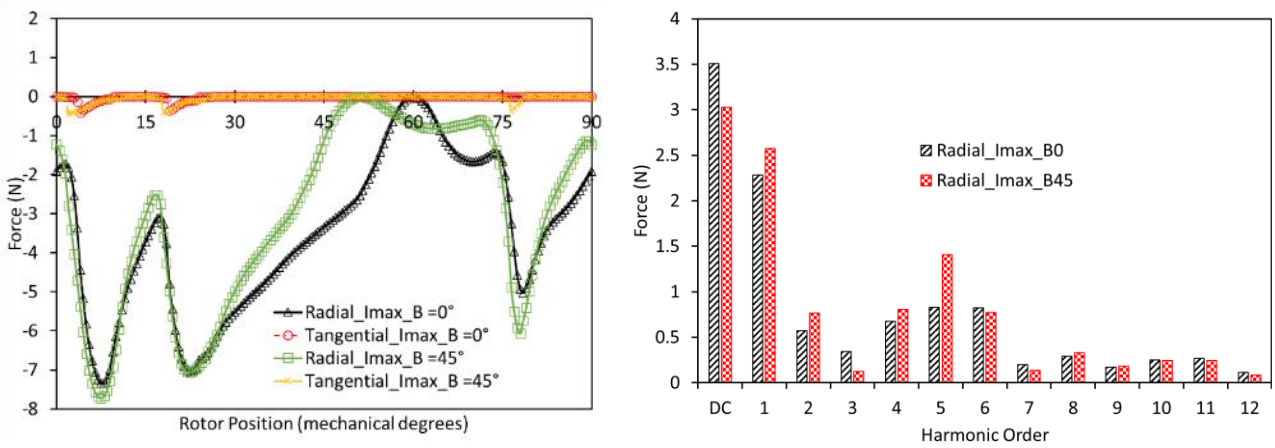

(a) Radial and tangential forces (b) Harmonics (radial)

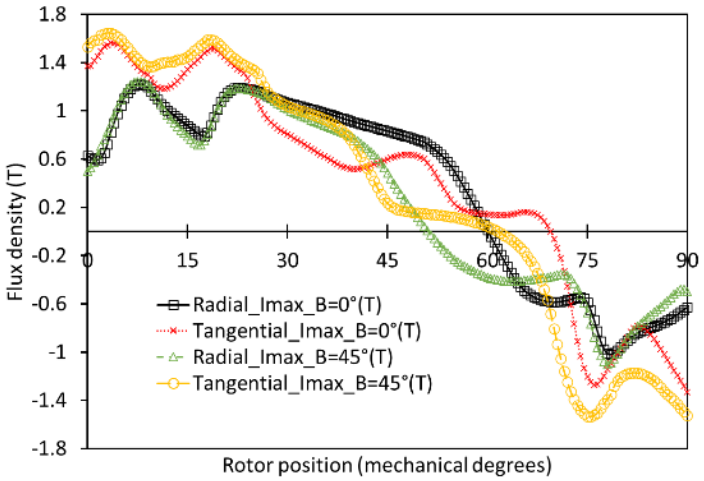

(c) Radial and tangential flux density at node

Fig. 3.4.18 Comparison of nodal force profiles at maximum current at β=0° and β=45°.

The profile for the β = 45° case shows a very similar distortion to the β = 0° case. The key difference shift in current angle has shifted the radial and tangential flux components such that they cross into the negative flux region much sooner. The DC component of the radial force is lower, and however, the fundamental, 2nd and 5th are all higher than the β = 0° condition. The differences can once again be better understood by looking at the rotor flux distribution at the different current angles, which is shown in Fig. 3.4.19.

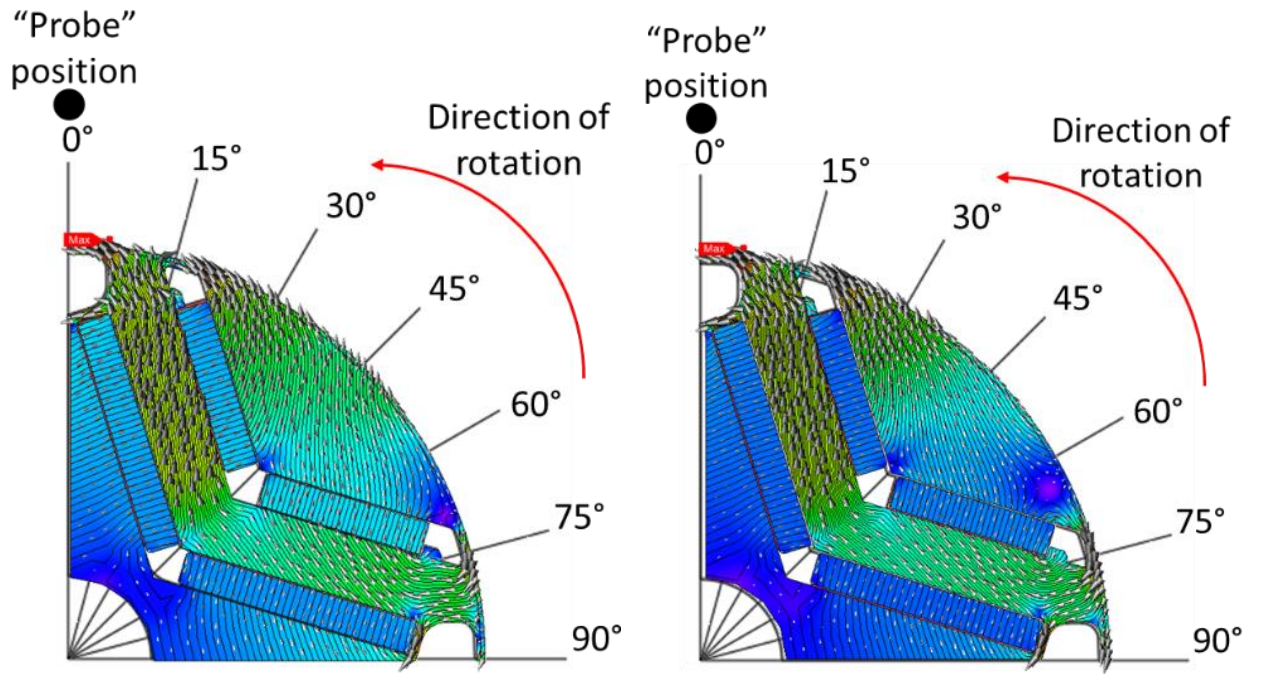

(a) β=0° (b) β=45°

Fig. 3.4.19 Comparison of flux densities in the rotor core at 1500rpm, I = 26.7Arms and the current angle changed from 0° to 45°.

The shift to a more tangential flux path within the rotor is well illustrated in Fig. 3.4.19, in the β = 0° condition. The rotor shows a reasonably high flux density up until around 60° where both the radial and tangential fluxes fall to 0, followed by a region of low flux density until the 2nd upper layer flux barrier passes at ~75°. When β = 45° (Fig. 3.4.19 (b)) this low flux region is shifted round ~15° and remains lower up to the same 75° point.

3.4.4 Summary of tooth force study

Using the Maxwell stress tensor applied to mid-air gap curve has allowed the radial and tangential tooth forces to be derived under different load conditions. Fig. 3.4.20 shows a comparison of the 3 load conditions with all the force values summarised in Table 3.4.4.

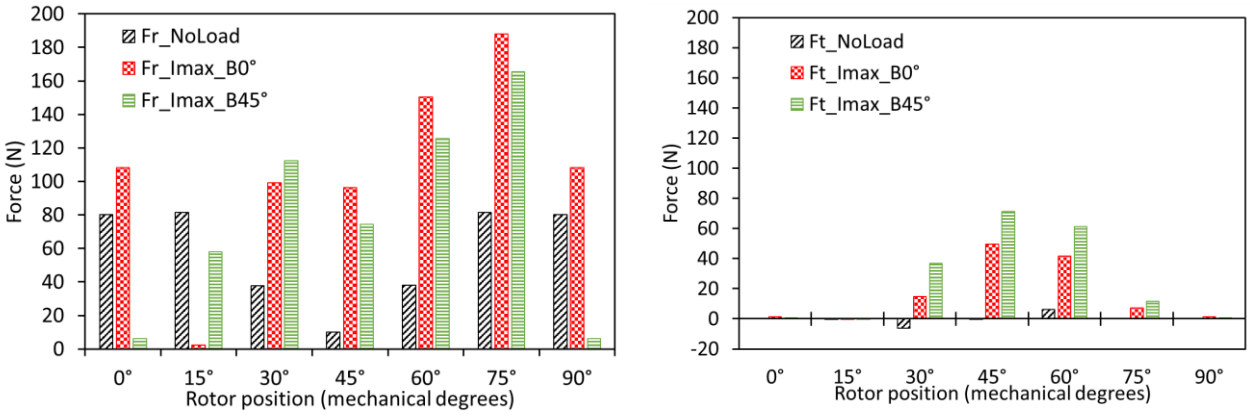

(a) Radial forces (b) Tangential forces

Fig. 3.4.20 Comparison of radial forces under no load, maximum current with β = 0° and β = 45°.

Table 3.4.4 Comparison of calculated radial and tangential forces at different load conditions at 1500rpm.

Rotor Position	No load		I = 26.7Arms, β = 0°		I = 26.7Arms, β = 45°	
	F_r (N)	F_t (N)	F_r (N)	F_t (N)	F_r (N)	F_t (N)
0°	80.20	0.01	108.11	1.36	6.11	0.60
15°	81.39	-0.15	2.48	-0.03	57.91	-0.31
30°	37.75	-6.12	99.24	14.90	112.48	36.97
45°	10.03	0.00	96.27	49.44	74.43	71.12
60°	37.91	6.14	150.52	41.79	125.68	61.19
75°	81.36	0.15	188.00	7.14	165.46	11.64
90°	80.21	0.00	108.11	1.36	6.10	0.59

From the results in Fig. 3.4.20 and Table 3.4.4:

- Under all load conditions the radial forces are dominant.
- Under no load conditions the radial forces are symmetrical about 45° with the variations in force due to the upper layer magnet and q-axis flux barriers.
- Applying the current with no current angle shift (β =0) shows a large increase in the radial component with high tangential forces at 30°, 45° and 60°, the peak being at 45°.
- Incrementing the current angle to β =45° shows an increase in the tangential forces, reflecting the increased torque due to the reluctance component but also a drop in the radial forces for all points with the notable exception of 30°.
- Interaction with non-salient aspects of the rotor (flux barriers etc) provide the source of the variations in radial and tangential forces. How much this influences the vibration will become clear in Chapter 6.

3.5 Summary

This chapter has detailed the modelling of the electromagnetic aspects of the machine using finite element analysis. A 2D FE model was implemented that utilised the mechanical drawings of the machine to take into account of features such as the magnet slot gap between the PMs and the rotor core due to the requirement to use a bonding epoxy to hold the magnets in place. This increased the net reluctance of the magnetic circuit and slightly reduced the magnet thickness. It was also noted that the 2D FE model cannot capture the influence of the end effect of a machine as it involves 3D flux paths; a 3D model would be required in this instance. Given the high number of different simulations that require to be run it was decided the high speed of the 2D simulation outweighs the increased accuracy but very low and processor intensive 3D FE model.

The FE model was then set to follow the same set of test scenarios that the physical machine was put through and comparisons made with the results provided in chapter 2 where possible. The resultant model shows excellent alignment to the measured results. The efficiency maps matched well, which are notoriously difficult to match. It was shown that the fact the copper loss is the loss leader of the machine means alignment of the net machine losses and therefore efficiency was much easier. Had the machine been an iron loss led machine then it would have proven much more difficult to match due to the non-linear nature of the loss and its sensitivity to external factors such as temperature.

With the FEA model in place the final step was to show the tooth forces acting on the machine. From the literature and an investigation on the developed 2D model, it was found that the optimum method of calculating the tooth forces was a curved surface one slot pitch in width which was located in the mid-air gap where the mesh density is high, the material homogenous and not prone to non-linear effects such as saturation. A brief investigation of the tooth forces based on no-load and load simulations was undertaken in order to characterise the force profile on the tooth under different load conditions.

The FE model has been shown to match the experimental results of the baseline machine well so is now ready to be used to generate the tooth forces for the dynamic model that will be described in chapter 6.

4 Experimental modal analysis of the baseline machine

4.1 Introduction

The work detailed so far has focussed on characterising the electromagnetic aspect of the baseline line machine in terms of both experimentation on the fabricated prototype and development of a 2D electromagnetic FE model of the machine in order to obtain the tooth forces. In this chapter the mechanical natural frequencies (eigen frequencies associated with eigen modes) of the baseline machine will be characterised to allow the development of a 3D mechanical FE model of the in chapter 5 of the thesis which forms the lower leg of the inputs to the dynamic vibratory model, shown in figure 4.1.1 .

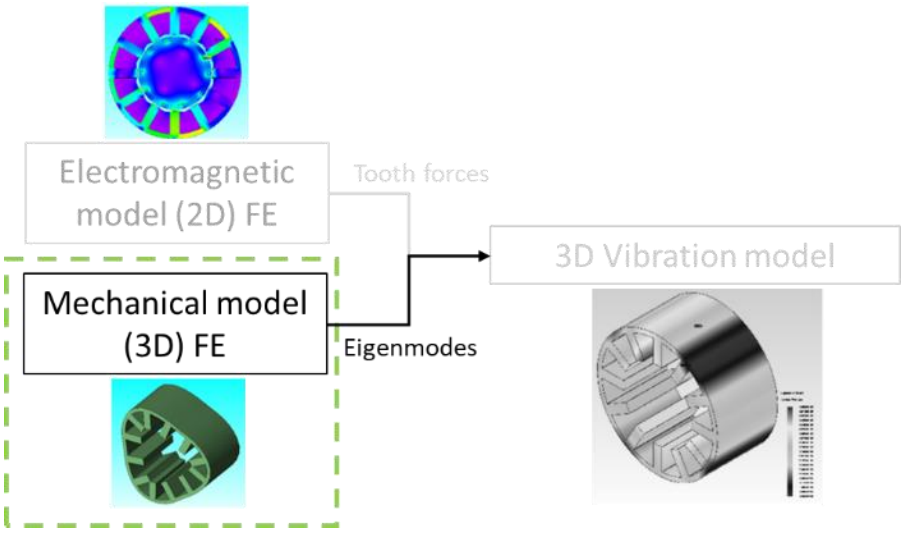

Fig. 4.1.1 Flow diagram of the vibratory modelling of an electrical machine.

The mechanical FE model provides the natural frequencies and eigenmodes of the machine structure. The final model takes the frequency domain tooth force data and the mechanical transfer function derived in this section to calculate the vibratory performance at several different load points in the machine.

To obtain these eigen values the process is very similar to the steps taken to characterise the electromagnetic performance of the baseline machine, namely:

- Characterisation of the physical machine eigenmodes by experiment.
- Development of finite element mechanical model whose performance is calibrated using the experimental results.

The two steps are split across 2 chapters, this chapter details the experimental phase, providing an overview of the equipment used, test procedure and of course the measured results. Chapter 5 details the subsequent development of the mechanical FE model.

4.2 Overview of the baseline machine structure, experimental setup, and procedure

4.2.1 The baseline machine structure

The electromagnetic investigation concentrated on the stator and rotor topologies of the baseline machine with the structure surrounding the magnetic circuit omitted from the model to reduce processing overhead. In reality of course there needs to be a structure surrounding the core of the machine that provides mechanical support and key functions such as providing a means of cooling the machine and supporting the bearings that hold the rotor within the stator bore with as tight geometric tolerancing as possible to mitigate some of the potential static and dynamic eccentricity issues discussed in chapter 1.

A cross section of the full assembly drawing of the motor can be seen in Fig. 4.2.1.

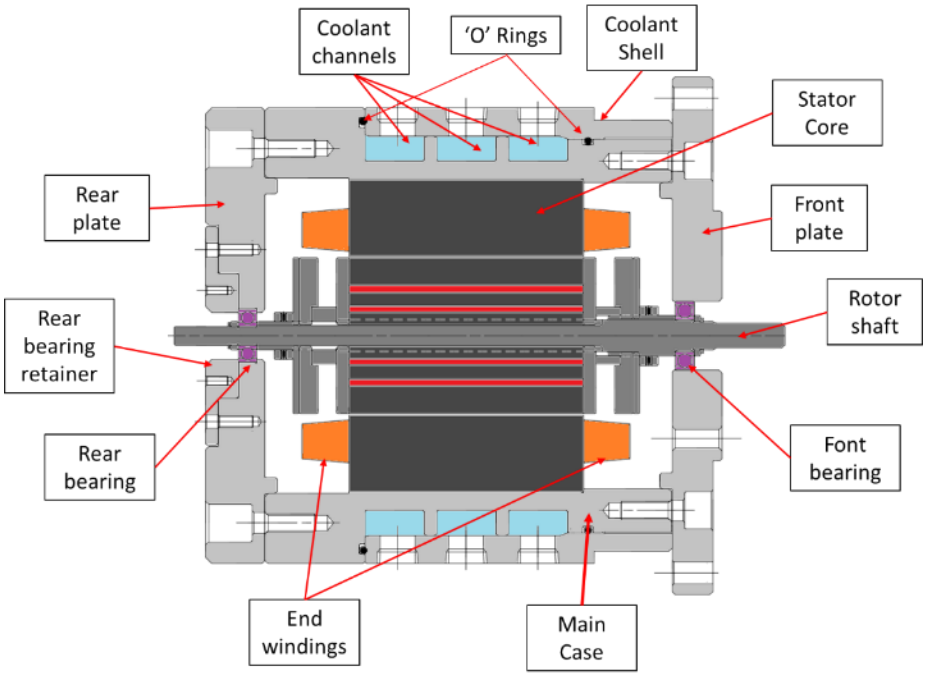

(a) Y-Z cross section of machine highlighting the casing components.

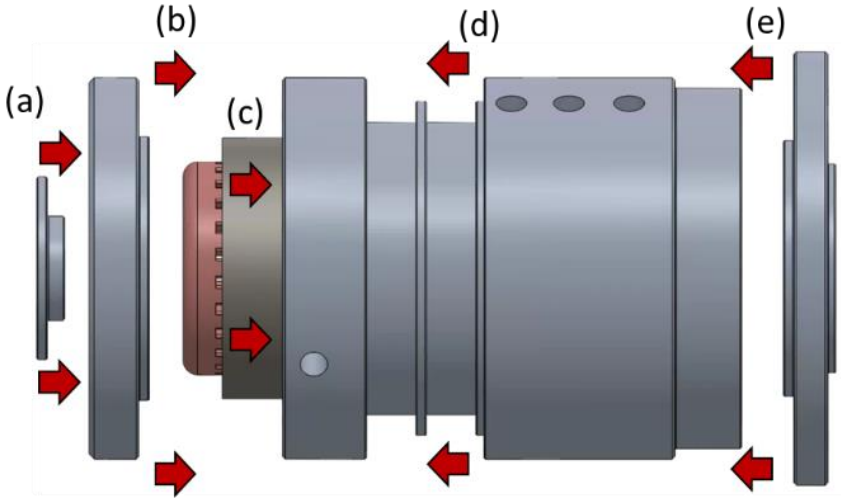

(b) Exploded view showing assembly sequence of parts (rotor omitted).

Fig. 4.2.1 Overview of the full baseline machine structure.

The need for a liquid coolant necessitates a more complex structure than an air-cooled system. The key features of the full machine assembly shown in Fig. 4.2.1 (a) are:

- The main case forms the central structure of the machine into which the stator is located.
- Over the casing sits a coolant shell jacket with two rubber 'O' rings to provide a seal. This allows coolant liquid to be passed around the outer diameter of the stator in the main case.
- A rear plate which is bolted on to the rear of the main casing. This retains the rear bearing and has a mounting point for the encoder required to control the machine.
- A front plate which again is bolted onto the main casing. This has several roles:
    - Like the rear plate it houses the front bearing.
    - Providing a clamp force to hold the coolant shell against the rear 'o' ring.
    - Providing a means of mounting the machine to the test rig.
- Rear bearing retainer pins the rear bearing controlling the rotor shaft axially. The front bearing housing provides some axial freedom to mitigate any axial load (thrust load) which can act as a brake on the bearing generating heat and damaging the bearings.

Fig. 4.2.1(b) shows the assembly sequence and is summarise in Table 4.2.1.

Table 4.2.1 Summary of the assembly sequence shown in Fig. 4.2.1(b).

Label	Component	Attaches to	Method
(a)	Rear bearing retainer	Rear plate	Bolted joint x4
(b)	Rear plate	Main case	Bolted joint x4
(c)	Stator sub-assembly	Main case	Heat shrink (interference fit)
(d)	Coolant Shell	Main case, front plate	Interference fit with inner 'O' ring on frame outer bore, clamped to rear 'o' using front plate
(e)	Front plate	Main case, coolant shell	Bolted joint x4, applies clamp force to coolant shell

The concern with the structure is the method by which the coolant shell is attached. It relies on the friction between the front and rear 'O' rings plus the clamp force from the front plate to be held in place against a thick end-bell at the rear of main case. This creates an asymmetry along the axial length of the part meaning that a 3D model will be required to portray the vibratory performance of the machine more accurately.

4.2.2 Baseline machine measurement test sequence

Fig. 4.2.1 highlighted the fact that the fabricated baseline machine has a complicated structure owing to the method of managing the liquid cooling requirements. The key concern here is given the structural complexity to just test the fully assembled motor and attempt to develop an FE model to match would be very difficult and prone to error. A better method would be to strip the machine down to as basic a level as possible and then test the machine at select stages of reassembly such that the FE model complexity can be built up in a similar manner. This allows the influence of difference aspects of the machine assembly such as the laminated stator core, windings and case fixtures to be observed and adjusted as the complexity increases to maintain as close a parity between the FE model and the actual machine as is possible. Sequence is shown in Fig.4.2.2.

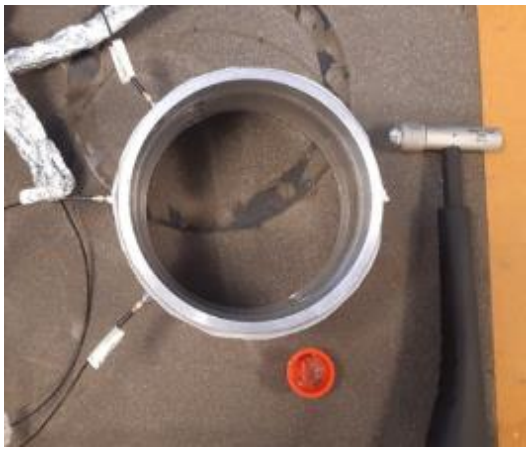

(a) Coolant shell.

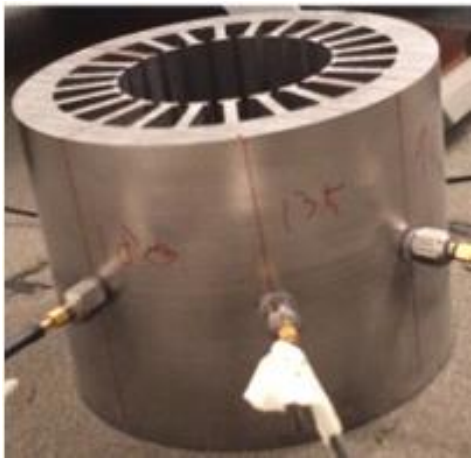

(b) Stator only.



(c) Wound stator in frame.



(d) Rear plate attached only.



(e) Front and rear plates attached, no coolant casing.



(f) fully assembled.



(g) Machine mounted to rig only.



(h) Machine fully dressed, ready for operation.

Fig. 4.2.2 Test sequence of the baseline machine showing the increasing complexity of the machine to the full system.

From the sequence shown in Fig. 4.2.2 one key stage of the assembly is missing between Fig. 4.2.2(b) and Fig. 4.2.2(c) which is the stator inserted into the frame prior to winding. On the original project 2 stators were fabricated (one spare in case of concerns) but only one casing and subsequent winding process was made due to time constraints. This therefore means that whilst the stator can be characterised directly the comparison of the structure before and after the winding process cannot be measured, making the modelling process a little more challenging for the transition from the simple stator to the wound stator in the frame.

Figs. 4.2.2 (g) and (h) both show the machine mounted to the dynamometer face plate:

- Fig. 4.2.2(g): The machine is mounted to the test stand only, the shaft is not connected to the driveline, the encoder is not attached, and the coolant lines are not installed.
- Fig. 4.2.2(h): The machine is attached to the driveline; coolant lines are installed, and coolant filled, and the encoder has been attached and aligned.

4.2.3 Overview of hammer, test bench and test equipment

The full rig utilised for the modal test experiments is shown in Fig. 4.2.3.

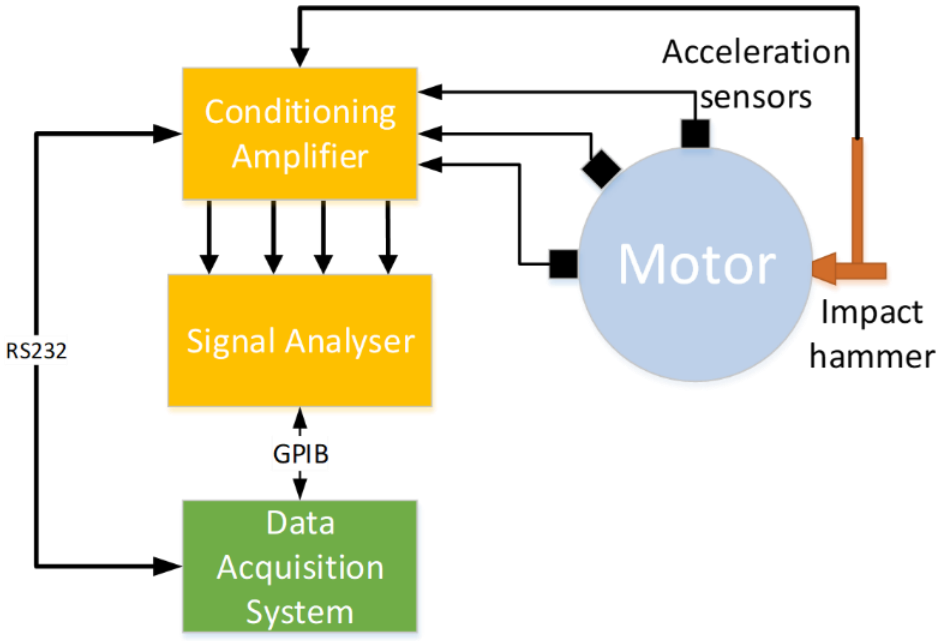

(a) System block diagram.

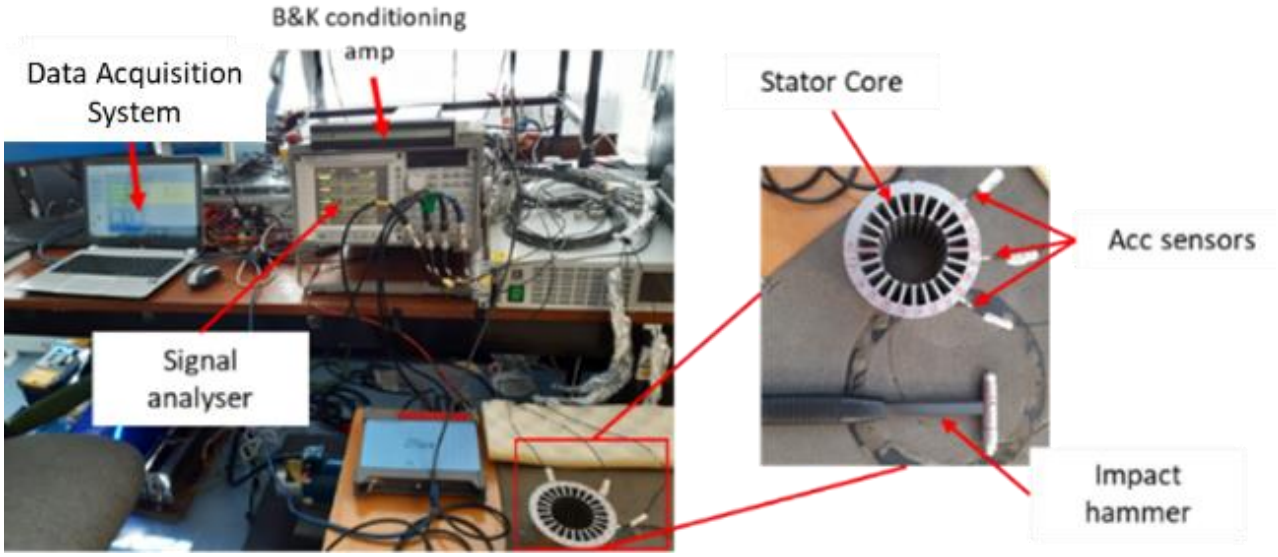

(b) Photograph of the experimental setup.

Fig. 4.2.3 Experimental setup for modal measurement of the baseline machine.

The rig contains several key components, highlighted in the system diagram shown in Fig. 4.2.4(a):

- **Impact hammer** (aluminium tip applied): applies and measures the impact force applied to the machine.
- **Acceleration sensor(s)**: captures the reaction of the structure to the force applied by the hammer
- **Conditioning amplifier**: Powers the acceleration sensors and hammer as well filtering the captured signal(s) to remove parasitic factors such as common mode noise.
- **Signal Analyser**: captures the time-domain signal from the hammer and sensors and generates frequency domain aspects such as phase and amplitude using FFT techniques.

- **Data acquisition system**: PC based acquisition written by author using National Instruments LabVIEW development tool allowing setup and control of the conditioning amplifier and signal analyser and capture all data from the analyser after each test.

The following sections will briefly outline the specifications and functionality of each block of the experimental setup.

4.2.3.1 Impact hammer

The impact hammer used in the experiments utilises a piezoelectric sensor located in the head of the hammer which generates a voltage directly proportional to the impact force, typically given in mV/N. The key specifications of the impact hammer used are highlighted Table 4.2.3 [BK05].

Table 4.2.3 Impact hammer specifications [BK05].

Manufacturer	Bruel & Kjaer	
Model	8206	
Measurement technology	Piezoelectric	
Output type	Voltage	
Voltage sensitivity @160Hz	25 mV/N	
Full scale output	+5V	Frequency response of different tip materials
Linear error @ full scale	+/-1%	
Tips available	Aluminium, Plastic (Delrin), rubber (polyurethane)	
Connector	BNC	

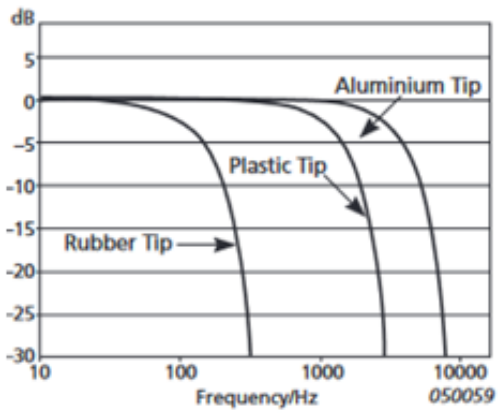

The frequency response curves of each tip from the supplier [BK05] in Table 4.2.3 highlights one of the limitations of the hammers in terms of the frequencies that can be excited. The stiffness of the test piece is fixed so the frequency response is controlled by varying the stiffness of the hammer tip. Utilising a hard, metallic tip, lowers the pulse duration of the impact thus increasing the frequency content [AT00], [AB11]. The cost of using the harder tip is the increased risk of damage to the test part and the risk of the hammer bouncing off the target surface giving multiple strikes which distorts the results. From the data provided by the supplier the maximum frequency from the B&K 8206 hammer with the aluminium tip is around 7kHz. The actual value will very much depend on the test piece and conditions.

4.2.3.2 The acceleration sensors

The system response to the impact from the hammer is measured using acceleration sensors distributed around the machine. The core of the sensor is a small mass attached several piezoelectric shear accelerometers which produce a small voltage directly proportional to the acceleration the sensor experience, typically given as mV/g or mV/ms^{-2}. The key specifications are provided in Table 4.2.4 [BK06].

Table 4.2.4 Specification of acceleration sensor [BK06].

Manufacturer	Bruel & Kjaer	
Model	4518-003	
Measurement technology	Piezoelectric	
Output type	CCLD* (Deltron)	
Frequency range	1Hz -> 20kHz	
Measurement range	+/- 50g	
Voltage sensitivity	100 mV/g (+/-10%)	
Mounting method	Adhesive	
Connector	M3 BNC	
*CCLD = Constant Current Line Driver		

These sensors operate on a single axis, more sophisticated (and expensive) sensors can operate on up to 3 axes to give full 3D measurement of the motion of the test body which is beyond the scope of this experiment. One of the key aspects of the sensor specification is the mounting methodology. There are numerous methods but the 3 most popular methods of mounting the sensor are [AT00]:

- Threaded stud: small holes are drilled and tapped with appropriate thread and the sensor is screw in place creating a tight mechanical bond.
- Adhesive: Cement or petroleum wax is utilised to bond the sensor to the target surface.
- Magnetic: A magnet integrated into the sensor head is used to hold the sensor to the target surface.

A general guide to the effectiveness of each mounting method is given in Fig. 4.2.5 [AT00].

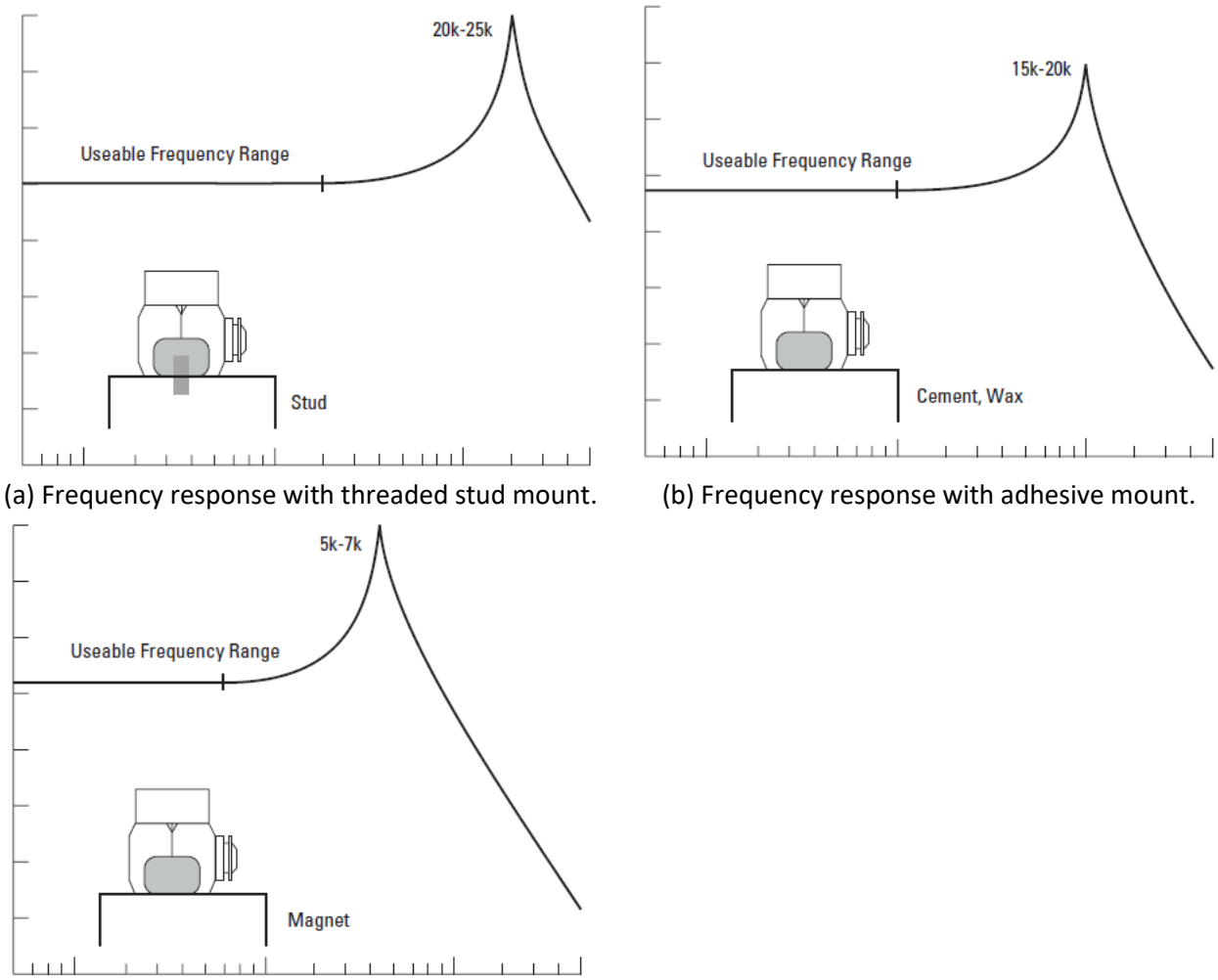

(a) Frequency response with threaded stud mount.

(b) Frequency response with adhesive mount.

(c) Frequency response with magnet mount.

Fig. 4.2.4 General guide to acceleration sensor frequency response VS mounting method [AT00].

The threaded stud method (Fig. 4.2.4(a) is commonly seen as being the most effective method [AT00], [OD88a]. However, it requires tapped holes to be drilled into the structure, which is difficult for this application due to the risk of damaging the coolant shell and creating leaks. Stud connections can also be very sensitive to tightening torques which can pre-load the sensor, inducing errors and potentially damaging the sensor.

Utilising adhesives is the next most effective method and has a big advantage in that it can be used on pretty much any surface. Care must be taken during the bonding process as the adhesive material (wax, epoxy, cement etc.) can act as a damper adding error to the measured acceleration. The magnetic solution offers the greatest convenience but has the lowest frequency response (Fig. 4.2.4(c)), there is also the key concern that it relies on the target surface being magnetic.

For the static test, a petroleum mounting wax is utilised. These waxes offer good force transmission characteristics and are very easy to manipulate; the wax is warmed by hand becoming soft, placed at the target position and the sensor is pushed into place. The wax then cools and hardens creating a good bond with surface. The caveat to this is the target surface must be smoothed and cleaned of any dirt or particulates

to ensure a good, uniform bond. The primary concern with utilizing the wax is that the thermal performance of the bond is poor, from experience anything above ~35°C causes the wax to soften, weakening the bond and creating unreliable results at best and having the sensor simply fall off the structure at worst. This is a minor irritant for the static testing as this is all performed at room temperature (~22°C) but is a big concern for dynamic testing when the case temperature of running continuously on load can easily exceed 40°C during load testing. The alternative mounting methodology for the dynamic case will be covered in chapter 6 of this thesis.

4.2.3.3 The conditioning amplifier

The transducers in both the acceleration sensor and the force hammer require power and although both use shielded cabling both are susceptible to noise which can distort the signals from the transducer. A conditioning amplifier is therefore employed to both power the transduces and clean the signals to mitigate the effects of noise on the measured data and maximise accuracy. The amplifier specification is shown in Table 4.2.5.

Table 4.2.5 Specification of conditioning amplifier [BK18].

Manufacturer	Bruel & Kjaer
Model	Type 2694-B
Channels	16
Inputs	Voltage CCLD* (Deltatron)
Channel Gains	0dB or 20dB
High Pass filter	1st order (1Hz)
Communications	RS232
*CCLD = Constant Current Line Driver	



The amplifier is manufactured by the same supplier as the force hammer and acceleration sensors and as such is well matched. With 16 channels it has more than enough capacity for the purposes of these experiments.

The main concern with this amplifier is there are no external controls to enable channels or set the gains for each channel. This is achieved using a serial data link (RS232) and a computer with proprietary software installed. Unfortunately, the software supplied was incompatible with the modern operating system used on the data acquisition PC, so the setup of the amplifier was achieved using a function written by the author using National Instruments LabVIEW to allow the amplifier to be setup. A brief overview of the functionality is provided in the data acquisition description later in the chapter.

4.2.3.4 The signal analyser

The signals outputted by the amplifier is then fed into a signal analyser. In terms of processing the signals there are a large range of options available. The options can be split into roughly 3 categories:

- Oscilloscope used to capture the time domain signal, FFT performed in post processing.

- Rapid Application Development (RAD) tool with high speed A2D ports (e.g. dSPACE or NI Compact RIO) to capture, process and store all logs.
- Dynamic signal analyser (DSA), a powerful tool that performs high speed FFT on input signals.

As with all things each of the 3 methods have their advantages and disadvantages, the major ones being summarised in Table 4.2.6.

Table 4.2.6 Comparison of different methods of capturing the impact force and acceleration signals.

	Oscilloscope	dSPACE/CompactRIO	Dynamic signal analyser
Advantages	✓ Very simple to setup ✓ Can support high number of channels ✓ Relatively low cost	✓ High number of input channels ✓ Generation of bespoke functionality ✓ Access to large number of prewritten analysis tools (LabVIEW or MATLAB)	✓ Fourier transform based tool ✓ Instant feedback of strike results ✓ Integrated functions for N&V measurement
Disadvantages	X Typically requires post processing for FFT X Post processing requires script to be written (e.g. Matlab) X Difficult to judge quality of strike	X Time consuming to develop & debug software X Needs specialist engineer to fully utilise X Requires expensive development software X Hardware expensive	X Low channel number X Complex tool: can be difficult to correctly setup X Expensive

Tools such as dSpace, Labview and Matlab offer powerful solutions to many applications. However, the general-purpose nature of the tools is potentially a large source of error. For example, when analysing the time domain data, the windowing methodology [AT00] is particularly important to mitigate concerns such as leakage [AB11], [JFG06], [OD88a] or truncation of the time data [AB11], [AT00]. [OD88a]. The time domain data from the impact hammer is very different from that of the acceleration sensors. As highlighted previously the nature of the impact means it must be very quick to maximise the excitation bandwidth [AT00], lasting microseconds whereas the acceleration sensor can take tens of milliseconds to settle, the difference is highlighted in Fig. 4.2.5.

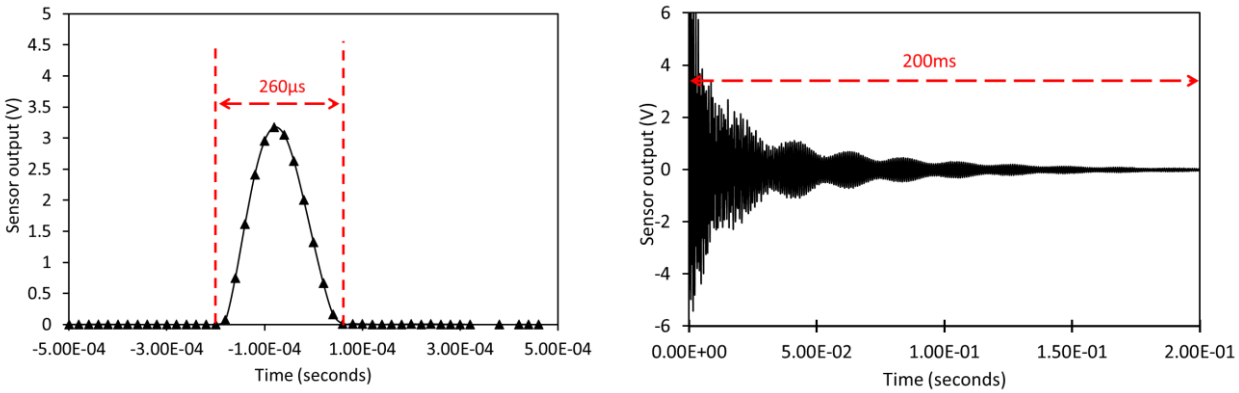

(a) Impact hammer time domain signal (raw). (b) Acceleration sensor time domain signal (raw).

Fig. 4.2.5 Comparison of the raw time domain signal from the force hammer and an acceleration sensor.

The amplitudes in Fig. 4.2.5 are the raw voltage values but the difference in settle time is stark. From Fig. 4.2.5(a) the hammer settle time is 260 µs whereas the acceleration sensor settle time in Fig. 4.2.5(b) is 200ms. Using the same windowing for both sensors results in either a larger error on the force hammer due to the very large number of redundant sample points dragging the average down when using windowing techniques such as Hanning [AB11] or severe truncation of the acceleration signal. Dynamic signal analysers tend to have specialist force window modes [AT00] that allow the system to differentiate between the different signals.

Given the above concerns plus the time required to develop and debug bespoke software the dynamic signal analyser was chosen as the tool to proceed with. The Signal analyser available in the group was designed with the express purpose of measuring vibratory measurement and comes with many features installed to support the analysis. The additional benefit is that the system was designed and optimised by specialists in the field eliminating some of the sources of error from using the 3rd party or in-house developed analysis tools. Table 4.2.7 gives the key specifications of the signal analyser utilised.

Table 4.2.7 Dynamic signal analyser specifications [KT17].

Manufacturer	Agilent (now Keysight tech)
Model	35670A Dynamic signal analyser
No. of channels	4 (BNC)
Frequency range	102.4 kHz (1 channel) 51.2Khz (2 channel) 25.6 kHz (4 channel)
Dynamic range	90 dB
accuracy	+/- 0.15dB
Resolution	100, 200, 400, 800 & 1600 lines
RT bandwidth	25.6 kHz/1 channel
Output	3.5” floppy disk, GPIB



Whilst well suited to the application, there are several concerns with the chosen signal analyser, the first is that there are only 4 channels, with one being the force hammer there can only be 3 acceleration sensors. This clearly limits the number of positions the sensors can occupy without either repositioning the sensor or shifting the strike location. The second is the main methodology of extracting data from the tool, the primary drive on the tool is a 3.5” floppy disk. The file system when using the floppy disk within the tool is dated and very clunky as each channel must be manually selected and saved making data logging time consuming. Fortunately, the signal analyser has a GPIB (General Purpose Interface Bus) on the rear which can be used to both remotely control the signal analyser and capture the data from all 4 channels to an external PC, a feature greatly exploited in this project. The final issue is the complexity of setting up the tool. Initial hammer tests using the tool yielded very noisy and difficult to interpret results. This led to a great difficulty in identify the different modes of the test piece and made development of the FE model very difficult and slow. After some experiments using simple sinusoidal sources and simple test pieces the concern was found to be the

automated limit setting on the tool and the windowing. Upon solving this issue, the identification of the modes was much simpler. Fig. 4.2.6 highlights the clear difference in results.

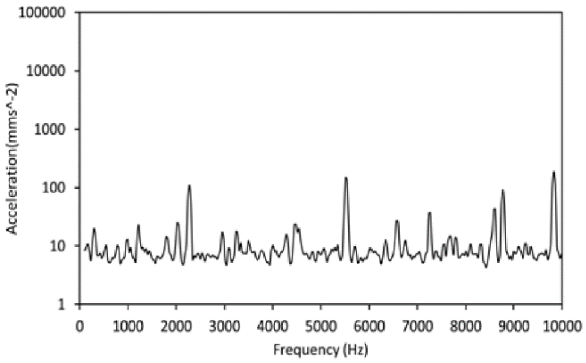

(a) Result of stator core strike with incorrect voltage limit and windowing.

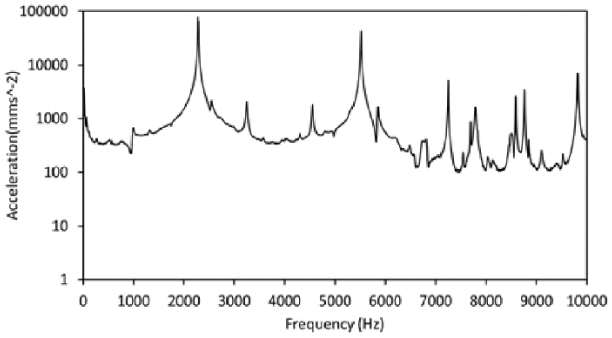

(b) Result of core strike with correct voltage limits and windowing.

Fig. 4.2.6 Illustration of windowing and limit errors with hammer testing the stator core.

4.2.3.5 The data acquisition system

The data acquisition system is a standard PC that utilises software written by the author using National Instruments LabVIEW to control, trigger and capture the data from the Signal Analyser using a USB to GPIB connection. Functional LabVIEW software libraries are provided for free by Agilent which are used to allow complete remote control of the signal analyser as well as capturing all data in the device. In addition, the software written communicates with the conditional amplifier to enable channels as well as functions such as the gain of each channel. A short summary of the tool is provided in Fig. 4.2.7 which shows the main screen of the tool and the high-level state machine diagram.

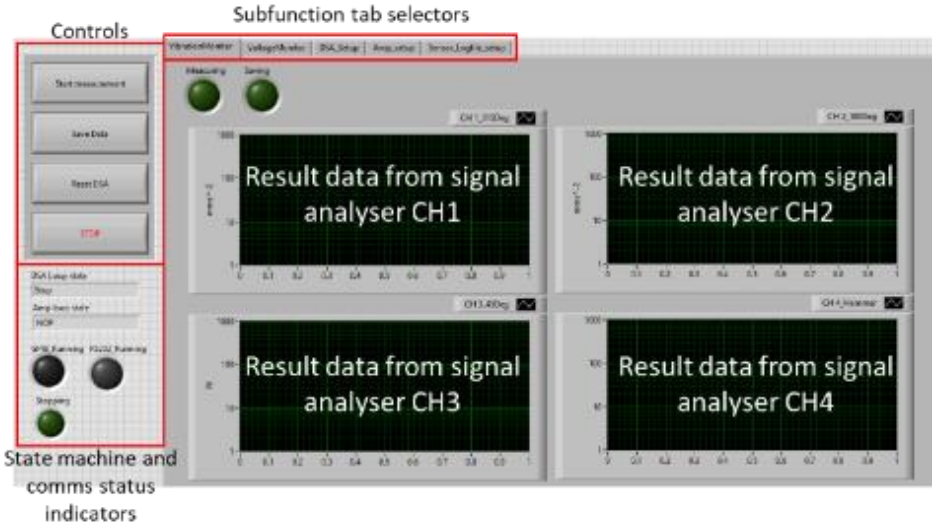

(a) Main screen and controls

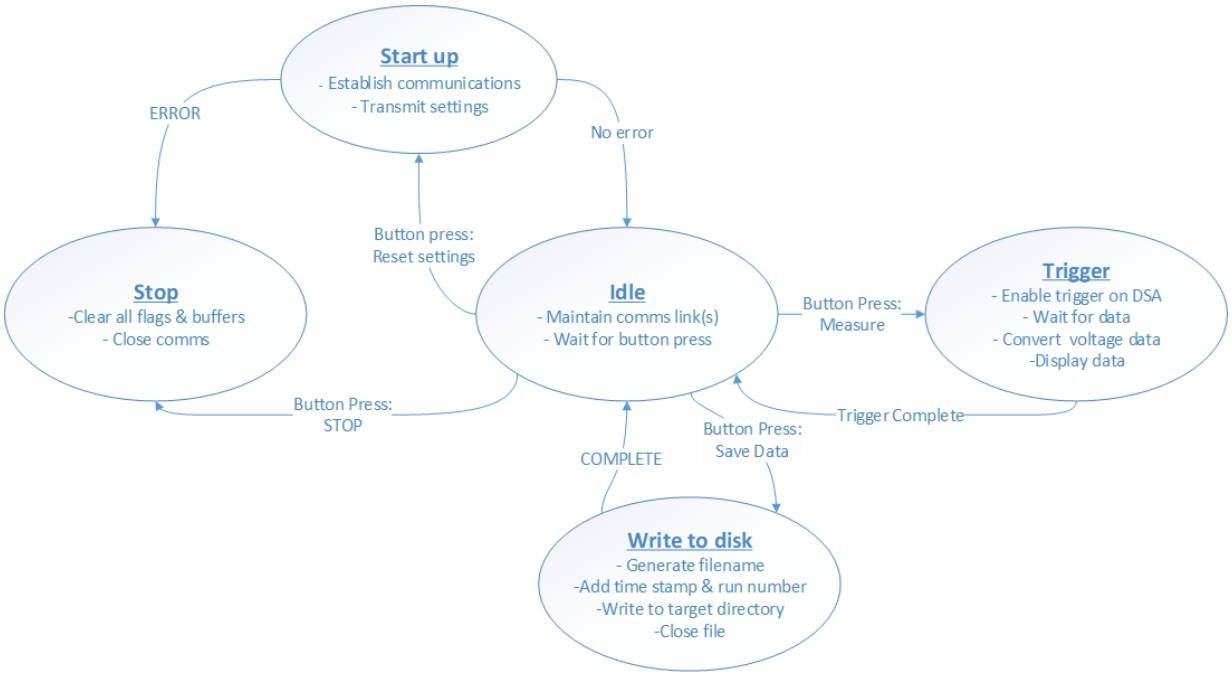

(b) High level state machine for the data acquisition operation.

Fig. 4.2.7 Overview of the data acquisition system for the force hammer and acceleration sensors.

Operation of the tool is very simple. The desired settings for the amplifier and signal analyser are inputted using the “DSA_Setup” and “Amp_setup” tabs. This can be done before running the program or during operation by pressing the “Reset DSA” button when the new settings are required.

Once the program is running the data is captured by pressing the “Start measurement” button which moves the state machine to the “Trigger” state. In this state the trigger command is transmitted to the signal analyser and the state machine then waits until the signal analyser sends the channel data back and the buffered data is converted from volts to the correct units and shown in the charts in Fig. 4.2.7(a), in which each chart shows the results from each channel respectively.

If there are no concerns with the results, then the “Save Data” button is pressed. This moves to the “Write to disk” state where the recorded data is stored as an Excel workbook file to with a filename and location previously set in the “Sensor Logfile Setup” tab. The system automatically adds a timestamp and run number to prevent confusion when re-visiting the results. Once testing is complete the “Stop” button is pressed and the system stops all communications and sets the signal analyser back to the manual mode.

For the trigger there are many options available with the Signal analyser but only 2 options are utilised during the capture of data for this thesis:

- Trigger by channel.
    - Used for the static analysis (hammer test).
    - The trigger is set to trigger on channel 4, which by default is the impact hammer.
    - Striking the machine with the hammer triggers the analyser and captures the impact force and the acceleration results.

- Trigger by external source.
    - Used during dynamic analysis when motor is in operation.
    - Rising edge from encoder triggers analyser and channel data captured.

More details on the capture of the acceleration sensor data for the dynamic test setup is provided in chapter 6 of this thesis.

- **Supporting the structure**

The final aspect to be considered concerns the method of supporting the target structure when its being measured. When using CAE techniques such as FE to perform modal analysis on a structure it can be free-bodied, that is the structure is essentially floating in space completely unconstrained. However, in the physical world this is not feasible as gravity means that the structure must be supported by some means. What it is supported by is important as this can have some influence on the measured response.

For the case when the machine is mounted on the rig then the support is very clear. The machine is constrained by the front plate of the machine being bolted to the mounting bracket on the dynamometer, as illustrated in Fig. 4.2.8.

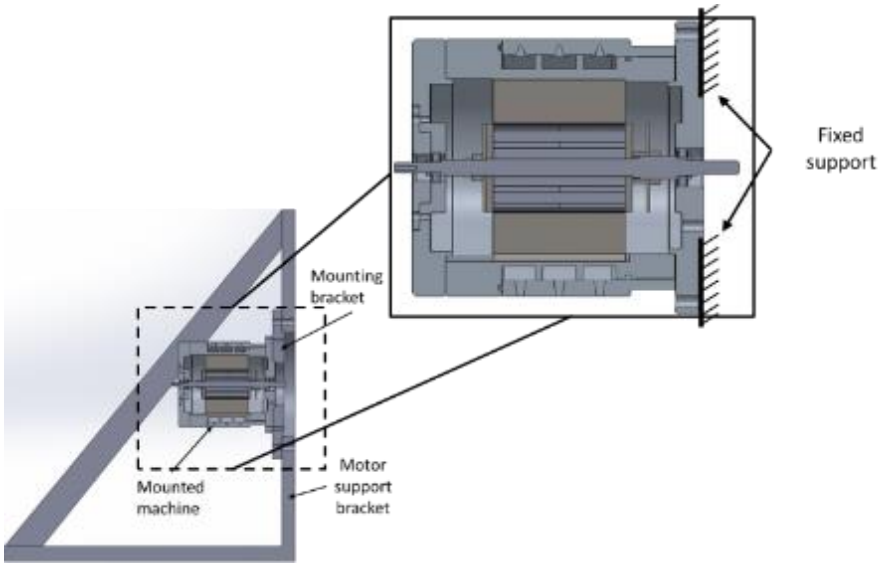

Fig. 4.2.8 Mounted machine constraint.

The mounted case is relatively easy to model in FE as a fixed support can be applied to the faceplate given the stiffness and mass of the support bracket in comparison to the machine.

For the case where the machine is being tested off rig it is more of a challenge. To try to approximate the free body motion of the structure methods such as suspension from elastic cords in a space frame or placing the structure on to a pliable material such as foam [AT00], [AB11]. These methods apply some degree of constraint to the structure and the rigid body modes will no longer have zero frequency [AT00], [AB11]. The trick is to ensure that the support structure is sufficiently soft such that any rigid body modes are significantly lower than the flexible modes and therefore have negligible influence on the structure. A good example is

provided in Fig. 4.2.9 where the rigid mode is non-zero but is significantly lower than the 1st flexible mode and as such can be neglected [AT00].

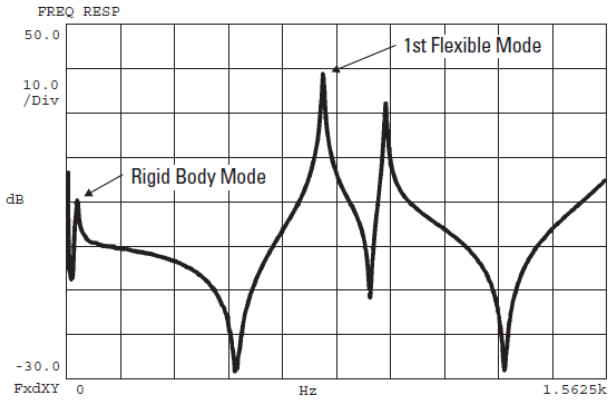

Fig. 4.2.9 Example of supporting the structure with a soft foam to mitigate the influence of rigid modes [AT00].

The method used to support the structure during the initial test phase is a rubberised mat with a soft foam coating, illustrated in Fig. 4.2.10.

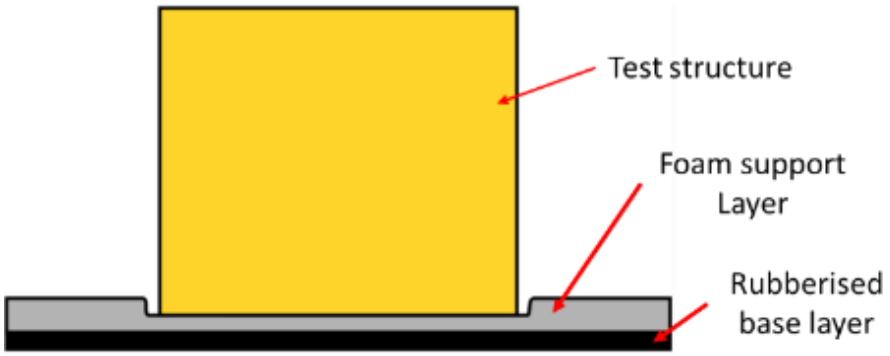

Fig. 4.2.10 Cross section of support material used for the testing.

This provides a soft material for the structure to sit on to mitigate the influence of any induced rigid modes. The rubberised base layer acts as a high friction interface with the table onto which the structure is being tested preventing the part sliding around following impacting and to act as a damper to de-couple the test structure from the test bench.

4.2.4 Measurement procedure

On the face of it the hammer test is rather simple. It is literally striking the target structure with the impact hammer and measuring the reaction. On closer inspection there are subtleties about the test process that needs to be considered to give good, and importantly consistent results. Some of the key concerns with setup such as the hammer tip selection, mounting methodology of the acceleration sensors or the windowing settings for the FFT have already been covered but there are a number of other concerns to consider whilst executing the test a sample of which are given in Table 4.2.8.

Table 4.2.8 Concerns with hammer test setup.

Test aspect	Concern	Results
Strike	Strike force too soft	Impulse does not excite all frequencies, modal frequencies missed
	Strike force too hard	High distortion in signal, overload acceleration sensors, damage to target structure, hammer bounce generating multiple impacts and erroneous data
Sensor attachment	Too much wax	Wax material acts as a damper producing error in system response measurement
	Too little wax	Poor adhesive force with structure surface means sensor can feely move or even fall off after a strike
Test temperature	Room temp >30°C	Softens wax reducing the adhesive quality of the material resulting in reduced constraint of the sensor or the sensor simply falling off
Test piece mounting	Part sat on hard surface (e.g. worktop)	Surface acts as a constraint on the structure changing the motion and modal frequencies VS a free body mount

An additional concern lies in keeping the sensor and strike positions consistent as the assembly complexity increases to enable a fair comparison between the progress of the different modes. This is achieved in 2 parts:

1. A guide attached to the top of the case aligned to the stator keyway which acts as the datum for the guide. This allows the tooth positions to be marked onto the side of the case.
2. Circumferential guide is aligned to the markings to provide the strike guide.

Using the guides, the sensor placement and strike locations is of higher accuracy. Fig. 4.2.11 details the radial and circumferential angle guide.



(a) Tooth alignment aid.

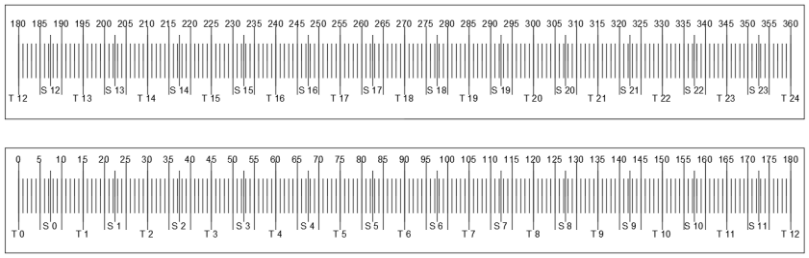

(b) Circumferential tooth and slot guide imposed onto angle guide.

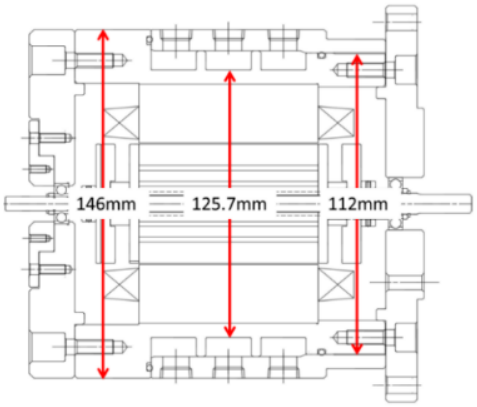

(c) Location of angle guides.

Fig. 4.2.11 Radial and circumferential angle guides for physical testing (not to scale).

Table 4.2.9 shows the differences in specification for each strip at the locations in Fig 4.2.11(c).

Table 4.2.9 Specification of angle strike guides.

Band location	Machine outer diameter (mm)	Shell ID (mm)	Coolant channel OD (mm)
OD of part	146	125.7	112
Circumference (full)	458.67	394.9	351.86
Circumference (1/2)	229.34	197.45	175.93
mm/deg	1.27	1.1	0.98
mm/tooth (15°)	19.11	16.45	14.66
mm/half tooth (7.5°)	9.56	8.23	7.33

The biggest concern during the creation of the strips was where the printed guides were at a different scale due to some internal defaults; different strips had to be printed with different plotter settings and carefully measured to find the closest match to reality and minimise error.

4.2.4.1 Averaging the hammer strikes

A key concern with the hammer test, as highlighted in Table 4.2.2 and Table 4.2.8 is that producing consistent, accurate strikes with just the right amount of force to excite the maximum number of frequencies without distortion can be difficult depending on the structure. To mitigate this concern is common practise [OD88a], [AT00], [AB11] to strike the target several times and use the average of the series of strikes. The 35670A Dynamic Signal Analyser has an averaging function, from trial and error 10 to 15 strikes were a good balance between test time and accuracy. Fig. 4.2.12 shows the test procedure.

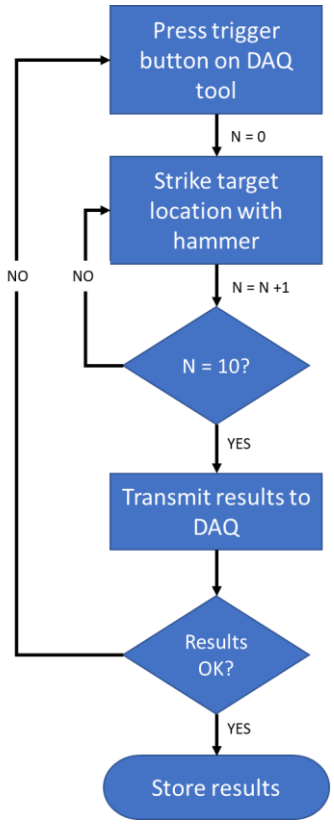

Fig. 4.2.12 Test procedure for averaging the hammer strikes.

After the set number of strikes are complete the signal analyser generates the average results and then sends the results to the data acquisition tool. Care must still be taken when using the hammer, even with many averages a single heavy-handed strike or multi-strike (hammer bounce) can distort the results. This is the reason the software written for the DAQ system the unit does not automatically save the data, rather it lets the user inspect the results first. To establish trends and root out any problems with the setup the procedure shown in Fig. 4.2.12 is repeated 3 or 4 times allowing for any inconsistencies to be identified. For example, during one of the runs an acceleration sensor may not have been properly mounted giving erroneous results which can be identified when several different runs are compared.

4.3 Impact hammer test results

With the test setup and procedures established the testing can begin, following the sequence of increasing structure complexity established in Fig. 4.2.2.

4.3.1 Coolant shell

The represents the simplest part of the structure however it has the most complicated relationship with the assembly of the structure owing to how it is fitted to the machine. It is important therefore to understand the modal frequencies of this part in the case that they arise during testing of the fully assembled machine. It was also fabricated from the same aluminium billet as the rest of the machine meaning it allows for a quick and easy way to calibrate the material properties of the motor casing. Fig. 4.3.1 shows the test setup.



(a) Top view of test with B&K hammer shown.

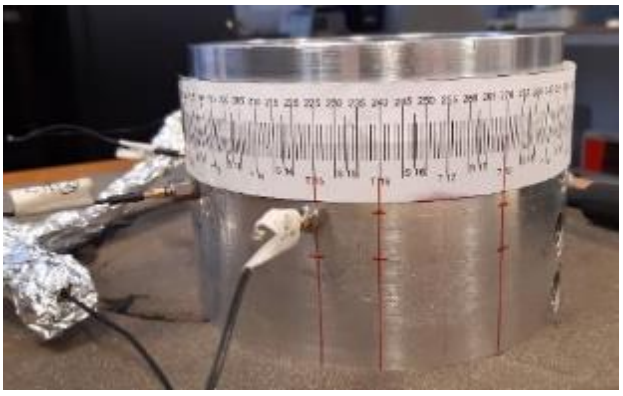

(b) Side view of test with sensor mounted in setup 1 orientation.

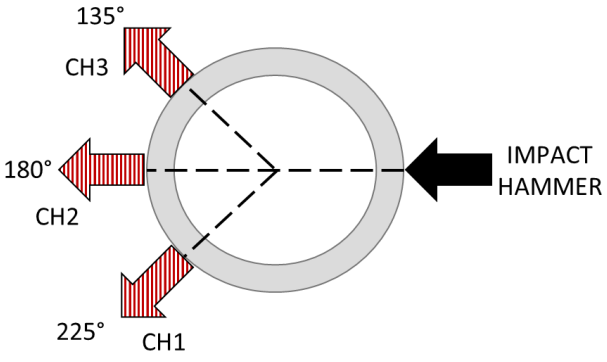

(a) Setup 1: sensors distributed at 45° angles, channel 2 sat 180° from impact and Ch1 and Ch3 45° either side.

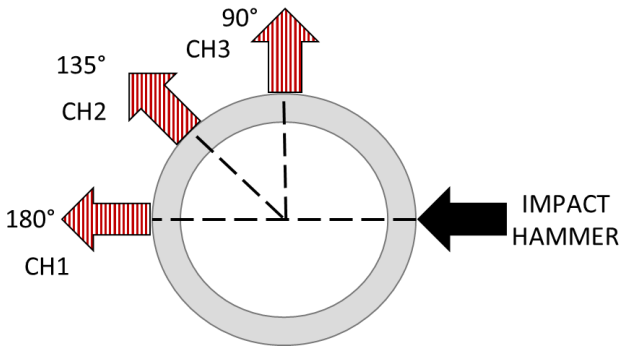

(b) Setup 2: sensors distributed at 45° angles, Channel1 is moved to 180° and CH2 and CH3 sat 45° anti-clockwise.

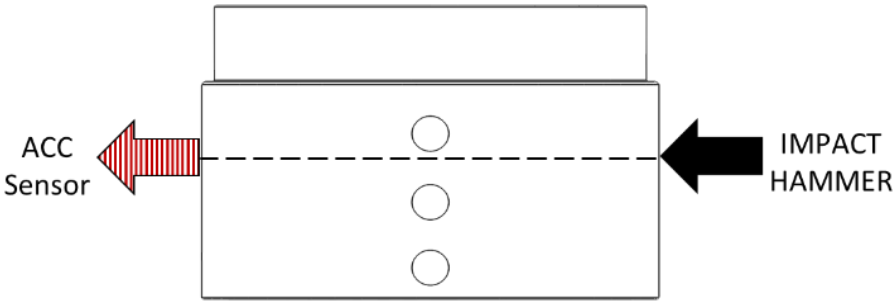

(c) Axial position of sensors and impact point – mid shape.

Fig. 4.3.1 Test setup of the coolant shell.

As highlighted in the specifications for the dynamic signal analyser (Table 4.2.6) only 4 channels are available on the device, so to cover as much of the stator as possible two setups are run, shown in Fig. 4.3.1 (b) and (c). Rather than move the sensors the impact point is shifted so channel 1 in Fig. 4.3.1 (b) moves from being 225° (counter-clockwise direction) from the impact point to 180°, i.e. diametrically opposite from the impact point. This avoids all the potential concerns with moving the sensors and re-bonding them to the stator outer surface. Testing is carried out using the process flow shown in Fig. 4.2.12.

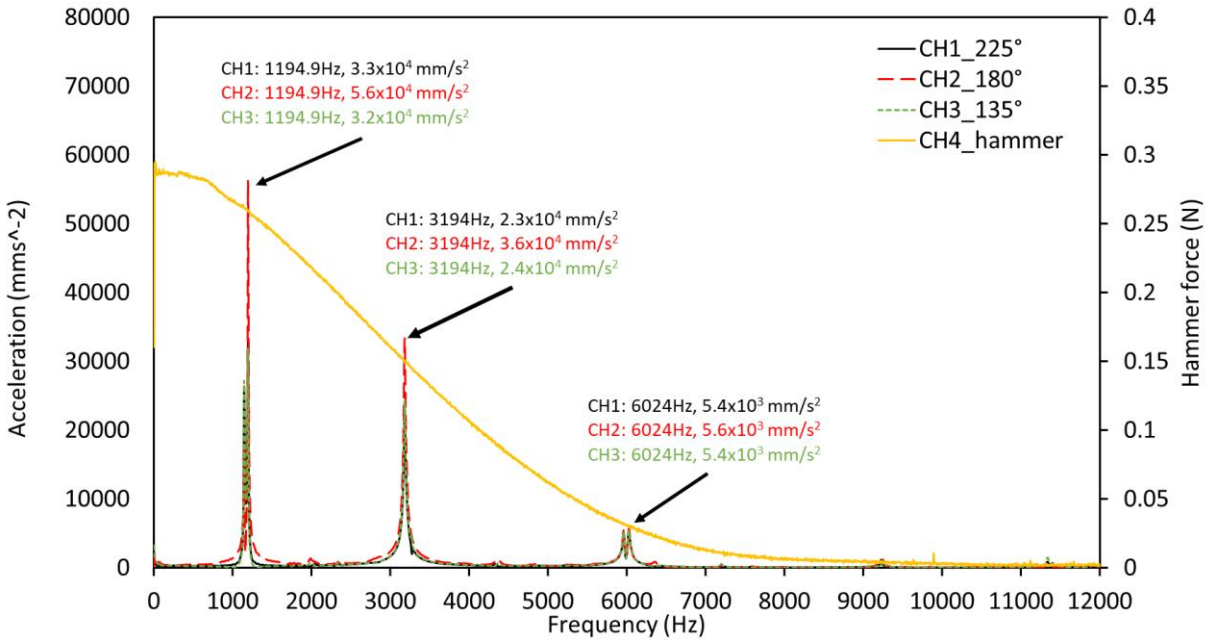

(a) Test 1 results FFT showing the acceleration sensors modal frequencies and the impact hammer force.

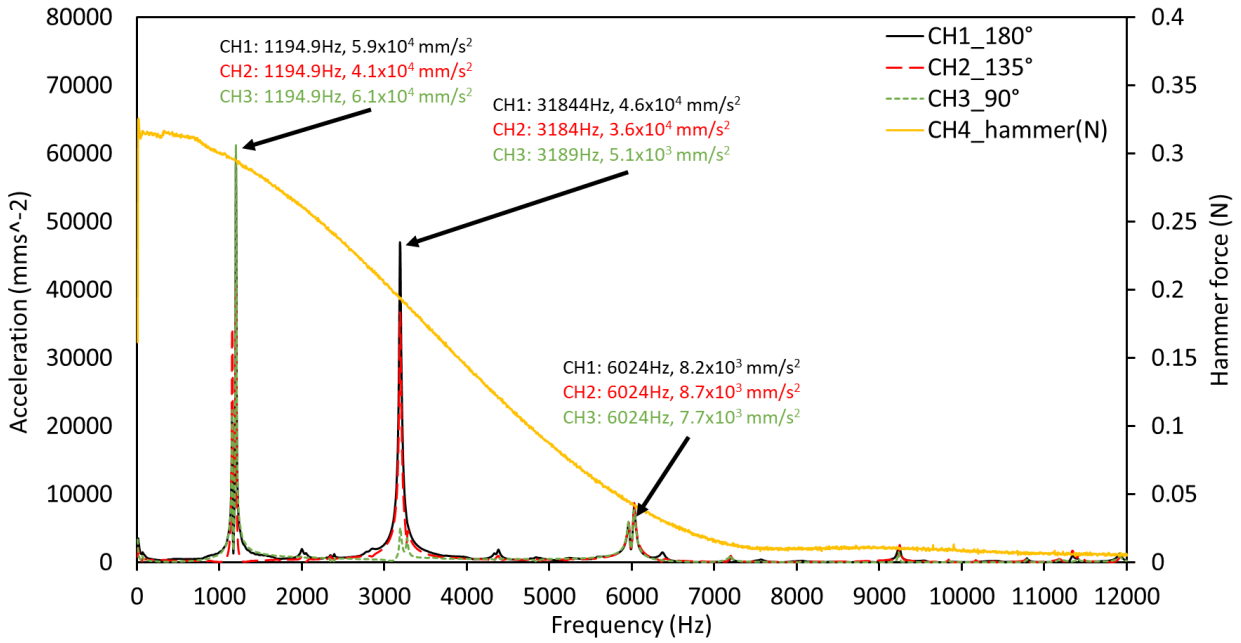

(b) Test 2 results FFT showing the acceleration sensors modal frequencies and the impact hammer force.

Fig. 4.3.2 Measured modal results for the coolant shell only.

Table 4.3.2– shell only measured modal frequencies and accelerations.

	Channel1 (225deg)		Channel2 (180deg)		Channel3 (135deg)	
Setup 1	Frequency	Maximum	Frequency	Maximum	Frequency	Maximum
	1194	32689	1194.9	55560	1194.9	31775
	3194	22555	3184	36296	3194	23904
	6024	5427	6024	5654	6024	5376
	9224	1163	9224	1241	9249	1455
	Channel1 (180deg)		Channel2 (135deg)		Channel3 (90deg)	
Setup 2	Frequency	Maximum	Frequency	Maximum	Frequency	Maximum
	1194.9	59233	1194.9	40583	1194	60692
	3184	46086	3184	36606	3189	5075
	6024	8163	6024	8710	6024	7705

The impact results are good with nice and clear modes identified at 1194Hz, 3189Hz and 6024 Hz, representing circumferential modes 2,3 and 4, respectively. The flexible frequencies are clear and there appears to be no rigid body modes indicating the structure support strategy is working as desired. The low stiffness and mass of the aluminium means that the key modes are all under the maximum bandwidth of the hammer and there is little excitation of frequencies above 6kHz.

4.3.1.1 Frequency response function of the coolant shell

With the impact testing complete the frequency response function (FRF) can be determined using (4.23) and measurement data from the impact hammer and the acceleration sensors. The accelerance (mms^{-2}/N) is shown in Fig. 4.3.3.

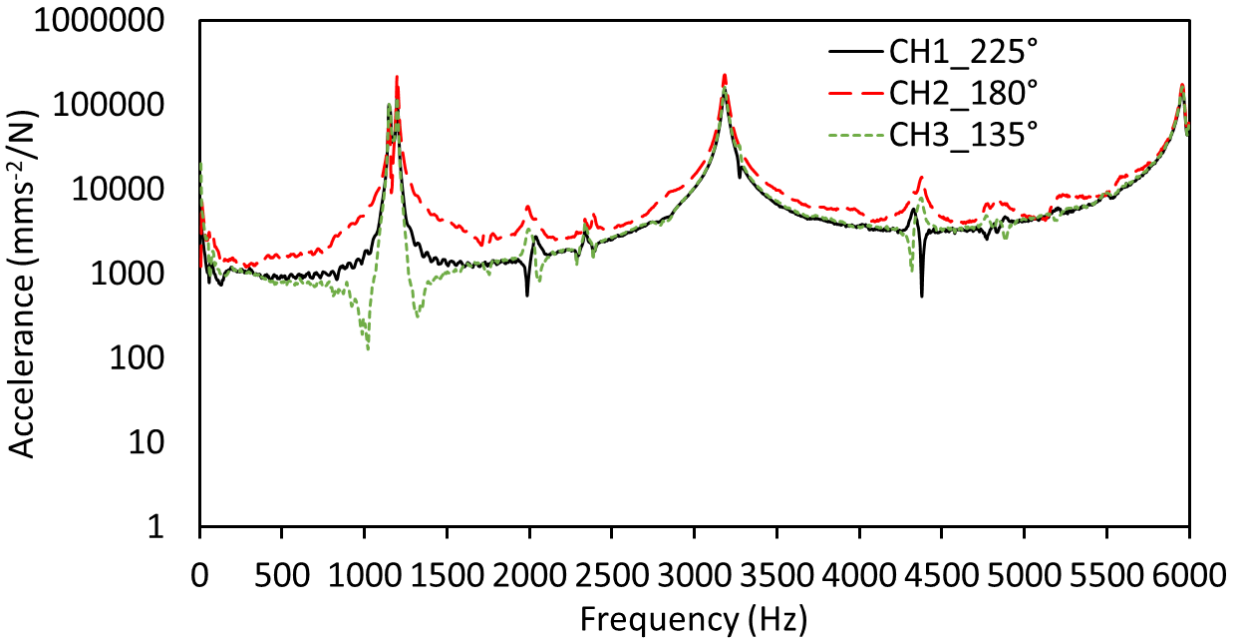

(a) Accelerance of channels 1 to 3 (225° to 135°) of setup 1.

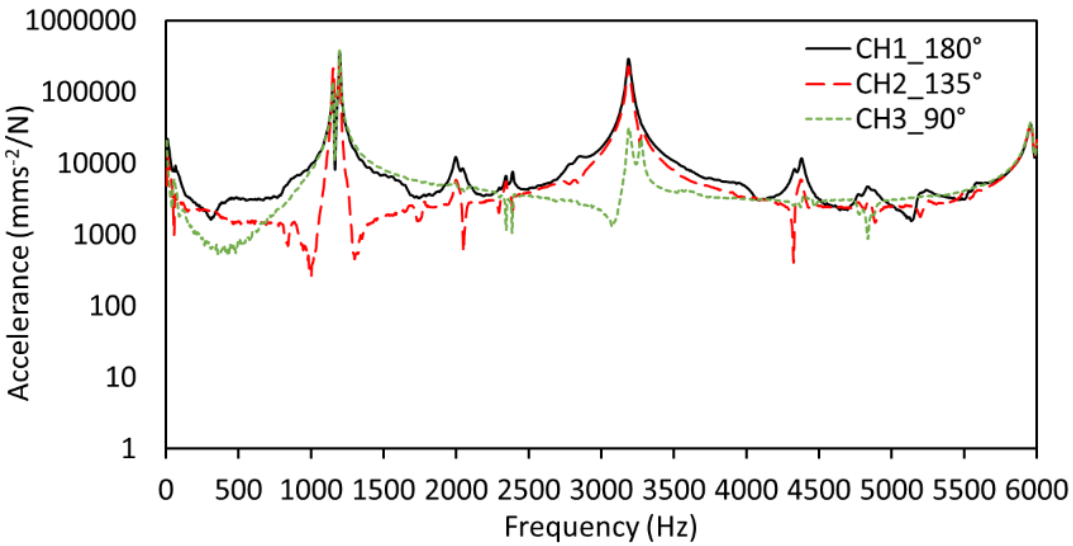

(b) Accelerance of channels 1 to 3 (180 °to 90°) of setup 2.

Fig. 4.3.3 Frequency response function for the coolant shell.

Following the rule of thumb on the cut off frequency [AT00] the bandwidth of the FRF is limited to 6kHz. A log-scale is utilised on the Y-axis as the maximum accelerance of the circumferential mode 2 and mode 3 dominates the spectrum by a factor of several thousand allowing the sidebands of the peaks to be observed.

4.3.2 The Stator

The measurement of the stator is arguable one of the most important given the dominance of the modal performance of the part, as discussed in chapter 1. The stator is set up as shown in Fig. 4.3.4.

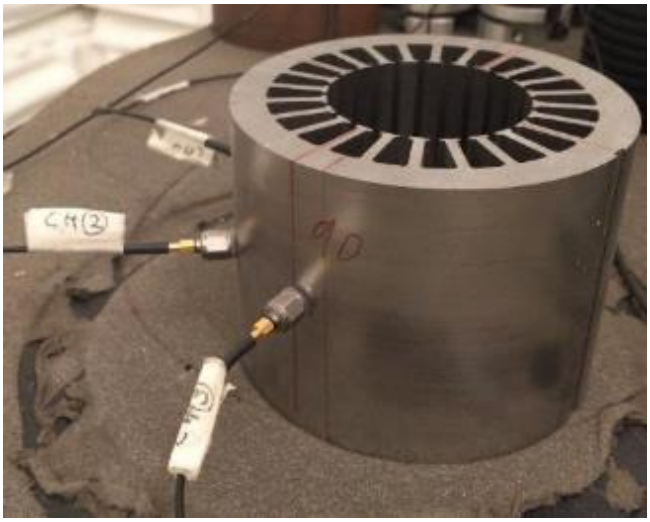

(a) Part with sensors attached ready for test.

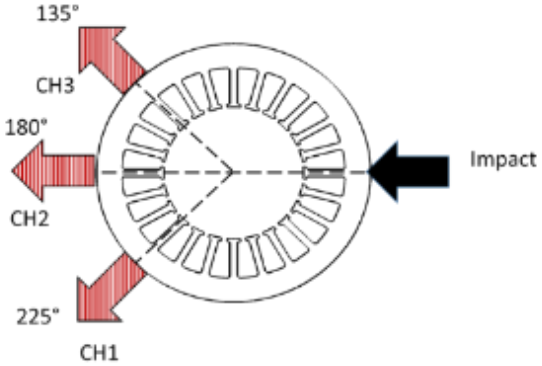

(b) Setup 1: sensors distributed at 45° angles, channel 2 sat 180° from impact and Ch1 and Ch3 45° either side.

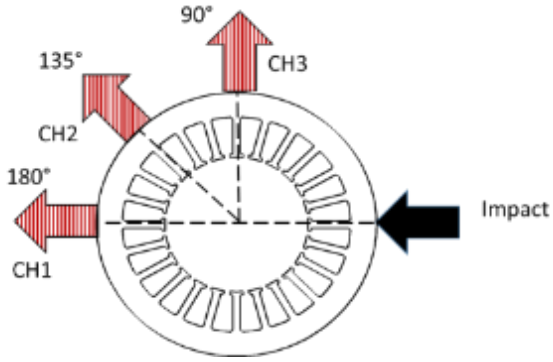

(C) Setup 2: sensors distributed at 45° angles, Channel1 is moved to 180° and CH2 and CH3 sat 45° anti-clockwise.

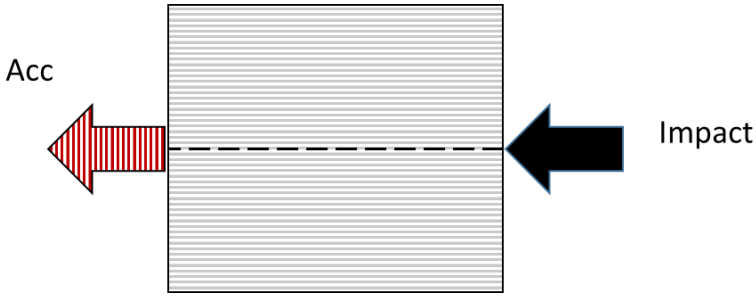

(d) axial position of sensors and impact point.

Fig. 4.3.4 Stator ONLY test setup.

The setup is identical to the Coolant shell. The results of the hammer test results are shown in Fig. 4.3.5 and key frequency and amplitude values in Table 4.3.2.

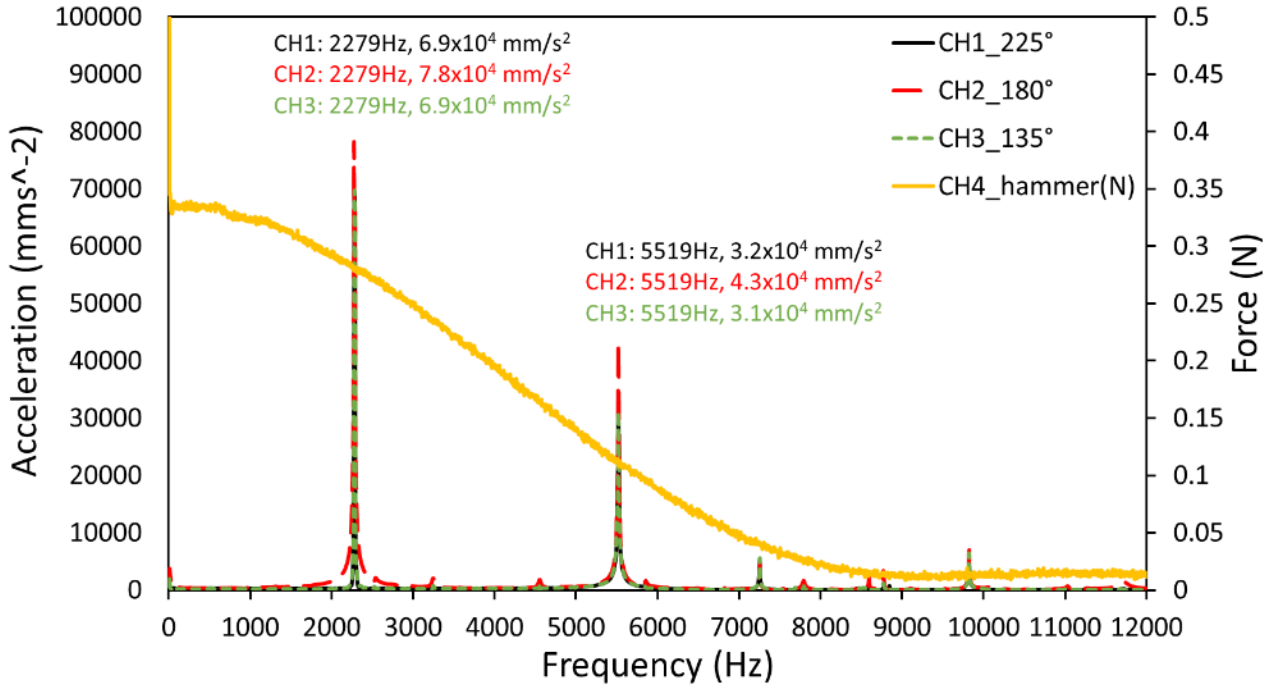

(a) Setup 1 results FFT showing the acceleration sensors modal frequencies and the impact hammer force.

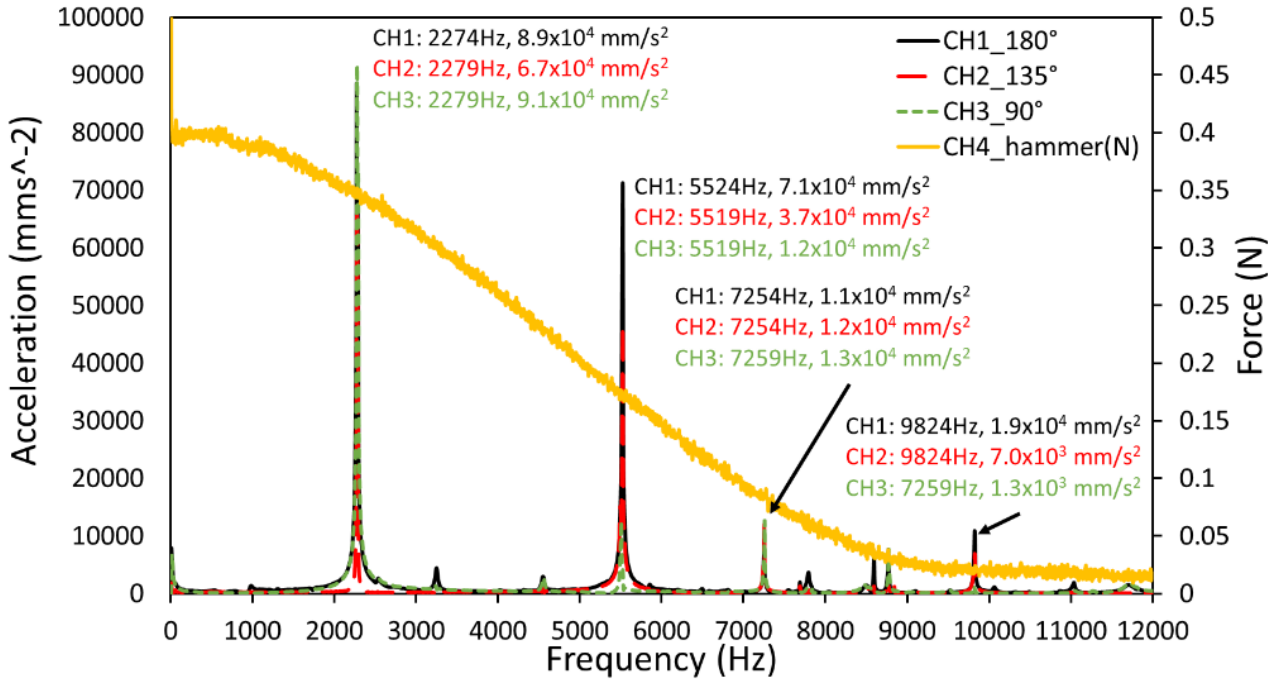

(b) Setup 2 results FFT showing the acceleration sensors modal frequencies and the impact hammer force.

Fig. 4.3.5 Measured modal results for the stator only.

The peak amplitudes and associated frequencies are summarised in Table 4.3.2.

Table 4.3.2 Results of impact hammer tests on stator core.

	Channel1 (225°)		Channel2 (180°)		Channel3 (135°)	
Set 1	Frequency (Hz)	Maximum (mms^{-2})	Frequency (Hz)	Maximum (mms^{-2})	Frequency (Hz)	Maximum (mms^{-2})
	2279	68969	2279	78194	2279	69577
	5519	32613	5519	43375	5519	31079
	7254	5511	7254	5204	7254	5578
	9824	4706	9824	6961	9824	6392
	Channel1 (180°)		Channel2 (135°)		Channel3 (90°)	
Set2	Frequency (Hz)	Maximum (mms^{-2})	Frequency (Hz)	Maximum (mms^{-2})	Frequency (Hz)	Maximum (mms^{-2})
	2274	88527	2279	66970	2279	91572
	5524	70172	5519	36724	5504	12509
	7254	10895	7254	11971	7259	12585
	9824	10898	9824	6960	9824	1305

From the results the peak modal frequencies shown in Figs. 4.3.5(a) and (b) are consistent, and the amplitudes clearly dominate the frequency domain. The key peaks correspond to circumferential modes 2, 3 and 4 respectively neatly following the expected output of a relatively simple structure, given the excitation band of the hammer. In Table 4.3.2 a further mode is observed at 9824Hz. The acceleration amplitudes at this point follow a very similar pattern to the 1st mode 3 at ~5519Hz, albeit at a significantly lower amplitude, indicating that this is a 2nd mode 3. So, the mode at -5519Hz would be circumferential mode 3 (a) and the mode at ~9824 would be circumferential mode 3(b). Care must be taken analysing peaks beyond 6kHz as excitation force drops below 10dB, which is typically seen as the cut off for matching frequencies [AT00], [OD88a] meaning the signal to noise ratio becomes very low and it becomes difficult to differentiate potential modes with noise in the system.

Another point to notice is that whilst the hammer force curve looks similar in both Figs. 4.5.5 (a) and (b) the strike force in (b) is higher than that of (a) which of course means the resultant accelerations are higher. So, whilst the modal frequency data yielded from the experiment is important care must be taken when comparing the acceleration data.

4.3.2.1 Frequency response function for the stator core

Like the coolant shell the frequency response function for the core can be calculated, again using (4.13) and using the force data from the hammer as the input parameter and the acceleration data from each measured channel as the output parameters. Fig. 4.3.6 shows the results for each setup.

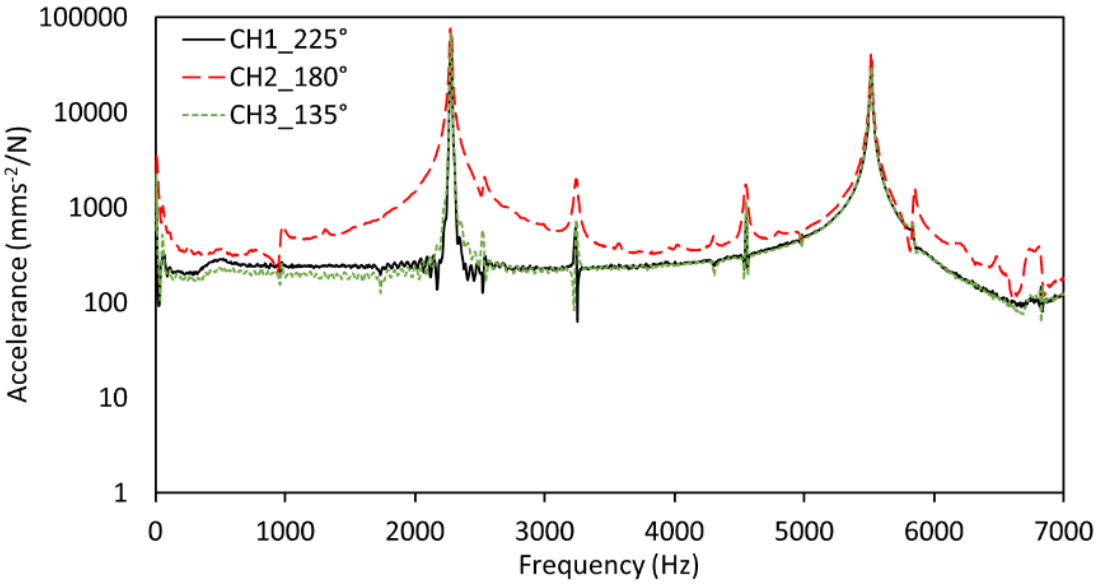

(a) Accelerance of channels 1 to 3 (225° to 135°) of setup 1.

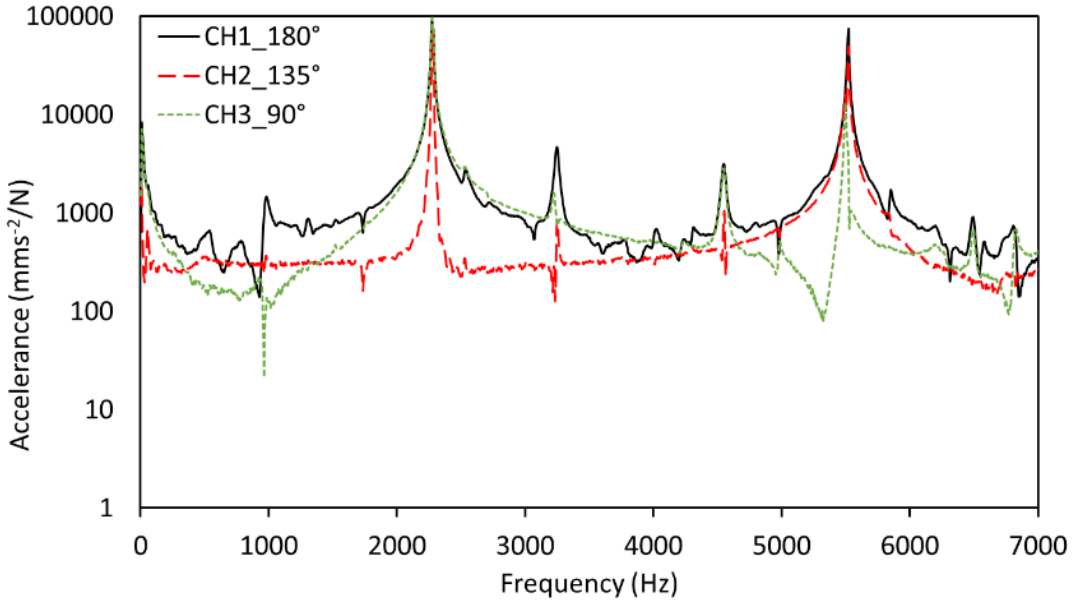

(b) Accelerance of channels 1 to 3 (180 °to 90°) of setup 2.

Fig. 4.3.6 Frequency response function for the stator core.

The peaks on each channel follow much the same trends as the simple aluminium cylinder of the coolant shell. The key difference is the frequency cut off occurs at 7kHz giving a much wider bandwidth and allowing the 3 key modes to be observed. In addition, the higher stiffness and mass of the stator mean the modal frequencies have shifted right to higher frequencies.

4.3.3 Wound stator in frame.

As highlighted in section 4.3 of this chapter the step in the assembly between the stator being shrunk fit into the frame and the machine being wound cannot be tested so the next step that can be tested is the fully wound stator fit in the frame. Fig. 4.3.7 shows the setup.



(a) axial position of sensors.



(b) radial position.

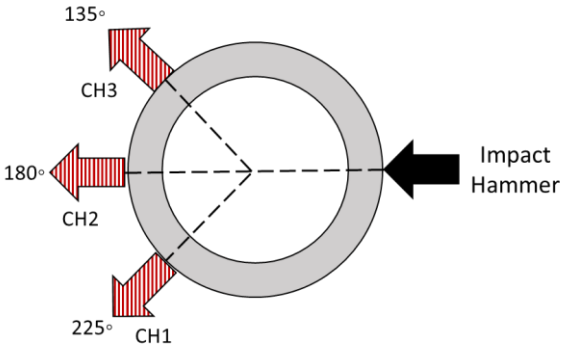

(b) Setup 1: sensors distributed at 45° angles, channel 2 sat 180° from impact and Ch1 and Ch3 45° either side.

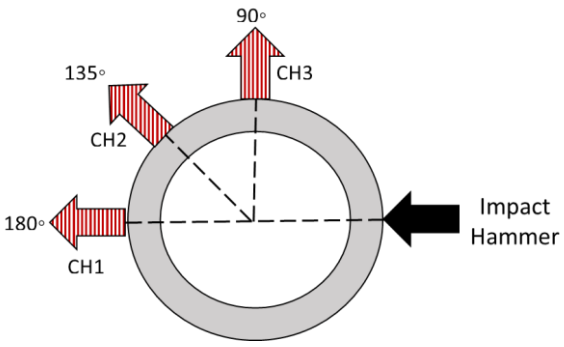

(C) Setup 2: sensors distributed at 45° angles, Channel1 is moved to 180° and CH2 and CH3 sat 45° anti-clockwise.

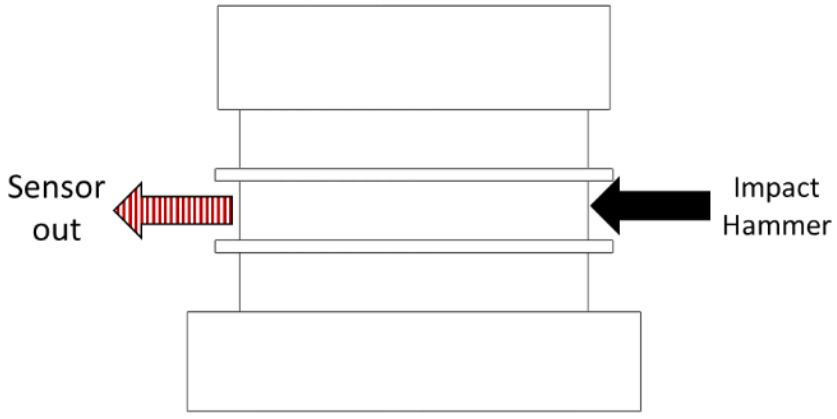

(d) axial position of sensors and impact point.

Fig. 4.3.7 Setup of the modal testing on the frame with wound stator installed.

The results are shown in Fig. 4.3.8 and Table 4.3.3.

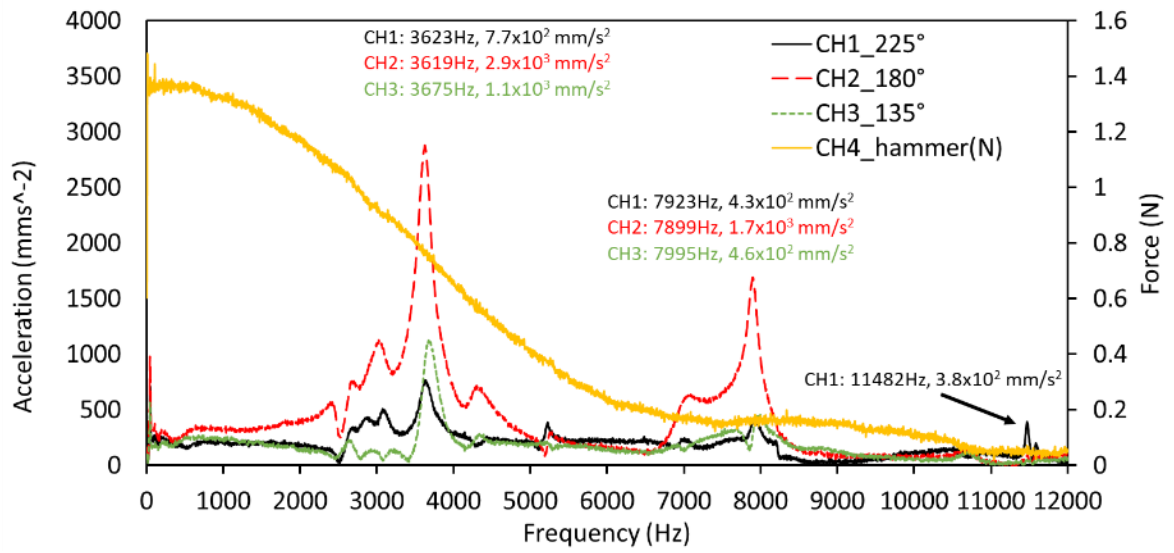

(a) Test 1 results FFT showing the acceleration sensors modal frequencies and the impact hammer force.

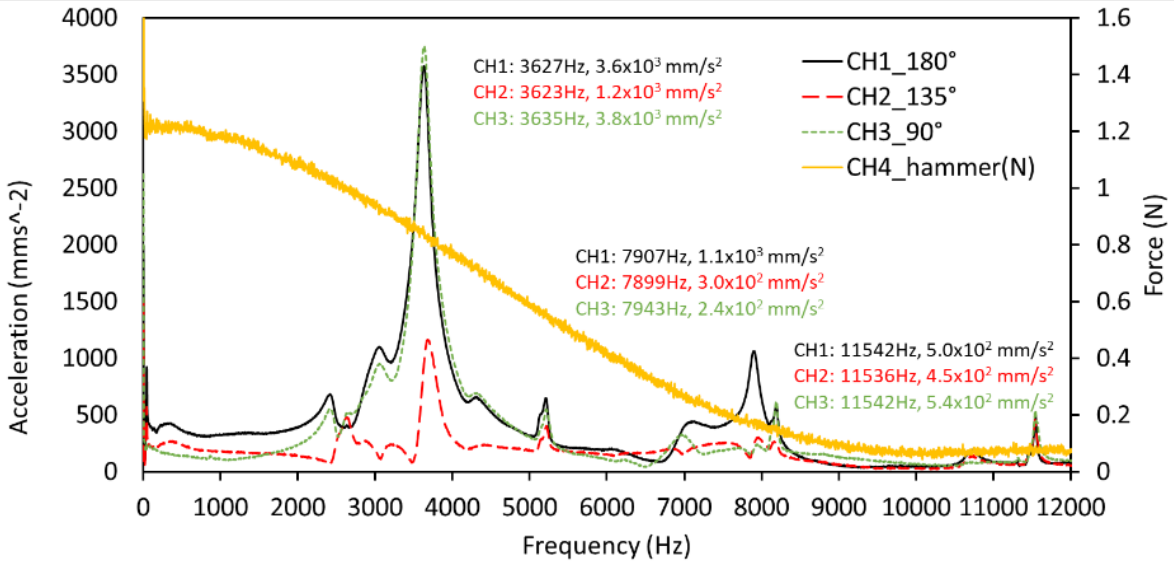

(b) Test 2 results FFT showing the acceleration sensors modal frequencies and the impact hammer force.

Fig. 4.3.8 Measured modal results for the wound stator in the frame.

Table 4.3.3 Results of impact test on wound stator in the frame.

	Channel1 (225°)		Channel2 (180°)		Channel3 (135°)	
Set 1	Frequency (Hz)	Maximum (mms^{-2})	Frequency (Hz)	Maximum (mms^{-2})	Frequency (Hz)	Maximum (mms^{-2})
	3627	766.6	3627	2878.7	3675	1124
	7923	427.3	7899	1689.8	7995	460.1
	11482	376	N/A		N/A	
	Channel1 (180°)		Channel2 (135°)		Channel3 (90°)	
Set 2	Frequency (Hz)	Maximum (mms^{-2})	Frequency (Hz)	Maximum (mms^{-2})	Frequency (Hz)	Maximum (mms^{-2})
	3607	3573	3623	1161	3635	3751
	7907	1061	7995	300	7943	240
	11542	498	11536	453	11542	538

This test proved to be one of the more difficult to implement, the primary concern being the width of the hammer head to strike the target surface is only a few millimetres thinner than the gap between the ribs on the middle coolant channel. This led to a high number of mis-strikes due to accidentally glancing off a rib or bouncing. In addition, considerably higher impulse forces had to be applied to the structure to excite the modes as can be seen from the force results in Fig. 4.3.8 compared to the stator impact results in Fig. 4.3.2 or Fig. 4.3.5. Even with the high impulse force the measured acceleration is much lower, reflecting the large increase in complexity of the structure.

Despite the above concerns the results in Fig. 4.3.8 clearly show mode 2 and mode 3. The frequencies of both have shifted significantly, mode 2 has increased ~1300Hz and mode 3 by ~2300hz reflecting the increased stiffness of the structure due to both the potted windings in the slots and the interference fit with the frame. A very small peak can be seen around 11500, this could align with the missing mode 4, though given the low amplitude and noise around this value it is difficult to judge. The aligned FE model later should give a good indication.

4.3.3.1 Frequency response function for the wound stator in frame

The FRF for the stator in frame is calculated in the same manner as the previous cases and the results shown in Fig. 4.3.9.

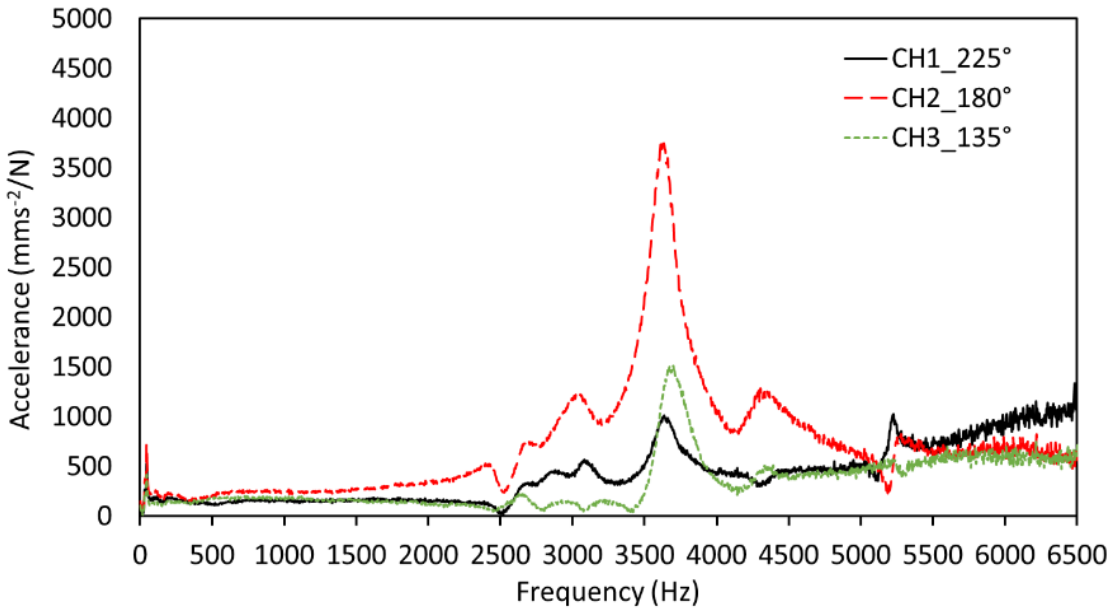

(a) Accelerance of channels 1 to 3 (225° to 135°) of setup 1.

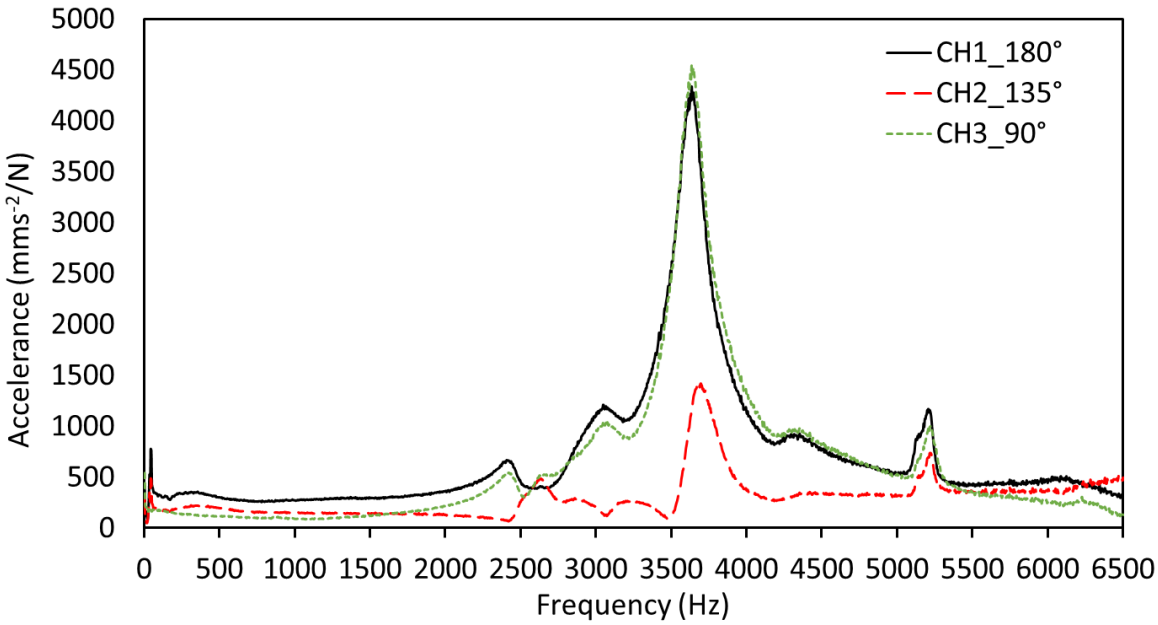

(b) Accelerance of channels 1 to 3 (180 °to 90°) of setup 2.

Fig. 4.3.9 Frequency response function for the wound stator in frame.

The first and most obvious observation is how sparse the FRF is compared to the stator and coolant shell. The cut off frequency of the excitation bandwidth is 6.5kHz means that only the mode 2 can really be observed. It should be noted that the cut-off frequency for both charts in Fig. 4.3.9 is based on the impact results of setup 1. The higher impact on setup 2 means the cut-off frequency here is slightly higher but the same value is used to ease comparison. The biggest difference between the results is the noise in setup 2 is less apparent, this highlights the fact that by the 2nd setup the strikes were more consistent and stronger giving a cleaner average impulse on the output which of course gives a smoother output.

4.3.4 Rear end plate attached

The next stage has the rear-end plate attached to the back of the frame. The plate is affixed to the rear of the frame using four M6 bolts which are tightened to 8Nm using a calibrated torque wrench. Using the set torque is important to ensure the structure rigidity remains as constant as possible during the different tests as the plates must be removed multiple times. Once the plate is attached the partially assembled machine is returned to the bench and setup as shown in Fig. 4.3.10.

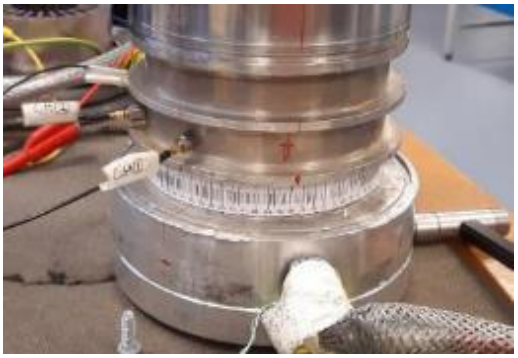

(a) Axial position of sensors

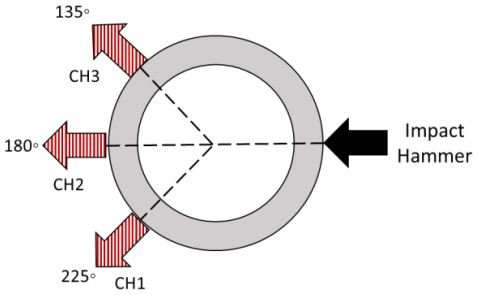

(b) Setup 1: sensors distributed at 45° angles, channel 2 sat 180° from impact and Ch1 and Ch3 45° either side.

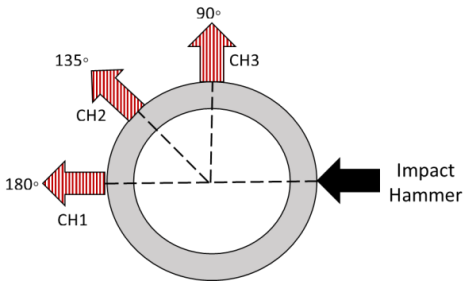

(C) Setup 2: sensors distributed at 45° angles, Channel1 is moved to 180° and CH2 and CH3 sat 45° anti-clockwise.

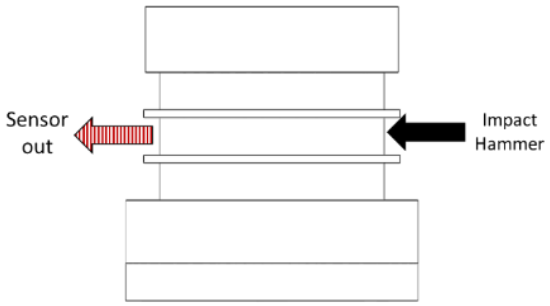

(d) Axial position of sensors and impact point.

Fig. 4.3.10 Setup of the modal testing on the machine assembly with the rear plate fitted only.

The results of the impact hammer tests are shown in Fig. 4.3.11 and Table 4.3.4.

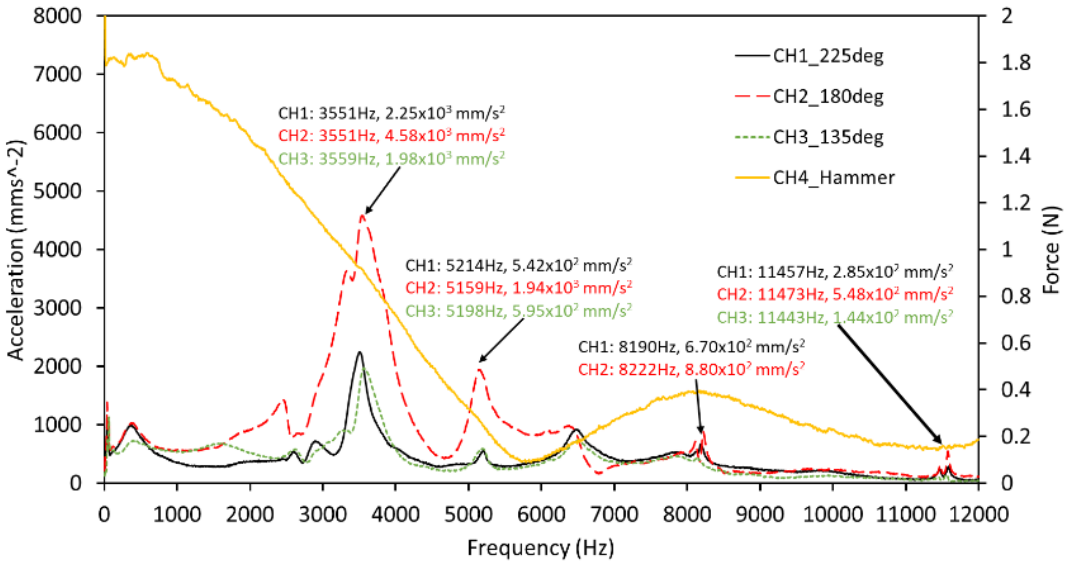

(a) Test 1 results FFT showing the acceleration sensors modal frequencies and the impact hammer force.

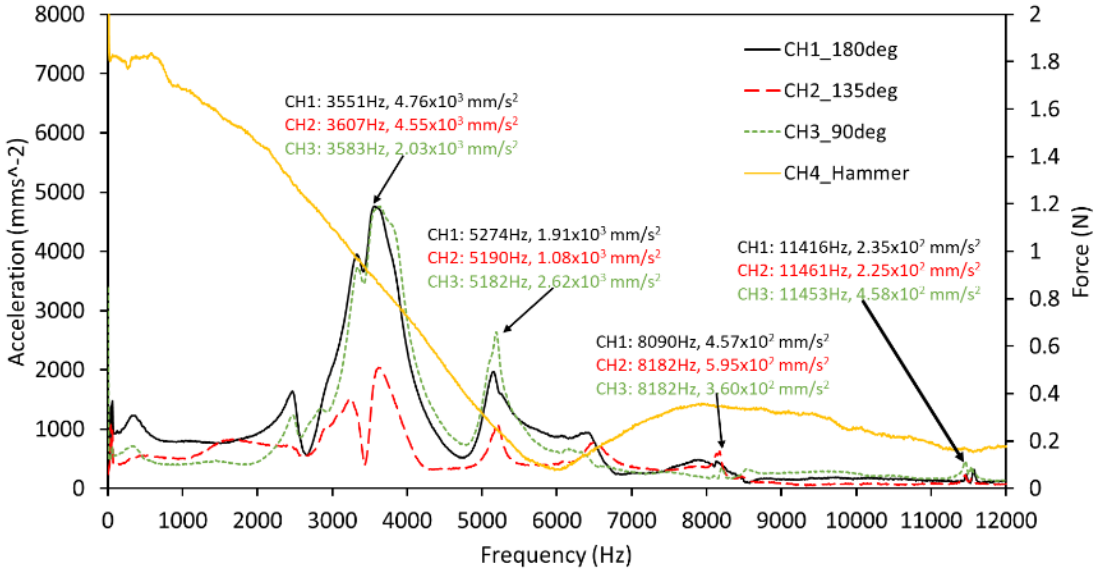

(b) Test 2 results FFT showing the acceleration sensors modal frequencies and the impact hammer force.
Fig. 4.3.11 Measured modal results for the wound stator in the frame.

Table 4.3.4 Results of impact test on wound stator in the frame

	Channel1 (225°)		Channel2 (180°)		Channel3 (135°)	
Set 1	Frequency (Hz)	Maximum (mms^{-2})	Frequency (Hz)	Maximum (mms^{-2})	Frequency (Hz)	Maximum (mms^{-2})
	3551	2248	3551	4583	3559	1975.8
	5214	541.9	5159		51898	
	8150	669.9	8182		N/A	-
	11457	285.3	11473	548	11433	458
	Channel1 (180°)		Channel2 (135°)		Channel3 (90°)	
Set 2	Frequency (Hz)	Maximum (mms^{-2})	Frequency (Hz)	Maximum (mms^{-2})	Frequency (Hz)	Maximum (mms^{-2})
	3551	4761	3607	4552	3583	2032
	5174	1907	5190	1076	5182	262
	8090	457	8182	595	8182	359
	11416	235	11461	225	114563	458

The concerns with mis-strikes and hitting the ribs continued with this test. To get a reasonable response from the assembly the strike force had to be higher than the previous tests making accuracy tougher. Increasing the number of averages per run proved to mitigate the concern. From the results the modes are reasonably clear, but the amplitudes are low, in part due to the high number of averages but also due to mis-strikes.

Even with the above concerns the mode 2 is clearly dominant over the other modes. The next highest peak sits at around 5200 Hz, its proximity to mode 2 suggests this is an axial mode. The shape of the structure in this case is a can, one end has a high rigidity from the attached plate whilst the other end is open. This creates an asymmetry in the shape stiffness making it more prone to axial modes. Thus, the axial mode observed is likely to be a mode 1. Very small peaks at ~8200Hz and ~11500Hz point to circumferential modes 3 and 4 respectively but this will require conformation using the aligned FE model.

4.3.4.1 Frequency response function for frame with rear plate attached

The FRF for both setups is generated and shown in Fig. 4.3.12.

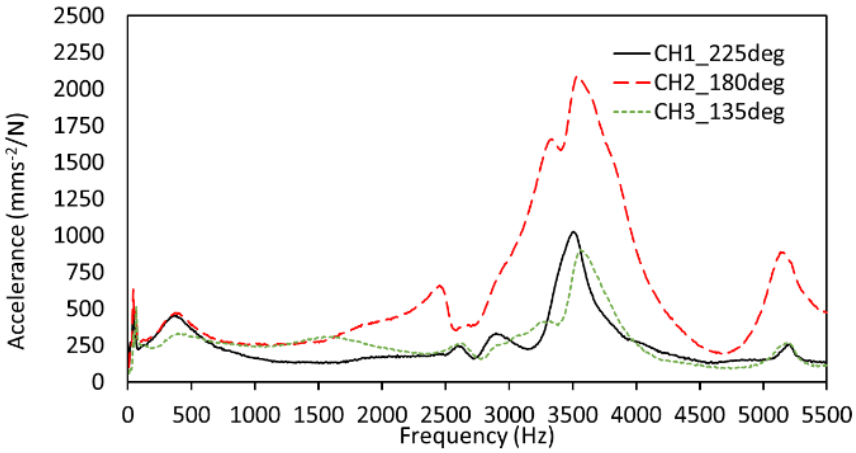

(a) Accelerance of channels 1 to 3 (225° to 135°) of setup 1.

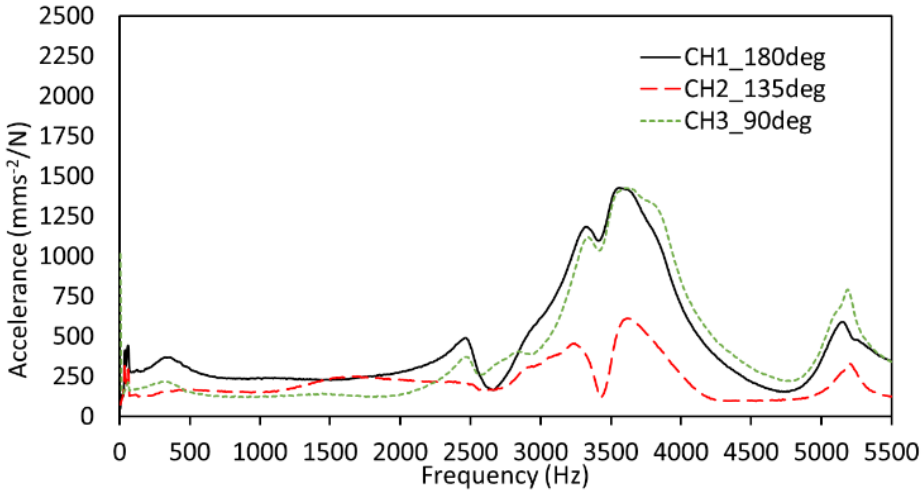

(b) Accelerance of channels 1 to 3 (180 °to 90°) of setup 2.

Fig. 4.3.12 Frequency response function for the frame with the rear plate attached.

The results further highlight the concerns with testing this stage of the assembly process, despite the higher force the bandwidth is much lower. The rounded nature of the mode 2 is still apparent indicating the damping in this case is high.

4.3.5 Front and rear end plates attached, no coolant shell

Prior to the fitment of the coolant shell the front plate is attached. Like the rear plate the front plate is fastened onto the machine structure using four M6 bolts for each of the plates and tightened to a set torque of 8Nm, again using a calibrated torque wrench. This allows the full effects of the end plates to be observed before adding the coolant shell and therefore allowing the influence of the shell to be determined. The setup follows the same procedure as the previous steps and is shown in Fig. 4.3.13.



(a) Front and rear plates attached and ready for hammer test.

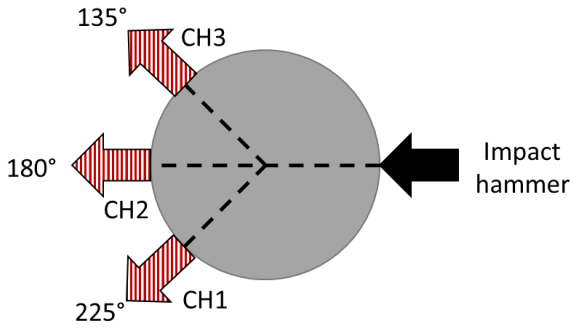

(b) Setup 1: sensors distributed at 45° angles, channel 2 sat 180° from impact and Ch1 and Ch3 45° either side.

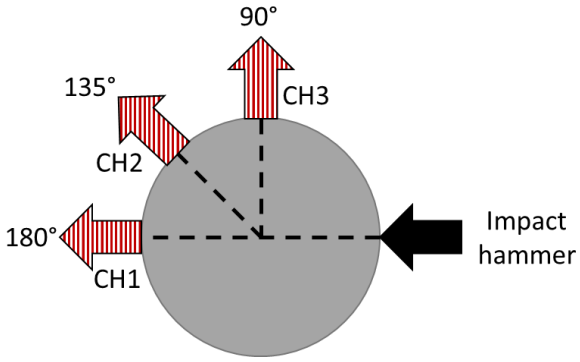

(c) Setup 2: sensors distributed at 45° angles, Channel1 is moved to 180° and CH2 and CH3 sat 45° anti-clockwise.

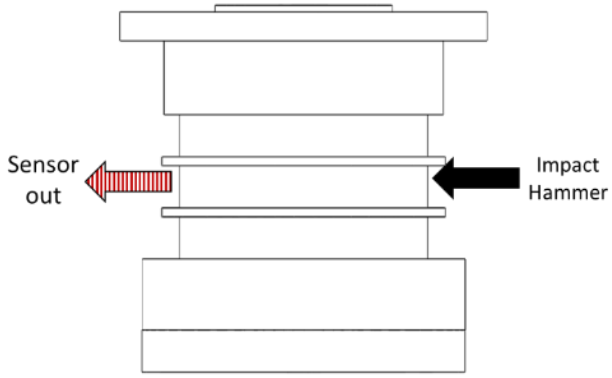

(d) Axial position of sensors and impact point.

Fig. 4.3.13 Hammer test of frame with front and rear end plates attached.

The test results can be seen in Fig. 4.3.14 and key frequencies and amplitudes given in Table 4.3.5.

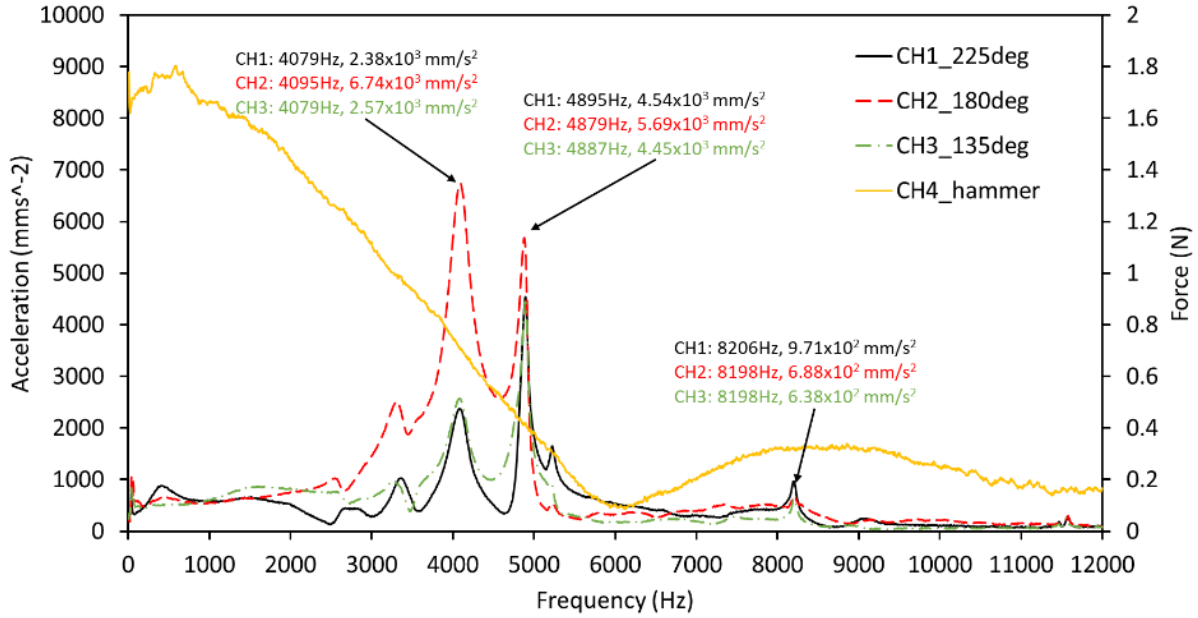

(a) Results of hammer test on frame with both end caps attached with setup 1.

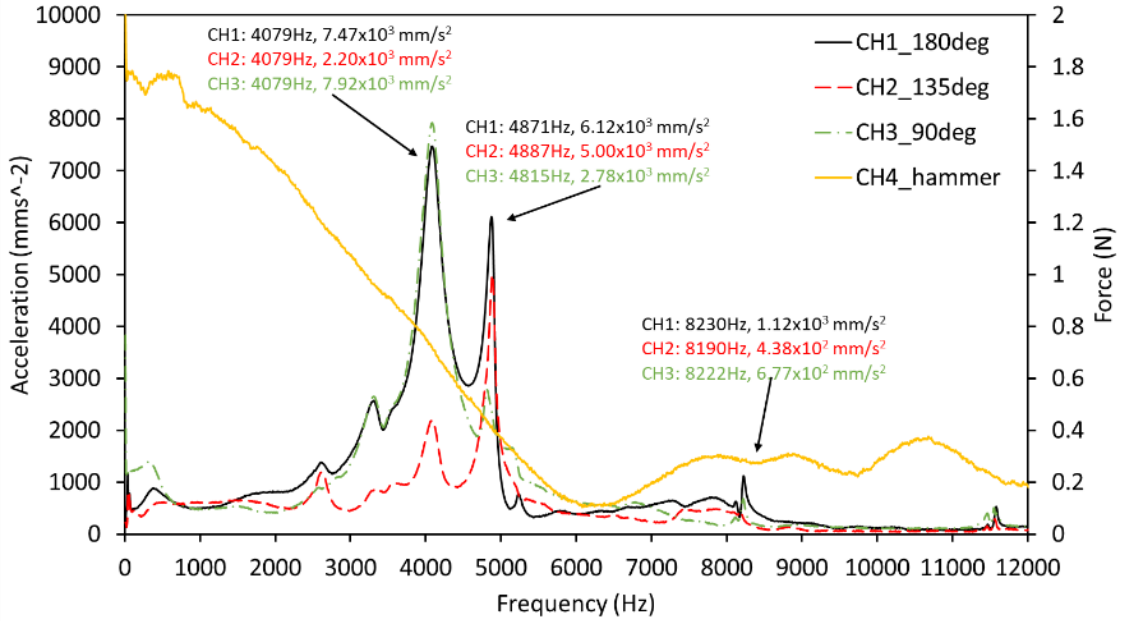

(b) Results of hammer test on frame with both end caps attached using setup 2.

Fig. 4.3.14 Measured modal results for frame with both end caps attached.

The key modal frequencies and their associated amplitudes on the various sensors can be seen in Table 4.3.5.

Table 4.3.5 Results of impact test on frame with end plates attached.

	Channel1 (225°)		Channel2 (180°)		Channel3 (135°)	
Set 1	Frequency (Hz)	Maximum (mms^{-2})	Frequency (Hz)	Maximum (mms^{-2})	Frequency (Hz)	Maximum (mms^{-2})
	4079	2380	4095	6740	4079	2570
	4895	4540	4879	5690	4887	4450
	8206	970	8198	688	8198	638

	Channel1 (180°)		Channel2 (135°)		Channel3 (90°)	
	Frequency (Hz)	Maximum (mms^{-2})	Frequency (Hz)	Maximum (mms^{-2})	Frequency (Hz)	Maximum (mms^{-2})
Set 2	4079	7470	4079	2200	4079	7920
	4871	6120	4887	5000	4815	2780
	8230	1120	8190	438	8222	677
	11581	497	11565	291	11549	506

This test suffered the same concerns as the previous in terms of difficulty of getting good, strong, and consistent strikes. Adding the front and rear plates acts to turn the structure from a hollow tube to a cylinder reflected, stiffening the structure which is reflected in the higher peaks and the higher frequencies of circumferential modes 2 and 3 which have both shifted around 300Hz each from 3627Hz to 4097Hz in the case of mode 2 and ~7900 to 8200Hz in for mode 3. A peak is observed at around 11581 Hz in setup 2, potentially highlighting mode 4 however the amplitude is small.

From the results there is clearly a mode at around 4850Hz. This appears to be similar to the 5200Hz mode observed in the previous case. The addition of the front plate means the radial stiffness front of the assembly is much higher, but the large increase in mass due to the front face plate being attached to the thin front of the frame with no coolant shell has changed the dynamic. An impact around the mid-point of the assembly would cause the relatively unconstrained extra mass to move in such a manner as to induce an axial mode, likely an axial mode 2 or perhaps some mode with the front plate inducing a response.

4.3.5.1 Frequency response function for the front and rear plates attachment

The frequency response function for this case is calculated and shown in Fig. 4.3.15.

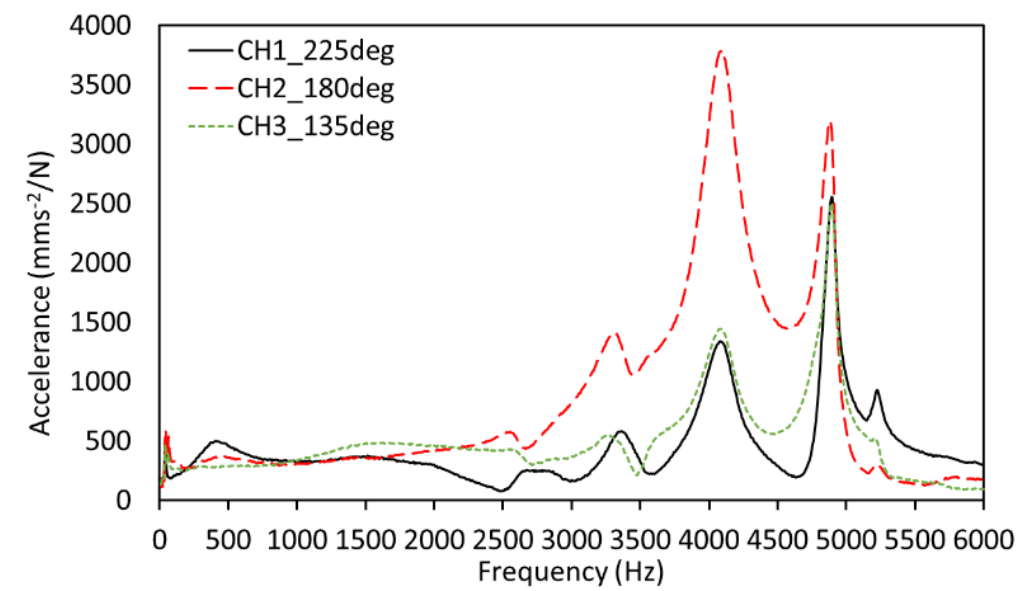

(a) Accelerance of channels 1 to 3 (225° to 135°) of setup 1

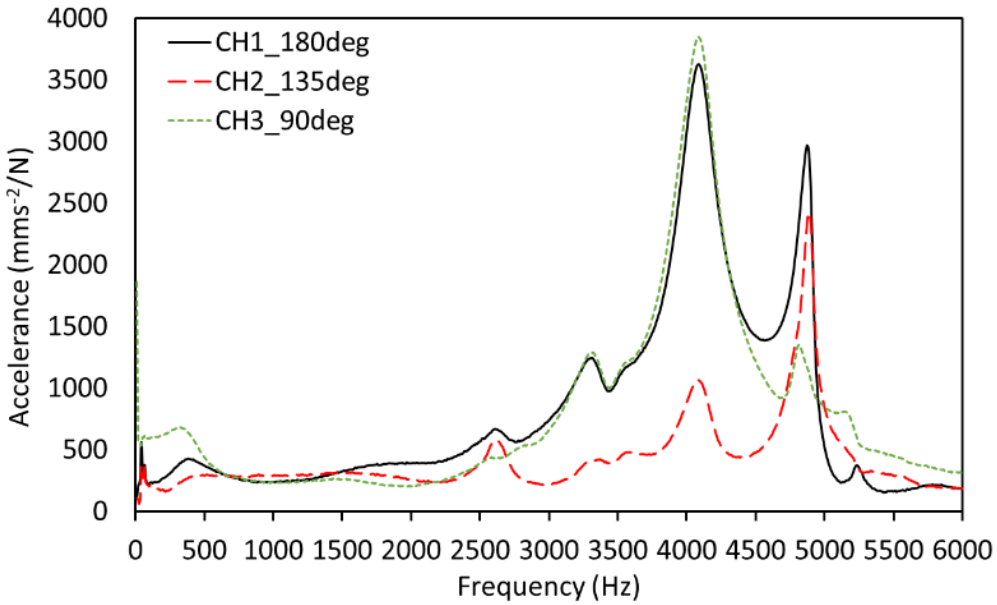

(b) Accelerance of channels 1 to 3 (180 °to 90°) of setup 2.

Fig. 4.3.15 Frequency response function for the front and rear plate attachment to the frame.

The increased stiffness is reflected in the higher frequency and, shaper peaks of the modes and the increase of the cut off frequency of the hammer response up to 6kHz. The modes previously discussed are much cleaner than in the case with only the rear plate attached.

4.3.6 Full machine, no rotor

The final test off rig is the full assembly. For this test, the front plate is removed, the 'O' rings are installed, and the coolant shell affixed. There are 2 tests that will be undertaken:

1. Fully assembled casing with NO rotor installed.
2. Fully assembled casing WITH rotor installed.

For test 1 the front plate is simply screwed back into place at the set torque and the hammer test repeated using the standard setup which is shown in Fig. 4.3.16.



(a) Fully assembled machine under test

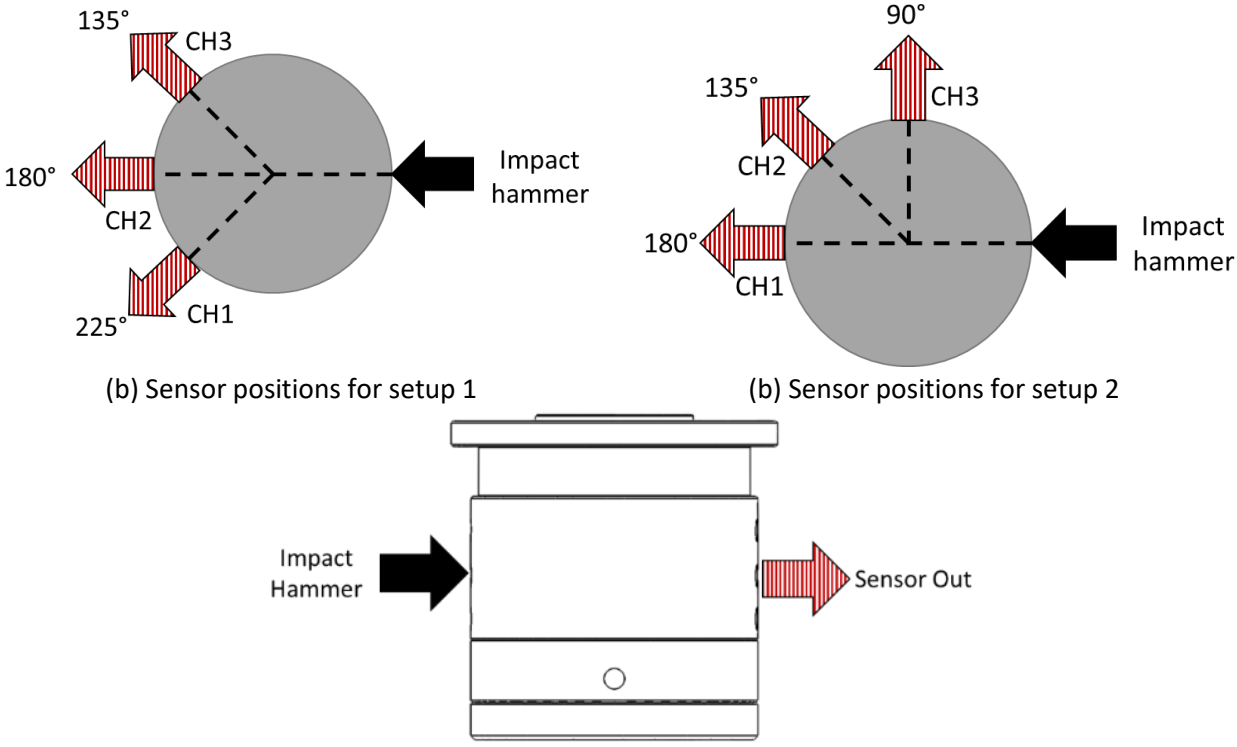

(b) Sensor positions for setup 1

(b) Sensor positions for setup 2

(c) Axial position of strike

Fig. 4.3.16 Full machine hammer test set up.

The impact results are shown in Fig. 4.3.17 and Table 4.3.6.

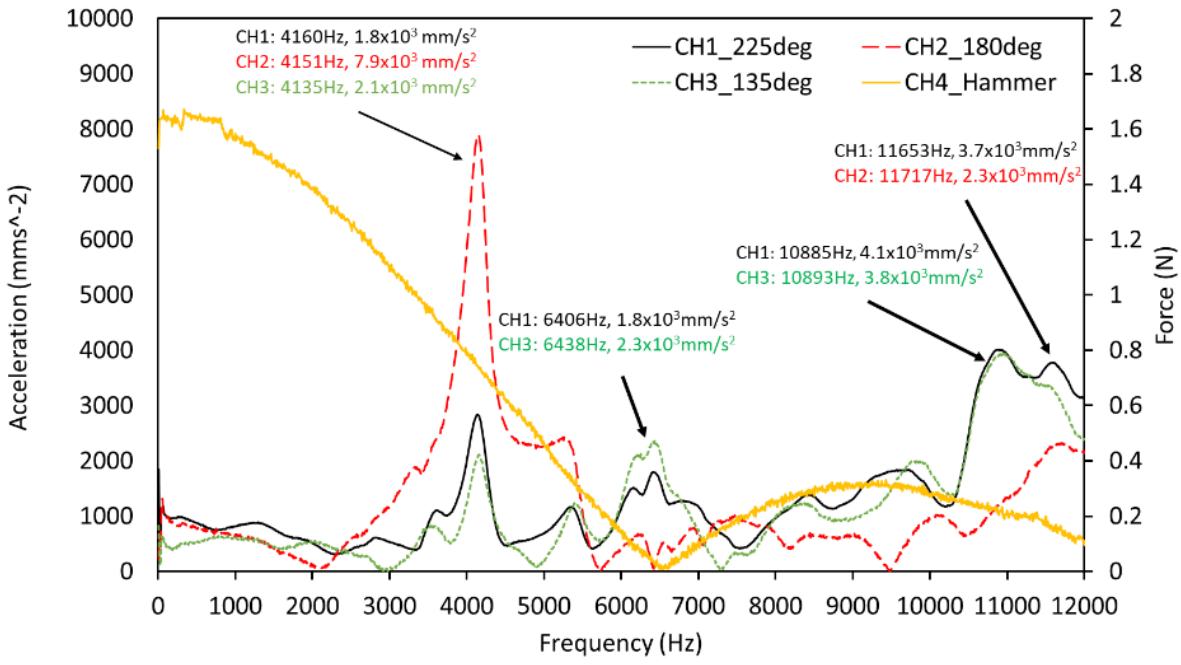

(a) Setup 1 impact results on the full machine assembly with no rotor installed.

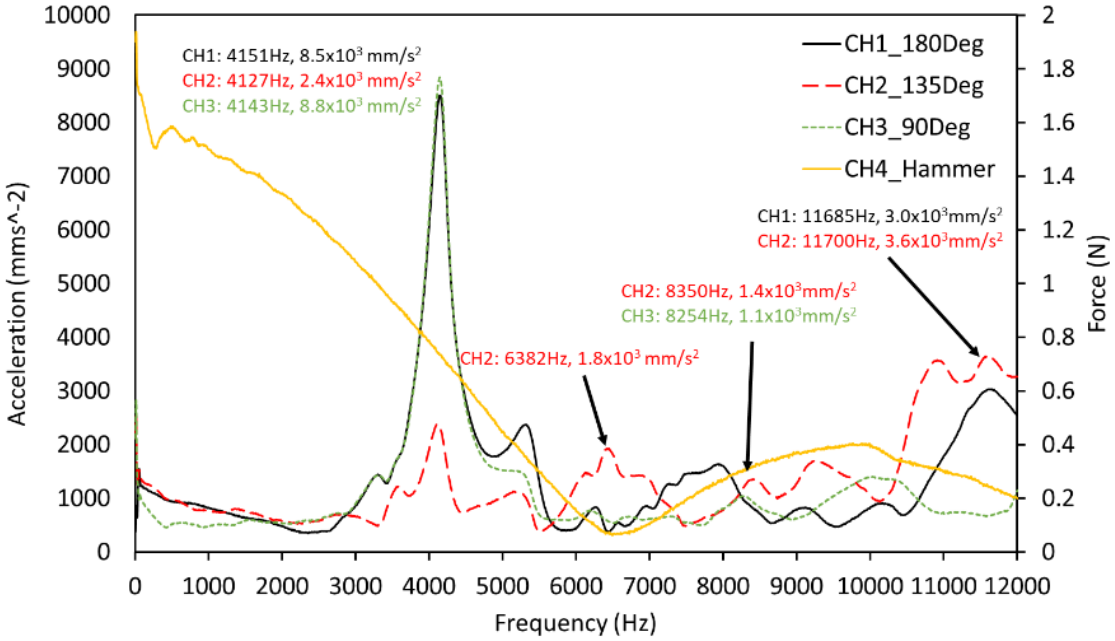

(b) Setup 2 impact results on the full machine assembly with no rotor installed.
Fig. 4.3.17 Impact results on the full machine with no rotor.

Table 4.3.6 Results of full machine hammer test with NO rotor.

	Channel1 (225°)		Channel2 (180°)		Channel3 (135°)	
Set 1	Frequency (Hz)	Maximum (mms^{-2})	Frequency (Hz)	Maximum (mms^{-2})	Frequency (Hz)	Maximum (mms^{-2})
	4160	1800	4151	7906	4135	2079
	6406	1800	N/A	-	6438	2300
	10893	4100	N/A	-	10893	3800
	11653	3700	11717	2300	N/A	-
	Channel1 (180°)		Channel2 (135°)		Channel3 (90°)	
Set 2	Frequency (Hz)	Maximum (mms^{-2})	Frequency (Hz)	Maximum (mms^{-2})	Frequency (Hz)	Maximum (mms^{-2})
	4151	8504	4127	2378	4143	8834
	N/A	-	6382	1830	N/A	-
	N/A	-	8350	1380	8254	1058
	N/A	-	10909	3600	N/A	-
	11685	2969	11700	3633	N/A	-

The fitting of the coolant shell meant that many of the concerns with avoiding the ribs on the previous test were no longer there; the test was much more straight forwards. The ease of hitting a smooth cylinder was tempered by the amount of force required to generate a response from the part leading to a concern with overloading the force hammer transducer and the acceleration sensors giving non-linear behaviour. In addition, the force hammer maximum excitation frequency has dropped considerably from the 1st test on the coolant shell with the frequency response of the hammer dropping rapidly such that the noise surrounding any modes above around 6kHz is difficult to judge.

Despite the concerns, circumferential mode 2 can still be clearly seen and the frequency has shifted upwards by around 80Hz reflecting the influence of the coolant shell mounting on the stiffness of the structure and the increased mass of the machine. Both traces show a modal frequency at ~6400Hz at the sensor positioned at 135 degrees.

An apparent peak is consistent at ~10.9kHz at 135deg in both tests though the crest is poorly formed making the exact frequency difficult to determine. Similarly, a further peak is seen around 11.7kHz which would align with the mode 4 observed in the previous two tests. Once the mechanical FE model has been established the FE should be able to confirm these modes.

4.3.6.1 Frequency response function for the full machine with no rotor

Fig. 4.3.18 shows the derived accelerance for the fully assemble machine with no rotor installed.

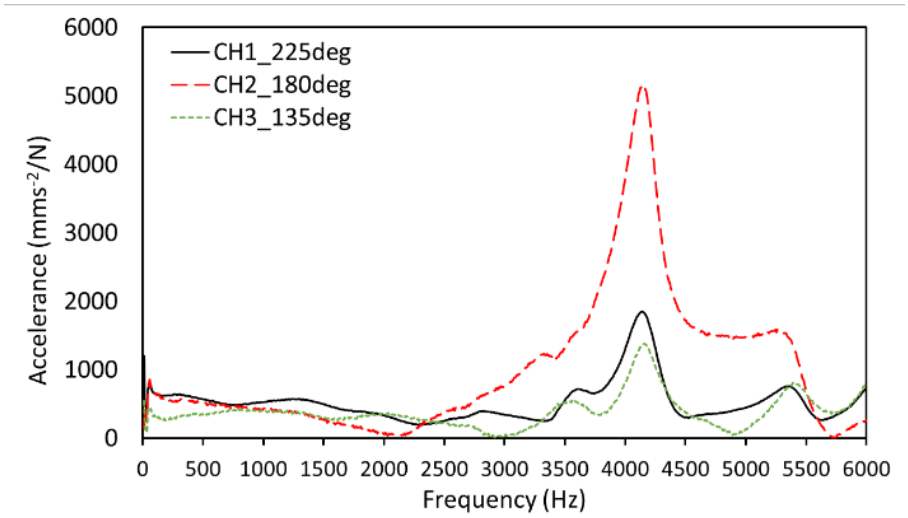

(a) Accelerance of channels 1 to 3 (225° to 135°) of setup 1.

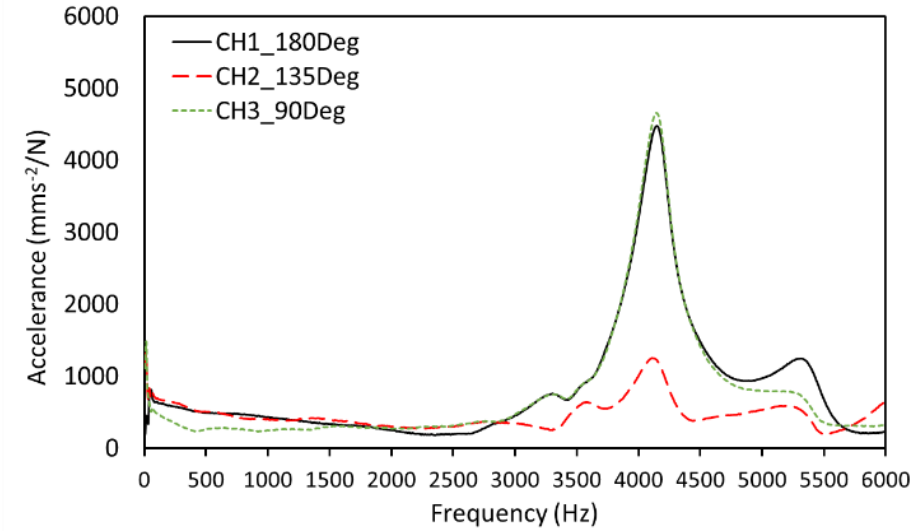

(b) Accelerance of channels 1 to 3 (180 °to 90°) of setup 2.

Fig. 4.3.18 Frequency response function for the full assembly with no rotor.

The addition of the coolant casing has changed the dynamics of the structure allowing for a 6kHz bandwidth from the hammer and much smoother waveform than the previous 3 cases. The addition of the casing has

adjusted the structure, so the mode observed a 4900 Hz has disappeared leaving only the mode 2 within the excitation bandwidth.

4.3.7 Full machine assembly with rotor installed.

With a baseline set for the machine with no rotor the 2nd and final off-rig test requires that the rotor be installed, as illustrated in Fig. 4.3.19.

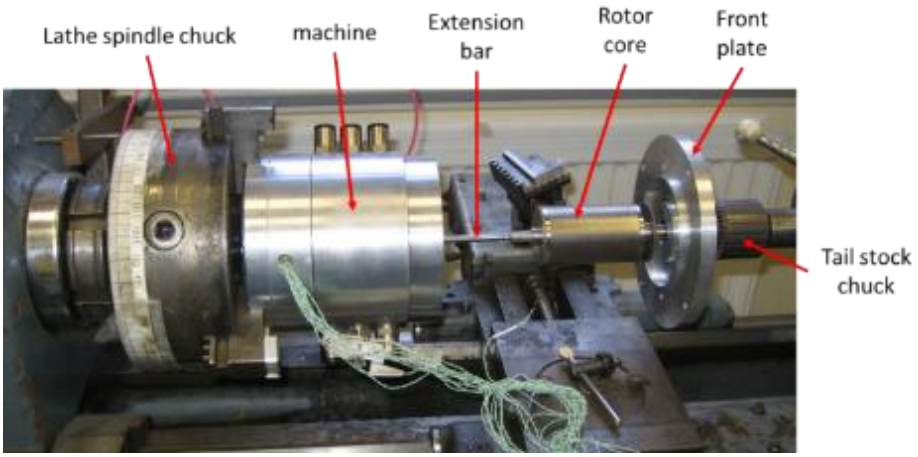

Fig. 4.3.19 Insertion of the rotor using a lathe.

The rotor is inserted using a lathe, with the stator placed in the chuck on the spindle and the rotor held by the tail stock. Using the lathe ensures good concentricity and alignment during the insertion process. The rotor is then carefully inserted into the stator assembly by sliding the tail stock towards the spindle, with a small extension bar at the rear of the rotor shaft engaging with the rear bearing to keep the rotor core concentric to the stator bore. This method counters the high magnetic forces between the PMs in the rotor and the stator preventing the cores coming into contact during the insertion and damaging the machine. When the rotor is fully engaged in the rear bearing the screws on the front plate are re-attached, set to the target torque and the full machine carefully removed from the spindle. A ‘C’ clip is used to secure the rotor shaft axially to the rear bearing and the rear stub shaft is removed, to allow the encoder to be attached later. Given that the machine now has a rotor shaft protruding from both axial ends of the assembly the support method is adjusted to allow the shaft to pass through the supporting material such that the main contact area has the same characteristics as the previous steps. With the machine ready the testing is repeated, and the results are shown in Fig. 4.3.20 and Table 4.3.7.

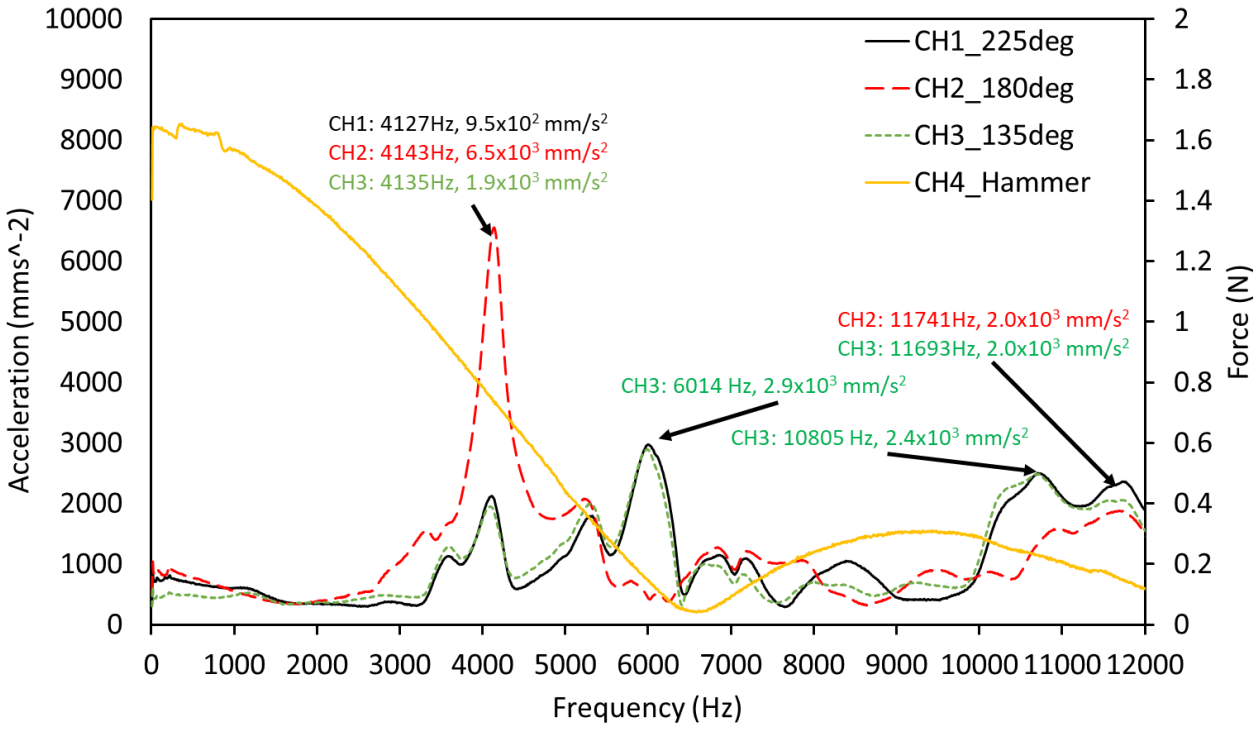

(a) Results of setup 1 impact test with full machine WITH rotor installed.

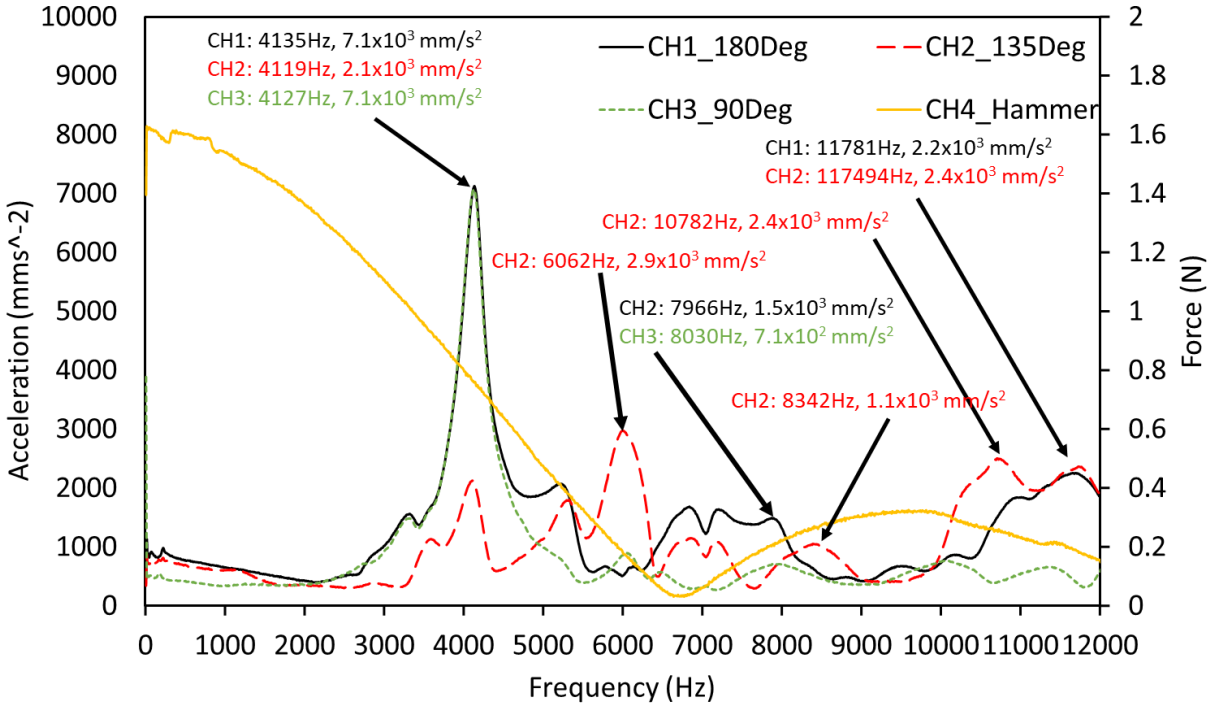

(b) Results of setup 2 impact test with full machine WITH rotor installed.

Fig. 4.3.20 Impact results on the full machine with the rotor.

Table 4.3.7 Results of full machine hammer test with rotor

	Channel1 (225°)		Channel2 (180°)		Channel3 (135°)	
Set 1	Frequency (Hz)	Maximum (mms^{-2})	Frequency (Hz)	Maximum (mms^{-2})	Frequency (Hz)	Maximum (mms^{-2})
	4160	950	4143	6553	4135	1921
	5382	4935	N/A	-	N/A	-
					6020	2887
					10805	2445
			11741	2031	11693	2046
	Channel1 (180°)		Channel2 (135°)		Channel3 (90°)	
Set 2	Frequency (Hz)	Maximum (mms^{-2})	Frequency (Hz)	Maximum (mms^{-2})	Frequency (Hz)	Maximum (mms^{-2})
	4135	7125	4119	2116	4127	7069
			6062	2864		
	7966	1500	8342	1062	8030	710
			10782	2454		
	11781	2190	11749	2391		

For this test, the strike force was much better controlled giving less distortion on the lower frequencies of the hammer and a smoother force curve.

Taking measurement error due to the fact the machine had to be taken apart and reassembled to install the rotor into consideration the results align very well with the test with no rotor installed, indicating that in the case of this machine the rotor has little influence on the overall modal performance of the machine. The only slight difference between the two tests is the peak seen at ~6kHz at 135 degrees. This has reduced by around 5% from the previous test, perhaps due to slight differences in assembly of the front plate or more likely due to the influence of the rotor mass and stiffness on the overall structure which would make this frequency and axial mode.

4.3.7.1 Frequency response function for the machine with rotor installed

Fig. 4.3.21 shows the derived accelerance for the fully assembled machine with the rotor installed.

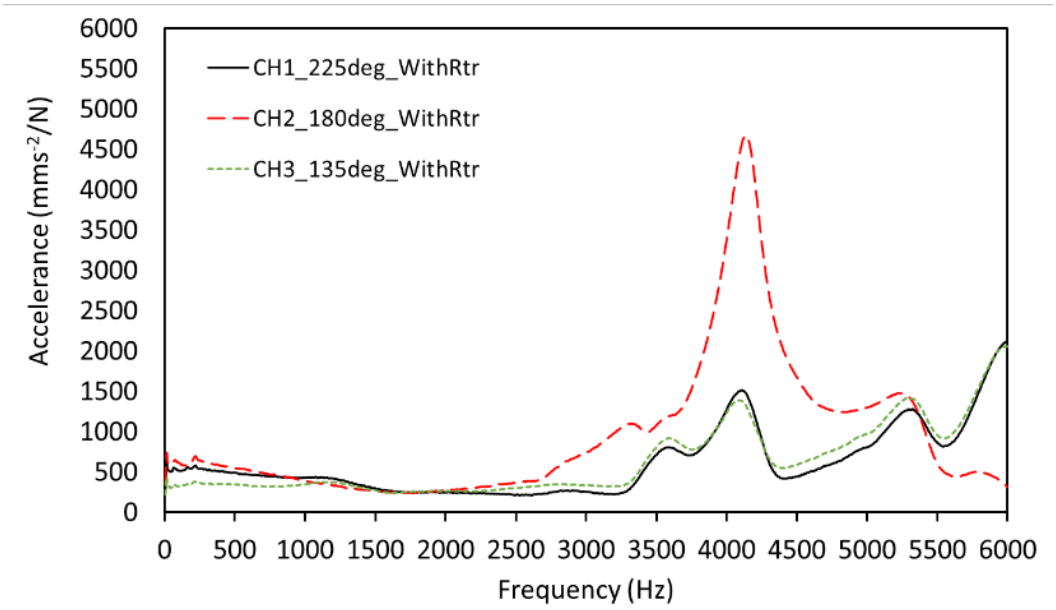

(a) Accelerance of channels 1 to 3 (225° to 135°) of setup 1.

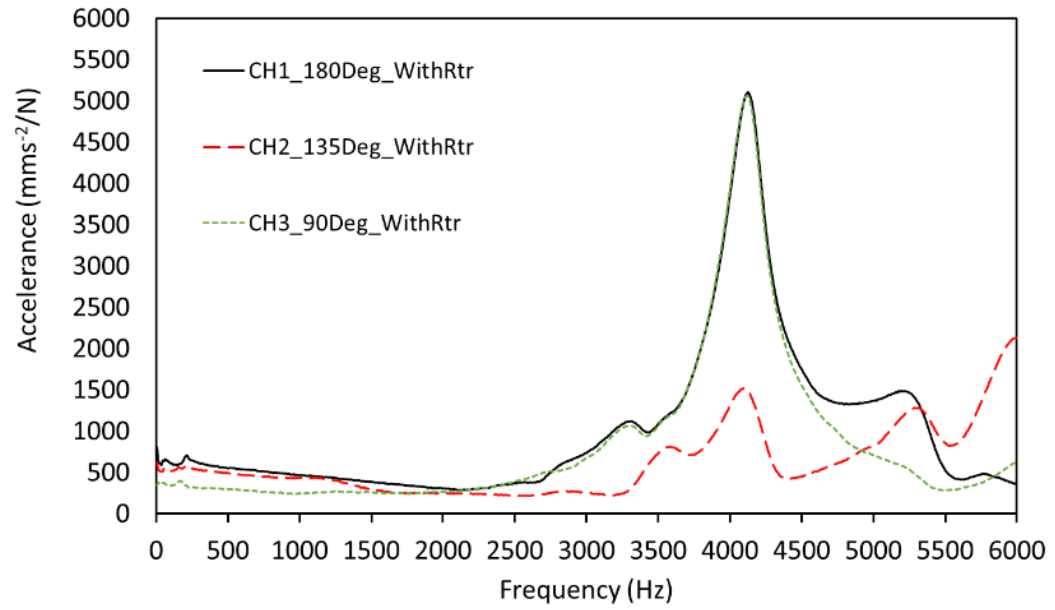

(b) Accelerance of channels 1 to 3 (180 °to 90°) of setup 2.

Fig. 4.3.21 Frequency response function for the full machine assembly with the rotor installed.

On inspection of the graphs in 4.321(a) and (b) it is very difficult to discern any difference between the mode 2,0 observed in the cases with and without. A direct comparison is drawn to try and better judge the impact of the rotor on the modal performance and is shown in Fig. 4.3.22.

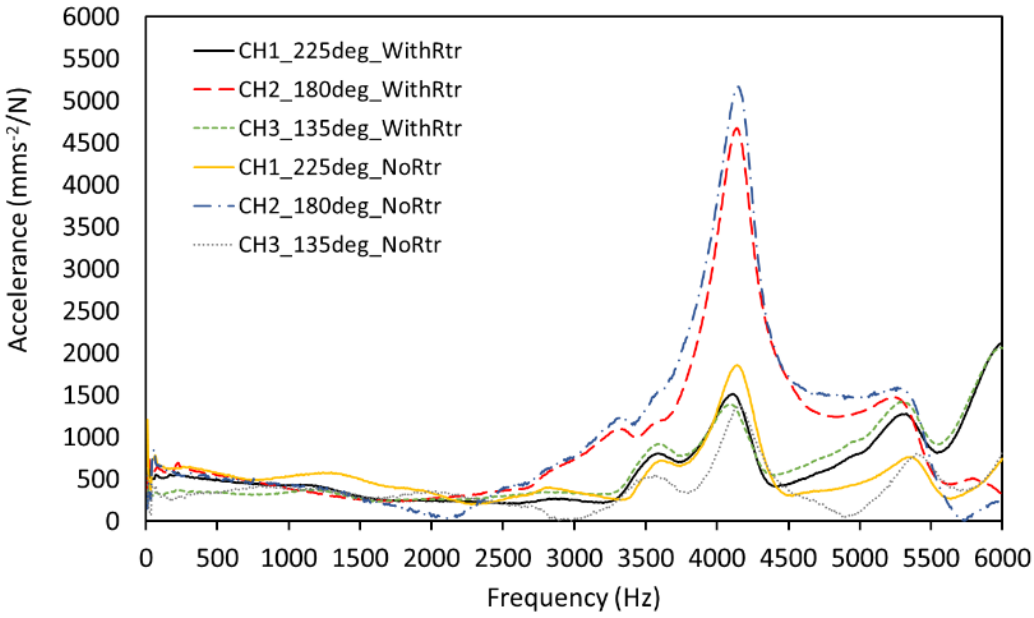

(a) Comparison of setup 1 with and without the rotor installed accelerance.

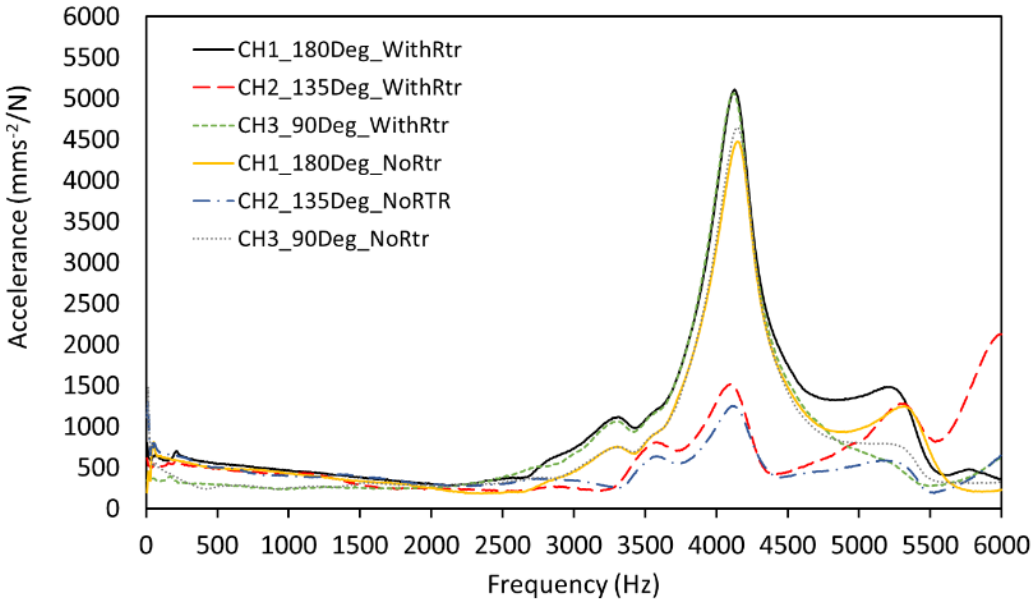

(b) Comparison of setup 1 with and without the rotor installed accelerance.

Fig. 4.3.22 Comparison of FRF for the full machine assembly with and without the rotor installed.

The comparison shows little to no changes in the mode 2 frequency between the test, as previously mentioned the sensors had to be stripped off and re-attached following the rotor insertion process so any variation is likely to be due to that. Similarly, there are differences in amplitude but again this is most likely test related as the average impact force recorded will differ from each test. From an FRF perspective it can therefore be judged that the rotor has no influence on the function within the excitation bandwidth of the hammer.

4.3.8 Machine mounted on dynamometer rig

The machine is now moved to the machine dynamic testing chamber and mounted to the support bracket that aligns the machine to the output shaft of the dynamometer. There are 2 conditions tested here:

1. Machine attached to the support bracket only.
2. Machine linked to the Dynamometer, encoder attached, and coolant system filled.

In the first test the machine is bolted to the mounting bracket and the hammer test is undertaken. This allows the influence of the new mounting position to be observed. Following this the machine is linked to the dynamometer via a coupling, the encoder is attached and clamped to the rear shaft from the rotor and finally the coolant lines are installed, and the system filled. The procedure and setup for both hammer tests is very similar to the previous tests.

4.3.8.1 Machine mounted to rig only

The machine is setup as shown in Fig. 4.3.23 and the hammer test is repeated.

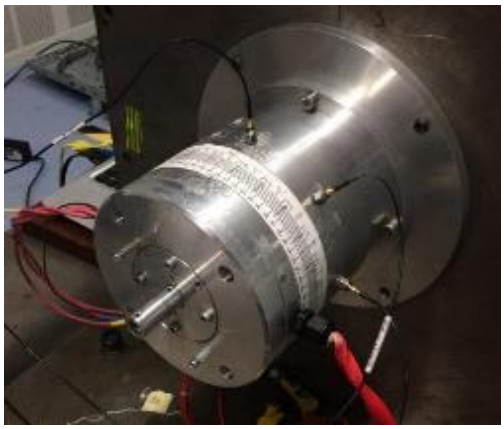

(a) machine mounted to rig (sensor setup 2).

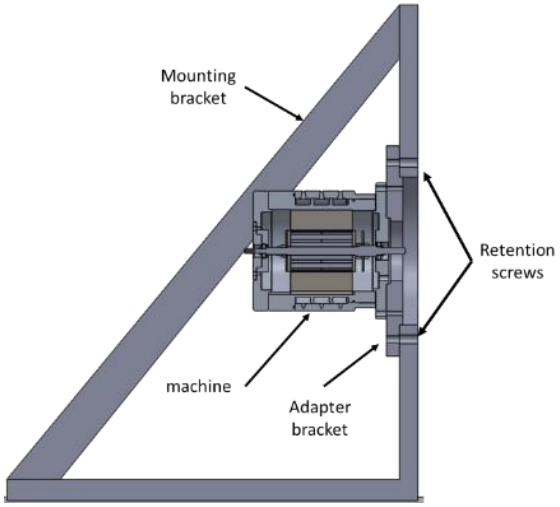

(b) Mounting condition.

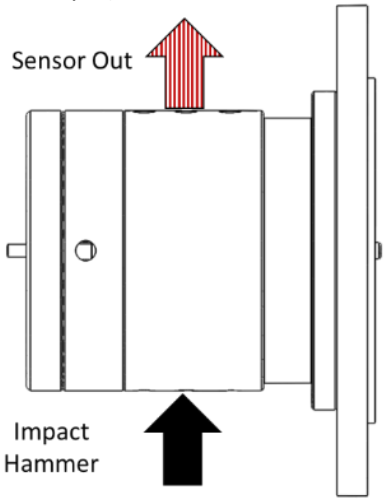

(c) Axial position of strike.

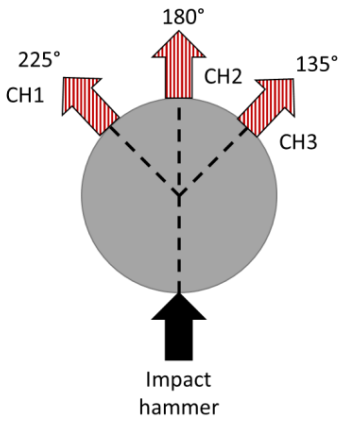

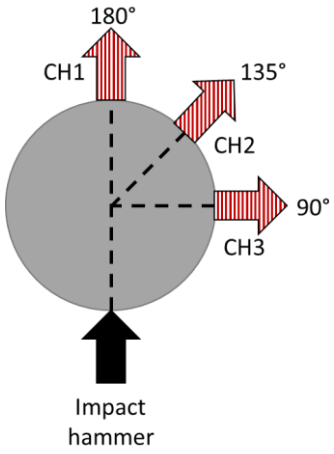

(d) Sensor positions for setup 1. (e) Sensor positions for setup 2.

Fig. 4.3.23 Setup of the hammer test on the rig only.

Aside from the obvious change in mounting condition it can be seen from Fig. 4.3.22 (c), (d) and (e) that the sensor and strike positions have changed in that the hammer is struck from below the motor. Initially the test was run such that the hammer struck from above, but the results typically contained a high number of distortions, typically from double strikes, and more critically, the acceleration sensors had a bad habit of falling off the motor during the test. Whether this was due to the room temperature or humidity in the test chamber influencing the bond of the wax or degradation in the wax material is unclear. Experimentation with different strike positions showed striking from the bottom mitigated much of the concerns. The cost of this setup is the sensors had to be re-arranged between the tests

The impact results are shown in Fig. 4.3.24 and the key frequencies and amplitudes in Table 4.3.8.

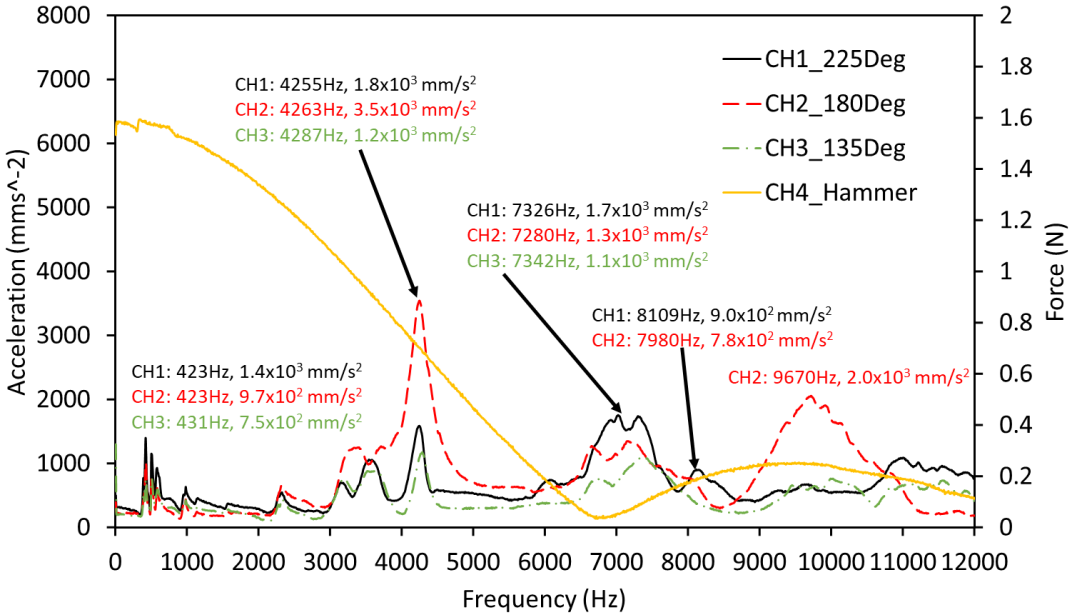

(a) Results of setup 1 impact hammer test on the mounted machine

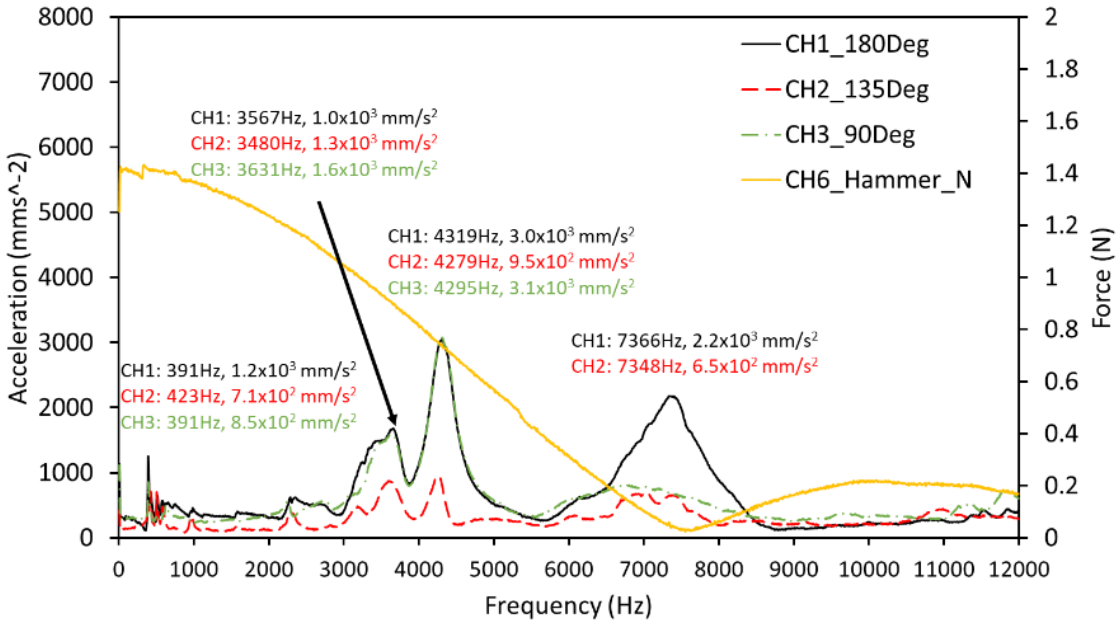

(b) Results of setup 2 impact hammer test on the mounted machine
Fig. 4.3.24 Impact for the full machine mounted to the rig only.

Table 4.3.8 Result summary of the machine mounted to the rig only

	Channel1 (225°)		Channel2 (180°)		Channel3 (135°)	
Set 1	Frequency (Hz)	Maximum (mms^{-2})	Frequency (Hz)	Maximum (mms^{-2})	Frequency (Hz)	Maximum (mms^{-2})
	423	1398	423	967	431	750
	3267	1034	3480	1251	3631	873
	4255	1751	4263	3502	4287	1173
	7326	1724	7280	1343	7342	1091
	8109	903	7980	783		
			9670	2028		
	Channel1 (180°)		Channel2 (135°)		Channel3 (90°)	
Set 2	Frequency (Hz)	Maximum (mms^{-2})	Frequency (Hz)	Maximum (mms^{-2})	Frequency (Hz)	Maximum (mms^{-2})
	391	1251	423	712	391	846
	3663	1673	3623	860	3663	1605
	4319	2997	4279	950	4295	3068
	7366	2173	7348	647		

The first observation from the test is the response is quite weak, a large impulse was required to sufficiently excite the structure leading to many repeat tests due to overloading either the hammer force transducer or the acceleration sensors. A distinction from the previous tests is the appearance of a low frequency peak at around 420Hz, a significantly lower frequency than anything observed to this point. It is consistency in all the testing and the clear amplitude mean it is unlikely to be noise, also all components are tightly fastened to the rig, so it is highly unlikely to be a rigid mode. Given how low the frequency is it is unlikely to be from the stator or frame as measured to this point which leaves either some aspect of the test rig being excited or

some previously unseen mode of the rotor. The shift in position from vertical to horizontal plus the change in mounting condition means there is some chance a rotor mode is being excited.

Mode 2 is clear and dominant in both setups, and the amplitude is lower than pervious tests and the slightly higher frequency (increase of around 100Hz) indicting that the new mounting position has adjusted the stiffness of the structure very slightly. A low amplitude peak is shown at around 3500Hz. However, its prominence is low, only being clear in the 2nd setup. Given the low amplitude of the highest peak (4.3kHz) it is difficult to determine whether the peak is a mode or background noise. The matched FE model later may shed some light on this. Beyond 6kHz the signal is very noisy, a relatively high peak is observed at around 7.3kHz. A peak is also observed at 9.7kHz on channel 2 in the 1st run.

4.3.8.2 Frequency response function for the rig mounted only condition

In line with the previous setups the FRF is calculated and shown in Fig. 4.3.25.

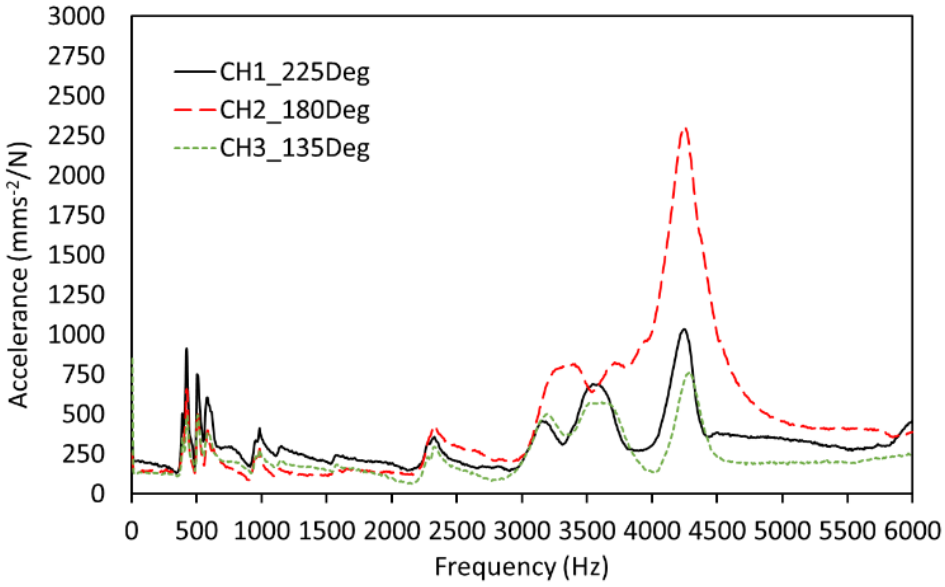

(a) Accelerance of channels 1 to 3 (225° to 135°) of setup 1

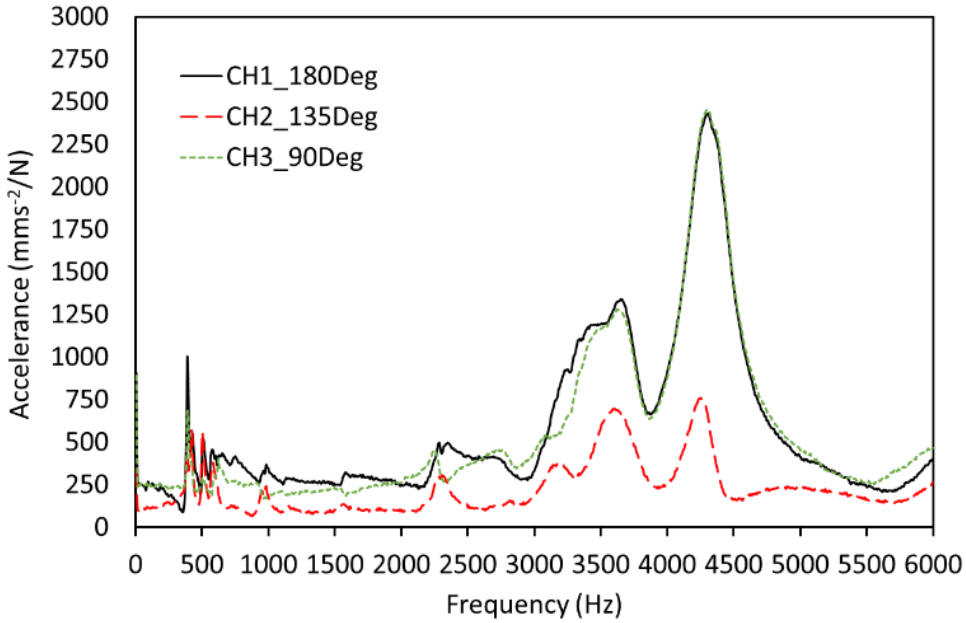

(b) Accelerance of channels 1 to 3 (180 °to 90°) of setup 2

Fig. 4.3.25 Frequency response function for the machine mounted to the dynamometer bracket only

The muted response in the acceleration data is of course reflected in the accelerance. The circumferential mode 2 dominates but is so low on the 225° and 135° positions that it is difficult to discern the points over any noise in the system.

4.3.9 Fully dressed machine

The final test is the machine fully setup and ready for dynamic measurement. The output shaft is linked to the dynamometer drive line via a coupling, the encoder is mounted and clamped to the rear of the rotor shaft, coolant lines are inserted, and the coolant system is filled. Fig. 4.3.25 shows the machine setup.

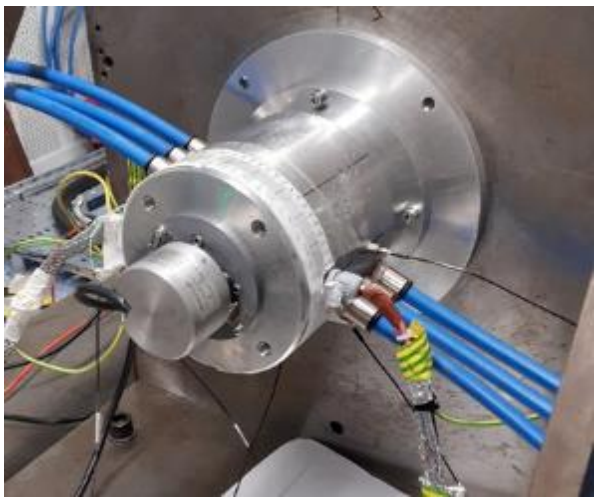

(a) Sensors being added to fully dressed and fluid filled machine

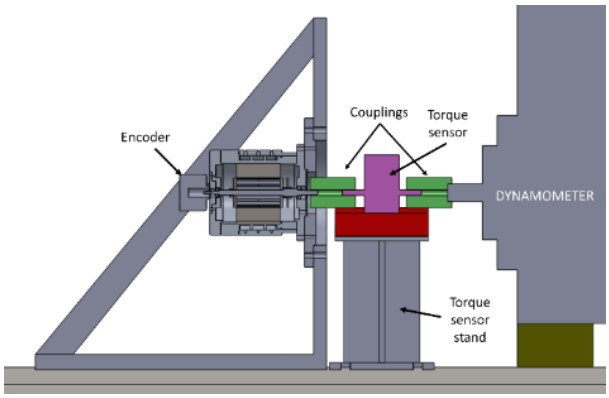

(b) Cross section of fully mounted condition highlighting the coupling to the dyno and the connection of the encoder to the rear of the machine.

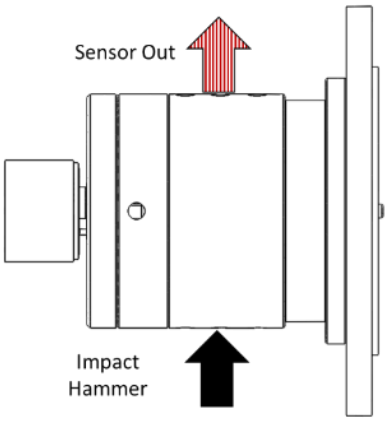

(b) Axial position of the strike.

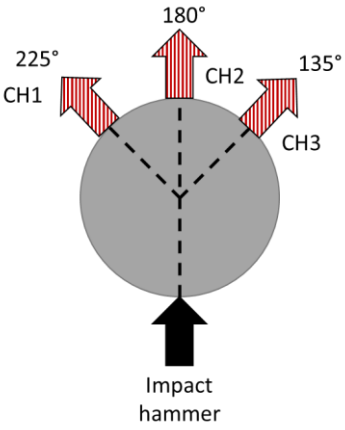

(c) Sensor layout for setup 1.

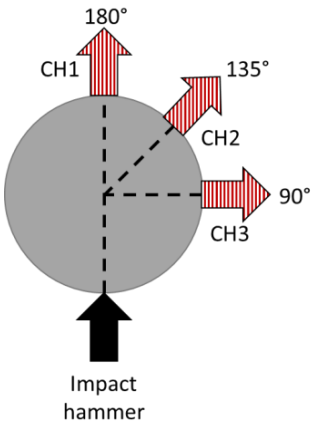

(d) Sensor layout for setup 2.

Fig. 4.3.26 Setup of the hammer test for the full machine.

The setup is identical to the previous tests. The results are shown in Fig. 4.3.26 and Table4.3.7.

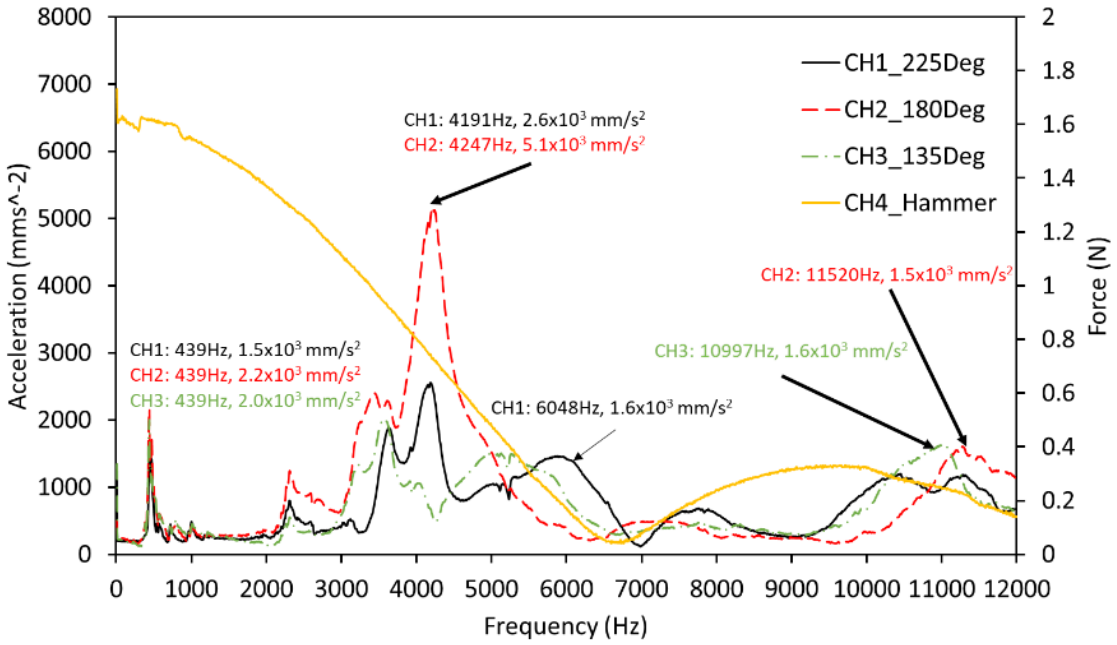

(a) Results of setup 1 impact hammer test on the full machine setup

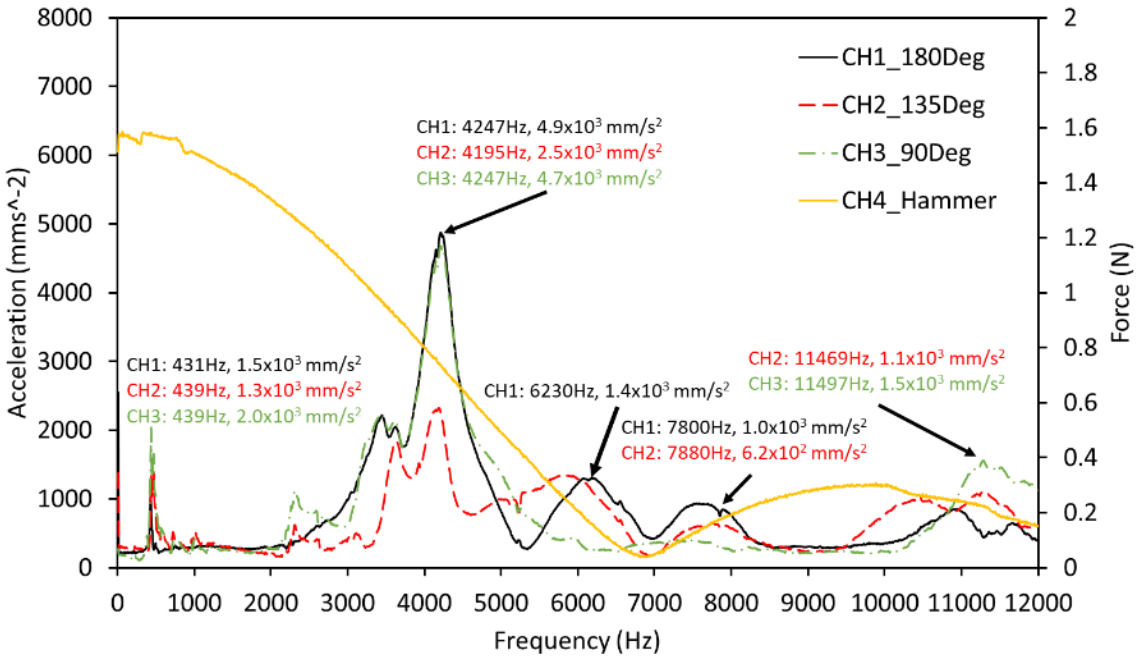

(b) Results of setup 2 impact hammer test on the full machine setup
Fig. 4.3.27 Impact for the full machine setup

Table 4.3.9 Result summary of the full machine setup

	Channel1 (225°)		Channel2 (180°)		Channel3 (135°)	
Set 1	Frequency (Hz)	Maximum (mms^{-2})	Frequency (Hz)	Maximum (mms^{-2})	Frequency (Hz)	Maximum (mms^{-2})
	431	1470	439	2154	439	1989
	3615	1873	3607	2269	3615	1916
	4191	2552	4247	5128	N/A	-
	6048	1600	N/A	-	N/A	-
	N/A	-	11520	1459	10997	1622
	Channel1 (180°)		Channel2 (135°)		Channel3 (90°)	
Set 2	Frequency (Hz)	Maximum (mms^{-2})	Frequency (Hz)	Maximum (mms^{-2})	Frequency (Hz)	Maximum (mms^{-2})
	439	1046	439	1330	439	2032
	4247	4875	4195	2314	4247	4679
	6230	1421	6100	1380	N/A	-
	7800	1012	7880	623	N/A	-
	N/A	-	11469	1075	11497	1550

The results of the fully filled machine show the circumferential mode 2 results have shifted slightly from the mounted only, by around 50Hz. This may be due to the additional mass from the coolant and encoder but could equally be due to the fact that between the mounted only and fully filled tests the acceleration sensors had to be removed to prevent damage during the process of linking the machine to the dynamometer and then remoted, the process of which could induce errors. In addition, applying the coolant to the machine dropped the surface temperature a few degrees making the wax a littler stiffer so perhaps a little less susceptible to background noise. The low frequency mode observed at ~420Hz has shifted slightly to ~440Hz,

the additional mass added to the machine plus the stiffness of the driveline due to the connection with the coupling would account for this. Beyond the mode 2 the waveforms appear more subdued than the mounted only condition reflecting the reduced noise apparent in the test. The results show some evidence of a modal frequency at around 10kHz and perhaps mode 4 around 11.4kHz which was alluded to in the un-mounted and mounted only conditions but similar to these results the frequencies are so far from the impact hammer response frequencies that the resultant waveshape and amplitudes make it difficult to give a precise judgment. The aligned FE model should shed more light on this.

4.3.9.1 Frequency response function for the final setup

The final frequency response is shown in Fig. 4.3.28.

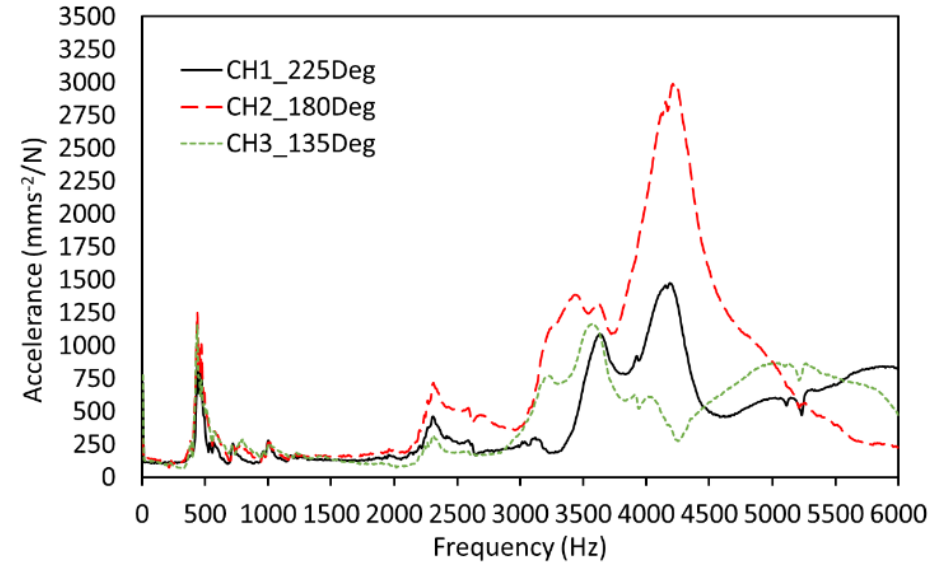

(a) Accelerance of channels 1 to 3 (225° to 135°) of setup 1.

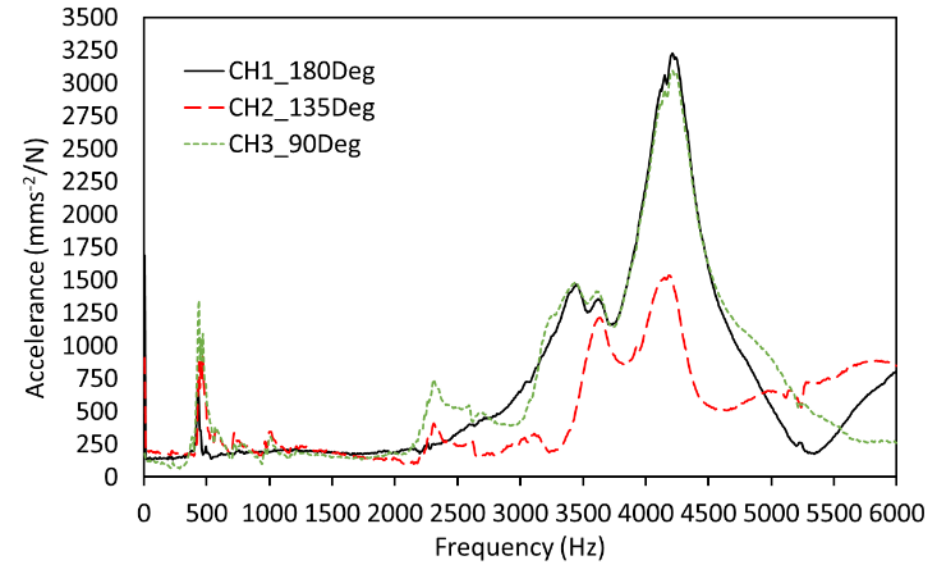

(a) Accelerance of channels 1 to 3 (180 °to 90°) of setup 2.

Fig. 4.3.28 Frequency response function for the final machine setup.

The response of the machine is much sharper in this final impact test compared to the mounted only condition. Mode 2 is much clearer on all channels and the small shoulder frequency at ~3500Hz is till apparent but much its prominence is greatly reduced compared to the previous case. Given the complexity of the setup and the fact the excitation band of the impact hammer is reaching its limit the results are OK.

4.4 Summary

The build-up of the complexity of the machine has highlighted the nature of the hammer test on complex structures. The stator core and coolant shell tests were very straight forward and showed clear results making interpretation of the data easy, a light tap of the hammer was enough to generate clear peaks for each mode. As the complexity of the assembly increased the difficulty of establishing the modes increased. Initially the main problem was mis-strikes due to the need to strike between the ribs of the coolant ducts in the machine but as the end plates and later the full coolant shell was added the concern became striking with enough force to sufficiently excite the structure without saturating either the force transducer or the acceleration sensors.

Despite the concerns there are some clear trends from the data a comparison of the different circumferential modes is provided in Fig. 4.3.28 and all values are shown in Table 4.3.10.

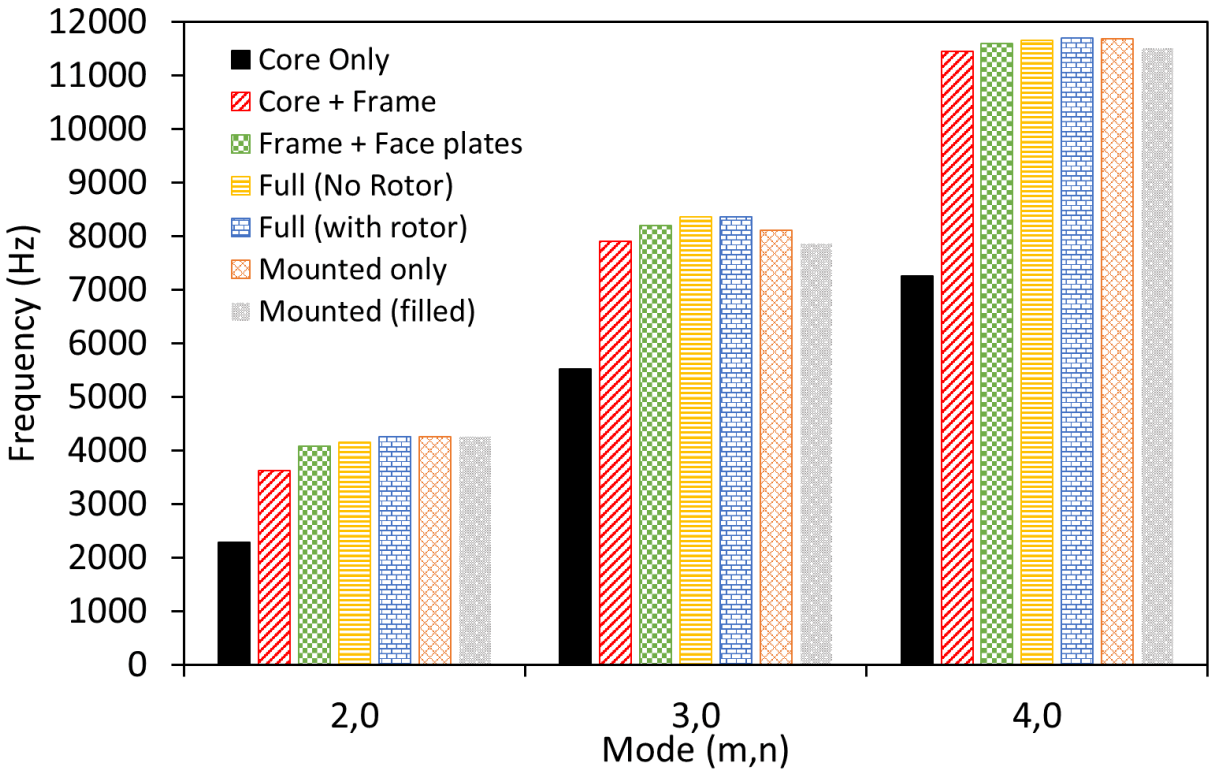

Fig. 4.3.28 Comparison of circumferential modes for each assembly stage of the baseline machine.

Table 4.3.10 comparison of circumferential modal frequencies for each stage of assembly for the baseline machine

Mode	Core Only	Core + Frame	Frame + Face plates	Full (No Rotor)	Full (with rotor)	Mounted only	Mounted (filled)
2,0	2279	3627	4079	4151	4255	4247	4247
3,0	5519	7899	8198	8350	8360	8100	7850
4,0	7254	11450	11589	11650	11700	11685	11500

The results in Fig. 4.3.28 show the move from a bare stator core to case with the wound core heat shrunk in the frame is very large across all modes. The larger step up is indicative of the increased stiffness provided by the casing and the influence of the windings on the overall structure. For the rest of the points there are some variations, adding the face plates further increases the stiffness of the part, having the largest influence on modes 2 and 3.

The addition of the coolant shell shows a small increase in the measured modal frequencies. In terms of the circumferential modes the addition of the rotor shows very little influence on the circumferential modes.

Finally, mounting the machine sees the constraints of the machine move and a slight shift in the modal frequencies, the mode 2 increases by around 100Hz whereas the mode 3 and mode 4 are less influenced. The mounted condition also shows additional around the 7kHz mark, indicating a potential secondary mode 2 or similar however given the low prominence of the peaks past 6kHz it is difficult to judge precise frequencies. The FE analysis, assuming it is correctly aligned to the identified modes should help identify any missing modes, albeit with some error attached.

5 Development of mechanical finite element model of baseline machine

5.1 Introducing the 3D machine model

Following the experiments on the baseline machine the task of developing a mechanical finite element model to represent the machine is the next step. To achieve this the mechanical FE tool ANSYS® workbench will be utilised. 3D modelling was achieved using Solidworks as the 3D assemblies were previously developed using this tool and the ANSYS® tool has excellent integration with Solidworks allowing seamless importing of the model geometry and parameters. During the experimentation, the complexity was slowly increased by assembling the machine assembly in stages in order to aid the development of the 3D model. The model geometry for each stage is shown in Fig. 5.1.1.

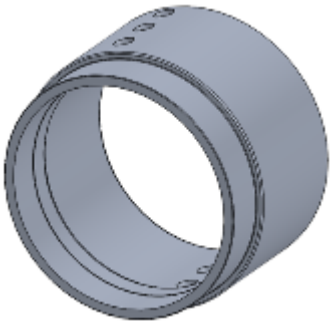

(a) Coolant shell only.

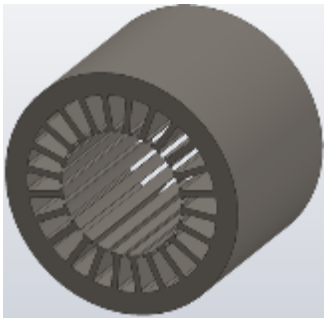

(b) Stator only.

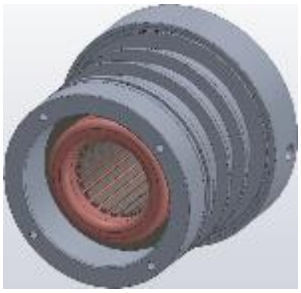

(c) Wound stator in frame.

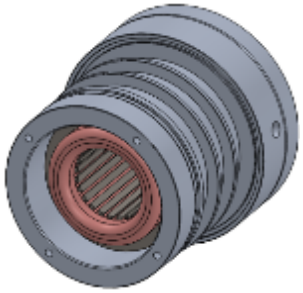

(d) Rear end plate attached.

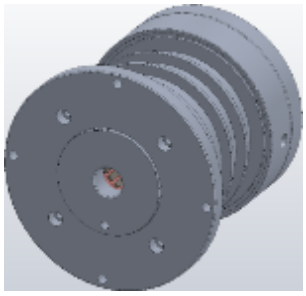

(e) Front and rear end plates attached, no Shell.

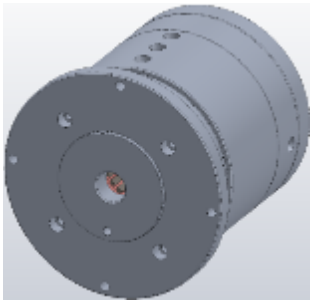

(f) Full machine assembly.

Fig. 5.1.1 3D models of the baseline machine structure at increasing levels of assembly.

As was highlighted in the development of the electromagnetic model getting the material data correct is essential in ensuring high accuracy of the FE model so this forms the first step in the development of the model.

5.1.1 Defining the materials

The FE solver uses (5.1) in order to solve each step within the calculation [JG06].

$$[M]\{\ddot{q}\} + [C]\{\dot{q}\} + [K]\{q\} = \{F(t)\} \tag{5.1}$$

where q is a vector (N,1) expressing the displacement of N degrees of freedom, {F(t)} is the force vector applying to the degrees of freedom, [M] is a mass matrix, [C] is the damping matrix and [K] is the stiffness matrix. It bears a strong resemblance to (1.6) introduced for the simple spring-mass damper system introduced in chapter 1 but encompasses N degrees of freedom, rather than the single degree of freedom on the simple example.

The accuracy of the model is therefore dependant on the key mechanical attributes of the part, namely the Young's modulus, density, and Poisson ratio of the component. Within the machine the case structure is the most straight forward part as casing is formed of aluminium and is isotropic, so the material properties apply in all directions and planes. The specification of the aluminium used is shown in Table 5.1.1 [MW18].

Table 5.1.1 Case material properties [MW18].

Item	Value	Units
Material	A6061-T4	
Density	2700	kg/m^3
Young's modulus	68.9	GPa
Bulk modulus	67.6	GPa
Shear modulus	25.9	GPa
Poisson's Ratio	0.33	-

For the stator laminations and windings, they are less straight forward as both these materials are non-homogenous so as such require further work to characterise. Before the challenging task of deriving these material properties the casing material specifications in Table 5.1.1 means that the first set of modal analysis can be undertaken using the coolant shell to verify the shape and material properties match those of the actual machine. It also provides a simple shape to set out a standard process of aligning each stage of the model to the test data.

5.1.1.1 Modal analysis of the coolant shell

Two models were made and meshed with the ANSYS® modal analysis tool, the meshed models are shown in Fig. 5.1.2

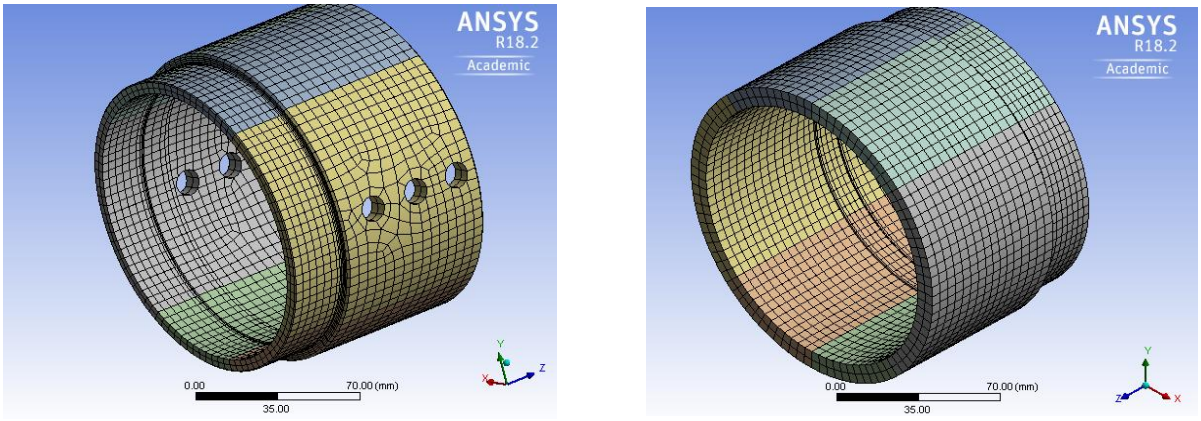

(a) Complex model with coolant inlet holes. (b) Simple mode – holes removed.

Fig. 5.1.2 Coolant shell models for modal analysis.

The differences between the two models lie in their complexity: the first shape (Fig. 5.1.2(a)) is directly from the mechanical drawing of the shape so includes the mounting points for the coolant inlets and all the chamfers and fillets required to ensure a smooth fit and finish the part. The 2nd shape (Fig. 5.1.2(b)) has the same overall profile but the features such as the coolant holes and fillets etc. are removed. This yields a much neater mesh; however, it potentially lowers the accuracy of the part so a comparison can be made by running the two models and comparing with the measured data. In both models a frictionless support type is applied to the back of the model to represent the constraint applied by the part being sat on the test bench.

Fig. 5.1.3 shows the mode shape results of the complex model and Fig. 5.1.4 shows the mode shape results of the simplified model.

ISO X-Y cross section Z-Y cross section

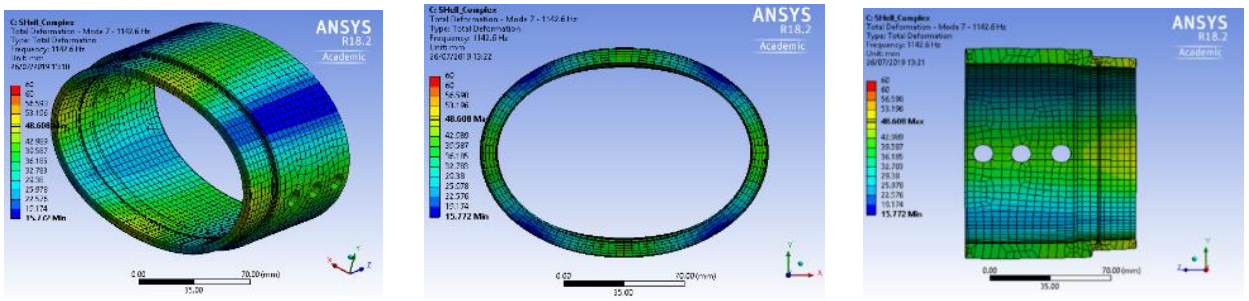

(a) Complex shape, mode (2,0) @ 1142.6Hz

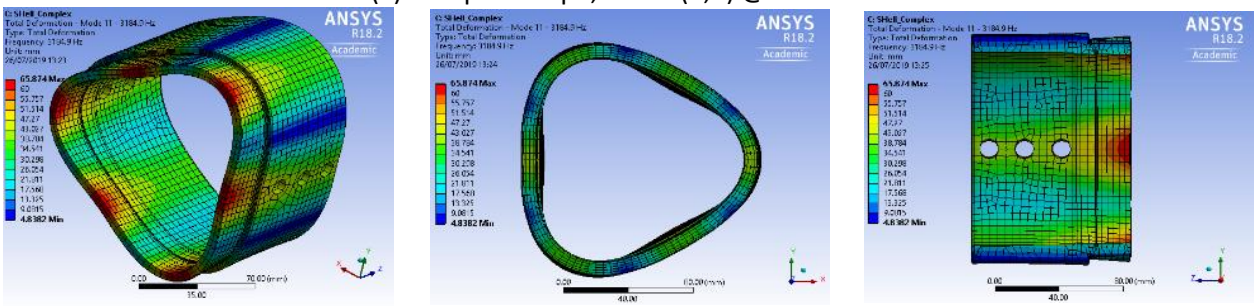

(b) Complex shape, mode (3,0) @ 3184.9 Hz

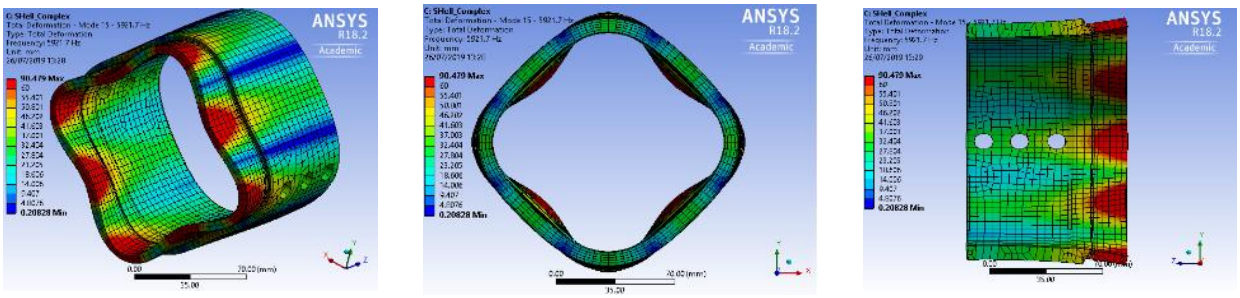

(c) Complex shape, mode (4,0) @ 5927Hz

Fig. 5.1.3 Circumferential modes 2 to 4 results for complex coolant shell shape.

ISO X-Y Cross section Y-Z Cross section

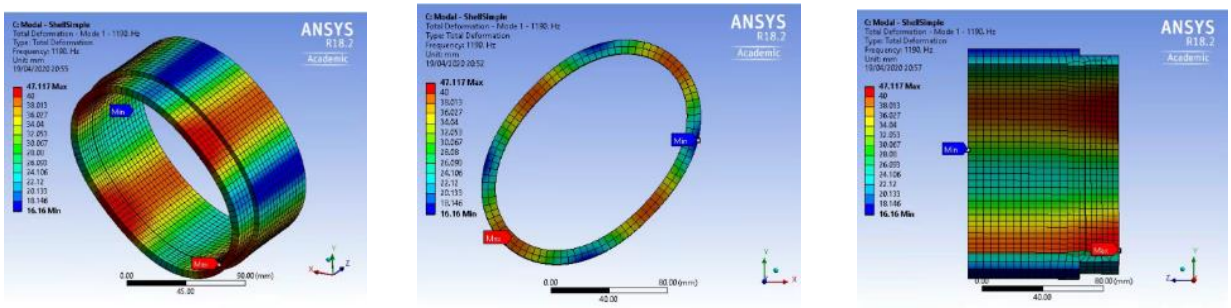

(a) Simple shape, mode (2,0) @ 1190Hz

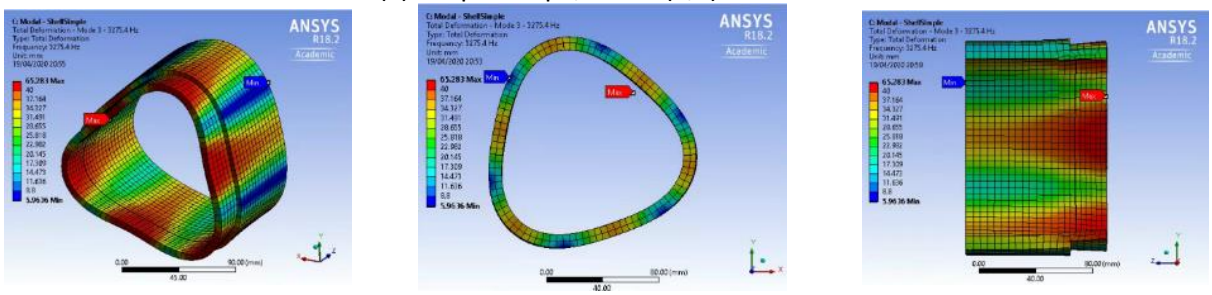

(b) Simple shape, mode (3,0) @ 3275.1Hz

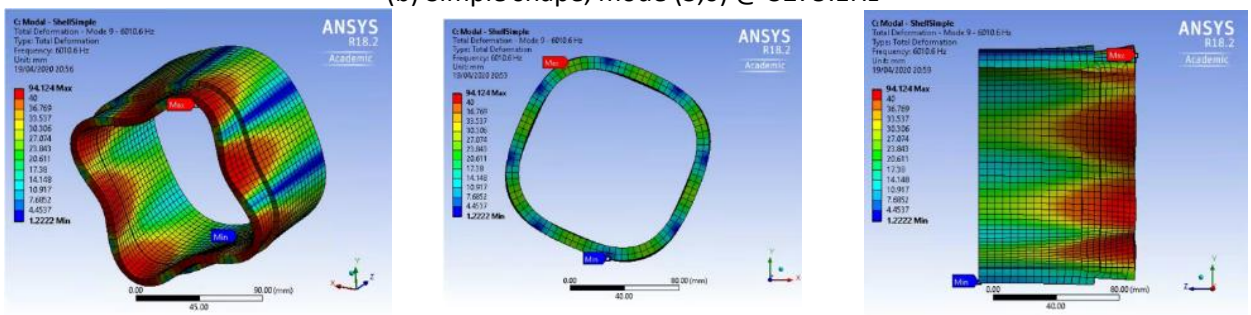

(c) Simple shape, mode (4,0) @ 5992.6Hz

Fig. 5.1.4 Circumferential modes 2 to 4 results for simplified coolant shell shape.

The differences in modal frequencies between the shapes and the measured data are summarised in Fig. 5.1.5 and Table 5.1.2.

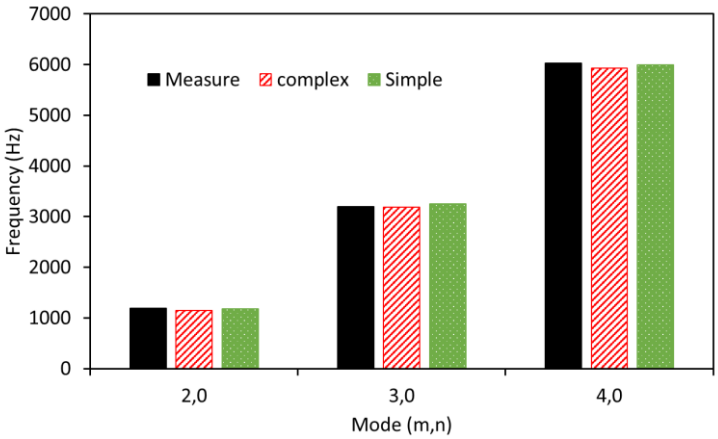

Fig. 5.1.5 Comparison of mode shapes frequencies between the measured data and the 2 FE models for the coolant shell.

Table 5.1.2 Comparison of mode shape results for the coolant shell

Mode	Measured	Complex shape		Simple shape	
		F (Hz)	Error (%)	F(Hz)	Error (%)
0,2	1194	1142.6	4.4%	1190	0.41%
0,3	3194	3184.9	0.28%	3275	2.5%
0,4	6010	5927	1.61%	5992.6	0.23%

Both models show good alignment with the measured data with the simpler shape proving to have the lower error at mode 2. The differences lie in the meshing of the parts, with the mounting holes on the complex shape giving an unevenness to the mesh which may have contributed to the slight difference in results. A direct comparison between the mesh complexity and the computational performance is shown in Fig. 5.1.6.

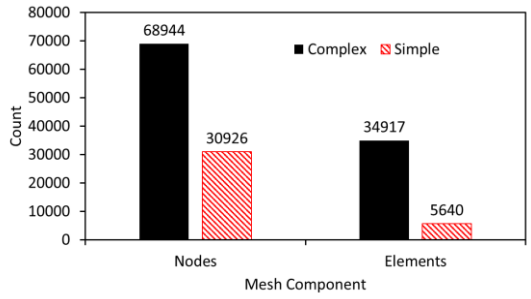

(a) Comparison of mesh complexity between the two models

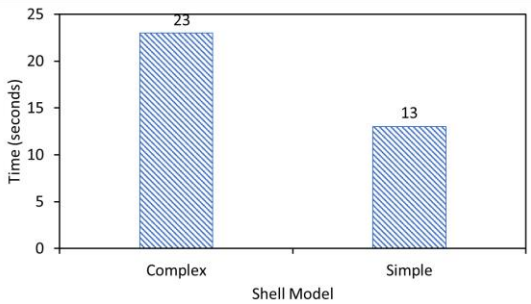

(b) Comparison of run time

Fig. 5.1.6 Comparison of mesh complexity and run time for the 2 coolant shell models.

The results show the complex shape utilises a correspondingly higher mesh complexity to encompass all the features of the shape, whereas the simple shape has under half the number of nodes and around 1/6th the number of elements. The reduced computational load is reflected in the faster processing time of the simple shape. Given the above data the simple model is chosen as the model to take forward for further analysis and ultimately used in the final assembly.

5.1.2 Modelling the stator laminations

In Chapter 1 it was shown that the state-of-art for modelling the stator laminations is to represent the material as an orthotropic composite, with different mechanical properties on the radial plane to that of the axial plane. The stator for this machine was bonded. At the design phase there was some concern that welding the outer diameter, whilst potentially stronger, could cause the plates at the inner bore to splay creating issues with the magnetic circuit which was very important for the design brief. Thus, with a bonded core the composite methodology matches well and will be used here. The material properties of the stator core are shown in Table 5.1.3.

Table 5.1.3 Lamination stack material properties [CP08]

Property	Stator core	Epoxy	Units
Material	M250-35	Epoxy (E645)	
Density	7600	1186	Kg/m^3
Young's modulus	200	3.44	GPa
Poisson's ratio	0.3	0.3	
Shear modulus	80.8	1.32	GPa

Using the above material properties and the equations in Chapter 1 (see Table 1.5.5) the mechanical properties can be derived. A concern with the stack is the stack factor was estimated as being 0.98 by the supplier but was not actually measured. This is a concern as changes to the stack factor can lead to large variations in stiffness, especially for axial modes. To check this the mechanical properties from 0.9 to 0.98 were calculated. The resultant values are shown in Table 5.1.6 and the trends of the key aspects plotted in Fig. 5.1.7.

Table 5.1.6 Influence on mechanical parameters of stack with increase of stack factor from 0.90 to 1.

Stack factor	Density (kg/m^3)	E_{xy} (MPa)	E_z (MPa)	Poisson ratio (X-Y)	Poisson ratio (Z)	G_{xy} (MPa)	Gz (MPa)
0.90	6958	$1.89x10^5$	$3.00x10^4$	0.3	0.048	$7.28x10^4$	$1.15x10^4$
0.92	7087	$1.93x10^5$	$3.62x10^4$	0.3	0.056	$7.44x10^4$	$1.39x10^4$
0.95	7279	$2.00x10^5$	$5.25x10^4$	0.3	0.079	$7.68x10^4$	$2.02x10^4$
0.96	7343	$2.02x10^5$	$6.17x10^4$	0.3	0.092	$7.76x10^4$	$2.37x10^4$
0.97	7407	$2.04x10^5$	$7.50x10^4$	0.3	0.110	$7.84x10^4$	$2.88x10^4$
0.98	7471	$2.06x10^5$	$9.54x10^4$	0.3	0.139	$7.92x10^4$	$3.67x10^4$
1	7600	$2.10x10^5$	$2.10x10^5$	0.3	0.3	$8.08x10^4$	$8.08x10^4$

Note: A stack factor of 1 has been added in Table 5.1.6 and Fig. 5.1.7 as a reference to a solid piece of steel; this is clearly not used due to the eddy current risks. Plotting the key variables above shows the general trend.

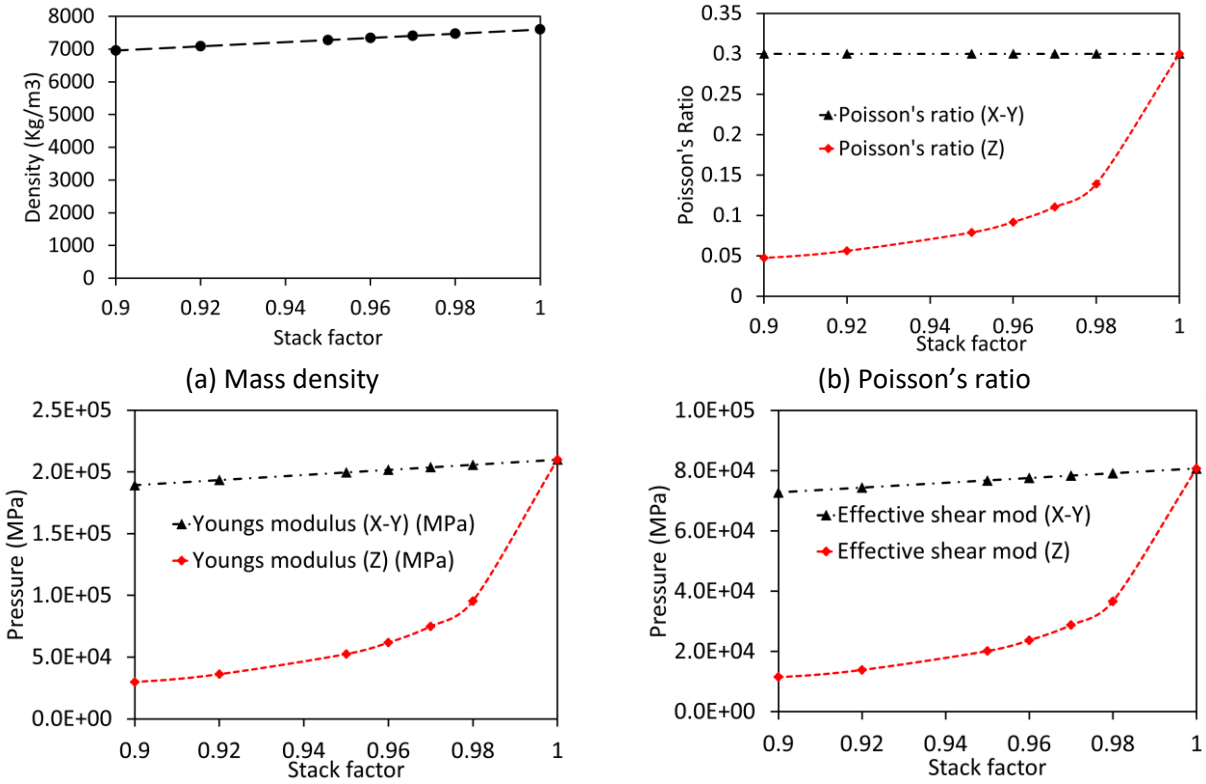

(a) Mass density (b) Poisson's ratio

(c) Young's modulus (d) Effective shear modulus

Fig. 5.1.7 Characteristics of the derived composite with varying stack factor (0.9 -> 1).

To conclusions can be made from the plots in Fig. 5.1.7:

- The radial (X-Y) plane is linear and gradually increases as the stack factor nears 1.
- The composite structure Z-axis is non-linear and markedly lower than a solid (stack factor = 1) for all key characteristics as seen in Fig. 5.1.7 (b), (c) and (d).

Given the dominance the stator has on the overall modal performance of the machine the importance of getting the stack factor correct is clear. Beyond modelling the stator in this project this also highlights the need for careful control and tight tolerances of the manufacturing processes, two bonded stators with slightly different stack factors due to some variation in assembly can lead to large differences in performance..

5.1.2.1 Modal analysis of the stator core

The stator core is modelled in ANSYS® and meshed, as shown in Fig. 5.1.7. A frictionless support is added to the rear face of the model to represent the constraint applied by the test bench.

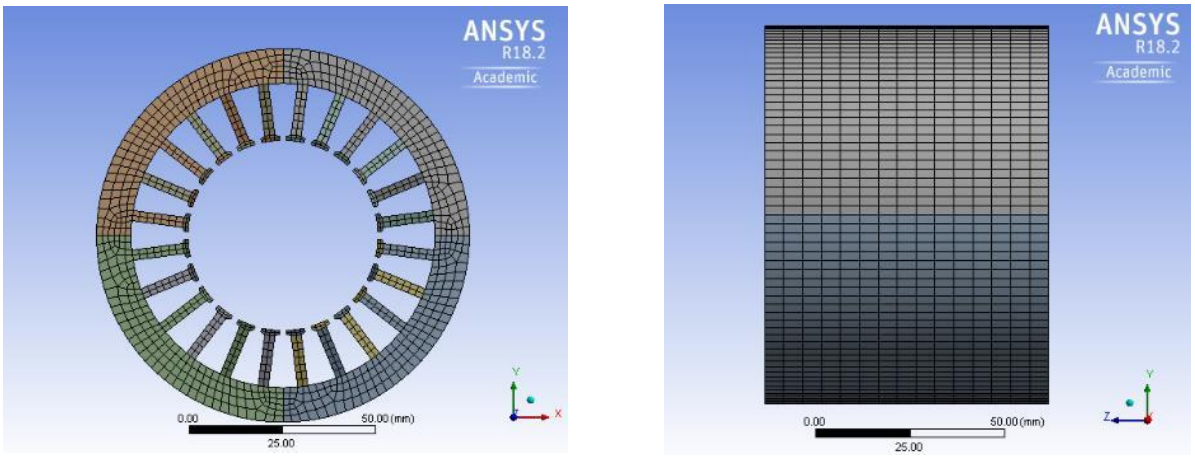

(a) Top view of core

(b) Side view of core

Fig. 5.1.7 Meshed model of the stator.

The material data derived in Table 5.1.6 are added to the FE tool and each material is run through modal analysis. Using the 3 key modal frequencies measured in the hammer test experiment (Fig.4.4.2) the results can be compared with the measured data.

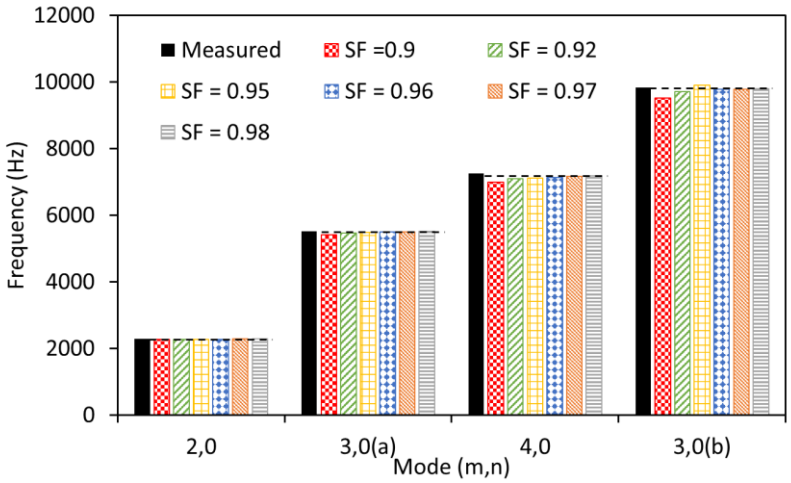

(a) Comparison of the measured modal results and the different stack factors

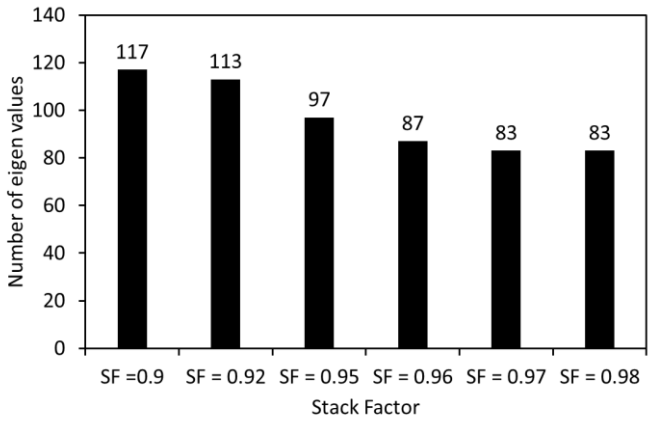

(b) Number of eigen values generated for a sweep to 12kHz for each stack factor

Fig. 5.1.8 Comparison of FE calculate modal frequencies and the measured results.

The results in Fig 5.1.8 are summarised in Table 5.1.7.

Table 5.1.7 Comparison of modal frequency of increasing stack factor with measured stator core

Mode	Measured	SF =0.9	Error (%)	SF = 0.92	Error (%)	SF = 0.95	Error (%)	SF = 0.96	Error (%)	SF = 0.97	Error	SF = 0.98	Error (%)
2,0	2279Hz	2261Hz	0.79%	2268Hz	0.48%	2274Hz	0.22%	2277Hz	0.09%	2281Hz	-0.09%	2287Hz	-0.35%
3,0(a)	5519Hz	5417Hz	1.85%	5464Hz	1.00%	5480Hz	0.71%	5489Hz	0.54%	5497Hz	0.40%	5512Hz	0.13%
4,0	7254Hz	6996Hz	3.56%	7086Hz	2.32%	7107Hz	2.03%	7121Hz	1.83%	7162Hz	1.27%	7183Hz	0.98%
3,0(b)	9828Hz	9521Hz	3.12%	9711Hz	1.19%	9897Hz	-0.70%	9778Hz	0.51%	9786Hz	0.43%	9804Hz	0.24%
Modes to 12kHZ:		117		113		97		87		83		83	

From the results it can be seen that there is little variation for mode (2,0), showing good alignment at all stack factors. For the higher modes, the accuracy increases as the stack factor increases until 0.98 where the best alignment is found. An additional interest was the number of eigenvalues found during the FE calculation. The stator cores with the lower stack factors have a larger number of modes, mostly in the form of tooth modes. Given that the axial characteristics of the tooth are much weaker it appears the lower stack factor means the teeth are more likely to hit a mode and begin moving at relatively low frequencies. Using this study, the stack factor of 0.98 is chosen as it best aligns with the measured. The mode shapes and frequencies are shown in Fig. 5.1.9.

ISO X-Y cross section Y-Z Cross section

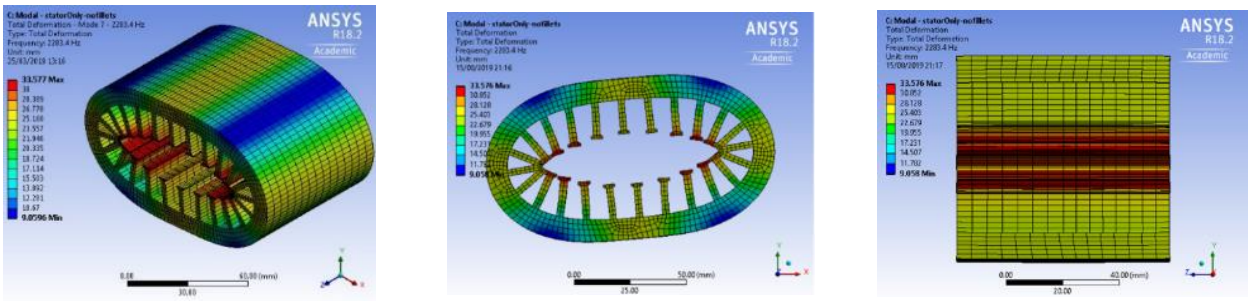

(a) Mode 2,0 @ 2287Hz

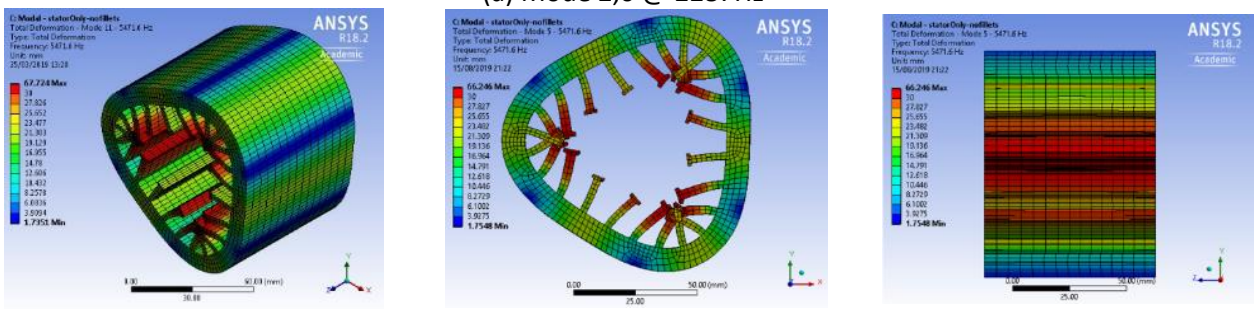

(b) Mode 3,0 (a) @5512Hz

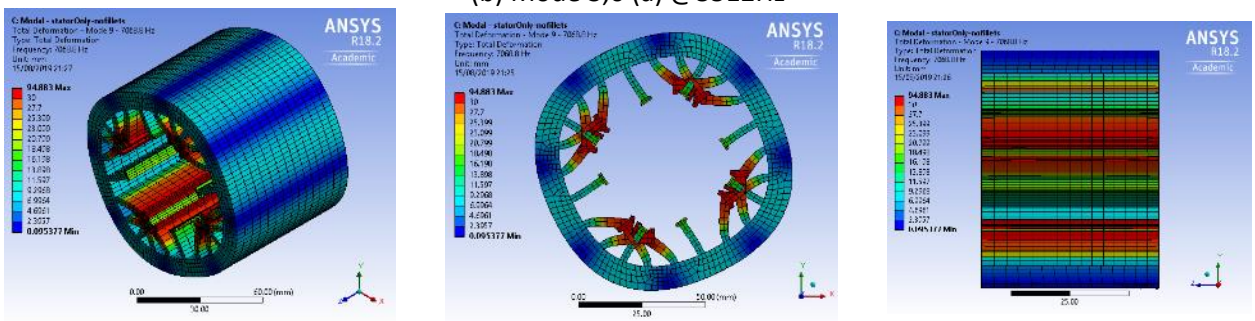

(c) Mode 4,0 @ 7183Hz

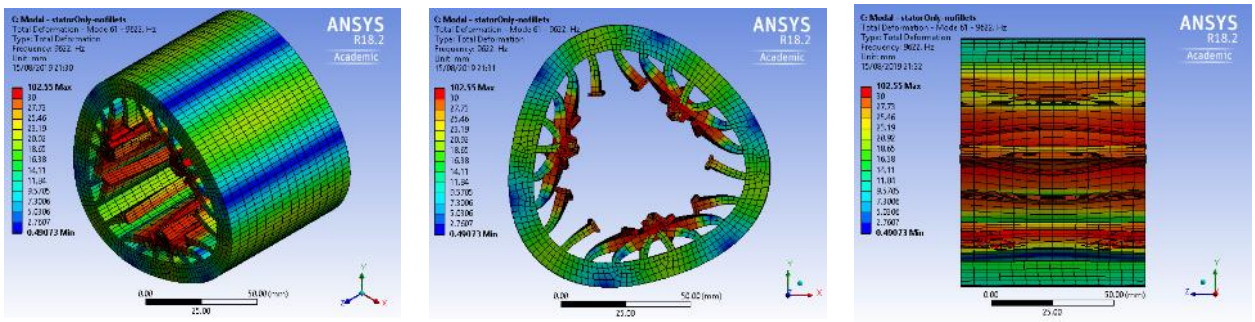

(d) Mode 3,0(b) @ 9804Hz

Fig. 5.1.10 Modal shapes of stator core generated using ANSYS® modal analysis.

5.1.3 Modelling the windings

Similar to the stator core, the literature review in Chapter 1 revealed a large number of studies on modelling the material properties of the stator windings with [KI02] providing an equation (see Chapter 1,(1.48)) based on a large empiric study of many different stators for induction machines. Key to this equation is the slot fill factor, that is the ratio of copper to the total slot area (1.53). In order to utilise the equation derived by [KI02] the fill factor must be derived, starting with the slot area which can be very simply obtained using a CAD tool and the resultant area is shown in Fig. 5.1.13.

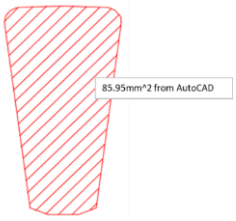

Fig. 5.1.13 Total area of one slot derived from CAD (85.95mm^2).

The next step is to work out the cross-sectional area of the winding occupying each slot. For this the winding specification is required to determine the number of strands per slot and the datasheet from the winding material supplier [HM17] is required to determine the overall thickness of strand including the coating as this varies highly from supplier to supplier. These are summarised in Table 5.1.8.

Table 5.1.8 In slot winding calculation

Item	Values	Unit
Wire diameter (copper)	1	mm
Number of wires in parallel	2	
Number of turns per coil	24	
Total number of wires per slot	48	
Thickness of coating	0.032	mm
Total wire diameter	1.064	mm
Total wire cross sectional area	0.89	mm^2
Total winding area per slot	42.68	mm^2

Given a slot area of 85.95mm^2 as calculated from CAD and a total in-slot area of 42.68 mm^2 in Table 5.1.8 the stack factor can be calculated by (5.13) to be 49.7%. It should be noted the influence of the enamel on the

individual wires in the coil increases the overall fill factor of the winding, and if the above calculations are repeated using only the copper diameter (1mm) then the fill factor sits at around 44%.

The calculated fill factor of 49.7% is plugged into (1.52) [KI02] giving a resultant E_{slot} of 0.628 GPa.

With the Young's modulus calculated the next aspects are the density and Poisson's Ratio. For these the Poisson ratio of copper is used [HM17] whilst the density is calculated using (1.43) (see chapter 1) like the stator core. The material properties of the winding structure are shown in Table 5.1.9 [HM17].

Table 5.1.9 Material properties of the winding [HM17]

Item	Conductor	Coating	Potting	Units
Material	Copper	Polyamide-imide	CR1035	-
Density	8960	1450	1300	Kg/m^3
Young's modulus	130	5.02	4.3	GPa
Poisson's ratio	0.343	0.3	0.3	

At this point an assumption must be made on how to represent the potting material. In the actual machine the efficiency of the potting process will not be 100%, small air pockets will sit within the slot, especially in the difficult to reach mid-axial region but it is very difficult to accurately predict the distribution of the air pockets and their influence on the mechanical attributes of the machine. To decide a comparison is drawn between the two extreme cases, one with no epoxy (air) and one which assumes the potting process was 100% efficient, Fig. 5.1.14 shows the resultant densities.

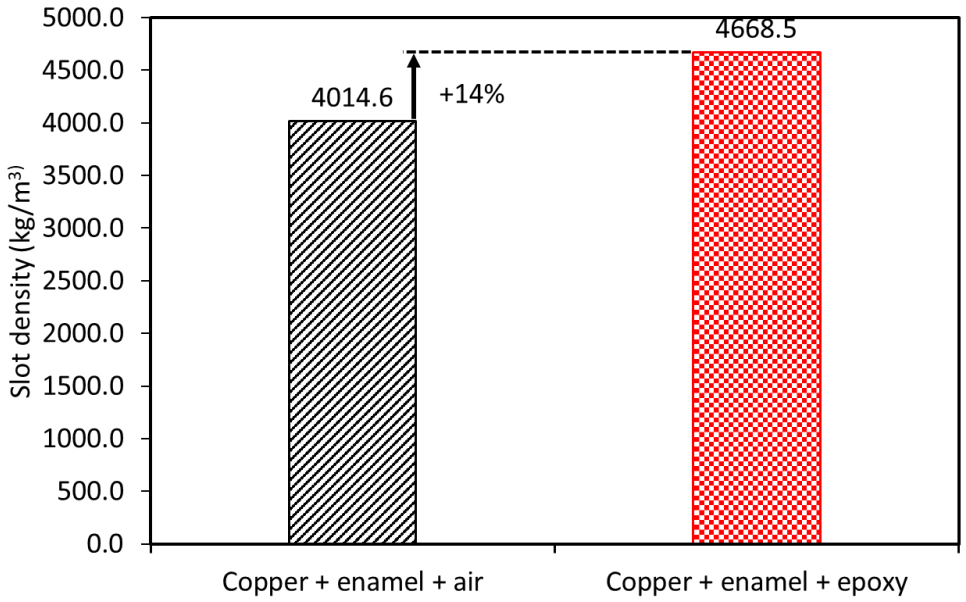

Fig.5.1.14 Comparison of slot densities with and without potting epoxy.

A brief review of the literature [KI02], [SN87], [MEHB93] that focus on the mechanical and thermal attributes of potting shows that in each case the machines are shown with or without potting, with no real cases in between so for this study the assumption will be made that the potting has filled 100% of the void within the slot that is not winding. Table 5.1.10 shows the final material settings for the composite.

Table 5.1.10 Final material settings for winding material equivalent composite

Item	Winding composite	Units
Density	4668.5	kg/m^3
Young's modulus	0.628	GPa
Poisson's ratio	0.343	

These values are inputted into the ANSYS® materials database which automatically calculates the shear modulus etc.

5.1.3.1 Modelling the end windings

As previously highlighted this machine is a distributed wound machine so has large end windings at both axial ends of the stator core. As with much of the stator core, representing the windings in a 3D model is difficult owing to the complexity of the structure. In much of the literature the end windings are disregarded and the windings represented as either an additional mass on the tooth or core [ZT04], [WC03] or the stator core [SAL01a], though it is important to note these machines are all concentrated wound switched reluctance (SRM) machines. On a distributed machine such as the machine understudy on this project the windings represent a substantial structure, so it is important to understand if this has a significant impact on the modal performance of this machine.

To establish the end winding geometry data the winding dimensions can be calculated by using data from the supplier for the winding [HM17] on recommended bend radii as well as approximations using the winding specifications such as the coil span of each coil for each pole of each phase to create an analytical approximation of the end winding. This is ok during the initial design phase but given that this machine is already fabricated it is much easier to simply measure the windings directly. Using a set of digital Vernier callipers the windings were measured with the resultant measurements shown in Fig. 5.1.15 and the key values shown in Table 5.1.11.

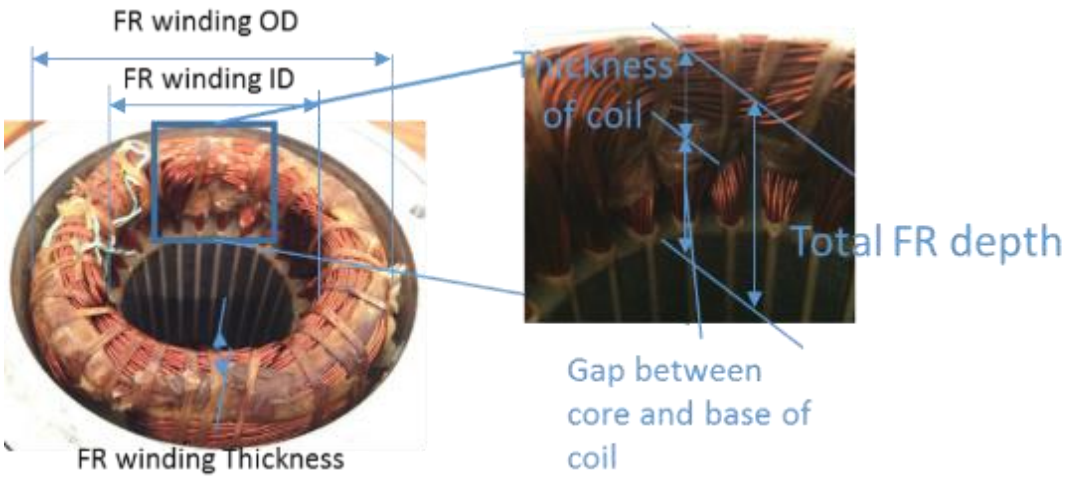

(a) Measured variables of the FR end winding.

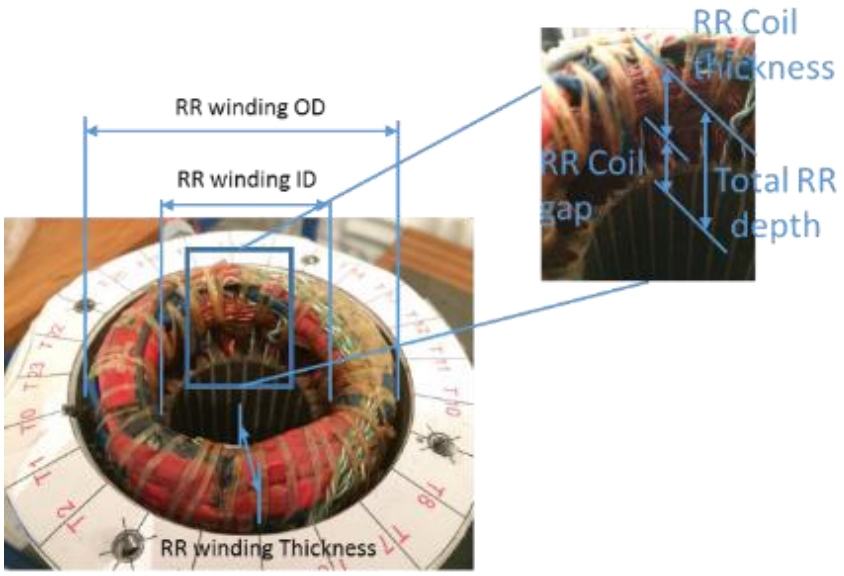

(b) Rear end winding – same aspects are measured on this as the FR winding.

Fig. 5.1.15 Measured aspects of front (a) and rear (b) end windings on fabricated baseline machine.

Table 5.1.11 Measured values from the fabricated machine end windings.

Measured aspect	Front end winding	Rear end winding
End winding inner diameter (ID)	56mm	56mm
End winding outer diameter (OD)	90mm	92mm
End winding width	34mm	36mm
Coil height (coil upper to coil lower)	10.3mm	16mm
Gap between bottom of coil and stator face	18.6mm	18.2mm
Total height (Coil depth + gap)	28.9mm	34.2mm

From the measurements the following observations can be made:

- The rear end windings are larger than the front windings.
    - The rear end of the stator is where the coils are terminated and the 3-external phase lines to the inverter are attached. Thus, more space is required to package these aspects.
- The total height of each end winding is much longer than the design estimation.
    - Design estimation was 22mm front and rear versus 28.9 mm measured on the front and 34.2mm on the rear.
    - During fabrication additional grooves had to be cut into the front and rear face plates to package the larger than anticipated windings.

The windings on the fabricated machine were hand wound making the structure irregular in nature as the winder worked to fit all the coils in whilst meeting the packaging requirements.

So given this information, how best can the end windings be represented? Using the CAD tools available there were essentially 2 options available:

- Utilise a special coil template tool from JMAG (2016 onwards)
- A “cage” type model created using the measurements from the physical machine to create a simpler model where the end windings are represented as solid lumps linked by 24 “bars” that represent the in-slot winding shape to form a single, solid model.

The resultant shapes are shown in Fig. 5.1.16 below.

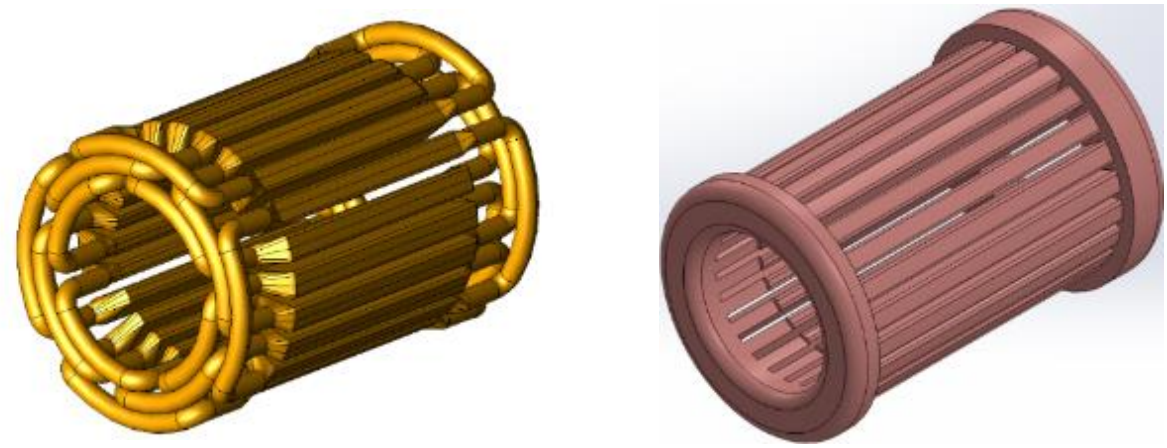

(a) Coil template model using JMAG tool set (b) Simple “cage” type model

Fig. 5.1.16 3D models for end windings.

Comparing the two models the JMAG model looks very impressive and does a good job of routing the coil ends but has some big concerns with regards to the larger mechanical model that is the goal of this exercise:

- Mesh complexity: the shape, number of wires and links means the mesh complexity and density will have to be high greatly increasing the processing time required to calculate the modes and mode shapes.
- End winding structural stiffness: the model does not account for the end windings being strapped and squeezed together, nor does it represent the influence of the potting on the structure. This means any modal analysis will likely return a high number of modes as each of the different end coils interact with each other according to how the casing/stator is moving in addition to the modes of each coil.

The JMAG model works well for understanding 3D phenomena such as the end effect or thermal modelling of the end windings but for modal analysis it is too complicated. Thus, for modelling the end windings utilised in the machine the simpler model will be used in the first instance as not only will it reduce the mesh density of the model but also better represents the fact that the binding and potting of the end windings forms a fairly uniform structure.

Given the material properties and geometry of the full windings are available a comparison with the different methods of representing the windings can be drawn to understand both the impact on the complexity of the

model and of course the accuracy of each compared to the measured static hammer test. There are several different methods of representing the windings within the mechanical model:

- Add the mass of the windings to the whole stator.
- Add the mass of winding to each tooth of the stator.
- Add model of windings to the slots only.
- Add full winding model (Cage type, see Fig. 5.1.16(b)).

Each of these methods approaches the problem with a different angle; the first two look at merely adjusting the material properties of the stator by increasing the mass density so from a modelling point of view the there is no need for any additional geometry, reducing the overall load on the PC when processing. The concern with method is that the model fidelity is clearly much lower as without the windings in the slot it is difficult to judge how the teeth will move as the system resonates, especially as this machine has very thin teeth and the mass of the windings is relatively large. The four models to be compared are shown in Fig. 5.1.17.

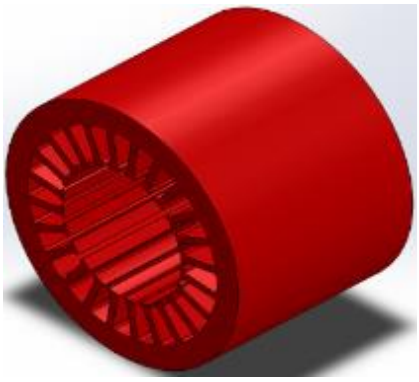

(a) Mass of windings added to stator core

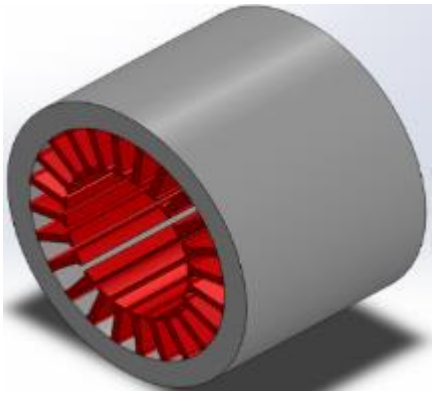

(b) Mass of windings added to stator teeth

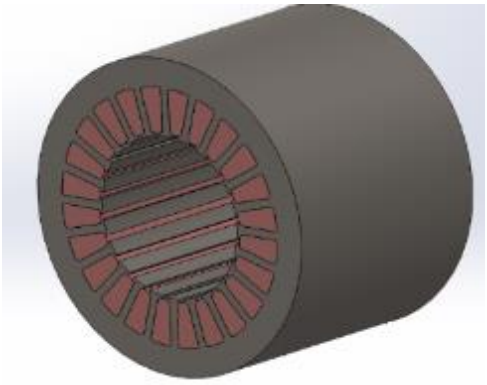

(c) Windings modelled in slot only

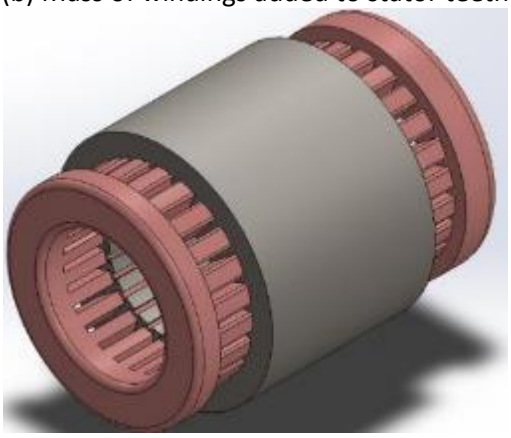

(d) End winding (simplified model)

Fig. 5.1.17 Stator models for comparison.

- Fig. 5.1.17 (a) and (b): the red highlighted areas show where the mass density of the part has been changed from that of the lamination material to encompass the properties of the winding.

- Fig. 5.1.17 (c): the slot is filled with the copper/epoxy composite material calculated in the previous section. Improving the fidelity of the model to (a) and (b) but neglecting the end windings.
- Fig. 5.1.17 (d): shows the full winding model developed is applied to the stator.

For the models in Figs. 5.1.17(c) and (d) it is simply a case of applying the models and materials developed but for Figs. 5.1.17 (a) and (b) the increase in mass density of each component needs to be calculated. Effectively this is achieved by adding the mass of the windings to that of the stator (or teeth) and re-calculating the density based on this new mass with the existing part volume. Table 5.1.12 shows the calculated and resultant values.

Table 5.1.12 Stator mass density increase calculations.

Winding mass added to full stator			
Area of stator (X-Y)	3.7×10^{-3}	m^2	(From CAD)
Stack length	7.5×10^{-2}	m	
Volume	2.78×10^{-4}	m^3	
Mass of stator	2.1	kg	
Mass of windings	1.45	kg	
Combined mass	3.55	kg	
New density	1.26×10^{4}	kg/m^3	
Winding mass added to teeth only			
Area of tooth (X-Y)	4.43×10^{-5}	m^2	(From CAD)
Stack length	7.5×10^{-2}	m	
Tooth volume	3.32×10^{-6}	m^3	
Mass of tooth	2.48×10^{-2}	kg	
Mass of winding per tooth	6.05×10^{-2}	kg	Total winding mass/no of teeth
New mass of tooth	8.54×10^{-2}	kg	
New tooth Density	2.57×10^{4}	kg/m^3	

Using the above settings, the models can now be run in ANSYS® mechanical. To ease the calculations the following common parameters are used:

- Stator and frame assembly used to allow comparison with the measured data.
- The same mesh parameters are applied to each model.
- Mesh size function added to stator: max size = 5mm.
- The models are run to find all eigenmodes up to 12kHz.

The models used are shown in Fig. 5.1.18.

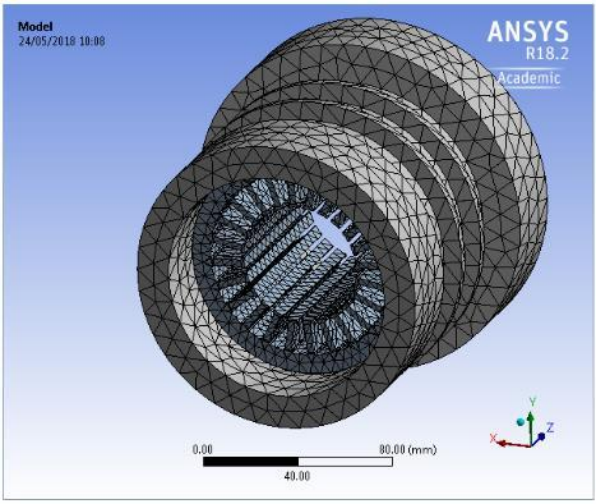

(a) Mass density of full stator increased

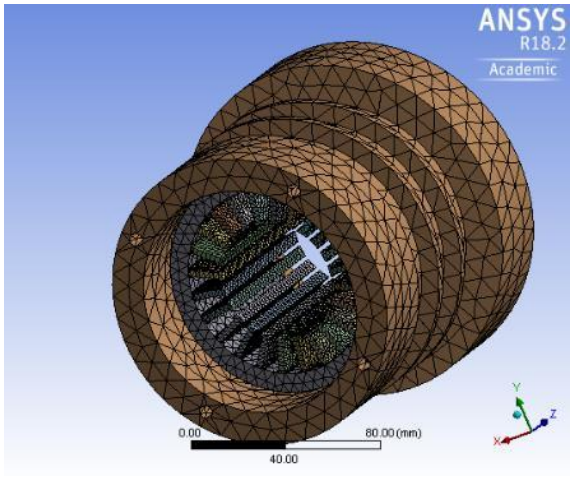

(b) Mass density of teeth increased

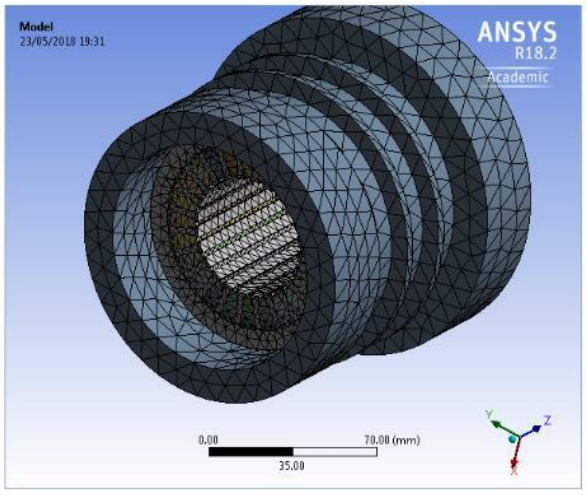

(c) Windings modelled in slot only

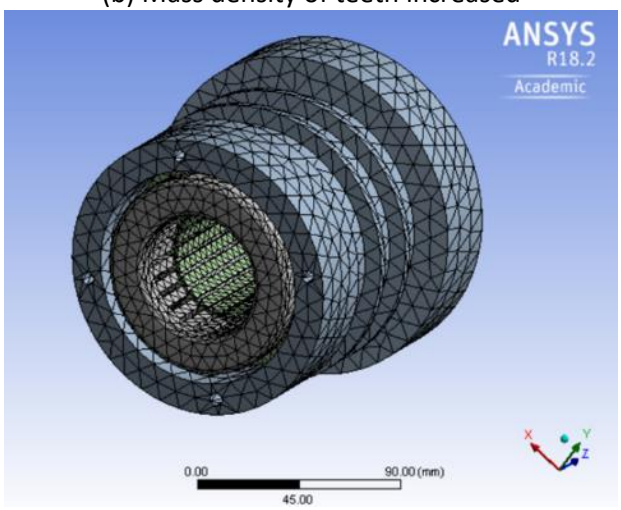

(d) Full windings modelled (V1)

Fig. 5.1.18 Meshed models of each of the different winding cases.

Figs. 5.1.18 (a) and (b) are essentially the same model with different material properties required. In Fig. 5.1.18(c) the slot area identified in Fig. 5.1.13 is extruded to form a component part which is then applied to each slot. Fig. 5.1.18(d) uses the “cage” type full winding from Fig. 5.1.16(b).

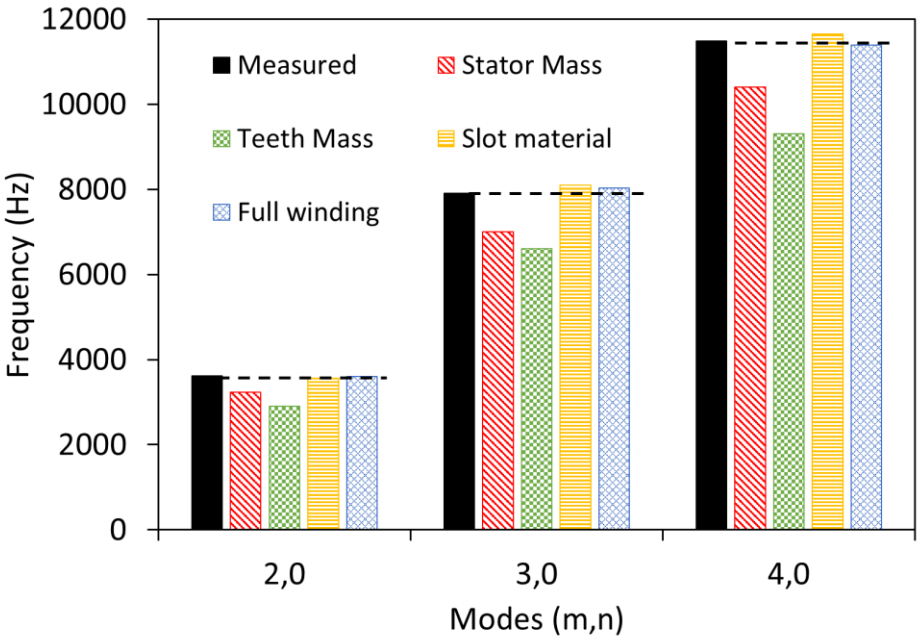

Fig. 5.1.19 Comparison of circumferential modes of each representation of the windings in the core

A summary of the modes compared to the measured data can be found in Table 5.1.13.

Table 5.1.13 Comparison of circumferential mode frequencies

Mode (m,n)	Measured	Winding mass added to stator	Mass density added to teeth	In-slot windings	Full windings model
2,0	3623	3189	2907	3560	3597
3,0	7907	6997	6602	8101	8024
4,0	11482	10600	9303	11649	11389

The results in Fig. 5.1.19 allow the following conclusions to be drawn:

- Adding mass to the teeth is the least accurate method with a large difference in modal frequencies between the measured data and the calculated values, especially at the higher modes.
- Adding the mass density of windings to the whole stator is an improvement but the increased mass with the same core stiffness drags the frequencies lower.
- The addition of the coils to the stator and to the “cage” model with the end windings have good alignment with the results and are almost identical to each other.

Using the material properties derived from [KI02] shows there is good alignment with the methods where the winding has been included. Significant differences are found when the number of calculated eigenmodes from the FE calculations are compared, highlighted in Fig. 5.1.20.

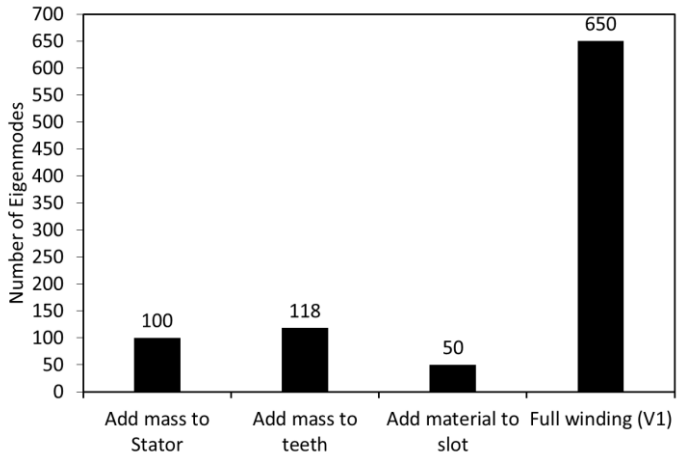

Fig. 5.1.20 Comparison of Eigenmodes generated in ANSYS® for each model (0-> 12Khz)

From the results there are clear differences in the number of calculated eigen values from the FE tool. Addition of the stator mass to the entire core and the teeth generates many eigenmodes, the vast majority of which are tooth modes. With only air surrounding the teeth there is little to prevent the relatively long, thin teeth in the core from swinging around generating large numbers of different tooth modes across the calculated frequency band. Adding the winding material to only the slot decreases the number of tooth modes as the material acts to dampen the tooth motion. The full winding model, whilst marginally accurate has an extremely high number of calculated modes which made identifying the full body modes very difficult. The vast majority number of eigenvalues calculated are the different modes of the end winding, this is reinforced by similar observations in the literature [SAL01a], [SN87]. Each eigenmode calculated takes a certain amount of processing time, so it can clearly be seen that the case where the full end winding model is utilised the high number of calculated eigenvalues and the increased mesh elements due to the additional geometry of the end windings means it takes hours to do one run. In the context of having to run the model multiple times to simulate the machine at different load conditions the full winding model is not suitable for this application. Thus, the best-balanced solution in terms of accuracy and processing time is the model where the calculated winding material is added to fill the slot.

5.2 Modelling the full machine assembly

During the analysis of the different end winding models it became clear that the processing times for each model was very long, taking 30 minutes or more to run. Given these models only contain the 2 core parts of the full assembly this run time and associated computational load would only rise as more parts are added making FE analysis of the full machine extremely time consuming and limit what could be modelled within the time frame of the project. Thus, some shape and mesh optimisation are required.

5.2.1 Simplifying the geometry and optimising the mesh

The first aspect to look at is the 3D models of the parts. These were imported into the FE tool from the CAD tool wholesale with all the features (chamfers/fillets/clearance holes etc) required for the fabrication and assembly of the machine. Each of these features, whilst important for the fit and finish of the real machine represents a challenge to the meshing tool with the ANSYS® package. Features such as fillets or even drill holes create a complex geometry which challenges the meshing tool and generates a sometimes irregular and dense mesh. By eliminating these features, the shape and therefore the mesh can be greatly simplified. Fig. 5.2.1 shows the initial “full” model and the simplified model.

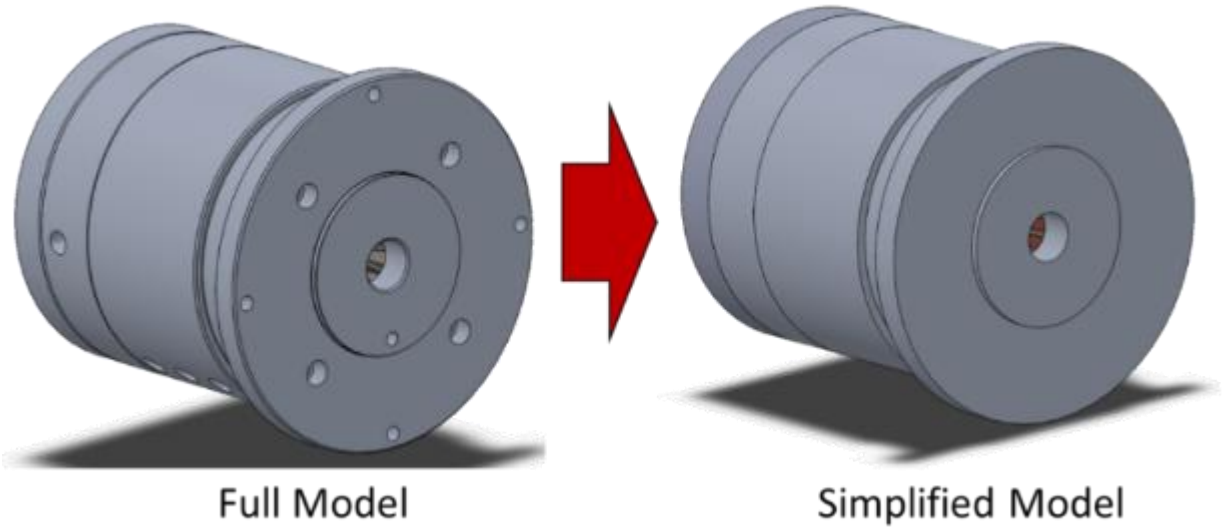

(a) 3D iso-view showing initial full motor assembly shape and simplified model.

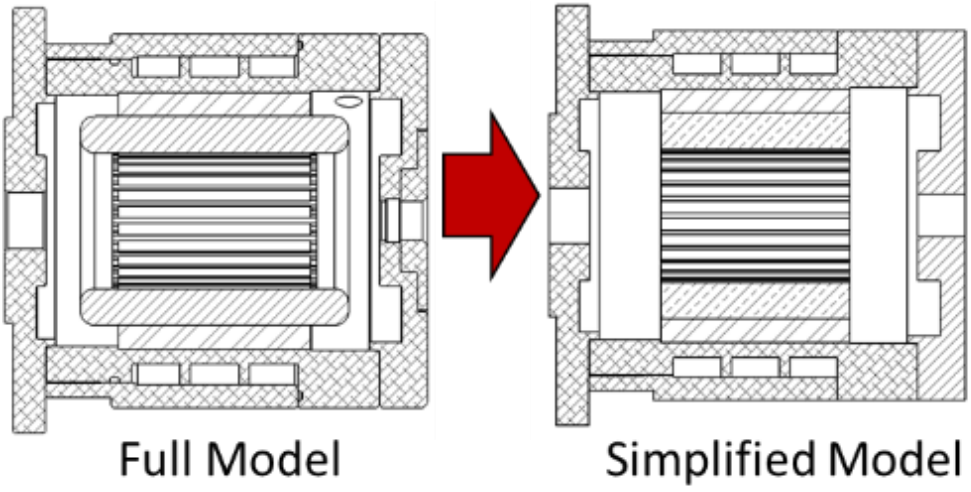

(b) X-Z cross section of the initial and simplified model.

Fig. 5.2.1 Comparison of original and simplified machine shapes.

From Fig. 5.2.1 the fundamental shape and key features of the model remain unchanged but there are many changes, some clear and some subtle:

- The rear bearing holder plate is integrated into the rear mounting plate of the machine.
    - The bore shape and all diameters are maintained.
- All chamfers and fillets at the edges of parts are removed.
- Holes for mounting bolts on the front and rear of the main frame and front and rear plates removed.
- Holes for the phase line and thermal sensors removed.
- Grooves for the 'O' rings on the main frame of are removed.

In addition to the simplification of the part a very important aspect to consider is the mesh density. The task of optimising the mesh, known as mesh convergence [ANS18], plays a very important role in reducing the processing load and hence increase the speed of running a model. This topic is heavily covered in the literature [SJY78], [SAL01b], [DSHL13] with considerable effort into meshing and convergence strategies for different applications. With modern computers the raw processing power and complex meshing algorithms with the latest FE tools optimization of the mesh often occurs internally without the user having to manually. The concern found with modal analysis is that these automated routines tend to favour common mechanical problems such as stress analysis or CFD problems and the trend was for much higher complexity meshes to be generated that may be necessary. Fortunately, ANSYS® workbench provides 2 methods to further converge the mesh:

- Mesh Convergence tool.
    - Optimisation tool dedicated to converging the mesh.
    - Very efficient for optimising mesh on standard mechanical analysis applications.
    - Not always compatible with Modal analysis due to non-static nature of eigenvalues at different mesh densities [ANS18].

- Standard mesh optimisation.
    - Mesh size set as parameter and minimum and maximum specified.
    - Highest amplitude modal frequency set as target.
    - Internal optimisation algorithms used to hunt for optimal value.

With modal analysis a change due to adjustments to mass or stiffness or large changes in mesh density may add or remove calculated eigenvalues from the result set meaning the target modal frequency can jump from different mode indexes making convergence difficult. This was a problem when using the internal convergence tool which would regularly generating errors when trying to converge, typically at the extremes of the densities when the calculated eigenvalue can shift. Thus, for the modal analysis the more manual optimisation option was favoured. Fig. 5.2.2 shows the initial auto-generated mesh compared to the converged mesh.

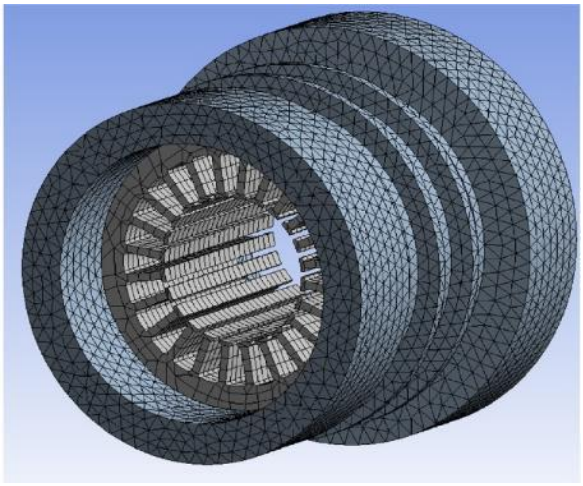

(a) Adaptive mesh.

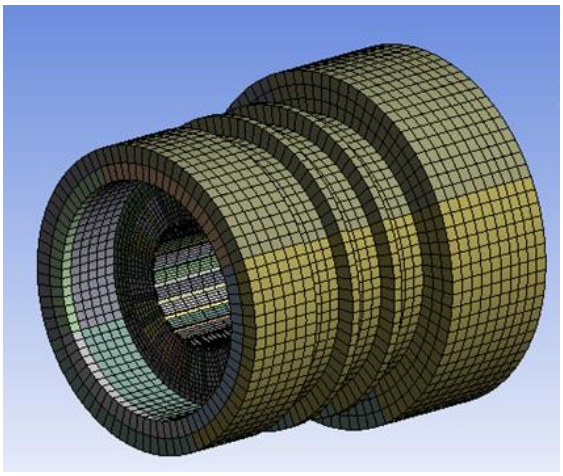

(b) Converged mesh.

Fig. 5.2.2 Comparison of the different meshing techniques to be compared.

The mesh density in Fig. 5.2.2 (a) is visibility higher than that of the mesh in Fig. 5.2.2(b). The effect of the mesh optimisation and model simplification can be illustrated with a simple set of comparisons. The models compared are:

- Two complex models, one with automatic mesh and one with converged uniform meshing.
- Two simple models, same mesh combinations as the complex model.

In each case the modal analysis tool is utilised, and the models run up to 12KHz. The results are shown in Fig. 5.2.3.

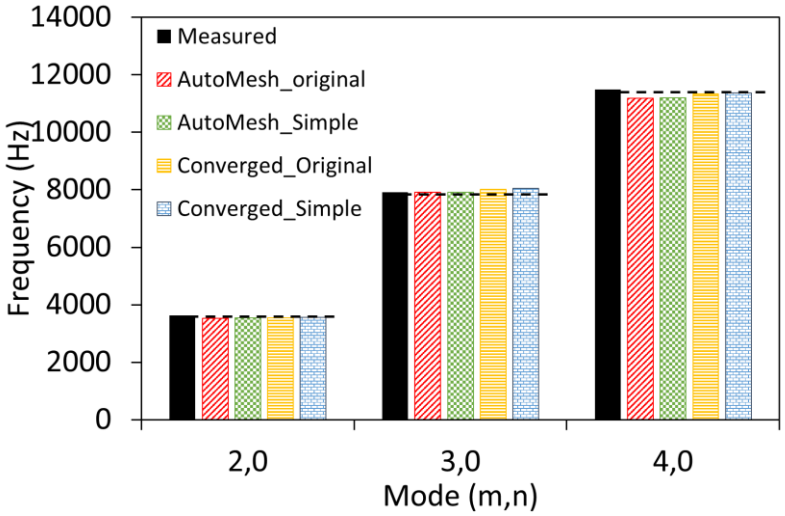

(a) Comparison of circumferential modes between the measured machine, different models, and mesh types.

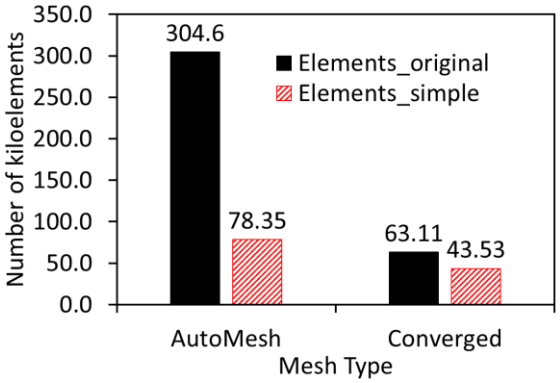

(b) Comparison of mesh densities between the different models and mesh types.

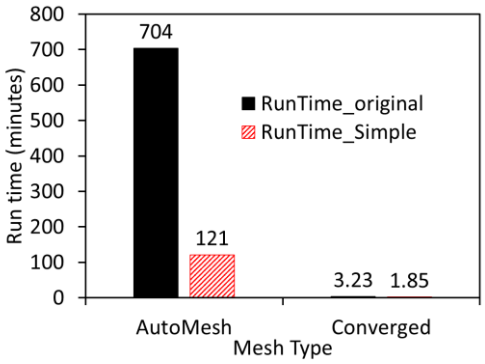

(c) Comparison of mesh densities between the different models and mesh types.

Fig. 5.2.3 Comparison of the different models and mesh types.

In Fig. 5.2.3(a) there is little to differentiate the modal results of the different model and mesh variations. This is to be expected as the major aspects of the geometry and the material are not changed from before so the different variations should match closely. Where the differences are starkly contrasted is when looking at the mesh statistics and the run times in Figs. 5.2.3 (b) and (c) respectively. Using the default meshing on the complex model takes almost 12 hours to generate all eigenvalues whereas the same settings on the simplified model takes 2 hours, a considerable difference in time. Looking at the converged mesh results the difference in processing time is glaring. The converged model is much faster in both the complex and simplified models. The clear winner is the simplified model with converged mesh with a run time of 1 minute 51 seconds. As was previously noted the run times will only increase as the model complexity increases so minimising the run time is a key performance indicator. It is good practise to undertake mesh convergence for each stage of the modelling as the model complexity increases to ensure the optimal mesh density is being utilised.

With the materials, structure and mesh now established for this more complex model the mode shapes can be seen in Fig. 5.2.4.

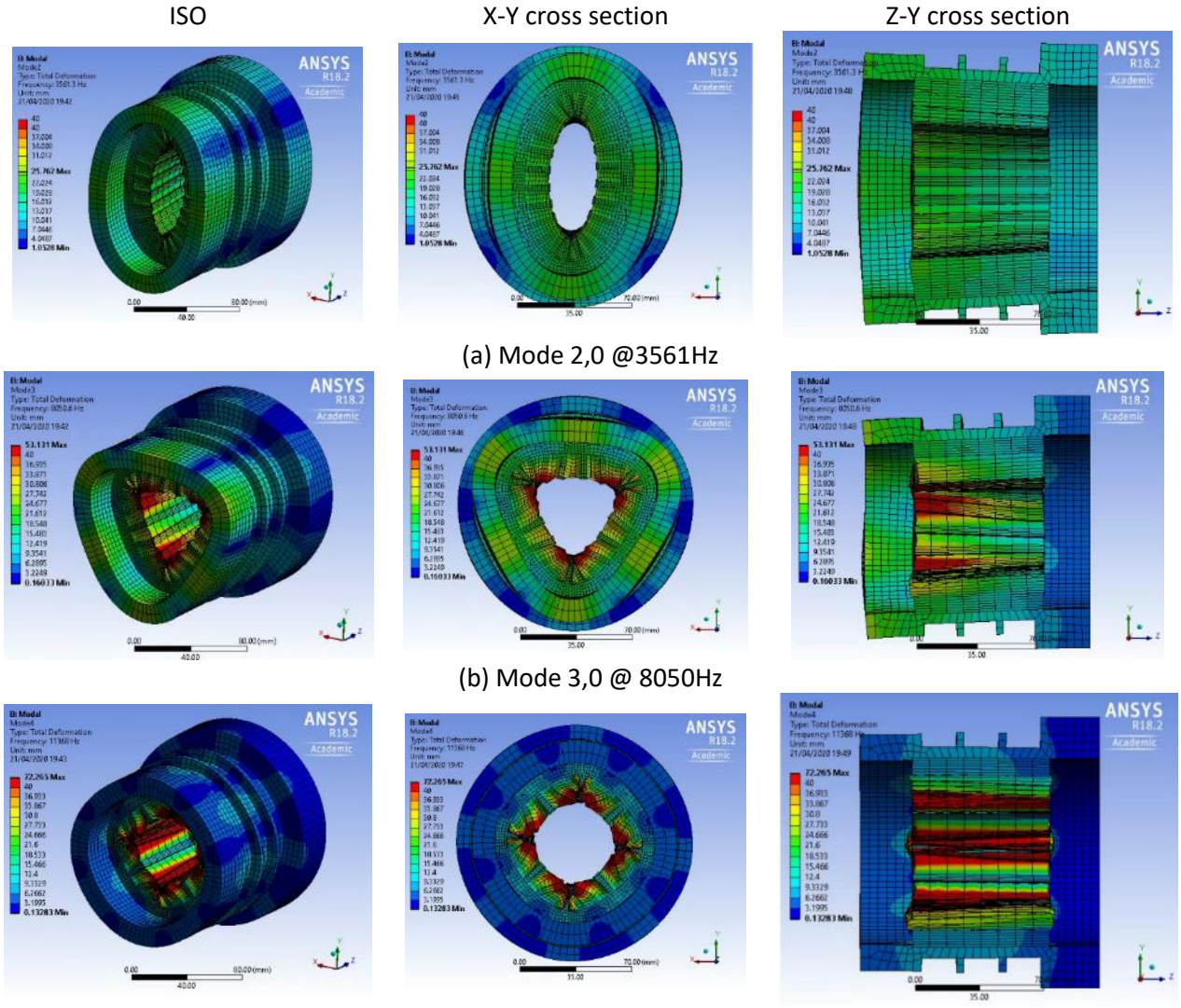

(a) Mode 2,0 @3561Hz

(b) Mode 3,0 @ 8050Hz

(c) Mode 4,0 @ 11368Hz

Fig. 5.2.4 Key modes generated for FE modal analysis of the stator in frame only.

Table 5.2.1 gives the raw frequency values for each mode.

Table 5.2.1 Comparison of measured modal frequencies with final FE model of the wound stator in frame.

Mode	Measured (Hz)	FE calculation (Hz)	Error
2,0	3623Hz	3561Hz	1.71%
3,0	7907Hz	8050Hz	1.81%
4,0	11482Hz	11368Hz	0.99%

The results show a good alignment with the measured data, a maximum error of 1.8% is very good given the relative complexity of the part and the problems encountered when trying to measure the part.

5.2.2 Representing the fixtures – attaching the rear plate

The next step in the assembly of the machine is the attachment of the face plates. During the hammer test the rear plate was attached, and the hammer test taken and then the front plate was attached without the coolant shell and the test repeated to allow the influence of the shell to be better understood. The concern

with modelling these stages of the assembly is that a key aspect of the simplification of the component shapes that form the motor assembly was the elimination of the bolt holes and associated clearance holes etc. in the face plates. This makes for a much simpler shape for the frame and face plates but given that the end plates on the fabricated machine are held in place by bolts screwed into it presents a problem, how can the fixtures be represented?

Before answering this, it is worth briefly looking in more detail at the interface between the face plate and the frame. The face plates perform 3 essential functions:

1. House the front and rear bearings and by extension control the concentricity and axial alignment of the rotor core to the stator core.
2. Provide structural stiffness to maintain the cylindricality of the machine.
3. Protect the machine core from the ingress of particulate matter from the surrounding environment.

The protection from the core of particulates is self-evident. However, the methodology of controlling concentricity and cylindricity of the machine relies on the fit between the lips on each the plates and the inner bore of the front and rear sides of the frame. Fig. 5.2.5.

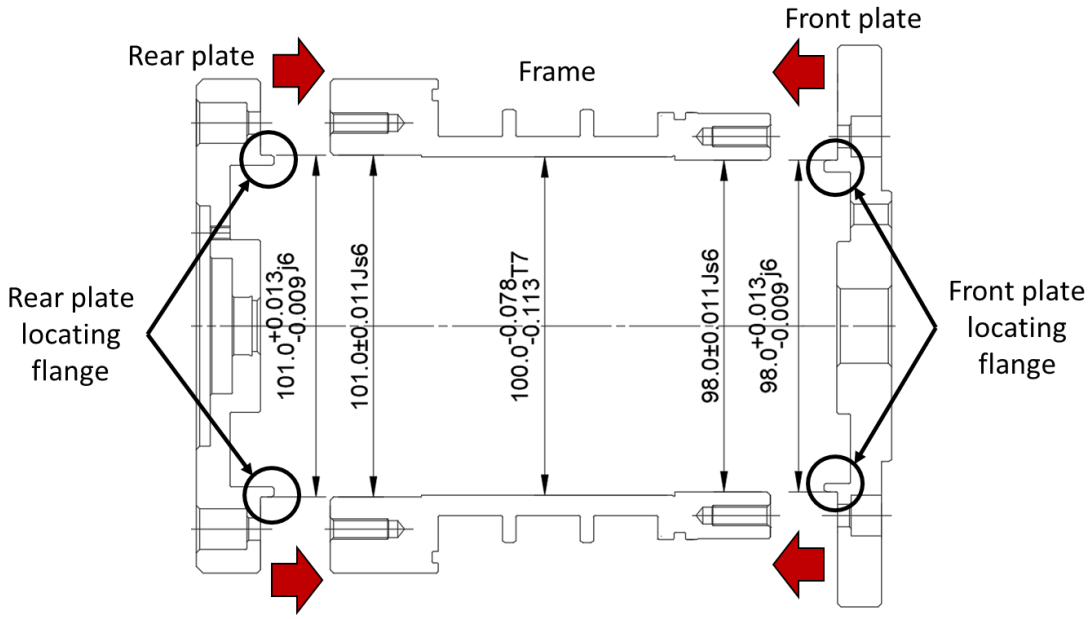

Fig. 5.2.5 Exploded view of frame and face plate assembly showing ISO fit specifications.

The drawing in Fig. 5.2.5 shows the tolerancing using the ISO system of limits and fits [CHS09]. The symbols “J6” and “Js6” provide a standard set of tolerances for the type of fit required and the diameter of the bore and shaft. There are essentially 3 types of fit, clearance, transition, and interference fits. A simple illustration of the 3 types is shown in Fig. 5.2.6.

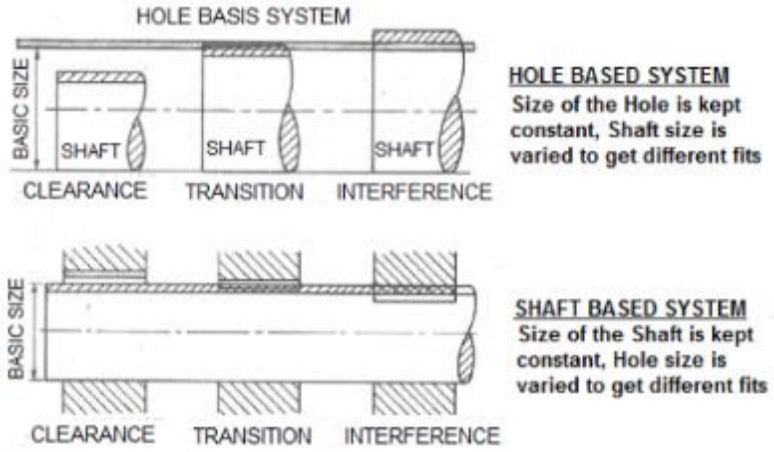

Fig. 5.2.6 Illustration of the 3 main classifications of fit, with hole and shaft basis fit [CHS09].

In the case of the face plates the "shaft" is the lips on the face plate and "hole" is the bore diameter at either end of the frame. The J6/Js6 ISO tolerance applied ensures a tight fit but not so much that the plate cannot be removed again so as such is defined as a transition fit. The specified fit requires the 4 bolts to be tightened to push and clamp the plate into place. Removal requires quite a high force, typically requiring "persuasion" with a soft-headed mallet. Therefore, the fit between the frame bore and the lips on the end plate controls the concentricity whilst the structure of the plates helps maintain the structural stiffness, and both contribute to the overall cylindricity. The plates are held in place axially by the fixing bolts which also act to locate the parts. These attributes must be replicated in the model.

Fortunately, given how common this problem is the ANSYS® mechanical FE tool uses the contact methodology to replicate the different types of fit which are summarised in Table 5.2.2.

Table 5.2.2 Different contact types available in ANSYS®.

Type	Separation	Sliding	Initially touching	Inside pinball region
Bonded	No gap	No sliding	Bonded	Bonded
No separation	No gap	Sliding allowed	No separation	No separation
Frictionless	Gap allowed	Sliding allowed	No separation	Free
Frictional	Gap allowed	No sliding	No separation	Free
Rough	Gap allowed	sliding allowed	η >0, bonded η =0, no separation	Free

For the interface between the lips on the front and rear plates and the inner bore of the frame the "bonded" type is utilised to represent the tight fit of the part. This bond is more linear in nature reducing the calculation load on the FE solver. Fig. 5.2.7 highlights the application of the bonded contact type to the rear face plate and the inner bore of the frame.

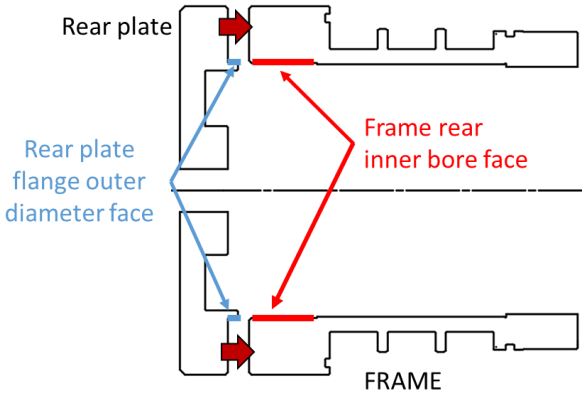

Fig. 5.2.7 Application of the bonded contact type to the rear face plate flange and frame rear inner bore.

For the fixtures it is less straightforward but there are several common techniques:

- Apply the bonded contact types in ANSYS® to the entire interface between the frame and the face plates.
- Use the spot weld function using mesh nodes at the bolt positions to link the face plates to the frame.
- Simple circles added to the face plates and frames representing the bolt diameter, the faces of the circles are bonded together to simulate the bolt but without the 3D bore etc.

The first option is quite simple, the interfaces of the plates and the frame are linked using the same method as the locating lip on the inner bore of the frame. The 2nd option is a bit more convoluted, initially a script within the ANSYS® tool was used that identified mesh nodes located approximately where the centre point of each screw hole was but this was run at the same time as the modal analysis making it difficult to verify the position of the weld matched the actual model. A better method was to split the 3D geometry of the casing such that the centre points were a feature of the geometry that could be manually selected, and the weld points applied, as shown in Fig. 5.2.8.

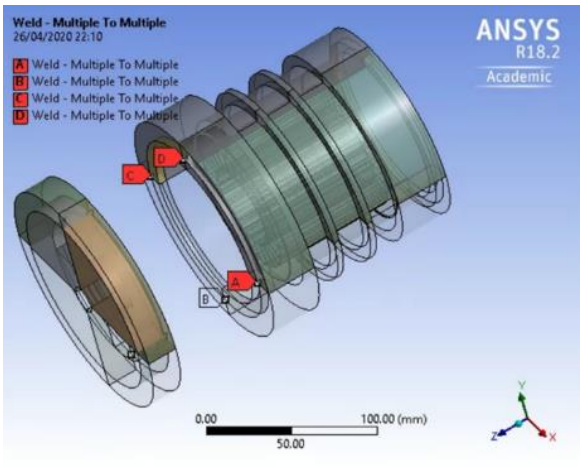

(a) Weld points applied to the rear frame body

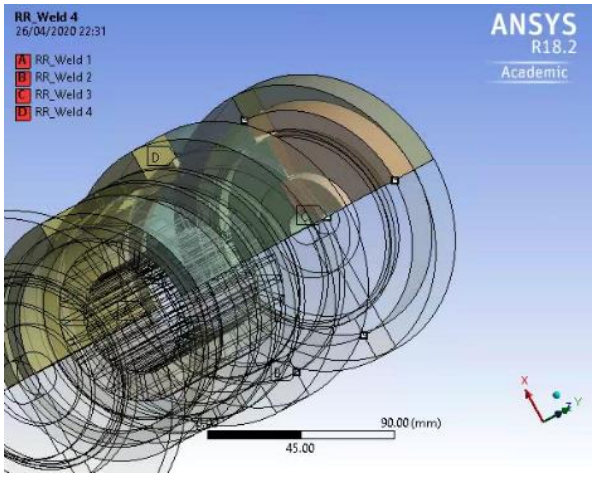

(b) Weld point applied to the rear plate

Fig. 5.2.8 Addition of the weld points to link the rear plate to the frame.

The final method combines the previous 2 methods by adding the screw points as simple 2D circles on the faces of the frame and plates and then bonding the resultant faces together. This is shown in Fig. 5.2.9.

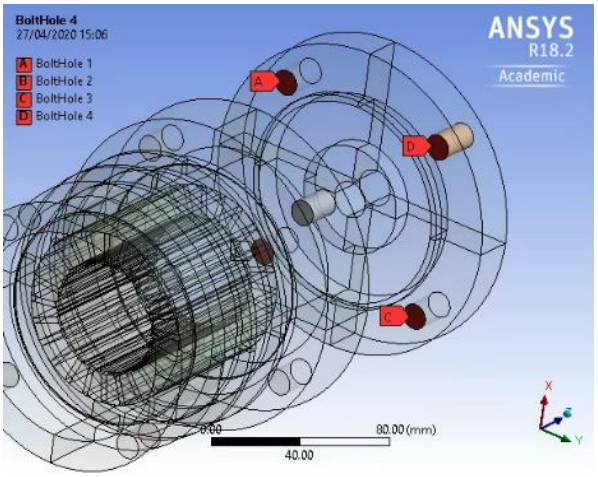

Fig. 5.2.9 Screws points added to the frame and rear face plate.

The three methods are compared with the measured data to observe the influence on the performance. Like the previous analysis the mesh and processing times are taken into consideration to find the best balance between accuracy and processing time the results are shown in Fig. 5.2.10.

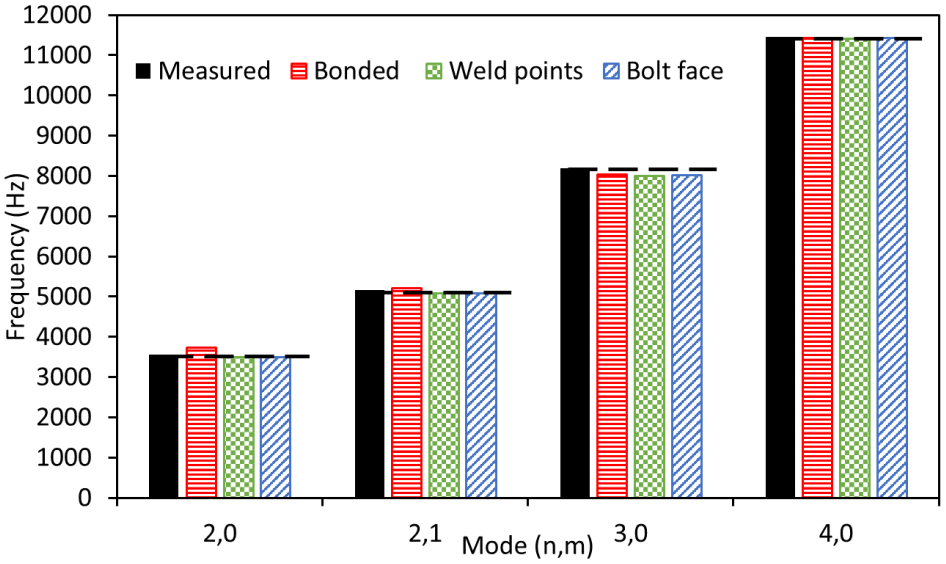

(a) Comparison of the modal frequencies from the different plate linkage methods with the measured results for the attachment of the rear plate.

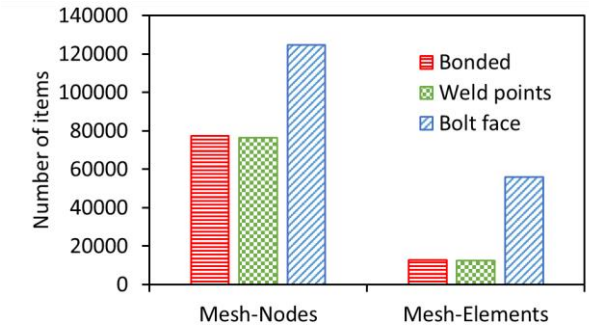

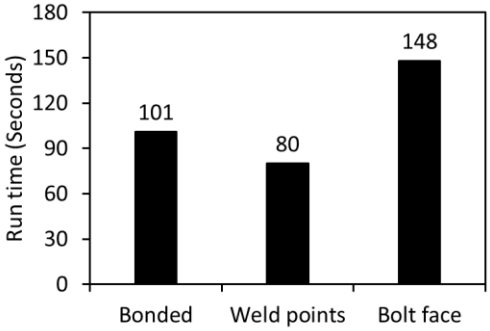

(b) Comparison of mesh complexity. (c) Comparison of run time.

Fig. 5.2.10 Comparison of the different methods to affix the rear plate to the frame body.

Table 5.2.3 provides the actual values and error margins for the modes shown in Fig. 5.2.10(a).

Table 5.2.3 Comparison of modal frequencies between the measured results and the different attachment methods

Mode	Measured	Bonded plate		Weld points		Bolt face	
		Freq(Hz)	Error (%)	Freq(Hz)	Error(%)	Freq(Hz)	Error(%)
2,0	3551	3726	-4.93%	3494	1.61%	3498	1.49%
2,1	5159	5207	-0.93%	5074	1.65%	5088	1.38%
3,0	8190	8028	1.98%	7999	2.33%	8010	2.20%
4,0	11457	11419	0.33%	11417	0.35%	11418	0.34%

The results show the full-face bonding method renders the structure too stiff compared to the other methods. Between the weld point method and the bolt face bonding method there is little difference in the modal results, and both show good alignment to the measured results. Where the differences do lie is in the meshing and given the implication of a denser mesh, the run time. Fig. 5.2.11 shows the meshed models for the spot weld and bolt face bonded models. The bonded mesh is almost identical to the spot weld model so is omitted for clarity.

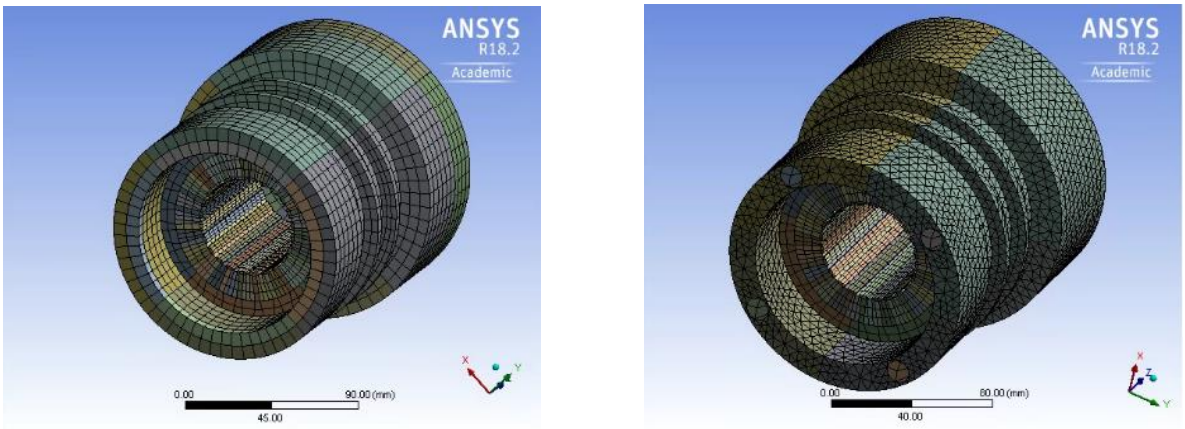

(a) Mesh from Spot weld method (b) Mesh from Bolt face bonding method

Fig. 5.2.11 Comparison of mesh between the spot weld and face bonding method.

The problem that arose with the bolt face method was simply drawing 2D shapes on the faces of the front and rear faces resulted in large numbers of error being generated by the meshing tool within ANSYS®. Using the slice feature converted the circles into short cylinders within the frame and face plate geometry which gives the 3D meshing tool a clearer boundary to generate the mesh within the shape. The uniform method which gave rise to the nice neat mesh on the bonded and spot weld models does not work well with the addition of circular shapes into the model so the tool automatically switches the mesh from the prism hexahedron type to the triangular base prism giving the denser appearance to the mesh observed in Fig. 5.2.11 (b).

The conclusion from the above study is that the welded methodology provides the best balance between accuracy and processing time. The final mode shapes are shown in Fig. 5.2.12.

ISO X-Y cross section Z-Y Cross section

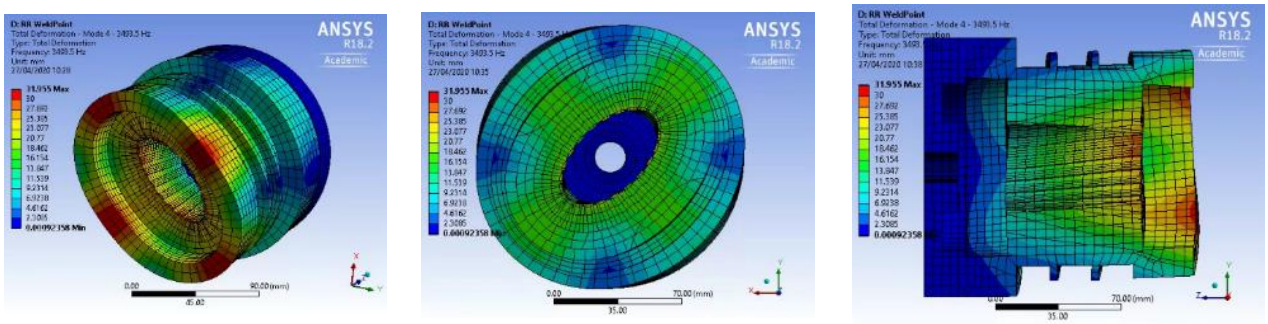

(a) Mode 2,0 @3494 Hz

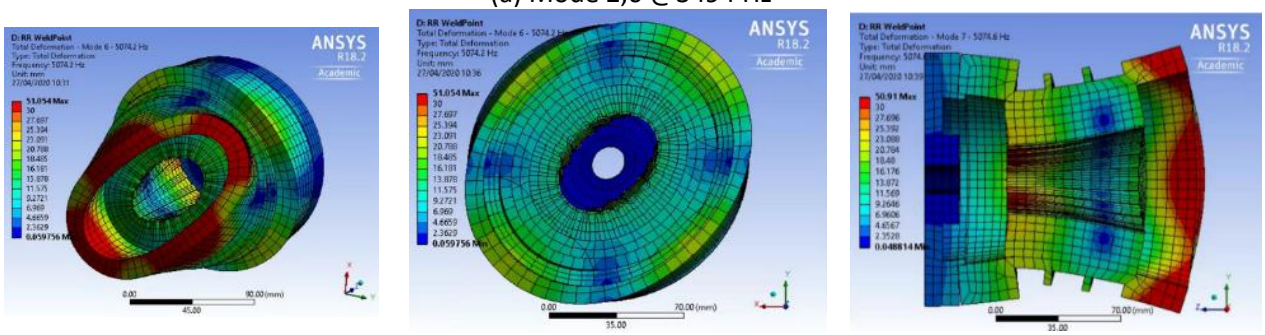

(b) Mode2,1 @5074Hz

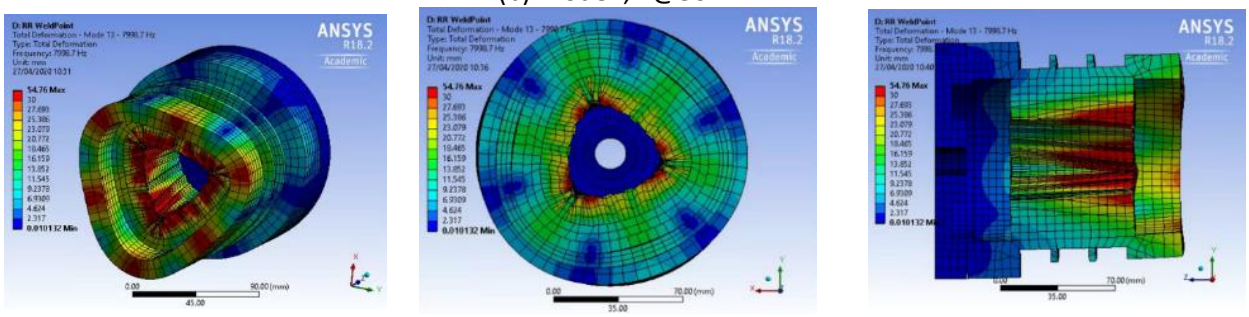

(c) Mode 3,0 @7999Hz

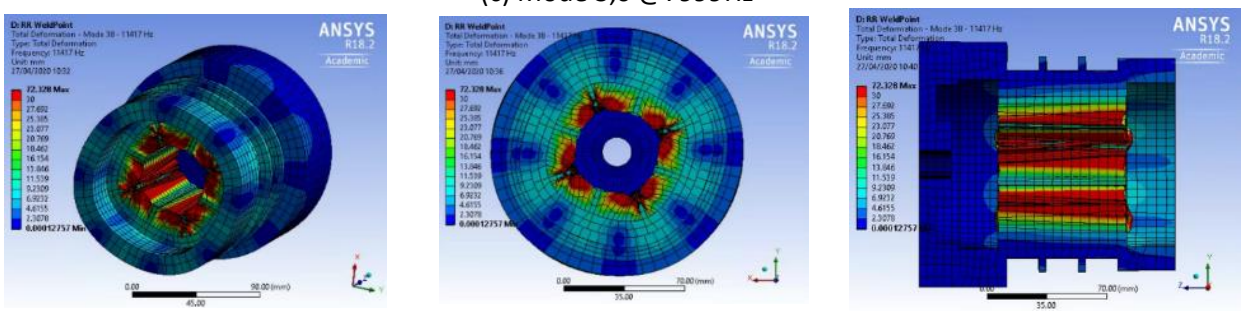

(d) Mode 4,0 @ 11417Hz

Fig. 5.2.12 Key modes generated for FE modal analysis of the frame with rear plate attached.

The 4 modes identified in the measurement can be clearly seen. This stage of the assembly is the first where a strong axial mode can be seen with mode 2,1 appearing at around 5kHz. The shape reinforces the analysis during the measurement that the open-top cylinder arrangement means there is an asymmetry in the stiffness of the part making it prone to axial modes.

5.2.3 Representing the fixtures – attaching the front plate

Following on from the attachment of the rear plate, the front plate is added using the same techniques applied to the previous model. The rear weld points are maintained from the previous section and the front weld points are applied and shown in fig 5.2.13 along with the meshed model.

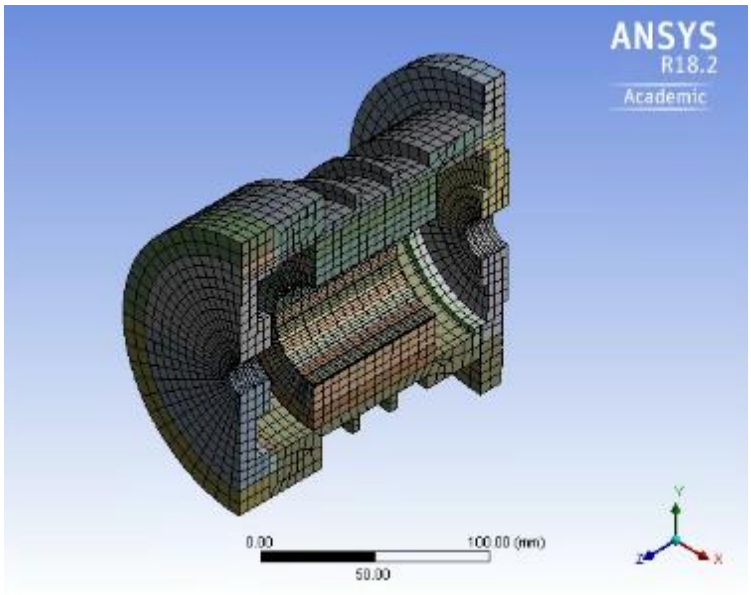

(a) Meshed model, sectioned on Y-Z plane

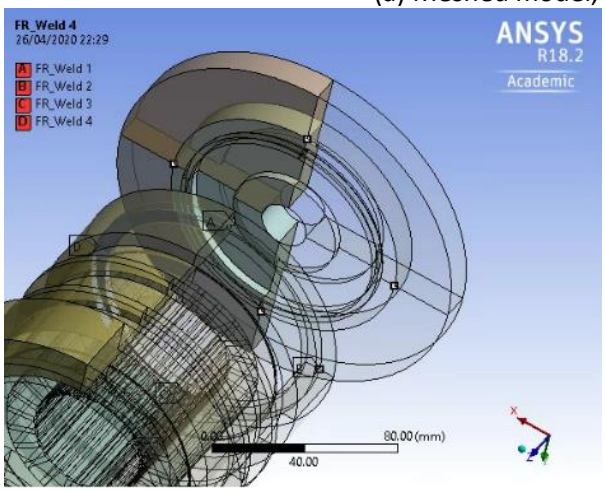

(b) Weld points on front plate

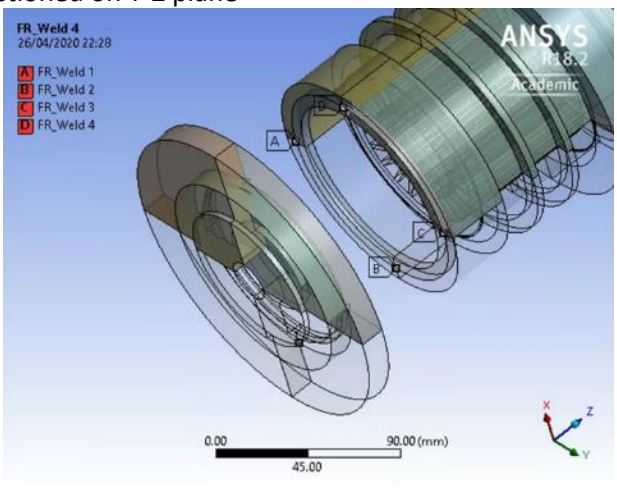

(c) Weld points on front face of frame

Fig. 5.2.13 Meshed model and weld points on the frame and front plate.

With the model in place the frictionless support constraint is applied to the rear of the machine to replicate the test condition and the modal analysis is run. The results can be seen in Fig. 5.2.14 and the actual values and errors are shown in Table 5.2.4.

ISO X-Y cross section Z-Y Cross section

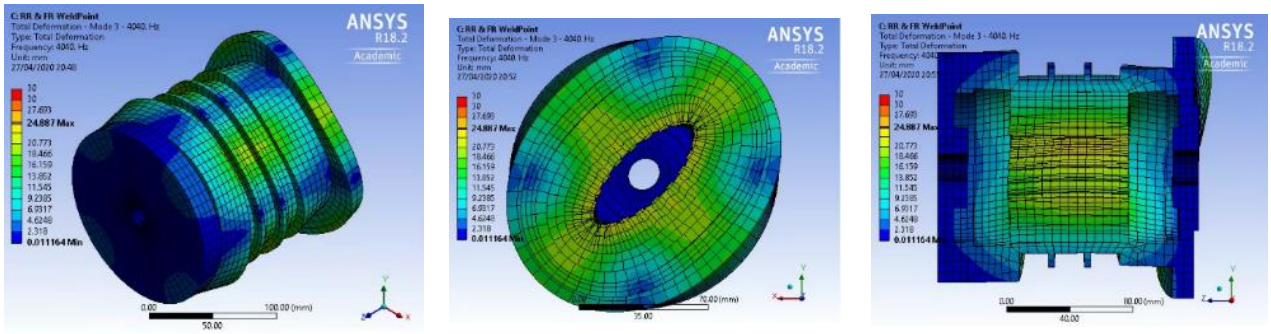

(a) Mode 2,0 @4040Hz

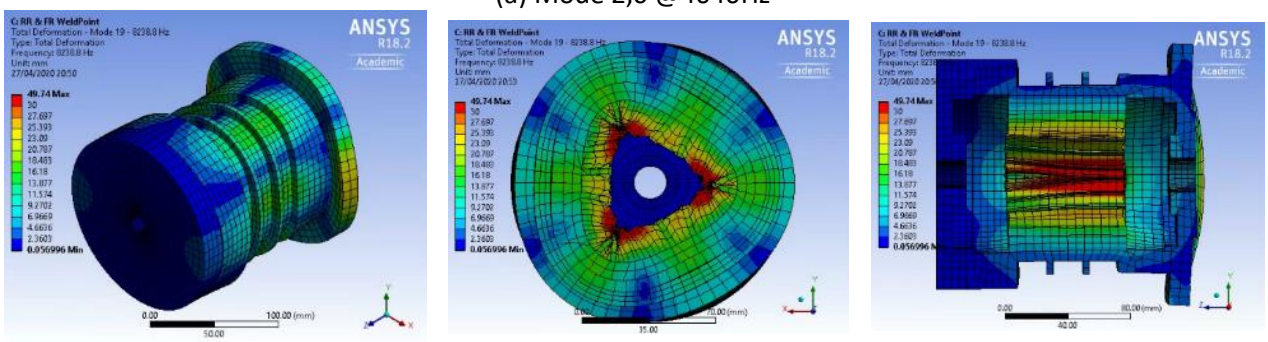

(b) Mode 3,0 @8238Hz

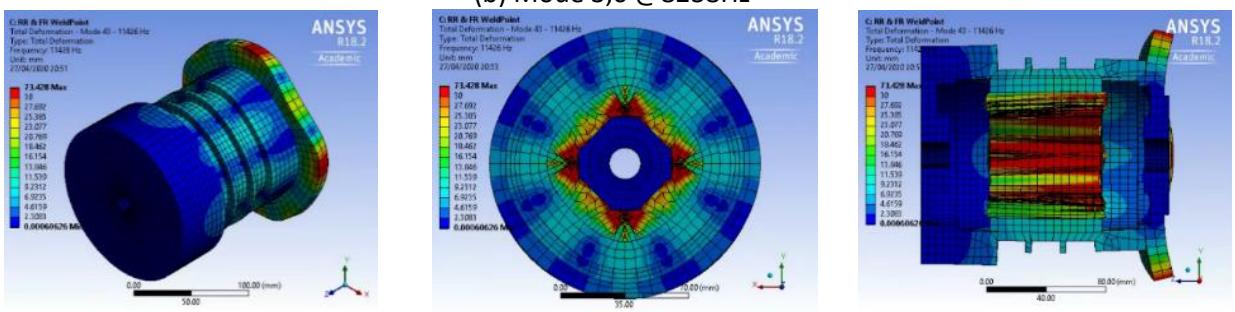

(c) Mode4,0 @11426Hz

Fig. 5.2.14 Key modes generated.

Table 5.2.4 Comparison of measured modal frequencies with final FE model of the wound stator in frame

Mode	Measured (Hz)	FE calculation (Hz)	Error
2,0	4079	4040	0.96%
0,2*	4895	5169	-5.49%
3,0	8198	8238	-0.49%
4,0	11549	11426	1.07%

*= assumed mode from analysis of measured data

The circumferential modal frequency results show good agreement with the measured data. Fitting the top plate changes the shape of the structure from an open-ended frame to a full closed cylinder stiffening the structure and shifting the modal frequencies which is reflected well in both the measured and FE calculated results.

The omission of the coolant shell means the front end of the frame onto which the front plate is fixed is much thinner that the rear leading to an asymmetry that is reflected in a high mode at ~4900Hz on the

measurement which was assumed to be a mode 2 axial mode. From the FE the nearest mode to this occurs at 5169Hz the mode shape of which is shown in Fig. 5.2.15.

ISO X-Y Cross section Z-Y Cross section

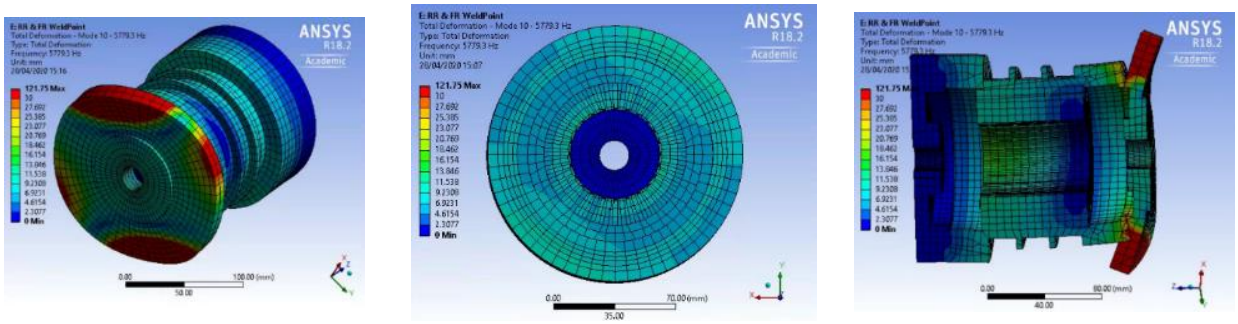

Fig. 5.2.15 Bending mode of the front plate flange at@5169Hz.

What the mode shows is that the front face plate of the assembly hits a bending mode, at 5169Hz which has a knock on effect to the rest of the structure making the top end move and inducing motion into the rest of the structure in a shape similar to an axial mode 2.

One reason for this may be that the frictionless support used up to this point may not accurately represent the support this model. On the rear of the machine there are four M4 socket head cap screws that protrude from the back of the machine. Whilst not a concern in the previous case it may be that the extra weight from the front plate has caused the foam on the support mat to bottom out, meaning the weight of the machine rests on the four screw heads instead of the foam distributing the load around base of the machine. To check whether the mounting is a concern 4 different test calculations were run with the following settings

- Fixed support applied to rear face plate
- Frictionless support applied to rear face of rear plate
- Shapes representing the rear bearing plate screws added and constraint added to screw head
- Free bodied, no support applied

The range of mountings goes from one extreme with the fixed support (e.g. the machine is securely fixed to the test bench) to free bodied wherein the structure is floating in space. The rear bearing screws are represented by extruding small cylinders from the P.C.D of the bearing plate. The dimensions are derived from [EE00] which utilises ISO 4762 for the M4 hexagon socket head cap screws used on the actual machine. The location of the screws is highlighted in Fig. 5.2.16.

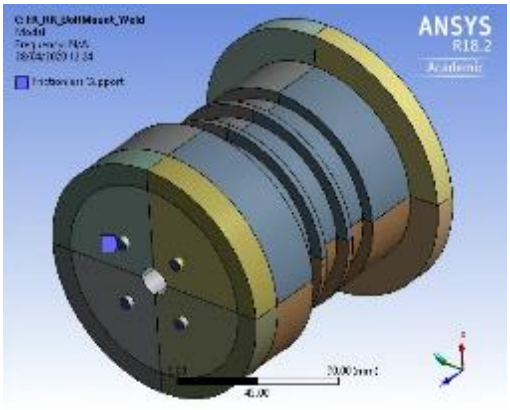

Fig. 5.2.16 Addition of the bolt heads for the rear bearing plate as mounting point.

With the models in place the modal analysis is run for each case and compared with the measured data and the initial frictionless constraint. Fig. 5.2.17 shows the resultant frequency modes and Table 5.2.5 gives the values and errors compared to the measured data.

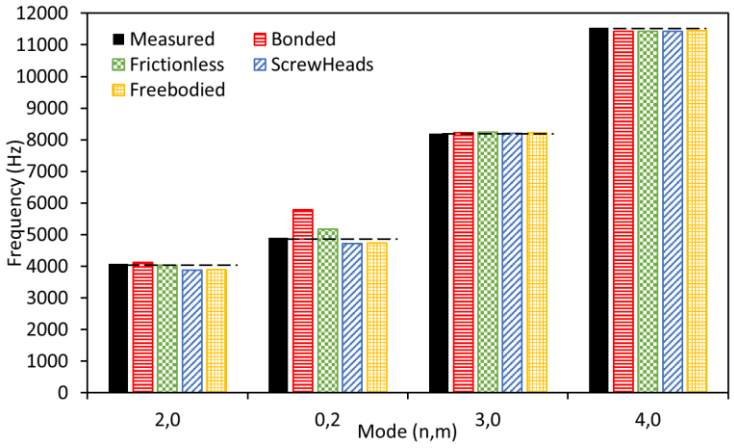

Fig. 5.2.17 Influence of the structure support methodology on the key modes.

Table 5.2.5 Resultant values from structure support comparison study

Mode	Measured	Bonded Support		Frictionless Support		Screw Head		Free Bodied	
		Freq (Hz)	Error (%)	Freq (Hz)	Error (%)	Freq (Hz)	Error (%)	Freq (Hz)	Error (%)
2,0	4079	4127	-1.18%	4040	0.96%	3873	5.05%	3900	4.39%
0,2	4895	5779	-17.94%	5169	-5.49%	4719	3.69%	4728	3.51%
3,0	8198	8230	-0.39%	8238	-0.49%	8200	-0.02%	8215	-0.21%
4,0	11589	11427	1.06%	11426	1.07%	11431	1.02%	11446	0.89%

The resultant mode shapes at the concern axial mode frequency shown in Table 5.2.5 are captured to allow comparison to be drawn. Fig. 5.2.18 shows the results.

ISO X-Y cross section Z-Y Cross section

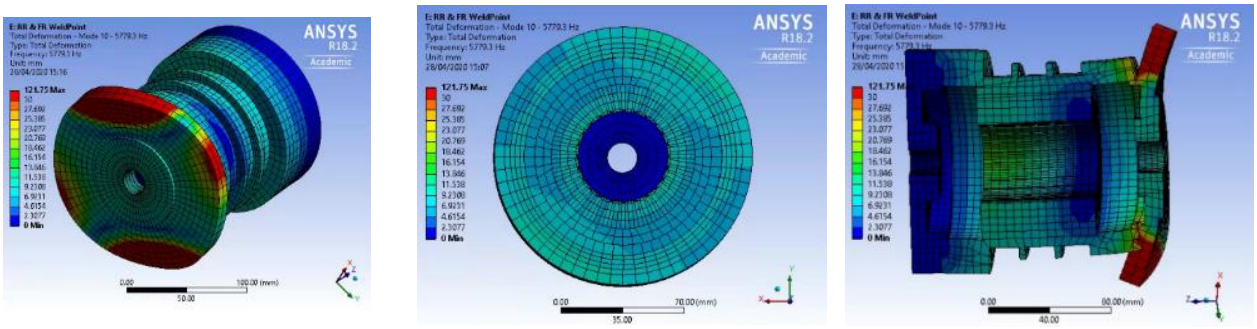

(a) Bonded support, FR plate bending mode @ 5779Hz

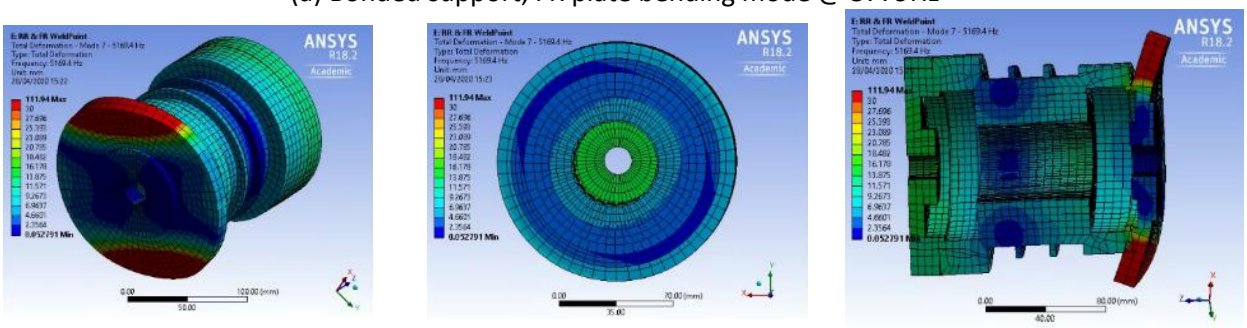

(b) Frictionless support, FR plate bending mode @ 5169Hz

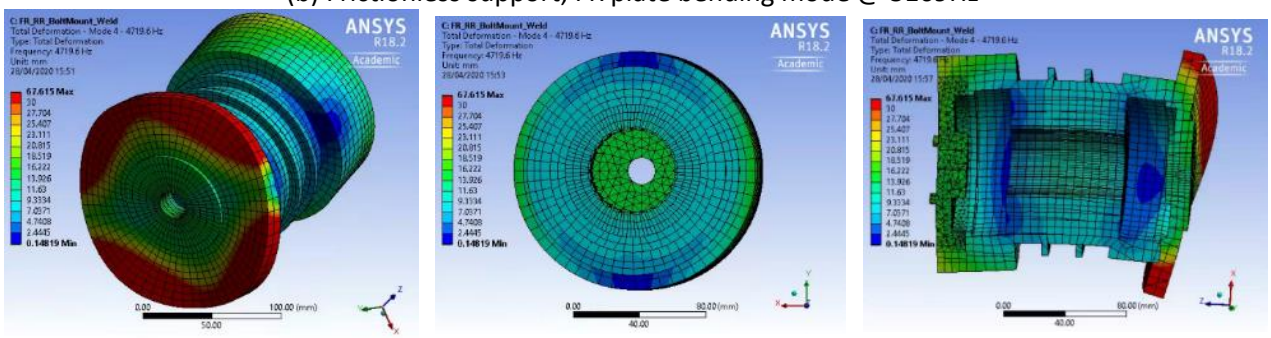

(c) Screwhead support, FR plate bending mode @ 4719Hz

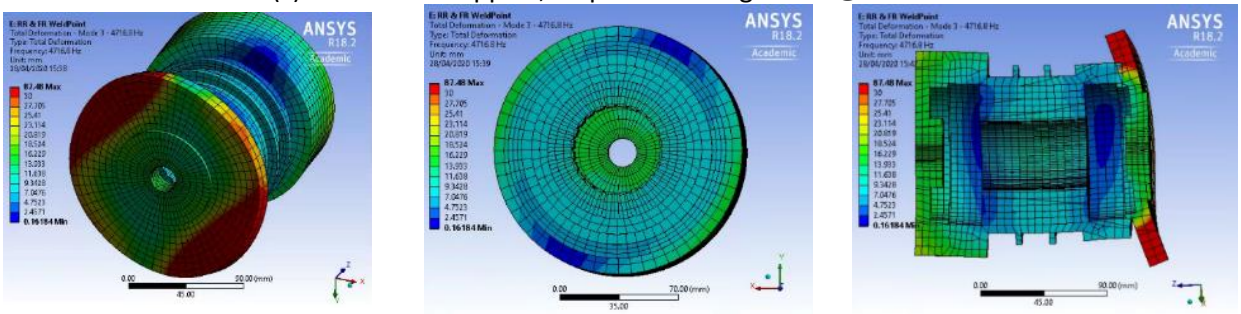

(d) Free bodied model, FR plate bending mode @ 4728Hz

Fig. 5.2.18 Key modes generated for FE modal analysis of the frame with rear plate attached.

The support chosen clearly has an influence on the excitation of the plate with the frequencies ranging almost 1 kHz between the extreme cases of the bonded support and the free-bodied. Based on the mode shapes the bolt mounted and free bodied model (Figs. 5.2.18 (c) and (d)) give the clearest indication of the mode shape of the structure.

From Table 5.2.5 the influence on the circumferential mode 2 can be observed to swing by ~300Hz between the extreme cases with the initial frictionless support on the rear face plate maintaining the closest alignment to the measured data. Mode 3 and Mode 4 are relatively unaffected by the support methodology.

Therefore, from the FE analysis the root cause of the peak at ~4900Hz is the excitement of the front plate mounting flange which has the knock-on effect of moving the rest of the machine structure to form an axial mode. The lack of support due to the omission of the coolant shell means the face plate is much freer to move so the input on the structure is greater than it would otherwise be. This is further backed up by the fact this mode was not observed in any of the subsequent measurements.

5.2.4 Modelling the coolant shell linkage

The final assembly can now be completed by adding the coolant shell to the assembly. The meshed model can be seen in Fig. 5.2.19.

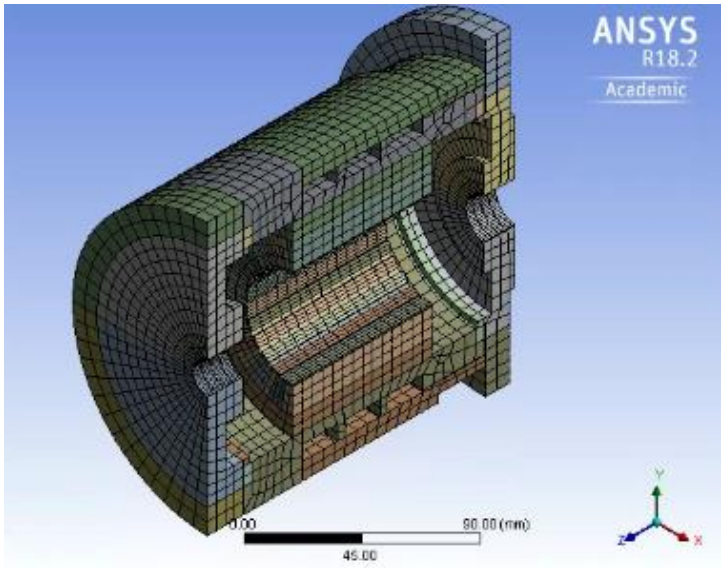

Fig. 5.2.19 Meshed full model (Y-Z section).

The welded points to represent the bolted joints are utilised from the previous models and the model run in modal analysis. The addition of the new shape increased the shape complexity so the mesh convergence operation is run once more to obtain the mesh in Fig. 5.2.19 the resultant modes can be seen in Fig. 5.2.20.

ISO X-Y cross section Z-Y Cross section

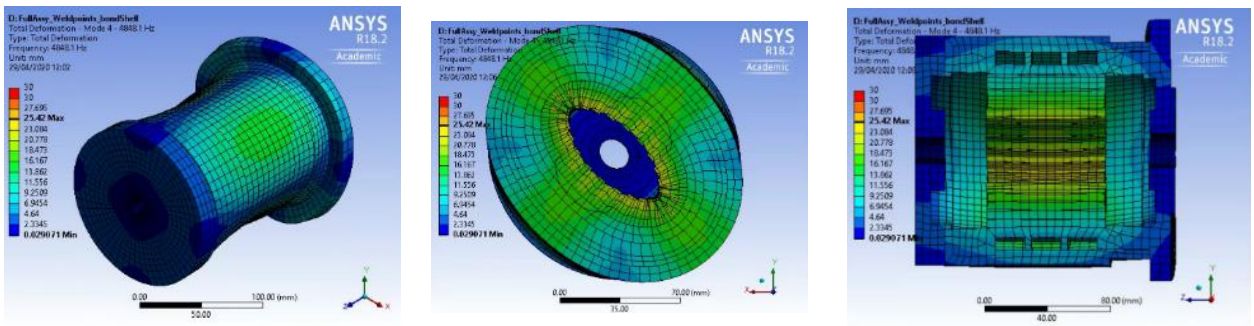

(a) Full assembly mode 2,0 @ 4848Hz

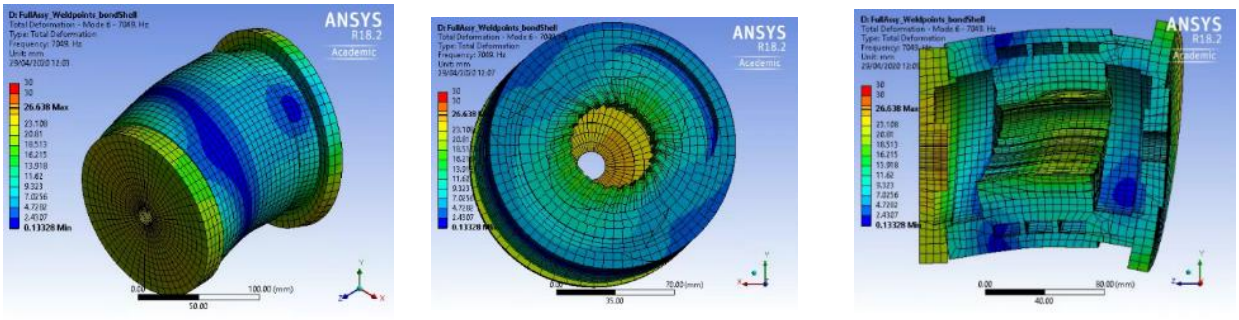

(b) Full assembly mode 0,2 @ 7049Hz

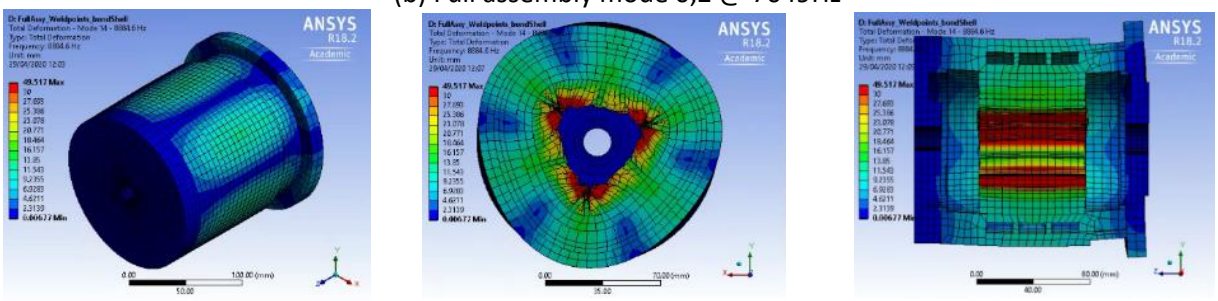

(c) Full assembly mode 3,0 @ 8984Hz

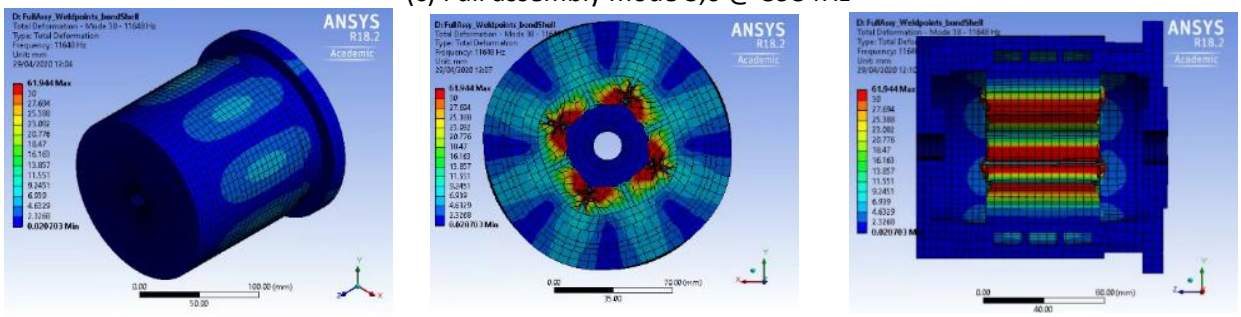

(d) Full assembly mode 4,0 @ 11648Hz

Fig. 5.2.20 Key modes generated for FE modal analysis of the frame with rear plate attached.

Table 5.2.6 comparison of modal frequencies for full assembly with bonded contacts between the coolant shell and joined parts

Mode	Measured	All bonded	Error Vs measured
2,0	4160	4848	-16.57%
0,2	6380	7049	-17.02%
3,0	8350	8984	-7.6%
4,0	11685	11648	0.32%

The measurement of the full machine was very noisy with mode 2,0 being the most prominent mode and some hints towards modes at ~6024Hz, ~8000Hz and ~11600Hz although amplitudes were low for all. The FE calculation results show the equivalent modes to be much higher frequencies than the measured with considerable errors indicating the addition of the coolant shell has rendered the structure far too stiff. Interestingly the mode 4,0 has good alignment, a trend that has followed the entire assembly process, more than the other modes this mode appears to be strongly led by the stator structure so as such modifications to the surround structure appears to have less impact than the lower modes.

5.2.4.1 Reducing the system stiffness

When importing a model into the ANSYS® mechanical workbench the system will automatically generate contacts between the sub-components of an assembly and default those contacts to “bonded” type, which was described in the previous section. The bonds generated are shown in Fig. 5.2.21.

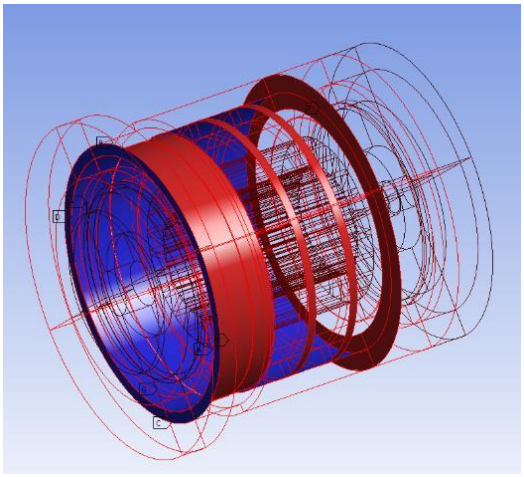

Fig. 5.2.21 Coolant shell contact regions automatically generated by ANSYS® mechanical.

What the image in Fig. 5.2.21 shows is that all surfaces within a given proximity of the shell inner bore and the frame and front face plate are automatically bonded with the nearest surface of the nearest part.

This is not reflective of the actual structure of the assembled machine; not every face of the coolant shell inner bore forms such a strong bond with the features on the outer diameter of the main casing, to do so would make it very difficult to assemble the machine. This means that the automatically generated contacts are rendering the structure unrealistically stiff. The full assembly drawing of the motor, shown in Fig. 5.2.22, highlights the key contact points between the frame (Case Main) and the coolant shell.

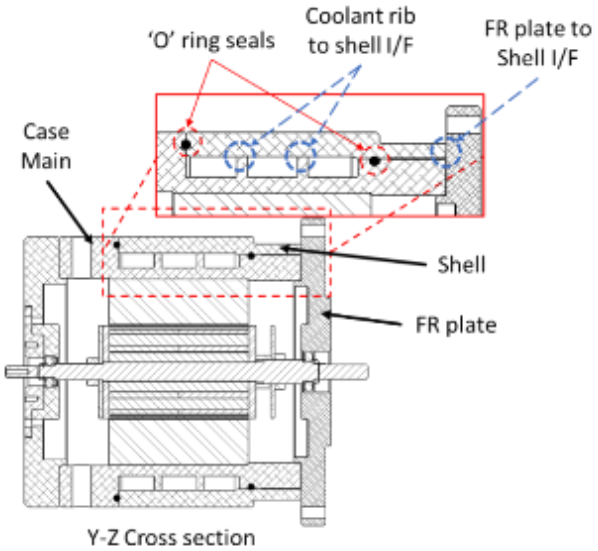

Fig. 5.2.22 Full assembly drawing of baseline machine showing the actual contact interfaces between the shell and the rest of the structure.

From Fig. 5.2.22 it can be seen that there are essentially 2 main types of fit between the outer coolant shell and the rest of the machine assembly:

- Cylindrical fit: tolerance between the outer OD of the CaseMain part and the inner IDs of the shell.
- Axial pressure fit: front plate forces shell axially into 'O' ring located on rear face of rear main.

Within the ANSYS® tool the interfaces highlighted in Fig. 5.2.22 can be achieved on the simplified model by isolating each contact region and assigning different contact characteristics according to the nature of the interface between the parts, which is summarised in Table 5.2.7.

Table 5.2.7 Overview of the contact interfaces between the coolant shell and the rest of the motor assembly.

Rear 'O' ring interface		Front plate clamp to shell	
CaseMain RR	Shell RR face	FR plate RR face upper	Shell FR plate
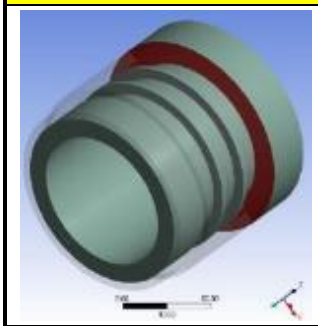	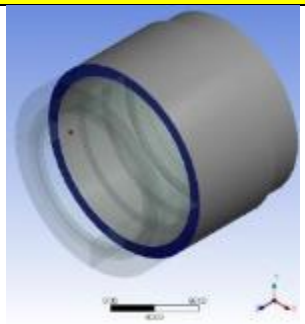	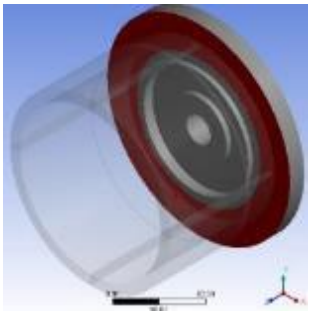	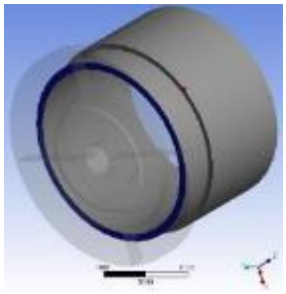
Contact interface material	**Target interface material**	**Contact interface material**	**Target interface material**
Nitrile	Aluminium	Aluminium	Aluminium
Contact control: pressure from bolting of FR plate to CaseMain.		Contact control: pressure from bolting of FR plate to CaseMain.	
Main coolant channel bore interface		**Front 'O' ring interface**	
CaseMain Ribs OD	Shell inner bore	CaseMain 'O' ring housing	Shell 'O' ring bore
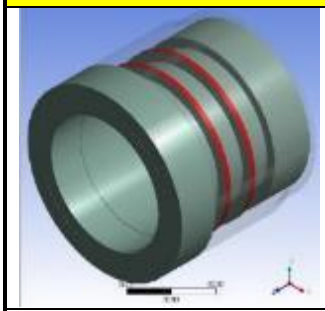	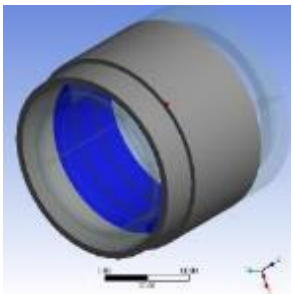	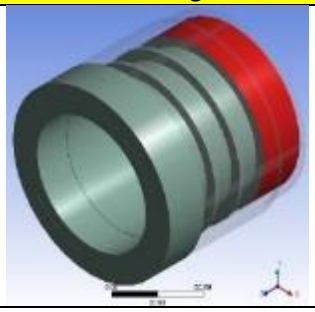	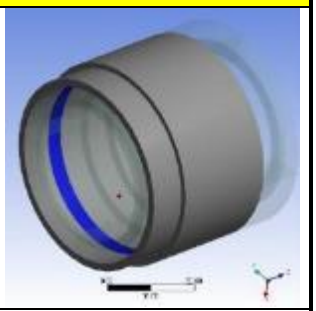
Contact interface material	**Target interface material**	**Contact interface material**	**Target interface material**
Aluminium	Aluminium	Nitrile	Aluminium
Cylindrical & concentricity tolerance between shell ID and ribs OD.		Interference fit between shell ID and 'O' ring.	

Manual assignment of the contact areas and the contact type is therefore more prudent.

From the list of ANSYS® contact types (see Table 5.2.2) the frictional contact method was deemed the best methodology to handle the 'O' ring interfaces and the fitting between the bore as in both these cases the motion of the shell in relation to the case main is dictated by the interference between the two parts. Using

the frictional contact method allows the coefficient of static friction between the different parts to be adjusted to allow for a more accurate representation of the assembly.

The coefficient of friction is used to describe the force of friction between two objects when a normal force is applied. It is utilised in the following equation (5.2)

$$F_f = \mu_s F_n \tag{5.2}$$

where F_f is the frictional force, μ_s is the coefficient of friction and F_n is the normal force. The effect is to create a non-linear dynamic of an object as highlighted in Fig. 5.2.23 [ETB04].

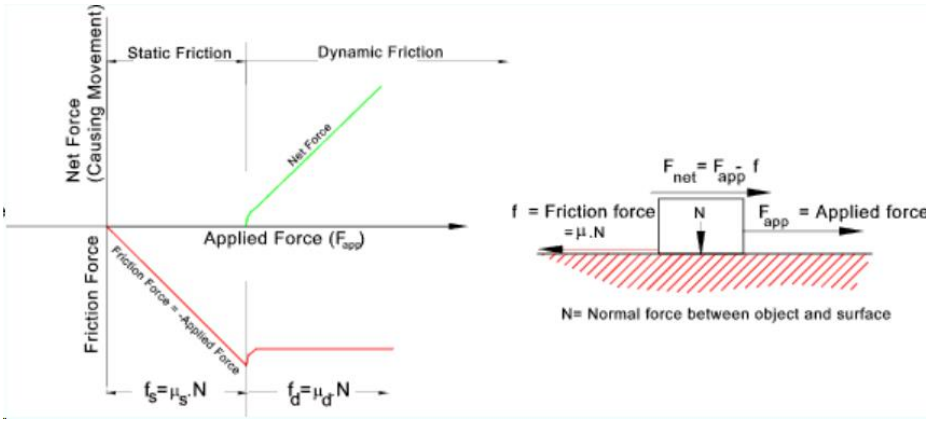

Fig. 5.2.23 Influence of friction on the dynamics of a part [ETB04].

The coefficient of friction ranges from 0 to 1, where 0 is no friction at all and 1 is where the frictional force equals the normal force. This is a general guide however as all objects placed together will have some friction so can never reach zero and some objects can have coefficients of friction much greater than one, for example some types of silicon rubber can have coefficients of friction well above 1 [ETB04].

The influence of a variation of the coefficient of friction on the part can be seen in Fig. 5.2.24 where μ_s for the different joints is varied to observe the influence the parameter has on the overall stiffness of the machine.

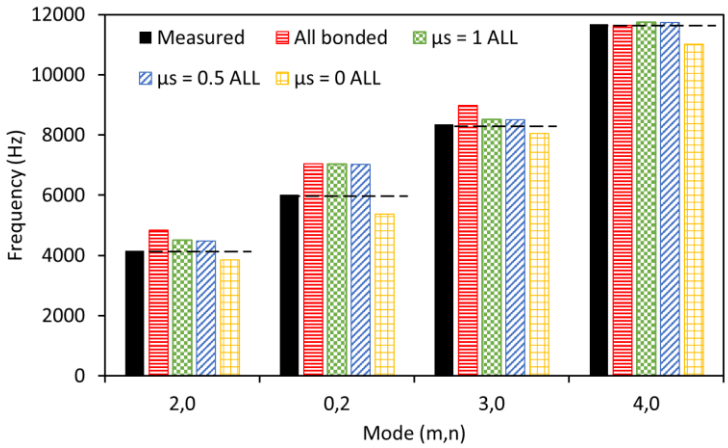

Fig. 5.2.24 Comparison of the first 3 modal frequencies and friction coefficient of the contact between the shell and the machine assembly.

Table 5.2.8 summarises the values of the data in Fig. 5.2.24.

Table 5.2.8– influence of frictional contact type with varying coefficient of friction.

Mode	Measured	Bonded contact	Frictional contact (ALL contact points)		
			$\mu_s = 1$	$\mu_s = 0.5$	$\mu_s = 0$
2,0	4160	4848	4497	4485	3857
0,2	6430	7049	7026	7015	5366
3,0	8350	8984	8515	8500	8041
4,0	11685	11648	11736	11736	11013

As can be observed the move from bonded contact type to the frictional with $\mu_s = 1$ sees the frequency drop significantly. Further reductions in μ show the drop in stiffness is distinctly non-linear as between $\mu_s = 1$ and $\mu_s = 0.5$ the drop in frequency is small but between 0.5 and 0 the drop in stiffness is significant. At $\mu = 0$ the stiffness drops significantly below the measured. This indicates that the assumption that the bonded methodology was over stiffening the structure was correct and that accuracy can be increased by utilising the frictional contact type to tune the assembly to match the measured. The results also show the axial mode to be more sensitive to the different friction coefficients than the circumferential modes.

The results shown above are from a simplified study where in the coefficient of friction was the same for all the different contact regions between the shell and the rest of the motor structure. To improve the fidelity μ_s of the different contact regions needs to be adjusted according to the type of contact and the materials involved

Obtaining the coefficient of friction is dependent on several factors and is best found through measurement of the exact piece to be modelled but fortunately as with many of these things the most common materials have empiric data available. Using material databases [ETB04] and [EL18] a range of the coefficient of friction values for a very large array of different materials can be found, a short sample of which is given in Table 5.2.9.

Table 5.2.9 Static coefficient of friction for sample materials [ETB04]

Materials and material combinations		Static frictional coefficient μ_s	
		Clean & dry surface	Lubricated surfaced
Aluminium	Aluminium	1.05 – 1.35	0.3
Brake material	Cast iron	0.4	
Car Tyre (general)	Asphalt	0.72	
Rubber	Dry Asphalt	0.9	
Rubber	Wet Asphalt	0.25 - 0.75	
Rubber	Dry Concrete	0.6 – 0.85	
Rubber	Wet Concrete	0.45 – 0.75	
Rubber	steel	0.64 – 0.9	

The values in Table 5.2.9 are best viewed as a guide. “Aluminium” or “Rubber” can cover a wide range of different materials and composites plus machining aspects such as the surface texture or the nature of the fit between the components means that the actual coefficient of friction can vary by quite some margin from

the values in the table. Using the optimisation functionality within ANSYS® Workbench the empiric values in Table 5.2.9 can be used as the initial start point for a full optimisation of the different contact points using Mode 2,0 (4160Hz) with an error of +/-2% as the target of the process. The materials for each contact point, the type of fit and the range of coefficient of friction values used are shown in Table 5.2.10.

Table 5.2.10 Coefficient of friction based on empiric data from [ETB04], [EL18]

Component		Material		Fit type	Coefficient of friction range
Contact	Target	Contact	Target		μ_s
Frame rear	Coolant shell rear face	Nitrile	Aluminium	Interference	0.6 to 1
Front plate face	Coolant shell front face	Aluminium	Aluminium	Interference	0.9 to 1.35
Frame front region outer diameter	Coolant shell 'o' ring interface inner diameter	Nitrile	Aluminium	Transition	0.1 -> 0.4
Coolant rib outer diameter	Coolant shell inner diameter	Aluminium	Aluminium	Clearance	>0.01

From Table 5.2.10 the range of coefficient values are based on the fit and the materials at each interface point. The different fits are dictated by the structure. The front and rear faces of the coolant shell have an interference fit with the front plate and the rear portion of the frame respectively which is derived by the axial force of the front plate pushing the coolant shell in place using the 4 bolts. This creates a strong link, but as was previously observed not a bonded link so a high coefficient of friction is required. Between the outer diameter of the coolant ribs on the main frame and the inner diameter of the main bore on the coolant shell the fit is a clearance fit to allow the part to slide over easily during fitment. There is some resistance during the fitment procedure indicating some contact, but it is relatively minor hence the low range provided. The link between the 'O' ring on the outer bore of the front region of the frame and the inner bore of the coolant shell is necessarily tight to ensure a good seal and prevent leakage, but not so tight that special press fit tools or similar are required, and hence the tight transition fit. Using these values, a NLPQL (Nonlinear Programming by Quadratic Lagrangian) optimisation method is utilised from the ANSYS® Workbench tool set. This method is well suited where optimisation has a small number of objectives and low number of parameters such as the case here. The optimised values are shown in Table 5.2.11.

Table 5.2.11 Optimised coefficients of friction for the attachment of the shell to the frame

Components		Optimised coefficient of friction
Contact	Target	μ_s
Frame rear	Coolant shell rear face	0.5
Front plate face	Coolant shell front face	0.95
Frame front region outer diameter	Coolant shell 'O' ring interface inner diameter	0.1
Coolant rib outer diameter	Coolant shell inner diameter	No contact

Interestingly the coefficient of friction between the 'O' ring on the outer diameter of the front region of the frame proved to be the most sensitive with values of above 0.1 strongly influencing the circumferential modes of the structure. The full results set of key modes calculated is shown in Fig. 5.2.25.

ISO X-Y cross section Z-Y Cross section

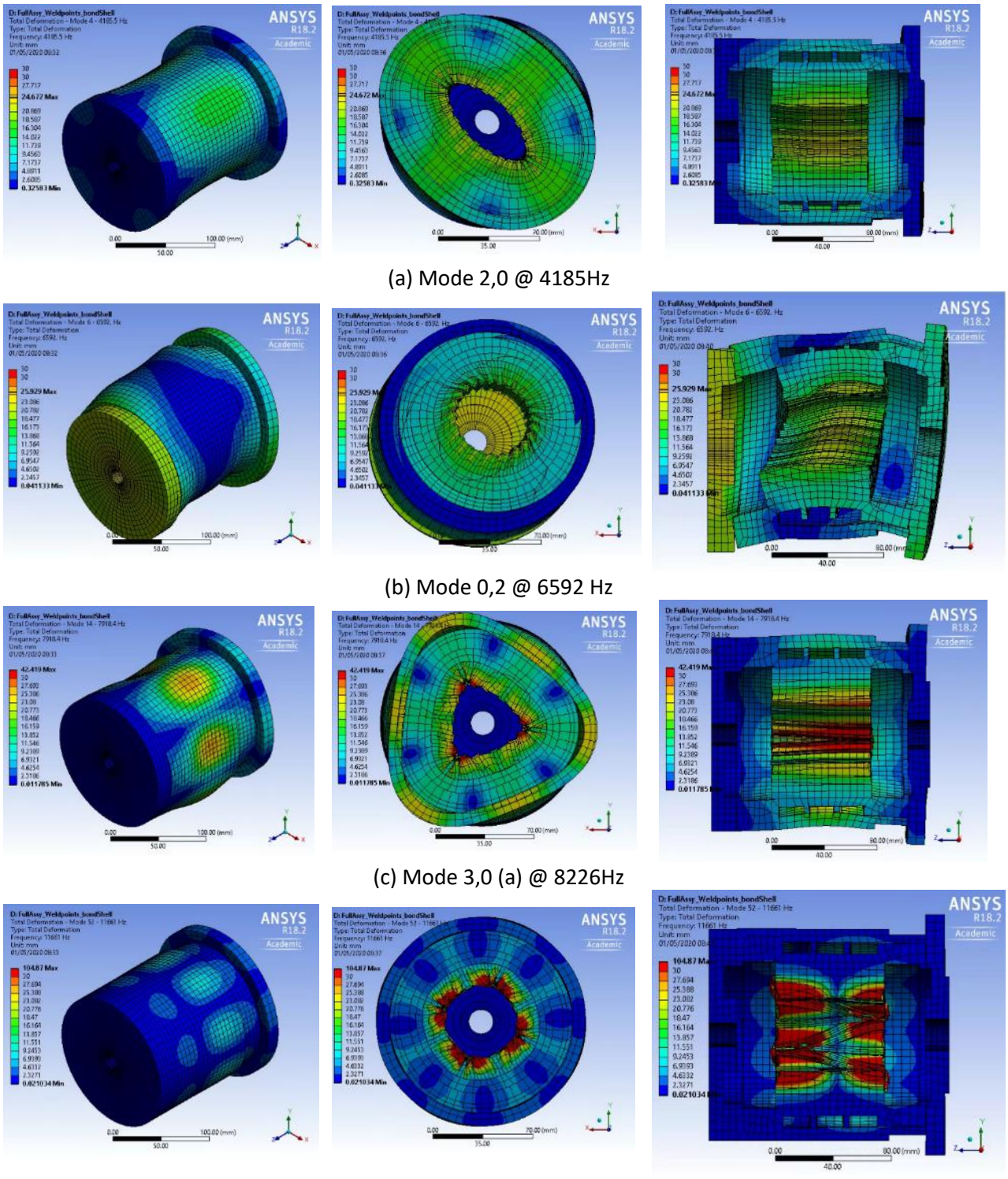

(a) Mode 2,0 @ 4185Hz

(b) Mode 0,2 @ 6592 Hz

(c) Mode 3,0 (a) @ 8226Hz

(d) Mode 4,0 @ 11661Hz

Fig. 5.2.25 Full Assembly with optimised friction settings for shell interface.

The results are compared with the measured and default bonded contact setting and shown in Fig.5.2.26.

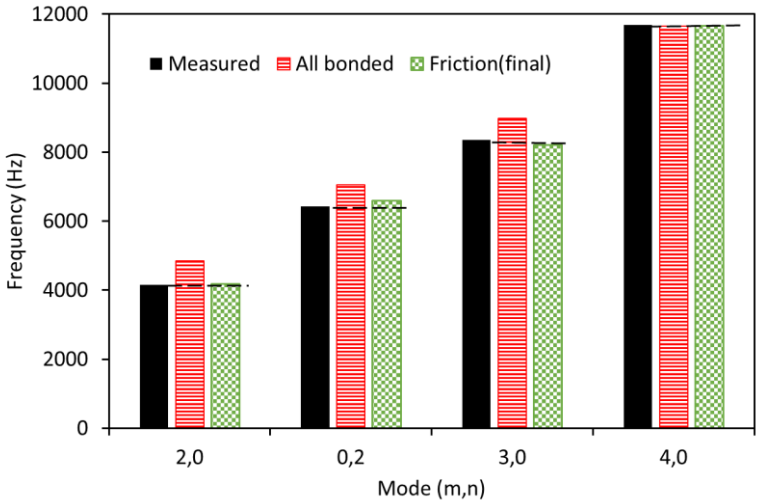

Fig. 5.2.26 Comparison of Friction contact type with optimised μ_s versus bonded contact type and measured data.

The values of the frequency modes compared above are shown in Table 5.2.12 below.

Table 5.2.12 Comparison of measured with the initial bonded type contact and frictional type

Mode	Measured frequency	Bonded		Frictional type (optimised)	
		Frequency	Error	Frequency	Error
2,0	4159	4848	-16.6%	4185	-0.6%
0,2	6430	7049	-10.1%	6592	-2.5%
3,0	8350	8884	-10.2%	8226	1.5%
4,0	11685	11648	0.3%	11661	0.2%

From the results the errors for the optimised frictional type has been dropped significantly for all modes to within acceptable values.

5.2.5 Representing the rotor

The measured data showed the influence of the rotor was minor on the circumferential modes of the machine as was discussed during the measurement phase the small difference these modes between the case with no rotor and the case with the rotor installed could as easily be attributed to measurement error due to the fact the front plate had to be removed and re-attached to allow the rotor to be installed. The only clear difference was the identified axial mode which dropped by around 5.7% from ~6430Hz to ~6060Hz. That the frequency dropped is interesting, the expectation would be the addition of the rotor would lead to a stiffening of the structure due to the hardened steel shaft utilised and bearings therefore a slight increase in the modal frequency. That the frequency dropped indicates the increased overall mass of the machine has had a big effect but the stiffness less so. The reasoning for this becomes clear when the constraints for the bearings are considered, highlighted in Fig. 5.2.27.

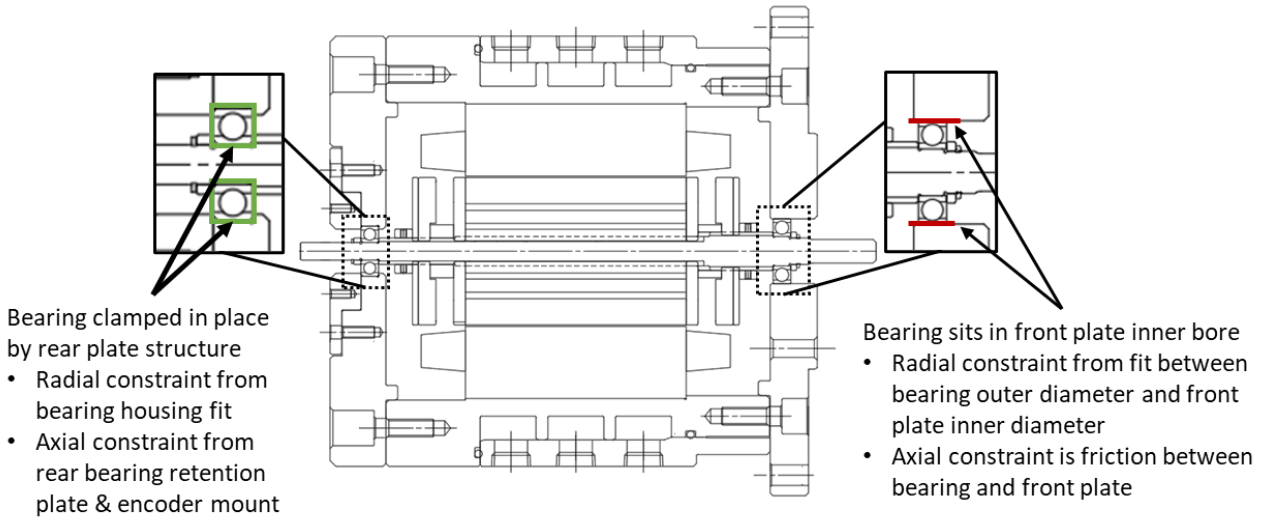

Fig. 5.2.27 Assembly drawing of the baseline machine highlighting the bearing retention methodology.

From Fig. 5.2.27 it can be seen that the rotor is relatively free to move in the axial direction, the motion is dictated by the friction between the outer diameter of the bearing and the inner diameter of the bore on the front plate which is much lower than if both bearings were clamped. It is also clear from the results that for this machine at least the bearings have little influence on the radial stiffness of the machine.

To represent the rotor there are two methods used:

1. Create a simple representation of the rotor and add to the assembly in the correct position.
2. Represent the core as a mass split between the front and rear bearing housings.

For (1) a simple shape is used rather than using the full rotor drawing to mitigate the additional processing load and eigenvalues this would generate. Rather 2 bearing shapes are linked by a shaft of the maximum diameter of the output shaft is used and the mass of the rotor core is added as an applied mass within ANSYS®. The setup is shown in Fig.5.2.28.

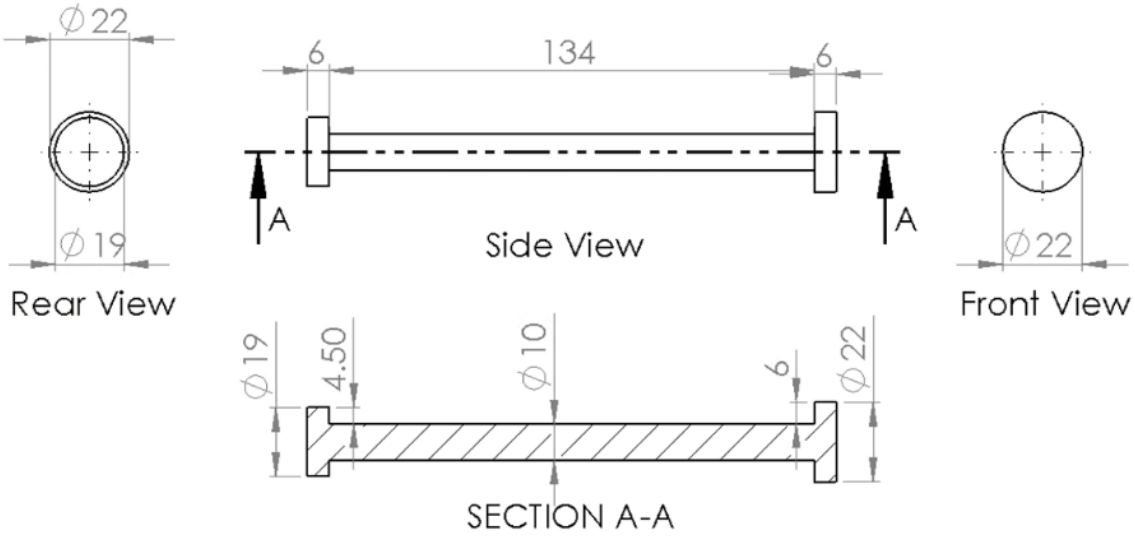

(a) 2D drawing of simple rotor

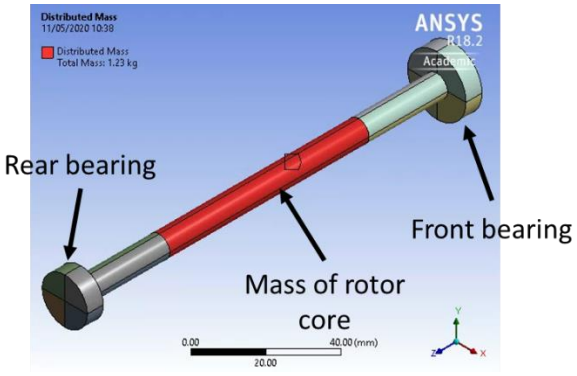

(b) 3D model showing mass distribution. Mass is added to where the active length of the rotor core sits

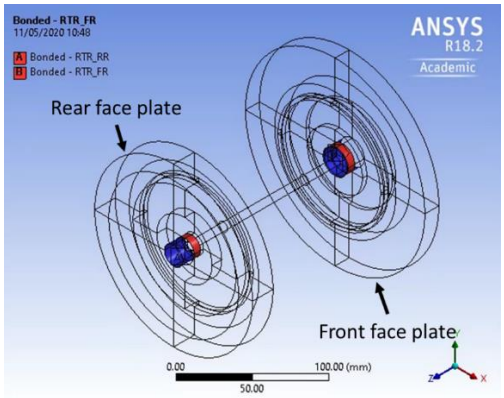

(c) Constraints applied to the rotor in the front and rear end plates

Fig. 5.2.28 Application of simple rotor shape to the machine model.

In Fig. 5.2.28 it can be seen that the shaft has no output shafts from the machine, the rotor ends with the bearings. Previous experience has shown the unconstrained output shafts can generate large number of irrelevant eigenvalues greatly increasing the processing time, and thus the model omits these features. The materials used in the part are shown in Table 5.2.13.

Table 5.2.13 Shaft material specification

Material	Shaft	Units
Type	EN43B	-
Hardness	HRC40	
Density	7850	kg/m^3
Young modulus	$2.03x10^5$	MPa
Poisson's ratio	0.29	-
Shear modulus	$7.86x10^5$	MPa
Tensile yield strength @HRC 40	1280	MPa

The material is applied to the full shape. To further save on processing overhead the bearings are assumed to be rigid and of the same material as the shaft. In terms of the mass, the core is weighed on a set of scales and was found to have a mass of 1.23kg.

Representation of the rotor as mass is a much simpler process, the distributed mass tool seen in Fig. 5.2.28 (b) is used to split the mass of the rotor across the front and rear bearings. The assumption made here is that both bearings support the same mass. The setup can be seen in Fig. 5.2.29.

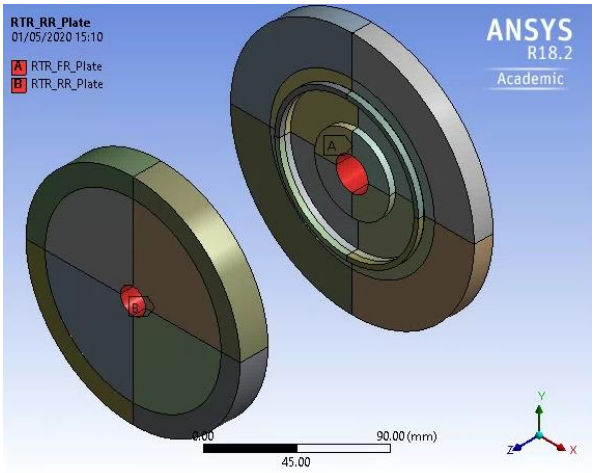

Fig. 5.2.29 Representation of the rotor mass on the inner bore of the front and rear face plates of the machine.

The modal analysis is run for the case with the simple rotor model is added and the mass only and the results are shown in Fig. 5.2.30 and Table 5.2.14.

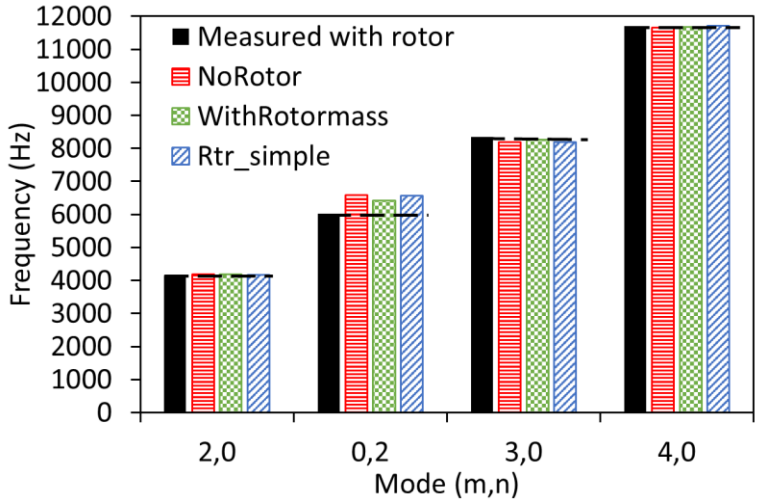

Fig 5.2.30 Comparison of measured and FE calculated modal frequencies with the rotor as a simple shape or represented as a mass.

The frequency values from the graph in Fig. 5.2.30 are shown in Table 5.2.14. Note in this table the values for the frictional contact between the front bearing and front plate are used as the results were identical to those of the bonded and better represents the condition of the front bearing in the inner bore of the front plate.

Table 5.2.14 Comparison of measured modal frequencies and FE calculated with rotor mass added to the face plates of the machine

Mode	Measured	No rotor		Rotor mass added only		Simple rotor shape	
		Frequency (Hz)	Error Vs measured	Frequency (Hz)	Error Vs measured	Frequency (Hz)	Error vs measured
2,0	4135	4183	-1.0%	4195	-1.3%	4174	-0.7%
0,2	6050	6592	-9.6%	6411	-6.6%	6564	-9.1%
3,0	8342	8190	1.8%	8260	1.0%	8185	1.9%
4,0	11700	11661	0.3%	11671	0.2%%	11671	0.2%

The results show that like the physical testing the rotor has had very little influence on the radial modes. Where the greatest error lies is in the axial mode identified with the case with the rotor mass being added As discussed in the measurement phase the measured drop in frequency for this mode maybe more due to the disruption to the structure caused by the rotor insertion process rather than a direct influence of the rotor. The increased mass does have a significant influence on the axial mode, dropping ~1kHz from the case without the rotor fitted. This drop is almost double that of the measured results indicating that the stiffness of the bearings and rotor shaft do indeed play a role in the performance. Given that the circumferential modes of the model are so closely matched for all shapes and that the error on the identified axial mode is less around 5% for the mass only option the benefits in applying the additional effort of adding a more complex rotor model do not outweigh the costs in overall system complexity and the knock-on effects to processing time. In addition, adding the mass only has the benefit of having negligible impact on the processing time of the FE calculation as the distributed mass tool has no influence on the mesh of the model.

5.2.6 Mounting the machine

The final stage in the modelling is the case where the machine is mounted to the test rig. Given that the assembly has been developed and tuned this step represents the most straight forward analysis in terms of the setup. The mounting of the machine is adjusted from the frictionless support attached to the rear of the machine from the previous analysis to 2 different supports on the front plate.

- Fixed support on the front face of the front plate representing the link to the face of the dynamometer mounting bracket
- Cylindrical support representing the link between the centring feature on the front plate of the machine assembly and the through hole on the Dynamometer mounting bracket

The two constraints are shown in Fig. 5.2.31.

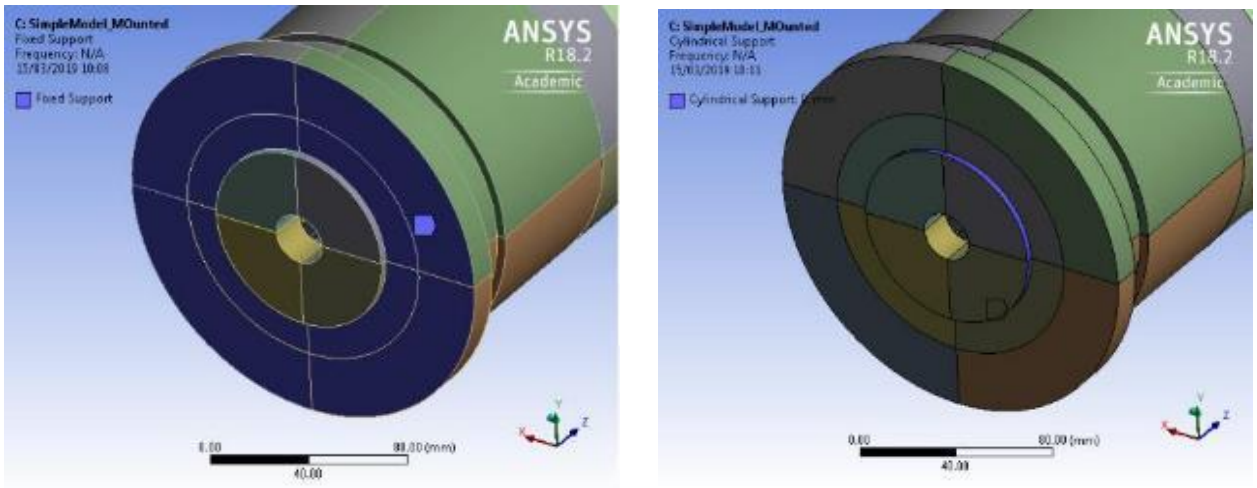

(a) Fixed support on front plate face

(b) Cylindrical support on front plate location feature

Fig. 5.2.31 Constraints applied to model for mounted only condition.

The connection between the centering feature is quite loose and is designed to ease the mounting of the machine to the rig, and it only constrains the machine in the radial direction. Hence, the cylindrical is set to allow axial motion, tangential motion but not radial. The axial and tangential constraints are effectively controlled by the fixed support on the front plate.

With the constrains in place the FE calculation can once again be run and the resultant modal frequencies compared with the measure data.

ISO X-Y cross section Z-Y Cross section

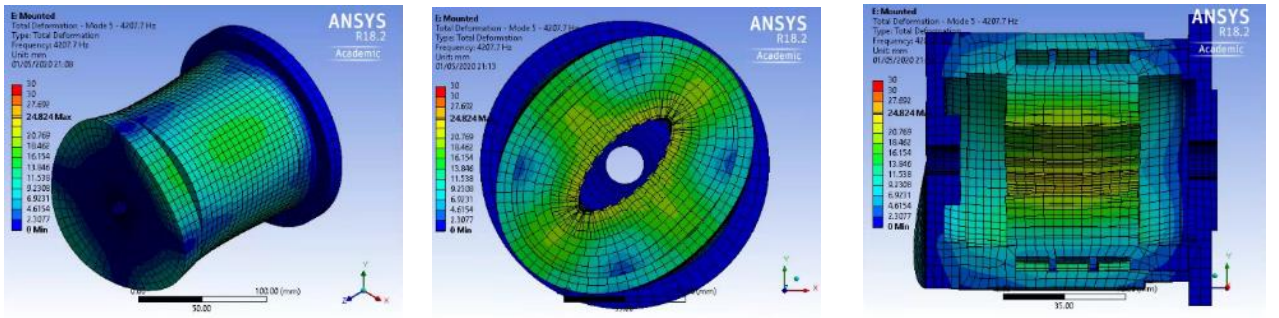

(a) Mode 2,0 @ 4207Hz

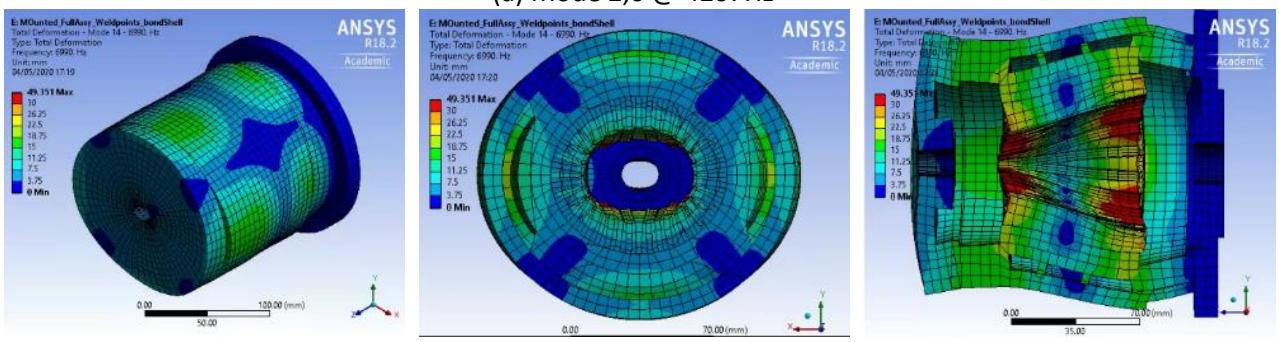

(b) Mode 2,1 @6990Hz

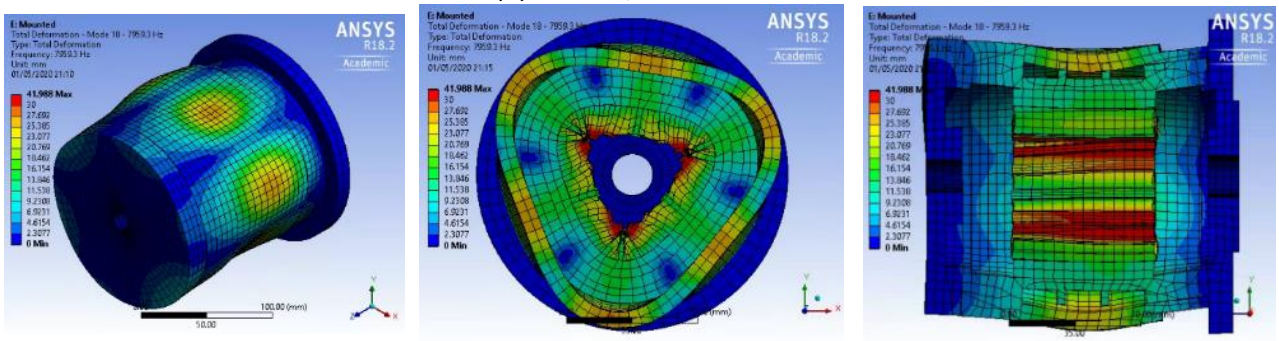

(c) Mode 3,0 (a) @ 7960

Fig. 5.2.32 Mode shapes with frictional contact mode applied.

Table 5.2.15 Comparison of measured and calculated modal frequencies for mounted ONLY condition.

Mode	Measured	FE	Error
2,0	4263	4207	1.3%
2,1	7200	6990	2.9%
3,0	8100	7960	1.7%

As discussed during the testing identifying the physical modes past 6kHz was difficult owing to the low excitation of the hammer in the fully mounted condition. One mode that was quite clear was at

approximately 9600Hz on channel 2 (180°) of the setup 1 of the hammer test (Fig. 4.3.24(a)). The peak is relatively high compared to the rest of the data but only seemed to occur at that test making it difficult to determine whether it was noise or an actual mode. Inspection of the calculated results show two potential candidates: a secondary mode 2 and a secondary mode 3, illustrated in Fig. 5.2.33.

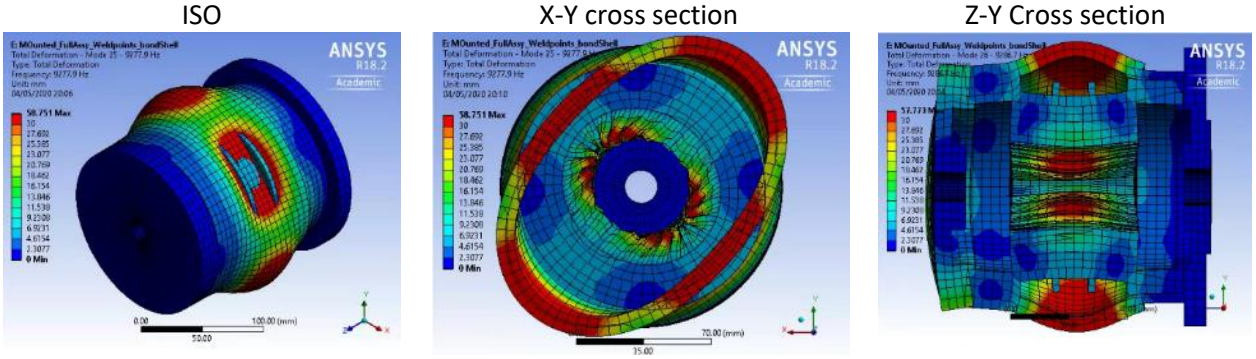

(a) Candidate 1: mode 2(b),0 @ 9278 Hz

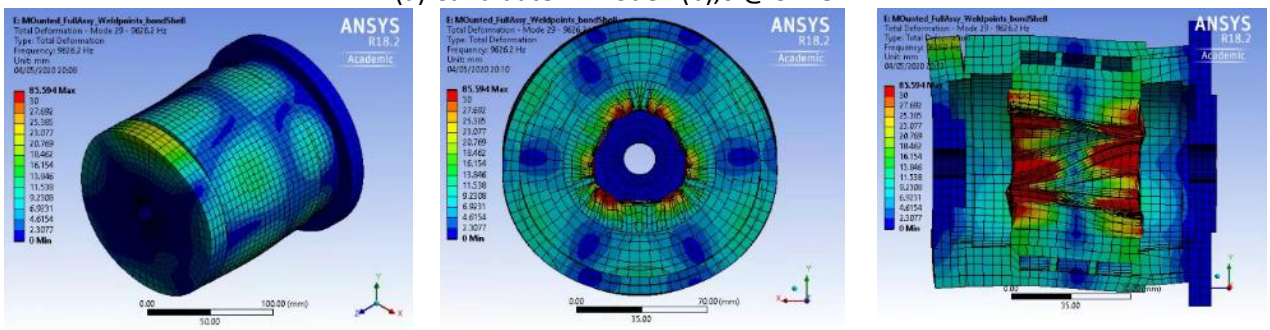

(b) Candidate 2: mode 3(b) @ 9626 Hz

Fig. 5.2.33 Candidate modes calculated by FE around 9.6kHz.

The general trend of the results has been the calculated modes are slightly lower, which would indicate the mode 2(b) at 9278Hz (Fig. 5.2.33 (a)) is the most likely candidate for the peak observed in the measurement.

5.2.7 The fully dressed machine

The final aspect to look at is the machine fully linked to the dynamometer with the coolant system filled. Like the addition of the rotor to the machine off rig the measured results show little difference on the circumferential modes between the mounted only and fully dressed machine. Indeed, the difference could simply once again be measurement error due to the need to remove the acceleration sensors to prevent them being damaged during the process of fully integrating the motor into the test rig. Differences do lie between the two, between ~6kHz and 10kHz there is much less noise with some weak peaks before the recurrence of mode 4 can be seen, plus a new value at around 10.9kHz. The key question is whether these differences are due to the addition of the coolant acting as a mass damper to remove some of the noise observed on the mounted only condition or whether the coolant in the machine acted to stiffen the wax of

the acceleration sensors and make them less noise prone. The main options available to approach this problem are:

- Model the mechanical properties of water or equivalent substance.
- Model the coolant as an additional mass in the machine.

A study of the literature shows much of the work for machines on this topic focusses primarily on the thermal characteristics [BB18], or coolant pumps [JSP10], or the mechanical losses due to forced air methods [KD01]. Widening the search to the oil and gas industry, where characterising and modelling fluids is central to most critical processes reveal computational fluid dynamics (CFD) techniques are used, [KI08], [KI09]. The reasoning for this is simple, as a liquid many of the mechanical features required such as the Young's modulus simply do not apply, and water can be shown to have a Poisson ratio of 0.5 assuming a perfect liquid and a bulk modulus [DE06] but this is not sufficient to represent the fluid in this model. Hence, the need for specialist methods such as CFD. For this project modelling the coolant as a CFD model is beyond the scope of the project, the effort required to learn and use complex CFD software is completely disproportionate to the small difference in results highlighted by the measurement. Also adding a CFD layer to the tool makes the dynamic modelling even more complex than it currently is. Thus, the focus lies on the contribution of the mass. Before calculating the mass, some basic assumptions are made to simplify the study:

1. The fluid is composed of pure water.
2. The fluid is at 20°C and 1 atmosphere pressure.
3. The fluid occupies 100% of the coolant channels (no air pockets).
4. No inlet/outlet pipes: The fluid is completely contained within the coolant channels.

Using the above assumptions, the relevant properties of the water can be given in Table 5.2.16 [DE06].

Table 5.2.16 Selected properties of water [DE06]

Item	Symbol	Value	Units
Density	ρ	998	Kg/m^3
Bulk modulus	B	2.2	GPa
Viscosity	μ	1.005	mPa.s
Surface tension	ɣ	0.07275	N/m

The mass of the water is obtained from the simple formula (5.3).

$$M_{water} = \rho_{water} V_{channel} \tag{5.3}$$

where M_{water} is the mass of water, ρ_{water} is the density of the water and $V_{channel}$ is the volume of one water channel. From Table 5.2.16 the density is known so the volume is required. To obtain this is simple using the CAD, illustrated in Fig. 5.2.34.

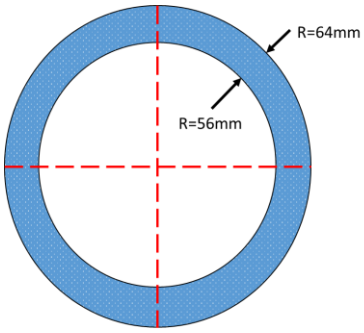

(a) 2D section of coolant channel showing inner and outer diameters

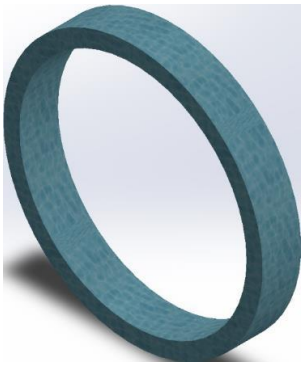

(b) Extruded shape showing 1 channel (depth = 19mm)

Fig. 5.2.34 Overview of the coolant channels in the machine.

From the shape in Fig. 5.2.34 the volume was found to be $5.73 \times 10^{-5} m^3$, using the density data in Table 5.2.16 and (4.38) gives a mass of 5.72×10^{-2}kg per channel. Given there are 3 coolant channels the total mass is $3 \times 5.72 \times 10^{-2} = 0.712$kg.

The mass is applied as a distributed mass, in a similar manner to the rotor mass previously discussed. Fig. 5.2.35 shows the mass applied.

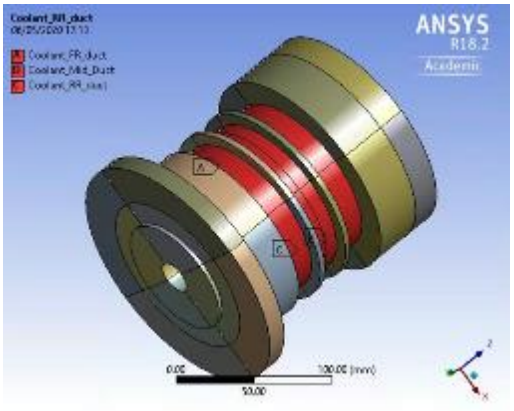

Fig. 5.2.35 Coolant mass applied to each channel (coolant shell hidden for illustrative purposes).

The modal analysis is repeated using the same mesh and constraints as the previous case. Fig. 5.2.36 and Table 5.2.17 provide the comparison of the resultant calculation.

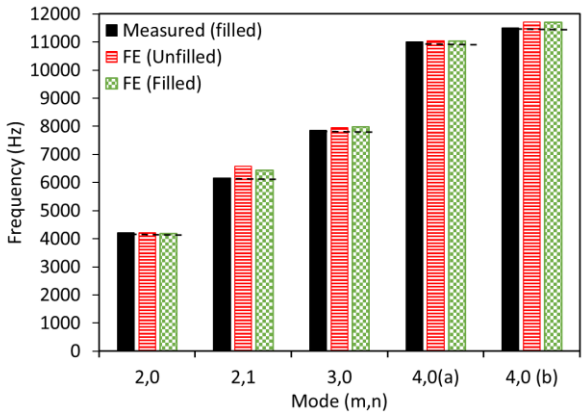

Fig. 5.2.36 Comparison of measured results of full rig with FE of mounted only and FE of water filled.

Table 5.2.17 Comparison of the measured machine and the FE calculated modal frequency results with and without the coolant mass added

Mode (n,m)	Measured (filled)	FE, mounted only		FE, coolant mass added	
		Frequency	Error VS Measured	Frequency	Error VS Measured
2,0	4216	4207	-0.21%	4174	-0.97%
2,1	6150	6569	-6.81%	6427	-4.5%
3,0	7850	7961	-1.41%	7980	-1.66%
4,0 (a)	10997	11036	-0.35%	11036	-0.35%
4,0 (b)	11500	11710	-1.83%	11698	-1.72%

From the results the increased mass causes a general drop in frequency, as would be expected, however, the impact on the circumferential modes is minimal. These are still very much dictated by the stator. For the identified axial mode (2,1) the error has dropped to below 5% versus the measured. Looking at the impact of adding the mass on the computational time of the analysis shows the calculation time to be 5 seconds slower for the additional mass which is negligible. The mesh is identical in both cases so the only effect the mass has is on the initial generation of the matrix used to solve the eigenvalues. Given the improvement to the axial mode the model with the coolant mass added is used as the final model.

5.3 Tuning the final model

The modal analysis tool used thus far allows the natural frequencies to be matched to the measured data. However, the modal analysis tool does not utilise any real-world forces in its operation. It operates by solving a large matrix equation to find all the eigen values, the majority of which may not even appear on a sensor. To obtain the final mechanical model the harmonic analysis tool is required. This takes in frequency based forced data and simulates the frequency response of the structure. Here, the damping factor can be tuned to ensure the response of the machine matches that of the measured data. The analysis tool requires a number of additional steps to operate compared with the modal analysis tool:

- Remote force tool applied to 3D shape.
- FFT Forces and frequencies captured during testing is inputted into the tool along a fixed vector.
- Frequency response (acceleration) probe is attached diametrically opposite the remote force tool.
- Analysis is setup and run.

To evaluate the tool and its performance the stator core is chosen to do the initial comparison as it is a relatively simple shape and reasonably quick to process. The setup is shown in Fig. 5.3.1.

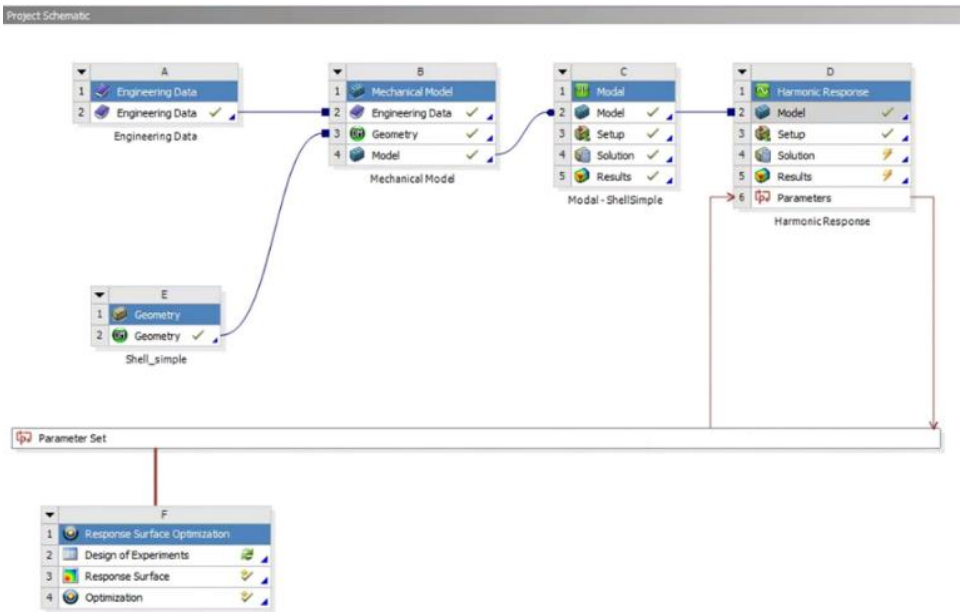

(a) Setup of the harmonic response function in ANSYS® Workbench (V18)

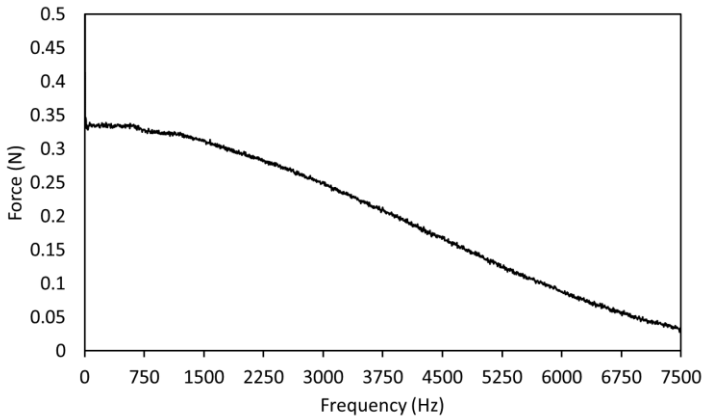

(b) Measured impact force frequency domain trace from hammer test

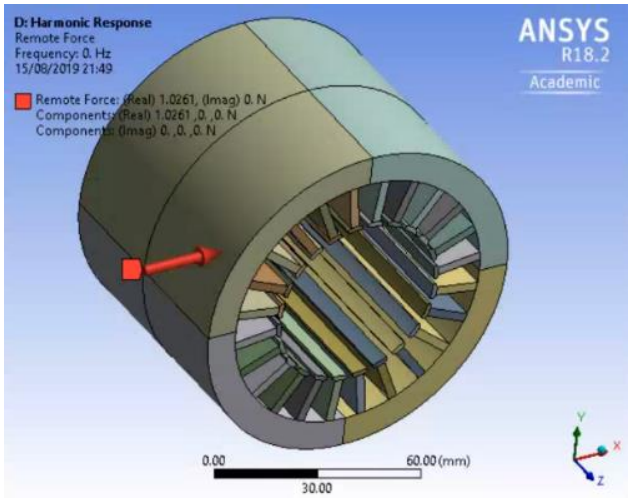

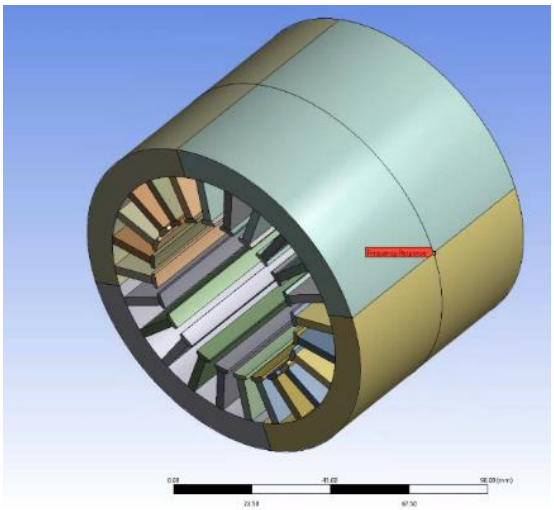

(c) Impact hammer force input point. (d) Response probe location.

Fig. 5.3.1 Setup of harmonic response and impact and pick up point on stator core model.

As with the FRF calculations performed during the test phase the hammer response is cut off such that only the excitation bandwidth of the hammer impulse simulated, and in this case the cut off frequency was 7000Hz. The analysis tool requires the minimum and maximum frequencies and the number of steps. i.e. the frequency resolution of the trace. For this model, the resolution from the signal analyser is replicated to ease comparison, which is 8Hz, so the number of steps required is 7000/8 = 875 steps.

A single probe is used to represent the sensor at 180Deg. The program is initially run undamped to ensure the frequency alignment is OK. Following this the optimisation function within ANSYS® workbench is utilised to derive the damping factor. The results of the study are shown in Fig. 5.3.2.

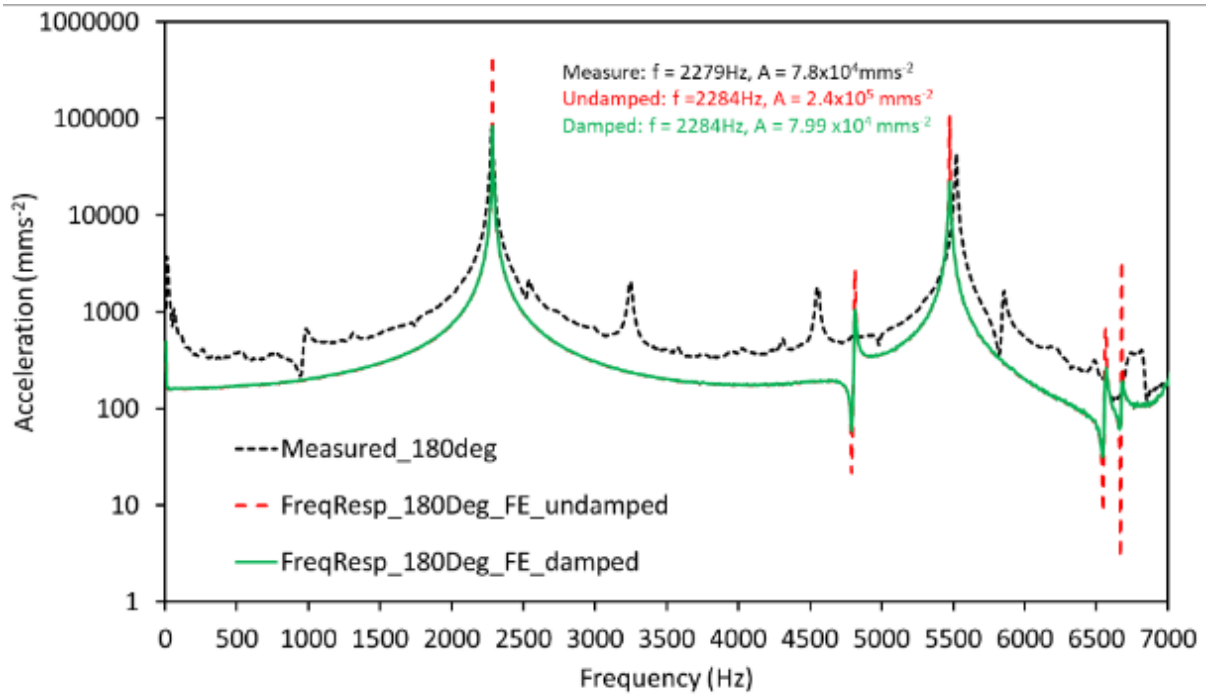

Fig. 5.3.2 Optimised damping factor versus measured data for the stator core.

The optimisation found a damping factor of **$\underline{1.08\text{x}10^{-3}}$**.

This gives good alignment with the measured mode 2,0 results. The acceleration results for mode 2 before and after the tuning is shown in Table 5.4.1

Table 5.3.1 Measured amplitude versus FE undamped (initial) and optimised damping factor

Mode 2,0 measured (mms^{-2})	Undamped		Optimised (DF = $1.08\text{x}10^{-3}$)	
	Acceleration (mms^{-2})	Error Vs measured (%)	Acceleration (mms^{-2})	Error Vs measured (%)
78193.74	237960	-204%	79906	2.14%

Good alignment is observed with both the frequency and the amplitude for circumferential mode 2 indicating the model of the stator has acceptable alignment with the measured data.

A key observation from the study is that the harmonic analysis takes a considerable period of time to run compared to modal analysis. Where the modal analysis on the stator core takes just under 30 seconds the harmonic analysis takes 15 minutes. As the model complexity expands with the growing assembly this time

increases significantly, up to an hour or more each run. Thus, the stator provides the template and format for running the simulation but there is little to gain in the larger scope of the project to run each stage through the harmonic response function within ANSYS® so the process will be applied to the ultimate goal of this whole exercise which is the machine on the rig.

5.3.1 Tuning the complete machine assembly

With the procedure in place and good results from the stator core the model representing the full machine set up and ready for testing can now be tuned. The developed model is applied to a harmonic analysis block, similar to Fig. 5.3.1(a). The system is then setup similar to the stator core, as shown in Fig. 5.3.3.

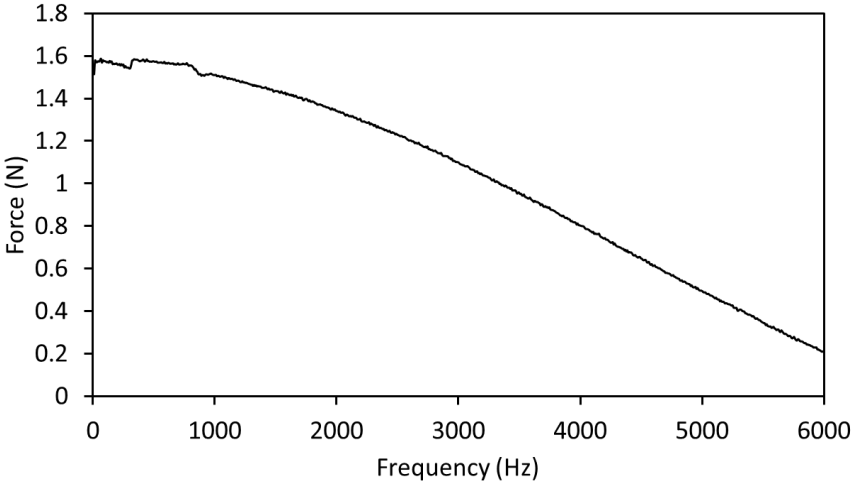

(a) Measured impact force spectrum from hammer test

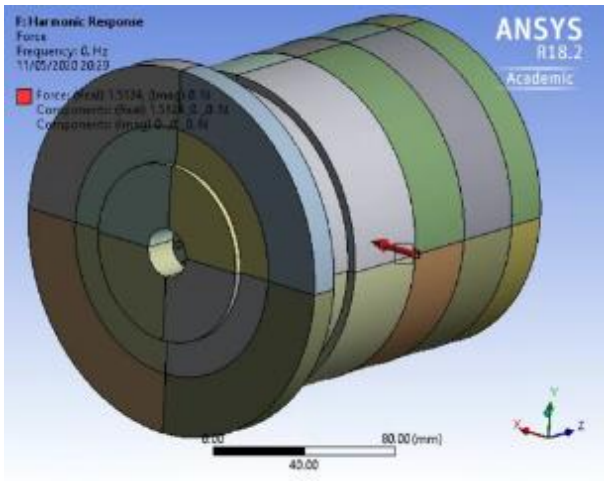

(b) Force tool applied to impact point

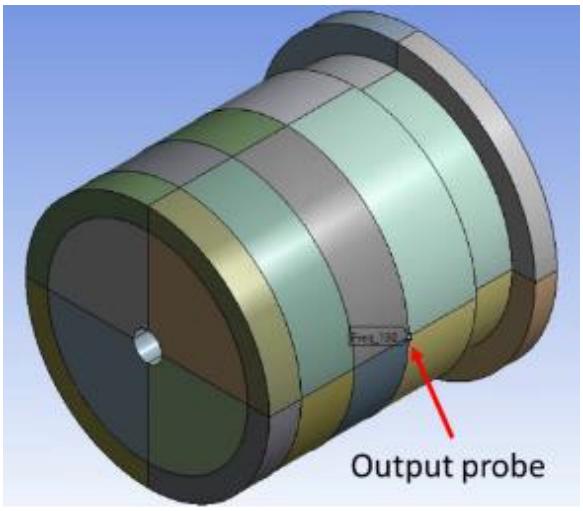

(c) Acceleration probe applied to 180° point

Fig. 5.3.3 Setup of the full machine for damping factor tuning.

From the measured data the cut off frequency from the hammer impact was 6kHz which is shown in Fig. 5.3.3(a). This is inputted into the force tool in Fig. 5.3.3(b). Similar to the rotor core the frequency of the signal analyser is matched so 6000/8 = 750 steps. The machine is run undamped then the optimisation tool utilised to find the damping rate for the peak mode (2,0). The resultant waveform is shown in Fig. 5.3.4 below.

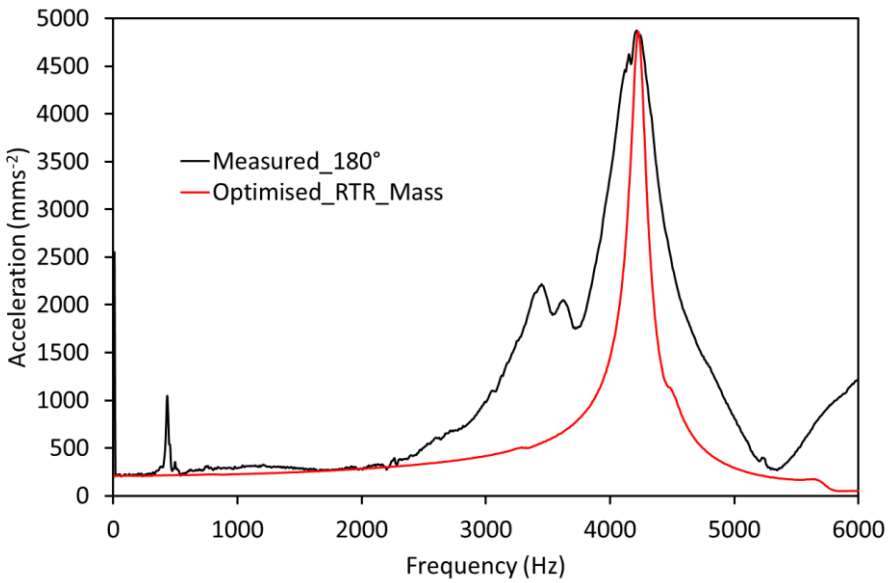

Fig. 5.3.4 Comparison of measured full machine measured and the FE model with the rotor as a mass.

The optimal damping factor for mode 2 was found to be **1.47x10^{-2}**.

The results are shown in Table 5.3.2.

Table 5.3.2 Measured amplitude versus FE undamped (initial) and optimised damping factor

Mode 2,0 measured (mms^{-2})	Undamped		Optimised (DF = 1.47x10^{-2})	
	Acceleration (mms^{-2})	Error Vs measured (%)	Acceleration (mms^{-2})	Error Vs measured (%)
4900	6.47x10^{5}	-13103%	4902	-0.04%

Fig 5.3.4 and Table 5.3.2 show optimisation of the damping factor has aligned the amplitude of the circumferential mode 2 very well. The profile of the wave does differ somewhat from the measured data in Fig. 5.3.4 which is different from the results of the stator core only results in Fig 5.3.2 where the profiles were a close match. Given the complexity of the fully mounted machine there are a multitude of potential reasons for this.

- **Influence of the test rig**: the hammer test in the rig revealed a number of modes, in particular the "shoulder" observed at ~3.5kHz which is attributed some aspect of the test rig as it was not observed off-rig or in the FE model, this distorts the waveform of the measured results versus the calculated.
- **Optimisation method:** The ANSYS optimisation methodology is very powerful and for the simpler models was very effective, however the limitation of only being able to select one frequency and target amplitude in this case lowers the degrees of freedom available to further tune the model and therefore the profile.
- **Model fidelity**: The battle between the need for high accuracy and the need for speed of processing means that some compromise must be made. The need to simplify the geometry and mesh of the model to maximise speed means some aspect of the dynamics of the model is lost.

The above is not an exhaustive list but despite the limitations the results are reasonable and indicate the model is a good candidate for the next stage of modelling the machine.

5.4 Summary

This chapter provided an overview of the development of a finite element model to replicate the frequency response of the baseline machine measured in chapter 4 of this thesis. The focus on circumferential modes should have allowed for a much simpler 2D FE model. However, the machine structure was shown to be too complex in nature for a 2D representation primarily due to the liquid cooling requirements of the machine. The coolant flows over 3 grooves in the frame of the machine directly over the fitted stator core which is sealed by an aluminium shell fitted with inlet and outlets to allow fluid flow through the machine. The method of holding the shell in place and forcing the shell against 2 sets of 'O' rings to maintain a good seal creates an asymmetric structure along the longitudinal axis of the machine meaning the machine is best represented using a 3D model.

Much like the development of the electromagnetic FE model the first and arguably most important step in the development of the 3D mechanical model is the establishment of the materials properties which are the foundation onto which the rest of the model lies. The challenge here lies with the stator core and the windings. For the stator core the need to laminate the core to mitigate iron loss means the structure cannot be represented as an isotropic material as the very large difference between the dense, strong steel plates and the much weaker inter-plate bonding material means the properties are orthotropic, that is they differ on the circumferential plane from the axial plane. The windings are arguably the most complicated structural aspect of any machine being made of strands of copper coated in a ceramic insulation material, wound into the stator core slots, end windings tied, and then potted with an epoxy. Both these aspects are very challenging to model, but as the literature review highlighted in chapter 1 they are not new problems and there have been a large number of methods proposed over the years.

- For the stator, the material is treated as an orthotopic composite the characteristics of which are centred on the stacking factor. The axial characteristics were found to be highly sensitive to the stack factor in particular between stack factors of 0.9 and 1 where even small changes to the stack factor lead to very large shifts in elasticity and density with implications on manufacturing tolerances etc.
- For the windings, the approach used for the stator is unwieldy due to the sheer number of parameters involved. Fortunately, within the literature a number of works derive a characteristic equation for the elasticity of the material based on a large number of empiric measurements that are based on the fill factor of the windings. Calculation of the fill factor using the slot area and winding data provides a value for the key data.

With the material in place the FE models were generated using the 3D models drawn during the initial design of the machine. The initial run utilised the stator model and found good agreement between the measured data and the calculate modes, validating the method of calculating the material.

From the stator onwards the process followed the same sequence as the measurement, starting with the wound stator heat shrunk into frame all the way to the final machine mounted on the rig. The salient points from the study were:

- On this machine the windings are best represented as the composite material filling each slot; addition of the end windings gives marginal improvement in accuracy at the cost of very high numbers of largely irrelevant eigenvalues.
- Shape simplification and mesh convergence at each stage of the process is as important now as ever to balance the requirement for maximum accuracy with minimum processing time.
- For this machine, the fasteners for the front and rear plates are well represented as weld points.
- The fitment of the cooling shell proved to be a large disruption to the modal performance, using the default (bonded) connection type results in too stiff a structure. Optimisation of the coefficient of fiction for each contact point yielded good results.
- The addition of a simple rotor shape gave negligible improvement on the circumferential performance of the model. However, adding the mass of the rotor into the front and rear bearing housing gave some improvement to the alignment of the identified axial mode.
- The coolant was found to have some effect and was best represented by adding the mass of the coolant (assuming the coolant channels are completely full of pure water). This adds limited overhead to the computation of the modes (no change to mesh) but improves accuracy.

Finally, the harmonic analysis tool was utilised to tune the damping factor of the final model such that the transfer function of the model closely matches that of the measured machine for the mode 2,0 results.

This process has produced the mechanical FE model of the machine which combined with the previously developed electromagnetic FE model allows the dynamic performance of the machine to be simulated which is the topic of the next section of the thesis.

6 Measurement and Simulation of the vibratory performance of the baseline machine

6.1 Introduction

This chapter details the steps taken to integrate the electromagnetic model developed in Chapter 3 and the 3D mechanical model developed in Chapter 5 in order to obtain the final vibration model of the machine. The aspect focussed on is shown in Fig. 6.1.1.

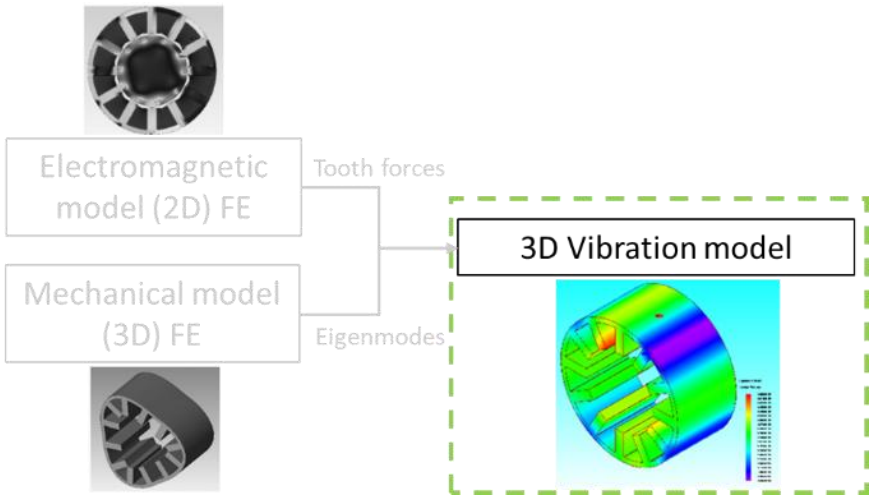

Fig. 6.1.1 - Flow diagram of the vibratory modelling of an electrical machine.

The methodology of modelling the vibratory modelling of the machine utilises the same harmonic response tool used in Chapter 5 with the key difference that rather than using the recorded force hammer data the tooth force data calculated by the electromagnetic FE tool is utilised. Using the ANSYS® Workbench (V18) the force data calculated by the electromagnetic FE tool is converted into the frequency domain using an in-built tool which are then mapped to the corresponding tooth surface of the 3D mechanical FE model. The harmonic response tool then calculates the mechanical response of the structure to the vibratory force in order to estimate the vibratory behaviour of the machine. This performance can then be compared with the vibratory behaviour captured during the measurement of the machine on the dynamometer allowing the model to be tuned in order to match the real-world data as closely as possible.

This chapter is split into 2 parts:

- Setup and analysis of the vibration measurement of the baseline machine on the dynamometer.
- Creation of the final vibratory model and the steps taken to create the final model.

6.2 Baseline machine vibration measurement results

The capturing of the vibratory performance occurred during the measurement of the baseline machine characteristics on the dynamometer, as detailed in Chapter 2. Whereas the primary focus in Chapter 2 was on the more general performance aspects of the machine with a brief highlight of the vibratory measurement in the full rig system diagram, shown in Fig. 2.3.10, this chapter will focus on the aspects of the rig relevant to capturing the vibratory data. A brief overview of the vibration measurement sub-system will be provided before the different measured scenarios summarised and resultant sensor data analysed.

6.2.1 Overview of measurement setup

The setup uses the same equipment employed during the impact hammer testing in Chapter 4, with the notable omission of the impact hammer as the excitation forces come from the machine. As reminder the key equipment's utilised include:

- Acceleration sensors: Bruel & Kjaer 4518-003 Piezoelectric sensors [BK06].
- Signal conditioning amplifier: 16 channel Bruel & Kjaer Type 2694 [BK18].
- Signal analyser: Agilent 35610A [KT17].
- PC with National Instrument LabVIEW installed to capture the data.

The block diagram for the acceleration sensor signal capture sub-system is shown in Fig. 6.2.1.

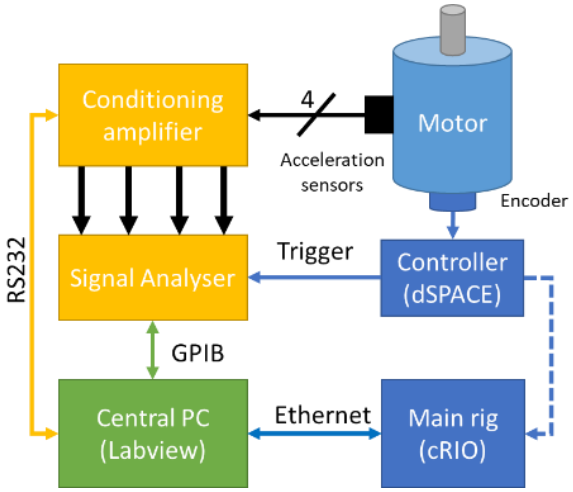

Fig. 6.2.1 Block diagram of the key components used in the vibration measurement.

The setup in Fig. 6.2.1 bears a very close resemblance to the hammer test setup shown in Fig. 4.2.3(a) in Chapter 4 with some key differences:

- No impact hammer means there is a free channel on the signal analyser for an additional sensor, bringing the total number of acceleration sensors to 4.
- The functionality of the data acquisition (DAQ) system detailed in Chapter 4 to capture the acceleration sensor data is integrated into the full machine DAQ system to increase test efficiency.

- The falling edge from the encoder is used as the trigger for the signal analyser.
- The methodology of attaching the acceleration sensors to the machine is changed from the petroleum wax used in the hammer test to a hot melt adhesive.

Most of these changes are self-explanatory, however some, such as the change to the triggering method and the means of mounting the sensors to the machine casing, merit a more detailed explanation.

6.2.1.1 Acoustic noise measurement omission

The keen observer will quickly notice that the vibration measurement system diagram in Fig. 6.2.1 and the main system diagram in Chapter 2 shows only acceleration sensors, there is no microphone to capture audible emissions. The reason for this is not lack of measurement equipment; a directional microphone was available and indeed the power analyser utilised has a dedicated channel for such a microphone. The problem was the test rig environment in which the machine was operated. Whilst the Electric Machines and Drives Group have a semi-anechoic chamber available the dynamometers that can operate in the chamber are unsuitable to operate the baseline machine, the machine was designed to operate at EV battery voltages (~300Vdc) and operate at high speeds (11,000rpm). Thus, the only facilities available at the time of testing that meets these requirements was the previously described AVL dynamometer. The chamber in which the test rig set has a large amount of noise isolation installed in order to meet building regulations but is non-anechoic in nature meaning there is not much in the way of noise absorption within the chamber. The AVL dynamometer used as the load machine is force air cooled, running a large fan when the dynamometer is powered up and in addition the room contains all the power and drive electronics both for the dynamometer and the drive and coolant pumps for the baseline machine. When the door of the test chamber is closed and the coolant system for the machine and drive engaged then the AVL drive and cooling system is turned on the resultant cacophony made any measurement of the acoustic noise from the machine very difficult to isolate.

6.2.1.2 Integration of data acquisition systems

In Chapter 4 a software tool developed by the author was introduced that allowed the remote control and acquisition of the data captured by the signal analyser using a General-Purpose Interface bus (GPIB) connection. This was developed to increase test speed and efficiency given that the alternative was to store the results data on a 3.5” floppy disk which was limited in capacity, slow, and tediously required each channel to be manually selected to store the results. For the dynamic testing, the need to manually operate the tool to store results becomes an even bigger disadvantage as the safety protocols and interlock system on the dynamometer forbids entry to the test chamber when the rig is powered and running. Remote controlling the power analyser via the software written became essential to allow the signal analyser to be setup,

triggered and the resultant data to be transmitted back to the PC safely outside the test chamber with the dynamometer and machine running.

The remote access tool was developed separately from the main machine data acquisition tool discussed in Chapter 2. However, it was quickly decided to integrate the functionality of the vibration acquisition tool into the main machine acquisition tool in order to increase test efficiency. This simplifies the test process and has the added advantage that whilst the trigger and averaging process for the acceleration sensors is running in the signal analyser all other aspects of the machine (torque, speed, voltage, current, temperature etc.) are synchronised and recorded allowing the conditions under which the machine was operating at the time of the measurement to be recalled for later analysis. The process flow for the integrated acquisition tool is shown in Fig. 6.2.2.

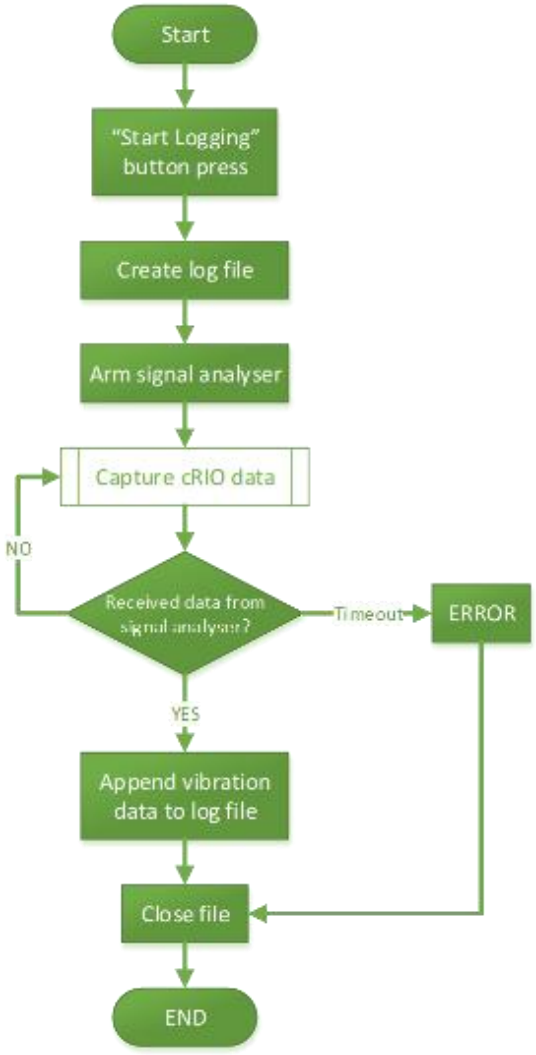

Fig. 6.2.2 High level flow chart of integrated data acquisition tool.

Note: the "cRIO" in Fig. 6.2.2 stands for Compact RIO, the National Instruments hardware which serves as the main hub of the machine measurement system. From the flow diagram in Fig. 6.2.2 it can be seen that the instant the "Start Logging" button is pressed the signal analyser is armed and the data from the different sources feeding into the cRIO is recorded by streaming the data to a log file. This streaming process continues

until either the acquisition software receives the processed frequency domain data from the signal analyser, or the system is judged to have waited too long for results. In the case where the processed data is received the recorded acceleration data is appended to the recorded machine data and the file is closed ready for future reference. In the case the time taken to receive the results data is too long it is judged that an error has occurred, the machine data is recorded, the log file closed and an appropriate error message to the user is generated.

6.2.1.3 Adjustment to signal analyser trigger source

With the removal of the impact hammer from the rig the trigger utilised in the static impact testing is clearly no longer valid. The concern here is the signal generated by the impact hammer during a static test acted as an excellent trigger point; it is clear and ensures the response waveform is fully captured. On the dynamic rig it is much more difficult to find such salient points using just the acceleration sensors; the risk of defining some arbitrary amplitude is the signal analyser may be triggered randomly due to some background noise or similar aspect leading to skewed and erroneous average data. Fortunately, the Agilent 35670A contains a number of options for triggering [KT17] including an external analogue trigger and a tachometer input which can be linked using a standard BNC co-axial cable.

From Fig. 6.2.3 it can be seen the encoder is linked to the dSPACE controller. The dSPACE controller uses standard hardware to interpret the signals from the encoder to generate a saw tooth wave, counting the encoder pulses from 0 to maximum (2048 pulses in this case) before resetting to 0 again. Each pulse step represents 360/maximum degrees, or 0.18 deg/pulse for the encoder used. This is illustrated in Fig. 6.2.3 and is used internally by the controller to determine both the rotor position and the rotor speed for the vector control of the machine.

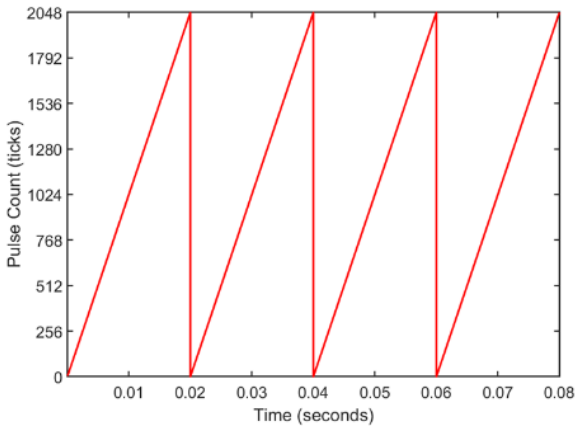

Fig. 6.2.3 Encoder saw tooth waveform with the machine rotating at 1500rpm.

In order to align the encoder to the ‘A’ phase of the machine the saw tooth waveform is outputted from one of the digital to analogue (D2A) channels on the dSPACE board as a 0 to +5V signal to a channel on an oscilloscope with a 2nd channel connected to the ‘A’ phase of the machine allowing the alignment procedure detailed previously (see Chapter 2) to be undertaken. Once the encoder is aligned there is little use for the

signal outside of the controller so the formerly redundant D2A channel can be plugged into the signal analyser and used as the trigger source. The falling edge is a good salient trigger point and has the added advantage of being aligned to the A-phase of the machine meaning the trigger occurs at regular intervals according to the position of the rotor giving a much better average on the signal analyser.

6.2.1.4 Acceleration sensor mounting and positions

For the hammer test the acceleration sensors were attached to the casing of the machine using a petroleum wax, the reasoning for which was detailed in Chapter 4. The main disadvantage of the wax used is that as its temperature exceeds around 35°C it softens, becoming very pliable weakening the bond between the sensor and the casing. For the hammer test this was no concern as the testing was always undertaken at room temperature (~18°C to ~22°C) with the machine unpowered so the wax was stable. For the dynamic performance testing the heat generated by the relatively high current density of the machine under load conditions means the thermal characteristics of the wax becomes a big concern. As the machine is operated at higher loads the case temperature can easily exceed 40°C even with the liquid cooling system, melting the wax and causing the sensor to fall free. An alternative was therefore required. Based on the study in Chapter 4 the different methods available are shown in Table 6.2.1.

Table 6.2.1 Pros and cons of alternative sensor mounting methods

	Threaded stud mount	Epoxy resin	Hot melt adhesive
Pros	✓ Good frequency response. ✓ Reliable linkage. ✓ Not sensitive to temperature.	✓ Strong bond to casing. ✓ No additional parts or modifications.	✓ Strong bond to casing. ✓ Very low risk of damage to sensor or machine to remove.
Cons	X No stud on sensor- additional part required. X Risk tapping hole will damage casing and create coolant leak.	X Time required for resin to set. X High risk of damage to the sensor and machine during removal.	X Risk high temperature of glue can damage sensor. X Bonding surface needs to be very clean to ensure good bond. X Risk of burns to the user during fitment.

Balancing the pros and cons listed in Table 6.2.1 the chosen method was hot melt adhesive; it avoids the complexity and risk of tapping fixings into the casing and the risk of damage to the sensor from the epoxy, in particularly during removal. A careful check of the sensor maximum temperature, 100°C [BK06], shows the sensor can withstand the high temperature of the glue (80°C) as it comes out the heat gun. The risk with using either the epoxy of the hot glue is that the surface on which the sensor is to be bonded must be as smooth and clean as possible. Otherwise, the bond is compromised increasing the risk the sensor comes loose. Thus, before applying the glue each target surface was smoothed using emery paper and then thoroughly cleaned with alcohol-based cleaner to remove any debris. One of the bonded sensors can be seen in Fig. 6.2.4.

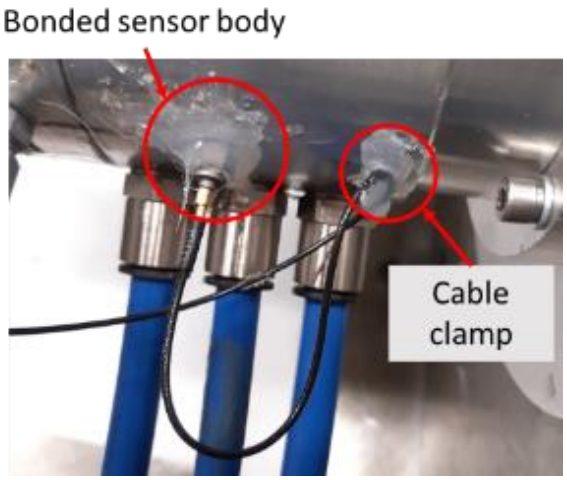

Fig. 6.2.4 Photo of sensor hot glued on to the machine surface

The photograph in Fig. 6.2.4 shows two bonded points: the largest part is the sensor itself and the second is one end of a loop of the cable to the sensor. This is a standard procedure and ensures that any snags or tugs on the long cable running to the conditioning amplifier does not pull off or damage the sensor, rather the cable clamp acts to absorb the shock. This method also keeps the length of cable linked to the sensor to an optimal length: long enough to allow the sensor to move freely but short enough to reduce the risk of any vibration along the long cable length inducing a signal on the sensor and giving false information about the machine.

The sensor positions are based on the positions established in the hammer test in Chapter 4. With the 4th channel on the Agilent scope available the two setups shown in Chapter 4 are combined.

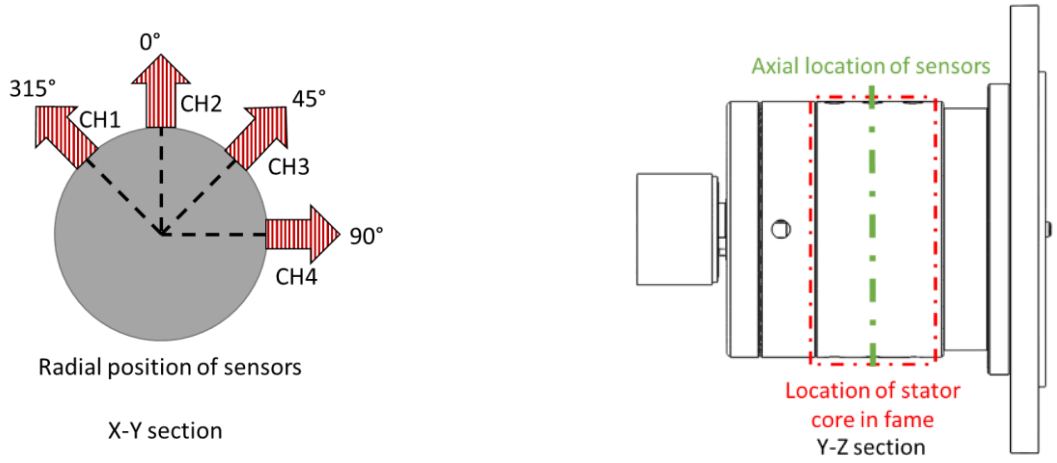

(a) Radial position of the 4 acceleration sensors (b) Axial position of the 4 acceleration sensors

Fig. 6.2.5 Mounting position of acceleration sensors on the machine.

The same angle guides created for the hammer test are utilised. 0° is the top and, looking at the machine from the rear the angle increments in a clockwise direction. Attaching the sensor to the 180° position from the hammer test proved unpractical, using the wax proved problematic with the sensor falling off on a regular basis but using the hot glue was even more precarious given the tendency for the very hot glue in fluid form to drip off the sensor risking burns and a poor connection with the casing.

6.3 Results of vibration measurement

The test results covered in Chapter 2 effectively covered the mapping of the efficiency of the machine using the maximum torque per ampere (MTPA) and maximum efficiency per ampere (MEPA) methodologies. For the vibration testing a large number of additional tests were undertaken to try to understand the effect of different load and control scenarios on the vibration of the machine. The different scenarios measured and undertaken are listed in Table 6.3.1.

Table 6.3.1 Summary of the scenarios measured.

Test no.	Scenario	Load condition	Description
1	Open circuit	No load	Understand vibration of machine on open circuit at different speeds.
2	Constant speed, variable torque	Load	Machine is held at constant speed; the current angle is held to 0° (where possible) and the torque incremented; vibration is measured at each point.
3	PWM sideband investigation	No Load	Investigation into high peaks observed at PWM side bands. Machine linked to inverter and controller set to 0 (no load). Machine measured with PWM frequency of 10kHz, 8kHz and 12kHz.
4		Load	Machine operated at a number of different speeds and torques at 8kHz, 10kHz, and 12kHz switching frequency to observe effect of adjusting the PWM switching frequency on vibration.
5	Current angle sweep	Load	Machine is set to a given speed and torque then the current angle is incremented in 10° steps from 0° to 60° (70° for very high speeds). Vibration measured at each step. Repeated for a number of different speeds and torques.
6	TN Curve	Load	Vibration measured at maximum torque/speed envelope of the machine.
7	MTPA	Load	Measure the vibration at select points of the torque & speed map created using the MTPA method.

Table 6.3.1 shows only the MTPA results are analysed, rather than the MEPA and MTPA methods. The reason for this is that the analysis of the performance shown in Chapter 2 highlighted that there was negligible difference in the current angle used by both methods meaning the load condition of the machine was identical for both, so there is no merit in comparing the vibratory performances. The order of the testing slowly increases the complexity if the testing such that a picture of the different aspects of operating the machine can be clearly understood, starting with the machine running open circuit, through operating the machine using mutual torque only up to the conditions under which the machine would operate under real-world conditions i.e. MTPA which includes complications such as flux weakening, the reluctance torque component due to the variation in saliency (L_q/L_d) with the increasing current angle and non-linear factors such as core saturation.

6.3.1 No load testing

No load testing was covered in Chapter 2 where the primary goal was to establish the back EMF of the machine at a given speed in order to record the voltage and hence the flux linkages between the PMs in the rotor and the coils in the stator to be measured. The test occurs with the machine being open circuit, i.e. the 3-phase contactors between the machine and the inverter are open. This both ensured the machine had been correctly wound and that the machine matched the performance expectation. For measuring the vibration, the no load testing is a bit more involved and essentially has the following goals:

- Understand the baseline mechanical performance of the rotor and associated driveline.
- Understand any background vibration or noise emanating from the rig (i.e., any vibration external to the machine).
- Understand the influence of the PMs on the vibration of the machine.

To achieve the above the machine is rotated using the dynamometer at higher and higher speeds and the vibratory performance captured at regular intervals. For this test, the machine is isolated from the drive by ensuring the 3-phase contactor to the inverter is open (i.e., the machine is open circuit) the machine is then rotated at the following speed steps: 1000rpm, 1500rpm, 2000rpm, 3000rpm, 4000 rpm, 4500rpm, 5000rpm, 6000rpm, 7000rpm, and 7500rpm. 7500rpm is the imposed maximum speed due to the rotor concern found during the initial testing.

Before discussing the results some terminology regarding the different frequencies of interest needs to be established and is summarised in Table 6.3.2.

Table 6.3.2 Definition of the key frequencies

Symbol	Name	Definition	Description
f_m	Rotor (mechanical) frequency	RPM/60	mechanical frequency of rotor in rev/s or Hz.
f_e	Electrical frequency	f_r*N_{pp}	number of electromagnetic cycles per rotor revolution, equal to rotor frequency (f_r) times number of pole pairs (N_{pp}).
f_c	PWM switching frequency	-	Switching frequency of PWM carrier wave.

The results can be seen in Fig. 6.3.1 with the salient frequency and amplitudes shown in Table 6.3.3. It should be noted that the charts in this chapter use a log-scale on the Y-axis as the high amplitudes observed in the on-load tests necessitate a logarithmic scale to improve the readability of the charts, a problem that was not apparent during the hammer tests.

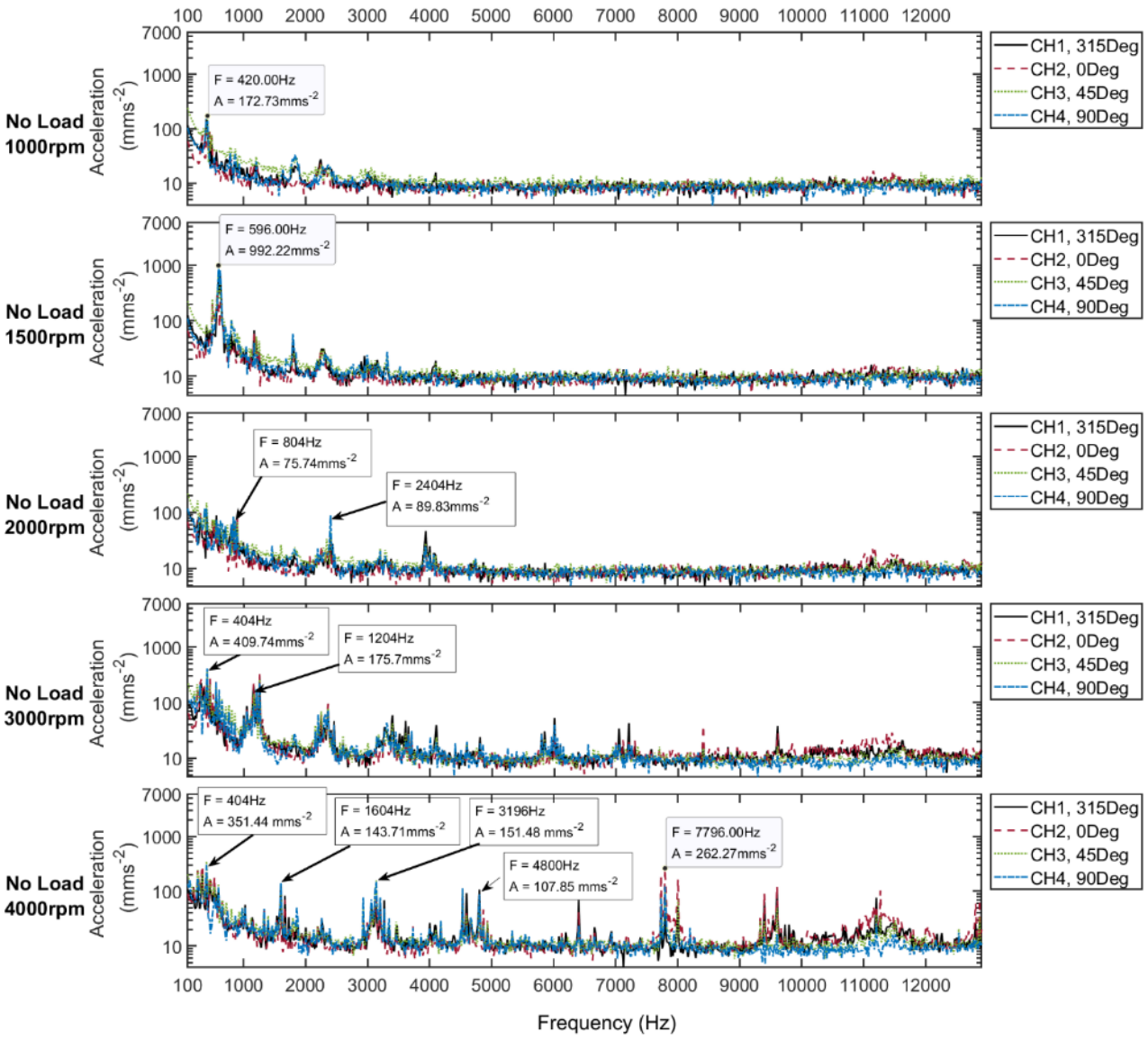

(a) No load, open circuit, 1000 to 4000 rpm

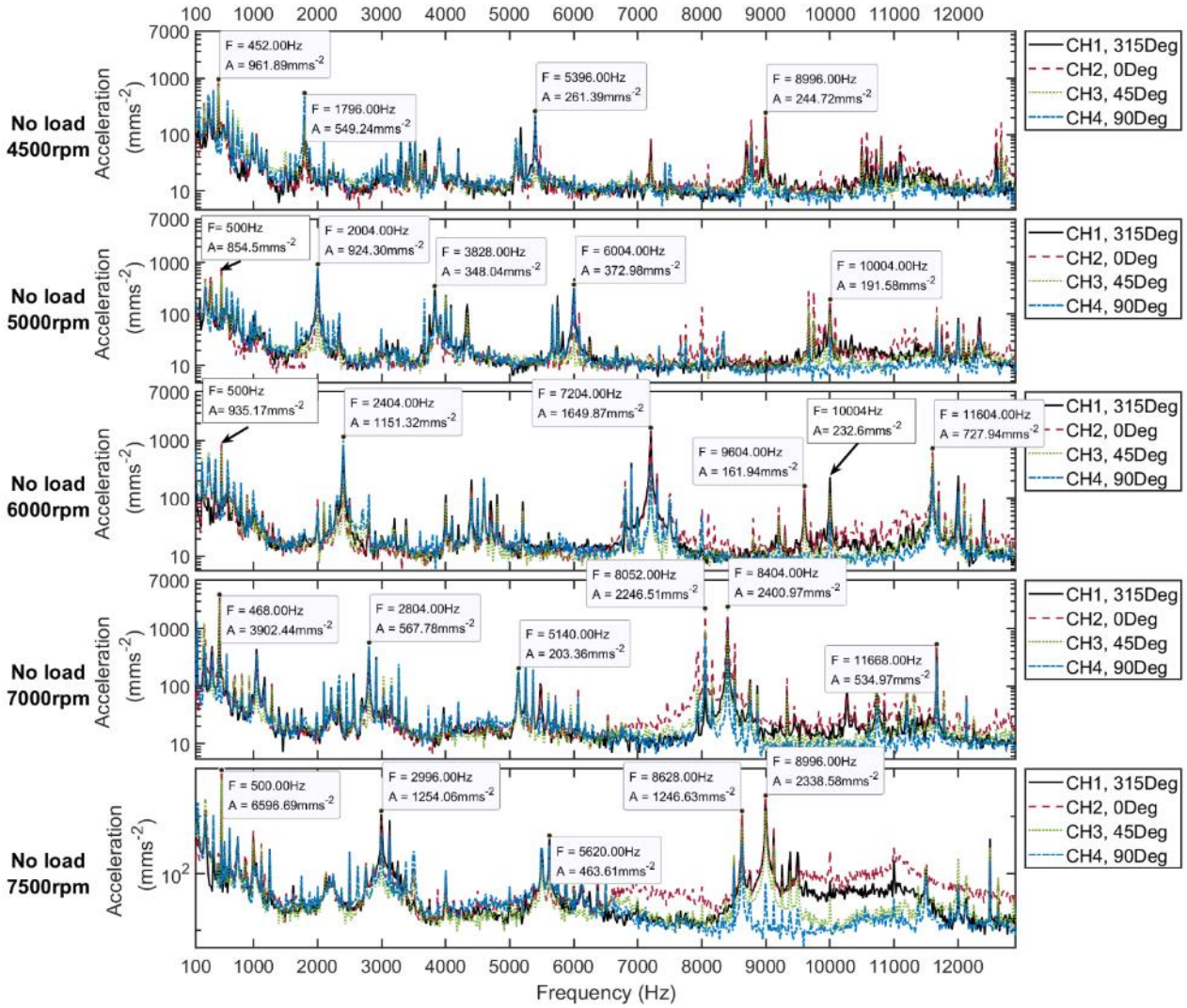

(b) No load, open circuit, 4500 to 7500 rpm

Fig. 6.3.1 No load vibration measurement, open circuit.

Table 6.3.3 Summary of no-load measured frequencies and accelerations

1000rpm		1500rpm		2000rpm		3000rpm		4000rpm	
Freq. (Hz)	Acc. (mms^{-2})	Freq. (Hz)	Acc. (mms^{-2})	Freq. (Hz)	Acc. (mms^{-2})	Freq. (Hz)	Acc. (mms^{-2})	Freq (Hz)	Acc. (mms^{-2})
404	189.44	596	992.2	804	85.8	404	409.8	404	351.4
				2404	89.83	1156	218.6	1604	143.7
						1204	175.7	3196	151.8
						1252	218.4	4804	107.85
								7996	262.6
4500rpm		5000rpm		6000rpm		7000rpm		7500rpm	
Freq. (Hz)	Acc. (mms^{-2})	Freq. (Hz)	Acc. (mms^{-2})	Freq. (Hz)	Acc. (mms^{-2})	Freq. (Hz)	Acc. (mms^{-2})	Freq. (Hz)	Acc. (mms^{-2})
452	961.9	500	854.5	500	935.2	468	3902.4	500	6596.7
1796	549.2	2004	924.3	2404	1151.32	2404	567.8	2996	1524
5396	261.39	3828	348	7204	1649.9	8052	2247	5620	463.6
8996	244.7	6004	491.6	9604	161.9	8404	2400.9	8628	1247
		10000	216.7	11600	727.9	11670	557.4	8996	2488.9

Given the machine is open circuit the only sources of excitation are the mechanical components (bearings, encoder etc.), the dynamometer and of course the interaction of the PMs with the stator teeth. From the results some general observations:

- The peak machine frequencies at each speed correspond to $n12f_e$ ($n24f_m$) where n is a harmonic order (1,2, 3...).
    - This is logical given the high cogging torque the non-skewed machine produces and agrees with similar work on the topic [SW18], [JFG06].
    - Beyond 4000rpm clear peaks can be observed at higher harmonic orders, in particular the 3rd and 5th ($36f_e$ and $60f_e$ respectively) as the harmonic frequencies excite modes on the machine structure. The 3rd harmonic in particular appears to produce the highest peaks at 7200Hz, 8400Hz, 9000Hz when the machine is at 6000rpm, 7000rpm and 7500rpm, respectively. These frequencies align to modes alluded to in the hammer test.
- Amplitudes below 4000rpm are very low making the peaks difficult to discern over the general background noise emanating from the rig, the exception being 1500rpm where the $12f_e$ (cogging) component appears to hit either a rotor mode or a mode on the rig assembly.
- As the rotor moves past 7000rpm the amplitudes of the lower frequencies between 468Hz and 500Hz have very large amplitudes, dominating the spectrum.
    - These frequency line up with the magnetic force from the PMs, equal to N_pf_m, where N_p is the number of poles, 4 on this machine. At 7000rpm the frequency is 4x166.67 = 466.67Hz, and at 7500rpm the frequency is 4x125Hz = 500Hz.
    - It is clear these frequencies hit some resonance frequency on the rig as the amplitudes observed are extremely high.

As the machine is accelerated past 7000rpm an audible roar is heard clearly from outside of the test rig which builds in amplitude with speed, despite all the sound proofing indicating that some aspect of the rig has hit a resonance frequency. Passing 7500rpm the sound is very loud; indeed, it was an attempt to pass through the noise band to 8000rpm that the rotor rear stub-shaft to the encoder failed. Referencing the hammer test there were a series of modes on the rig observed between 400Hz and 500Hz and it appears that the rotor is exciting this resonance frequency. In fact, for all tests there is a peak sat between 450Hz and 500Hz in the low end of the spectrum.

6.3.2 On load vibration measurement: Constant speed, variable torque

As current is applied to the machine the influence of the stator coils and the additional magnetic loading this implies comes into play meaning the forces acting on the rotor and stator will increase and the complexity of the flux in the air gap increases greatly. As shown in Table 6.3.1 a number of load tests were undertaken

beyond the "standard" tests shown in Chapter 2 to allow the vibratory performance to be explored in more depth. The first, basic test, has the machine held at a constant speed, the current angle is fixed to zero, i.e. I_d = 0A (where possible) and the torque incremented in steps. This means the machine is operating using only the mutual torque component (below base speed) allowing the basic vibratory performance along with the influence of aspects such as the PWM switching frequency to be evaluated. The test points evaluated are shown in Fig. 6.3.2 and summarised in Table 6.3.4.

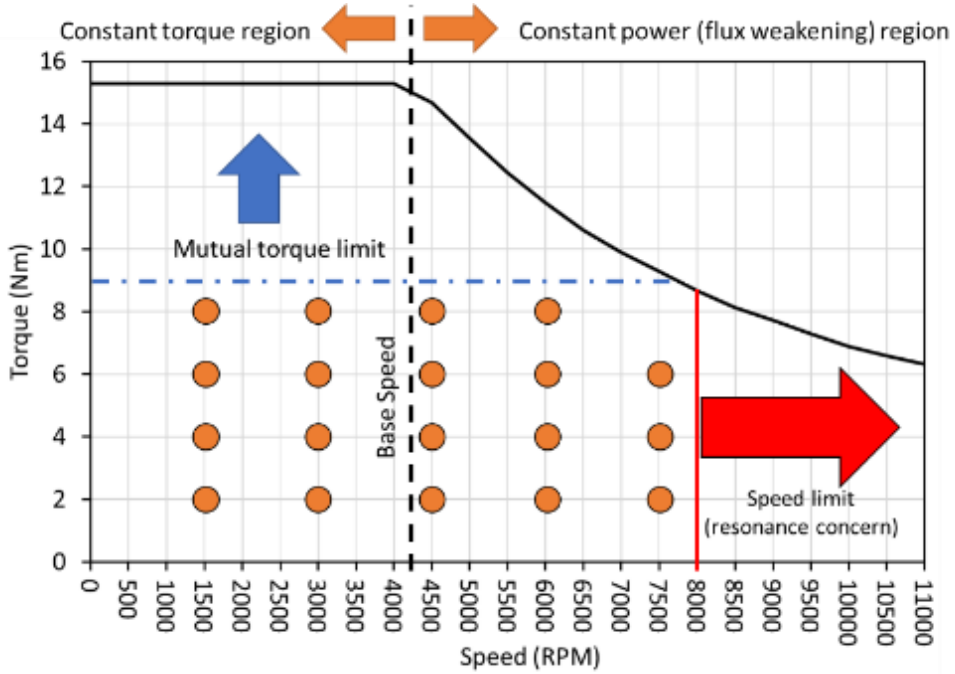

Fig. 6.3.2 Constant speed, variable torque

Table 6.3.4 Constant speed, variable torque measured points

	Speed				
Torque	1500rpm	3000rpm	4500rpm	6000rpm	7500rpm
2Nm	✓	✓	✓	✓	✓
4Nm	✓	✓	✓	✓	✓
6Nm	✓	✓	✓	✓	✓
8Nm	✓	✓	✓	✓	✗

The five speeds shown in Table 6.3.4 and Fig. 6.3.2 represent two speeds in the constant torque region (1500rpm, 3000rpm) one speed sitting around the base speed (4500rpm) and two speeds in the flux weakening region (6000rpm and 7500rpm). Given that the I_d current is held to zero the maximum torque chosen is 8Nm, a nice round number slightly below the maximum torque the machine can achieve with no reluctance torque contribution. It also allows the same torques to be measured deep into the flux weakening region with the notable exception of 7500rpm where measuring at 8Nm proved a little too unstable to get good results. Each speed point is analysed in turn, starting with 1500rpm which is shown in Fig. 6.3.3 and Table 6.3.5.

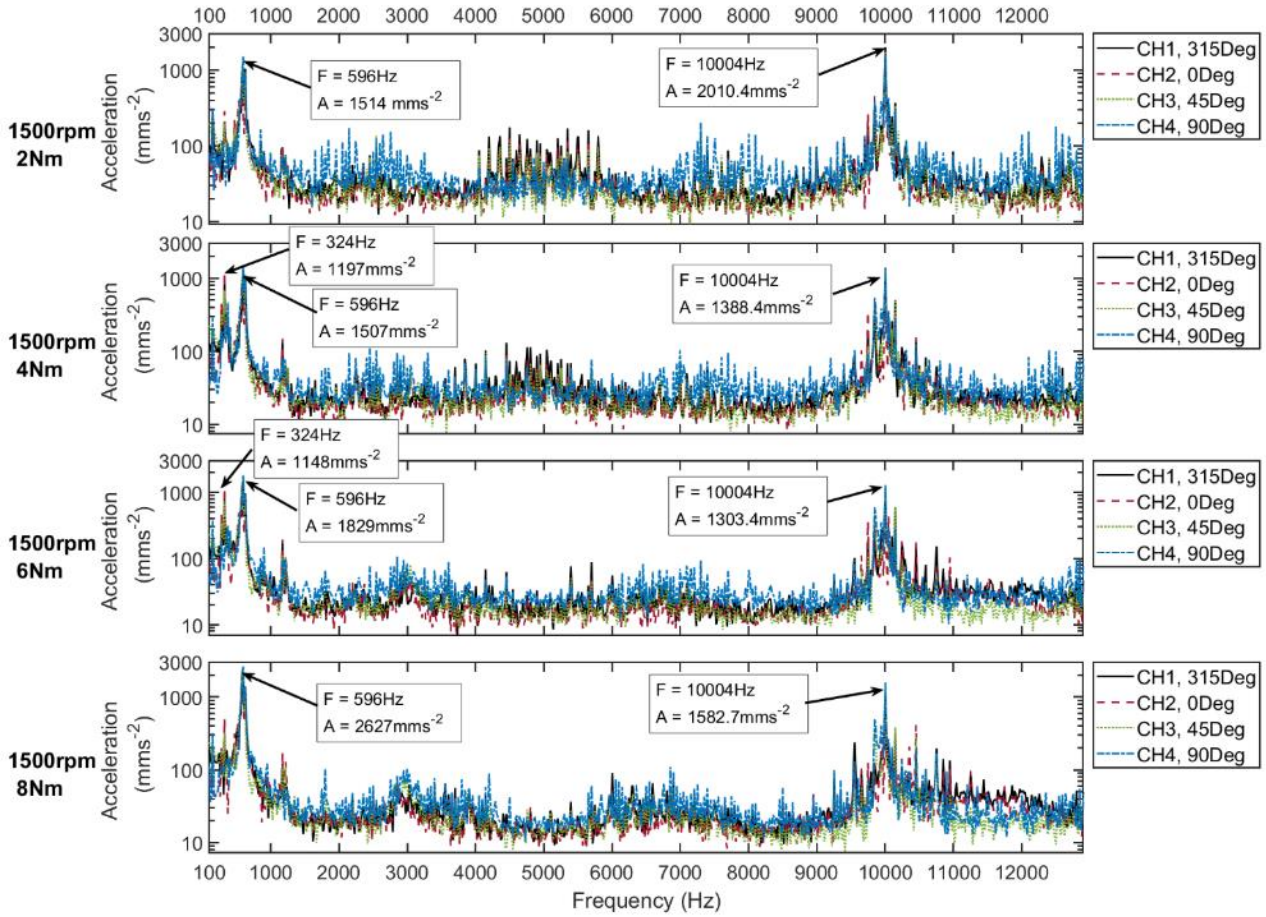

Fig. 6.3.3 Constant speed 1500rpm with torque varied between 2 -> 8Nm, I_d set to 0A.

Table 6.3.5 Measured acceleration with machine held at 1500rpm and incrementing torque

2Nm		4Nm		6Nm		8Nm	
Freq (Hz)	Acc (mms^{-2})	Freq (Hz)	Acc (mms^{-2})	Freq (Hz)	Acc (mms^{-2})	Freq (Hz)	Acc (mms^{-2})
596	1514	324	1197	324	1148	596	2627
10004	2010.4	596	1507	596	1829	10004	1582.7
		10004	1388.4	10004	1303.4		

From Fig. 6.3.3 and Table 6.3.5 the following observations can be made:

- The 600Hz peak corresponding to $12f_e$ observed in the no load test is clearly present in each torque point.
    - The amplitude of the peak rises proportional to the torque which is of course a function of the current being applied to the machine.
- The influence of the PWM switching frequency, f_c, can be clearly observed at 10kHz.
    - Either side of the 10kHz sits 2 side bands at 9844Hz and 10148Hz, accounting for measurement error this makes the lower band 150Hz lower than the switching frequency and the upper band 150Hz higher, corresponding to $f_c + 3f_e$ and $f_c - 3f_e$.
- A reasonably large peak is observed at 324Hz corresponding to $6f_e+f_m$, the peak is best observed at 4Nm and 6Nm but is present at all points.

The $6f_e$ point corresponds to a stator harmonic which fits the basic theory well [JFG06] interaction of 5th and 7th harmonics, $12f_e$ = interaction of 11th and 13th harmonics reinforced by the fact these peaks were not observed in the no load condition. The peak at 324Hz appears to correspond to a mode excited by a side band of the 6fe harmonic, matching 6fe+fm. Clearly this frequency aligns with some mode of the rig. The phenomena around f_c+3f_e and f_c-3f_e is explained later in this section.

The accelerometer results for the torque steps at 3000rpm can be seen in Fig. 6.3.4 and the key amplitudes summarised in Table 6.3.6.

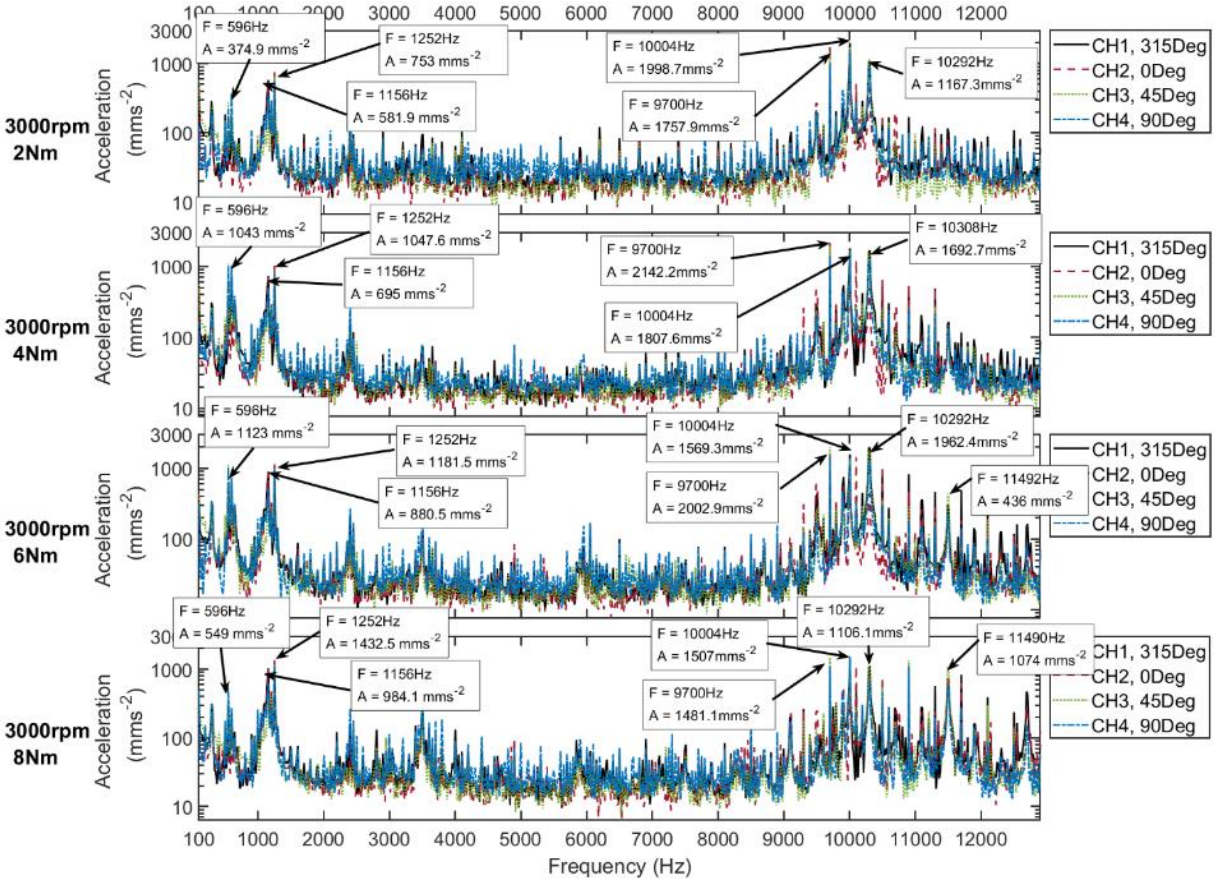

Fig. 6.3.4 Constant speed 3000rpm with torque varied between 2 -> 8Nm, I_d set to 0A.

Table 6.3.6 Measured acceleration with machine held at 3000rpm and incrementing torque

2Nm		4Nm		6Nm		8Nm	
Freq (Hz)	Acc (mms^{-2})	Freq (Hz)	Acc (mms^{-2})	Freq (Hz)	Acc (mms^{-2})	Freq (Hz)	Acc (mms^{-2})
596	374.9	896	1043	596	1123	596	549
1156	581.9	1156	695	1156	880.5	1156	984
1252	753	1252	1047.6	1252	1181.5	1252	1432.5
9700	1757.9	9700	2142.2	9700	2002.9	9700	1481.1
10004	1998.7	10004	1807.6	10004	1569.3	10004	1507
10292	1167.3	10308	1692.7	10292	1962.4	10292	1106
		10900	554.4	10900	825.2	10900	1336.6
						11490	1074

The pattern observed at 1500rpm is repeated in the 3000rpm test summarised in Fig. 6.3.4 and Table 6.3.6. The lower frequency peak corresponding to $6f_e$ is much clearer with the frequency aligning with the same mode excited by the ripple torque ($12f_e$) at 1500rpm. Around the ripple frequency (1200Hz) at 3000rpm two side bands corresponding to $12f_e$-f_m and $12f_e$-f_m are observed, indicating that the machine is exciting a mode either side of the 1200Hz ripple frequency, most likely a mode of the rotor or some sub-component of the driveline (balance plate or similar).

The influence of the side bands from the PWM can be much better observed here. Once again, they correspond to f_c+3f_e and f_c-3f_e to represent the upper and lower bands, respectively. The upper band appears to be coming into alignment with a machine mode (~10300Hz) whereas the lower side band, whilst showing a clear peak, does not fit the profile of a mechanical mode, and the peak may be due to EMI generated by the PWM at this frequency. At the maximum measured torque (8Nm) some of the higher frequencies around 11500Hz are excited around the mode (4, 0) highlighted in the hammer test.

The machine is accelerated up to 4500rpm and the test repeated with the results shown in Fig. 6.3.5 and summarised in Table 6.3.7.

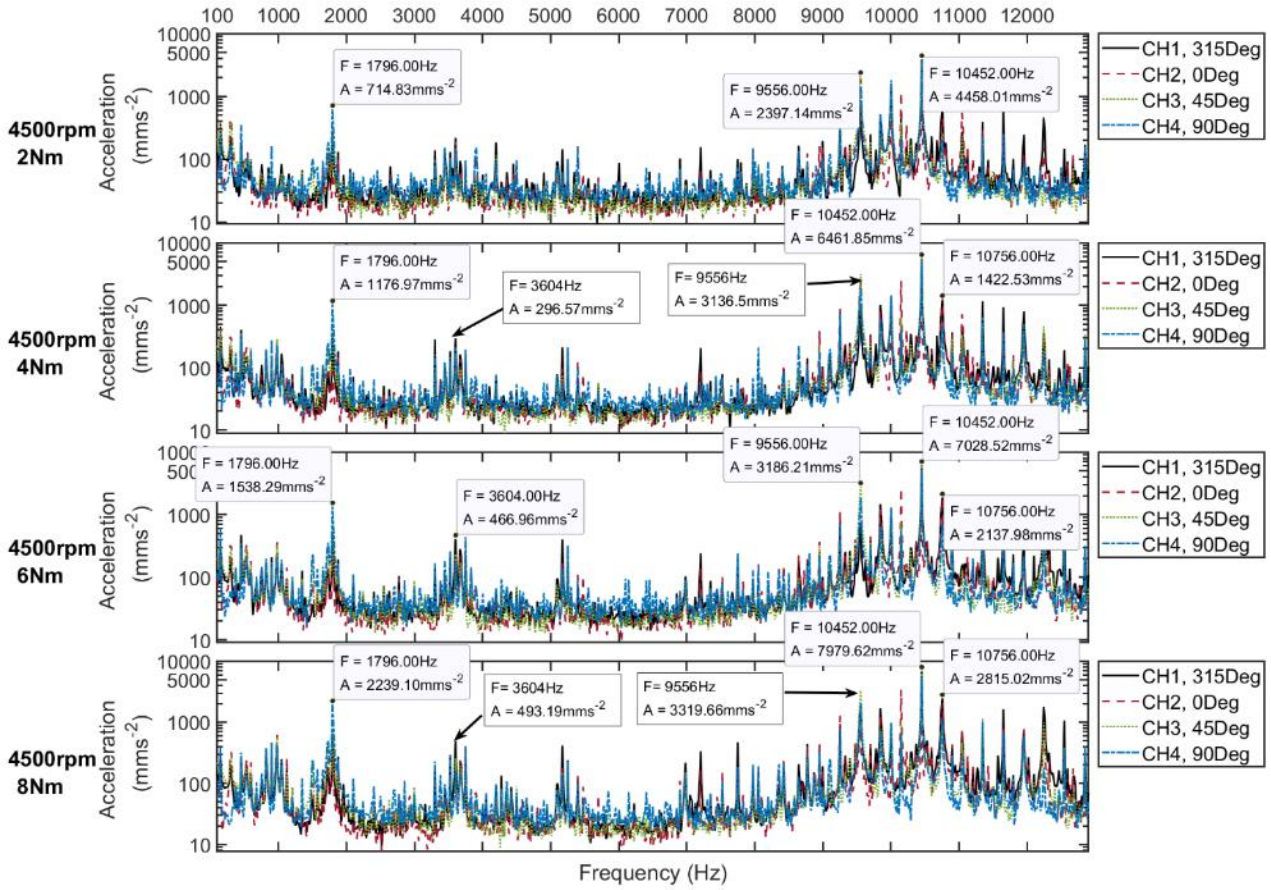

Fig. 6.3.5 Constant speed, 4500rpm, with torque varied between 2 -> 8Nm, I_d set to 0A.

Table 6.3.7 Measured acceleration with machine held at 4500rpm and incrementing torque

2Nm		4Nm		6Nm		8Nm	
Freq (Hz)	Acc (mms^{-2})	Freq (Hz)	Acc (mms^{-2})	Freq (Hz)	Acc (mms^{-2})	Freq (Hz)	Acc (mms^{-2})
1796	714.83	1796	1176.97	1796	1538.29	1796	2239.1
9556	2397.14	9556	3186.2	9556	3186.21	9556	3319.66
10452	4458	10452	6461.85	10452	6461.85	10452	7979.6
		10756	1422.5	10756	1422.5	10756	2815

The 4500rpm follows the same trend as the previous two speed points:

- The $12f_e$ frequency from the interactions with the stator teeth can be clearly observed at 1800Hz.
- The lower frequency $6f_e$ component is still present, but at 900Hz the frequency has clearly moved away from the excitation frequencies of the rig or driveline assembly excited in the previous two speed points and as such the amplitude has dropped considerably.
- The PWM side bands have neatly expanded proportionally to the rotor speed, following the trend from previous results.
    - The upper band ($f_c + 3f_e \approx 10450Hz$) is clearly sat at very close to a machine mode given the high amplitude at this frequency.
    - The low band ($f_c-3f_e=9550Hz$) shows the characteristics of a mechanical peak rather than a noise component, though the amplitude is much smaller than that of the upper band.

Accelerating the machine to the next speed point, 6000rpm moves the machine into the flux weakening region which necessitates adjusting the test procedure. Whilst all the testing up to the base speed thus far could operate purely on mutual torque ($I_d = 0$) moving up into the flux weakening region means some d-axis current must be applied to clamp the PM flux such that control of the machine can be retained. To achieve this the minimum amount of I_d required to maintain the target torque is applied. Table 6.3.8 shows I_d, I_q and the resultant current angle used for each torque point measured at 6000rpm.

Table 6.3.8 Id, Iq and resultant current angle used for each torque point at 6000rpm

	2Nm	4Nm	6Nm	8Nm
I_d	-2A	-7A	-13A	-19A
I_q	5A	9A	11A	12A
β°	21°	37°	49.5°	58°

Using the current values in Table 6.3.8, the machine is operated at 6000rpm with the results are shown in Fig. 6.3.6 and summarised in Table 6.3.9.

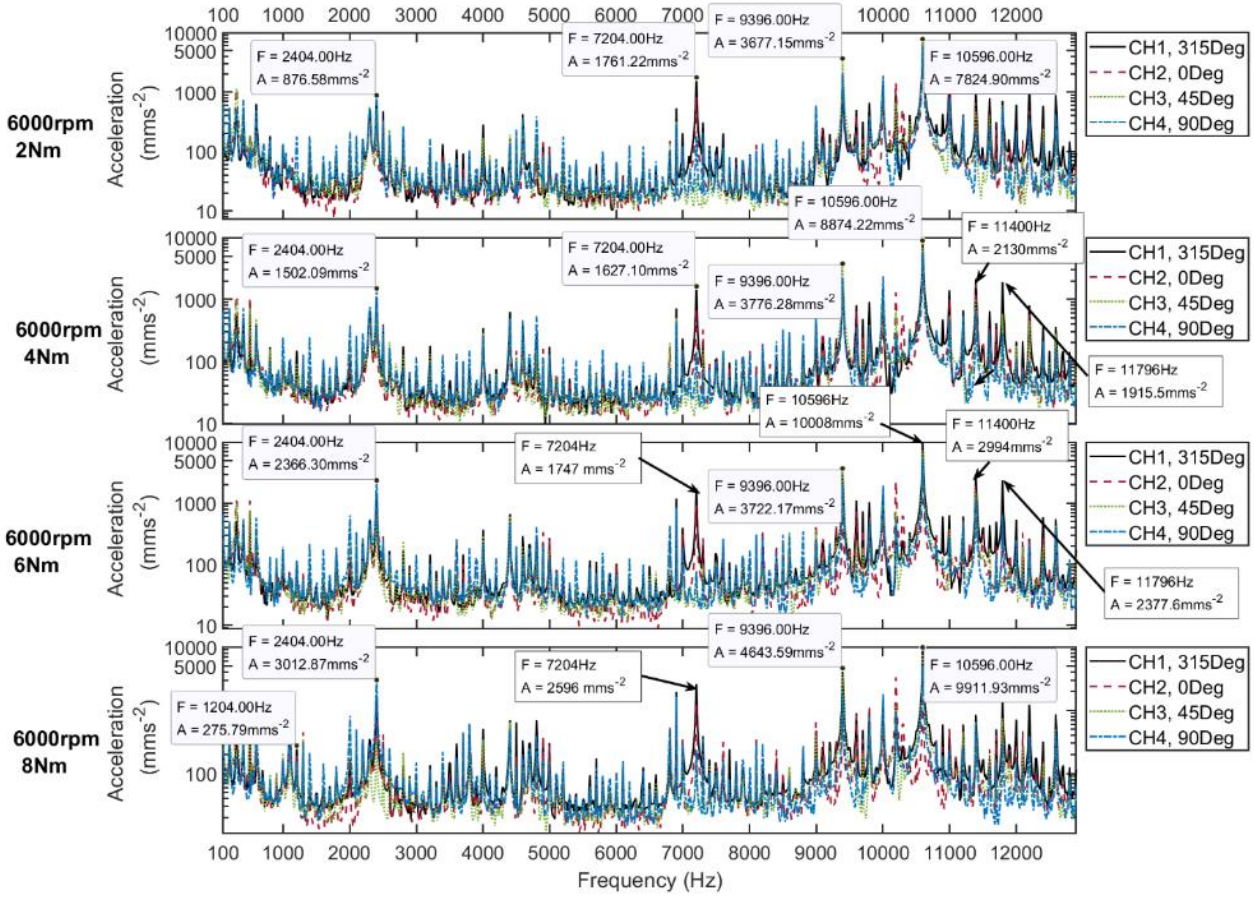

Fig. 6.3.6 Constant speed, 6000rpm, with torque varied between 2 -> 8Nm

Table 6.3.9 measured acceleration with machine held at 6000rpm and incrementing torque

2Nm		4Nm		6Nm		8Nm	
Freq (Hz)	Acc (mms^{-2})	Freq (Hz)	Acc (mms^{-2})	Freq (Hz)	Acc (mms^{-2})	Freq (Hz)	Acc (mms^{-2})
2404	876.5	2404	1502.1	2404	2366.3	1204	275.79
7204	1764.2	7204	1627.1	6900	1194	2404	3012.87
9396	3677.15	9396	3776.28	7204	1747	6900	1949
10596	7824.9	10596	7824.9	9396	3776.28	7204	2596
		11400	2130	10596	10008	9396	4643
		11796	2378	11400	2994	10596	9911
				11796	2377.6		

Entering the flux weakening region the spectrum is changed from the lower speed points:

- The noise levels on the measured data are much higher than the previous test points with Ch4 (90deg) in particular affected.
- The $6f_e$ component is present, however amplitude is low.
- The $12f_e$ peak is observed at the expected 2400Hz, with the amplitudes increasing with the torque as previously observed.

- The $36f_e$ (7200Hz) peak observed in the no-load at 6000rpm is once again present, showing a reasonable amplitude that is once again proportional to the torque. This indicates a harmonic of the ripple torque is exciting a machine mode at this frequency.
- The PWM side bands (f_c+3f_e and f_c-3f_e) show high amplitudes with the upper band frequency (10.6kHz) dominating the spectra clearly indicating the side band has aligned with a mode of the machine.

Similar to the 6000rpm moving up to the final and imposed maximum speed of 7500rpm requires a higher injection of flux weakening current to maintain control of the machine. The current settings used by the controller can be seen in Table 6.3.10.

Table 6.3.10 I_d, I_q and resultant current angle used for each torque point at 7500rpm

	2Nm	4Nm	6Nm
I_d	-8	-14	-19
I_q	4	6	8
β°	63°	64.5°	67°

Using these values, the final torque and speed values are measured and shown in Fig. 6.3.7 and summarised in Table 6.3.11.

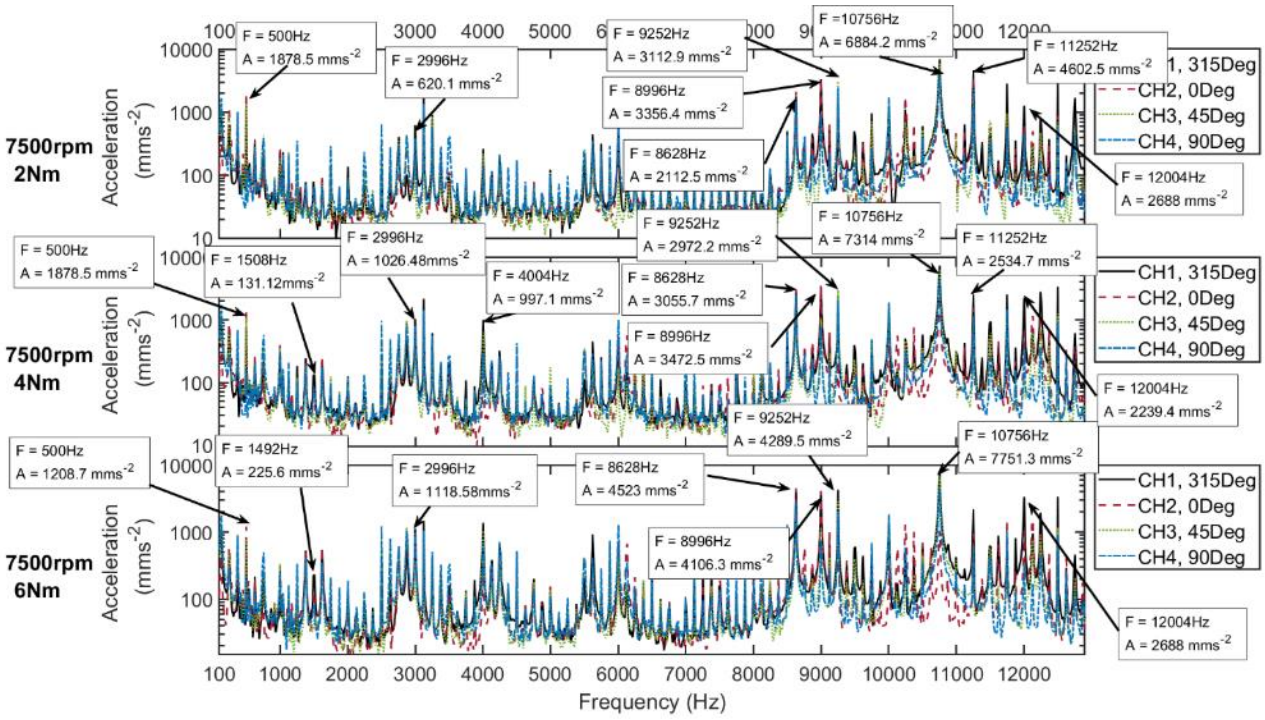

Fig. 6.3.7 Constant speed, 7500rpm, with torque varied between 2 -> 6Nm.

Table 6.3.11 Measured acceleration with machine held at 7500rpm and incrementing torque

7500rpm, 2Nm		7500rpm, 4Nm		7500rpm, 6Nm	
Freq (Hz)	Acc (mms-2)	Freq (Hz)	Acc (mms-2)	Freq (Hz)	Acc (mms-2)
500	1878.5	500	1878.5	500	1208.7
3124	1796.5	1508	131.12	1492	225.6
8628	2112.5	3124	2154.9	3124	1407.4
8996	3556.4	4004	997.1	4004	1377.6
9252	3112.9	8628	3055.7	8628	4523
10756	6884.2	8996	3472.5	8996	4106.3
11252	4602	9252	2972.2	9525	4289.5
12004	2688	10756	7314	10756	7751.3
		11252	2534.7	11252	2172.6
		12004	2239.4	12004	2688

At 7500rpm the background noise levels on the captured waveform become significant making it a more difficult to discern the key frequencies below 6kHz, as with the 6000rpm trace the sensor attached to channel 4, 90°, is the worst offender. One immediate observation is the application of current to the coils has had the effect of eliminating the resonance problem with the machine at 500Hz observed during the no-load test. Whilst the frequency is still excited, the loading of the rotor and driveline has had the effect of shifting the resonance frequency, in effect stiffening the structure. An additional observation is that whilst there is certainly more activity in the upper frequency region of the sampled bandwidth the very high peaks observed at 6000rpm around the upper PWM band has dropped, indicating that the frequency has now come out of phase with the machine mode observed at 6000rpm.

To summarise this section:

- The harmonic $12f_e$ clearly still induce vibrations in the structure, highlighting the high ripple rate of the machine.
- The $6f_e$ harmonic can be found at most speeds with two side bands $6f_e+f_m$ and $6f_e-f_m$ but the magnitudes tend to be low compared to the ripple torque, only showing with any significance at 1500rpm and 3000rpm when the frequencies align with a rotor or rig mode.
- The addition of the PWM and current in the coils clearly changes the picture observed in the no load:
    - Higher flux due to the MMF from both the PMs and the coils means the measured acceleration is much higher across all points, due of course to the higher forces.
    - The PWM side bands represent a significant source of noise, in particular around 6000rpm with the upper band (10.6kHz ($f_c + 3f_e$)) finding alignment with a machine mode.

6.3.3 Influence of the PWM switching on the machine

In all the load testing undertaken thus far a trend has appeared with the presence of two side bands sat symmetrically either side of the switching frequency, f_c, and are represented by the frequency's $f_c + 3f_e$ and sat at $f_c - 3f_e$. These are clearly related to the rotating speed of the machine, which can be illustrated by plotting each of these frequencies against each of the rotor speeds tested and can be seen in Fig. 6.3.8.

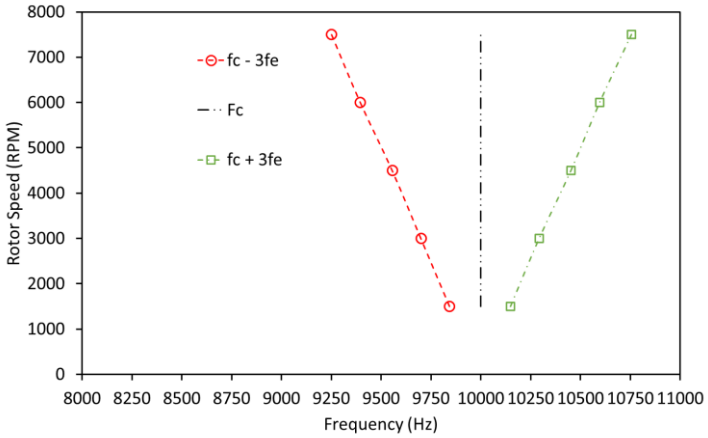

Fig. 6.3.8 Comparison of upper and lower frequency bands versus rotor speed.

The points in Fig. 6.3.8 are shown in Table 6.3.12 along with the difference between the upper and lower bands.

Table 6.3.12 Comparison of PWM switching frequency (f_c) upper and lower bands

Rotor Speed	Mechanical frequency (f_m)	Electrical frequency (f_e)	Lower band	Switching frequency (f_c)	Upper band	Fc – lower	Upper – Fc
1500rpm	25Hz	50Hz	9844Hz	10000Hz	10148Hz	156Hz	148Hz
3000rpm	50Hz	100Hz	9700Hz	10000Hz	10292Hz	300Hz	292Hz
4500rpm	75Hz	150Hz	9556Hz	10000Hz	10452Hz	444Hz	452Hz
6000rpm	100Hz	200Hz	9396Hz	10000Hz	10596Hz	604Hz	596Hz
7500rpm	125Hz	250Hz	9252Hz	10000Hz	10756Hz	748Hz	756Hz

Allowing for the errors typical in vibration measurement, in particular on such a complicated setup the results show clearly that the upper and lower bands are the 3rd harmonics of the electrical frequency (f_e) super imposed onto the carrier frequency from the PWM. A check of literature shows this phenomenon has been encountered by other researchers, appearing in some of the literature [AK16], [CL19], indicating this is not some unique problem with this setup. So, the key question is where do these frequencies derive from? The answer lies the Space Vector PWM (SVPWM) method that was discussed in Chapter 1. As highlighted in one of the benefits is the addition of a 3rd harmonic [JTB90] to increase the voltage utilisation and effectively increase the base speed. This method is utilised in the control for this machine and the evidence from these

results and also the results in the literature [WL14], [WL18] show it is having an effect on this machine. Further verification can be obtained by observing the voltage waveforms at the difference speeds. Using the power analyser and using a LabVIEW program written by the author to trigger and capture the data from the power analyser the voltage and current waveforms can be captured from the machine. The power analyser contains a 3rd order Butterworth filter with adjustable cut-off frequency, 5.5kHz in this case, on all channels [YMIC14]. This feature can be remotely engaged allowing the voltage and current waveforms to be capture with and without the higher frequency components. Fig. 6.3.9 shows the measured unfiltered and filtered voltage waveforms with the machine at 4Nm running at 3000rpm.

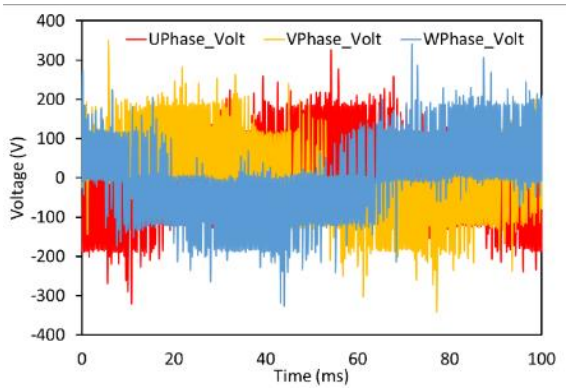

(a) Unfiltered voltage waveform @ 3000rpm, 4Nm, β = 0° (1 electrical cycle)

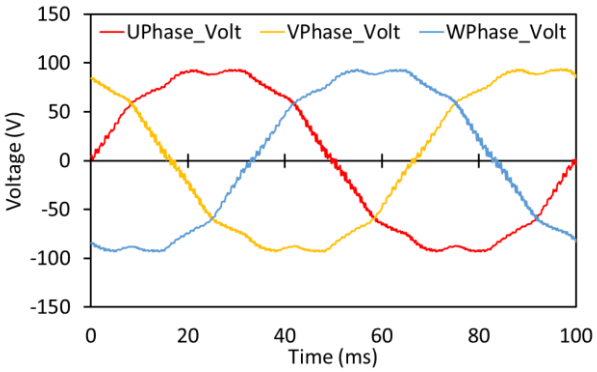

(b) 5.5kHz low pass filter applied to voltage waveform @3000rpm, 4Nm, β = 0° (1 electrical cycle)

Fig. 6.3.9 Comparison of the measured raw and filtered voltage waveforms at 3000rpm and 6Nm and the current angle set to 0°.

The unfiltered voltage waveform in Fig. 6.3.9(a) shows the actual voltage applied to the machine, which is very difficult to interpret, application of the 5.5kHz low pass filter eliminates much of the chatter generated by the switches and the underlying voltage waveform can be seen in Fig. 6.3.9(b). The flat top of the waveform from the SVPWM can be seen in 6.3.9(b), aligns to the theory in [JTB90] and [WL14].

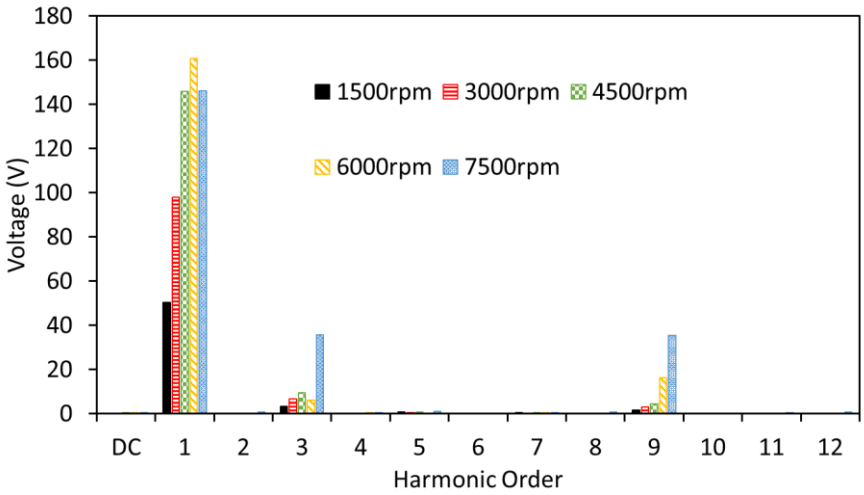

Fig. 6.3.10 Measured voltage harmonics in FILTERED voltages at 1500rpm, 3000rpm, 4500rpm, 6000rpm, 7500rpm @ 4Nm.

Fig. 6.3.10 shows the 3rd harmonic is clearly present in all cases. The FFT results in Fig. 6.3.10 also highlight the influence of the flux weakening function from the control. At 4Nm the flux weakening current at 6000rpm is relatively low, so the fundamental is still high but less of a step than the speeds below base speed. At 7500rpm high flux weakening currents are applied to operate at this speed so the fundamental has been lowered but a large step in the 9th harmonic a very large step on the 3rd harmonic can be seen.

6.3.3.1 Varying the PWM switching frequency: No load test

The analysis of the on-load test results shown previously highlighted the issues with the sidebands due to the SVPWM method on the machine and how with a switching frequency of 10kHz, the upper band in particular appear to excite key modes in the machine leading to large amplitudes on the acceleration sensors, in particular at speeds past 5000rpm. The logical question is, do these phenomena move with the switching frequency, as the theory would suggest, and are the high amplitudes unique to the 10kHz switching frequency? To test this the two additional switching frequencies were introduced, 8kHz and 12kHz. Time limitations on the test rig meant that a full suite of machine tests (T-N curve, MTPA map etc.) for the 8kHz and 12kHz switching frequency could not be undertaken but a few simple no load and load tests were undertaken to understand the impact on the vibratory performance of this machine.

6.3.3.2 Adjusting the PWM frequency under no-load conditions

The first test run is a no-load test. The no-load testing differs from the test described previously in that the inverter and controller are engaged (i.e., all circuit breakers closed) with the target I_d and I_q currents set to 0Amps. Under these conditions there is very little current in the coils. However, even with the PWM effectively set to 0% there will still be some switching. Thus, some peaks around the switching frequencies should be observed. The machine is operated at 1500rpm, 3000rpm, 4500rpm and 6000rpm and the frequency switched between one after another.

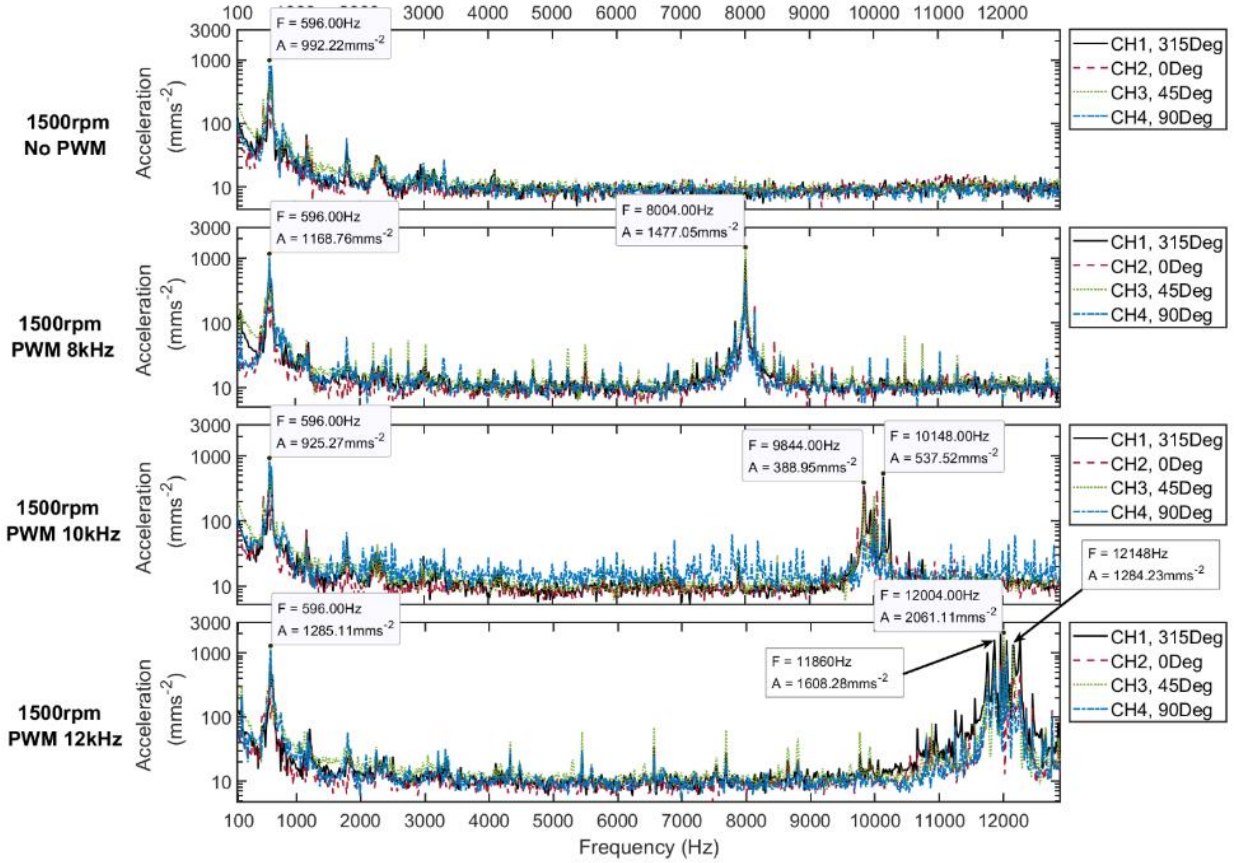

(a) No load, 1500rpm, comparing open circuit with 8kHz, 10kHz and 12kHz switching frequencies

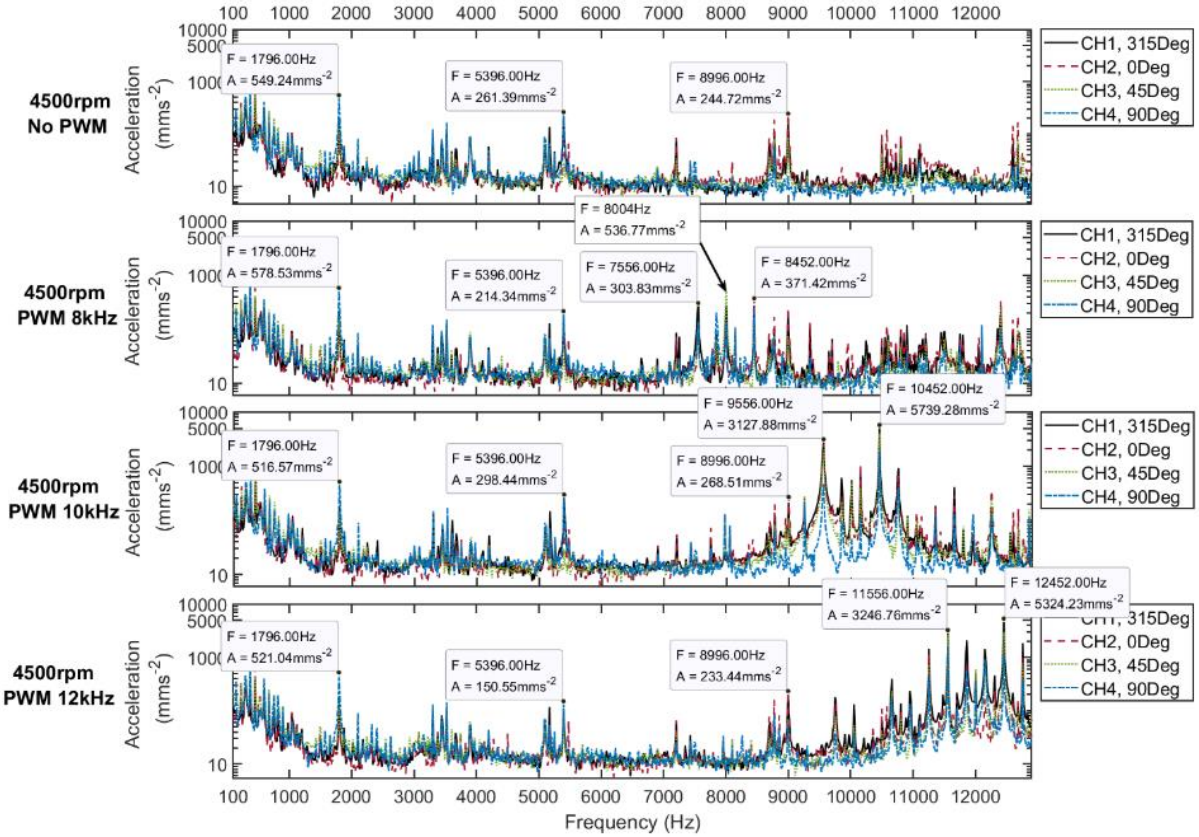

(b) No load, 4500rpm, comparing open circuit with 8kHz, 10kHz and 12kHz switching frequencies

Fig. 6.3.11 Comparison of no-load outputs of acceleration sensors with different PWM switching frequencies.

The trend for each of the frequencies follows the same pattern, with side bands forming either side of the PWM frequency. The frequencies and amplitudes are provided for each of the tests are shown in Table 6.3.12.

Table 6.3.12 Summary of the no-load PWM frequency bands at 8Khz, 10kHz and 12kHz switching frequencies and increasing rotor rpm.

Speed (rpm)	lower band, 8kHz switching frequency			Upper band, 8kHz switching frequency		
	Frequency (Hz)	Acc. (mms^{-2})	Fc – Lwr	Frequency (Hz)	Acc. (mms^{-2})	Upr – fc
1500	7844 Hz	107.5 mms^{-2}	156Hz	8148 Hz	200.1 mms^{-2}	148 Hz
3000	7700 Hz	245.2 mms^{-2}	300Hz	8292 Hz	198.2 mms^{-2}	292 Hz
4500	7556 Hz	303.8 mms^{-2}	444Hz	8452 Hz	536 mms^{-2}	452 Hz
6000	7396 Hz	259.2 mms^{-2}	604Hz	8596 Hz	223.2 mms^{-2}	596 Hz
Speed (rpm)	lower band, 10kHz switching frequency			Upper band, 10kHz switching frequency		
	Frequency (Hz)	Acc (mms^{-2})	Fc – Lwr	Frequency (Hz)	Acc (mms^{-2})	Upr – fc
1500	9844 Hz	388.9 mms^{-2}	156Hz	10150 Hz	537.5 mms^{-2}	148Hz
3000	9700 Hz	2040 mms^{-2}	300Hz	10292 Hz	1528 mms^{-2}	292Hz
4500	9556 Hz	6321 mms^{-2}	444Hz	10450 Hz	5739 mms^{-2}	450Hz
5000*	9508 Hz	1887 mms^{-2}	492Hz	10500 Hz	6321 mms^{-2}	500Hz
Speed (rpm)	lower band, 12kHz switching frequency			Upper band, 12kHz switching frequency		
	Frequency (Hz)	Acc (mms^{-2})	Fc – Lwr	Frequency (Hz)	Acc. (mms^{-2})	Upr – fc
1500	11854 Hz	1608 mms^{-2}	146 Hz	12148 Hz	1711 mms^{-2}	148 Hz
3000	11700 Hz	1934 mms^{-2}	300 Hz	12310 Hz	3625 mms^{-2}	310 Hz
4500	11560 Hz	3247 mms^{-2}	440 Hz	12450 Hz	5324 mms^{-2}	450 Hz
6000	11410 Hz	2883 mms^{-2}	590 Hz	12610 Hz	3453 mms^{-2}	610 Hz

*Note: The testing sequence started with 10kHz and due a concern with the dynamometer the maximum speed recorded was 5000rpm. The concern was resolved upon adjusting the controller to 8kHz switching frequency but unfortunately as these tests occurred at the end of the test sequence the no-load performance with the machine at 6000rpm was not re-measured with the 10kHz switching frequency due to time constraints on using the test rig.

The low frequency components at $12f_e$ and the rig components are identical for each case and the amplitude has only a little variation compared to the open circuit case. The PWM components can be clearly seen in each case, in particular on 4500rpm test with the 10kHz and 12kHz showing high amplitudes. Plotting the bands shown in Table 6.3.12 in a similar manner to Fig. 6.3.8 reveals the same pattern previously established for the increase in bandwidth as the speed increases, even under no load conditions this is illustrated in Fig. 6.3.12.

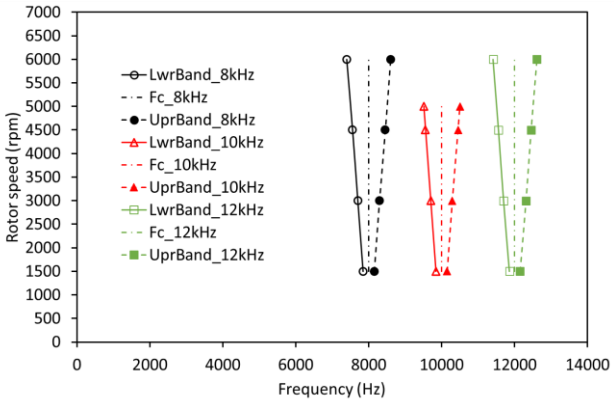

Fig. 6.3.12 Chart showing the sidebands generated by the SVPWM strategy at the 3 different PWM switching frequencies, 8kHz, 10kHz and 12kHz.

The band gap between the upper and lower frequencies are identical for each rotor speed, regardless of the switching frequency, further reinforcing the point the gap is a function of the 3rd harmonic due to the SVPWM switching strategy.

6.3.3.3 Adjusting the PWM frequency under load conditions

The results of adjusting the PWM switching frequency showed relatively large peaks forming on the 10kHz and 12kHz tests in particular on the upper bands, of each as the bands hit apparent alignment with different modes of the machine. Given the no load conditions there is very little current in the machine, aside from parasitic loads coming from the machine and the inverter. Thus, from the no-load results alone it is difficult to establish whether the spikes are a result of a force applied to the machine via the air gap flux or EMI induced on the sensor by the switching components of the inverter. To establish this, the machine was operated at load under the same conditions as the constant-speed, variable torque as the 10kHz switching frequency results previously detailed. Time restrictions limited the points that could be tested so a very simple set of 2 speeds, one in the constant torque region and one in the flux weakening region with 2 torques per speed were chosen, as detailed in Fig. 6.3.13.

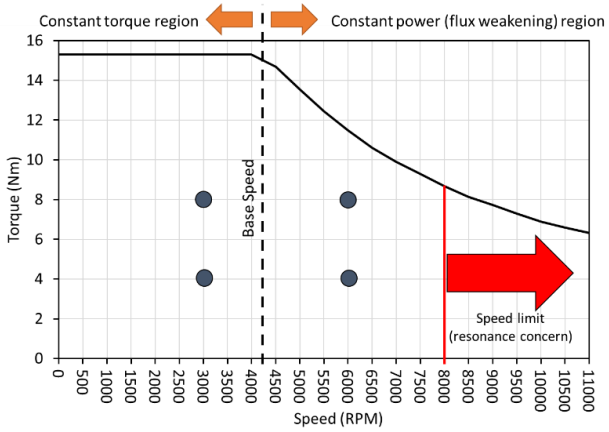

Fig. 6.3.13 Test points on T-N curve used to compare influence of varying PWM switching frequency on the vibratory performance of the machine under load conditions.

A summary of all the test points is provided in Table 6.3.13, note: the 10kHz switching frequency results are the same results from the previous load testing but included here for ease of comparison.

Table 6.3.13 Test points for each switching frequency

	4Nm			8Nm		
Speed (rpm)	8kHz	10kHz	12kHz	8kHz	10kHz	12kHz
3000	✓	✓	✓	✓	✓	✓
6000	✓	✓	✓	✓	✓	✓

The testing here is less comprehensive due to the aforementioned time restrictions on the rig but operating the machine at a few test points either side of the base speed should be sufficient to show any trends or concerns, in particular as the previous tests (constant speed, variable torque) showed relatively low amplitudes until the machine passed 3000rpm. The testing follows the same procedure as previously discussed, the major difference being that in order to change the switching frequency the controllers needs to be taken offline which means isolating the machine from the inverter, shutting down the dSPACE controller and re-compiling the Simulink code used to control the machine. Once the compilation process is completed the controller hardware can be re-started and the inverter once again linked to the machine via the contactors. Fig. 6.3.14 shows the comparison between the machine running at 3000rpm at 4Nm and 8Nm with different switching frequencies.

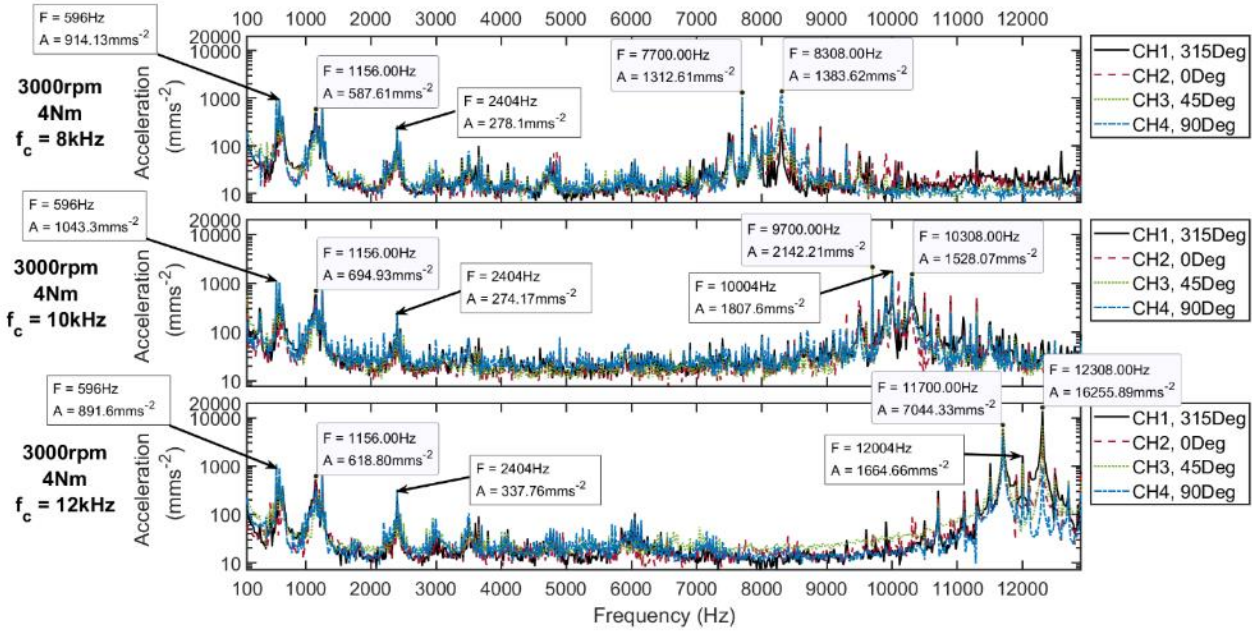

(a) Influence of PWM f_c at 8kHz, 10kHz and 12kHz on vibratory performance at 3000rpm, 4Nm

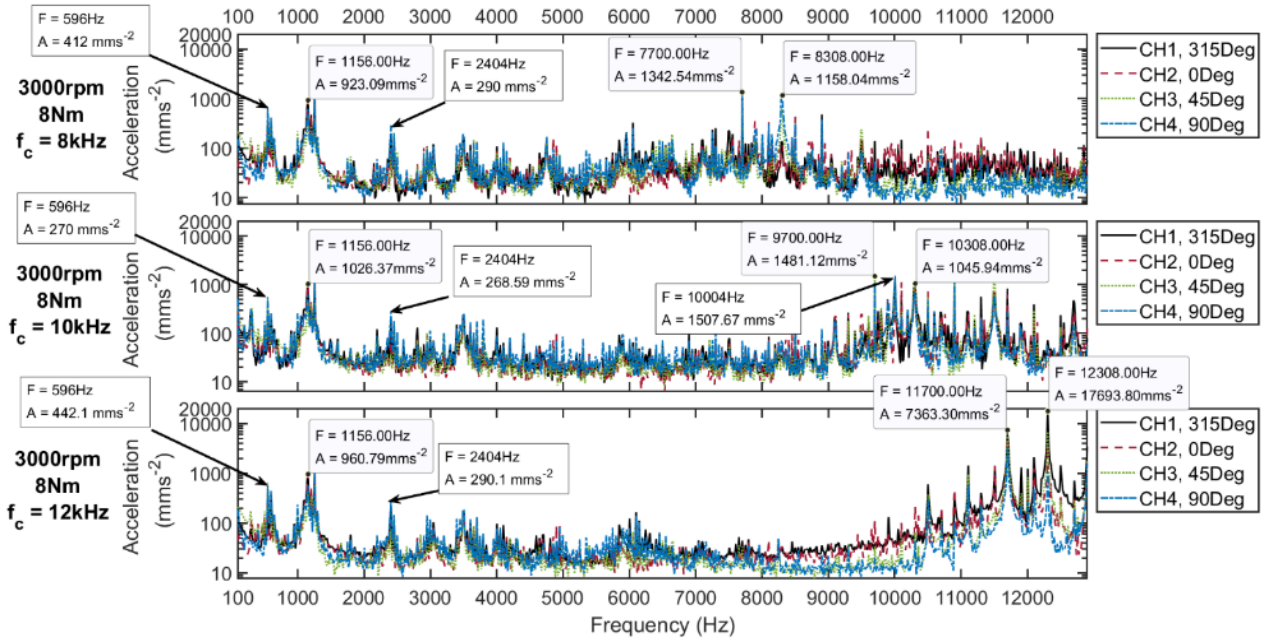

(b) Influence of PWM f_c at 8kHz, 10kHz and 12kHz on vibratory performance at 3000rpm, 8Nm

Fig. 6.3.14 Comparison of baseline machine vibration operating at 3000rpm, 4Nm, 8Nm with increasing PWM switching frequency (8kHz, 10kHz and 12kHz).

The key frequencies from the acceleration results in Fig. 6.3.14 are shown in Table 6.3.14.

Table 6.3.14 Summary of acceleration sensor results with varying PWM switching frequency at 3000rpm, 4Nm and 8Nm

Fc = 8kHz, 3000rpm, 4Nm		Fc = 10kHz, 3000rpm, 4Nm		Fc = 12kHz, 3000rpm, 4Nm	
Freq. (Hz)	Acc. (mms^{-2})	Freq. (Hz)	Acc. (mms^{-2})	Freq. (Hz)	Acc. (mms^{-2})
596	914.13	596	1043.3	596	891.6
1156	587.61	1156	694.9	1156	618.80
1204	231.65	1204	292.3	1204	332.4
1252	763.98	1252	794.19	1252	924.43
2404	278.1	2404	268.59	2404	337.76
7700	1312.18	9700	2141.2	11700	7044.33
8308	1383.62	10004	1807.6	12004	1664.67
		10308	1528.07	12308	16255.89
Fc = 8kHz, 3000rpm, 8Nm		Fc = 10kHz, 3000rpm, 8Nm		Fc = 12kHz, 3000rpm, 8Nm	
Freq. (Hz)	Acc. (mms^{-2})	Freq. (Hz)	Acc. (mms^{-2})	Freq. (Hz)	Acc. (mms^{-2})
596	412	596	270	596	442.1
1156	923.1	1156	1026.37	1156	960.79
1204	453.5	1204	472.16	1204	509.66
1252	1384.1	1252	1432.5	1252	1379.49
2404	290	2404	268.6	2404	290.1
7700	1342.54	9700	1481.12	11700	7363.3
8308	1158.04	10004	1507.67	12308	17693.8
		10308	1045.94		

From the results in Fig. 6.3.14 and Table 6.3.14, the following observations can be made:

- In terms of the modes due to torque ripple etc. there is no difference between both the frequencies and very minor differences in the amplitudes measured at the different frequencies.
    - Minor variations in the amplitudes at the 596Hz ($6f_e$) point likely relate to the aspect of the rig being excited than anything machine given electromagnetically they are under the same load and mechanically the setup has not been changed.
- The PWM side bands at f_c+3f_e and f_c-3f_e are clear and dominant at all frequencies.
    - At 10kHz and 8kHz the lower side band (f_c-3f_e) appears more as induced noise than a modal peak owing to the spike-like profile of the peak.
    - Amplitudes of the peaks and side bands at 8kHz and 10kHz f_c are very similar in amplitude indicating some impact but no alignment with any machine modes.
- 12kHz f_c shows extremely high amplitudes, in particular f_c+3f_e where the amplitude is greater than 10 times the nearest peak from the 8kHz and 10kHz f_c results.
    - The level of displacement for all acceleration sensors indicates alignment with a low order machine mode, likely mode 0.

Following on from the 3000rpm, the speed point in the flux weakening region, 6000rpm, is measured. The same methodologies for changing the PWM switching frequency and the method of applying some I_d current to clamp the rotor flux is utilised during this measurement. The results are shown in Fig. 6.3.15.

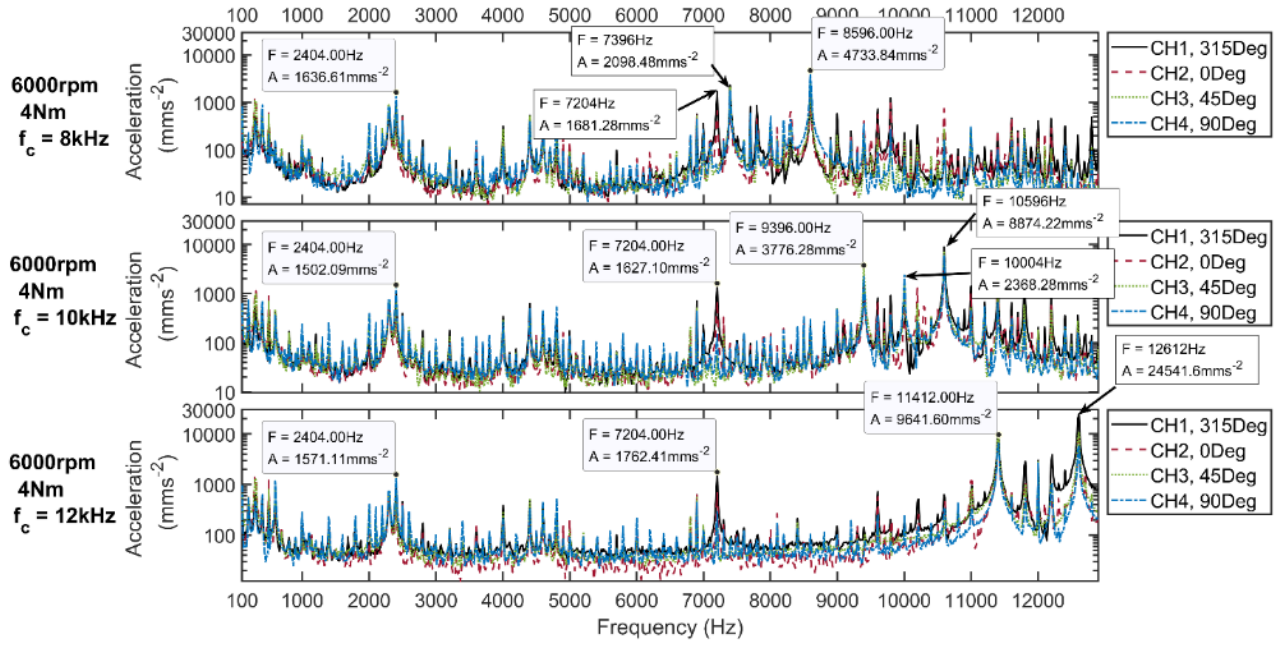

(a) Influence of PWM f_c at 8kHz, 10kHz and 12kHz on vibratory performance at 6000rpm, 4Nm

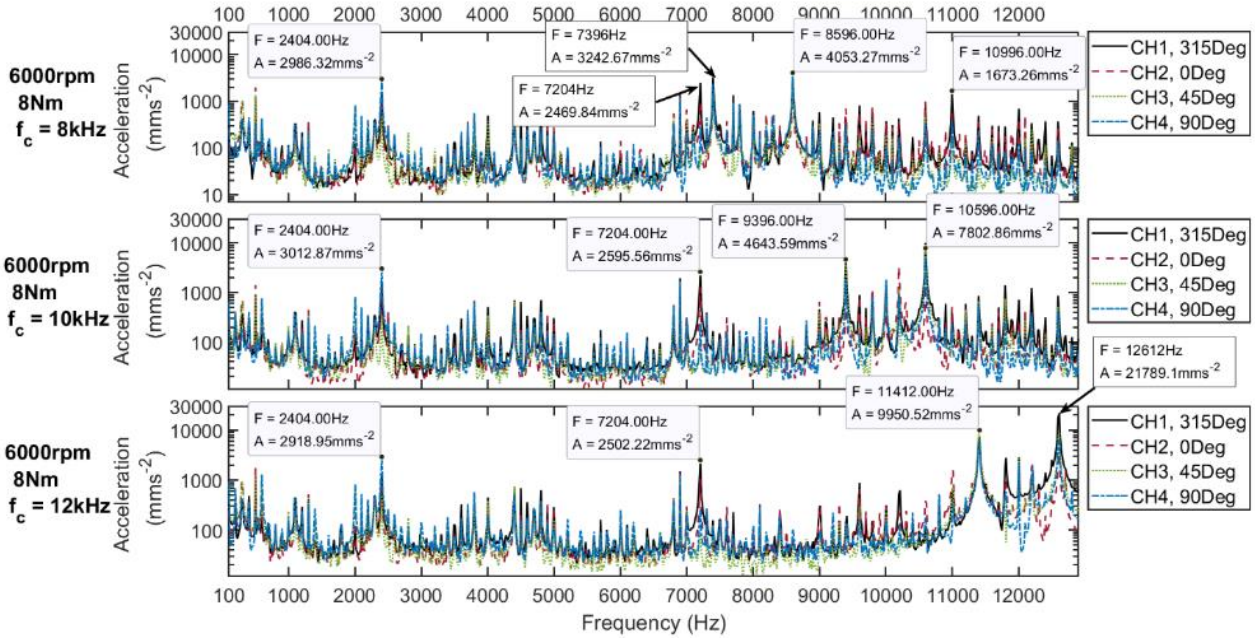

(b) Influence of PWM f_c at 8kHz, 10kHz and 12kHz on vibratory performance at 6000rpm, 8Nm

Fig. 6.3.15 Comparison of baseline machine vibration operating at 6000rpm, 4Nm, 8Nm with increasing PWM switching frequency (f_c) (8kHz, 10kHz and 12kHz).

Similar to the 3000rpm results the key frequencies with the machine running at 6000rpm, 4Nm, 8Nm and the PWM frequency incrementally increases are summarised in Table 6.3.15.

Table 6.3.15 Summary of acceleration sensor results with varying PWM switching frequency at 6000rpm, 4Nm and 8Nm

Fc = 8kHz, 6000rpm, 4Nm		Fc = 10kHz, 6000rpm, 4Nm		Fc = 12kHz, 6000rpm, 4Nm	
Freq. (Hz)	Acc. (mms^{-2})	Freq. (Hz)	Acc. (mms^{-2})	Freq. (Hz)	Acc. (mms^{-2})
2404	1636.61	2404	1502.1	2404	1571.11
7204	1681.28	7204	1627.1	7204	1762.41
7396	2098.48	9396	3776.28	11412	9641.60
8596	4733.84	10004	2368.28	12612	24541.6
		10596	8874.22		
Fc = 8kHz, 6000rpm, 8Nm		Fc = 10kHz, 6000rpm, 8Nm		Fc = 12kHz, 6000rpm, 8Nm	
Freq. (Hz)	Acc. (mms^{-2})	Freq. (Hz)	Acc. (mms^{-2})	Freq. (Hz)	Acc. (mms^{-2})
2404	2986.3	2404	3012.87	2404	2918.95
7204	2469.84	7204	2595.56	7204	2502.22
7396	3242.67	9396	4643.6	11412	9950.52
8596	4053.27	10596	7802.86	12612	21789.1
10996	1673.26				

The results in Fig. 6.3.15 and Table 6.3.15 show much the same trends as the 3000rpm with the frequencies attributed to the machine geometry at 6000rpm (2404Hz ($12f_e$) and 7200Hz ($36f_e$)) being constant for each switching frequencies and the amplitudes at each torque step align well given the nature of the testing. For the peaks found around the switching frequencies there is some difference with the results at 3000rpm.

- The lower bands (f_c-3f_e) when f_c = 10kHz and 8kHz appear to be close to machine modes and share similar amplitudes, the 10kHz being slightly higher.
- The upper band (f_c+3f_e) when f_c =10kHz is clearly in alignment with a machine mode at ~10600Hz, showing a much higher peak than the equivalent band at 8kHz.
- The side bands when f_c = 12kHz have clearly hit a machine mode, in particular the upper band sitting at ~12600Hz showing the highest peak recorded in all dynamic testing thus far.

Given the above results of the measurements the effects of adjusting the PWM frequency can be summarised as follows:

- The frequencies due to aspects such as the ripple torque (12f_e) are consistent for each test and the amplitudes sit in reasonable alignment.
- The PWM frequency, and in particular the f_c+3f_e and f_c-3f_e components from the SVPWM clearly have a large impact on the overall vibratory performance for this machine.
    - Setting the switching frequency, f_c, to 8kHz has the lowest impact on the machine as it sits in an apparent dead zone in terms of key machine modes.
    - Setting f_c to 10kHz shows more impact, in particular the f_c+3f_e band at 6000rpm which aligns with a machine mode at ~10.6kHz.
    - The switching frequency with the highest impact is quite clearly 12kHz where the upper band (fc+3fe) quite clearly aligns with a low mode of the machine generating very large acceleration on all sensors; the profile matches that of mode 0 (breathing).

The conclusion from these tests is that the 8kHz switching frequency appears to mitigate the impact of the PWM and the f_c+3f_e and f_c-3f_e bands the best. Unfortunately, this was established towards the end of the test window on the dynamometer, so the key lesson here is to evaluate the PWM switching frequency carefully as early as possible in the test phase as the general rule of thumb with selection of PWM frequencies clearly has an issue on this machine; the standard 10kHz utilised on traction applications aligns to a number of machine modes on the baseline machine which probably does not apply to full scale traction machines.

6.3.4 Current angle sweep

The previous tests effectively held the current angle at 0° to minimise the influence of the reluctance component on the vibration characteristics of the machine. For this test, the influence of the current angle is the focus of the study with the current angle swept from 10° to 60° (70° in the very high-speed region) and the vibration measured at each point. Given the high number of potential test points, the number of speeds for different torque points is limited to 4, i.e. 2 speeds in the constant torque region (1500rpm, 3000rpm) and 2 speeds in the constant power (flux weakening) region (6000rpm, 7500rpm). For each of the speeds, 3 torque values are used, 4Nm, 6Nm, and a maximum of 12Nm for the lower speed points to allow the

reluctance torque component to be observed. The lower torque values allow the same torque to be measured and compared at all the chosen test speeds. The points chosen are summarised in Fig. 6.3.16 and the full list of speeds, torques and current angles is shown in Table 6.3.16.

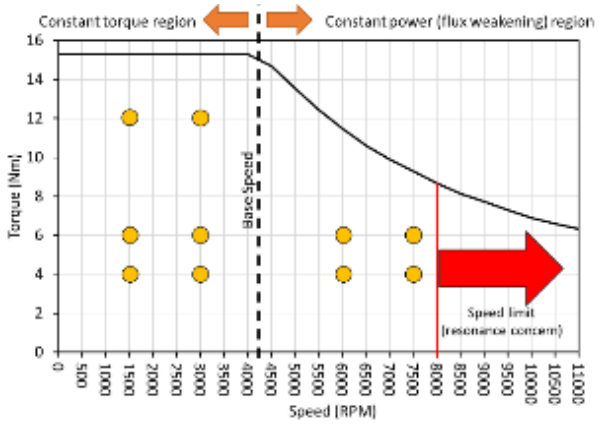

Fig. 6.3.16 Test points for the influence of changing the current angle on the vibration performance.

Table 6.3.16 Full list of measured test points for current angle sweep test

Torque	β°	1500rpm	3000rpm	6000rpm	7500rpm
4Nm	10°	✓	✓	✗	✗
	20°	✓	✓	✗	✗
	30°	✓	✓	✗	✗
	40°	✓	✓	✓	✗
	50°	✓	✓	✓	✗
	60°	✓	✓	✓	✓(65°)
	70°	✗	✗	✓	✓
6Nm	10°	✓	✓	✗	✗
	20°	✓	✓	✗	✗
	30°	✓	✓	✗	✗
	40°	✓	✓	✗	✗
	50°	✓	✓	✓	✗
	60°	✓	✓	✓	✗
	70°	✗	✗	✓	✓
12Nm	10°	✗	✗	✗	✗
	20°	✗	✗	✗	✗
	30°	✓	✓	✗	✗
	40°	✓	✓	✗	✗
	50°	✓	✓	✗	✗
	60°	✓	✓	✗	✗
	70°	✗	✗	✗	✗

Table 6.3.16 shows which current angles can be practically utilised, especially in the flux weakening region, meaning that the number of actual test points is 36, rather than 84 potential points. For the low speed points the maximum current angle was limited to 60° to reduce the risk of demagnetising the rotor; typically by the time the higher angles were reached the core machine temperatures were getting quite high so rather than risk permanently damaging the machine the angle was limited. The higher angle of 70° was only really utilised

for the higher speeds where very large current angles are required simply for the controller to maintain operation of the machine.

Given the large number of measured points the results will be split by speed with the first run at 1500rpm shown in Fig. 6.3.17 and the resultant summary shown in Table 6.3.17.

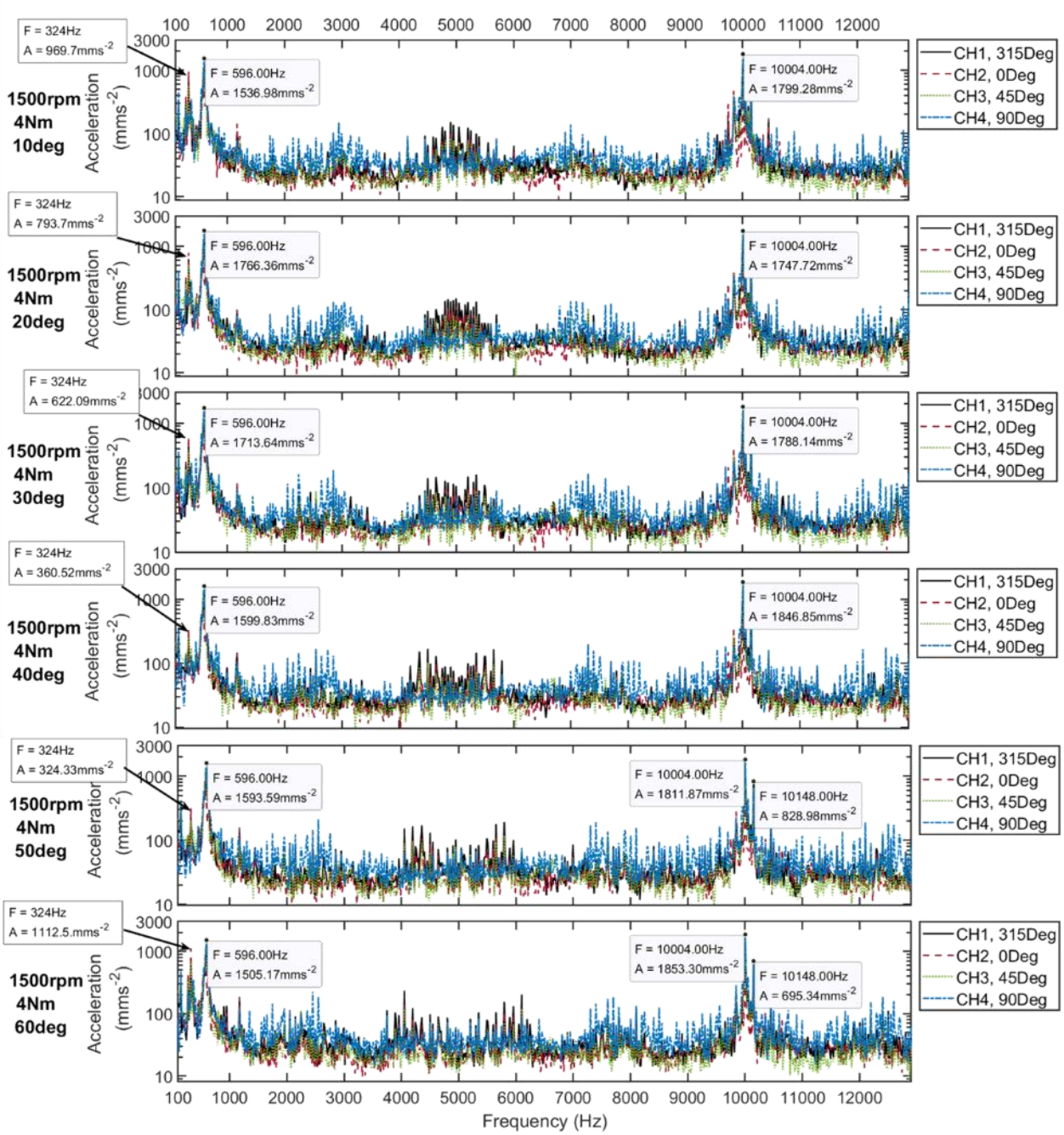

(a) Current angle sweep, 1500rpm, 4Nm, current angle swept 10° to 60°

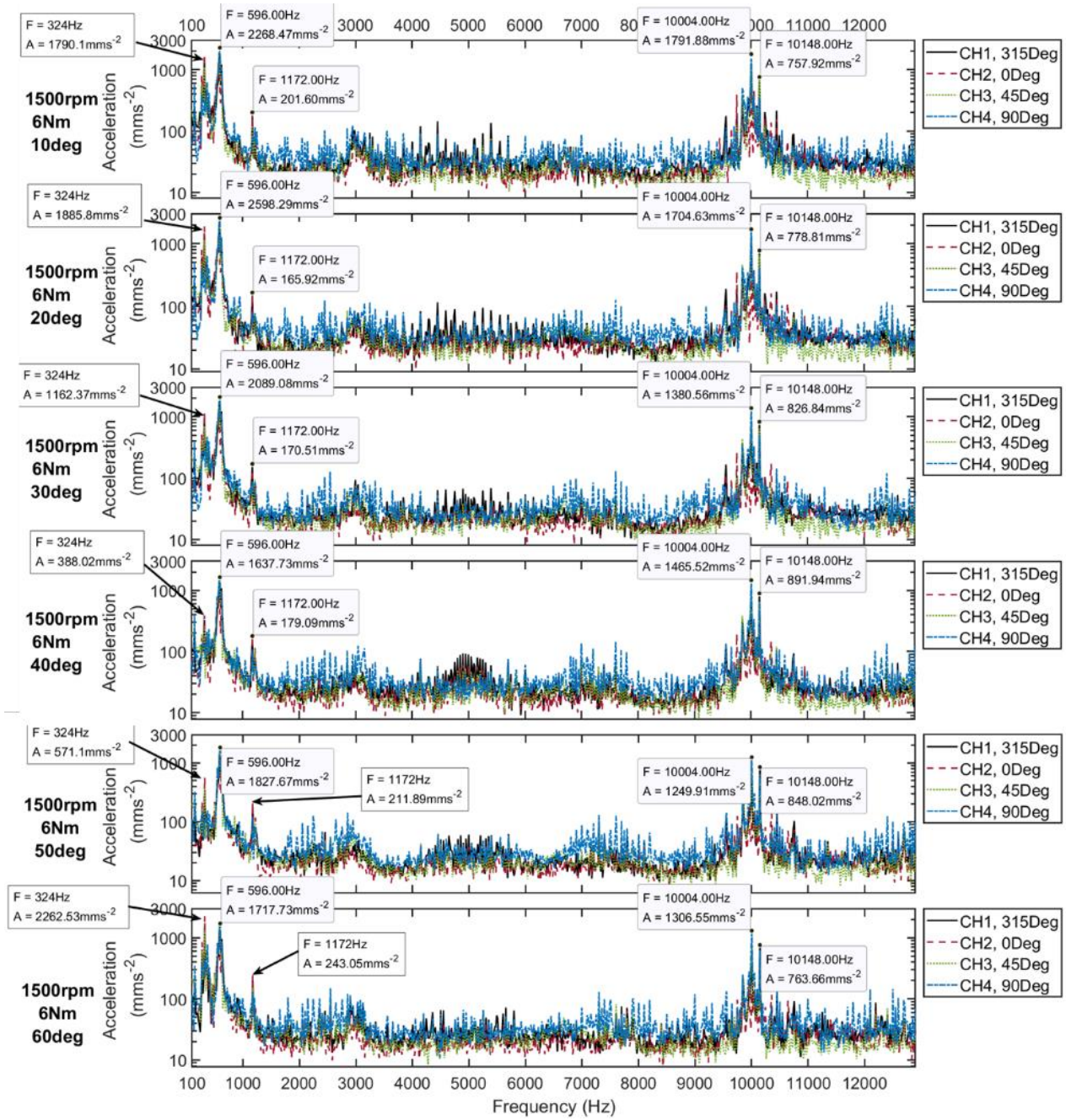

(b) Current angle sweep, 1500rpm, 6Nm, current angle swept 10° to 60°

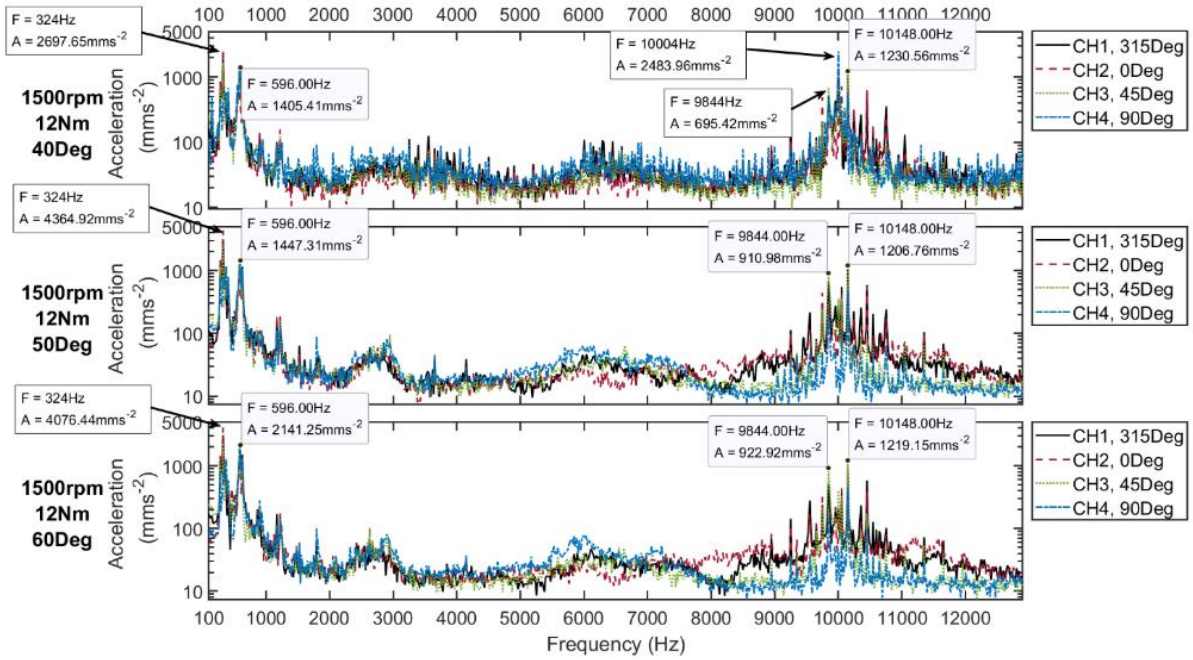

(c) Current angle sweep, 1500rpm, 12Nm, current angle swept 40° to 60°

Fig. 6.3.17 Vibratory performance of machine running at 1500rpm and 4Nm, 6Nm, and 12Nm with the current angle incremented.

Table 6.3.17 Measured acceleration at 1500rpm with incrementing current angle (10° to 60°) at 4Nm, 6Nm and 12Nm

	1500rpm, 4Nm		1500rpm, 6Nm		1500rpm, 12Nm	
β°	Freq (Hz)	Acc (mms^{-2})	Freq (Hz)	Acc (mms^{-2})	Freq (Hz)	Acc (mms^{-2})
10°	324	969.7	324	1790.1		
	596	1536.98	596	2288.5		
	10004	1799.3	1172	201.6		
			10004	1791.9		
			10148	757.92		
20°	324	793.7	324	1885.8		
	596	1766.36	596	2598.3		
	10004	1747.7	1172	165.9		
			10004	1704.6		
			10148	778.81		
30°	324	622.1	324	1162.4		
	596	1713.64	596	2089.1		
	10004	1788.14	1172	170.51		
			10004	1380.6		
			10148	826.84		
40°	324	360.5	324	388	324	2697.7
	596	1599.83	596	1637.7	580	1334.2
	10004	1846.85	1172	179.1	9844	695.4
			10004	1465.5	10004	2483.9
			10148	891.94	10148	1230.6
50°	324	318.33	324	571.1	324	4364.9
	596	1593.59	596	1827.7	596	1447.3
	10004	1811.87	1172	211.89	9844	911
	10148	828.98	10004	1306.5	10148	1232.4
			10148	848.02		

60°	324	1112.53	324	2262.5	324	4076.4
	596	1505.17	596	1717.7	596	2141.3
	10004	1853.3	1172	243.05	9844	922.9
	10148	695.34	10004	1306.6	10148	1219.2
			10148	763.66		

From the analysis, the same frequencies appear as in observed in every other test taken at this speed so far showing good repeatability. The observations from Fig. 6.3.17 are:

- At 4Nm, there is minimal impact on the overall vibratory performance of the ripple frequency, the only item of interest is the 324Hz ($6f_e+f_m$) peak, which drops considerably from 969.7 mms-2 to about 1/3 of that amplitude at 40° before rapidly increasing as the current angle passes 50°.
- As the torque increases to 6Nm this trend of the amplitude dropping at 324Hz is even more pronounced and the effect is seen at the $12f_e$ (~600Hz) frequency.
- At all torque points small peak can be observed at $24f_e-f_m$ (1172Hz), most noticeable at 6Nm indicating some small excitation on the rig assembly. However, compared to the above points and the influence of the PWM on the amplitude is negligible.
- For 12Nm, the lower frequency peaks start from a low and build as the current angle is increased, following the trend from the previous points.
- The PWM side bands provide no significant contribution for the 4Nm and 6Nm cases, and however, are present at the 50° and 60° steps.

The trend with the drop in amplitude on the $6f_e+f_m$, $12f_e$ and f_c harmonics observed in Fig. 6.3.17 is quite logical. As the current angle is increased from 10° towards 40° the reluctance component comes more into play meaning that to maintain the same torque the net current, I_{dq}, can decrease. Lower current means a lower MMF in the coil, and therefore, the electromagnetic forces acting on the stator are reduced. This is more pronounced at the 6Nm step due to the higher currents involved. As the current angle is moved past the point where the peak reluctance component can be found (between 40° and 50°) the controller has a concern as not only is the reluctance torque component dropping due to the change in the L_q/L_d ratio but the flux weakening effect is suppressing the PM flux meaning more current must be applied into the coils to achieve the target torque, boosting the coil MMF and causing the force amplitudes to rapidly increase past 50° compared to the gradual reduction moving from 10° to 40°. Fig. 6.3.18 illustrates the amplitude data observed in Table 6.3.17 for the $6f_e+f_m$ and 12fe harmonics, which are plotted against the current angle to better illustrate the trend.

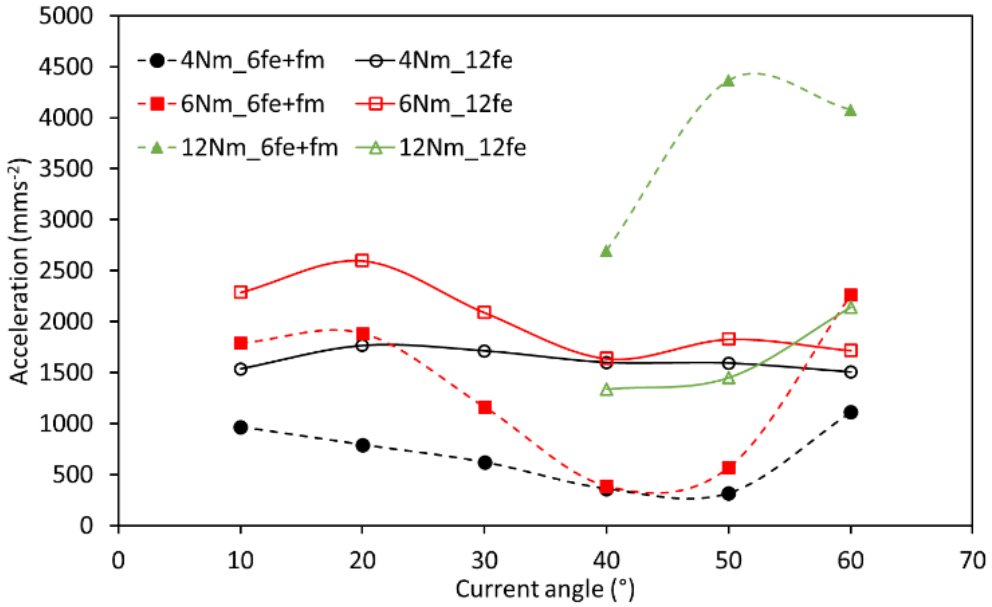

Fig. 6.3.18 Comparison of the $6f_e+f_m$ and $12f_e$ harmonic amplitudes for the tested torques versus current angle.

From Fig. 6.3.18, it can be seen that for the amplitudes for all points below 40° (omitting the 12Nm traces) the general trend is a reduction in amplitude, reflecting the drop in I_{dq} current. At 40° the acceleration measured at each harmonic is at a minimum and the curve of each rises at 50°. The effect is most pronounced on the 4Nm and 6Nm $6f_e+f_m$ harmonics. For the $12f_e$ harmonics a rise is seen at 50° but levels off a little at 60°. At the very high load 12Nm at 60° the amplitude drops a little, perhaps more related to the machine being quite saturated at this point than the lower torque points. The current angle sweep test process is repeated for 3000rpm and the results can be seen in Fig. 6.3.19 and the summary in Table 6.3.18.

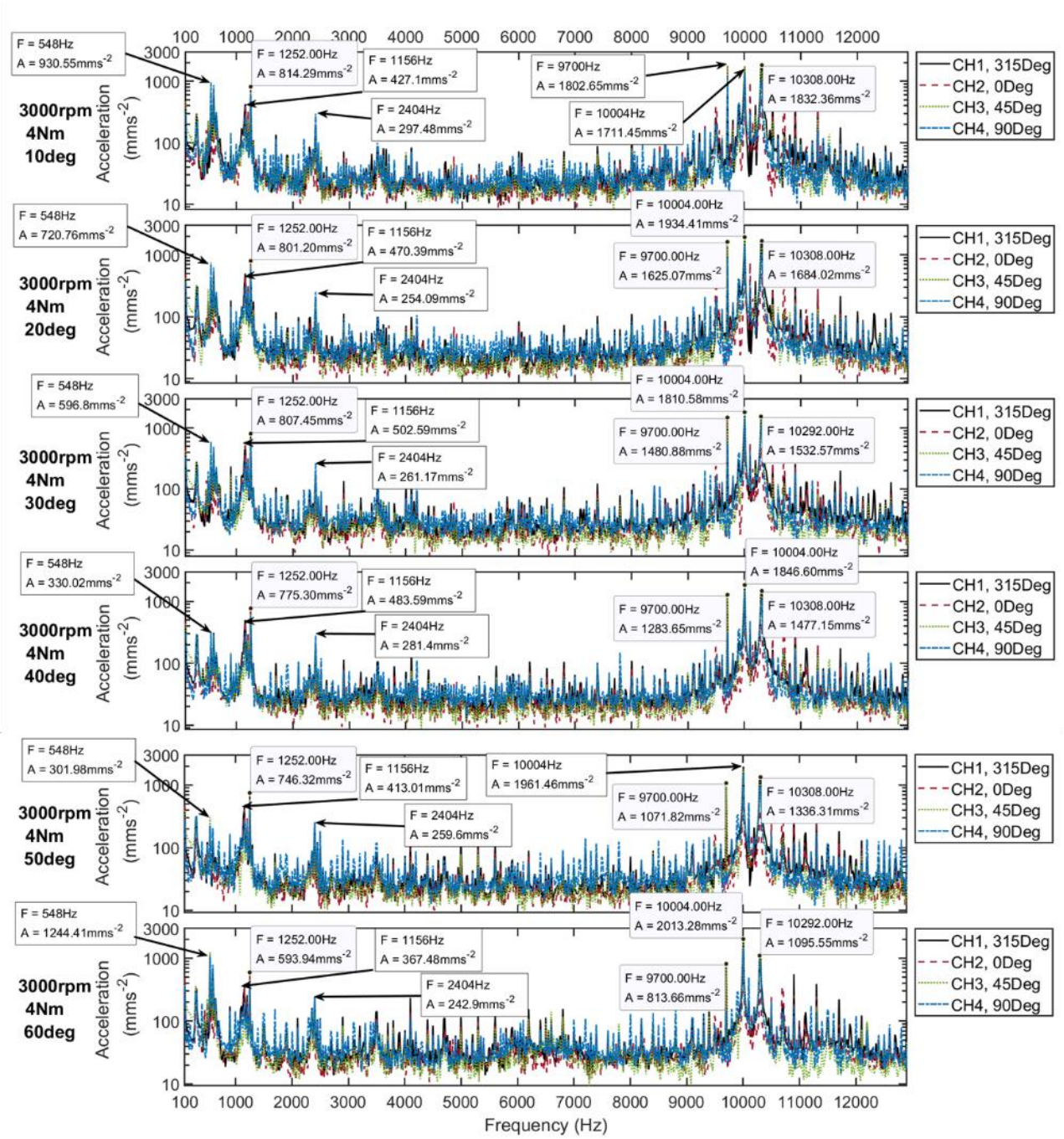

(a) Current angle sweep, 3000rpm, 4Nm, current angle swept 10° to 60°

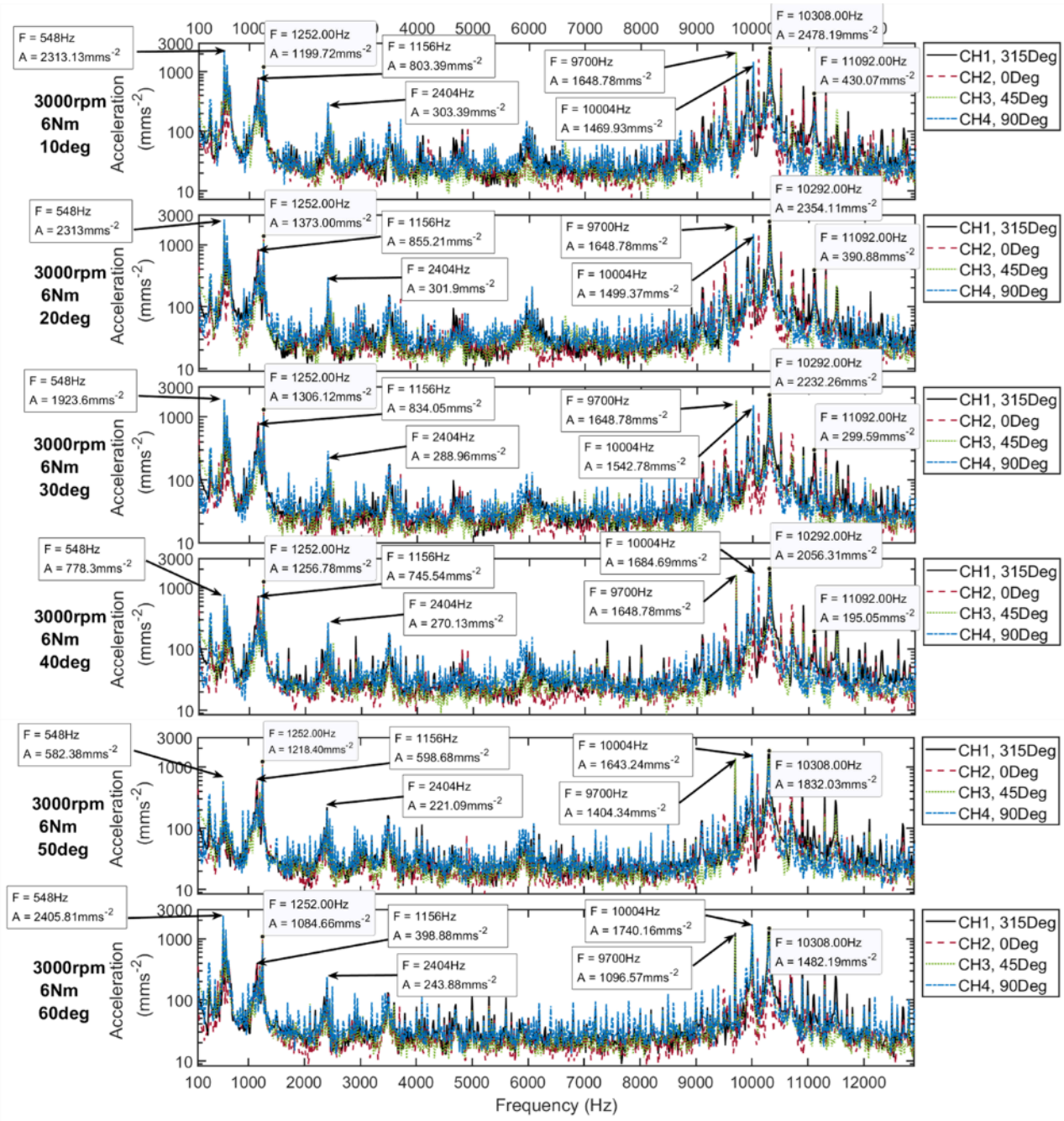

(b) Current angle sweep, 3000rpm, 6Nm, current angle swept 10° to 60°

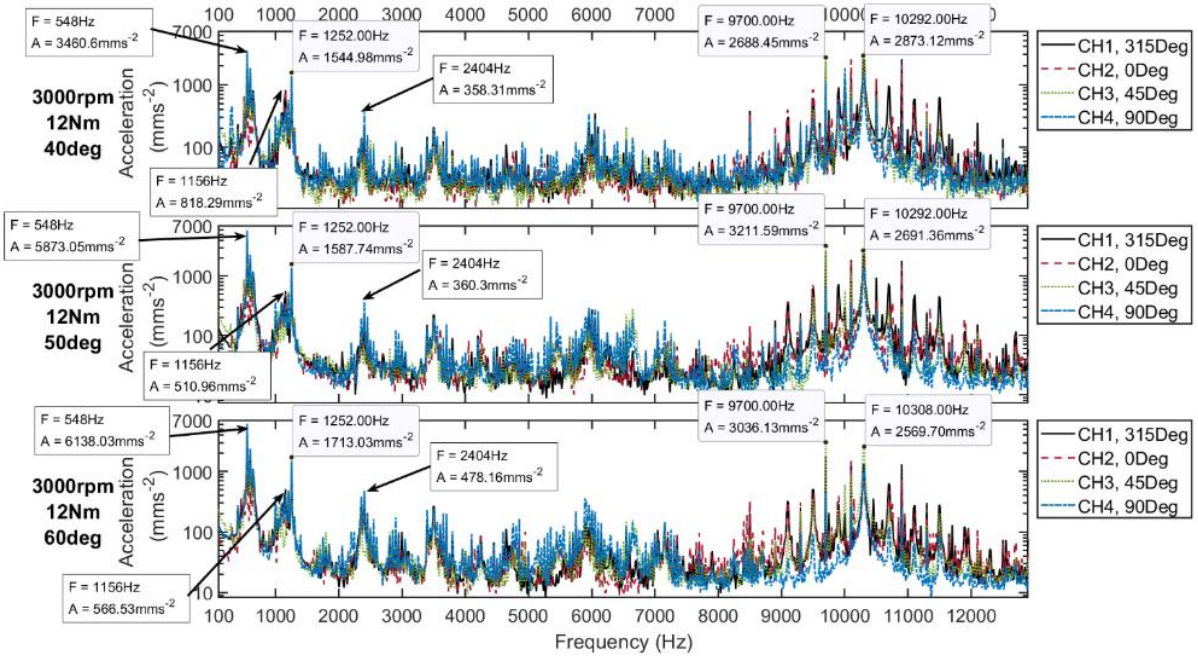

(c) Current angle sweep, 3000rpm, 12Nm, current angle swept 40° to 60°

Fig. 6.3.19 Vibratory performance of machine running at 3000rpm and 4Nm, 6Nm, and 12Nm with the current angle incremented.

Table 6.3.18 Measured acceleration at 3000rpm with incrementing current angle (10° to 60°) at 4Nm, 6Nm and 12Nm

	3000rpm, 4Nm		3000rpm, 6Nm		3000rpm, 12Nm	
β°	Freq (Hz)	Acc (mms^{-2})	Freq (Hz)	Acc (mms^{-2})	Freq (Hz)	Acc (mms^{-2})
10°	548	979.4	548	2313.13		
	1156	427.1	1156	803.39		
	1252	814.3	1252	1398.95		
	2404	297.5	9700	2137.86		
	9700	2001.7	10292	2437.6		
	10004	1737.4				
	10308	1832.36				
20°	548	796.5	548	2558.9		
	1156	470.39	1156	855.21		
	1252	801.2	1252	1373		
	9700	1747.38	9700	1967.25		
	10004	1934.4	10308	2359.78		
	10308	1684.02				
30°	548	596.8	548	1923.6		
	1156	502.59	1156	834.05		
	1252	807.45	1252	1306.1		
	9700	1493.7	9700	1842.1		
	10004	1924.7	10308	2232.32		
	10308	1570.83				
40°	548	330	548	778.3	548	3460.6
	1156	483.59	1156	745.54	1156	818.29
	1252	775.3	1252	1256.78	1252	1544.98
	9700	1283.65	9700	1648.8	9700	2712.99
	10004	2001.8	10292	2056.31	10308	2869.7
	10292	1453.4			10900	2509.8

50°	548	301.98	548	596.1	548	5873.1
	1156	413.01	1156	598.68	1156	510.96
	1252	746.32	1252	1218.4	1252	1587.7
	9700	1071.8	9700	1403.34	9700	3211.6
	10004	1961.45	10308	1832	10308	2677.1
	10308	1336.3			10900	1798.4
60°	548	1244.4	548	2405.81	548	6138
	1156	367.48	1156	398.88	1156	566.53
	1252	593.94	1252	1084.66	1252	1713
	9700	813.66	9700	1280.1	9700	3306
	10004	2013.28	10292	1483.6	10308	2569.7
	10308	1123				

For the 3000rpm the general trend observed at 1500rpm is repeated, obviously with a proportional increase in the frequencies concerned. The key differences here are:

- Similar to the previous test at 3000rpm the results show side bands of the $6f_e$ and $12f_e$ frequencies (600Hz and 1200Hz respectively) corresponding to $6f_e \pm f_m$ and $12f_e \pm f_m$, where f_m is 50Hz.
    - For each load and current angle swept, the $6f_e$-f_m (~550Hz) band shows a particularly high response, dominating the spectrum at the high torque/high current angle test.
    - These frequencies follow the same trend as the $6f_e$ harmonic in terms of the amplitude dropping and then rising rapidly as the current angle approaches and then passes 40°.
- At the 12Nm load, the 48fe component (2400Hz) appears to grow with increasing current angle suggesting a link with the reluctance component of the machine (variation in L_d and L_q inductances).
    - The frequency is present in the lower torque points but only becomes relevant at higher torque values.
    - Relative amplitudes are still low compared to the ripple and PWM components.
- The PWM switching frequency, f_c, is prominent and in line with the previous results the side bands $f_c \pm 3f_e$ are once again prominent.
    - The drop in amplitude with respect to current angle is present. However, compared to the $6f_e$ component the effect is more gradual and the amplitude does not rise again past 50°.

The sidebands at $6f_e$-f_m and $12f_e \pm f_m$ only appear prominent at this speed, and the highest amplitudes lie at frequencies within the concern band between ~400Hz and 600Hz which as discussed in the no load appears to be a mode of the rotor driveline or some subcomponent of the rig assembly, whereas the $12f_e \pm f_m$ excite modes around the cogging component ($12f_e \approx 1200$Hz) but the actual amplitude around that frequency is less prominent.

The machine is then accelerated past the base speed up to 6000rpm, well into the flux weakening region and the measurement repeated. As discussed previously, in order to operate at this high speed, the controller

needs to apply a negative I_d current such that it can operate within the voltage limit locus. The actual current angle that allows the machine to operate is around 33° but to keep in line with the angle steps used in throughout this stage of the testing the current angle is rounded up to start at 40°. The other key difference between the testing and the lower speed is the maximum current angle of the sweep which is increased to 70°, reflecting the fact that to achieve the elevated I_d current amplitudes means the current angles are more advanced at the higher torque points. The results can be seen in Fig. 6.3.20 and Table 6.3.19.

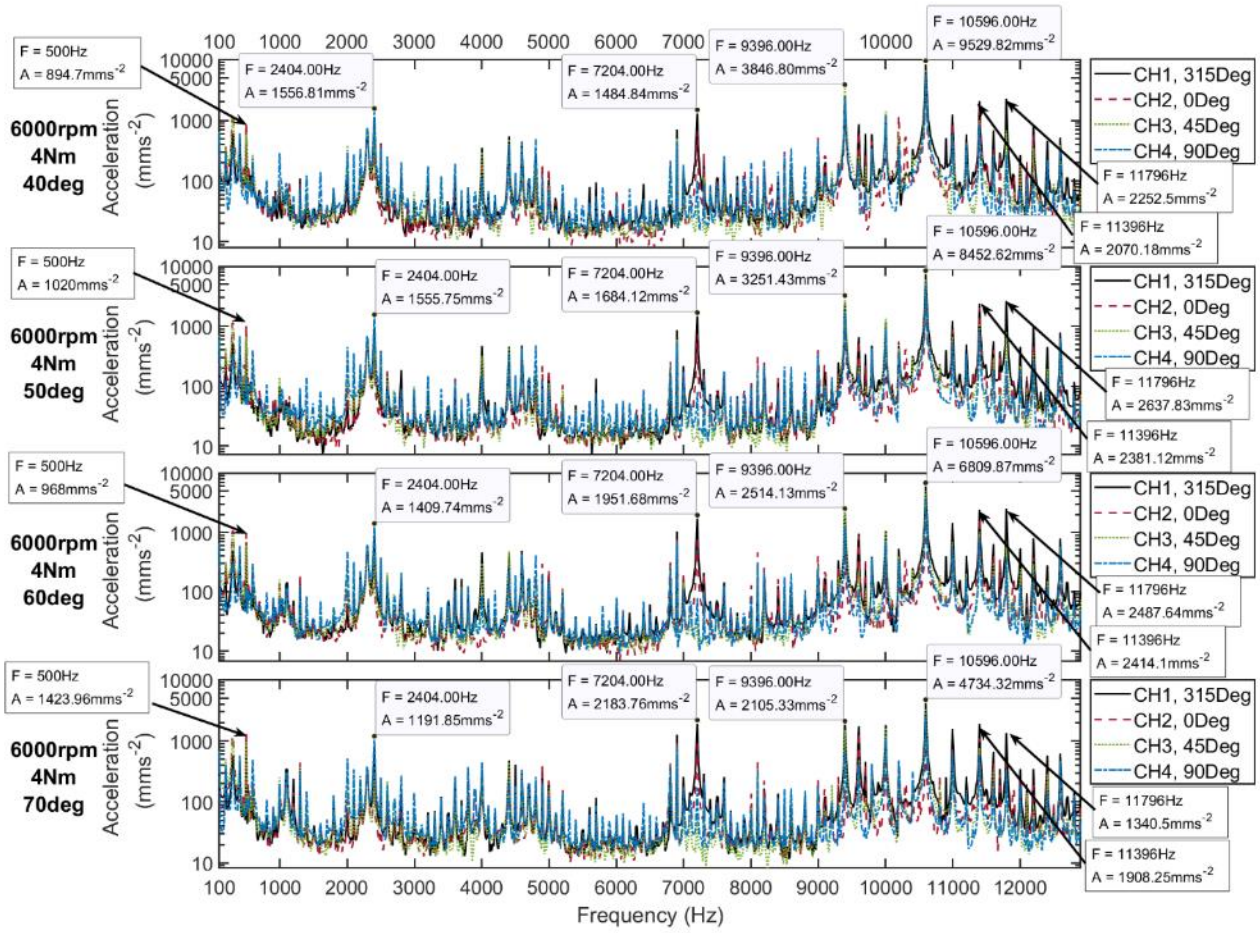

(a) Current angle sweep, 6000rpm, 4Nm, current angle swept 40° to 70°

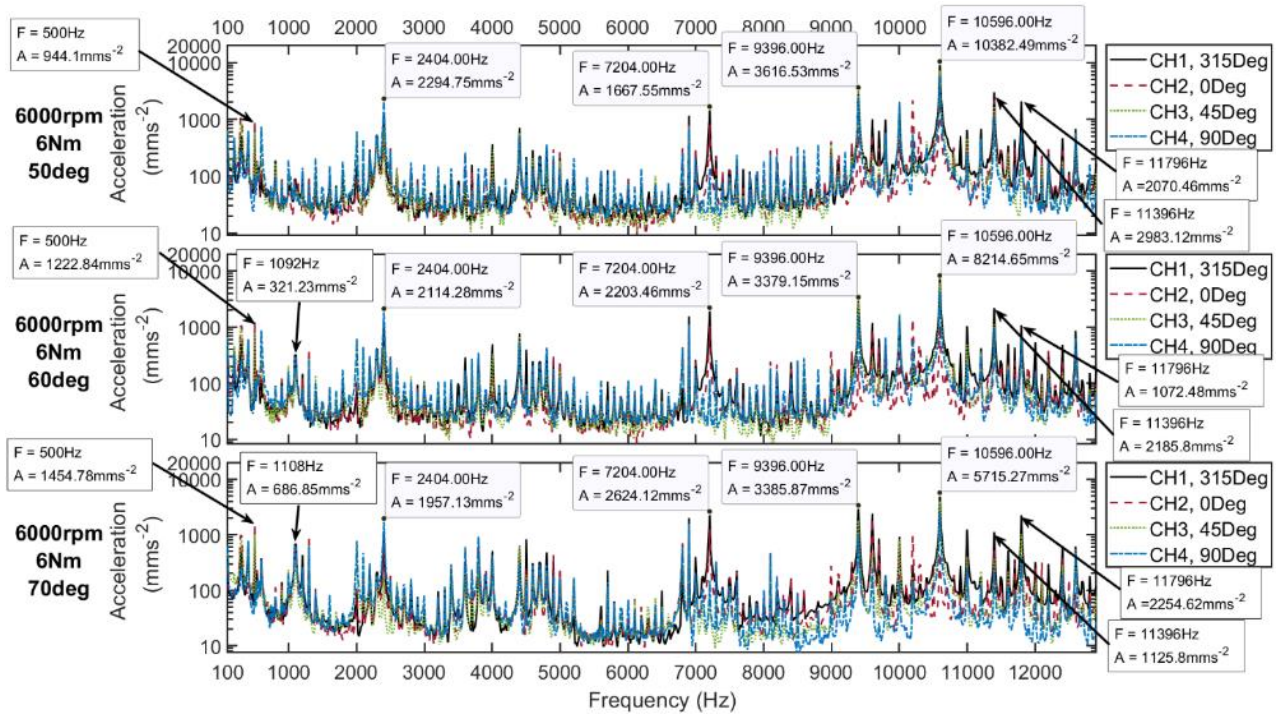

(b) Current angle sweep, 6000rpm, 6Nm, current angle swept 50° to 70°.

Fig. 6.3.20 Vibratory performance of machine running at 6000rpm and 4Nm and 6Nm with the current angle incremented.

Table 6.3.19 Measured acceleration at 6000rpm with incrementing current angle (40° to 60°) at 4Nm and 6Nm.

	6000rpm, 4Nm		6000rpm, 6Nm	
β°	Freq (Hz)	Acc (mms^{-2})	Freq (Hz)	Acc (mms^{-2})
40°	500	894.7		
	2404	1556.8		
	7204	1484.8		
	9396	3846.8		
	10596	9529.8		
	11396	2070.2		
	11796	2252.5		
50°	500	1020	500	977
	2404	1555.75	2404	2294.8
	7204	1684.12	7204	1667.6
	9396	3251.4	9396	3616.5
	10596	8452.6	10596	10382.5
	11396	2381.1	11396	2070.2
	11796	2637.8	11796	2252.5
60°	500	1020	500	1222.84
	2404	1409.7	2404	2114.28
	7204	1951.68	7204	2203.46
	9396	2514.13	9396	3379
	10596	6809.87	10596	8214.65
	11396	2414	11396	2158.8
	11796	2487.6	11796	1072.5

70°	500	1423.96	500	1454.8
	2404	1197.85	2404	1957.1
	7204	2183.8	7204	2624.1
	9396	2105.3	9396	3385.87
	10596	4732.3	10596	5715.27
	10996	1563.3	11396	1125.8
	11396	1908.25	11796	2254.6

The results in Fig. 6.3.20 are consistent with the previous results at this speed, again giving confidence in the measured results at this speed.

- The level of background noise has once again increased markedly, CH4 (90Deg) appears the most affected.
- Following the trend from the previous speeds, the minima of the amplitudes sits at current angles between 40° and 50°, which means the results here only show the amplitude of the 12fe increasing.
- The $6f_e$ component (1200Hz) is not present, only appearing as a low amplitude at the maximum current angle.
- The $36f_e$ (7200Hz) component is once again observed, the amplitude following the same trend as the $12f_e$ component.
- The $f_c + 3f_e$ PWM sideband component (~10.6kHz) again dominates the spectrum, showing a very high peak at 4Nm and 40°.
    - Clearly the upper frequency band has aligned with, or very close to a machine mode.
    - Similar to the previous cases the amplitude drops as the current angle increases.
    - The difference is the scale of the drop is much more significant, almost 50% from the machine at 40° and 70°.

The final test point is at the imposed speed, 7500rpm. For this test the current angle has to be very high to achieve even 4Nm in this test, so the machine is measured at 65°. An exemption was made at this point compared to the 6000rpm as to round up would mean there was only one test point. For the 6Nm point, the only test point available is at 70°. The results can be seen in Fig. 6.3.21 and Table 6.3.20.

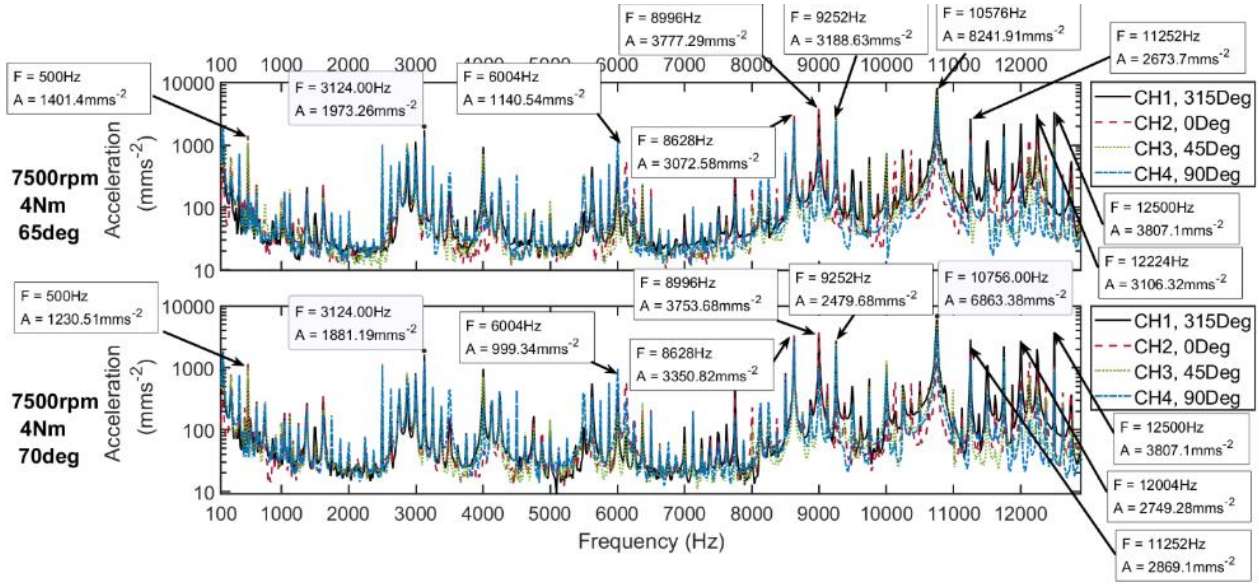

(a) Current angle sweep, 7500rpm, 4Nm, current angle swept 65° to 70°.

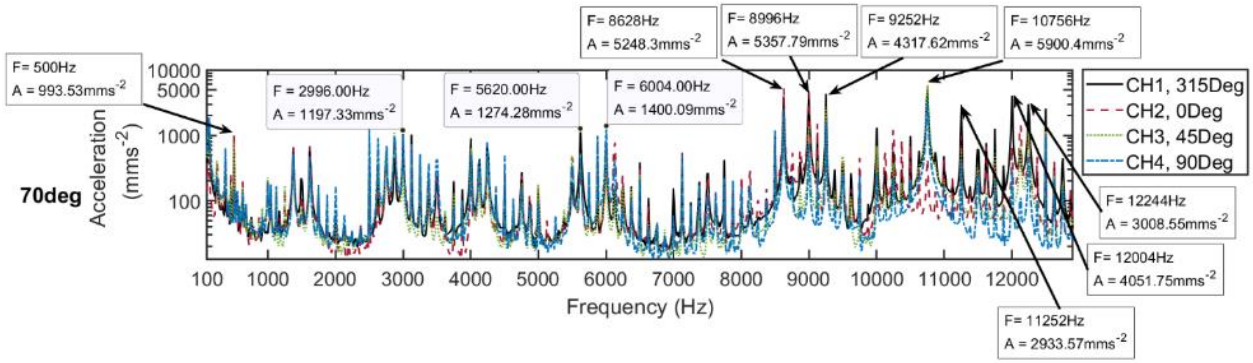

(b) Current angle sweep, 7500rpm, 6Nm, current angle at 70° only.

Fig. 6.3.21 Vibratory performance of machine running at 6000rpm and 4Nm and 6Nm with the current angle incremented.

Table 6.3.20 Measured acceleration at 7500rpm with incrementing current angle (65° to 70°) at 4Nm and 6Nm

	7500rpm, 4Nm		7500rpm, 6Nm	
β°	Freq (Hz)	Acc (mms^{-2})	Freq (Hz)	Acc (mms^{-2})
65°	500	1404.4		
	3124	1973.3		
	6004	1140.5		
	8628	3072.6		
	8996	3779.3		
	10756	8241.9		
	11252	2673.7		
	12224	3108.3		
	12500	3807.1		

70°	500	1250.5	500	993.5
	3124	1881.2	2996	1197.3
	6004	999.3	5620	1274.3
	8628	3350.8	6004	1400.1
	8996	3753.7	8628	5248.3
	9252	2773.2	8996	5357.8
	10756	6863.4	9252	4317.6
	11252	2869.1	10756	5900.4
	12004	2749.3	11252	2933.6
	12500	3807.1	12004	4051.75
			12244	3008.55
			12500	2566.7

The results in Fig. 6.3.21 show increased levels of noise over the 6000rpm, in particular at 6Nm. However, the frequencies established in the previous load test at this speed are clearly observed. The trends at 7500rpm follow much the same as those observed at 6000rpm including the large drop in amplitude when moving the current angle from 65° to 70°. The major difference being a large peak sat at 12kHz and the $36f_e$ (9kHz) component clearly interacting with a machine mode.

The summary of this section is as follows:

- Incrementing the current angle towards the MTPA point results in the net acceleration dropping for many of the excited frequencies, in particular 12fe, 6fe, fc and their associated sidebands.
    - The drop reflects the lower in current in the coils due to the contribution of the reluctance torque component to reduce the current required to achieve the target torque.
- As the current angle passes the MTPA and increases towards 90° the controller has to apply larger currents to compensate initially for the loss of mutual torque and as the current angle exceeds 50° then reluctance torque resulting in a rapid rise in the measured acceleration.
- The exception to the point above is the PWM side band amplitude ($f_c \pm 3f_e$) where the drop in amplitude becomes much greater at the higher current angles.
    - This effect is most prominent in the flux weakening region, partly due to the higher current angles required.

With the characteristics of the machine under different load conditions better understood the next phase is to observe the performance of the machine at the maximum torque-speed envelope of the machine and the mapped maximum efficiency points as these represent the machine performance if the machine were applied to a practical driveline.

6.3.5 T-N curve

The procedure for establishing the T-N curve of the machine was detailed in Chapter 2. The measurement of the vibratory performance of the machine occurred after the maximum operating points had been mapped. Given the risk to the machine operating at full load due the thermal loading etc. the maximum torque for each speed was established in one run to allow the optimal current angle to be found, the machine given time to cool then the established I_d and I_q values reapplied and the acceleration sensors were recorded. Fig. 6.3.22 shows the measured points on the TN-curve of the baseline machine.

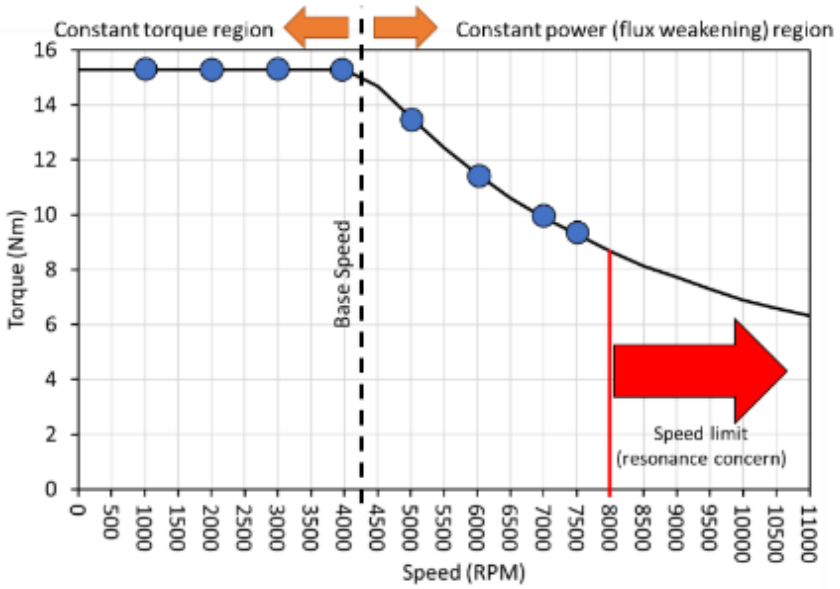

Fig. 6.3.22 Measured vibration points on the TN-curve of the baseline machine.

Table 6.3.21 below details the actual speed and torque values of each measurement point.

Table 6.3.21 Measured points on TN-curve

Speed (rpm)	1000	2000	3000	4000	5000	6000	7000	7500
Torque (Nm)	15.3	15.3	15.3	15.3	13.4	11.4	9.6	8.5
I_d (A)	-26.15	-26.27	-26.22	-26.32	-33.94	-34.17	-36.12	-31.47
I_q (A)	27.15	27.18	27.14	26.87	15.96	12.42	9.67	9
β (°)	43.9	44	44	44.4	64.8	70.1	75	74

The measured vibration at the points highlighted in Fig. 6.3.22 and Table 6.3.21 results can be seen in Fig. 6.3.23.

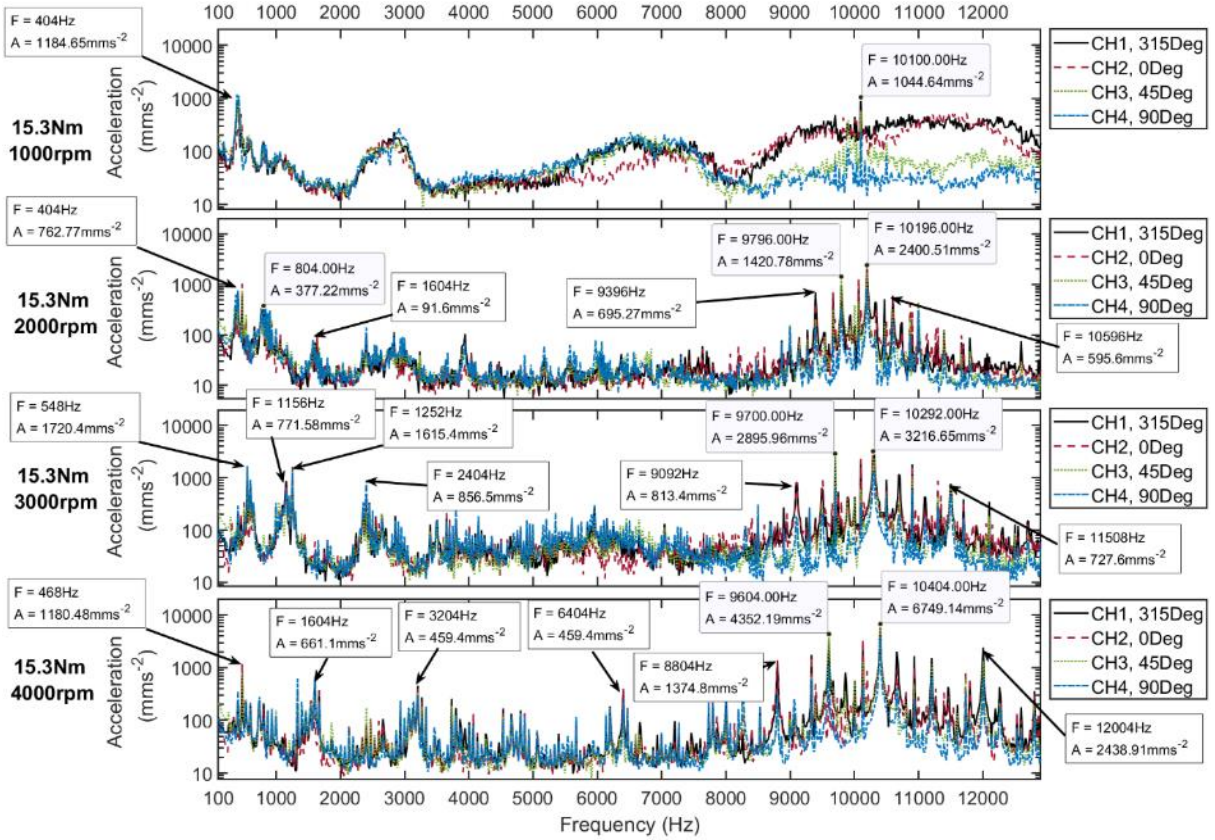

(a) Acceleration signals recoded at maximum torque between 1000rpm and 4000rpm

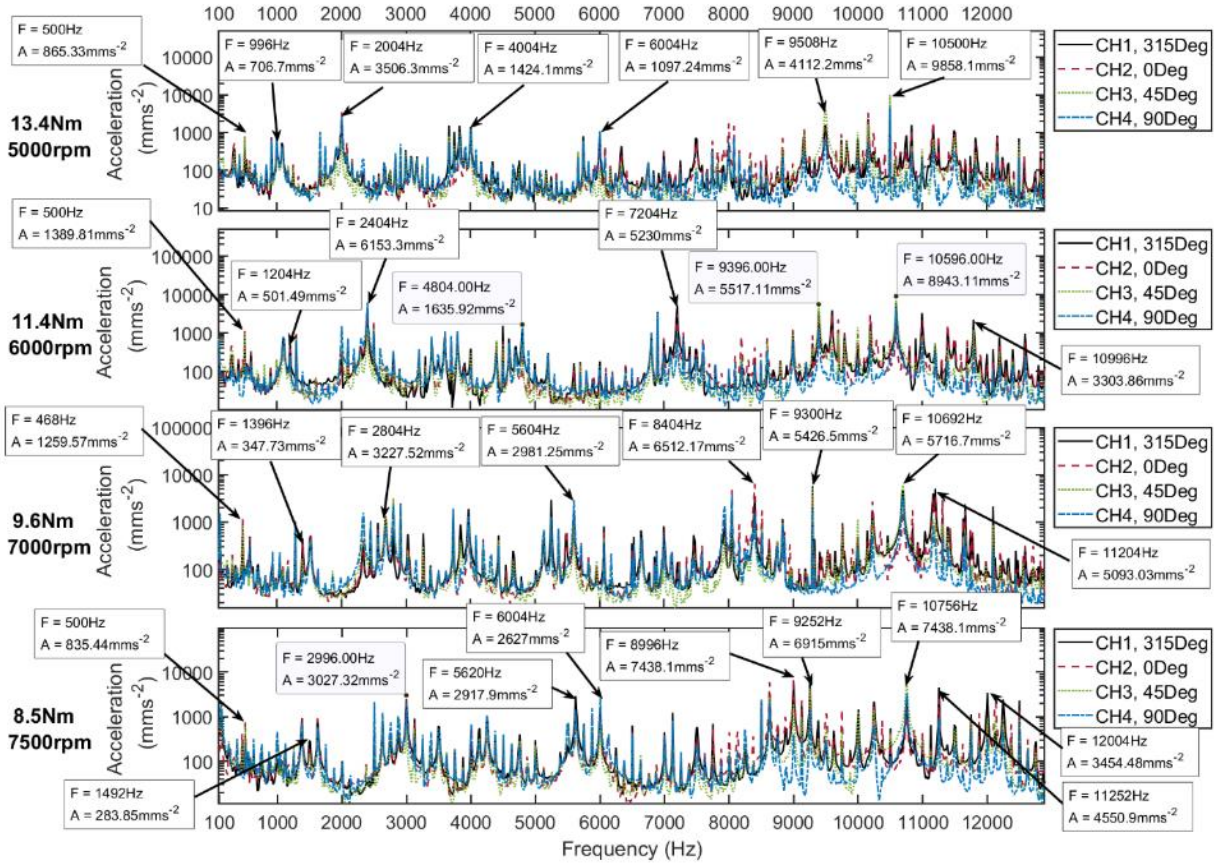

(b) Acceleration signals recoded at maximum torque between 5000rpm and 7500rpm

Fig. 6.3.23 Results of acceleration sensor measurement for the maximum torque of the baseline machine for incrementing speeds.

Table 6.3.22 shows the key frequencies and acceleration amplitudes for each of the speeds shown in Fig. 6.3.11.

Table 6.3.22 key vibration frequencies and amplitudes from the T-N curve measurement

1000rpm, 15Nm		2000rpm, 15Nm		3000rpm, 15Nm		4000rpm, 15Nm		5000rpm, 13Nm	
Freq. (Hz)	Acc. (mms^{-2})	Freq. (Hz)	Acc. (mms^{-2})	Freq. (Hz)	Acc. (mms^{-2})	Freq. (Hz)	Acc. (mms^{-2})	Freq. (Hz)	Acc. (mms^{-2})
404	1185	404	762.77	548	1720	468	1180	500	865.3
10100	1045	804	377.2	1156	771.58	1604	694	996	706.7
		9396	695.3	1204	1615	3204	459.4	2004	3506
		9796	1421	2404	865.5	6404	459.4	4004	1517
		10200	2401	9092	813.4	8804	1384	6004	1097
		10596	595.6	9700	3040	9604	4352	9508	4112
				10292	3267	10400	6749	10500	9858
				11508	727.6	12000	2439		

6000rpm, 11Nm		7000rpm, 10Nm		7500rpm, 9Nm	
Freq. (Hz)	Acc. (mms^{-2})	Freq. (Hz)	Acc. (mms^{-2})	Freq. (Hz)	Acc. (mms^{-2})
500	1390	468	1260	500	835.44
2404	6153	1396	347.7	1492	283
4804	1636	2804	3228	2996	3027
7200	5230	5604	2981	5620	2918
9396	5517	8404	6512	6004	2628
10600	8943	9300	5426.5	8996	7438
10996	3304	10690	5716.7	9252	6915
		11200	5093	10756	7453
				11250	4551
				12000	3454

The results follow the trends established in the previous more basic test points. The key points observed are:

- The noise level is very high across the whole speed range, much more than previous cases
    - The coil current is at maximum meaning all associated PWM harmonics are at peak amplitudes.
    - Aspects such as saturation of the core at maximum load provide further means of distorting the values recorded.
    - Channels 1&2 (315deg and 0deg) appear unsettled at 1000rpm, above 8kHz the sensors appear to saturate.
- The $24f_e$ frequency linked with the reluctance torque is clear for all speeds above 2000rpm, with amplitudes becoming quite large at speeds beyond 3000rpm.
- The $6f_e$ component with side bands $6f_e \pm f_m$ can be observed at most speed points. However, the relative amplitudes are very low compared to the ripple and PWM components.

- The exception being 3000rpm once again due to the $6f_e$ component alignment with a rotor/rig mode.

- Levels of distortion and noise are high for all speed points but in particular above 5000rpm.
  - The I_{dq} current in the machine is at the limit of the machine for each point so effects such as EMI and of course saturation of the core at full load contributes to high noise amplitudes.
- 6000rpm once again proves to have high amplitudes at the $12f_e$ (2.4kHz), $36f_e$ (7.2kHz), and the f_c+3f_e (10.6kHz) points where the machine operating at this speed appears to likely a series of modes both of the machine and the rig.

The results from the T-N curve measurement show good consistency with the previous analysis, and the key difference being with the machine at full load the forces are higher as is the overall background noise, in particular as the speeds exceed 5000rpm.

6.3.6 Maximum Torque Per Ampere (MTPA) measurement

Following the T-N curve mapping the Maximum Torque Per Ampere (MTPA) was mapped for a large number of points under the derived T-N map. Similar to the T-N map the measurement of the vibratory performance for the MTPA aspect occurred once the optimal I_d & I_q current points had been established. Again, this allowed for a more efficient mapping process. During the mapping process there were over 49 individual data points mapped to balance the need for mapping fidelity and the time constraints on the test rig. To show the vibration results for each of these points is a little unwieldy. Thus, instead for a select number of torque and speed points the vibrations in the map are selected to build a picture of the trends of the vibratory data. The points on the torque speed graph of the baseline machine mapped during the establishment of the MTPA map and the points selected to plot the vibratory data are summarised in Fig. 6.3.24 and Table 6.3.23.

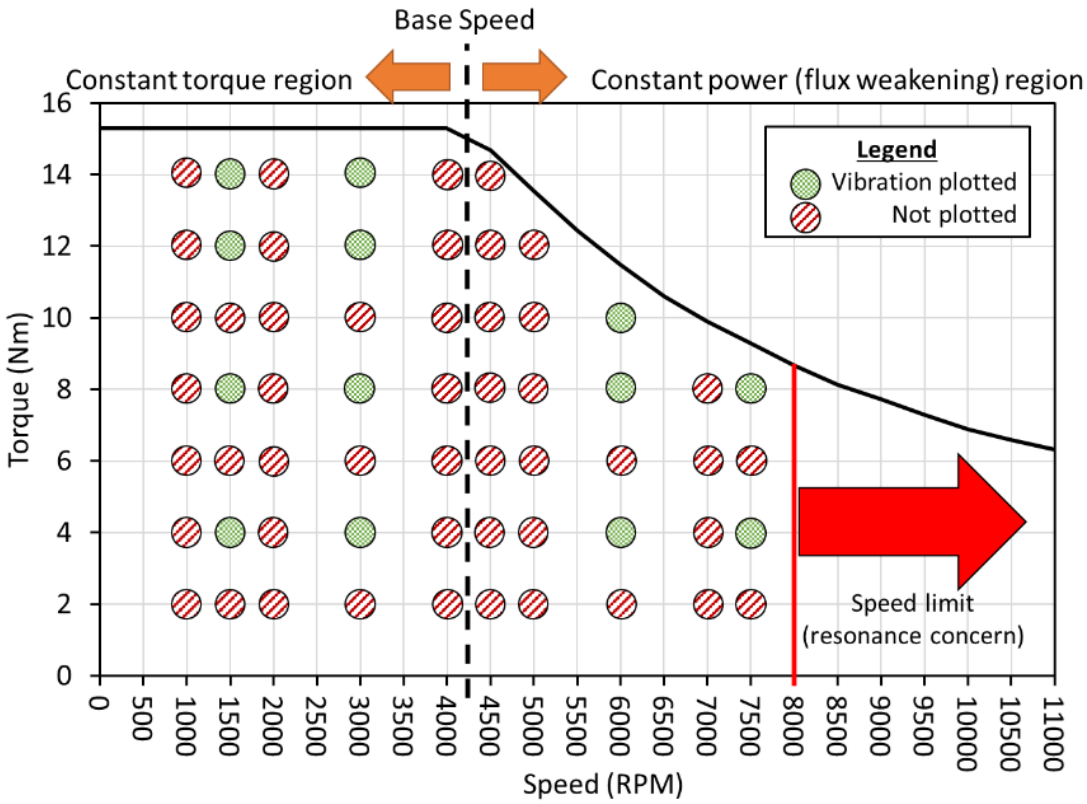

Fig. 6.3.24 Torque-speed points mapped during the MTPA

Table 6.3.23 MTPA sample points

	1500rpm	3000rpm	6000rpm	7500rpm
4Nm	✓	✓	✓	✓
8Nm	✓	✓	✓	✓
12Nm	✓	✓	**(10Nm)**	***X***
14Nm	✓	✓	***X***	**X**

From Fig. 6.3.24 and Table 6.3.23 it can be seen that the same speeds used in the current angle sweep test are used. The key difference is that the torques measured extend much higher than the more basic test stepping from 4Nm to 12Nm in 4Nm steps before measuring a maximum 14Nm. From Table 6.3.24 it can be noted that due to the need to flux weakening the 6000rpm and 7500rpm speed points cannot achieve the upper torque values. For 6000rpm the maximum torque possible is 11.4Nm so the maximum used here is 10Nm to mitigate the risk of exceeding the voltage limit. To try and simplify the analysis process each of the different speeds will be analysed in turn, starting with 1500rpm, as shown in Fig. 6.3.25 and Table 6.3.24.

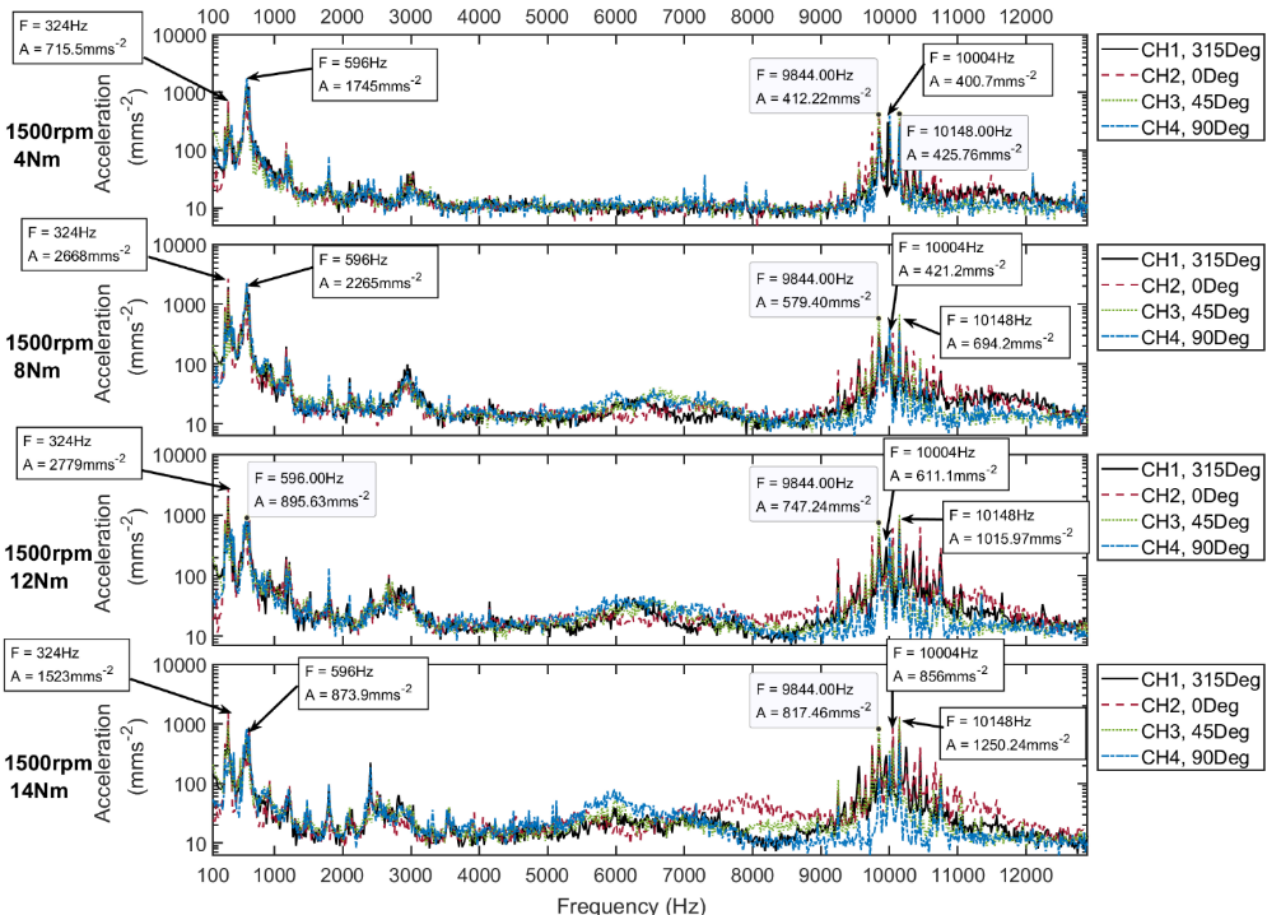

Fig. 6.3.25 Acceleration measurement from machine operating MTPA at 1500rpm and incrementing torque from 4Nm to 14Nm.

Table 6.3.24 Key frequencies and acceleration amplitudes during MTPA measurement at 1500rpm

4Nm		8Nm		12Nm		14Nm	
Freq (Hz)	Acc (mms^{-2})	Freq (Hz)	Acc (mms^{-2})	Freq (Hz)	Acc (mms^{-2})	Freq (Hz)	Acc (mms^{-2})
324	715.5	324	2668	324	2779	324	1523
596	1745	596	2265	628	1117	628	873.9
9844	412.2	9844	579.4	9844	747.3	9844	817.5
10004	400.7	10004	421.2	10004	611.1	10004	856
10148	425.76	10148	694.2	10148	1015.97	10148	1250.24

The frequencies identified match those of all previous on-load tests at this speed and, unsurprisingly the lower magnitudes in reflecting the findings from the current angle sweep test which found the optimal utilisation of the reluctance component reduces the overall amplitude owing to the lower forces involved with less current in the coils. The only significant peak is the suspected rotor and driveline assembly mode at 324 Hz, as discussed in length previously. Moving on from this the machine is accelerated to 3000rpm and the process is repeated for each of the torque points, the results can be seen in Fig. 6.3.26 and summarised in table 6.3.25.

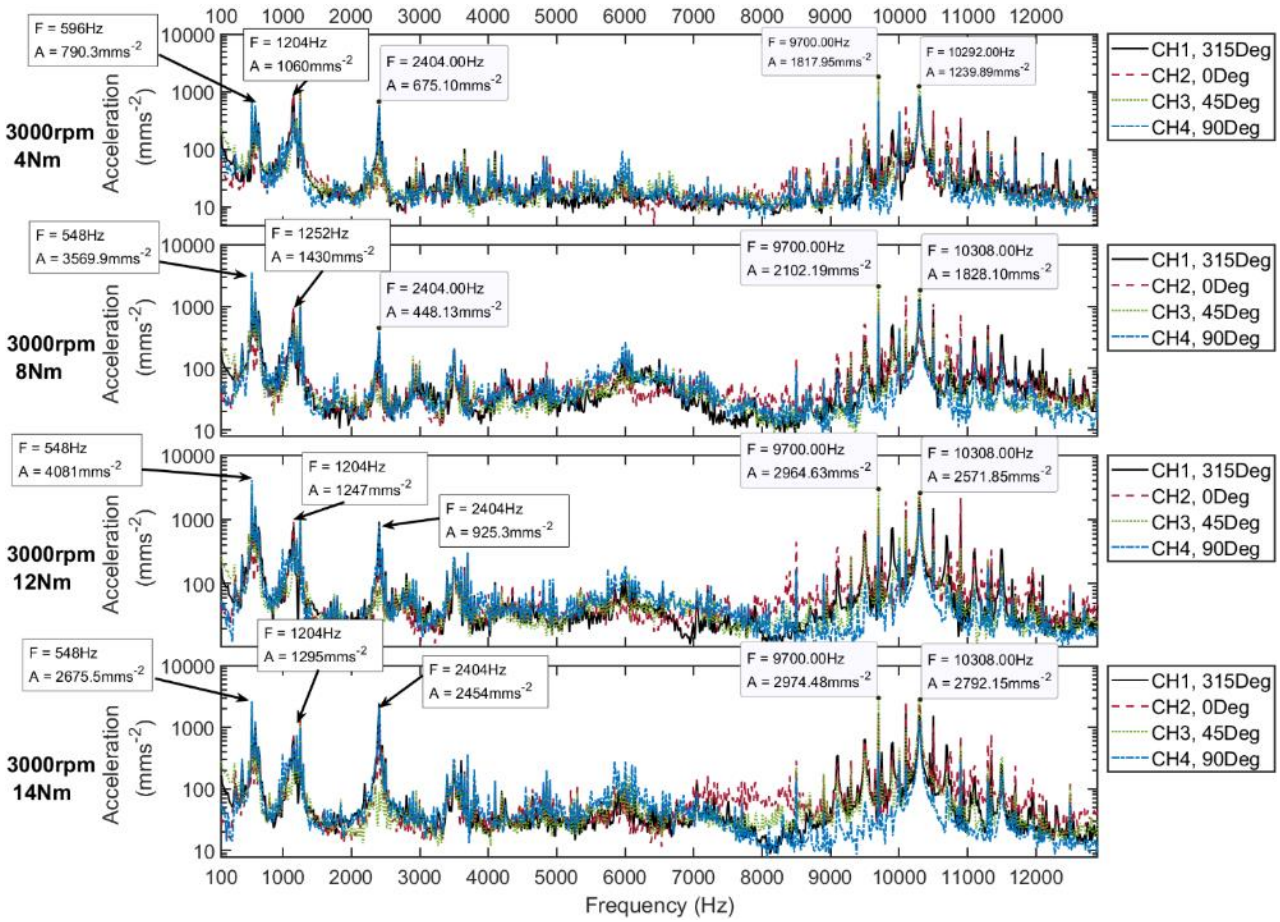

Fig. 6.3.26 Acceleration measurement from machine operating MTPA at 3000rpm and incrementing torque from 4Nm to 14Nm.

Table 6.3.25 Key frequencies and acceleration amplitudes during MTPA measurement at 3000rpm

4Nm		8Nm		12Nm		14Nm	
Freq (Hz)	Acc (mms^{-2})	Freq (Hz)	Acc (mms^{-2})	Freq (Hz)	Acc (mms^{-2})	Freq (Hz)	Acc (mms^{-2})
548	790.3	548	3569.9	548	4081	548	2675.5
1204	1060	1204	1430	1204	1247	1204	1295
2404	675.1	2404	448.1	2404	925.3	2404	2454
9700	1817.95	9700	2102.2	9700	2694.6	9700	2947.5
10308	1217.6	10100	1493.7	10100	1914	10100	2672.3
		10308	1828.1	10308	2571.85	10308	2792.15
		10500	1106.7	10900	2165	10500	1541.4

Similar to the 1500rpm results there are no real surprises with the 3000rpm MTPA results, again the consistency giving good confidence in the results. The 548 Hz peak attributed to a component on the test rig dominates as previously observed. The point of interest is the peak at $24f_e$ (2400Hz), the amplitude of which grows with the increasing torque, indicating a link with the reluctance component. This peak was observed previously at this speed, but it appears the MTPA point has hit a sweet spot giving it a higher amplitude, although given the complexity of the rig setup and the intensity of the testing it may be due some aspect of the rig changing slightly over the previous tests. The machine is accelerated up to 6000rpm and the process

is repeated for each of the torque points listed in Table 6.3.24. The results can be seen in Fig. 6.3.27 and summarised in Table 6.3.25.

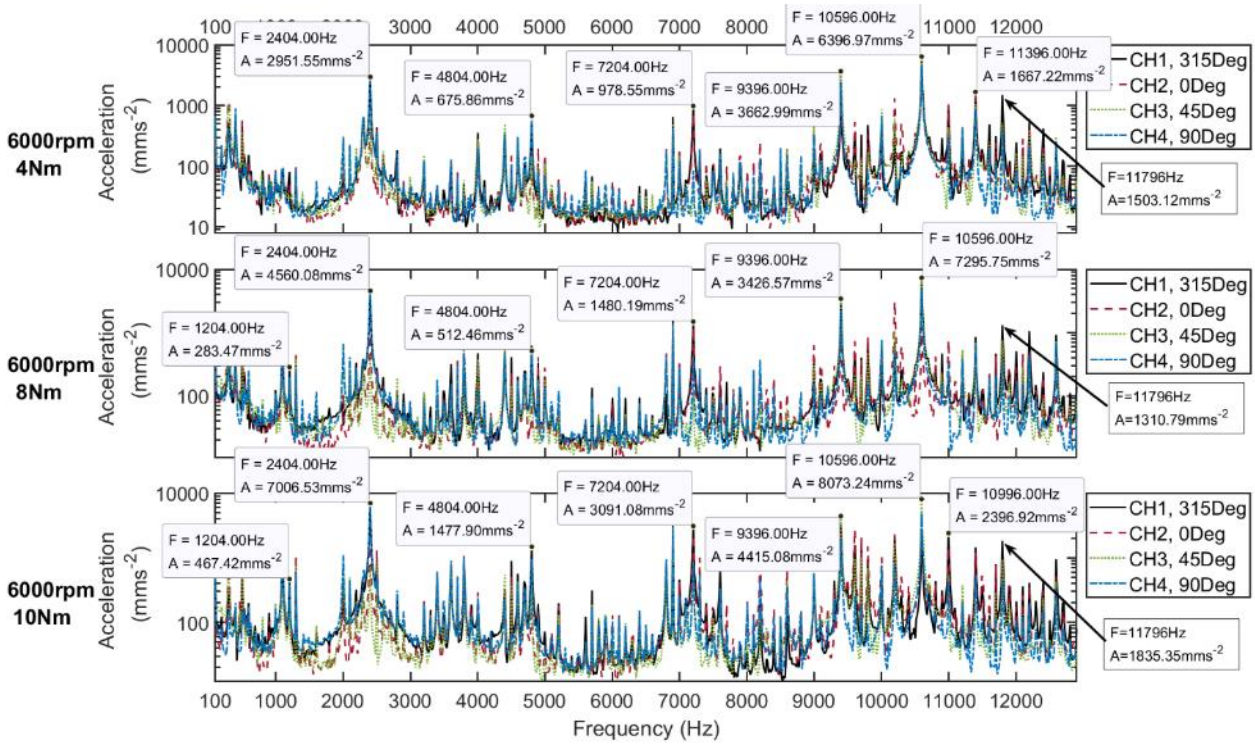

Fig. 6.3.27 Acceleration measurement from machine operating MTPA at 6000rpm and incrementing torque from 4Nm to 10Nm.

Table 6.3.25 Key frequencies and acceleration amplitudes during MTPA measurement at 6000rpm

4Nm		8Nm		10Nm	
Freq (Hz)	Acc (mms^{-2})	Freq (Hz)	Acc (mms^{-2})	Freq (Hz)	Acc (mms^{-2})
2404	2951.55	2404	4560.1	2404	7007
7204	978.55	6900	1614.55	4804	1477.9
9396	3662.99	7204	1480	6900	3122
10596	6393.97	9396	3426.6	7204	3091
		10196	3107.1	9396	4415.1
		10596	7295.75	10196	2314
				10596	8073.24
				10996	2396.9

The high peak at 2400Hz (12fe) is observed once again here with the magnitude much higher than the same frequency encountered at 3000rpm. Similar to the previous tests 6000rpm shows a high peak at 7200Hz ($36f_e$) and the PWM side band 10600 (f_c+3f_e) show high amplitudes due to alignment with machine modes. Similar to the 3000rpm point a component can be observed at 4800Hz ($24f_e$), appearing at 10Nm, again aligning with the reluctance torque of the machine.

The final speed point highlighted in the flux weakening region is at the maximum speed tested, 7500rpm. At this high speed the only comparable torque points are 4Nm and 8Nm, the results of which can be seen in Fig. 6.3.28 and Table 6.3.26.

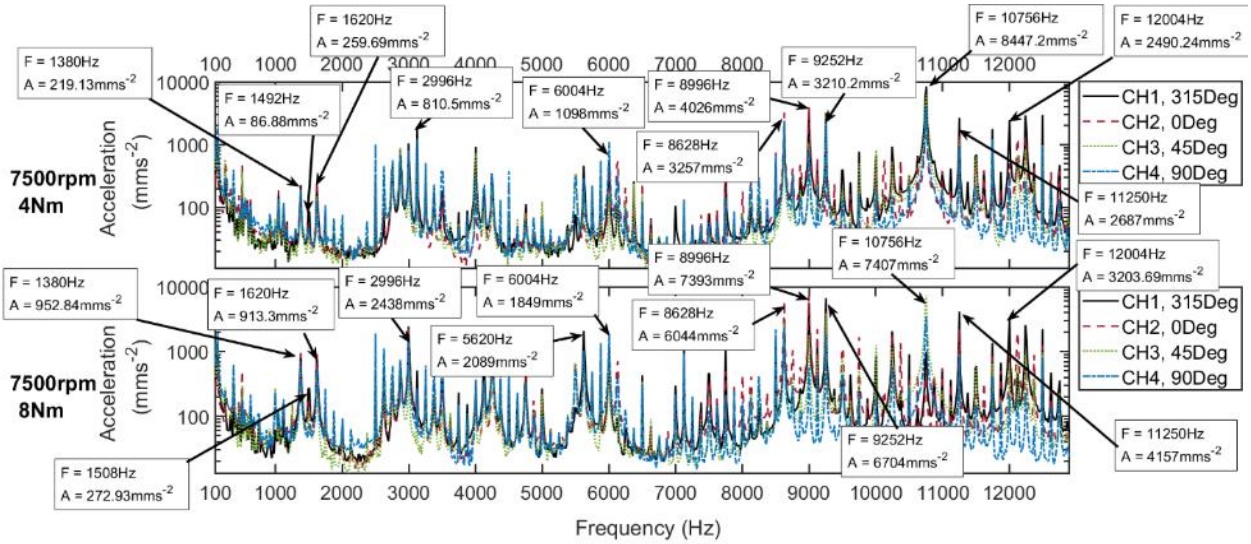

Fig. 6.3.28 Acceleration measurement from machine operating MTPA at 7500rpm and incrementing torque from 4Nm to 8Nm.

Table 6.3.28 Key frequencies and acceleration amplitudes during MTPA measurement at 7500rpm

4Nm		8Nm	
Freq (Hz)	Acc (mms^{-2})	Freq (Hz)	Acc (mms^{-2})
3124	1984	2500	1903
6004	1098	2996	2438
8628	3257	5620	2089
8996	4026	6004	1849
9252	3210	8628	6044
10756	8447.2	8996	1393
11250	2687	9252	6704
12004	2490.24	10756	7404
		11250	4157
		12004	3203.69

Fig. 6.3.28 shows the common theme of high noise at this speed point. However, as with the other speed points on this test the frequencies are consistent with all tests.

6.4 Simulating the vibratory performance of the baseline machine

With the detailed experimental investigation completed the final stage is to build the final dynamic vibratory model of the machine and compare the results of the model with that of the measured data.

6.4.1 The integrated FE models

To run the model the ANSYS® Workbench package is used. This package integrates the powerful ANSYS® mechanical FE tool sets and the Electromagnetic FE package, Maxwell. The workbench environment allows different facets of the package to be linked together, be it CFD methods or thermal modelling or, as in this case, electromagnetic forces applied to a 3D mechanical model. The model and its component parts are shown in Fig. 6.4.1.

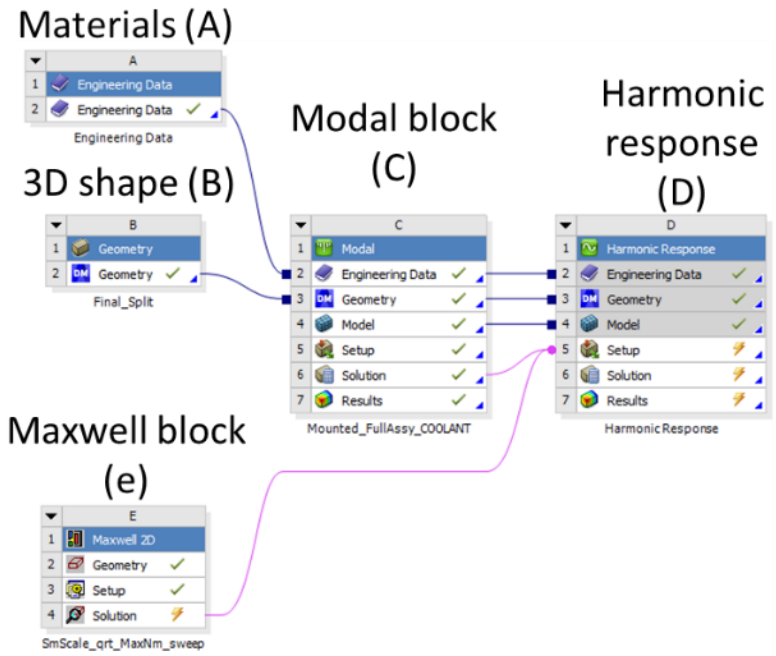

Fig. 6.4.1 ANSYS® Workbench model for calculating harmonic response of the machine.

Whilst much of the process is handled internally by the ANSYS® software it is a very complex tool so care must be taken when setting up the model. Both the electromagnetic and the mechanical harmonic response tool need careful setup to ensure there are no errors in the mapping of the force data.

6.4.1.1 Setting up the electromagnetic model

Setting up the model requires the use of the harmonic response tool within the ANSYS® Maxwell package. This tool performs the job of capturing the force data from the FE solver and performs a discrete Fourier transform on the results to generate the force harmonics that is sent to the mechanical model. The key steps in setup are:

- Modification of the model geometry.
- Modification of the step control.

One big advantage of the baseline machine is that the structure is symmetrical, and it has no skew so that a 2D quarter model of the machine can be used for the force calculations. Whilst a large benefit in terms of processing time the setup of the model is important. The standard way to model a fractional model of a machine is to set the symmetrical axis through the centre of a tooth (Fig. 6.4.2(a)), primarily as it is easier to draw and avoids issues with windings along the symmetrical boundaries.

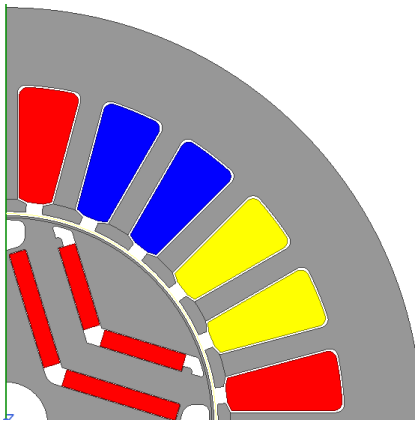

(a) "Standard" ¼ model arrangement.

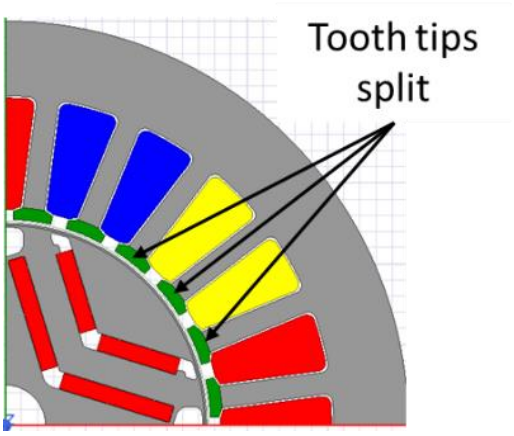

(b) Best practise for force model.

Fig 6.4.2 Orientation of the stator on the quarter model.

As the machine is a 4-pole machine the symmetrical boundary lies on the X and Y axis, respectively. In the force calculation it presents a problem as when a tooth tip or air gap curve (discussed below) sits at a line of symmetry.

- The symmetry multiplier function mirrors the force curves and treats the half teeth on the boundary as full objects, so when the symmetry is multiplied 7x4 = 28 tooth loads are generated instead of 24, creating problems when trying to map the force.
    - Rotating the stator eliminates this problem as 6 teeth are mirrored.
- Care must be taken with this method as the winding object will be mirrored, doubling the number of turns and creating a distorted back EMF waveform.
    - The winding in these slots along the symmetrical boundary should have their number of turns divided by two to countermeasure this.
    - Verification by running a no-load back EMF check is recommended.

The next step is to tell the system what parts of the geometry the force calculation needs to take. The method recommended by ANSYS® [EC19], [AN15], [YX14] for this application is the virtual work method which must be applied to magnetic objects, which are the stator tooth tips illustrated in Fig. 6.4.2(b). Fortunately, these were already in split from the main stator in the model to allow higher mesh densities at the air gap interface. The tool automatically determines which faces of the tooth are interfacing with the air gap and which are linked to the rest of the stator tooth, so the forces are only calculated on the relevant surfaces [ANS18].

The step control is also modified to support the force tool. In the standard analysis in chapter 3 the machine is set to run over a given cycle (e.g. electrical cycle or cogging cycle) and the time step for the solver is set to

dictate how many degrees/step the simulation must run. For the force analysis, the machine is operated over a single mechanical cycle. However, the step control is now used to dictate the maximum mechanical frequency range of the calculated harmonics (6.1) [EC19].

$$f_{max} = \frac{1}{2dT} \tag{6.1}$$

where f_{max} is the maximum frequency and dT is the time step.

To compare the model data to the measured data f_{max} has to be appropriately high, if f_{max} is known then (6.1) can be re-arranged to give the step time. The total simulation time is $1/f_m$, where f_m is the mechanical frequency and is dictated by the rotor speed.

Time limitations on the project meant that there was no time to implement a full inverter model in the electromagnetic FE simulation, so the phase currents are simulated as sinusoidal waveforms.

6.4.1.2 Setting up the mechanical model

The mechanical model is much more straight forward to set up. The key aspects are to set the faces as a apply the imported forces to tooth faces and to ensure the forces are applied in the middle of the stator axially, typically by setting up a default co-ordinate system. The resultant mapped forces on the model are illustrated in Fig. 6.4.4.

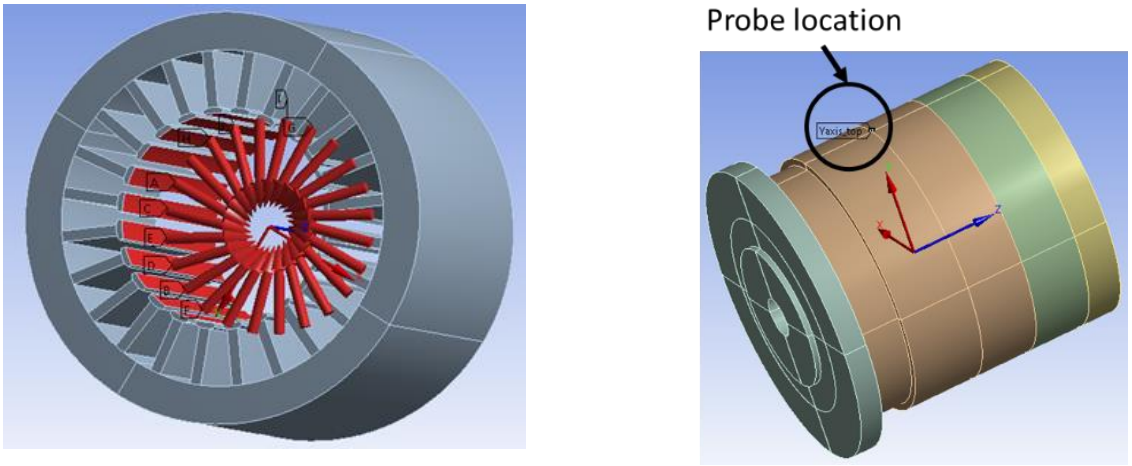

(a) Mapped tooth forces (frame hidden) (b) Acceleration probe location.

Fig. 6.4.4 Setup of the 3D model.

The probe location in Fig. 6.4.4(b) aligns with the sensor sat at the 0-degree position in the measurement so the acceleration data captured from this probe will be used in the comparison.

The key care point with the 3D model in Fig.6.4.4(a) is that it MUST share the same co-ordinate system and origin as the 2D electromagnetic model. Best practise is to import the 2D stator model into the FE tool and extrude the shape to the correct axial length as this guarantees the coordinates are aligned. Failure to do this risks the forces being mapped erroneously. This is highly relevant considering the process detailed in Fig. 6.4.2. If the 2D stator is rotated half a tooth pitch, then the 3D stator must also be rotated in the same manner or the calculated forces will be applied to the slot gap instead of the tooth.

6.4.2 Comparison of the model and measured data

The efforts in simplifying the mechanical model and utilisation of the various features of FE tool such as symmetry multipliers means the simulation times have been reduced but can still take a few hours to complete each set of calculations. Given the limited time a full replication of the detailed measurements carried out in the first section of this chapter is not possible. To try to verify the model, 4 speeds will be tested, 2 in the constant torque region and 2 in the flux weakening region. For each of these speeds the machine will be simulated at no-load and maximum torque, as summarised Table 6.4.1.

Table 6.4.1 I_d and I_q current settings for each speed and torque point

	1500 rpm		3000 rpm		6000 rpm		7500 rpm	
	I_d (A)	I_q(A)	I_d(A)	I_q (A)	I_d (A)	I_q (A)	I_d (A)	I_q (A)
0Nm	0	0	0	0	0	0	0	0
MAX	-26.1	27.0	-26.2	27.1	-34.2	12.4	-31.5	9.0
T_{max}	15.3Nm		15.4Nm		11.4Nm		8.6Nm	

The I_d and I_q currents in Table 6.4.1 are taken directly from the logged data from the experiments.

The bandwidth each speed runs at is also important. The higher the frequency band the more steps the FE tool has to run increasing the processing time. As the supply currents are sinusoidal in this machine there is no PWM component so the high frequency peaks observed in the testing will not be as prevalent. Looking at the test results from earlier in this chapter 1500rpm and 3000rpm have a large region of the bandwidth that is effectively noise between ~3kHz and 10kHz where the PWM influence lies. To give some overhead to this the band was extended to 5kHz for both speeds. For the high speeds, the higher harmonics are observed up to 10kHz, so this is the limit set on those speeds. With the limits and load levels set the simulations are run. The no-load results are observed in Fig. 6.4.5.

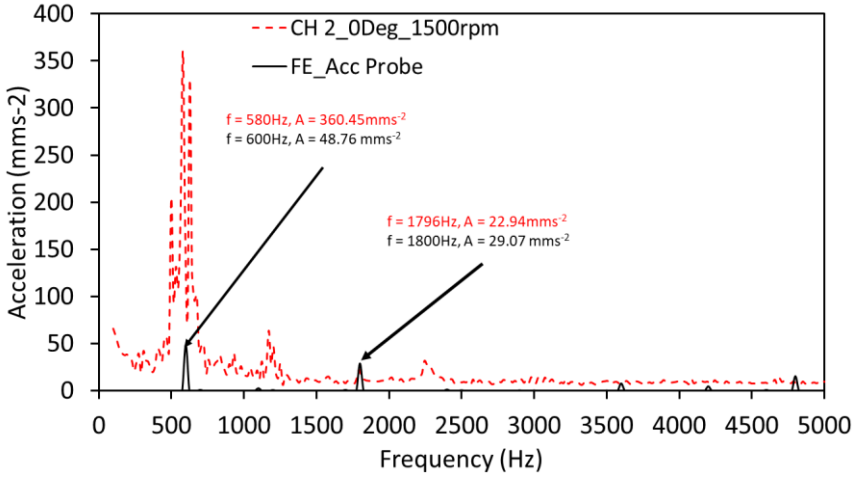

(a) 1500rpm, no load.

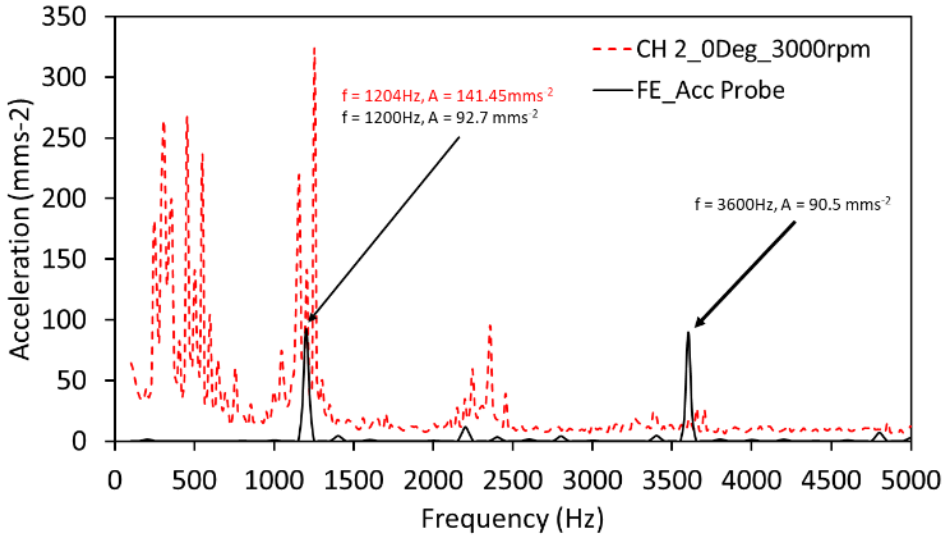

(b) 3000rpm, no load.

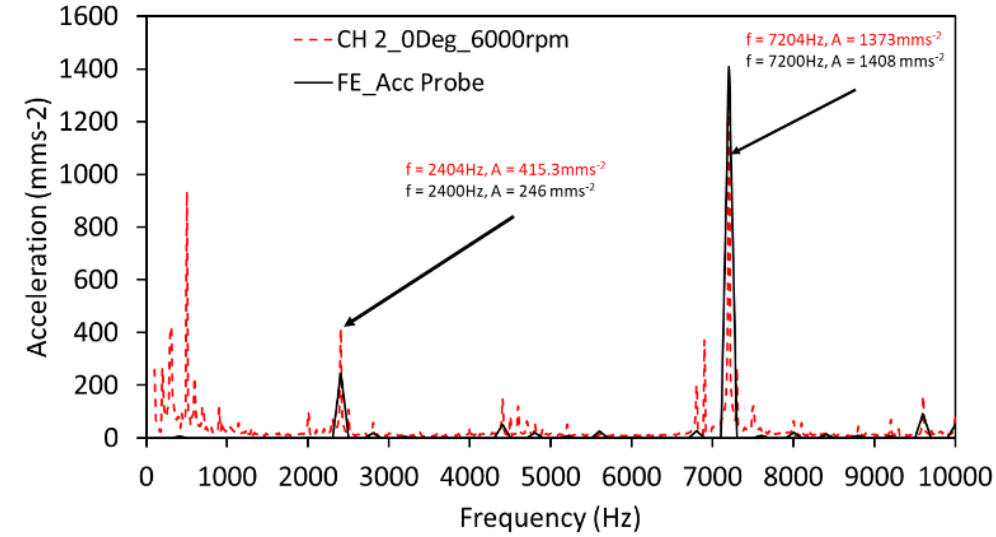

(c) 6000rpm, no load.

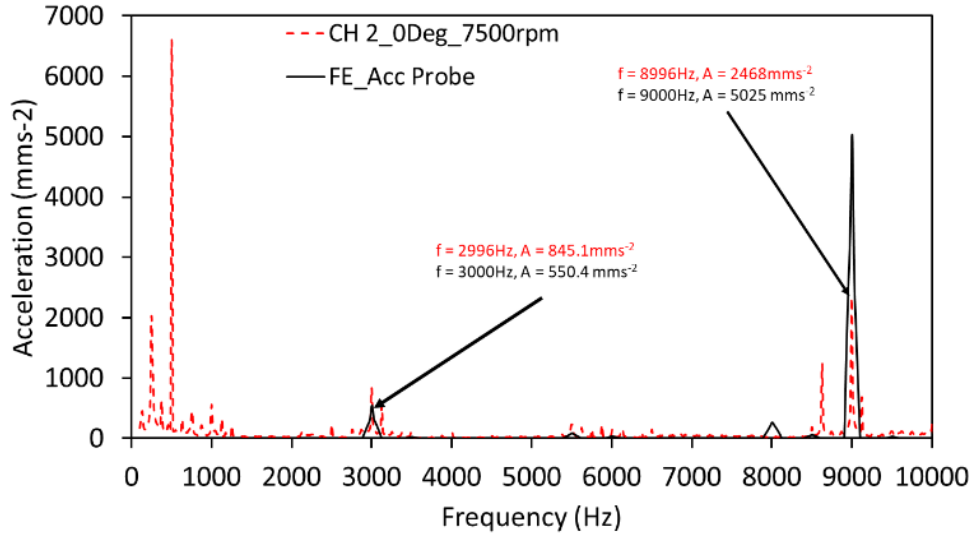

(c) 7500rpm, no load.

Fig. 6.4.5 Comparison of calculated harmonic responses and measured results under no load conditions at 1500rpm, 3000rpm, 6000rpm and 7500rpm.

Table 6.4.2 Comparison of FE and measured results for no load test.

	FE probe		Measured data	
Speed	Frequency	Amplitude	Frequency	Amplitude
1500rpm	600Hz	48.8mms^{-2}	580Hz	360.5mms^{-2}
	1800Hz	29.1mms^{-2}	1796Hz	22.9mms^{-2}
3000rpm	1200Hz	92.7mms^{-2}	1204Hz	141.5mms^{-2}
	3600Hz	90.5mms^{-2}	-	-
6000rpm	2400Hz	246mms^{-2}	2404Hz	415.3 mms^{-2}
	7200Hz	1408 mms^{-2}	7204Hz	1373mms^{-2}
7500rpm	3000Hz	550.4 mms^{-2}	2996Hz	845.1 mms^{-2}
	9000Hz	5025 mms^{-2}	8996 Hz	2468 mms^{-2}

The results show that in general the key $12f_e$ frequency, corresponding to the ripple frequency is correct with the 3rd harmonic ($36f_e$) also in alignment. The amplitudes also follow the pattern of the measured well, increasing as the speed increases, which given the extra energy in the system is to be expected. Whilst the trend is good, the amplitudes of the calculated values relative to the measured data are a little different.

- At 1500rpm the $12f_e$ component (600Hz) is sitting around the modes from the rig components that were discussed in the measured results previously. Between 500Hz and 600Hz there are some aspects of the rig being excited that is drowning out the machine reaction.
    - The $36f_e$ component (1800Hz) shows reasonable alignment, although the amplitudes are very low in both the FE and measured cases.
- At 3000rpm the $12f_e$ component (1200Hz) shows reasonable alignment with the same frequency on the measured. However, similar to the 1500rpm the surrounding modes drown out the 12fe component.
    - As discussed in the measurement these values are likely due to a dynamic mode of the rotor as the peaks are not observed in any of the impact hammer tests.
- At 6000rpm and 7500rpm the comparative performance is better; the modelled amplitudes are lower suggesting that at the $12f_e$ frequencies for both the machine is a little over damped.
- Conversely, the $36f_e$ component calculated overshoots the measured, a very small amount at 6000rpm and a significant amount at 7500rpm.

The machine is then run at the different speeds at maximum torque for each speed point, using the current data in Fig.6.4.2. The results are shown in Fig. 6.4.6.

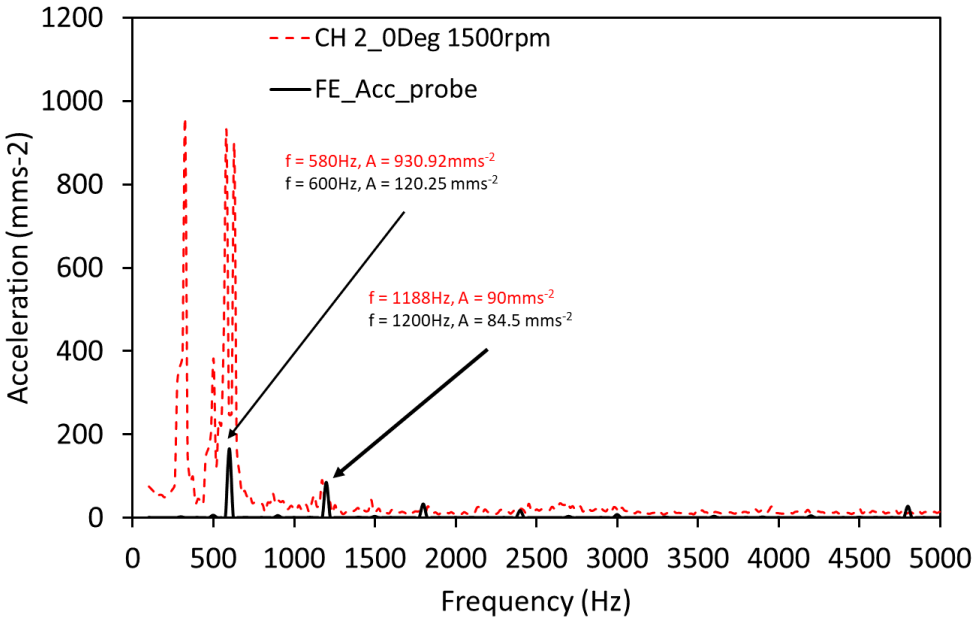

(a) 1500rpm, maximum torque.

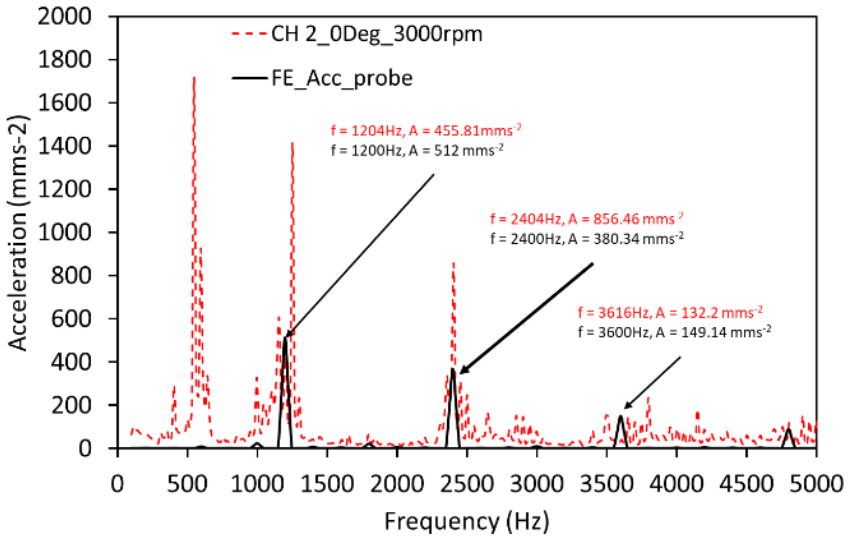

(b) 3000rpm, maximum torque.

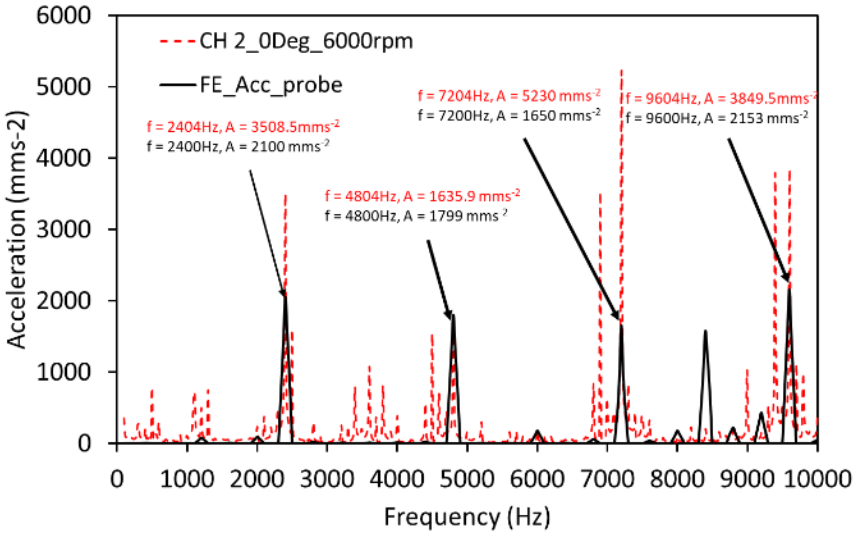

(c) 6000rpm, maximum torque.

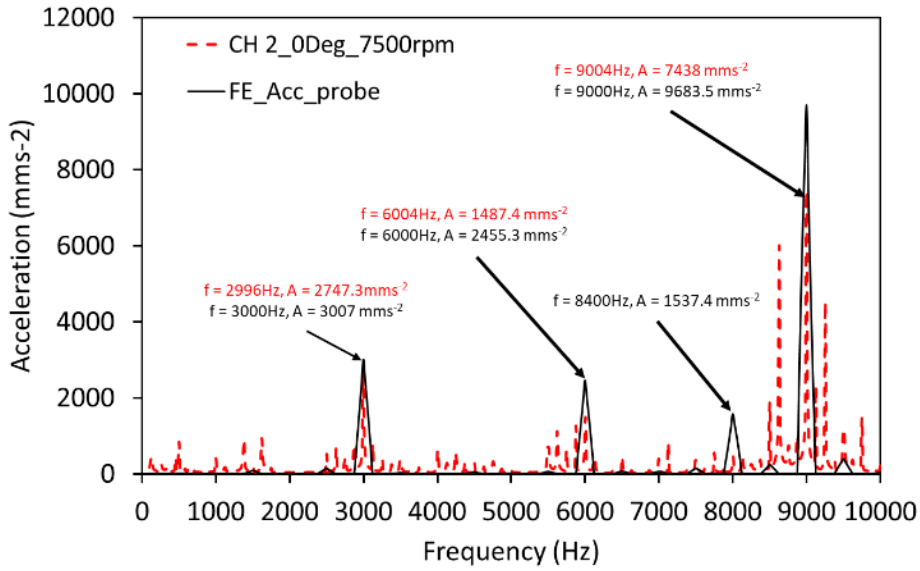

(c) 7500rpm, maximum torque.

Fig 6.4.6 Comparison of calculated harmonic responses and measured results under full load conditions at 1500rpm, 3000rpm, 6000rpm and 7500rpm.

Table 6.4.3 summarises the key points in Fig. 6.4.6.

Table 6.4.3 Comparison of FE and measured results for full load test.

	FE probe		Measured data	
Speed	Frequency	Amplitude	Frequency	Amplitude
1500rpm	600Hz	120.25mms^{-2}	580Hz	930.92mms^{-2}
	1200Hz	84.5mms^{-2}	1188Hz	90mms^{-2}
3000rpm	1200Hz	512.0mms^{-2}	1204Hz	455.81mms^{-2}
	2400Hz	380.34mms^{-2}	2404Hz	856.46mms^{-2}
	3600Hz	149.14mms^{-2}	3616Hz	132.2mms^{-2}
6000rpm	2400Hz	2100mms^{-2}	2404	3508.5mms^{-2}
	4800Hz	1799mms^{-2}	4804Hz	1635.9mms^{-2}
	7200Hz	1650mms^{-2}	7204Hz	5230mms^{-2}
	8400Hz	1574.6mms^{-2}		
	9600Hz	2153mms^{-2}	9604Hz	3849mms^{-2}
7500rpm	3000Hz	3007mms^{-2}	2996Hz	2747.3mms^{-2}
	6000Hz	2455.3mms^{-2}	6004Hz	1487.4mms^{-2}
	8000Hz	1573mms^{-2}	-	-
	9000Hz	9683.5mms^{-2}	9004Hz	7438mms^{-2}

The results follow much the same trends as the no-load data in that the key $12f_e$ frequencies and their harmonics are shown in good alignment with the measured. At the low speeds, the rig and rotor modes mean that whilst the $12f_e$ components align reasonably with the measured data the surrounding high peaks mean the component is effectively drowned out. At high speeds, the picture is much better with 7500rpm in particular showing good alignment.

The amplitudes of the different peaks are still different from the measured. However, the general trend in increase is observed, showing the effect the full load is having on the vibratory performance. Frequencies between ~3kHz and ~6kHz shown good agreement in terms of amplitude between the measured and calculated values. However, above and below this the general trend is the measured data is much higher in

amplitude than the calculated. Given the complexity of the rig and the mechanisms in place there a large number of potential reasons for this but following factors are likely strong contributors.

1. The damping factor for the model was tuned from the hammer test data for mode (2,0), which sits around 4200Hz.
    - The damping factor is a function of frequency, so whilst correct for the mode (2,0) it is likely under or over damping the amplitudes of frequencies above and below the frequency the mechanical transfer was calculated at.
2. Differences in the calculated and actual modal frequencies.
    - From the modal analysis it was seen that there are some errors between the developed model and the measured, given the effect of a natural mode on the amplitude the proximity of a mode will influence the size of the peak.
3. Test rig components and rotor dynamic modes. As highlighted in both the impact hammer test on the mounted machine and the dynamic test the setup shows
    - At 3000rpm the high peaks at $12f_e \pm f_m$ were indicated to be rotor dynamic modes during the analysis of the measured.
    - The machine model does not account for these and are not generated in the calculation.
4. Measurement error.
    - The acceleration sensors were bonded to the machine and operated in a very noisy environment in terms of mechanical and electrical noise, rendering the acceleration signals susceptible to being influenced by external factors.

Overall, given the complexity of problem, the results are quite reasonably representative of the frequencies and trends displayed by the measured machine. Future work will be useful to further investigate the causes of the differences between the measured and FE predicted vibration results. One possible way is to remove the water-cooling jacket to compare the measured and FE predicted vibration results directly on the stator frame since the thin structure of water jacket and water flow are also potential major sources of causing the differences.

6.5 Chapter summary

6.5.1 Summary of measured data analysis

The measurement of the machine passed through a series of different tests with complexity building at each point up to the full measurement of the machine under MTPA control which would be the conditions under which the machine would be operated given an application. The key outputs are:

- The high cogging torque of the machine is reflected in a high $12f_e$ component across the speed range of the machine.
    - Under no load conditions at speeds above 7500rpm the high ripple has the unfortunate effect of inducing very high levels of vibration causing damage to the machine.
    - This resonance was not observed during the load testing, indicating the resonance frequency had been shifted due to the combined load of the baseline machine and the dynamometer on the drive line. It should be noted audible noise levels were high at speeds above 7000rpm under load conditions but reduced compared to the no-load condition.
- The PWM switching components have the most significant impact on the vibratory performance of the machine.
    - The side band f_c+3f_e in particular appears to run through a series of eigen modes on the machine, in particular between ~10.5kHz and ~10.8kHz, generating very large amplitudes.
    - The f_c+3f_e sideband was shown to be a result of the SVPWM switching strategy utilised by the controller.
- Adjusting the PWM switching frequency, f_c, highlighted the importance of optimising the frequency to the machine.
    - Switching frequency f_c at 8kHz showed a large mitigation in overall acceleration. However, the maximum amplitudes were still significantly higher than other factors.
    - Switching frequency f_c at 10kHz was OK for low speeds but at higher speeds, in particular 6000rpm, the upper band fc+3fe appears to align with a machine mode generating a large amplitude.
    - Running the PWM frequency at 12kHz showed extremely large amplitudes at most speeds, in particular on the f_c+3f_e band which appeared to align with, or at least excite, mode 0 (breathing) on the machine.
- Adjustment of the current angle towards the MTPA point results in a net reduction in the acceleration measured across the key $6f_e$, $12f_e$ and PWM switching frequency, f_c, and their sidebands.
    - The high current density of the machine is reflected in these results; as the reluctance torque component is utilised the current required to obtain the target torque is reduced; lower current means lower coil MMF which means reduced forces on the stator core.

- As the current angle sweeps past the optimum point the acceleration rapidly increases reflecting the action of the controller having to pump more current into the machine to maintain the target torque.
- At higher torques the $24f_e$ component becomes more prominent indicating a link to the reluctance component. However, the amplitude never becomes significant, even at maximum torque.

The results have shown good consistency throughout the testing with the same frequencies appearing during different tests and after various resets and shutdowns of the test rig giving good confidence in the results.

6.5.2 Summary of dynamic model

The dynamic model was successfully implemented. It was shown that a fractional 2D model for the electromagnetic FE model works well for this machine however care must be taken to ensure the lines of symmetry are correct to avoid erroneous force vectors being generated and also to ensure that the co-ordinate systems of the 2D and 3D models are matched to prevent erroneous mapping of the forces.

The model was shown to give reasonable alignment with the measured data for the two extremes of no-load, full load and speeds in the constant torque and constant power region.

- The key ripple frequency, $12f_e$ and its harmonics are shown and give good alignment with the measured data.
- Amplitudes follow the trend from the measured data as speed and load changes.
- Amplitudes in the range 3kHz to 6kHz show good correlation to the measured data.
  - Above and below this band the accuracy falls off.
  - This is likely the effect of the calculated damping ratio only being effective for a given frequency band, as well as the influence of water-cooling jacket outside the stator frame.
- The $12f_e$ component at 1500rpm is in the same frequency range as the very high amplitudes due to suspected rig modes, in particular 580Hz, identified in the impact hammer and dynamic testing, this has the effect of drowning out the component.
- At 3000rpm the $12f_e$ component has reasonable alignment to the measured amplitude. However, the two side bands $12f_e \pm f_m$ suspected to be dynamic modes of the rotor or driveline mean that similar to the 1500rpm results the calculated band looks significantly lower than that it actually is.

Given the complexity of the models developed and the test rig used to measure the machine these results are reasonable but future work will be useful to further investigate the causes of the differences between the measured and FE predicted vibration results.

7 Investigation into the influence of IPM topologies on the vibratory performance of a machine

7.1 Introduction

All the measurements, analysis and modelling up to this point have focussed on the baseline IPM machine which, as was shown in the development of the baseline electromagnetic FE model, utilises a dual-layer 'V' arrangement for the permanent magnets. Fig. 7.1.1 shows the ¼ FE model covered in chapter 3 as a reminder.

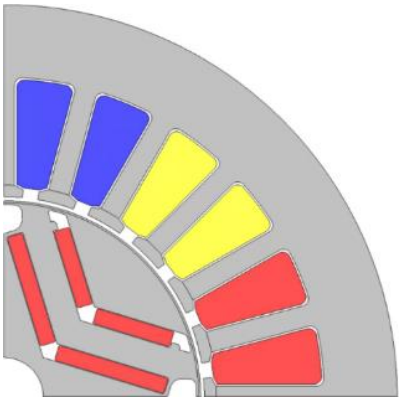

Fig. 7.1.1 Dual layered 'V' magnet topology of the baseline IPM machine.

This topology was chosen due to the requirements of the original design brief for which the prototype machine was developed and for the similarity to the characteristics of the MY09 Nissan LEAF motor, the design of which was still classified at the time of development. In chapter 1 of this thesis it was shown that there is a wide array of different possible IPM topologies which have been compared extensively in literature [LG09], [JQZ15], [AKJP16], [YY17], though the tendency is to focus on the electromagnetic performance aspects of each machine rather than aspects such as the vibratory behaviour. Given the time-consuming nature of the vibratory simulations, as highlighted in chapters 5 and 6, it is prudent to limit the number of different topologies investigated so care must be taken to choose the most relevant topologies for the application as this will yield the most useful results, the application in this thesis is of course electric machines for EV and HEV drivetrains.

The automotive industry tends to be very conservative in terms of the design and development of critical systems such as the traction machine, steering, brakes, chassis, etc. This conservatism is borne of necessity rather than a fear of change; the development of any new technology into a given market requires a very careful analysis of the risk and rewards. Releasing a new technology into the market only to find the customer has no interest, or even worse, it has some major unforeseen technical issue can be ruinous and history is strewn with organisations that tried to push the curve only to have it severely backfire [Kl08]. The powertrain and chassis departments tend to tread the most carefully when considering new technologies given the implications of reliability, safety, and the high cost to the company in terms of the recalls and loss of

reputation of that can occur when these aspects go wrong. This tendency to mitigate risk means that the number of machine topologies used within the industry for traction applications is actually quite limited and will be briefly reviewed here.

7.1.1 Common IPM designs for automotive powertrains

The availability of technical data on the electric machines utilised in production EV and HEV powertrains is limited; a highly competitive arena such as the automotive market mean secrecy is important for the reasons previously discussed so the selected topologies will be based on published public domain data. Much of this data comes from the Oak Ridge Nation Labs (ORNL) in the USA [OR20], initially part of the Manhattan project in the 1940's it has since evolved into a multi-faceted research group with a focus on low-carbon technologies such as electric powertrains. ORNL did a lot of work in the early 2010's of stripping down electric powertrains such as the Toyota Prius, Nissan LEAF and BMW i-series, doing detailed analysis and publishing them into the public domain. A number of different machines are reviewed, and the common topologies summarised in Table 7.1.1. Some well-known vehicles such as the Tesla Model S are omitted due to fact the Model S utilises an induction machine. The Tesla model 3 is reported to utilise an IPM machine [CR18] for at least one of its traction motors but at the time of writing details are a little sparse.

Table 7.1.1 Selected production BEV/HEV IPM topology comparison

Machine application	**Company**	Nissan/UoS[1]	Nissan	Toyota	Lexus	BMW	Honda	General Motors
	Vehicle(s)	N/A	LEAF/eNV200	Prius (Gen3)	LS 600h	i3	Accord	Bolt EV
	Production year	2011	2014	2010	2008	2014	2014	2017
	Drivetrain	BEV[2]	BEV[2]	HEV[3]	HEV[3]	BEV[2]	HEV[3]	BEV[2]
	Machine type	IPM[4] PMSM[5]	IPM[4] PMSM[5]	IPM[4] PMSM[5]	IPM[4] PMSM[5]	IPM[4] PMSM[5]	IPM[4] PMSM[5]	IPM[4] PMSM[5]
	Magnet topology	Dual layer 'V'	Delta	Single layer 'V'	Delta	Dual Bar	Single layer 'V'	Dual layer 'V'
Image			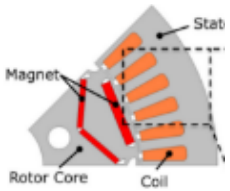					
Machine specifications	**Rated power**	80kW	80KW	60kW	110kW	125kW	70kW	150kW
	Peak Torque	280Nm	254Nm	207Nm	300Nm	250Nm	No Data	360Nm
	Max Speed	11000rpm	10400rpm	13500rpm	10230rpm	11400rpm	No Data	8810rpm
	Slot(S)/pole(P)	48S/8P	48S/8P	48S/8P	48S/8P	72S/12P	48S/8P	48S/8P
	Line voltage	$300V_{dc}$	$300V_{dc}$	$650V_{dc}$	$650V_{dc}$	$360V_{dc}$	No Data	$350V_{dc}$
	Phase current	$440A_{rms}$	$440A_{rms}$	$300A_{rms}$	No Data	375 A_{rms}	No Data	$400A_{rms}$
	Stator OD[6]	200mm	200mm	264mm	200mm	242mm	291mm	264mm
	Rotor OD[6]	130mm	130mm	160.4mm	129.1mm	178.6mm	No Data	No Data
	Stack length	150mm	150mm	50.8mm	135.9mm	132mm	No Data	125mm
	Skew:	1 step	1 step	None	1 step	6 step	No Data	None
Reference		N/A	[NT14]	[TAB11]	[TAB09]	[BO16]	[BO14]	[FM16]

1 = The University of Sheffield, 2 = Battery Electric Vehicle, 3 = Hybrid Electric Vehicle. 4 = Interior Permanent Magnet, 5 = Permanent Magnet Synchronous Machine, 6 = Outer Diameter.

It should be noted that the dual layer 'V' Nissan/UoS machine in Table 7.1.1 is the full scale (80kW) version of the baseline machine. From the review in Table 7.1.1 it can be seen that there are broadly 4 different topologies employed:

- Single layer 'V' (Prius et. al).
- Dual layer 'V' (Nissan/University of Sheffield prototype, General Motors).
- Delta arrangement (Lexus, Nissan).
- Dual bar arrangement (BMW).

These topologies will be utilised for the comparative analysis for the influence of the magnet topology on the vibratory performance of the machine. Referencing Table 7.1.1 and setting aside the fact the baseline machine is much smaller than the full sized traction machines listed, simply using the specifications gleaned from the literature will not create a fair comparison; the machines vary in power, size and application making direct comparison difficult. To understand the influence of each topology in terms of the vibratory and general machine performance aspects each topology needs to be scaled and adjusted such that they are as close to the baseline aspects as possible. To fairly compare the topologies the machines the variations between the topologies must therefore be limited to the layout of the magnets in the rotor core, meaning:

- The slot/pole combination is fixed.
- The same stator geometry and windings from the baseline is utilised.
    - The DC link voltage is held the same.
    - The same maximum current is used.
    - Same number of turns applied.
- The same rotor outer diameter (in effect fixing the air gap) and stack length is utilised.
- The same laminated steel and permanent magnet materials are utilised.
- All four machines target the same performance by targeting the baseline T-N curve profile.

The initial step of the investigation is therefore to design 3 topologies using the Delta, single layer 'V', and dual layer bar topologies that align with the baseline performance, using the T-N curve as the datum for the alignment of the selected topologies. The N-T curve for the baseline machine is shown in Fig. 7.1.2.

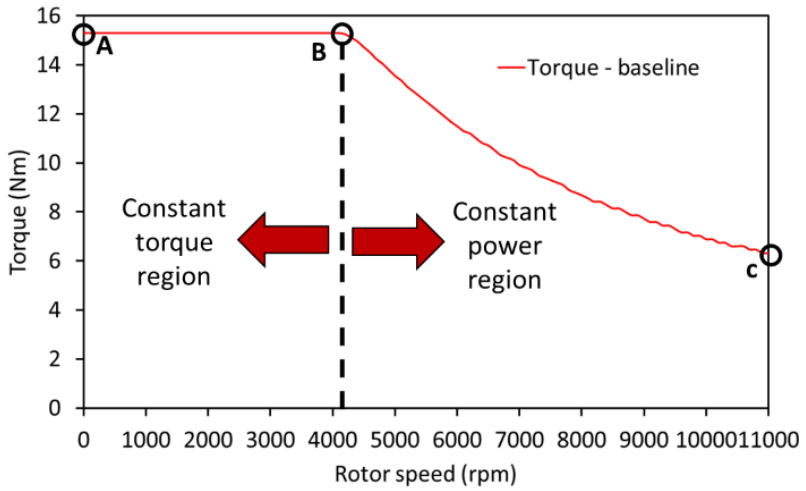

Fig. 7.1.2 T-N curve of baseline machine showing key performance points, 'A' is the maximum torque at 0 rpm, 'B' is the base speed of the machine and 'C' is the torque at the maximum rated speed.

From Fig. 7.1.2 the key aspect that need to be aligned:

1. Maximum torque in the constant torque region (A to B in Fig. 7.1.2)
    - The stator MMF is fixed as is the machine volume, split ratio, and stack length.
    - Thus, the only method of boosting or lowering the torque to adjust either the magnet volume to adjust the PM flux linkage (ψ_m) of the machine to adjust the mutual torque component and/or change the reluctance torque component by the adjusting saliency (L_q/L_d ratio) using methods such as the adjusting the magnet geometry (pitch angle, depth etc.) or adding flux barriers.
2. Constant power region (point B to C in Fig. 7.1.2).
    - Target is to match the constant power speed range (CPSR) of the baseline [WLS02].
    - Dictated by the so-called characteristic current of the machine, I_c (eq. 7.1) [AP17] which is the ratio of the PM flux linkage, (ψ_m) and d-axis stator inductance (L_d). The characteristic current point represents the centre of the voltage limit ellipses described in chapter 2 [AP17], [TM87], [SM89].

$$I_c = \frac{\Psi_m}{L_d} \tag{7.1}$$

In effect, to achieve the same CPSR the topologies have to match the PM flux linkage d-axis inductance ratio as closely as possible. Given the maximum current is fixed the control variables are once again the PM flux linkage and geometry of the magnets and flux barriers in the machine which influences the d and q axis inductances.

Analytical methodologies of designing IPM machines are subject to error due to the non-linear effects of saturation in the rotor and stator cores at high loads and cross coupling of the d and q axis flux [JRH10],

[DH12]. To avoid these complexities the method of matching the topologies is to utilise the literature to establish an initial design using best practise and then utilise the optimisation tools available within the electromagnetic FE tool to adjust the design such that the T-N curve requirement is met. The full methodology is described later in this chapter.

Following the establishment of the matched rotors further studies into the effects the different rotor features have on the vibratory performance of the machine can be determined, Fig. 7.1.3 outlines the workflow of the chapter.

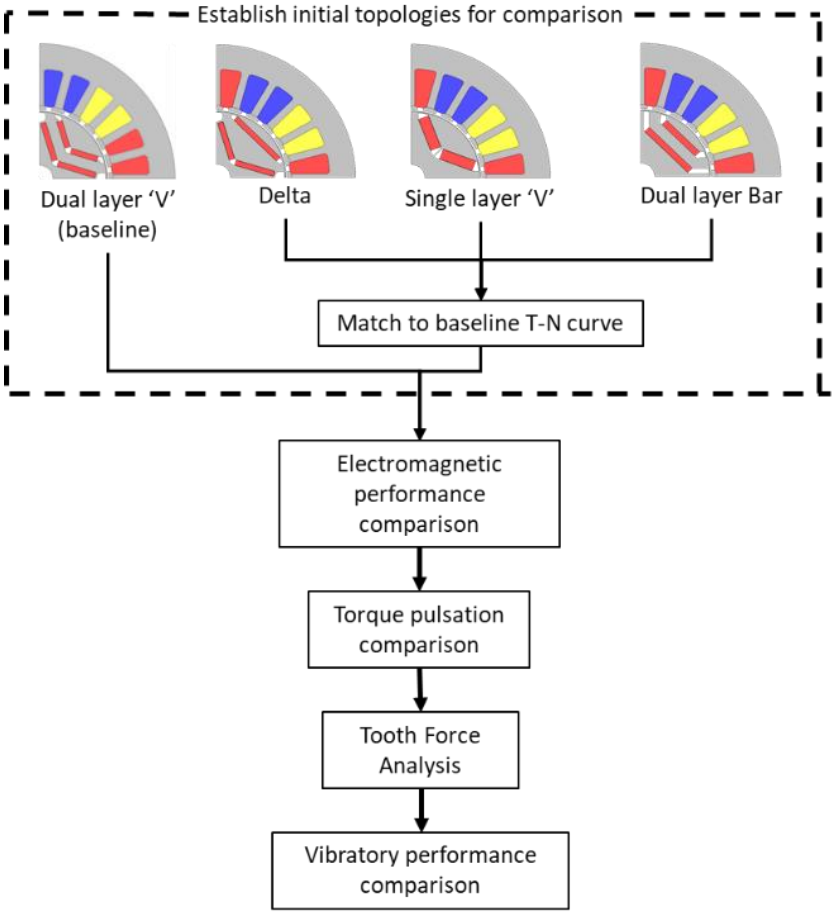

Fig. 7.1.3 Workflow of chapter 7.

From Fig. 7.1.3 following the initial step of matching the T-N curves a comparison of the initial machine designs is undertaken allowing for a more detailed examination of the differences between the different machines in terms of the general electromagnetic performance of the machine (back EMF, torque characteristics, efficiency, and loss, etc.) and of course the tooth forces and vibratory performance of the machine using the methods and models developed previously in the chapter.

.

7.2 Generating the IPM topologies

7.2.1 Establishing the constraints and procedure for the topology comparison

To allow for a fair comparison between the different topologies variations in the design parameters must be limited to the arrangement of the magnets in the rotor core, all other aspects must be fixed where possible. A list of the key constraints for the machine is provided in Table 7.2.1.

Table 7.2.1 Constraints for topology comparison

	Constraint	Value	Unit
Performance objectives (from baseline)	Rated power	20	kW
	Maximum speed	11,000	RPM
	Rated torque	15.3	Nm
	Maximum current	26.7	A_{rms}
	Max line voltage (@max speed)	600	V
Machine constraints (from baseline)	Slot(S)/Pole(P)	24S4P	-
	Stator outer diameter	100	mm
	Stator inner diameter	51	mm
	Rotor outer diameter	50	mm
	Air gap width	0.5	mm
	Stack length	75	mm
	Number of turns	24	Per coil
	Winding circuit	4S1P	S = series, P = parallel
	Winding connection	Wye	-
	Current density	17	A/mm^2
	Magnet material	N36Z	[SE16]
	Rotor core material	M250-35A	[CP08]
	Rotor core stack factor	0.98	-

To keep in line with the fabricated baseline machine all the designs are unskewed. In addition to the factors listed in Table 7.2.1 a key aspect of any FE analysis is the mesh and simulation settings. As was discussed in the development of the baseline electromagnetic FE model key aspects of the analysis such as the cogging torque and tooth forces are highly sensitive to the mesh density. It is of high importance therefore to ensure that when comparing these topologies, the mesh settings are held constant with particular priority given to the settings around the air gap.

In terms of the FE settings, aspects such as the rotor speed and the number of degrees per step of the simulation must be consistent. Again, careful control of these factors ensure the comparison between the different topologies is fair and based on any differences are based on the features in the rotor core, i.e. there is no bias of one design due to a difference in the FE tool setup rather than physical aspect.

With the constraints in place the different topologies need to be established and then optimised such that they match the T-N curve of the baseline machine. The flow diagram for the procedure is shown in Fig. 7.2.1.

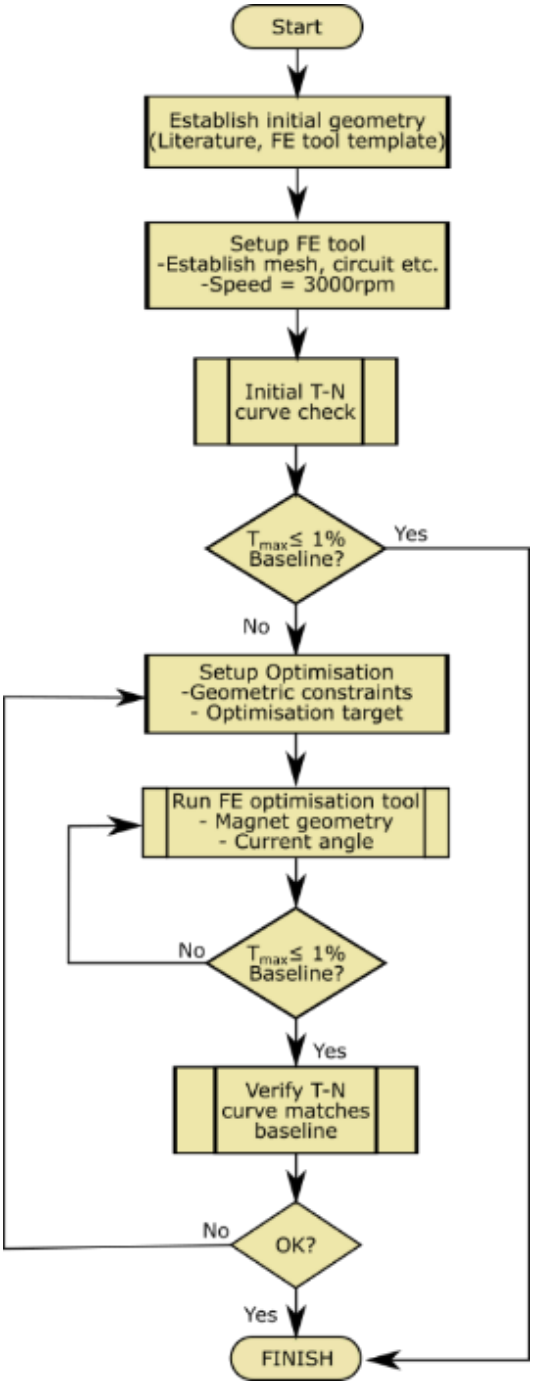

Fig. 7.2.1 Flow chart for matching the T-N curves of the different topologies

It can be seen in Fig 7.2.1 that for each topology an initial design is established, and the T-N curve calculated and compared with the baseline. If the topology matches the baseline then the process is complete, if not (more likely) the topology is optimised. The optimisation methodology is a multi-object generic algorithm (MOAG) that is provided by the JMAG FE tool [JM18b]. To use the function the user must provide some constraints for the tool to establish the search space and some objective functions such as a torque value or minimise ripple rate to act as the target. The process then follows the steps in Fig. 7.2.2 [JM18b] to establish which designs align closest to the objective function(s).

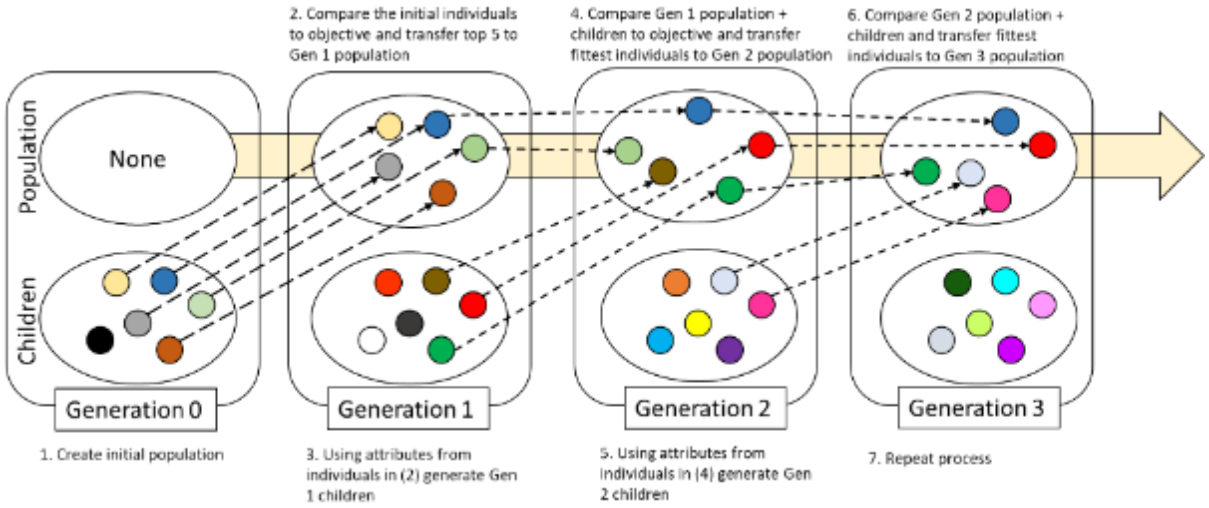

Fig 7.2.2. Overview of genetic algorithm process with population = 5 and children = 6.

Each individual in Fig. 7.2.2 is a different potential solution initially randomly generated using the constraint conditions. The process example in Fig. 7.2.2 has a "population" of 5 individuals, that is the number of individuals that are allowed to pass from one generation to the next and 6 "children" that represent the number of new individuals generated at each generation. It can be seen that at generation 0 there are 6 solutions made, of those only 5 can move to the next generation so the solutions that are "fitter" i.e., closer to the objective function are transferred to generation 1. Within generation 1 a new set of 6 children are generated using the attributes from the 5 fittest individuals from generation 0. These new individuals plus the 5 from generation 0 (11 total) are compared to the objective function and once again the fittest 5 individuals are moved to form the population of the next generation. This process will then continue until:

a) The objective function is met (within the set error band).
b) The maximum number of generations are met.

On completion, assuming the case (a) above has been met, a number of solutions equal to the population size are provided and ranked as closest to the objectives. Referring to Fig. 7.2.1 it can be seen that the top solutions are then fed through the T-N curve tool. The population is limited to 5 as the T-N tool needs flux data from the FE to run which can be quite time consuming to capture. The top 5 are then compared with the baseline T-N curve. If one of the results are aligned then the process is stopped, if not then the closest match is used to establish new constraints to allow finer tuning of the model and the optimisation process repeated. Experience showed that it was very rare to have to run more than one optimisation cycle, the MOAG method proved useful in producing good solutions.

Key to the process is the constraints and the targets. The bulk of the constraints are very much dependant on the geometry being optimised; the different machines will have different geometric maximum and minimum values to avoid clashes with other parts etc. However, all topologies have common objective functions as shown in Table 7.2.2.

Table 7.2.2 Common constraints and objective functions for all machines

Item	Parameter	Min	Max	Unit
Constraints	Current angle	42	55	°
Target/Objective	Average torque	Range	>= 15.2	Nm
			<= 15.4	Nm
	Ripple rate	Range	MINIMISE	-
Method	Multi-objective GA	-	-	-

It can be seen that a common constraint is the current angle. This is because the maximum average torque is the objective and changing the rotor geometry changes the saliency of the rotor and therefore the reluctance torque component. The current angle is included to ensure the mutual and reluctance torque components are maximised. The target torque is the average torque of the baseline (15.3Nm) with ± 0.1Nm error band added to assist the optimisation in convergence. The JMAG optimisation tool also requires at least one objective to “maximise” or “minimise” to meet the internal requirements of its algorithm so that the ripple torque was selected as this is always a good aspect to minimise. With the process established the design phase can begin.

7.2.2 Development of the delta topology

The delta topology is the first to be developed, which in theory at least, is the easiest to match given that as previously highlighted the dual layer design of the baseline machine is based on the original delta type topology of the MY10 Nissan LEAF machine. Rather than generating a new topology the baseline topology is used as a start point and modified. Essentially the lower layer 'V' is held constant whilst the upper layer of magnets is pivoted using the mid-point of the flux barriers at the tips of both upper magnets as the axis of rotation and rotated to form a straight bar. The magnet slot for the upper layer is already a single shape meaning the new shape neatly forms a single slot for the upper magnet; combining the two magnets to a single bar magnet finishes the process. The key concern from a CAD modelling point of view before the upper magnet slot could be rotated the geometry to the upper flux barrier at either edge of the upper layer had to be modified. The existing design is quite complex and is the result of an optimisation of the shape to balance the need to mechanically retain the magnet in the 'V' position at maximum speed whilst minimise flux leakage within the rotor core, the constraints used to control the resultant shape made it difficult to rotate the magnets in the desired manner. Thus, a simplified version is applied to ease the rotation of the upper layer and can be seen in Fig. 7.2.3 (a).

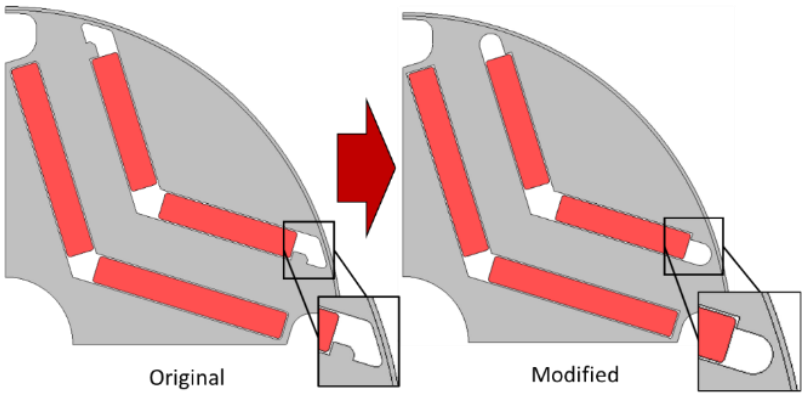

(a) Modification of the upper layer flux barrier to simplify the manipulation of the upper layer 'V'

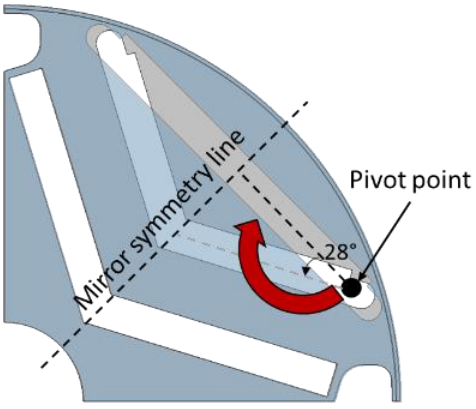

(b) Rotation of the upper layer to form the upper bar

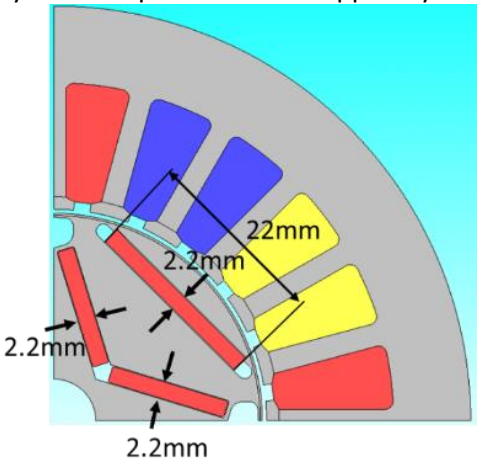

(c) Single magnet created to form upper layer

Fig. 7.2.3 Establishment of the initial Delta topology shape

From Fig. 7.2.3 (b) the modification of the upper layer is made clearer. The location of the pivot point fixes the upper layer pole arc; maintaining this reduces the complexity of the initial optimisation. The angle of the slot is then rotated from 28°, the initial position, to 0° forming a line perpendicular to the mid-pole symmetry line. Within the CAD tool the geometry is mirrored along the mid-pole symmetry line, primarily to make the drawing process more efficient so the resultant magnet slot in the lower portion of the drawing is reflected in the upper, forming one full magnetic pole of the machine. A new shape for the upper magnet is added and can be seen in Fig. 7.2.3 (c) with the key magnet dimensions of the initial delta topology.

7.2.2.1 Matching the Delta T-N curve to the baseline machine

The initial design is run through the FE tool to generate the initial T-N curve of the topology. As highlighted previously the methodology and tools utilised are identical to that used to calculate the baseline characteristics in chapter 3. The resultant maximum torque curve can be observed in Fig. 7.2.4 with the values summarised in Table 7.2.3.

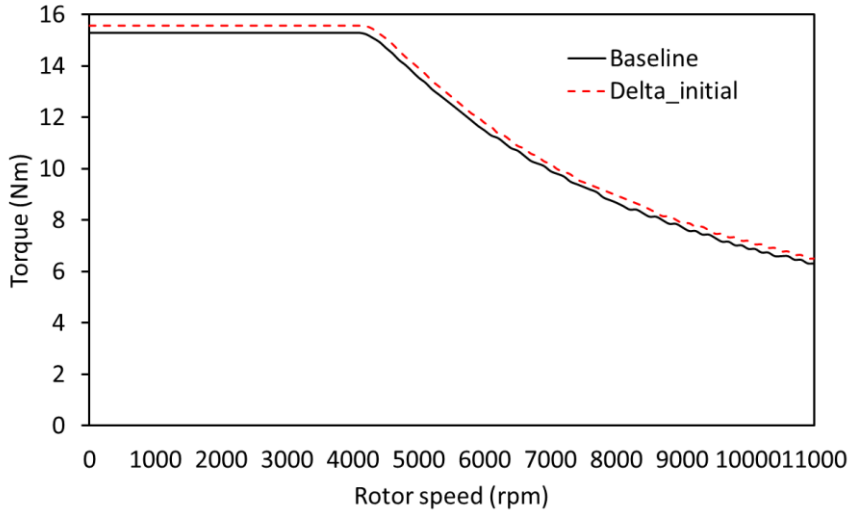

Fig. 7.2.4 Initial T-N curve of the delta type IPM topology VS the baseline machine.

Table 7.2.3 Comparison of maximum average torque and base speed of initial delta design and the baseline

	Baseline machine	Delta (initial)	Error (Delta initial Vs Baseline)
Max. average torque (Nm)	15.3	15.6	2%
Base Speed (rpm)	4200	4200	0%

It can be seen that the torque profile of the initial design is very close to that of the baseline, the key difference being the maximum torque is higher than that of the baseline. This can be brought into line with the baseline by some minor adjustments to the magnet thickness to drop the magnetic torque component slightly, so the thickness of the upper bar magnet and the two lower layer magnets are chosen to be adjusted. The current angle is also included in case changes in saliency mean the torque composition has changed from

the initial analysis. Given the error is ~2% the variation in magnet thickness only needs to be small. The constraints and objective functions can be found in Table 7.2.4.

Table 7.2.4 Constraints and objective functions for Delta topology optimisation

Item	Parameter	Min	Max	Unit
Constraints	LWR magnet slot thickness	1.5	2.2	mm
	UPR Magnet slot thickness	1.5	2.2	mm
	Current angle	42	55	°
Target/Objective	Average torque	Range	>= 15.2	Nm
			<= 15.4	Nm
	Ripple rate	Range	MINIMISE	-
Method	Multi-objective GA	-	-	-

With the targets set and the model ready the optimisation sequence detailed om Fig 7.2.1 is executed. The resultant shape is generated, and the calculated T-N curve shown in Fig. 7.2.5 and the final values in Table 7.2.5.

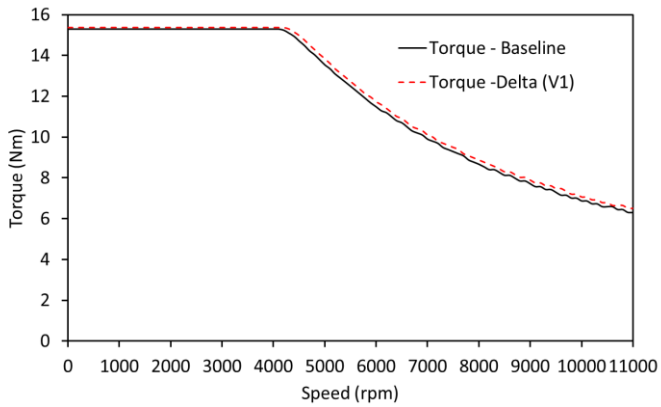

(a) Comparison of T-N curves between the delta and baseline topologies

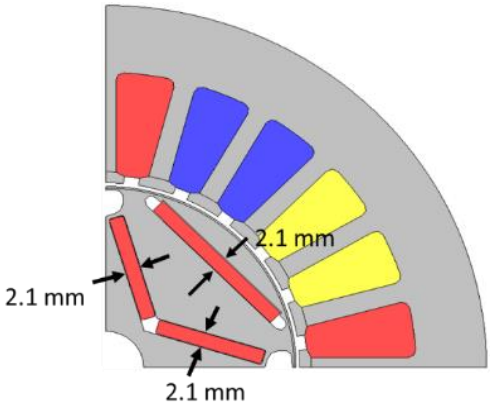

(b) Dimensions of the optimised machine

Fig. 7.2.5 Adjustment of magnets to reduce maximum average torque and align with baseline.

Table 7.2.5 Optimised magnet thickness

Parameter	Initial	V1	Difference Vs initial	Units
Lower magnet slot thickness	2.2	2.1	-0.1	mm
Upper magnet slot thickness	2.2	2.1	-0.1	mm
Max. average torque	15.6	15.33	-0.27	Nm

Table 7.2.4 shows the adjustments required to bring the T-N curve into line with the baseline are minimal to achieve a good match. A full comparison of all the different performance aspects will be provided later in this chapter following the establishment of the aligned single layer 'V' and dual bar topologies.

7.2.3 Development of single layer topology

Given the popularity of the single layer topology as highlighted in Table 7.1.1 there is a lot of literature available on the design [YY17], [KSI05] of a single layer 'V' machine. Given the prevalence of the topology many FE tools such as ANSYS® Electronics workbench or JMAG have templates of this and other basic IPM topologies pre-installed; the user needs only to define the key geometric parameters to generate the required shape. The advantage of using this method also means the different parameters can be inputted

directly into the optimisation tool reducing the effort to create the model. The initial topology is shown in Fig. 7.2.6.

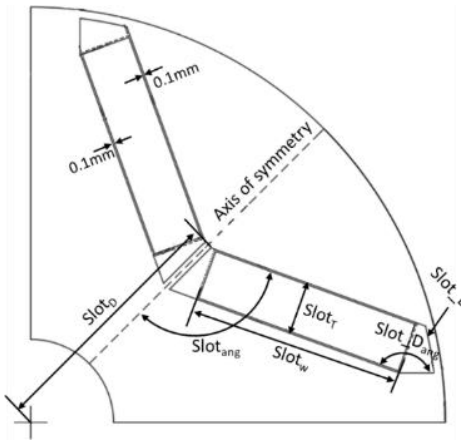

(a) Key dimensional aspects of the dual layer topology to maintain

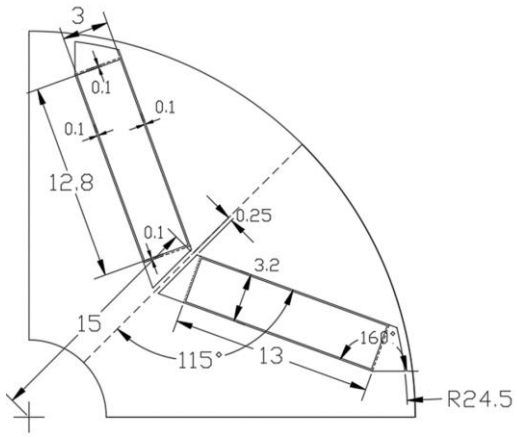

(b) Key dimensions of the single layer 'V' initial (dashed lines represent construction lines)

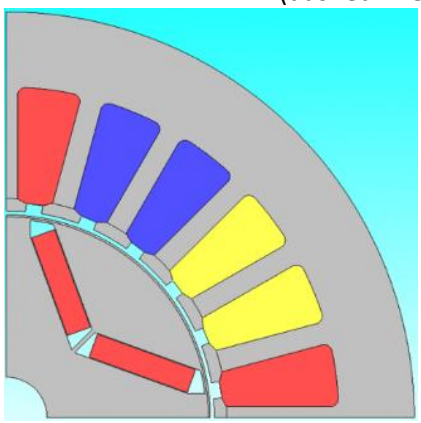

(c) Resultant single layer 'V' FE model (initial)

Fig. 7.2.6 Initial single layer topology.

Table 7.2.6 below summarises the key dimensions listed in Fig. 7.2.5(a) and (b).

Table 7.2.6 Key dimensions and initial values for the Single 'V' topology

Symbol	Parameter	Value	Unit
$Slot_{Ang}$	Magnet slot angle	115	°
$Slot_W$	Magnet slot width	13	mm
$Slot_T$	Magnet slot thickness	3.2	mm
$Slot_D$	Magnet slot depth (from rotor centre axis)	15	mm
Slot_D_{OR}	Magnet slot duct outer radius	24.5	mm
Slot_D_{ang}	Magnet slot duct lower pitch angle	160	°

The initial dimensions were generated using the baseline as a template; the initial magnet slot depth ($slot_D$) is the same as the depth of the upper layer magnets on the baseline with the magnet slot angle and width chosen so that the pole pitch sits between the upper and lower layers of the baseline. Similar to the Delta and the development of the initial baseline model a 0.1mm gap is maintained between the magnet slot and the magnet, representing the gap required for the bonding material. With the initial design in place the T-N curve matching process is undertaken

7.2.3.1 Matching the single layer 'V' machine T-N curve to the baseline machine

The procedure in Fig. 7.2.1 is followed as before. An initial run using the design shown in Fig. 7.2.5 is undertaken with the results shown in Fig. 7.2.7 and Table 7.2.7 shows the performance compared to the baseline topology.

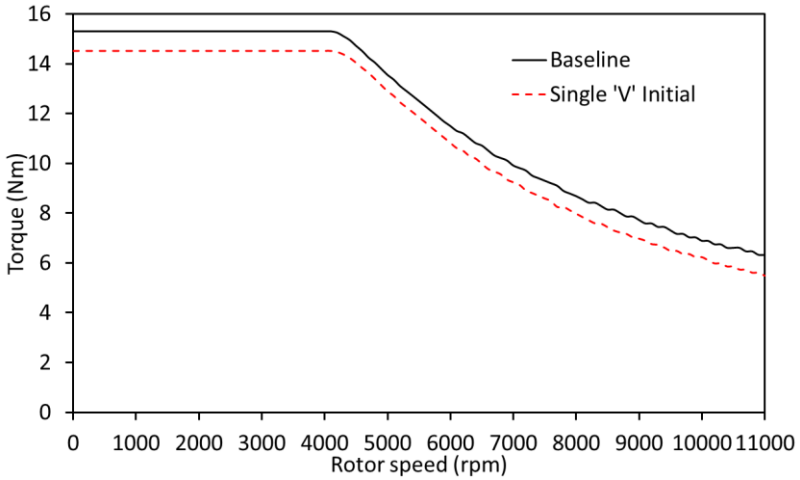

Fig. 7.2.7 T-N curve of the initial single layer 'V' machine.

Table 7.2.7 Comparison of maximum average torque and base speed of initial delta design and the baseline

	Baseline machine	Single 'V' (initial)	Error (Vs Baseline)
Max. average torque (Nm)	15.3	14.5	5.2%
Base Speed (rpm)	4200	4200	0%

From Fig. 7.2.6 it can be seen that the maximum average torque of the initial single layer 'V' topology design is 5.2% lower than the baseline, significantly lower than with the Delta topology so more effort is required to bring the T-N curve into alignment. The optimisation tool within the FE tool is once again utilised however the larger difference in torque means more effort is required to achieve the target. The constraints and objectives utilised are shown in Table 7.2.8.

Table 7.2.8 Constraints and objective functions for the single layer 'V' topology optimisation

Item	Parameter	Min	Max	Unit
Constraints	$Slot_W$	11	14	mm
	$Slot_T$	3	4.2	mm
	$Slot_D$	12	16	mm
	$Slot_{ang}$	105	117	°
	Current angle	40	50	°
Target/Objective	Average torque	Range	>= 15.2	Nm
			<= 15.4	Nm
	Ripple rate	Range	MINIMISE	-
Method	Multi-objective GA	-	-	-

The optimum solution was found and is detailed in Fig. 7.2.8 and Table 7.2.9.

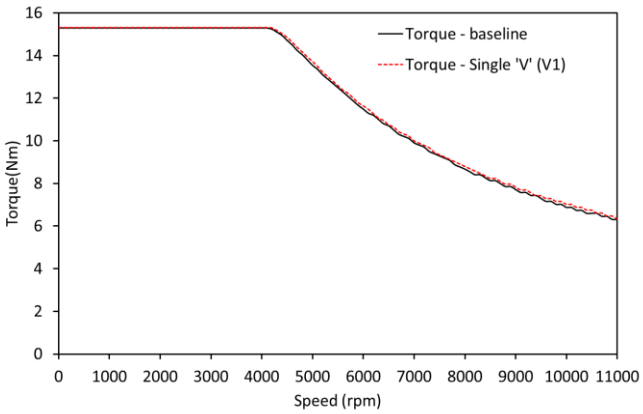

(a) Aligned T-N curves of the baseline and single layer 'V' topologies

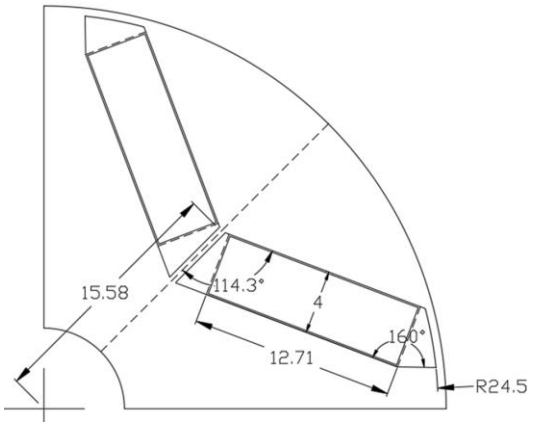

(b) Optimized geometry of the single layer 'V' topology to align with baseline T-N curve

Fig. 7.2.8 Final shape single layer 'V' versus baseline.

Table 7.2.9 Optimised parameter for matching single 'V' T-N curve to baseline

Parameter	Initial	V1	Difference Vs initial	Units
Magnet length	13	12.7	-0.3	mm
Magnetic thickness	3.2	4	+0.8	mm
Magnet depth in core	15	15.58	+0.58	mm
Magnet pitch	115	114.6	-0.74	°
Max average torque	14.5	15.32	+0.8	Nm

The resultant design matches the baseline T-N curve well, the adjustment to the magnet thickness and position boosted the torque up to the target of the baseline. Similar to the delta topology the full comparison of the characteristics of the matched rotor will be shown later in the chapter, following the establishment of the final topology, the dual layer bar type.

7.2.4 Development of dual layer bar topology

The final primary topology is the dual bar topology. Unlike the very popular single layer 'V' topology, literature on the design of a dual layer bar type topology was a little more challenging to find however [AKP16] provides a very good example with the key dimensions shown in Fig. 7.2.9 [AKP16].

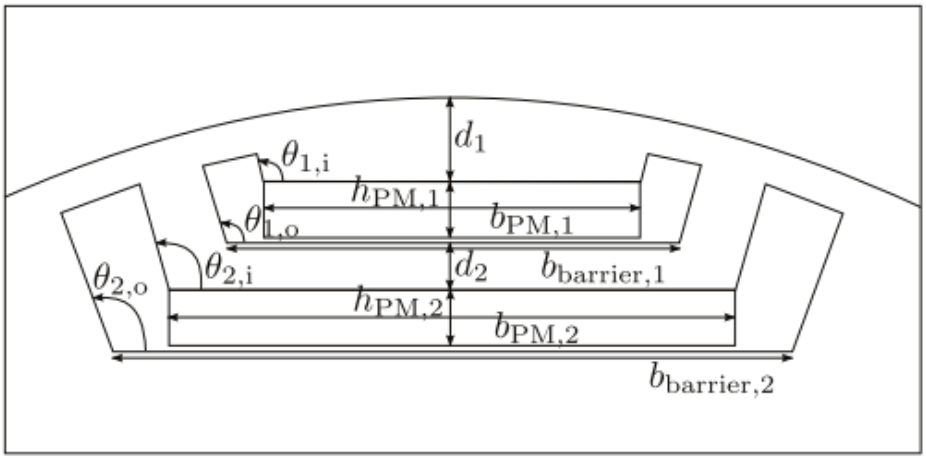

Fig. 7.2.9 Basic dual-layer bar type topology [AKP16].

The symbols in Fig. 7.2.9 represent:

- d_1 = Distance of upper (UPR) magnet from rotor outer diameter (OD).
- d_2 = depth of lower (LWR) magnet from upper magnet.
- $h_{pm,x}$ = Thickness (height) of PM_x, where x is 1 or 2 and 1 = the upper layer and 2 = lower layer.
- $b_{pm,x}$= Breadth (width) of PMx, where x is 1 or 2.
- $b_{barrier,x}$= breadth of flux barrier, where x is 1 or 2.
- $\theta_{x,I}$ = Angle of inner edge of flux barrier.
- $\theta_{x,o}$ = Angle of outer edge of flux barrier.

The template provided by [AKP16] serves as a good starting point for identifying the key geometric features. However, the layout as depicted in Fig. 7.2.9 requires some modifications for the purposes of this study:

- In common with all the other designs in this thesis the depth of the magnets in the core is set using the origin of the rotor as the datum rather than the rotor OD as depicted in [AKP16].
- The topology is symmetrical, and so all magnet slot lengths are referenced from the central line of symmetry running through the centre of the pole.
- Similar to the previous topologies a 0.1mm gap is placed around the magnet to better represent the actual magnetic circuit.

Fig. 7.2.10 shows the initial dimensions of the topology.

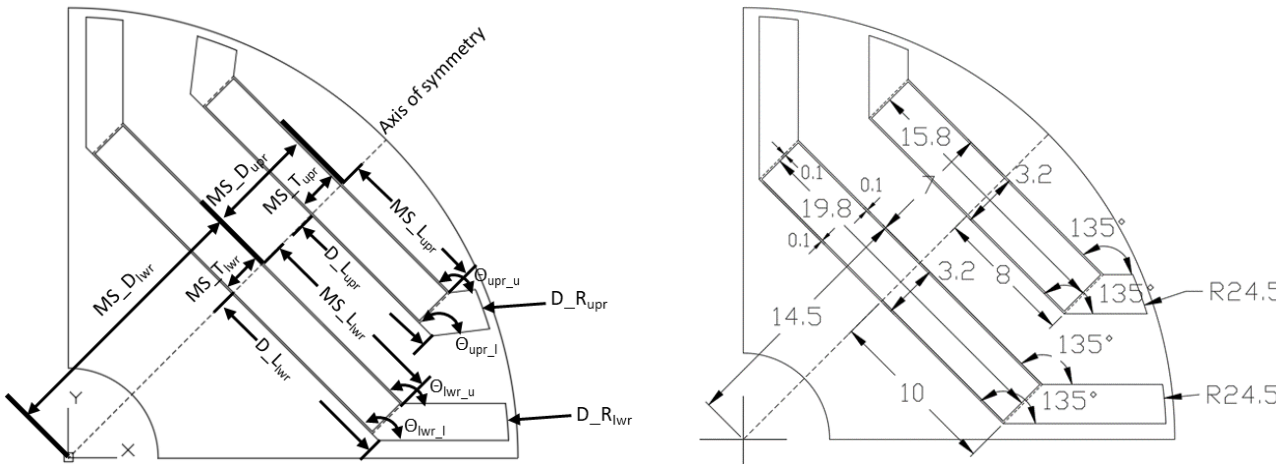

(a) Geometric parameters for dual layer bar type topology

(b) Initial dual bar dimensions

Fig. 7.2.10 Initial dual bar type topology design.

The meanings and values for the symbols in 7.2.10(a) are shown in Table 7.2.10. Similar to the single layer the baseline topology served as a template for the initial positioning of magnets, in particular the depth of each magnet layer in the core and the inter-magnet gap. The outer diameter of the flux barriers on each layer are the same as the q-axis and upper layer flux barriers on the baseline machine. The positions of these then dictate the magnet length and angle of the flux barrier.

Table 7.2.10 Parameters for the initial design of the dual layer bar-type machine

Parameter	Symbol	CAD Value	Full shape	Unit
Magnet slot depth, lower layer	MS_D_{lwr}	14.5	←	mm
Distance between upper and lower layer	MS_D_{upr}	7	←	mm
Magnet slot thickness, lower layer	MS_T_{lwr}	3.2	←	mm
Magnet slot thickness, upper layer	MS_T_{upr}	3.2	←	mm
Magnet slot length, lower layer	MS_L_{lwr}	10	20	mm
Magnet slot length, upper layer	MS_L_{upr}	8	16	mm
Duct length, lower layer	D_L_{lwr}	10	20	mm
Duct length, upper layer	D_L_{upr}	8	16	mm
Flux barrier, upper layer, outer radius	FB_OR_{upr}	24.5	←	mm
Flux barrier, lower layer, outer radius	FB_OR_{lwr}	24.5	←	mm
Angle of upper edge of upper layer flux barrier	θ_{upr_u}	135	←	°
Angle of lower edge of upper layer flux barrier	θ_{upr_l}	135	←	°
Angle of upper edge of lower layer flux barrier	θ_{lwr_u}	135	←	°
Angle of lower edge of lower layer flux barrier	θ_{lwr_l}	135	←	°

With the initial dimensions established the N-T curve can be calculated and compared to the baseline as the previous cases.

7.2.4.1 Matching the dual layer bar design T-N curve to the baseline machine.

The calculated initial T-N curve is shown in Fig. 7.2.11 and differences to the baseline shown in Table 7.2.11.

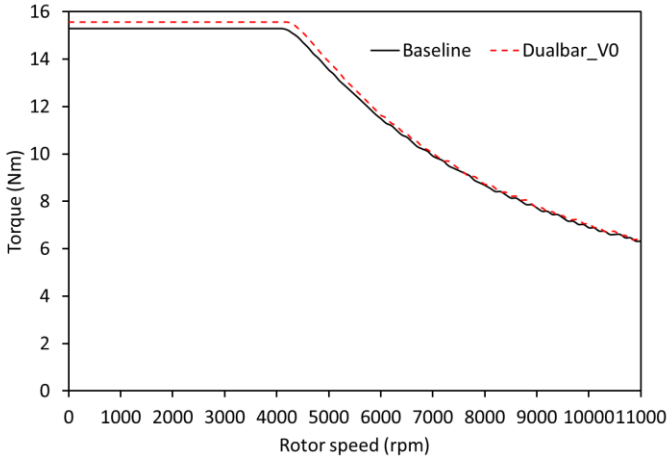

Fig. 7.2.11 Initial torque-speed curve of the dual layer bar type topology compared to the baseline machine.

Table 7.2.11 Comparison of maximum average torque and base speed of initial dual layer bar design and the baseline

	Baseline machine	Dual layer bar (initial)	Error (Vs Baseline)
Max. average torque (Nm)	15.3	15.6	2%
Base Speed (rpm)	4200	4200	0%

The comparison in Fig. 7.2.11 shows the maximum average torque of the dual bar topology to be slightly higher by around 2%. The small difference means that once again only minor adjustments to the initial geometry is required to bring alignment with the baseline T-N curve. The procedure in Fig 7.2.1 is once again

followed and Table 7.2.12 shows the list of geometric constraints. The objectives and methods are the same as the delta and single layer 'V' topologies.

Table 7.2.12 Constraints and objective functions for dual layer bar topology optimisation

Item	Parameter	Min	Max	Unit
Constraints	MS_D_{lwr}	14	16	mm
	MS_D_{upr}	5	8	mm
	MS_T_{lwr}	2.0	3.2	mm
	MS_T_{upr}	2.0	3.2	mm
	MS_L_{lwr}	8	11	mm
	MS_L_{upr}	6	9	mm
	D_L_{lwr}	8	12	mm
	D_L_{upr}	6	10	mm
	θ_{upr_u}	120	145	°
	θ_{upr_l}	120	145	°
	θ_{lwr_u}	120	140	°
	θ_{lwr_l}	120	140	°
	Current angle	45	55	°
Target/Objective	Average torque	Range	>= 15.2	Nm
			<= 15.4	Nm
	Ripple rate	Range	MINIMISE	-
Method	Multi-objective GA	-	-	-

The optimisation process finds a convergence that finds the best balance of the objective functions. The resultant T-N curve and geometry are shown in Fig. 7.2.12.

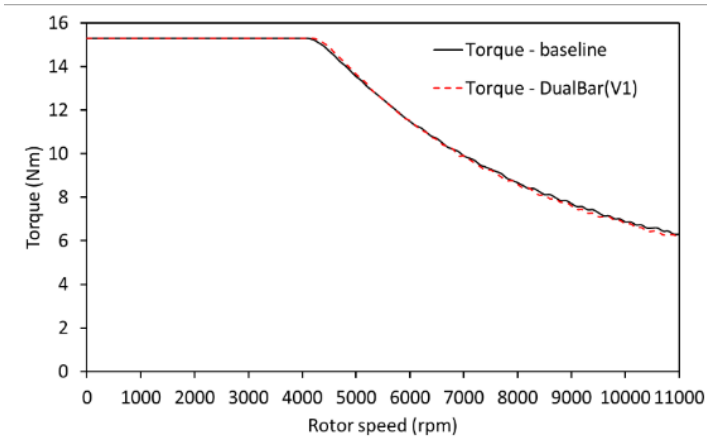

(a) Comparison of the T-N curve of the optimised dual-layer bar topology and the baseline

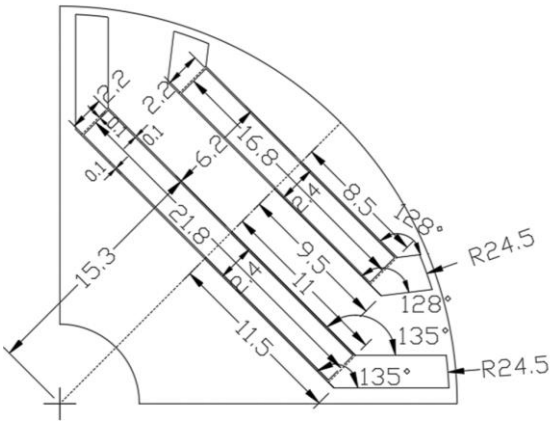

(b) Resultant geometry from the optimisation process

Fig. 7.2.12 Optimised dual bar topology and resultant T-N curve.

The maximum average torque is found to be 15.28Nm, bringing the dual bar neatly into line with the baseline with a mere 0.02Nm difference between the topologies. The changes to the geometry shown in Fig. 7.2.12(a) are summarised in Table 7.2.13.

Table 7.2.13 Optimised parameter for matching single 'V' T-N curve to baseline

Parameter	Initial	V1	Difference Vs initial	Units
MS_D_{lwr}	14.5	15.3	+0.8	mm
MS_D_{upr}	7	6.2	-0.8	mm
MS_T_{lwr}	3.2	2.4	-0.8	mm
MS_T_{upr}	3.2	2.4	-0.8	mm
MS_L_{lwr}	10	11	+1.0	mm
MS_L_{upr}	8	8.5	+0.5	mm
D_L_{lwr}	10	11.5	+1.5	mm
D_L_{upr}	8	9.5	+1.5	mm
θ_{upr_u}	135	128	-7	°
θ_{upr_l}	135	128	-7	°

From the optimisation the key changes are the magnets have reduced in thickness by 25% whilst the magnet lengths of both the upper and lower layers have been increased by 1.5mm. The lower layer depth was adjusted to move slightly closer to the upper layer and the flux barrier angle adjust slightly to maintain the magnet pole arc. The overall effect is to drop the net torque into good align with the baseline machine.

7.3 Comparison of the IPM topologies performance

The previous section showed the initial design process for the 3 topologies chosen that was undertaken to match the T-N curves with the baseline topology. With the designs in place a more detailed comparison of the key performance aspects of the machine can be drawn which follows the same machine performance aspects as those compared between the baseline machine and the measured data in chapter 3. As a reminder these are:

- Static air gap flux distribution.
- No load back EMF and flux linkages.
- Torque composition and machine inductance.
- Efficiency and loss maps.
- Torque pulsations.
    - Cogging torque.
    - Torque ripple at maximum current.
- Tooth forces and vibratory performance.

Similar to the development of the baseline machine FE model the FE analysis tool offers insight into the machines such as the core magnet flux densities and distributions that is difficult to achieve with a physical machine allowing any differences between the 4 topologies to be explored in greater depth.

7.3.1 Comparison of T-N curves

Given that the T-N curves were already generated in the previous section a quick comparison between all four can be drawn and is shown in Fig. 7.3.1.

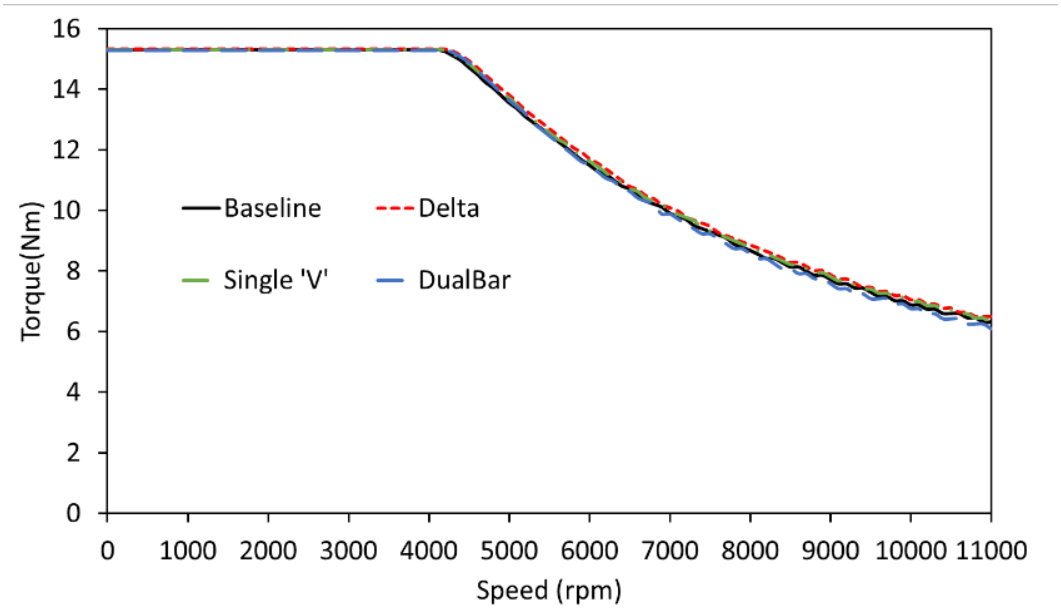

Fig. 7.3.1 Comparison of N-T curves for all 4 topologies.

Table 7.3.1 provides the maximum calculated torque and base speed for each of the 4 machines shown in Fig. 7.3.1.

Table 7.3.1 Comparison of maximum average torque and base speed for the 4 topologies

	Baseline	Delta	Single layer 'V'	Dual Bar
Max average torque	15.3	15.33	15.32	15.28
Base speed	4200	4200	4200	4300

Based on the design criteria for the topologies it comes as little surprise that the 4 machines are very closely matched; the Delta shows a maximum torque 0.03Nm higher than the base line and the Dual layer bar type is 0.02Nm. In terms of the base speed the dual layer bar type has a slightly higher base speed than the other 3 topologies reflecting that perhaps the net flux linkage of the dual layer bar is lower than that of the other machines. Given the low error between the different machines it is fair to judge the different rotor topologies as having the same performance envelope and therefore the initial objective of this activity has been satisfied.

7.3.2 Static air gap flux distribution

The PM flux in the rotor and stator cores of each rotor type can be visualised using the FE tool set to magnetostatic analysis and is the comparison is shown in Fig. 7.3.2.

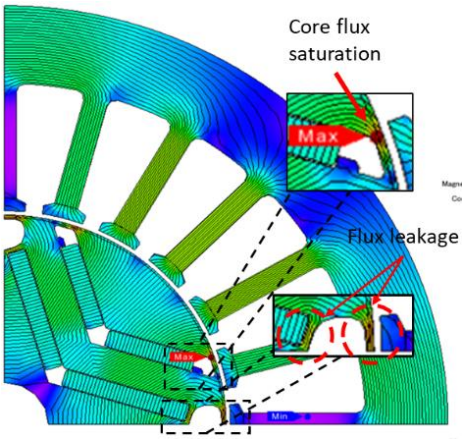

(a) Baseline. Max flux density = 2.07T

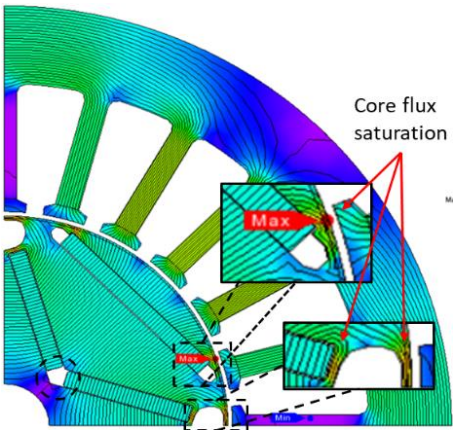

(b) Delta topology. Max flux density = 2.17 T

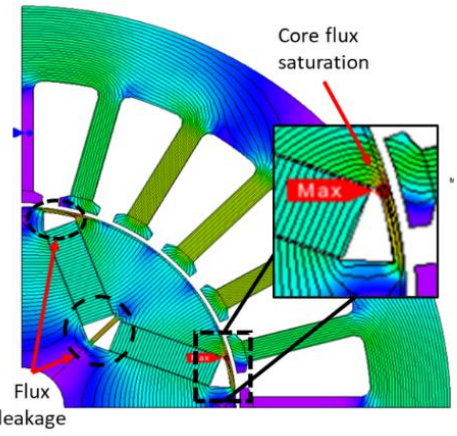

(c) Single layer 'V'. Max flux density = 2.21T

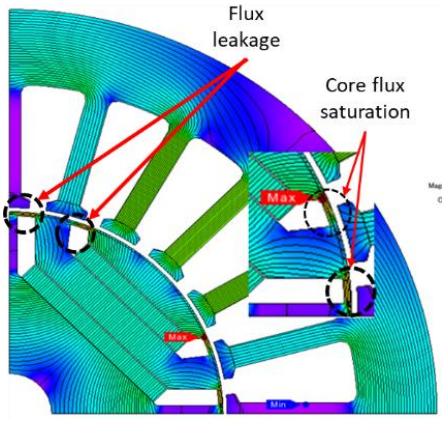

(d) Dual layer Bar. Max flux density = 2.06T

Fig. 7.3.2 Comparison of static flux distributions of the 4 topologies under study.

Each of the topologies in Fig. 7.3.2 shows good symmetry across the pole arc indicating the fundamental FEA model settings such a material and symmetry are all correct and in order. The flux distribution in the stator back iron is very similar, the only aspect of note is the dual layer bar has a lower flux density in the back iron, owing to the reduced PM content versus the other topologies. The other main observations are:

- Maximum flux density in each machine lies where the magnets are closest to the outer diameter of the rotor core and therefore the iron material is thinner and prone to saturation.
- This is most acute for the single layer 'V' machine which has a larger magnet and sees a peak flux density of 2.21 T at the magnet tip where the iron material is very thin.
- The single layer 'V' also has more leakage on the inner edges of the magnets compared to the delta and baseline designs, primarily due to the thin iron strip between the two magnets in each pole giving the flux a short circuit path. It can also be noted that the flux loading here is high indicating the material is saturating and mitigating the leakage.
- The similarities between the Delta and baseline topologies mean the flux distribution is very similar; the key difference is the higher flux density (2.17T vs 2.07T) observed at the tooth tips of the Delta upper bar magnet, again where the iron material is thinnest.
- The dual-layer bar type shows areas of flux saturation at the tips of the flux barriers on each layer and the peak flux density (2.06T) is comparable to the baseline machine.

Drawing a curve through the centre of the airgap allows the FE tool to calculate the mid-air gap flux density and capture the flux distribution with the air gap. Fig. 7.3.3 shows the resultant distribution across one pole pair for each machine and a comparison of the harmonic content of flux density.

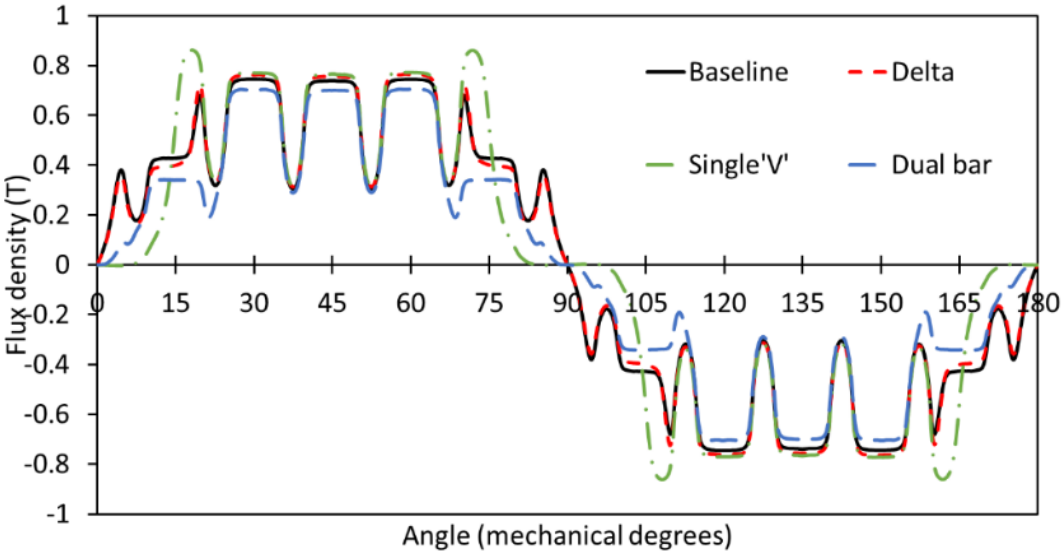

(a) Comparison of air gap flux density across one pole pair for each machine

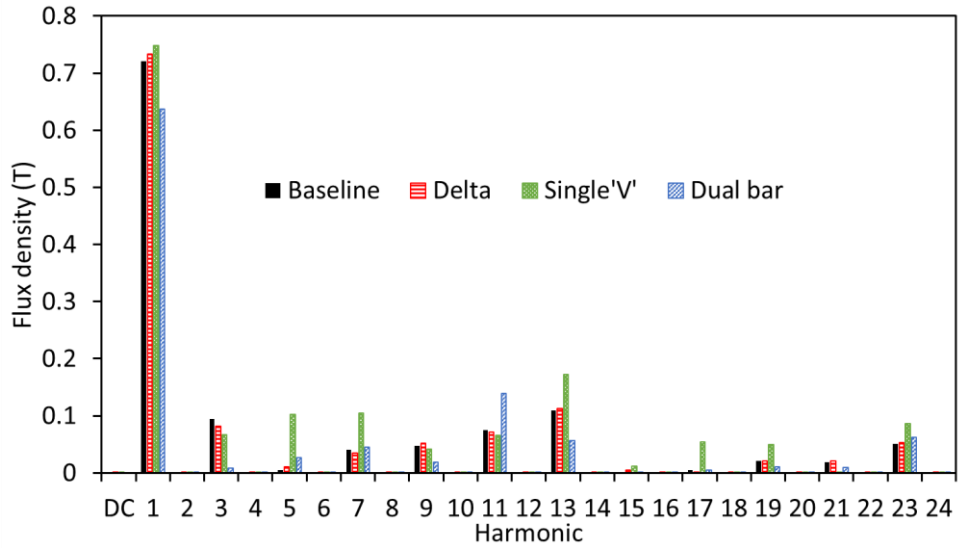

(b) Comparison of mid-air gap flux harmonics for each topology

Fig. 7.3.3 Comparison of static air gap flux density for one pole pair.

The amplitudes for the key harmonics in Fig. 7.3.3(b) are summarised in Table 7.3.2.

Table 7.3.2 Static air gap flux density amplitudes for key harmonics

Harmonic	Baseline	Delta	Single 'V'	Dual layer bar
Fundamental (T)	0.721	0.733	0.749	0.637
3rd (T)	0.095	0.082	0.067	0.008
5th (T)	0.005	0.011	0.102	0.027
7th (T)	0.040	0.035	0.105	0.045
9th (T)	0.047	0.052	0.042	0.019
11th (T)	0.075	0.071	0.066	0.139
13th (T)	0.110	0.112	0.172	0.056
23rd (T)	0.051	0.053	0.086	0.062

All four airgap flux density waveforms in Fig. 7.3.3(a) follow the same harmonic-rich non-sinusoidal profile of the baseline; the delta waveform is very similar to the baseline with some small differences in amplitude. This is also observed in the harmonic content where both topologies show spikes in the 3rd, 7th, 9th, 11th and 13th harmonics with minor differences in amplitudes between them. Again, this is in line with expectation given how the delta was formed by locking the flux barriers of the upper layer of the baseline machine and rotating the magnet ducts to form the delta geometry.

However, the single layer 'V' and dual layer bar types have significant differences from the baseline.

- Single layer 'V':
  - The large inter-pole gap means there is very low flux density for the first 7.5° where the 2nd stator tooth can be observed to align with the front end of the lower magnet and the flux density begins to rapidly rise.
  - A very large spike, forming a "horn", is formed, the peak of which aligns with the region of maximum flux density at the rotor edge, indicating flux is bridging the air gap at this point to link with the stator rather than remain with the heavily saturated region of the rotor core.

- This horn shape is symmetrical across the pole arc occurring at the tips of each magnet in the 'V' shape.
- Rich harmonic content with high amplitudes on the 3rd, 5th, 7th, 9th, 11th and in particular the 13th harmonic.

- Dual layer bar:
  - Smoother waveform that the other waveforms, reflected in the harmonic content with only the 11th harmonic showing any significant difference to the other machines.
  - For all other harmonics, the amplitudes are significantly lower than the other machines, including the fundamental.

Ignoring the two "horns" on the single layer 'V' for a second, the nature of the magnet arrangement means the flux density distribution is more trapezoidal in form compared to the waveforms of the other topologies as it does not have the benefit of a 2nd layer of magnets that the other topologies have that shape the flux density into a more sinusoidal form. This trapezoidal nature contributes significantly to the high harmonic content of the single layer 'V' shown in Fig. 7.3.3(b). The two "horns" indicate a potential design concern as it shows an irregular flux distribution along the rotor core circumference leading to possible concern with vibration. How much difference this makes to the performance versus the baseline under load conditions will be observed in the tooth force and vibratory performance comparison later.

The dual layer bar type shows a smoother waveform than the other machines, though it could not be described as sinusoidal owing to the variations in reluctance from the stator teeth and slots.

7.3.3 Magnet volumes

Given all 4 machine topologies utilise the same permanent magnet material (N36Z) the composition of which contains expensive rare earth materials such as dysprosium and neodymium, it is worth understanding the difference in PM volume of each topology compared to the baseline. This is of particular relevance given the target application of the machines is an automotive drivetrain which, as discussed before, is a highly competitive and cost sensitive market. The magnet volumes in four machines are calculated using the CAD data of each design. Fig. 7.3.4 and Table 7.3.3 show the calculated volumes.

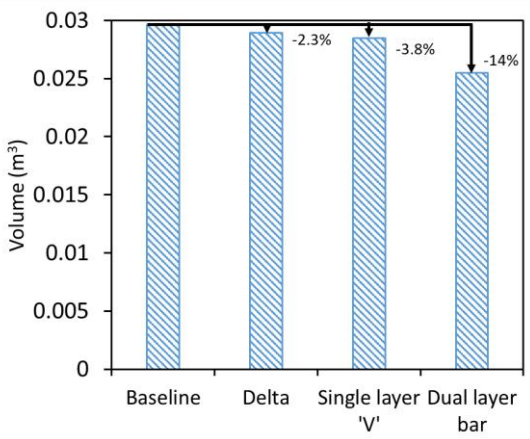

Fig. 7.3.4 Comparison of magnet volumes between the 4 topologies.

Table 7.3.3 Comparison of total magnet volumes between the 4 machines

Topology	Total magnet volume (m^3)	%diff to baseline	Total mass (kg)
Baseline	$2.96x10^{-2}$	-	0.228
Delta	$2.90x10^{-2}$	-2.3%	0.223
Single layer 'V'	$2.85x10^{-2}$	-3.8%	0.219
Dual layer bar	$2.55x10^{-2}$	-14%	0.196

Note: mass calculation based on N36Z magnet material density of 7700 kg/m^3 [SE16].

Each of the 3 topologies have lower magnet volume than the baseline with the dual layer bar showing the greatest reduction with a significant 14% reduction in overall magnet volume. Given these differences it can be seen that if pure cost was the deciding factor then the dual layer bar is the winning solution, this reduction in PM content must come with a price however so further investigation is required to see how the topology stacks up against the others in terms of performance.

7.3.4 No load flux linkage and EMF comparison

Following on from the static tests the no load analysis is the next item to compare. Similar to the comparison between the measured machine and the baseline in chapter 3 the FE is set to rotate the rotor at 1200rpm, ensuring all calculation step and mesh settings are the same between the different topologies and the calculations run. The results of the no-load flux linkage are shown in Fig. 7.3.4.

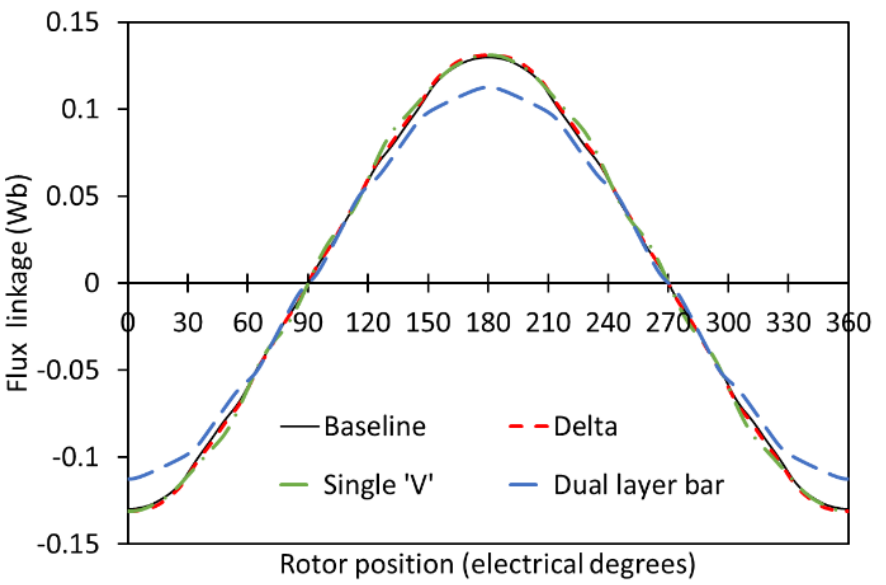

(a) Waveforms

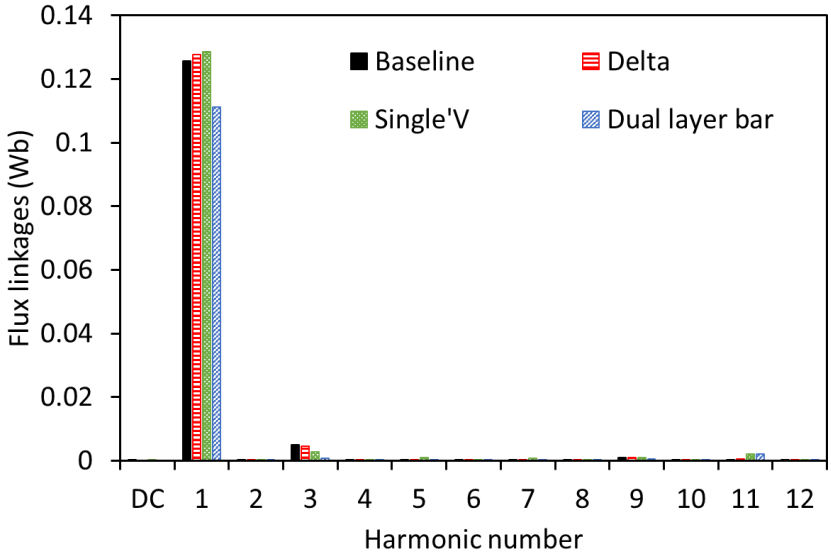

(b) Harmonics

Fig. 7.3.5 Comparison of no-load flux linkages at 1200 rpm.

From Fig.7.3.59(a) it can be seen that the outlier of the 4 topologies is the dual layer bar with a significantly lower amplitude than the other 3 machines; the other machines match very closely. The harmonics in Fig. 7.3.5(b) reflect this with the fundamental of the baseline being significantly lower and the 3rd harmonic evident on the other 3 machines is so small as to be negligible. Using the same methodology detailed in chapter 3 of this thesis the PM flux linkage can be calculated and is compared in Table 7.3.3.

Table 7.3.3 Comparison of ψ_m between the 4 topologies

Topology	ψ_m (mWb)	% difference from baseline
Baseline	153.8	-
Delta	156.4	+1.7%
Single layer 'V'	157.4	+2.3%
Dual layer bar	136.2	-11.4%

The induced EMF at 1200rpm is calculated by the FE tool by differentiating the flux linkage waveform. The resultant waveforms and FFT are shown in Fig. 7.3.6.

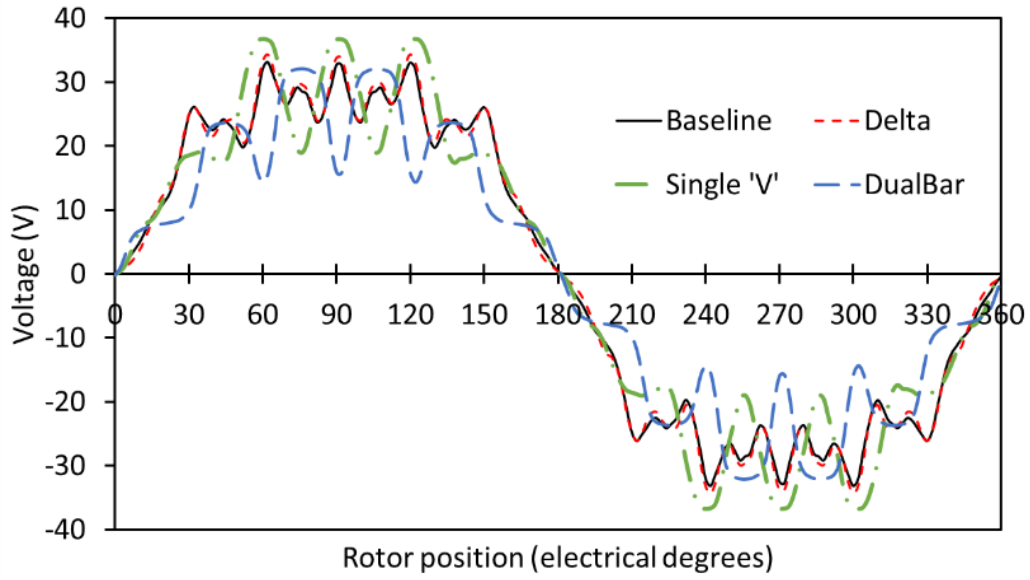

(a) Waveforms

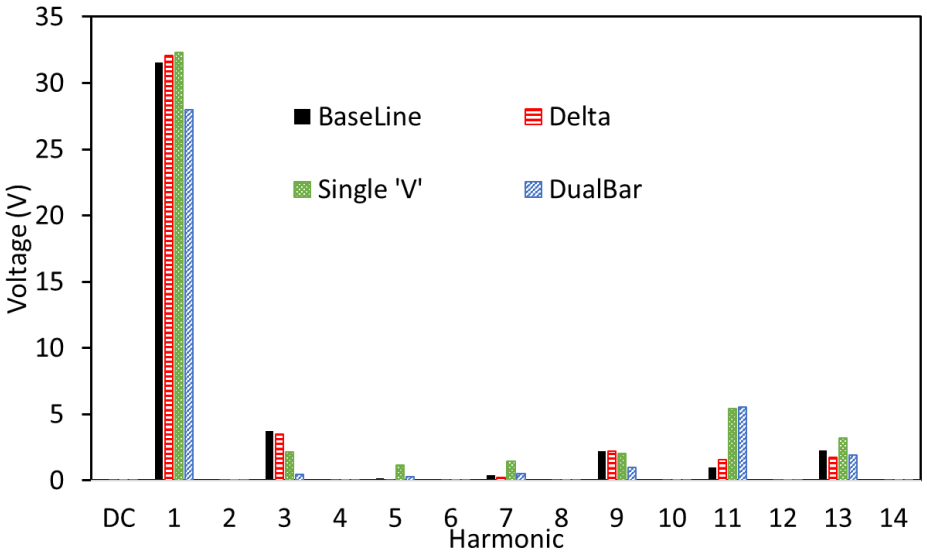

(b) harmonics

Fig. 7.3.6 Comparison of no-load EMF for all four machines at 1200 rpm.

The key attributes of the EMF are summarised in Table 7.3.4.

Table 7.3.4 Comparison of fundamental voltage and key harmonics

	Baseline	Delta	Single 'V'	Dual layer bar
Max (V)	33.18	34.30	36.8	32.1
Min (V)	-33.19	-34.3	-36.8	-32.1
PP (V)	66.37	68.61	73.61	64.19
Fund (V)	31.56	32.10	32.3	27.96
3rd (V)	3.75	3.48	2.13	0.48
9th (V)	2.20	2.21	2.03	0.98
11th (V)	0.99	1.58	5.45	5.57
13th (V)	2.29	1.77	3.24	0.01

The difference between the baseline and delta machines is very small, the delta has a slightly higher fundamental reflected by the slightly higher flux linkage and there are some small differences between the 11th and 13th harmonics. Between the baseline and the single layer 'V' and the dual layer bar type there are

significant differences, primarily in the large ripple observed in each waveform, reflected by the significantly higher 11th harmonic. The concern is that these high frequency harmonics mean that the machines are more prone frequency dependant losses such as eddy currents in the iron leading to higher losses than if the waveforms were more sinusoidal in nature.

7.3.5 Machine inductance and torque composition

Following on from the no-load performance the on-load characteristics of the machine needs to be compared. The torque-speed characteristic of each machine is shown in Fig. 7.3.1. There are a number of items of interest underlying the performance of the machine, namely the saliency of each topology, dictated by the L_q/L_d ratio as detailed in chapter 1 and the torque composition of each topology. Each of these aspects are calculated in the same manner to that detailed in chapter 3, that is the machine is operated at maximum current for one electrical cycle and the current angle is swept from 0° (i.e. I_d = 0A) to 90° (i.e. I_q = 0A). The results from this simulation are also used in the comparison of the ripple torque characteristics later in this section.

L_d and L_q are derived from the fluxes calculated by the FE tool in the same manner as described in chapter 3. To compare the inductance across the entire current range of the machine is very time consuming so the L_d and L_q inductances are compared with the machine at maximum current and the current angle swept; as the I_d and I_q currents change to move the current vector the d and q axis inductances will change as a function of the current and how the geometry of the high reluctance features such as magnets or flux barriers aids or inhibits the flux passing through the rotor at any given current angle. At maximum torque, the saliency of each machine can be calculated to show what the differences are in each machine. The results can be seen in Fig. 7.3.7 and the salience calculation in Table 7.3.5.

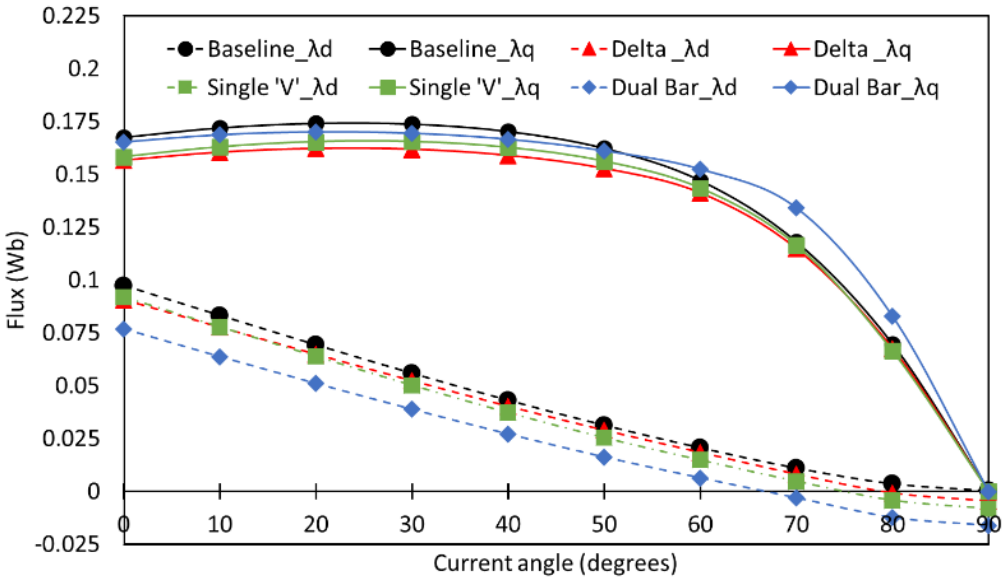

(a) Comparison of calculated d and q axis fluxes of each machine at maximum current (26.7A_{rms}) and increasing current angle

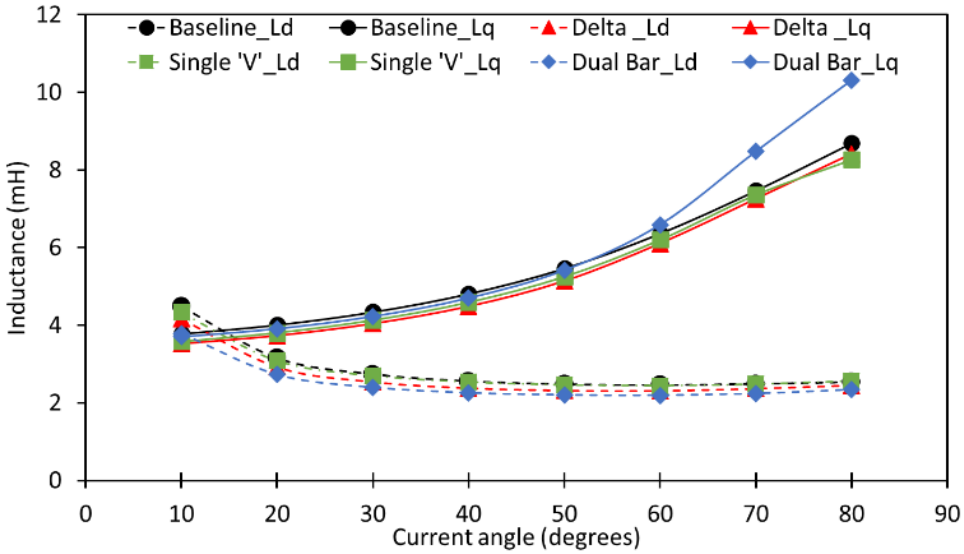

(b) Comparison of d and q axis inductances of each machine at maximum current (26.7A_{rms}) and increasing current angle from 0° to 90°

Fig. 7.3.7 Comparison of d and q axis fluxes and inductances at maximum current with increasing current angle.

Table 7.3.5 Comparison of Ld, Lq and resultant saliency of each machine at maximum current and β = 50°

	Baseline	Delta	Single 'V'	Dual layer bar
L_d @ β = 50°	2.41 mH	2.32 mH	2.46 mH	2.20 mH
L_q @ β = 50°	5.46 mH	5.14 mH	5.25 mH	5.42 mH
Saliency (L_q/L_d)	2.26	2.21	2.13	2.46

From Table 7.3.5 it can be seen that given the similarities in geometry of the delta and baseline machines the saliency is very similar. The dual layer bar type topology has the highest saliency, which given that profile of 'u' shaped magnet slots of the upper and lower layers bears a strong resemblance to a synchronous reluctance machine rotor is of little surprise. It also indicates how the dual-bar machine is able to achieve the same torque as the baseline by having a higher reluctance component which clearly compensates for the lower mutual torque due to the ψ_m component being significantly lower. The single layer 'V' has the lowest saliency, again a reflection of the geometry of the rotor core.

Using the d and q axis flux data calculated by the FE tool the torque components of each machine can be derived and compared. Again, this follows the same process detailed in chapter 3. The resultant torque curves can be seen in Fig. 7.3.8.

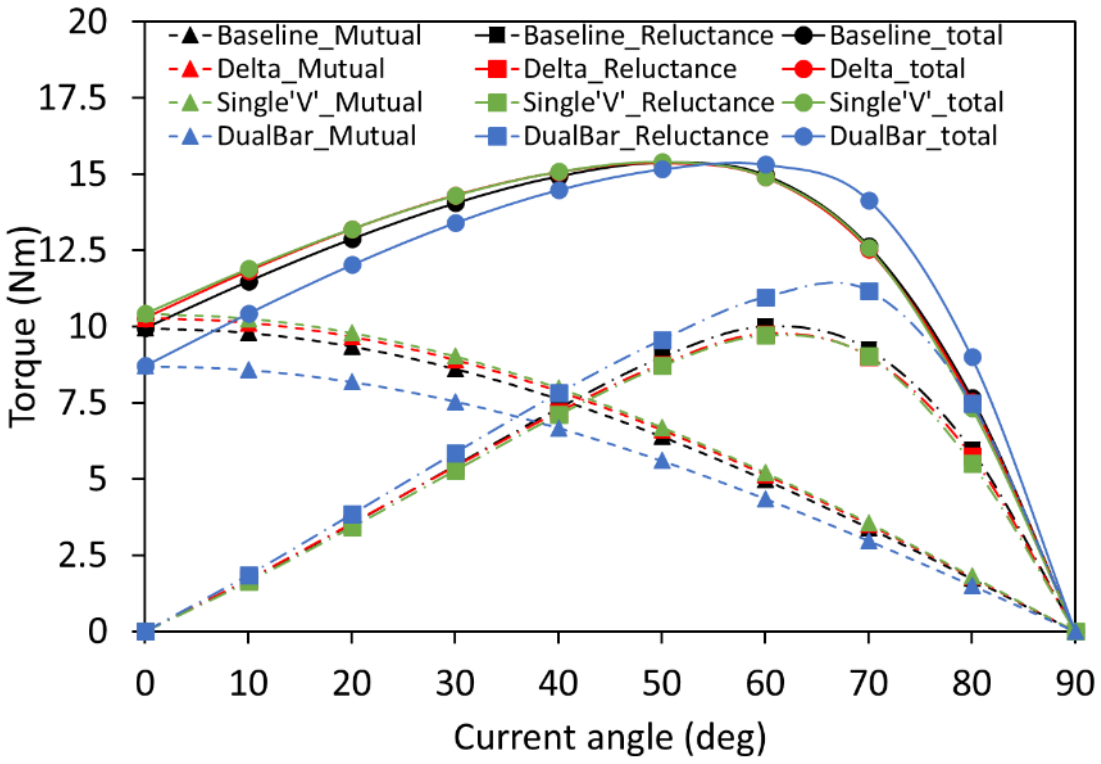

Fig. 7.3.8 Comparison of the torque components of each machine at maximum current (26.7Arms) and incrementing current angles.

In line with much of the results thus far the Delta, single layer 'V', and baseline topologies all cluster close together. The slightly lower PM flux linkage of the baseline machine, as seen in Table 7.3.3, means the torque when β = 0° (i.e. I_d = 0A) is slightly lower than that of the Delta and single 'V'. Once the current angle passes 30° the contribution from the reluctance torque, dictated by the saliency of the machine, begins to pull the baseline into alignment with the torque of the Delta and single 'V' until at maximum net torque the machines are full aligned. The dual bar delta follows a much different pattern. As highlighted previously the saliency of the machine means that the reluctance torque component is much stronger than the other 3 machines, significantly boosting the net torque beyond β = 30° allowing it to compensate for the lower mutual torque component and bringing the dual layer bar topology torque into alignment with the baseline at around 50°. The contribution of the mutual and reluctance torque components of the machine can be analysed. Fig. 7.3.9 shows the contribution of each component for each machine when the machine is at maximum current and β = 50°.

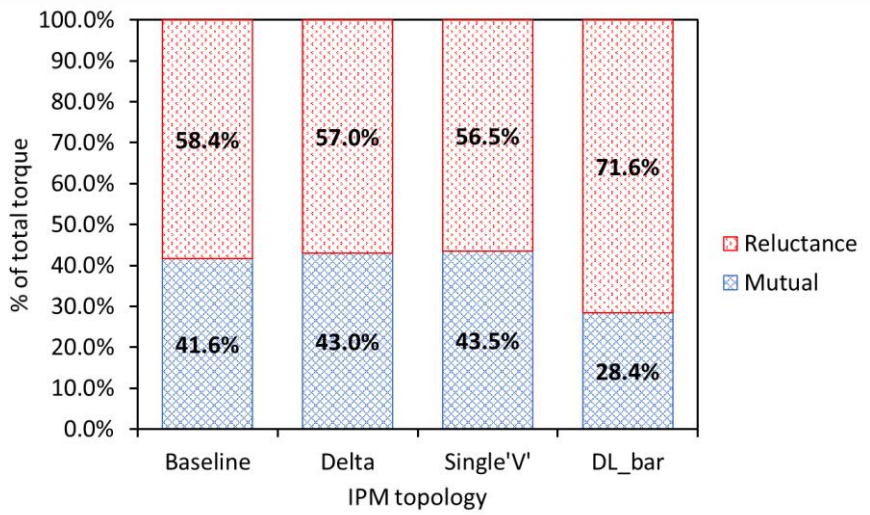

Fig. 7.3.9 Comparison of torque composition for each machine at maximum current and β = 50°.

From Fig. 7.3.9 the trends borne out from the saliency calculation and the torque composition in Fig. 7.3.8 can be more clearly seen. All 4 machines make effective use of the reluctance component however the dual layer bar clearly relies more heavily on the reluctance component to achieve the required torque whilst the single layer 'V' and delta topology utilise more mutual torque, slightly more than the dual layer 'V' of the baseline machine.

7.3.6 Comparison of efficiency and loss

The efficiency and loss maps of each machine is the next aspect to compare. The same loss mapping tool and methodology is followed as was shown in chapter 3, ensuring that aspects such as the winding resistance and maximum DC link voltage are the same for each machine. It should also be noted that magnet loss is not included in this study. This is due to a number of reasons. Firstly, in an IPM machine the magnets are largely shielded from key loss mechanisms such as the slotting effect [JRH10], [DH12], experiencing only the armature reaction magnetic field. Even with the armature reaction field the time varying component is much lower in the rotor core than that of the stator teeth and yoke [DH12], this is observed in the detailed tooth force study in chapter 3. This means the loss contribution due to the magnets would be expected to be lower which again is illustrated by the alignment of the calculated and measured efficiency map of the baseline machine in chapter 3. The other key reason lies in the complexity of calculating losses in PM materials, in particular the eddy current losses. The magnets used are sintered and as such difficult to segment in the same manner the steel rotor and stator cores; in the baseline machine the magnets are split into two segments along the axial length meaning that there is an inherent 3D effect to the core losses. This 3D nature makes it difficult to capture the core losses using 2D analytical and FEA methods which means a 3D electromagnetic FEA model would be required. Given this added complexity and the low contribution of the losses to the overall machine performance the PM losses were not included here. The implications of this are that the accuracy of the simulations at high load or extended periods of running the machine would drop;

losses in the magnets would mean the temperature in the rotor core would rise, changing the Br of magnet accordingly which of course has an impact on the magnetic circuit and therefore performance of the machine. Thus, whilst negating the loss is OK in this case, if the models were simulating drive cycles or similar then they would need to be included to maintain fidelity.

Fig. 7.3.10 shows the resultant efficiency maps.

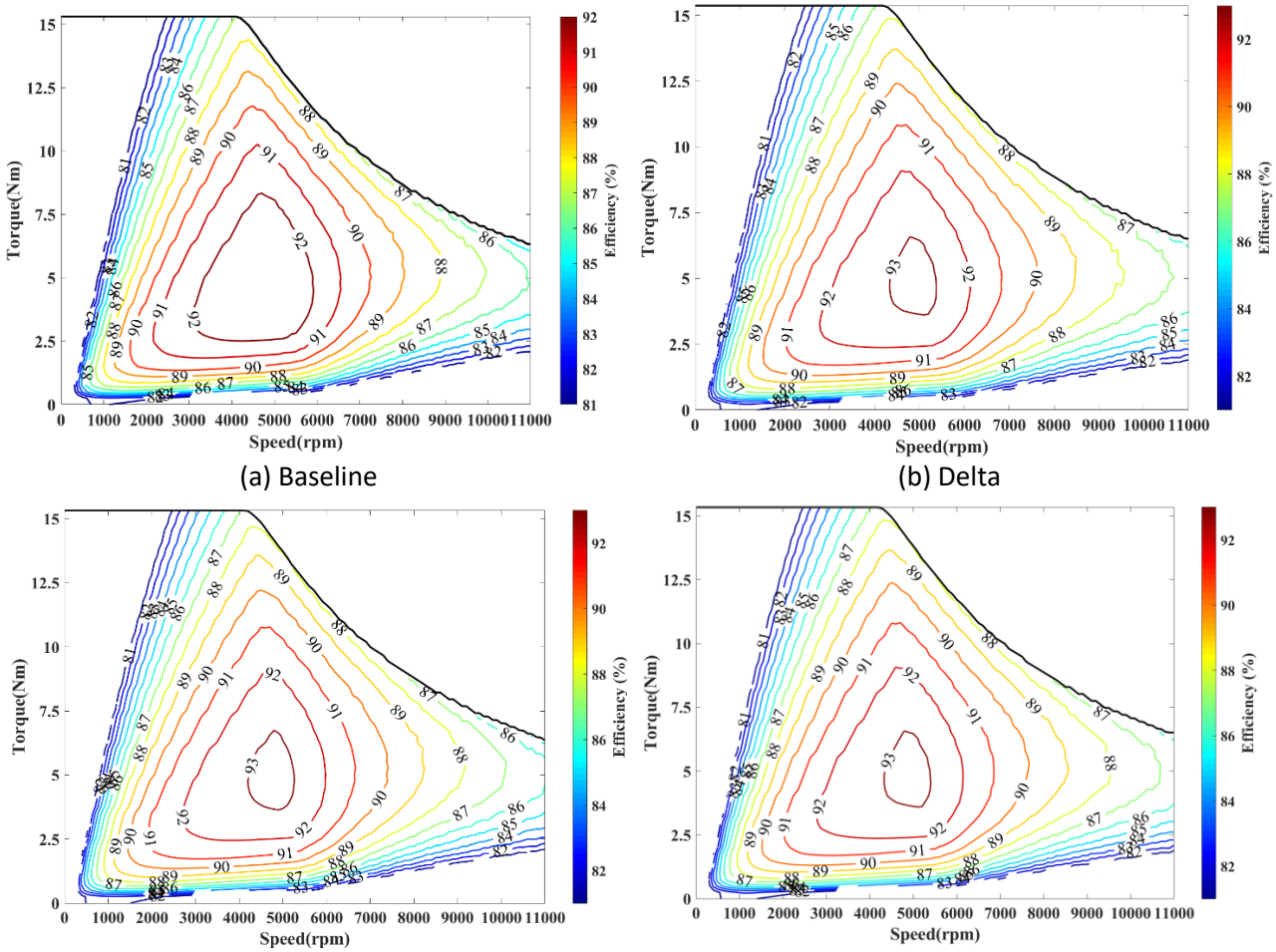

(a) Baseline (b) Delta

(c) Single layer 'V' (d) Dual layer bar

Fig. 7.3.10 Efficiency maps of the 4 machine topologies.

The four maps show very similar characteristics. This is not surprising given the development of the baseline model in chapter 3 showed the loss leader of this machine to be the copper loss and all four machines use the same stator. The 3 new topologies show a 93% efficiency region between ~4500rpm and 500rpm and ~3.5Nm to 7Nm which is not shown on the baseline machine. This is due to the methodology of creating the contour plots used in Fig. 7.3.10 which rounds down to the nearest 1Nm. Table 7.3.6 shows the maximum efficiency values and the associated speed and torque they appear.

Table 7.3.6 maximum efficiency of each machine with the associated speed and torque point

Topology	Max efficiency	Speed @ max efficiency	Torque @ max efficiency
Baseline	92.96%	5000rpm	4.8Nm
Delta	93.25%	5000rpm	5Nm
Single 'V'	93.26%	4900rpm	5Nm
Dual layer Bar	93.25%	5000rpm	5Nm

From the results in Table 7.3.6 it can be seen that there is very little difference between the maximum efficiency points of four machines, 0.3% is the maximum swing between the baseline efficiency (lowest) and the Single 'V' which shows the marginally highest efficiency. Overall, it can be said that there are only minor differences between the machines in terms of maximum efficiency.

7.3.6.1 Copper loss

The copper loss calculated by the efficiency mapping tool can be compared and the results shown in Fig. 7.3.11.

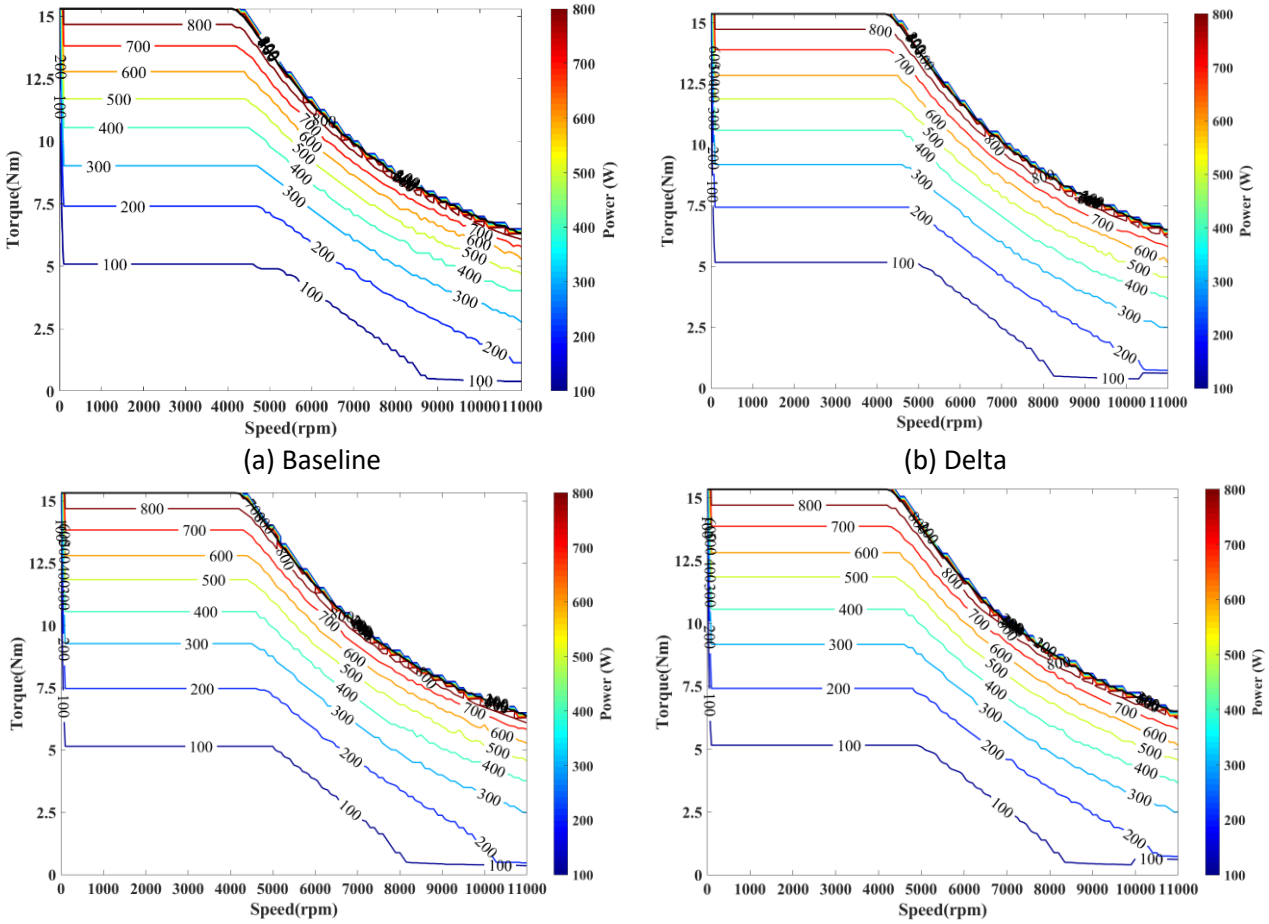

(a) Baseline (b) Delta

(c) Single layer 'V' (d) dual layer bar

Fig. 7.3.11 Comparison of copper losses for the 4 machine topologies. All values are in Watts

Table 7.3.7 shows the maximum copper loss for each machine.

Table 7.3.7 Maximum copper loss in each topology

	Baseline	Delta	Single layer 'V'	Dual bar
Max. copper loss(W)	887.6	887.6	887.6	887.6

The maps match very closely making it difficult to see what differences there are. As described in chapter 3 the loss tool calculates copper loss using I^2R so given the stator and stator windings are then it follows that the loss must be the same, as highlighted in Table 7.3.7. In the actual machine there will be some difference due to the harmonic content of the flux distribution of each machine generating different AC losses within

the windings, particularly at higher machine frequencies. However, this is a complex topic that is out of the scope of this study.

To try to draw better comparison the copper loss in each machine at 2 difference speeds at incrementing torques can be compared to highlight any differences. The speeds chosen are 3000rpm as it lies comfortably within the constant torque region and 7500rpm deep within the flux weakening region of the machine. At each speed, the torque is incremented in 3Nm intervals. The comparison can be seen in Fig. 7.3.12 and the calculated values in Table 7.3.8.

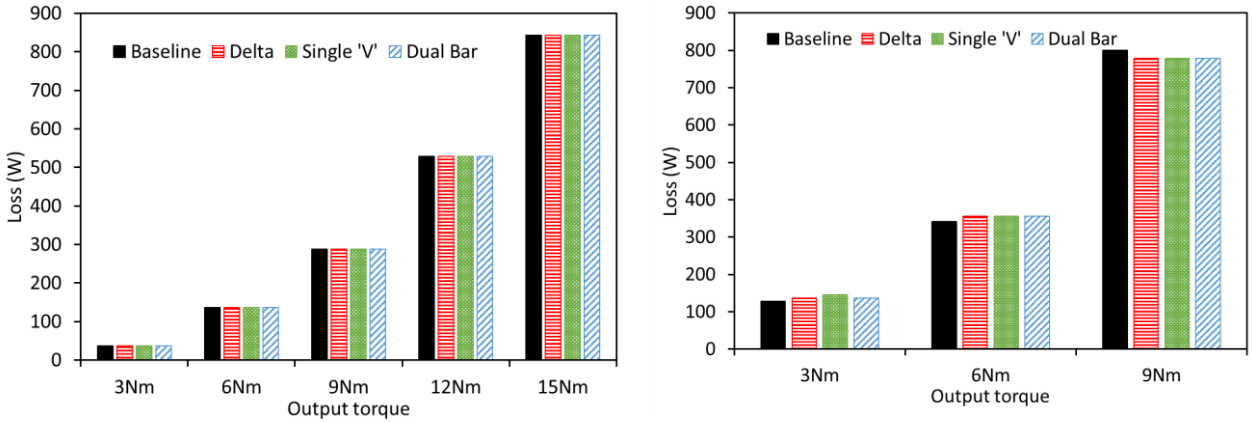

(a) 3000rpm (b) 7500rpm

Fig. 7.3.12 Comparison of copper losses for all machines at different torques, 3000rpm and 7500rpm.

The high flux weakening current at 7500rpm means the maximum torque in 7.3.12(b) is 9Nm for this comparison.

Table 7.3.8 Copper loss values for all machines at 3000rpm and 7500rpm with incremental torque. All values are in Watts (W)

	3000 rpm				7500 rpm			
Torque	Baseline	Delta	Single 'V'	Dual Bar	Baseline	Delta	Single 'V'	Dual Bar
3Nm	36.4	36.4	36.4	36.4	128.0	136.7	145.6	136.7
6Nm	136.7	136.7	136.7	136.7	341.5	355.5	355.5	355.5
9Nm	288.0	288.0	288.0	288.0	800.0	778.8	778.8	778.8
12Nm	529.2	529.2	529.2	529.2	-	-	-	-
15Nm	843.2	843.2	843.2	843.2	-	-	-	-

Within the constant torque region, the copper loss is identical for all machines which is confirmed both by Fig. 7.3.12 (a) and Table 7.3.8. At the higher speeds, some small variations in loss can be found reflecting slight differences in the net current due to differences in the required flux weakening current. These slight differences are amplified in terms of loss due to the squared current component of the loss equation.

7.3.6.2 Iron loss

The next key loss aspect is the iron loss, and the calculated loss maps are shown in Fig. 7.3.13.

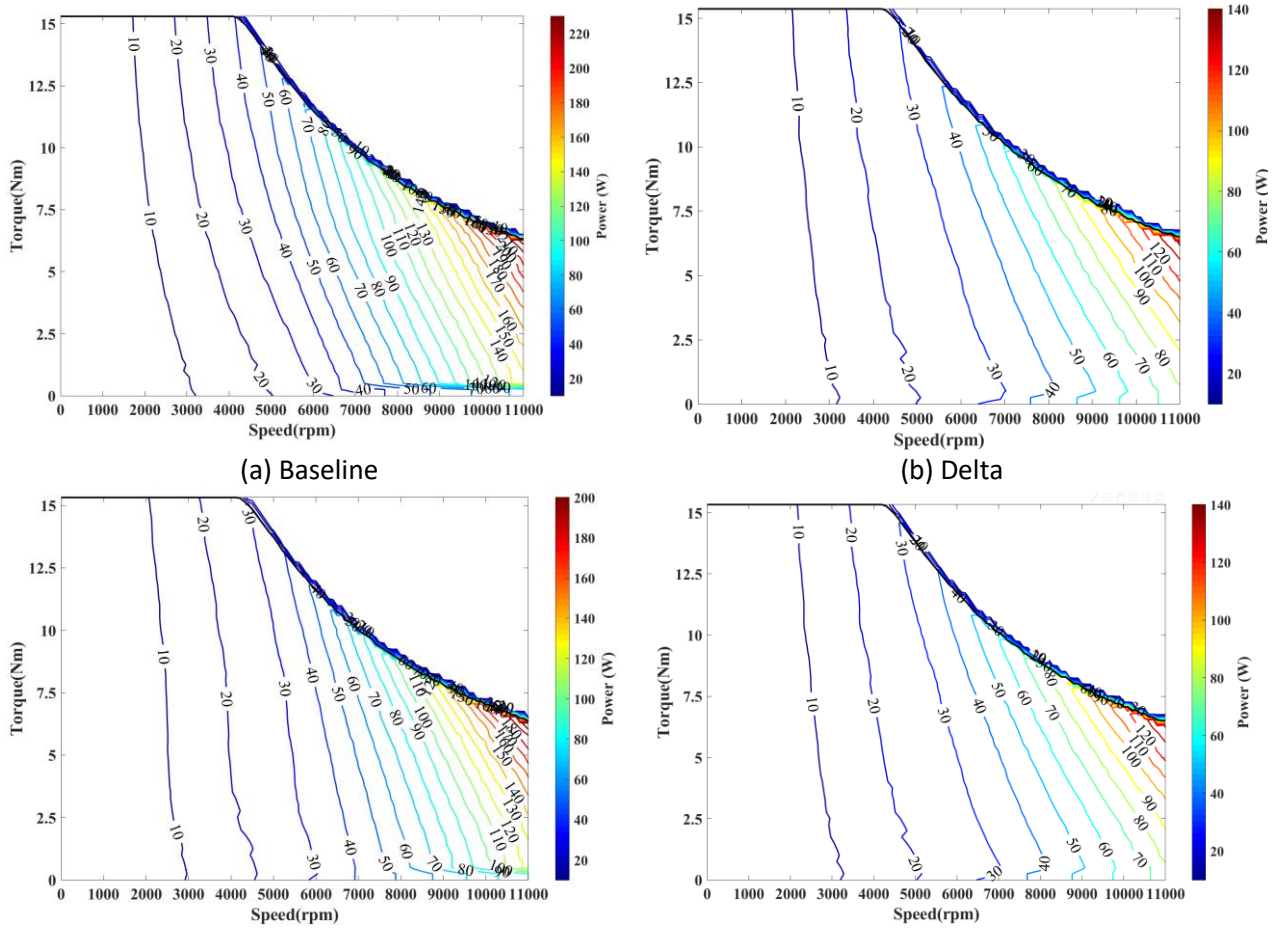

(a) Baseline (b) Delta

(c) Single layer 'V' (d) Dual layer bar

Fig. 7.3.13 Comparison of iron loss between the 4 topologies. All values are in Watts.

In contrast to the copper loss there are some notable differences between the machines in terms of iron loss, with the baseline and single layer 'V' exhibiting higher losses than the dual layer bar and Delta type. Table 7.3.9 shows the maximum iron loss values for each machine.

Table 7.3.9 Maximum Iron loss in each topology

	Baseline	Delta	Single layer 'V'	Dual layer bar
Max. Iron loss(W)	236.5	142.6	208.4	140.8

Both the delta and dual bar topologies show the lowest loss, with only 2W separating the Dual bar from the Delta. The baseline clearly has the highest iron loss, with a maximum around 28W higher than the next highest, the single layer. It is worth commenting at this point that both the single layer 'V' and dual bar type topologies exhibit significantly higher harmonic content than the delta and baseline topologies so there is an argument that further optimisation to mitigate these harmonics will lead to further reductions in loss. Similar to the copper loss the iron loss contour plots in Fig. 7.3.13 illustrate the loss distribution across the torque speed map but are difficult to compare, especially has the iron loss peaks at higher frequencies meaning the maximum losses are clustered in the top right of the high-speed region of the machine. The losses are compared again at 3000rpm and 7500rpm for the iron loss and shown in Fig. 7.3.14 with the loss values shown in Fig. 7.3.10.

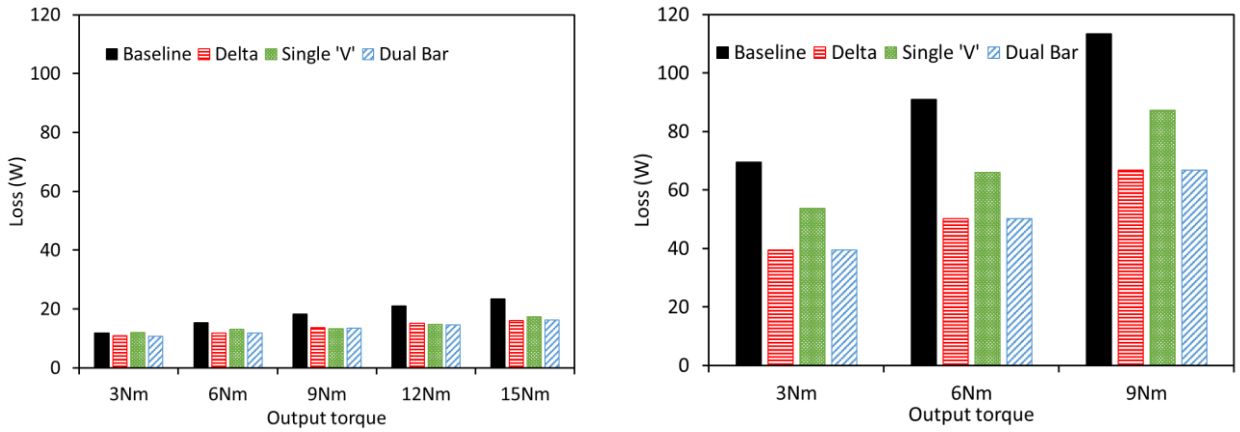

(a) 3000rpm (b) 7500rpm

Fig. 7.3.14 Comparison of copper loss for all machines at different torques, 3000rpm and 7500rpm.

Table 7.3.10 Iron loss values for all machines at 3000rpm and 7500rpm with incremental torque. All values are in Watts (W)

	3000 rpm				7500 rpm			
Torque	Baseline	Delta	Single 'V'	Dual Bar	Baseline	Delta	Single 'V'	Dual Bar
3 Nm	11.8	10.9	12.0	10.7	69.5	39.6	53.8	39.5
6 Nm	15.3	11.8	13.1	11.9	91.0	50.2	66.0	50.2
9 Nm	18.3	13.7	13.4	13.5	113.4	66.8	87.4	66.8
12 Nm	21.1	15.1	14.7	14.5	-	-	-	-
15 Nm	23.4	16.1	17.3	16.2	-	-	-	-

The trend shown in Table 7.3.9 with the maximum loss values is played out across the speed and torque ranges compared in Fig. 7.3.14. At 3000rpm the iron losses are very low compared to the copper losses and at the very low torque point the 4 machines have very small differences in loss, less than a Watt in some instances. At 7500rpm however the differences are much clearer with baseline showing the highest loss, followed by the single 'V' and the delta and dual bar showing near-parity in terms of the loss.

7.3.6.3 Total loss

The total loss is the combination of the iron loss, copper loss, and the mechanical loss. Given that all four topologies are using the same casing, bearings, and shaft etc. and the overall mass of the machines are very similar the same loss coefficients are utilised, so the mechanical loss is calculated to be the same for all machines at each speed. The total loss distribution maps for each topology can be seen in Fig. 7.3.15.

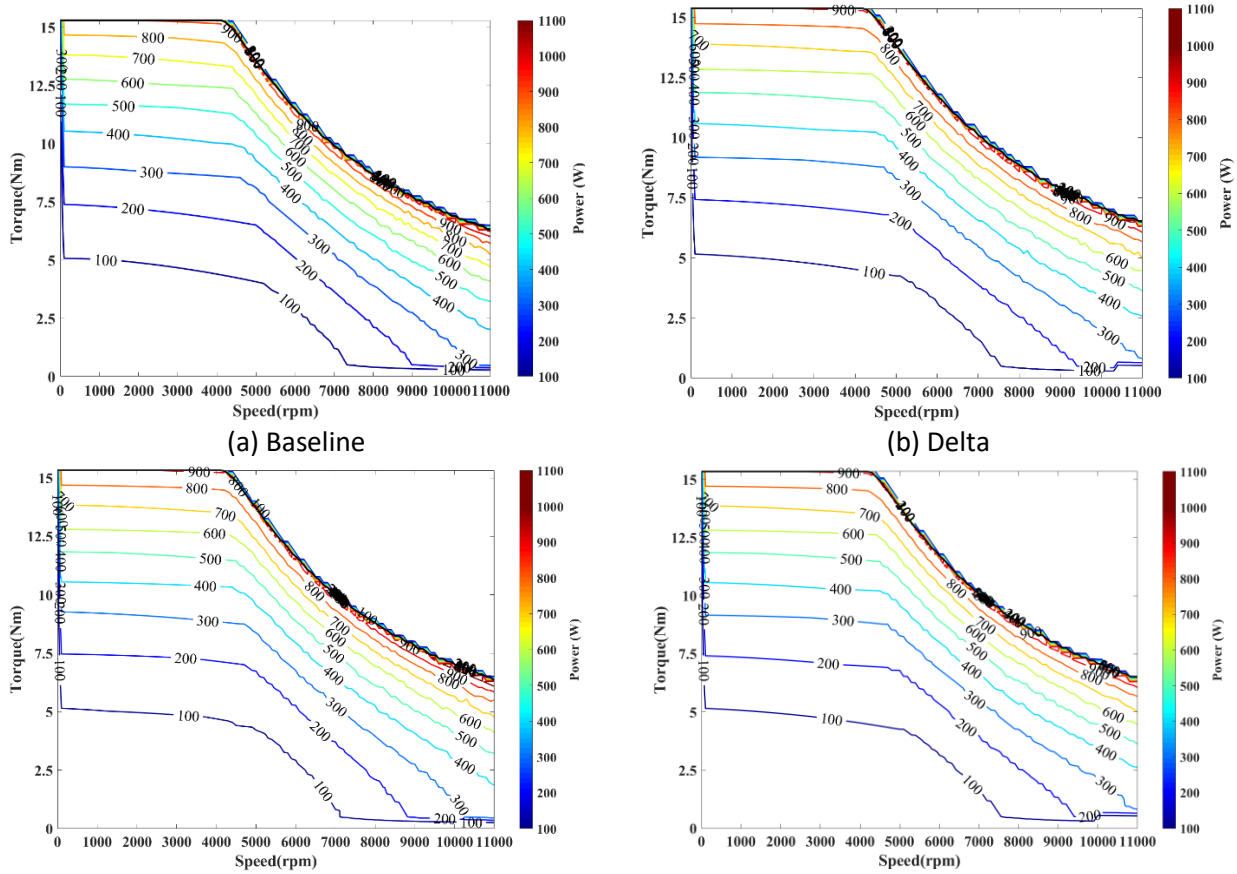

(a) Baseline (b) Delta

(c) Single layer 'V' (d) Dual layer bar

Fig. 7.3.15 Comparison of total loss between the 4 topologies. All values are in Watts.

Similar to the copper and iron loss comparisons the maps in Fig. 7.3.15 give a good overview of the loss distribution of each topology however direct comparison is again a little harder to make. In line with the previous loss comparisons the total losses are compared at incrementing torques at 3000rpm and 7500rpm, Fig. 7.3.16 and Table 7.3.11 show the results.

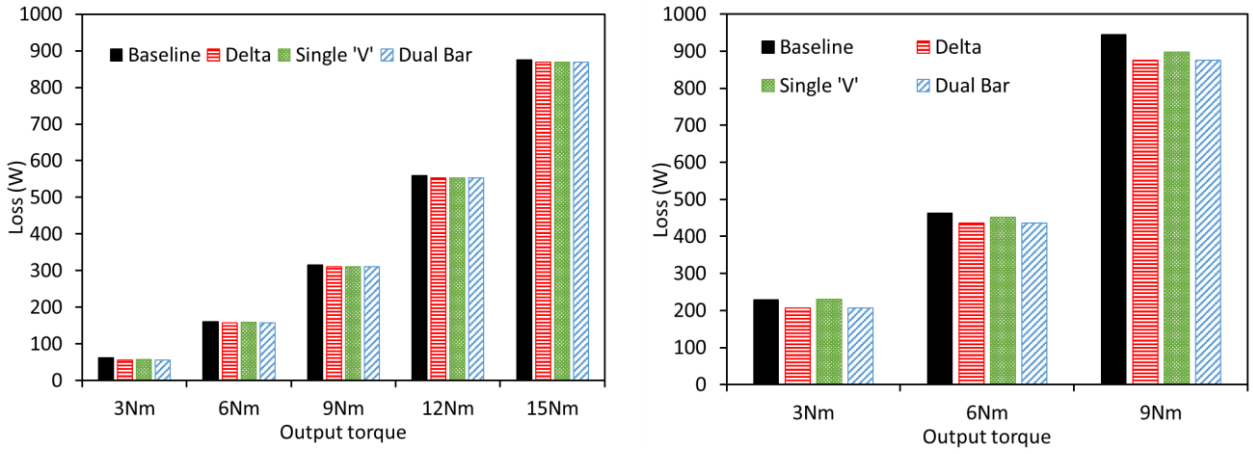

(a) 3000 rpm (b) 7500 rpm

Fig. 7.3.16 Comparison of calculated total machine losses for four topologies at different torque, 3000rpm and 7500rpm.

Table 7.3.11 Total loss values for all machines at 3000rpm and 7500rpm with incremental torque. All values are in Watts (W)

	3000 rpm				7500 rpm			
Torque	Baseline	Delta	Single 'V'	Dual Bar	Baseline	Delta	Single 'V'	Dual Bar
3 Nm	61.7	56.1	57.3	56.0	228.3	207.0	230.2	207.0
6 Nm	160.8	157.3	158.6	157.4	463.2	436.5	452.3	436.5
9 Nm	315.1	310.5	310.2	310.4	944.1	876.4	896.9	876.4
12 Nm	559.1	553.1	552.7	552.6	-	-	-	-
15 Nm	875.4	868.1	869.3	868.3	-	-	-	-

Using the calculated loss data, the percentage contribution of each loss component can be compared at different speeds and torques. The 4 topologies are compared at 3000rpm and 7500rpm and 3Nm and 9Nm at each speed to allow the influence each topology has on the loss breakdown. This is shown in Fig. 7.3.16.

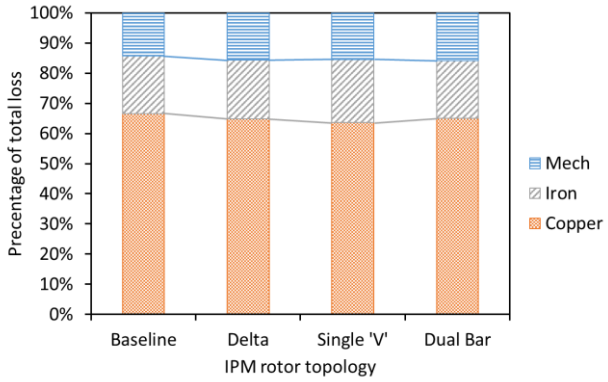

(a) 3Nm and 3000rpm

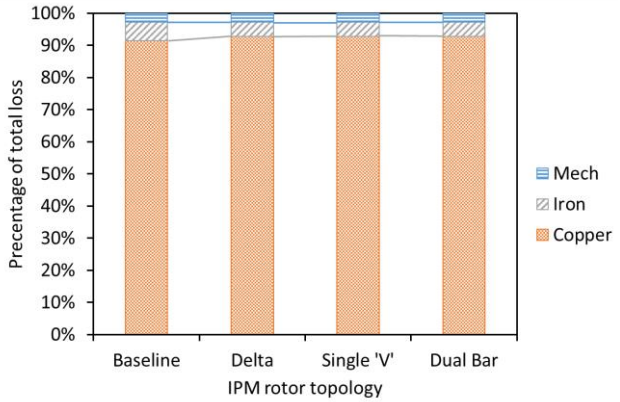

(b) 9Nm and 3000rpm

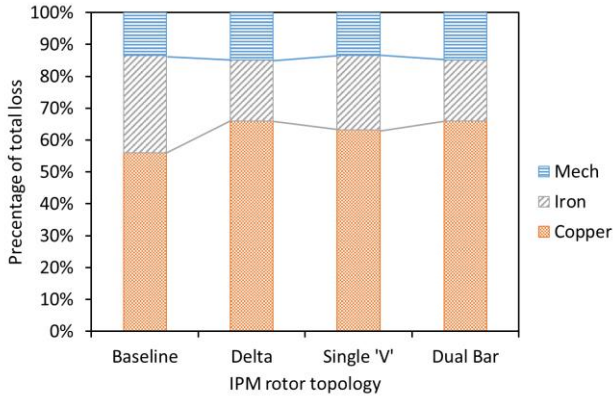

(c) 3Nm and 7500rpm

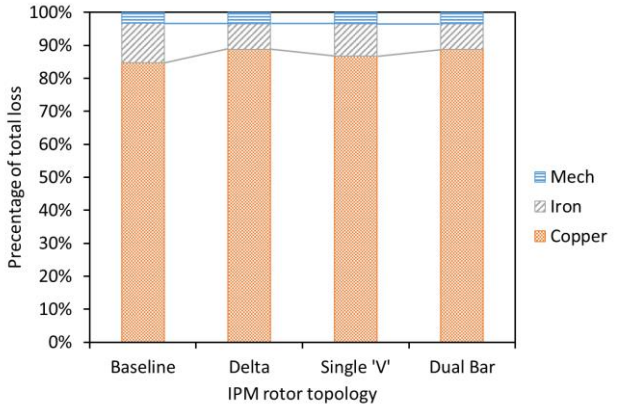

(d) 9Nm and 7500rpm

Fig. 7.3.16 Percentage distributions of key losses of four machines at 3Nm and 9Nm, 3000rpm and 7500rpm.

The copper loss can be seen to be dominant at 3000rpm at both 3Nm and 9Nm (Fig. 7.3.16 (a) and (b) respectively) with very minor differences due to the iron loss. At 7500rpm the higher iron losses of the baseline and single 'V' topologies become more apparent at the 3Nm point although the copper loss still contributes more than 50% of the total loss. Therefore, for all 4 topologies the variations in iron loss only contribute slight changes in the overall dominance of the copper loss which explains why both the efficiency and loss maps are so closely aligned for all 4 topologies.

7.3.7 Comparison of torque pulsations

With the higher-level performance aspects of the machines such as the efficiency maps and EMF compared the next stage of the comparison focuses on the torque pulsations generated by each of the four topologies, looking initially at the cogging torque and then the on-load torque ripple.

7.3.7.1 Cogging torque

The procedure for simulating the cogging torque in FE as detailed in chapter 3 is repeated for each of the machine topologies. As previously discussed, the cogging torque calculation is particularly sensitive to mesh requiring a high mesh density and very low rotation speeds. What is also important is that the mesh is as close as possible between the four machines to ensure that any differences between the machines can be judged as due to the magnet arrangement with high confidence. Fig. 7.3.17 shows the meshed machines.

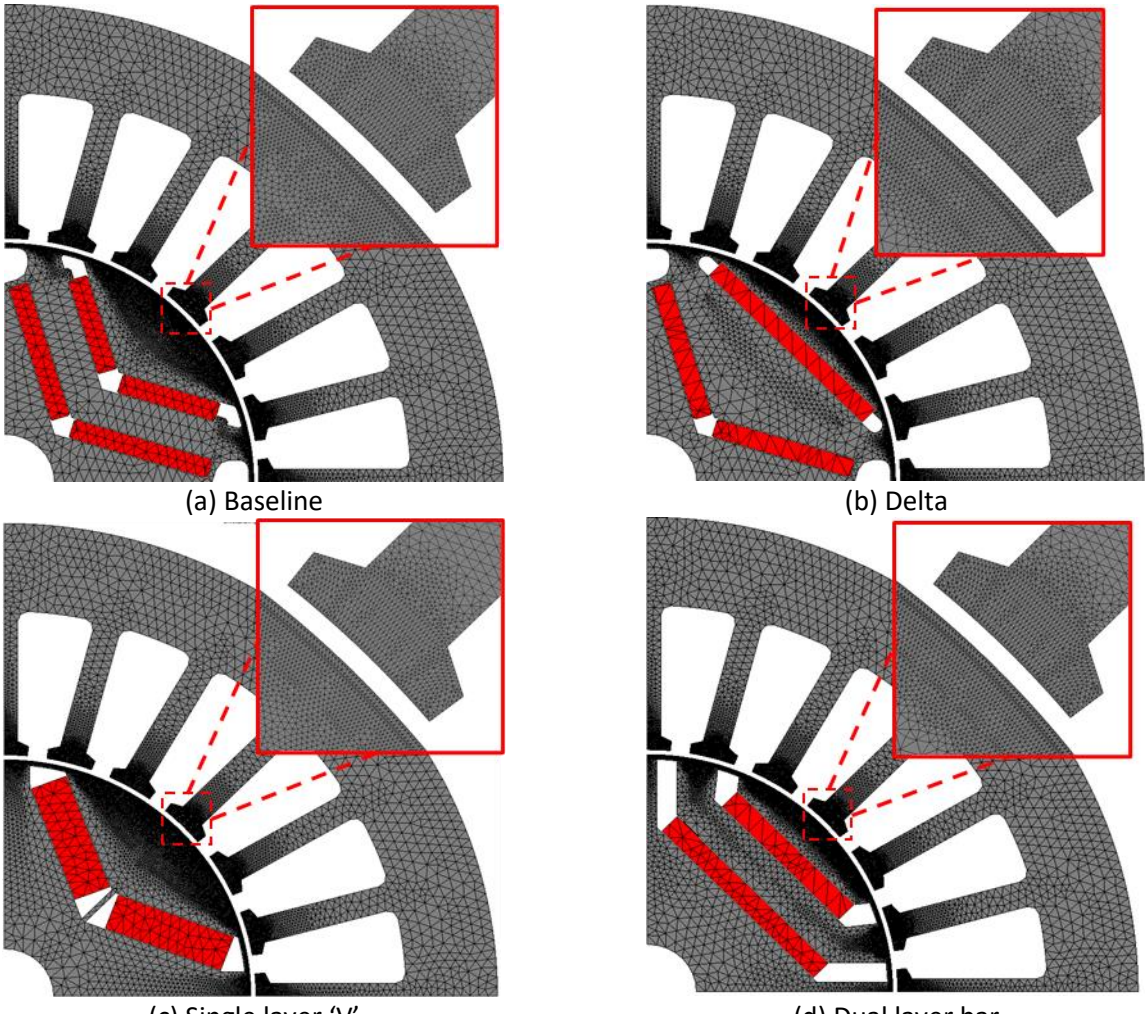

(a) Baseline (b) Delta

(c) Single layer 'V' (d) Dual layer bar

Fig. 7.3.17 Comparison of the meshed machines for cogging torque calculation

With the models in place the FE models are run. Given the number of runs and the freedom FE gives in terms of resolution each machine is only run for 1 cogging cycle (15° mechanical) allowing the profile of the cogging cycle to be observed. This is shown in Fig. 7.3.18.

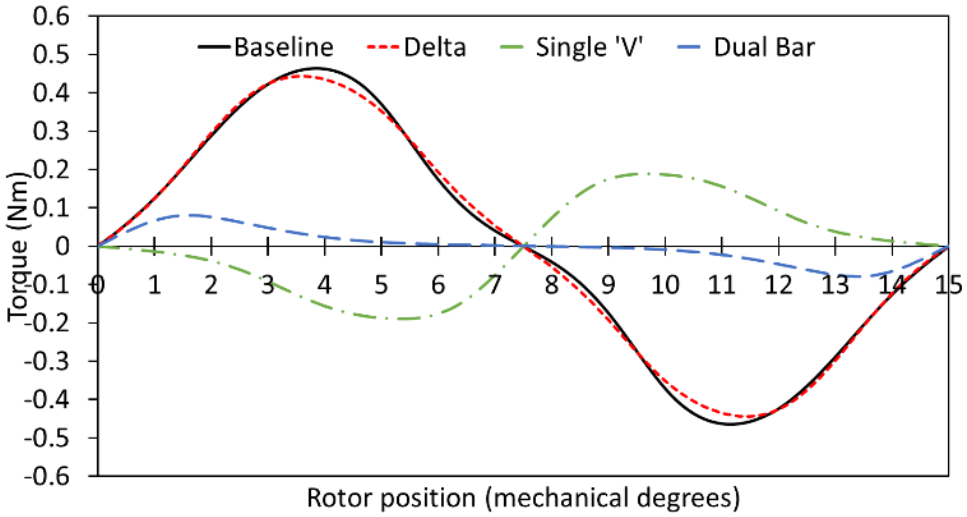

(a) Waveform over 1 cogging cycle

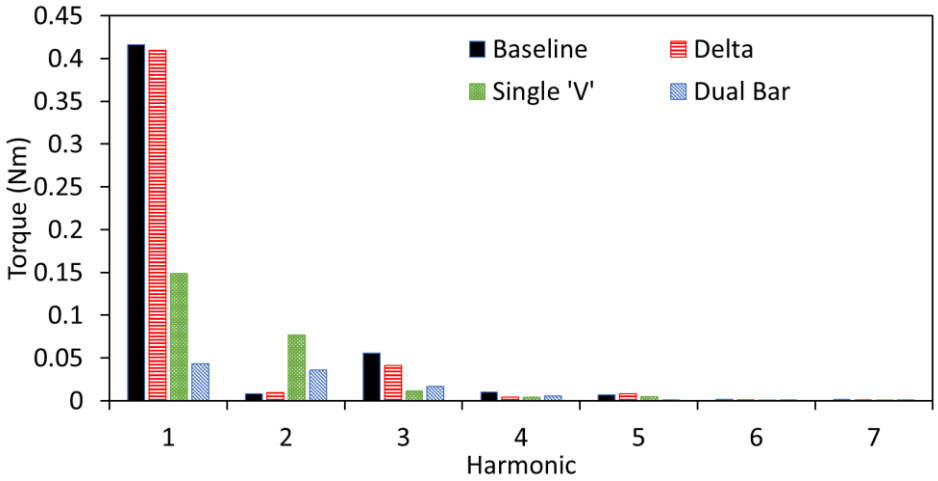

(b) Harmonics

Fig. 7.3.18 Comparison of calculated cogging torques for the four IPM machine topologies.

The key data from Fig. 7.3.18 can be seen in Table 7.3.12.

Table 7.3.12 Key values of cogging torque for four machines

		Baseline	Delta	Single 'V'	Dual Bar
Max/Min	Max (Nm)	0.464	0.443	0.189	0.080
	Min (Nm)	-0.464	-0.444	-0.189	-0.080
	PP (Nm)	0.928	0.887	0.378	0.160
Harmonics	Fund (Nm)	0.416	0.410	0.149	0.043
	2nd (Nm)	0.008	0.010	0.077	0.036
	3rd (Nm)	0.056	0.041	0.012	0.017

The results in Fig. 7.3.18 show that once again the delta lines up closely with the baseline line although the baseline exhibits a higher peak to peak than the delta. Slight differences in the low harmonics, in particular the 3rd harmonic, mean the waveforms are slightly different shapes.

With the dual bar topology there is a significant difference compared to the baseline with the peak to peak of the dual bar topology being 1/6th of that of the baseline. This may be attributed to the lower PM flux of

the dual bar design. Both the dual bar and the single layer topologies have different magnet pole arc to pole-pitch ratios to the baseline and delta machine for which the magnet pole arcs are identical. The significance of the pole arc to pole pitch ratio is explained well in [ZQZ00] and [ZQZ03] which highlights the significance in achieving the optimum ratio, α_p [ZQZ00], to greatly mitigate the peak cogging torque in the machine. Given both the single 'V' and dual bar topologies were optimised to reduce ripple the magnet pole arcs were adjusted, shifting the overall ratio away from the baseline and closer to a torque minimum as highlighted in [ZQZ00] and [ZQZ03]. Fig. 7.3.19 shows the pole pitch and magnet pole arc values from the CAD drawings of the machine and Table 7.3.13 shows the resultant ratios for each machine.

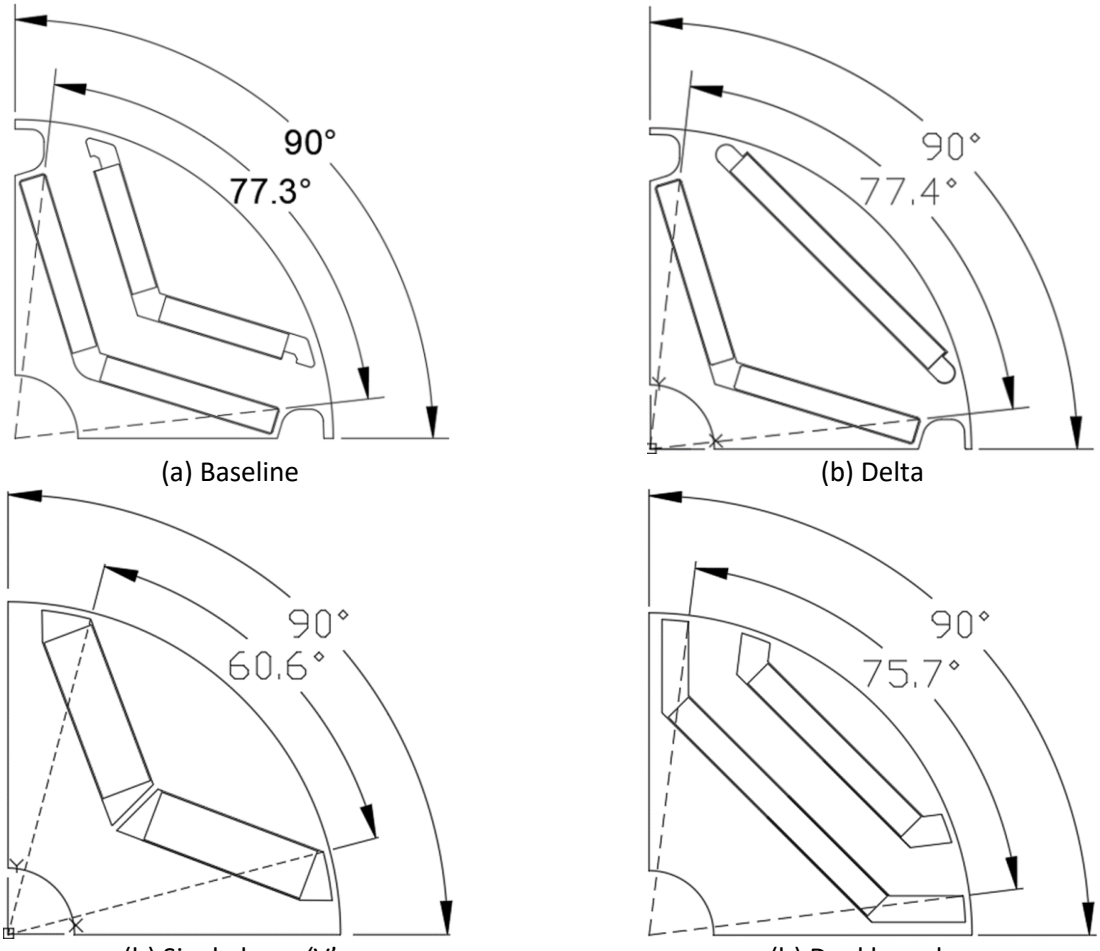

(a) Baseline (b) Delta

(b) Single layer 'V' (b) Dual layer bar

Fig. 7.3.19 Magnet pole arc and pole pitches in four machines.

Table 7.3.13 Magnet pole arc to pole pitch ratios for four machines

	Baseline	Delta	Single layer 'V'	Dual layer Bar
Pole pitch	90°	90°	90°	90°
Magnet pole arc	77.3°	77.4°	60.6°	75.7
magnet pole arc to pole pitch ratio	0.86	0.86	0.67	0.84

An interesting characteristic to the adjustment of the magnet pole arc to pole pitch ratio is highlighted in [ZQZ00] where at certain magnet pole to pole pitch ratios the waveform performs a phase reversal, which

can be clearly seen in the cogging waveform of the single layer 'V' topology indicating this is the case for this topology. Both the single layer 'V' and dual bar also exhibit reasonably high 2nd harmonic which provides much of the distortion of the waveforms away from the more sinusoidal form observed on the baseline and delta topologies.

7.3.7.2 Torque ripple

For the torque ripple the results from the analysis of the torque composition is used to obtain the torque waveforms at each current angle at maximum torque. Unlike the analysis in chapter 3, showing all the results for all 4 machines at each current angle means plotting 40 waveforms which is very difficult to read. What can easily be compared is the ripple rate, again defined in chapter 3, which is the ratio of the difference between the maximum and minimum torques and the average torque. The ripple rate for each machine at each current angle up to 80° can be seen in Fig. 7.3.20 and the values summarised in Table 7.3.14. When the current angle is at 90° the average current tends to be very small, << 1Nm generating very large or even negative ripple rate values making the comparison difficult so is omitted from Fig. 7.3.20 and Table 7.3.14.

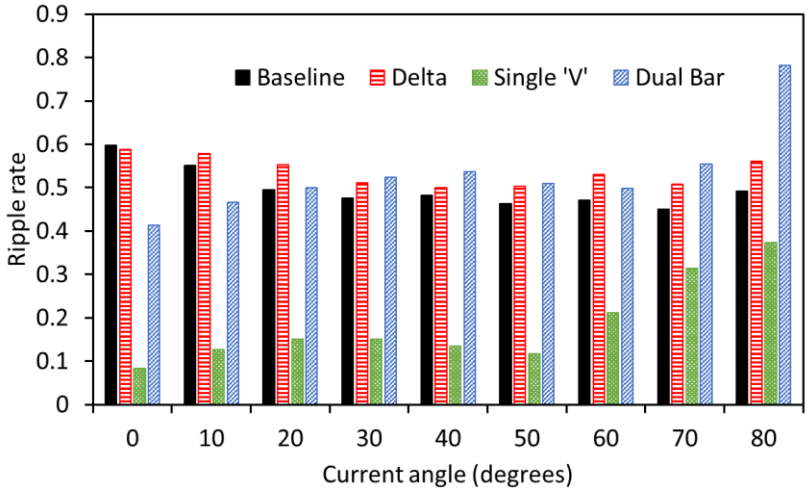

Fig. 7.3.20 Comparison of ripple rate for four topologies at maximum current and incremental current angles.

Table 7.3.14 Ripple rate values for each machine at maximum current and incrementing current angle

β	0°	10°	20°	30°	40°	50°	60°	70°	80°
Baseline	0.60	0.55	0.49	0.48	0.48	0.46	0.47	0.45	0.49
Delta	0.59	0.58	0.55	0.51	0.50	0.50	0.53	0.51	0.56
Single 'V'	0.08	0.13	0.15	0.15	0.13	0.12	0.21	0.31	0.37
Dual bar	0.41	0.47	0.50	0.52	0.54	0.51	0.50	0.56	0.78

From the results the following observations can be made:

- The single layer 'V' topology has a significantly lower ripple rate than the other machines, only rising above 0.15 at the current angle progresses past 60° and even in this case the ripple rate is lower than any of the other topologies.

- The dual bar topology shows a much higher ripple rate in particular between β = 30° and β = 50° and becomes very high beyond β = 70° indicating the higher reluctance torque aspect due to the saliency of machine is having a negative impact on the machine performance.
- With the exception of β =0° where the delta and baseline ripple rates closely match the delta topology exceeds the ripple rate of the baseline where it exhibits the highest ripple up to a current angle of ~30° where the dual bar topology overtakes the delta.

From the results it can be seen that the machines with higher saliency (baseline, delta, and dual bar) suffer compared to the single layer 'V' design. It also shows the optimisation of the rotor design for the single layer 'V' type detailed earlier in this chapter has achieved a good solution in terms of the ripple performance.

To compare the torque waveforms of each topology the machines are simulated running at maximum current (I_{rms} = 26.7A) and a current angle of 50°, approximately the maximum torque value for each machine, over 1 electrical cycle. The results are shown in Fig. 7.3.21.

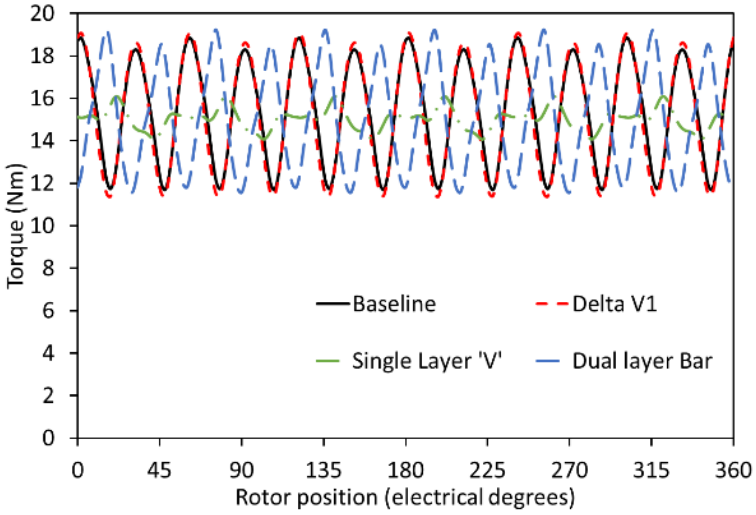

(a) Waveforms

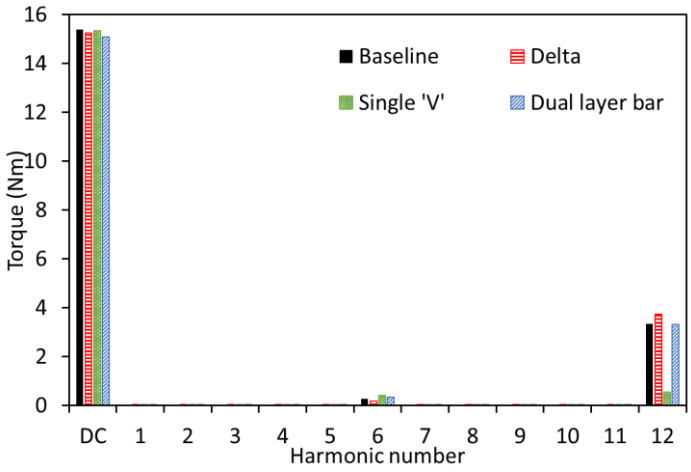

(b) Harmonics

Fig. 7.3.21 Comparison of torque ripples between the 4 rotor topologies at 26.7Arms and β=50°.

The key values from Fig. 7.3.21 are shown in Table 7.3.15.

Table 7.3.15 Comparison of key ripple aspects for the four topologies

		Baseline	Delta	Single 'V'	Dual Bar
Max/Min	Max (Nm)	18.84	19.08	16.07	19.24
	Min (Nm)	11.69	11.37	14.05	11.57
	PP (Nm)	7.15	7.71	2.02	7.67
	Ripple rate	0.46	0.5	0.13	0.54
Harmonics	DC (Nm)	15.39	15.24	15.33	15.09
	6th (Nm)	0.27	0.19	0.40	0.33
	12th (Nm)	3.34	3.74	0.55	3.31

At maximum torque, the following observations of the ripple can be made:

- The delta topology has the highest peak to peak torque ripple and the 12th harmonic, followed closely by the baseline machine
- The dual layer bar machine exhibits high torque ripple, showing a higher peak to peak, and a 12th harmonic very similar to the delta and baseline topologies
- The single layer 'V' has significantly lower ripple in terms of both the peak to peak and amplitudes at the 6th and 12th harmonics, producing the smoothest torque

From this analysis the single layer 'V' topology has emerged as the smoothest machine, despite early concerns with high harmonics in the EMF and static flux distribution. Further optimisation of this topology, and indeed all the topologies, should remove more of these concerns; the key task for this study is to understand the effectiveness of each strategy utilised and of course the impact on the vibratory performance of the machine. Before moving onto more detailed designs of each topology the next to understand is the influence each topology has on the tooth forces and by extension the vibratory behaviour of each machine, which is covered in the next section.

7.4 Tooth force comparison

The performance comparisons between the selected topologies up to this point has highlighted the fact that whilst the machines match in terms of the T-N curve and overall efficiency due to the dominance of the copper loss in each machine many of the other key attributes of the machine differ greatly, in particular the torque pulsations both in terms of the cogging and on-load ripple torques. In this section the tooth forces under different load conditions are calculated and compared in the same manner to that shown in chapter 3 on the base line machine.

7.4.1 Tooth force comparison setup

In chapter 3 a detailed analysis of the tooth forces of the baseline machine was undertaken using both the nodal force analysis tools in the FEA package and utilising a curve located in the mid-air gap and covering 1 slot pitch on to which the Maxwell stress tensor was applied calculate the net tooth force. In this chapter these techniques will be applied to all the topologies understudy to allow the tooth forces generated by each topology to be compared. Fig. 7.4.1 shows the meshed topologies of the machines, including the baseline machine, with the locations of the force probes and the air gap curves for each machine.

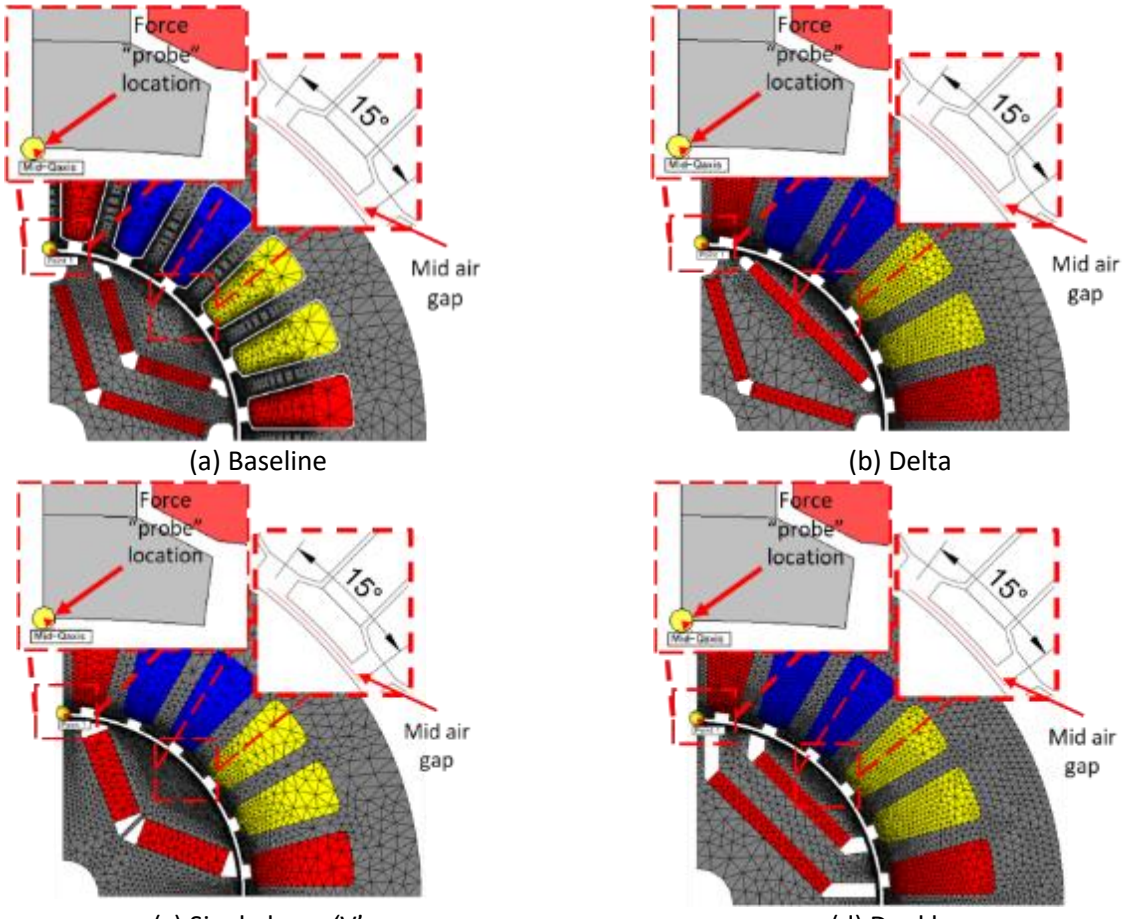

(a) Baseline (b) Delta

(c) Single layer 'V' (d) Dual bar

Fig. 7.4.1 Location of force probe and air gap flux sample points in the 4 machines.

From Fig. 7.4.1 it can be seen that the nodal force probe sits at the tooth edge in the middle of the tooth located at the q-axis of each topology at the starting point. The mid-air gap curves sit over the tooth aligned

with the d-axis. Both tools are used to capture the radial and tangential flux components and are in identical locations on each topology.

7.4.1.1 A note on the mesh settings

Generating the mesh within the FEA tool for measuring the tooth forces tends to be glossed over but can be one of the more difficult tasks of the setup, to accurately obtain a picture of the tooth forces the simulation must step the machine through a minimum of one force cycle (90° mechanical for these 4 pole machines) so to utilise the mesh density used for the cogging torque analysis (Fig. 7.3.17) would put extremely high processing loads on the PC running the simulation. Thus, mesh is adjusted such that the large areas of iron on the stator and rotor have a significantly lower mesh density whilst maintaining a high density at the rotor edge and stator teeth areas. These settings are shared with all 4 machine topologies ensuring the mesh is consistent. On the first comparison run however, there was a concern highlighted in Fig.7.4.2.

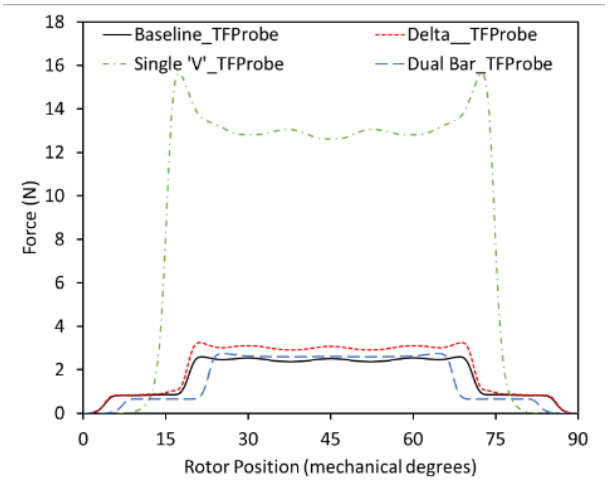

Fig. 7.4.2 Initial comparison of nodal force (absolute) probe results on the centre of the tooth for each rotor topology over 1 pole cycle.

Fig. 7.4.2 shows the calculated tooth force from the force probe on the single layer 'V' machine dominates the waveforms from the other machines by a factor of 4. Whilst the single layer 'V' showed some concern with back EMF harmonics no other aspect of the results thus far would indicate such a large disparity in the tooth force calculation. An inspection of the different models revealed the problem to lie in a mismatch between the mesh settings on the single layer 'V' topology compared to the other 3.

Whilst the manually set aspects of the mesh (tooth tip, rotor edge etc.) were all identical the problem lay in the air gap mesh. In modern FEA tools such as JMAG or ANSYS® ED (formerly MAXWELL) meshes in the air gap region are automatically generated by the software. The user has to identify the motion region(s) of the machine, i.e. the rotor, and using that the tool creates a "slide" condition which acts as a boundary between the static part of the model (stator) and the rotating part (the rotor) [JM18b] and is highlighted in Fig. 7.4.3(a). Typically, the slide edge sits in the middle of the air gap with a small section of air added to the rotor to reduce the complexity of adjusting the mesh at a material boundary [JM18b]. With the slide and motion established the air gap region mesh is derived by dividing the region circumferentially and radially, illustrated

in Fig. 7.3.3(b). By default, the circumferential and radial divisions are automatically generated by the tool. However, they can be set manually which is where the root cause of the concern lay. Fig. 7.3.3(c) shows the effect of adjusting the radial divisions from 360 radial divisions to 2880 divisions.

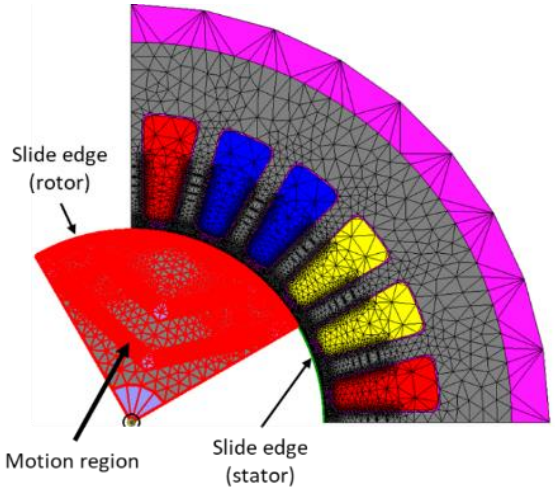

(a) Illustration of the motion region and the slide mesh

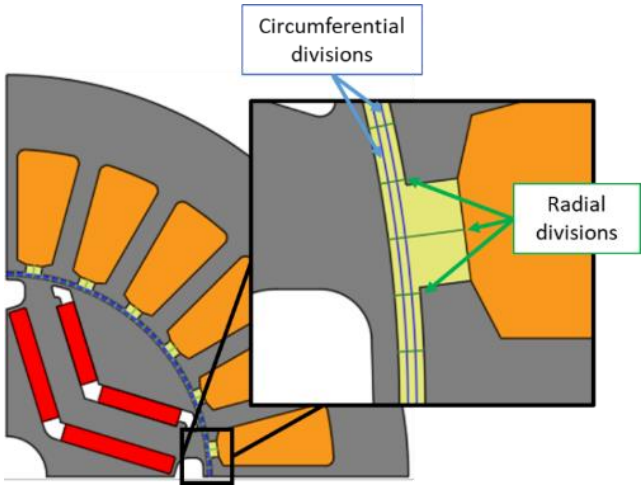

(b) Definition of radial and circumferential divisions

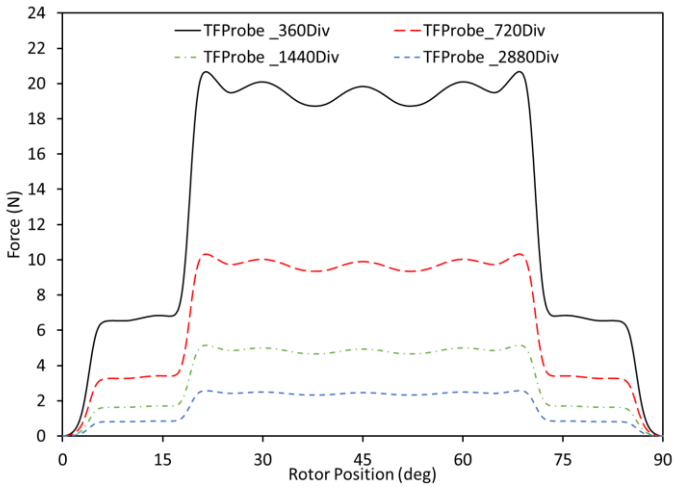

(c) Effect of increasing radial divisions on calculated absolute nodal force (Baseline machine, no load @ 1500rpm)

Fig. 7.4.3 Effect of radial mesh distributions on the baseline machine.

The machine geometry has not changed nor has the PM flux bridging the air gap so the net force acting on the tooth must be the same but looking at Fig. 7.4.3(c) it would be easy to mistake this as not being the case. The reason for the disparity is the force probe is using the flux data calculated at a single mesh node, that is an intersection point between cells of the mesh. As the mesh density increases the number of nodes climbs proportionally so the flux density across a given geometry, the tooth face in this case, is divided among a larger number of nodes. More mesh nodes mean the flux each node calculates is proportionally lower, and thus, given the Maxwell stress tensor the force calculated must drop accordingly. Resolving this concern has highlighted:

- Reinforcement of the point that as much care and attention must be given to ensure the mesh matches as the geometry and material when comparing different machine topologies, highlighted by the sensitivity of calculating the nodal forces on the tooth to mesh density.
- The nodal force probe provides a useful insight to the force profile at a point on the tooth as the rotor moves underneath it over a given cycle but the force density or pressure acting on the whole tooth face must be utilised in order to map the tooth forces more accurately to the mechanical model.

Following the investigation, the mesh settings were carefully checked and aligned and the simulation re-run.

7.4.2 No load tooth force comparison

With the models aligned in terms of the mesh settings the comparison of the machine can begin, starting with the no load condition. As with the no load test in chapter 3 the rotor speed is set to 1500rpm and the simulation run for 1 magnetic force cycle (90° mechanical or 180° electrical) with a step resolution of 0.5 mechanical degrees per simulation step, i.e., the FEA will run 180 steps to complete the 90° rotation of the rotor. The waveform and FFT results using the force probe for each machine is shown in Fig. 7.4.4, a summary of the key harmonics and amplitudes is provided in Table 7.4.1.

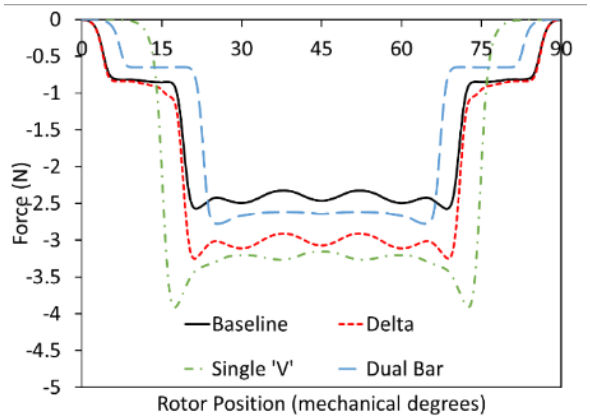

(a) Nodal force radial forces.

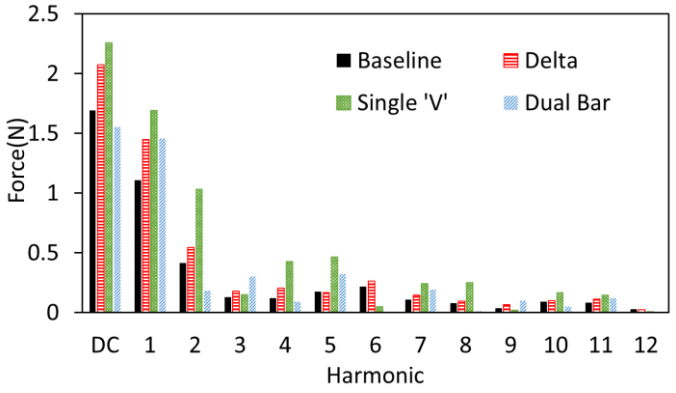

(b) Comparison of the radial force FFT.

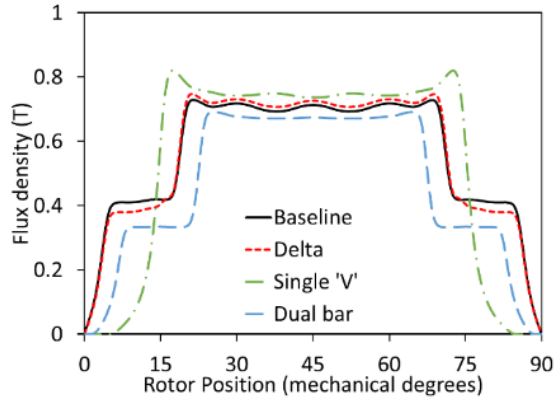

(c) Radial flux densities.

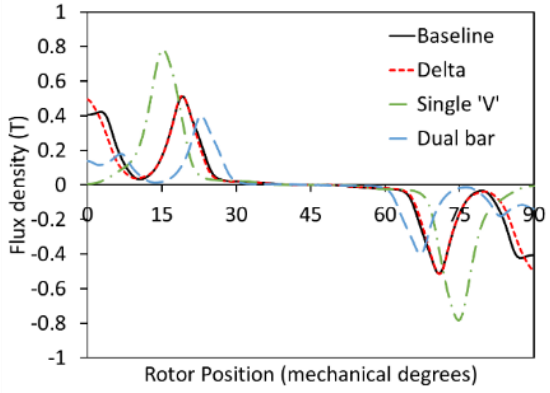

(c) Tangential flux densities

Fig. 7.4.4 Comparison of radial nodal force probe and calculated radial and flux density waveforms at 1500rpm and no load.

Table 7.4.1 Harmonic amplitudes from nodal force probe with machine rotating at 1500rpm and no-load conditions

Harmonic	Baseline	Delta	Single 'V'	Dual bar
Peak	-2.58N	-3.25N	-3.91N	-2.78N
Harmonics				
DC	1.69 N	2.07 N	2.26 N	1.55 N
1	1.11 N	1.45 N	1.69 N	1.45 N
2	0.41 N	0.54 N	1.03 N	0.18 N
3	0.13 N	0.18 N	0.15 N	0.30 N
4	0.12 N	0.20 N	0.43 N	0.09 N
5	0.18 N	0.17 N	0.46 N	0.32 N
6	0.22 N	0.26 N	0.05 N	0.00 N
7	0.11 N	0.15 N	0.24 N	0.19 N
8	0.08 N	0.10 N	0.25 N	0.01 N

From the results the following observations can be made:

- The single layer 'V' clearly shows the highest amplitude of the 4 machines
    - High harmonics on the 1st, 2nd, 4th, and 5th orders.
    - Single layer nature means the force profile is more trapezoidal than the dual layer topologies.
    - Large "horns" observed at ~15° and ~75° positions similar to observations from static flux comparison.
- The delta topology shows the 2nd highest amplitude of the compared topologies.
    - DC, 1st, and 2nd harmonics are high however the amplitudes quickly drop off to align more with the baseline machine as the order number increases.
    - Dual layer nature shows a more sinusoidal profile than the single 'V', the lower layer matching the baseline exactly. However, the difference in the upper layer between the baseline and delta is more apparent due to the higher force calculated as the upper layer is aligned with the force probe (between ~20° and ~70° of rotation in Fig7.4.4 (a)).
- Lower PM content means the dual bar has a lower DC component than the other 3 machines. However, the fundamental is high, equal to the delta.
    - The shorter length of the upper layer magnet is reflected in the force profiles.
    - The profile is the most sinusoidal in nature of the compared topologies, still harmonic rich but in general amplitudes are much lower.

Following analysis of the tooth force probe the forces on the mid-air gap curve are calculated using the Maxwell stress tensor method, with the results shown in Fig. 7.4.5.

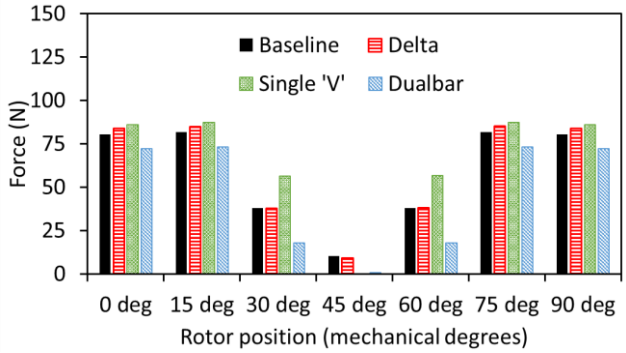

(a) Calculated radial forces.

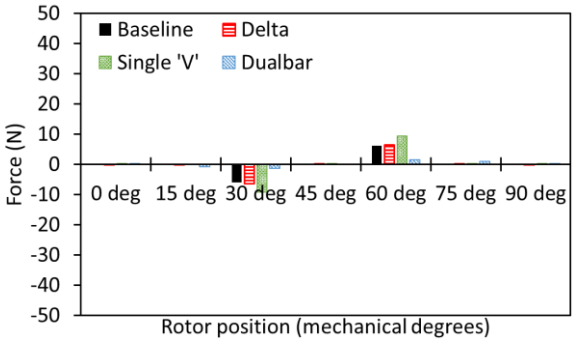

(b) Calculated tangential forces from

Fig. 7.4.5 Calculated tangential and radial force results for the 4 rotor topologies from the mid-air gap curve

The force results have much the same pattern exhibited by the base machine all machines showing at 90° and 90° due to the curve being aligned with the d-axis. As explained in chapter 3 the reason for this symmetry is the sole source of magnetic flux in the machine in this calculation is the PMs in the rotor cores which. There is some clear distinction between the different topologies at the radial forces 45° and the 30° and 60° point for the radial and tangential components from the single layer 'V' topology. Starting with the 45° position result it can be seen in Fig. 7.4.6 that the forces experienced by the baseline (dual layer 'V') and delta are due to flux leakage bridging the air gap and using the tooth to bypass the flux barrier on the rotor q-axis and link with the neighbouring PM pole. Given the delta topology design is a modification of the baseline the geometry is identical between the two so as such the characteristics are very similar. The marginally higher radial force on the delta is due to the flux barriers on the edges of the upper layer magnet having a slightly higher flux leakage than the baseline.

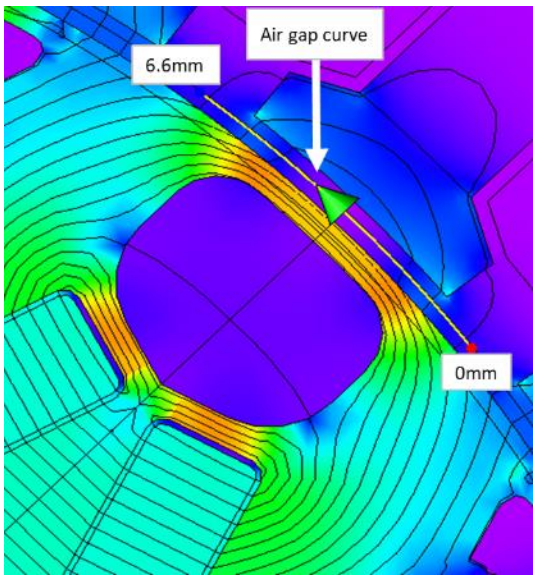

(a) Baseline

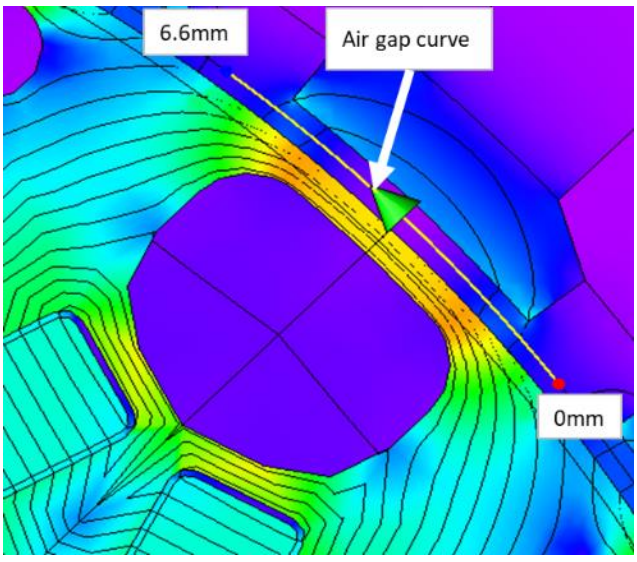

(b) Delta

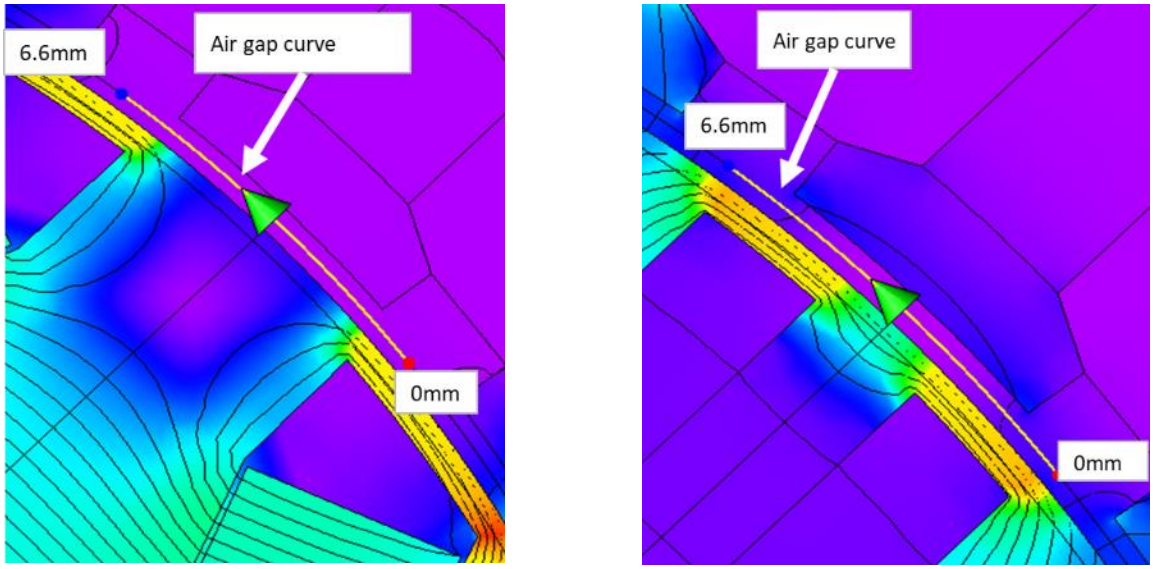

(c) Single layer 'V' (d) Dual bar

Fig. 7.4.6 Comparison of flux distribution of the different rotor topologies at the measured tooth with the rotor rotated 45° from the start position.

In Fig. 7.4.6 (c) it can be seen that the region of iron between the poles on the single layer 'V' gives a strong leakage path for the PM flux and as such no flux links with the tooth across the air gap. No flux density on the tooth surface means no force hence the lack of force observed at this position. On the dual bar topology in Fig. 7.4.6 (d) there is a very small amount of flux interacting with the measured tooth creating a very small radial force but significantly lower than that of the baseline or delta topologies. This is confirmed when looking at the radial and tangential flux densities around the measured tooth for each topology at the 45° rotor position in Fig. 7.4.7.

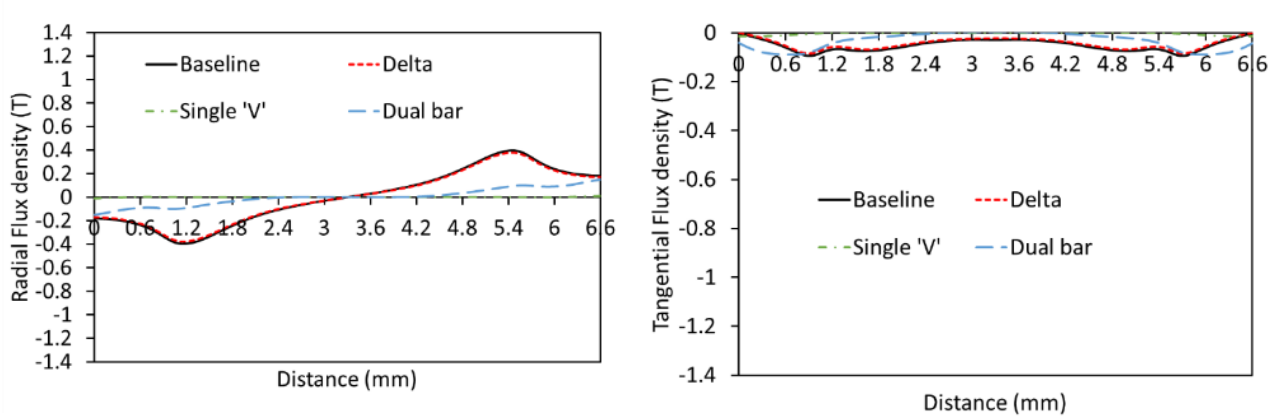

(a) Radial flux density (b) Tangential flux density

Fig. 7.4.7 Flux density calculated along the mid-air gap curve for all 4 topologies with the rotor positioned at 45°.

At 45° the mid-air gap curve is aligned to the rotor q-axis so as such is exactly halfway between the poles. Summing the forces generated due to the radial flux will equal 0N as the 2nd half of the curve cancels out the first half, given the equation for the tangential force is proportional to B_rB_t (eq. 1.3, chapter 1) if B_r is 0 then F_{tan} must be zero. Given that the radial force is proportional to B_r^2-B_t^2 (eq. 1.4, chapter 1) then the negative

flux on the first half of the curve is forced positive so there is a net positive radial force Fig. 7.4.5 (b), which is more apparent on the baseline and delta due to the higher flux density in the air gap.

From Fig. 7.4.5 (b) it can be seen that the single layer 'V' topology experiences a Larger force in the tangential direction when the rotor is at 30° and 60° than the other topologies. Fig. 7.4.8 shows the flux distribution at these rotor positions across the measured tooth as well as the calculated flux densities in the radial and tangential directions.

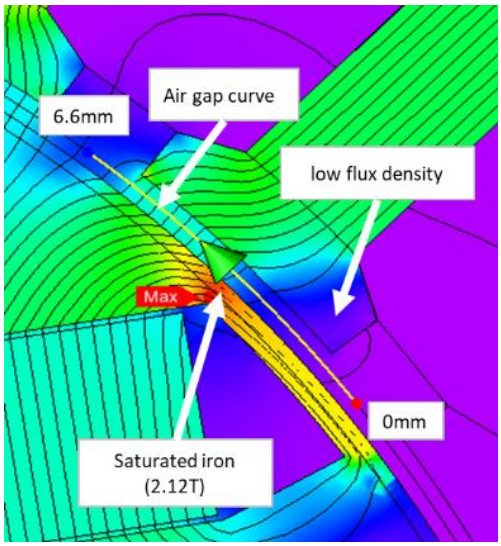

(a) Single layer 'V' flux density distribution around air gap curve at 30° from start position.

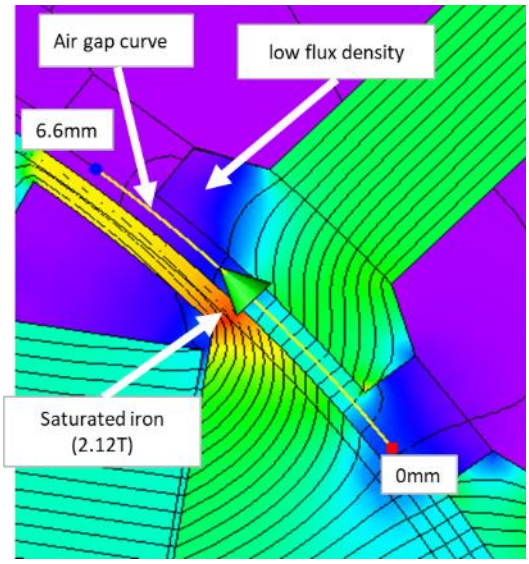

(b) Single layer 'V' flux density distribution around air gap curve at 60° from start position.

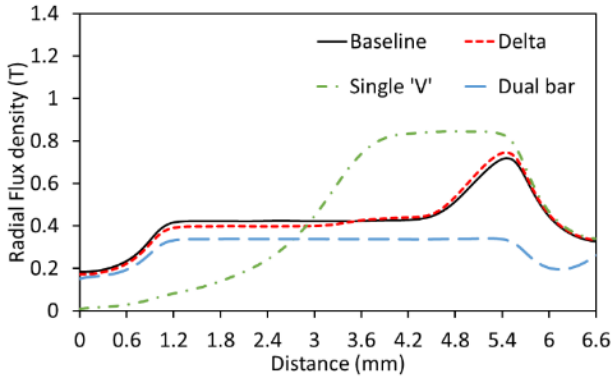

(c) Comparison of radial flux with rotor at 30°

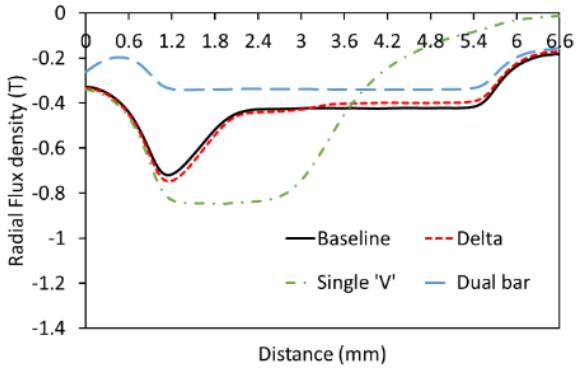

(d) Comparison of radial flux with rotor at 60°

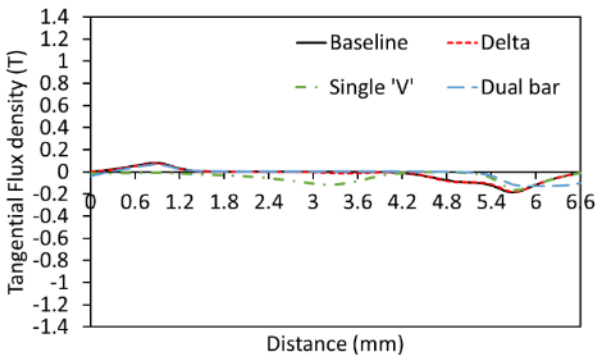

(e) Comparison of tangential flux with rotor at 30°

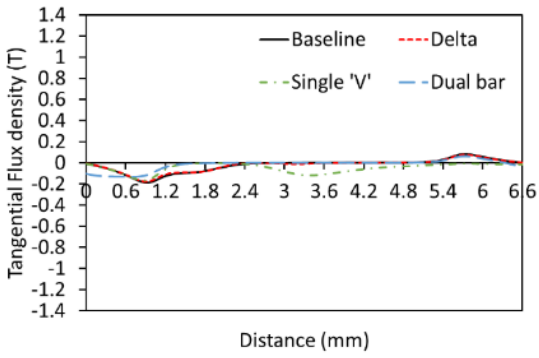

(f) Comparison of tangential flux with rotor at 60°

Fig. 7.4.8 Flux distribution and calculated flux density across air gap curve at no load.

Fig. 7.4.8 highlights the symmetry of the flux distribution in the machine under no-load conditions as the phenomenon is identical for both the 30° and 60° positions, just the direction has changed. From Fig. 7.3.6 (a) and (b) it can be seen that the effect is due to an unbalance in the force across the tooth, very similar to the phenomenon highlighted in chapter 3 with the baseline machine. The difference here on the single layer 'V' topology the region of iron just at the tip of the magnet is highly saturated, showing a peak flux density of ~2.12T, higher than the other topologies. The effect of the high saturation has greatly reduced permeance of the iron, that is $\mu_r \rightarrow \mu_0$ meaning more PM flux will bridge the air gap to the tooth from the area on the leading edge of the magnet rather than the rear, which is blocked by the tooth tip flux barrier. The effect is the tooth has a very large flux density on one edge but very low on the other creating a large imbalance and hence large tangential force. This phenomenon links to the "horns" observed in nodal force probe results in Fig. 7.4.4(a) and the static PM flux distribution comparison observed earlier in this chapter (Fig. 7.3.3).

7.4.3 On load tooth force comparison – I_{rms} = 26.7A, β=0°

Following on from the no load comparison the simulation maximum current is applied to the model and the current angle is held at 0°. The speed is held at 1500rpm. The current angle means the machine is at maximum electrical load, but the lack of reluctance torque means it is not yet at maximum torque. Fig. 7.4.9 shows the difference in flux distribution on the ¼ model of each topology with the rotor at the start position under no load and at the load condition being analysed.

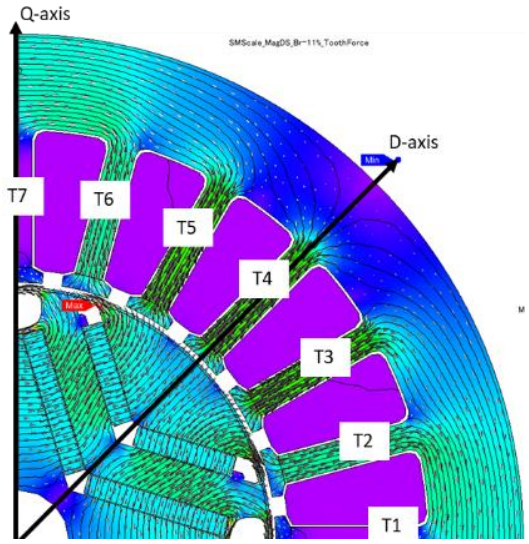

(a) Baseline rotor core no load

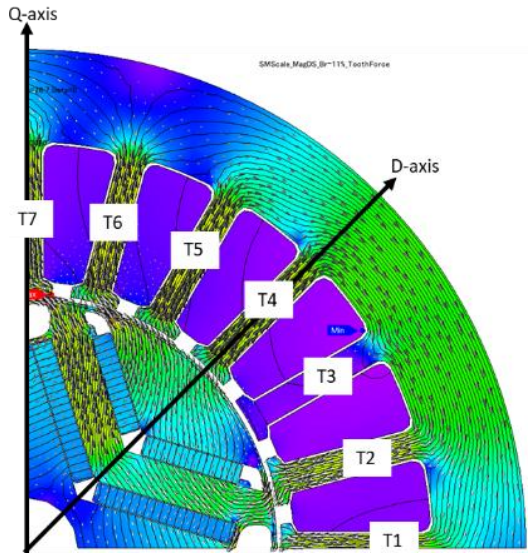

(b) Baseline rotor core I_{rms} = 26.7A and β = 0°.

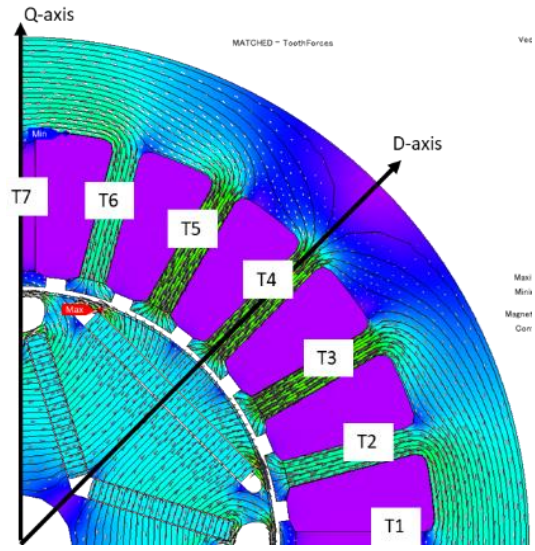

(c) Delta rotor core no load.

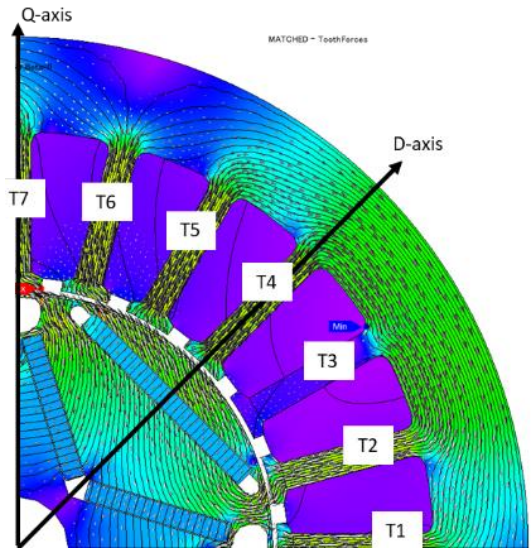

(d) Delta rotor core I_{rms} = 26.7A and β = 0°.

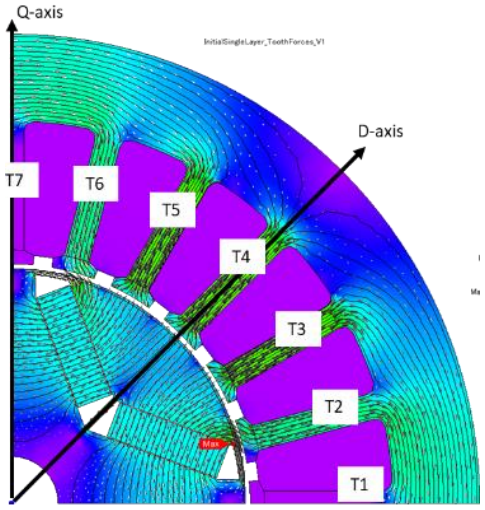

(e) Single layer 'V' rotor core no load

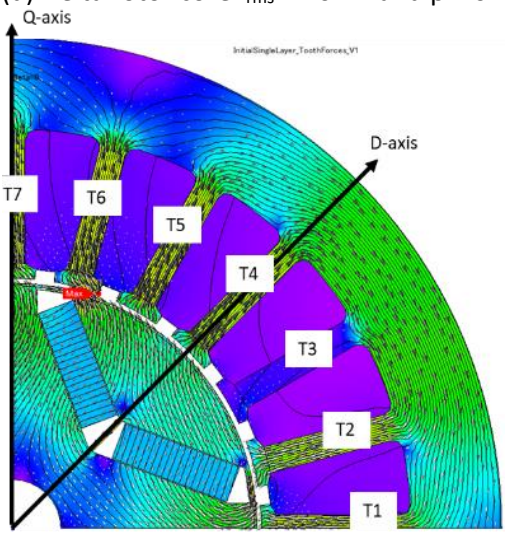

(f) Single layer 'V' rotor core I_{rms} = 26.7A and β = 0°.

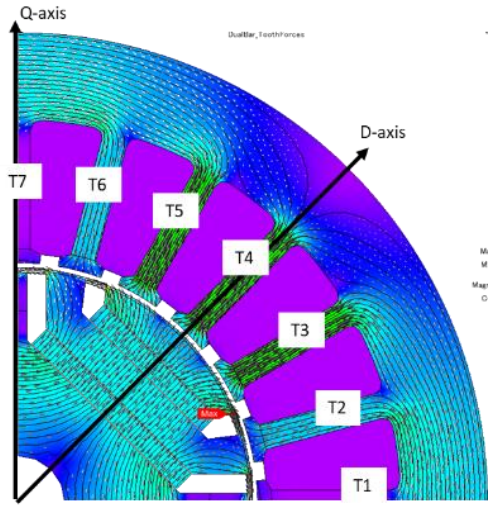

(g) Dual bar rotor core no load.

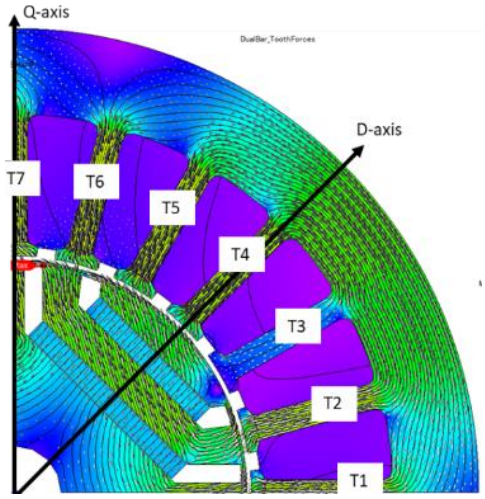

(h) Dual bar rotor core I_{rms} = 26.7A and β = 0°.

Fig. 7.4.9 Comparison of flux density distributions in each machine at no load and I_{rms} = 26.7A and β = 0° conditions.

In Fig. 7.4.9 (b), (d), (f) and (h) it can be seen that all machines follow the same trend as the baseline with tooth T3 in each case showing very low flux densities, the exception being the dual bar machine but the reasoning for this should come clear with more analysis.

Using the same nodal force probe on the tooth tip of tooth T7 and the mid-air gap curve as shown in the no load the performance of each rotor topology is compared. Fig. 7.4.10 shows the calculated force results from the probe.

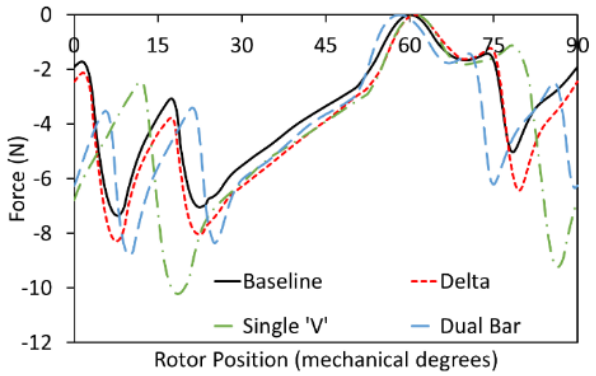

(a) Radial nodal force waveform.

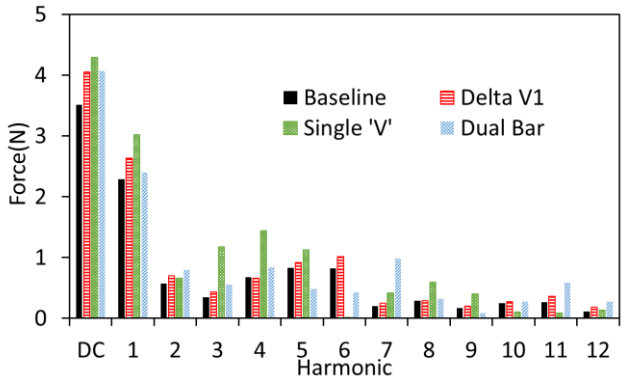

(b) FFT of radial forces.

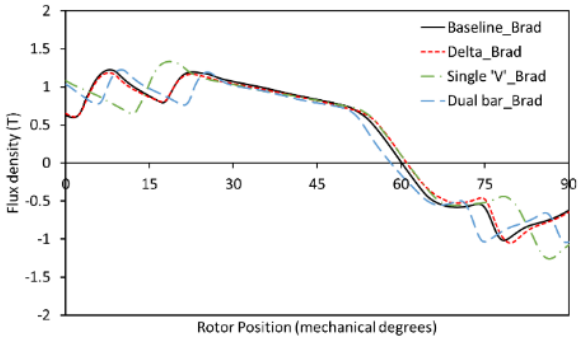

(c) Radial flux.

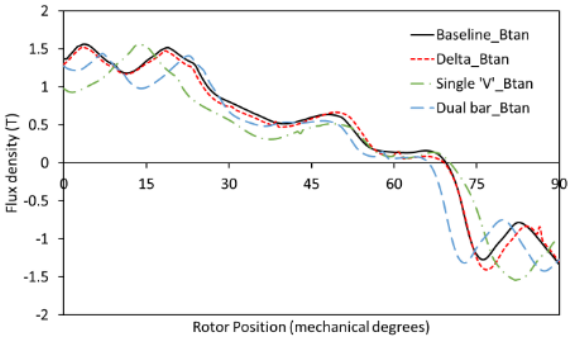

(c) Tangential flux.

Fig. 7.4.10 Comparison of force probe results for all 4 machines at 1500rpm and I_{rms} = 26.7A, β=0°.

Table 7.4.2 shows the harmonic amplitudes of the key harmonics shown in Fig. 7.4.8 (b).

Table 7.4.2 Harmonic amplitudes from radial nodal force probe with machine rotating at 1500rpm, I_{rms} = 26.7A, β = 0°

	Baseline	Delta	Single 'V'	Dual bar
Peak	-7.34 N	-8.28 N	-10.22 N	-8.79 N
Harmonic				
DC	3.51 N	4.05 N	4.29 N	4.07 N
1	2.28 N	2.64 N	3.02 N	2.40 N
2	0.57 N	0.70 N	0.66 N	0.80 N
3	0.35 N	0.44 N	1.18 N	0.56 N
4	0.68 N	0.66 N	1.44 N	0.84 N
5	0.83 N	0.92 N	1.12 N	0.48 N
6	0.82 N	1.01 N	0.01 N	0.43 N
7	0.20 N	0.25 N	0.42 N	0.98 N
8	0.29 N	0.29 N	0.60 N	0.32 N

The waveform shown in Fig. 7.4.10(a) was analysed in chapter 3 for the baseline machine where it was shown that the distortion was due to the PM flux moving tangentially from the d-axis towards the q-axis to link with

the rotating field generated by the coils. The high level of distortion leads to a very rich harmonic content reflected in the FFT seen in Fig. 7.4.10(b) and Table 7.4.2. In terms of the comparative differences between the 4 topologies, the following findings are highlighted:

- The delta topology follows much the same profile as the baseline with peaks slightly higher than the baseline, following the trend established in the no-load testing.
- The baseline, delta and dual bar topologies all show a set of 2 peaks at the start, the first peak coming from the lower layer coming into alignment, which then drops away only to rise again as the upper layer comes into alignment.
- The single layer 'V' shows only a single peak, as there is only 1 layer, but the maximum force is much higher than the other topologies, again in line with the no load findings.

Looking at the waveform for the single layer 'V' in Fig. 7.4.10(a) it can be seen that the force jumps to high value then as the force probe becomes more into alignment with the d-axis the force calculated on the single layer 'V' falls into line with the rest of the machine, showing that the peak force occurs around the upper flux barrier on the upper edge of the magnet. Fig. 7.4.11 highlights the flux density on the tooth on the single layer 'V' at the position of maximum force calculated by the force probe (rotor has moved 18.5° from start).

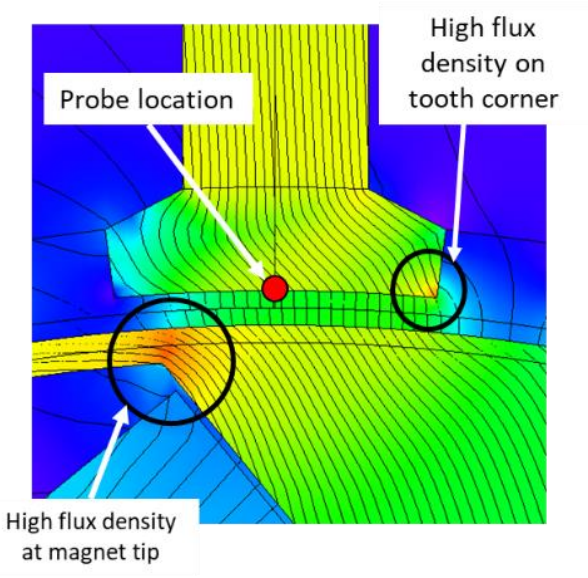

Fig. 7.4.9 Flux density on tooth and rotor at position of maximum calculated force on the force probe tool.

The saturated region of iron at the magnet tip highlighted in Fig. 7.4.11 is once again the area of concern on the machine as the high reluctance of the saturated iron and the barrier leads to an imbalance of magnetic loading on the tooth so as the nodal force probe comes into alignment with this region there is a large rise in the flux density across the air gap generating the high peaks on the force probe waveform described above. Fig. 7.4.11 also highlights the effects of fringing on the tooth as the bottom right corner of the tooth tip experiences high flux densities, most probably resulting in saturation of the region.

Following the same procedure as the no load comparison, Fig. 7.4.12 shows the calculated tooth forces on the mid-air gap curve with the machine on load at rotor positions 0° (start) to 90° in 15° steps.

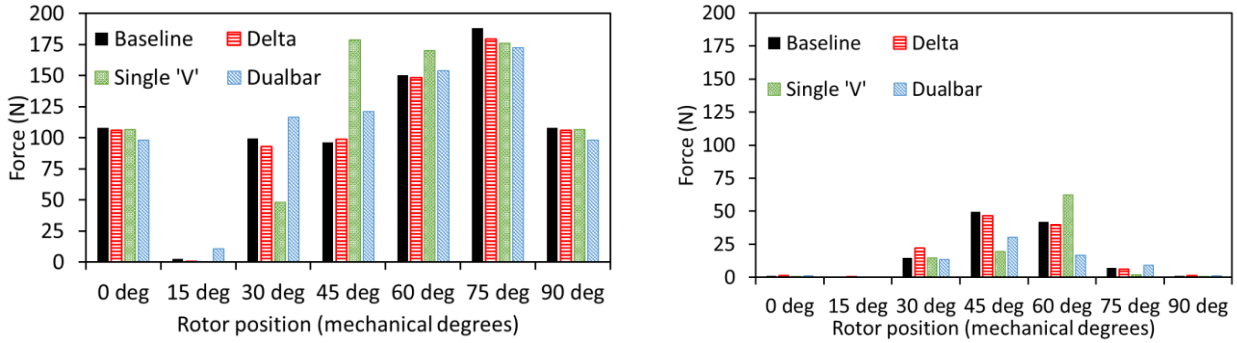

(a) Calculated radial forces (b) Calculated tangential forces

Fig. 7.4.12 Comparison of air gap curve forces for all 4 machines at 1500rpm, I_{rms} = 26.7A, β = 0°.

The key difference between the force profiles in Fig. 7.4.12 and that of the no-load in Fig. 7.4.5 is the force profile is non-symmetrical and tangential forces are significantly higher due to the MMF of the rotating stator field interacting with the PMs in the rotor, which again was detailed on the baseline machine study in chapter 3. The interest in this section is comparative performance differences in the 4 topologies. From figure 7.4.12 it can be seen that at rotor positions 30°, 45° and 60° there are large variations between the different topologies.

- With the rotor positioned 30° from the start position the single layer 'V' shows significantly less radial force than the other topologies, whereas the dual bar dominates.
- With the rotor positioned 45° from the start position the single layer 'V' shows a substantial radial force.
- With the rotor positioned 60° from the start position the dual bar tangential force drops significantly and whilst the single 'V' dominates.
- The delta topology tracks the baseline topology closely.

The first aspect to understand is why the single layer 'V' at 30° from the start position has such a different radial force characteristic than the other topologies. Fig. 7.4.11 shows the radial and tangential fluxes interacting with the tooth at this point and the flux distribution for each machine from the FE tool.

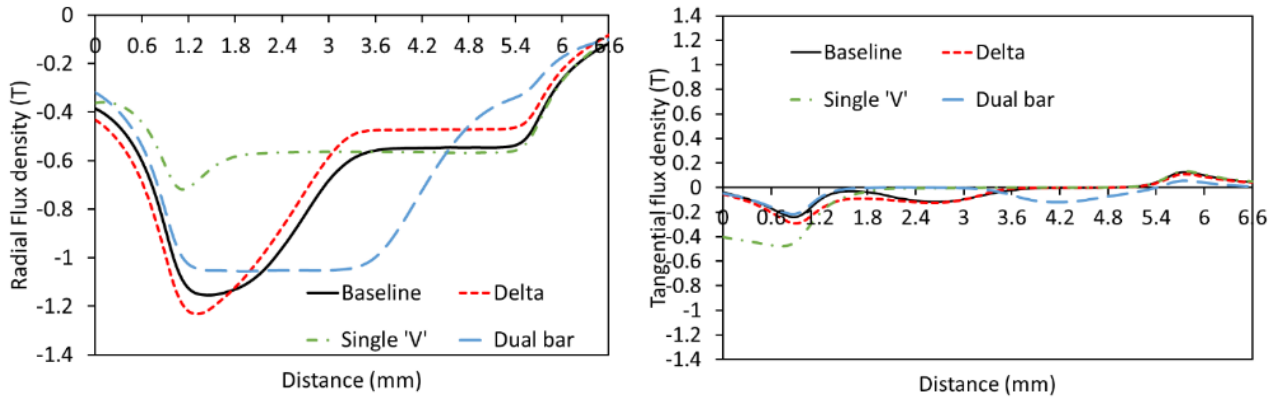

(a) Calculated radial flux densities.

(b) Calculated tangential flux densities.

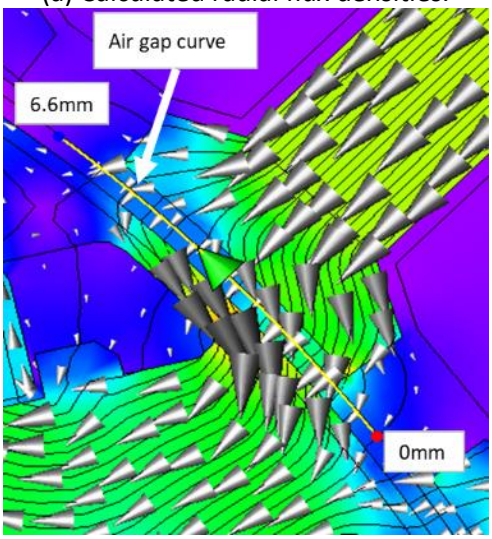

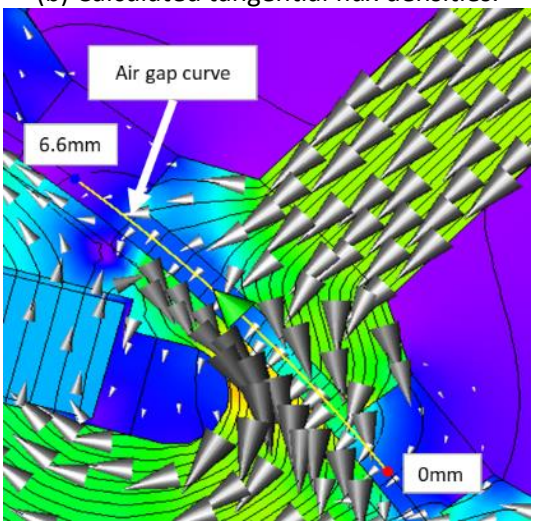

(c) Baseline machine, flux density and flux lines.

(d) Delta machine, flux density and flux lines.

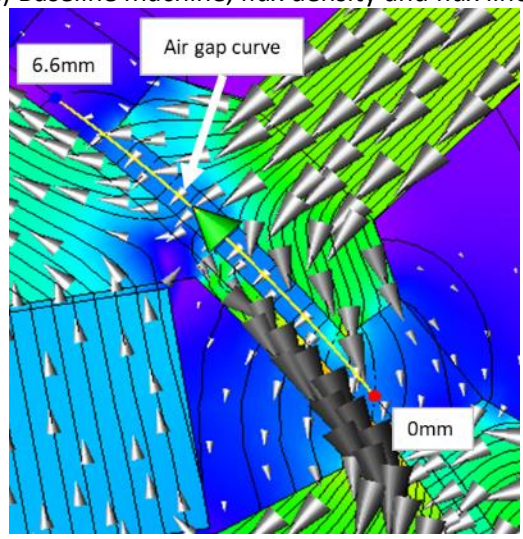

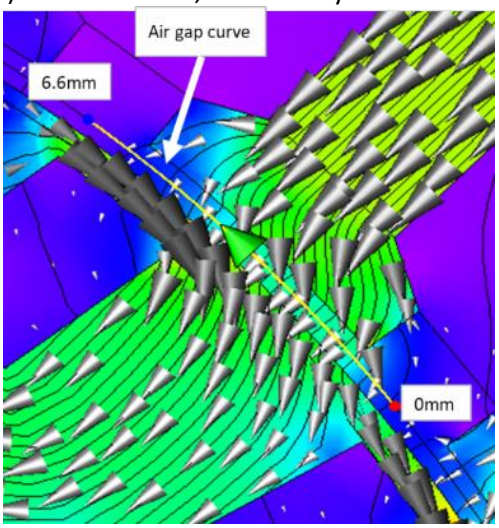

(e) Single layer 'V' machine, flux density and flux lines.

(f) Dual Bar machine, flux density and flux lines.

Fig. 7.4.13 Calculated flux densities on the mid-air gap curve and distributions for each machine with rotor at 30° and machine operating at 1500rpm, I_{rms} = 26.7A, β = 0°.

Figure 7.4.13(a) shows the radial flux density for the single layer 'V' is significantly lower across the profile of the measured curve than the other topologies, showing a high peak at the early section of the curve before dropping off much quicker than the other topologies. The reasoning for this can be better observed looking at the flux distribution around the tooth in Fig. 7.4.13(e).

- The primary reason is the tooth is aligned with the magnet end flux barrier a region of low but fairly constant flux density on the upper half of the mid-air gap curve
- The small rise at the ~1mm marks is the tooth edge interacting with the very edge of the highly saturated region on the rear of the magnet.

So once again the primary reason for differences in force lies in the magnet geometry, and in this case the difference in pole pitch and magnet slot thickness has played a role in dictating how the flux density changes

across the tooth tip curve. The flux generating the forces at the 45° point can be analysed in a similar manner, the results are shown in Fig. 7.4.14.

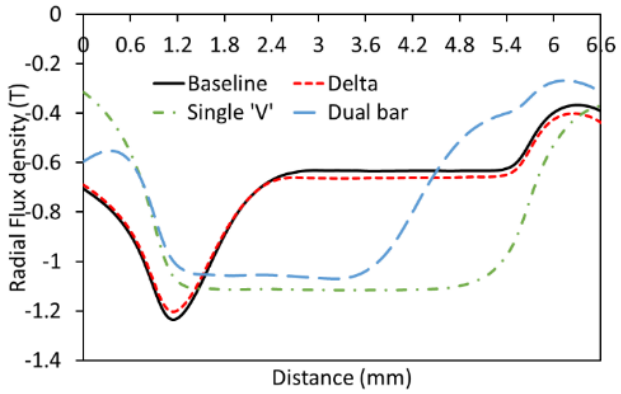

(a) Calculated radial flux densities.

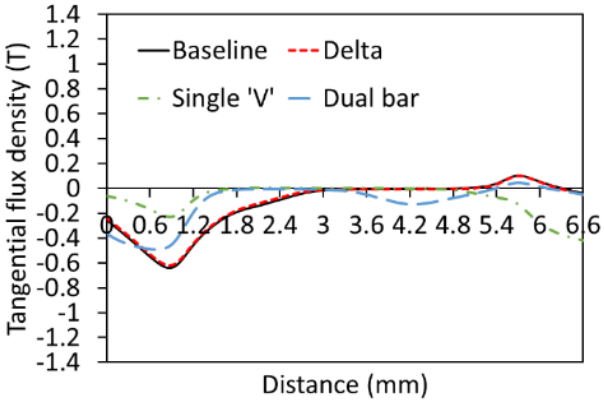

(b) Calculated tangential flux densities

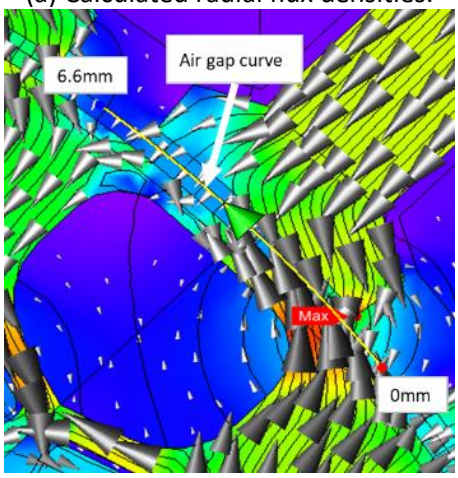

(c) Baseline machine, flux density and flux lines.

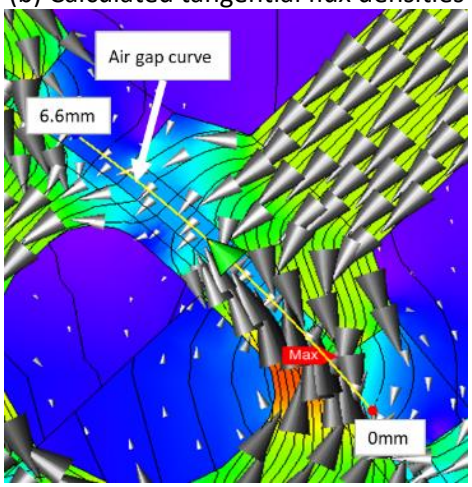

(d) Delta machine, flux density and flux lines.

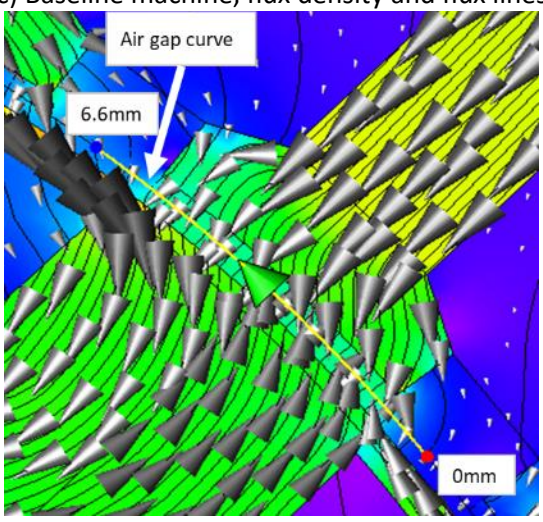

(e) Single layer 'V' machine, flux density.

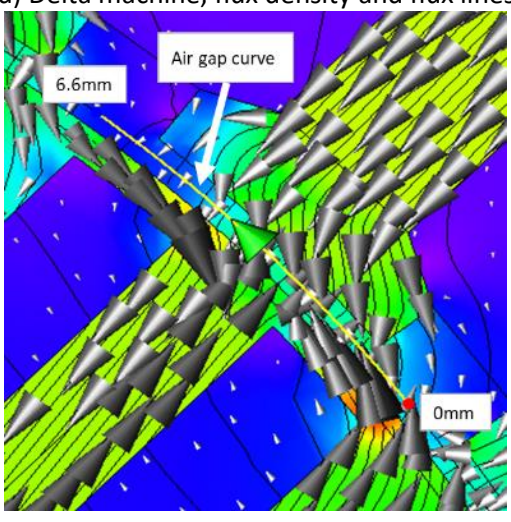

(f) Dual Bar machine, flux density.

Fig. 7.4.14 Calculated flux densities on the mid-air gap curve and distributions for each machine with rotor at 45° from the start position and the machine operating at 1500rpm, I_{rms} = 26.7A, β = 0°

At this point the rotor q-axis is aligned to each tooth on the 4 topologies, which as previously highlighted forms the main flux path through the rotor. The baseline and delta topologies, which share the same flux barrier geometry, have similar characteristics. The baseline shows a slightly lower flux density towards the

upper tooth edge (around 5.5mm along the curve) giving a slightly higher tangential force due to the increased imbalance across the tooth. The single layer 'V' and dual bar also share some common features at this position.

- The tooth aligns with the inter-pole iron on both topologies for which there is no q-axis flux barrier like that on the baseline and delta types.
- The tooth on the single layer 'V' is almost entirely aligned to the rotor iron so high levels of flux can be seen in the radial direction, producing a positive force in the radial direction, as shown in Fig. 7.4.14(a).
- The upper layer flux barriers on the dual bar topology acts to enhance the tangential flux path and block the radial flux on the upper half of the mid-air gap curve meaning the tooth experiences a higher tangential force but lower radial force than the single layer 'V'.

The final position of interest is 60°, the same analysis is repeated and shown in Fig.7.4.15.

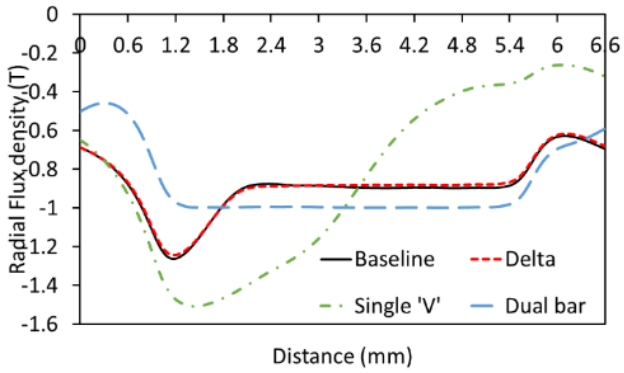

(a) Calculated radial flux density.

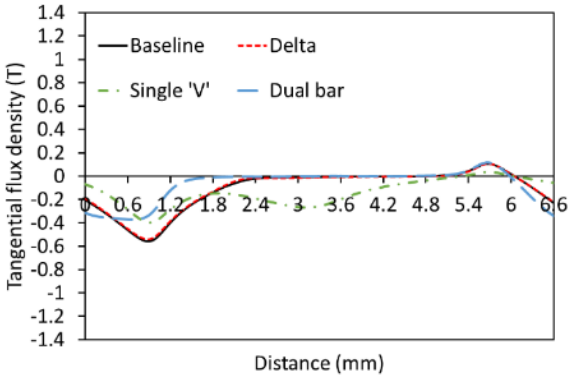

(b) Calculated tangential flux density.

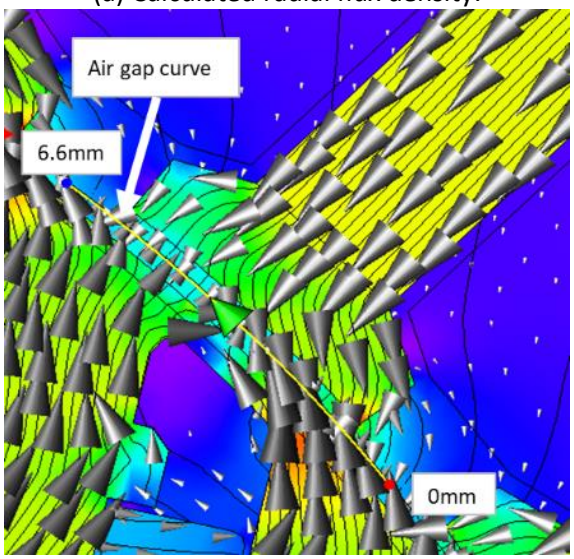

(c) Baseline machine, flux density and flux lines.

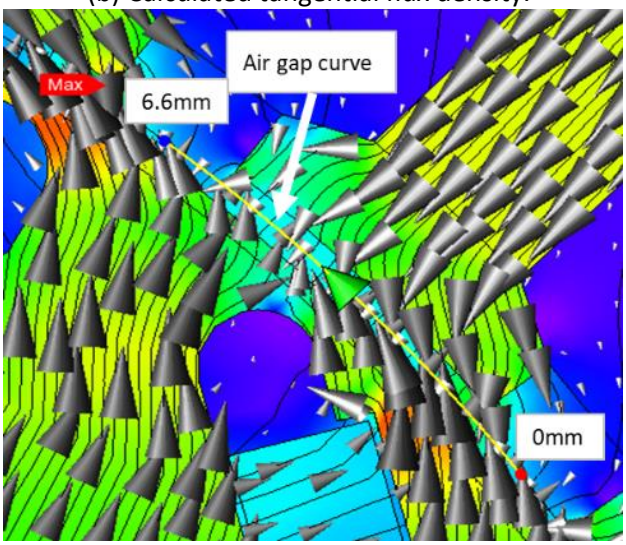

(d) Delta machine, flux density and flux lines.

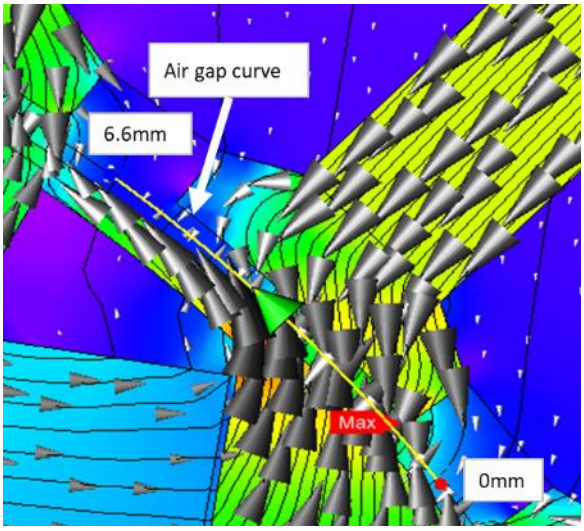

(e) Single layer 'V' machine, flux density and flux lines.

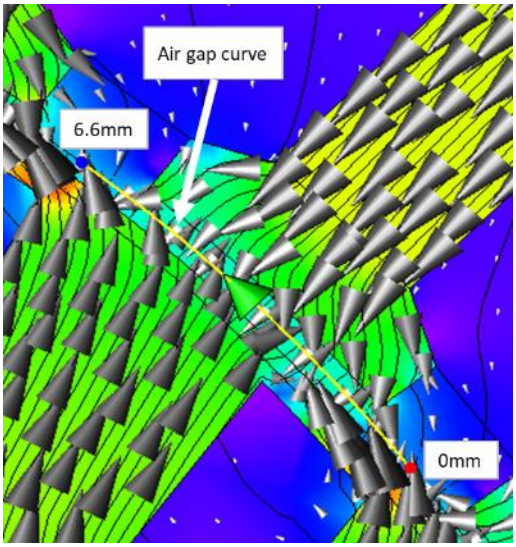

(f) Dual Bar machine, flux density and flux lines.

Fig. 7.4.15 Calculated flux densities on the mid-air gap curve and distributions for each machine with rotor 60° from start position and machine operating at 1500rpm, I_{rms} = 26.7A, β = 0°

Whilst the geometry at 60° is a mirror image of that at 30° the effect of MMF from the stator linking the stator flux to the PM flux means the flux distribution is distinctly asymmetric.

- The geometry of the flux barrier on the upper layer magnet of the delta topology shows higher leakage (Fig. 7.4.15 (d)) compared to the baseline machine (Fig. 7.4.15(c)) resulting in a slightly higher tangential flux on the upper side of the measured curve on the delta topology so the net force across the tooth is slightly lower so the tangential force is lower.
- The single layer 'V' has a very large imbalance of flux along the arc of the measured curve with very high flux density at the lower tooth edge around the ~1mm point.
    - Fig. 7.4.15(e) shows the bulk of the tooth lies above the very high flux density at the leading edge of the magnet which carries the bulk of the flux traversing the air gap.
    - This means the region of the tooth over the flux barrier on the upper edge of the measured curve has a very low flux density due to the flux barrier whilst the region aligned with the iron sees the highest flux density on the machine producing a high net tangential force, largest of all the machines.
- On the dual bar topology, the first portion of the tooth sits off centre from the flux barrier outside of the flux saturated region meaning the tooth does not interact with the large "bulge" in flux due to the flux on the leading edge of the flux barrier observed with the other topologies.
    - This is why despite the fact the tooth sees a higher, constant flux due to being mostly aligned with the interlayer iron the net radial forces are lower and the net tangential force is lower.

The results show the bulk of the variations between the machines occur due to the geometry of the flux barriers and magnet slots closet to the rotor outer diameter and the inter-pole (q-axis) region. These features strongly influence the flux density across the tooth tip and hence the forces that act on it.

7.4.4 On load tooth forces comparison – I_{rms} = 26.7A, β=45°

The second load point maintains the current at maximum (26.7A_{rms}) and speed (1500rpm) but moves the current angle to 45° shifting the stator field position relative to the PM field on the d-q axis plane, the effect on each topology is illustrated in Fig. 7.4.16. As with the previous case the mid-air gap curve and nodal force probe are located in the same positions as shown in Fig. 7.4.1

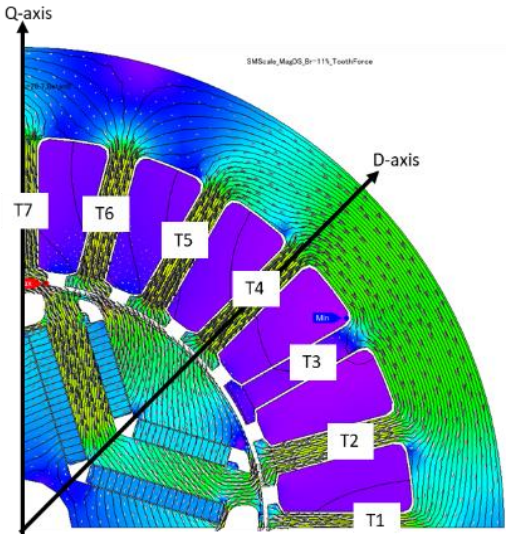

(a) Flux vectors in baseline rotor core I_{rms} = 26.7A and β = 0°.

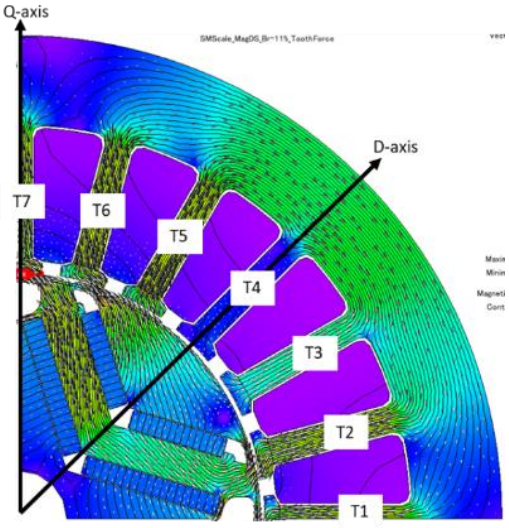

(b) Flux vectors in baseline rotor core I_{rms} = 26.7A and β = 45°.

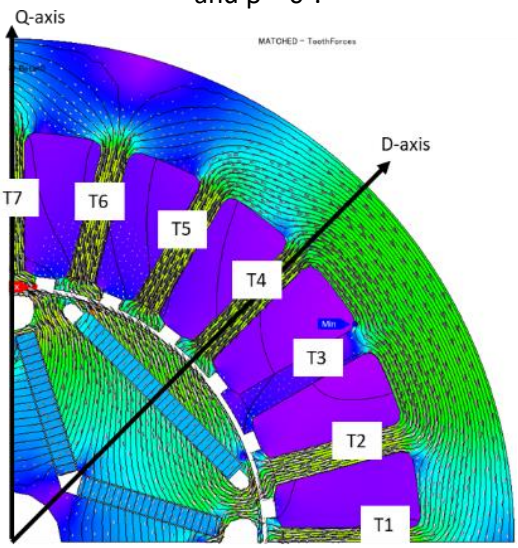

(c) Flux vectors in delta rotor core I_{rms} = 26.7A and β = 0°.

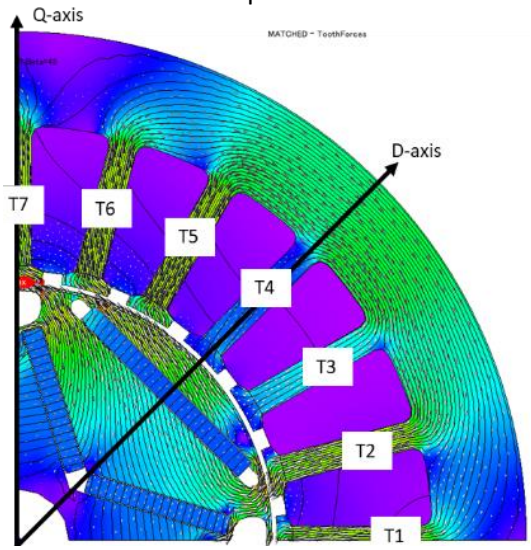

(d) Flux vectors in delta rotor core I_{rms} = 26.7A and β = 45°.

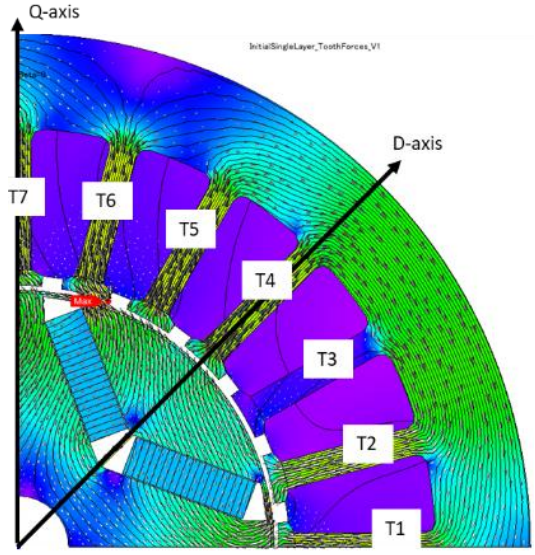

(e) Flux vectors in single layer 'V' rotor core I_{rms} =° 26.7A and β = 0°.

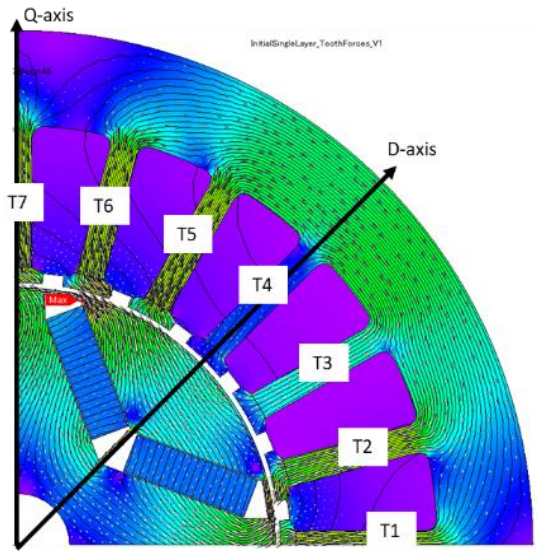

(f) Flux vectors in single layer 'V' rotor core I_{rms} = 26.7A and β = 45°.

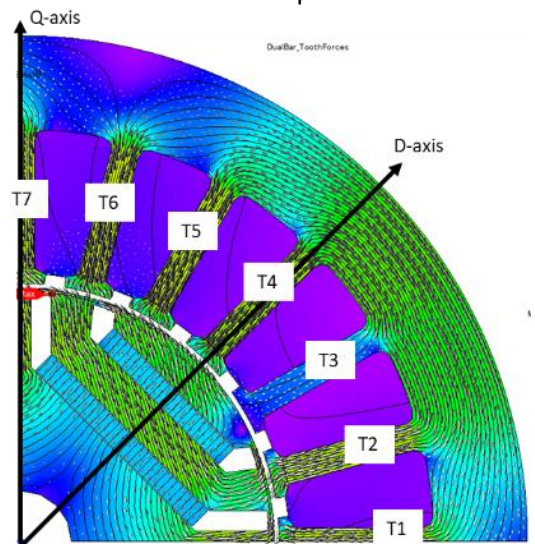

(g) Flux vectors in dual bar rotor core I_{rms} = 26.7A and β = 0°.

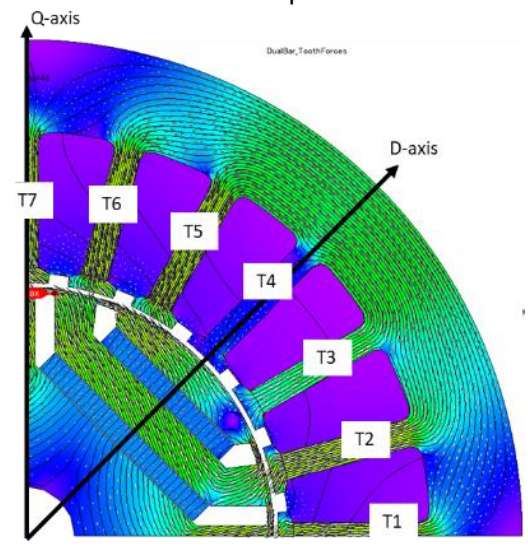

(h) Flux vectors in dual bar rotor core I_{rms} = 26.7A and β = 45°.

Fig. 7.4.16 Comparison of flux density distributions in each machine at the load points I_{rms} = 26.7A, β = 0° and I_{rms} = 26.7A, β = 45°.

Fig. 7.4.16 highlights that all machines follow the same trend as the baseline with a greater level of the magnetic flux deflecting in the tangential (q-axis) direction in the rotor cores and the vector change meaning that tooth T4 (the measured tooth) becomes the tooth with the lowest flux density at the initial position in all case.

A comparison of the forces calculated by the nodal force probe and the radial and tangential fluxes is shown in Fig. 7.4.17.

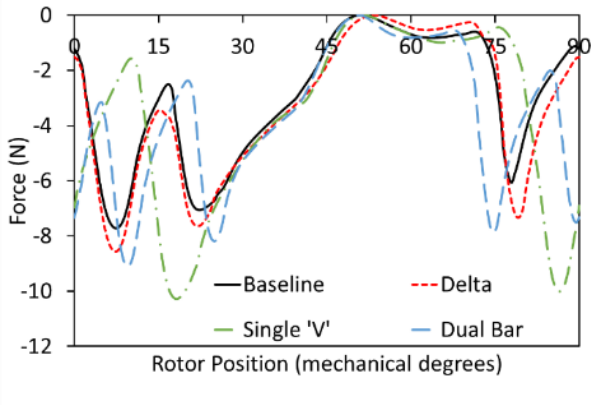

(a) Nodal force probe radial force waveforms.

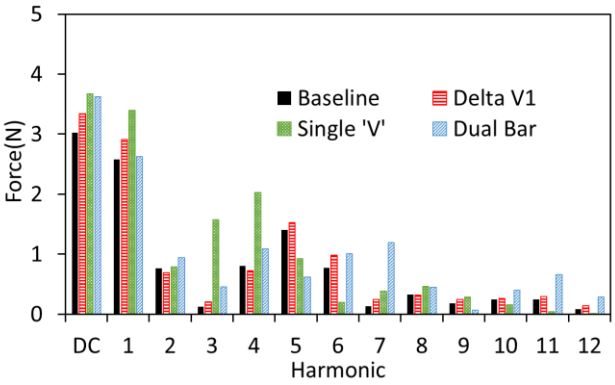

(b) Comparison radial force of the FFT.

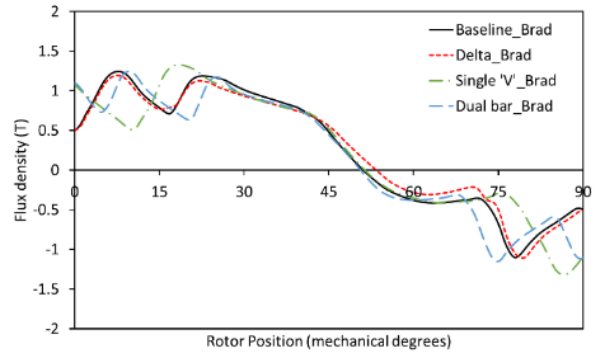

(c) Calculated radial flux.

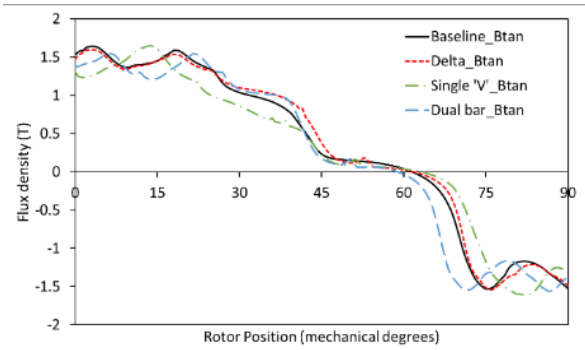

(c) Calculated tangential flux.

Fig. 7.4.17 Comparison of node probe radial force and flux component results for all 4 machines at 1500rpm, I_{rms} = 26.7A, β = 45°

Table 7.4.3 shows the maximum force calculated and the key harmonic force values.

Table 7.4.3 Harmonic amplitudes from stator tooth force probe with machine rotating at 1500rpm, I_{rms} = 26.7A, β = 45°

	Baseline	Delta	Single 'V'	Dual bar
Max				
Harmonic				
DC	3.03 N	3.34 N	3.67 N	3.62 N
1	2.58 N	2.91 N	3.40 N	2.62 N
2	0.76 N	0.69 N	0.79 N	0.94 N
3	0.12 N	0.21 N	1.58 N	0.46 N
4	0.80 N	0.73 N	2.03 N	1.09 N
5	1.40 N	1.52 N	0.93 N	0.62 N
6	0.77 N	0.98 N	0.20 N	1.01 N
7	0.13 N	0.25 N	0.38 N	1.20 N
8	0.33 N	0.32 N	0.46 N	0.44 N

The force probe waveform in Fig. 7.4.17(a) shows that as the rotor moves from the start position to around 30° the force profile remains much the same as the previous load case; the peak values are higher but only by ~0.5N per topology. Much of this is due to the fact that at the rotor initial position the force probe is sat on the q-axis for each machine and has much the same magnetic loading as the β = 0° case which is illustrated well in Fig. 7.4.18 (a) and (b). As was shown in chapter 3, the effect of shifting the current angle at 45° is the q-axis becomes a much more attractive path to the flux in the rotor core pulling the flux more strongly tangentially from the rotor d-axis meaning the bulk of the flux traversing the air gap is calculated between 0°

and around 25° after which the flux density and therefore the force drops much quicker than the previous case, reflected in the waveform in Fig. 7.4.17(a). As the rotor rotates to around 60° from the start position on the dual layer machines the force probe aligns with upper layer barriers causing a slight rise in force which levels off as the top of the flux barriers pass under the probe until around 70° on the dual bar and ~75°on the delta and baseline topologies where in the probe aligns with the high flux density on the back edge of the flux barrier and the sudden increase in air gap flux density results in the force rapidly increasing. On the single layer machine, the same effect is observed but the difference in magnet geometry means the spike occurs around a rotor position of 85°.

The calculated forces from the radial and tangential fluxes acting on the mid-air gap curve can be seen in Fig. 7.4.18.

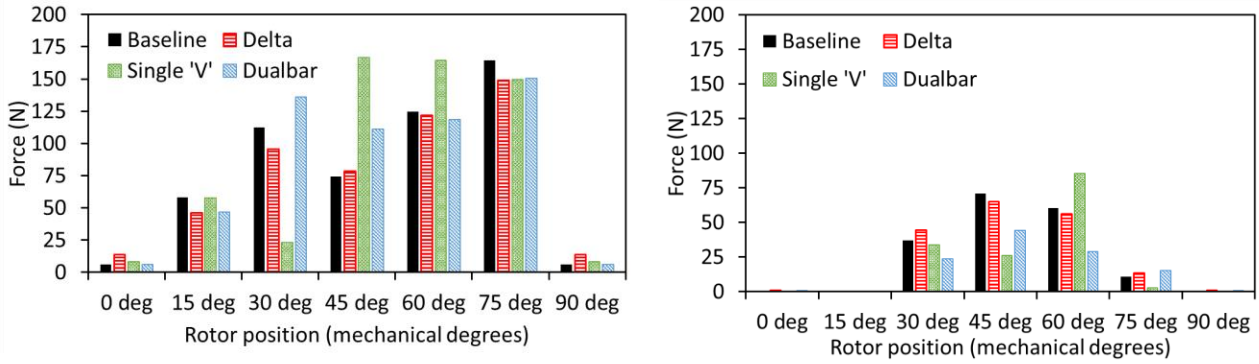

(a) Radial forces. (b) Tangential forces.

Fig. 7.4.18 Comparison of air gap curve results for all 4 machines at 1500rpm and I_{rms} = 26.7A, β=45°

Much of the major differences between the results of running the machine with β= 0° and β= 45° were covered in chapter 3, and all the machines follow the same trend. The shift in the stator field means that the magnetic loading on the measured tooth changes such that in general all machines display a higher tangential force at the 30°, 45° and 60° positions than the β=0° condition. The differences in force on the stator tooth at each position for both simulation conditions are shown in Table 7.4.4.

Table 7.4.4 Comparison of calculated radial and tangential tooth forces at I_{rms} = 26.7A, with current angle set to β = 0° and β = 45°

Radial forces								
Rotor Position	Baseline		Delta		Single 'V'		Dual bar	
	β = 0°	β = 45°	β = 0°	β = 45°	β = 0°	β = 45°	β = 0°	β = 45°
0°	108.11N	5.98N	106.19N	13.85N	106.74N	8.13N	98.04N	6.25N
15°	2.48N	57.92N	0.29N	46.27N	0.57N	57.75N	10.79N	46.88N
30°	99.24N	112.45N	93.04N	95.48N	48.14N	23.12N	116.40N	136.08N
45°	96.27N	74.13N	98.87N	78.68N	178.89N	166.51N	121.03N	110.87N
60°	150.52N	124.85N	148.48N	121.71N	170.38N	164.40N	153.85N	118.67N
75°	188.00N	164.68N	179.38N	148.84N	176.23N	149.49N	172.63N	150.26N
90°	108.11N	5.97N	106.19N	13.85N	106.73N	8.11N	98.04N	6.25N

Tangential forces								
Rotor Position	Baseline		Delta		Single 'V'		Dual bar	
	β = 0°	β = 45°	β = 0°	β = 45°	β = 0°	β = 45°	β = 0°	β = 45°
0°	1.36N	0.53N	1.44N	0.98N	0.83N	0.40N	1.04N	0.56N
15°	-0.03N	-0.30N	0.16N	-0.11N	0.12N	-0.15N	0.06N	0.32N
30°	14.90N	36.96N	22.01N	44.48N	14.70N	33.90N	13.64N	23.73N
45°	49.44N	71.01N	46.56N	65.12N	19.70N	26.08N	30.29N	44.32N
60°	41.79N	60.20N	39.79N	56.32N	62.52N	85.51N	16.70N	28.75N
75°	7.14N	10.83N	6.18N	13.56N	2.11N	2.85	9.37N	15.12
90°	1.36N	0.53N	1.44N	0.98N	0.83N	0.39N	1.05N	0.56N

Comparing the force results from the two load conditions reveals:

- The curve used to calculate the tooth forces is aligned to the surface of tooth T4, which from Fig. 7.4.18 (b), (d), (f) and (h) is shown to have very low flux densities, and hence the negligible radial and tangential force at this point.
- Tangential forces are significantly higher with the rotor positioned at 30°, 45°, 60° and 75° from the start position.
- The peak radial forces observed at the higher rotor angles have all dropped, though the single layer 'V' only sees marginal reductions at 45° and 60°
- The single 'V' is also unique in seeing a more significant drop in radial force when the rotor is at 30° from start position, sharply contrasting the dual layer bar type which sees a significant increase.
- The delta topology follows the trend of the baseline faithfully, the only significant in trend change between the cases of β = 0° and β = 45° is the tangential force of the delta drops compared to the baseline when the rotor is at the 30° position.

Given the above a more detailed investigation of the flux distribution of the measured tooth for each topology at the 30°, 45° and 60° would provide more insight into the difference. Fig. 7.4.19 shows the calculated radial and tangential at the mid-air gap curve and the flux distribution of on each machine at this point.

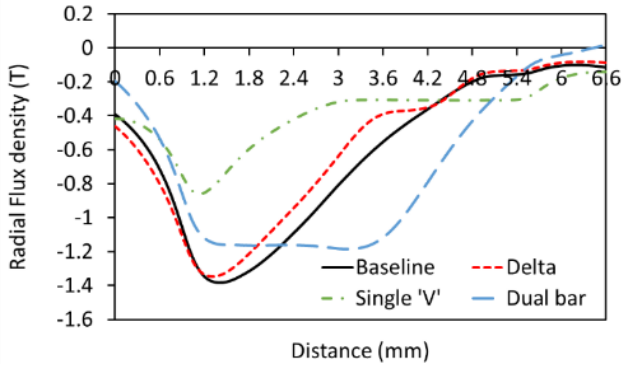

(a) Calculated radial flux density.

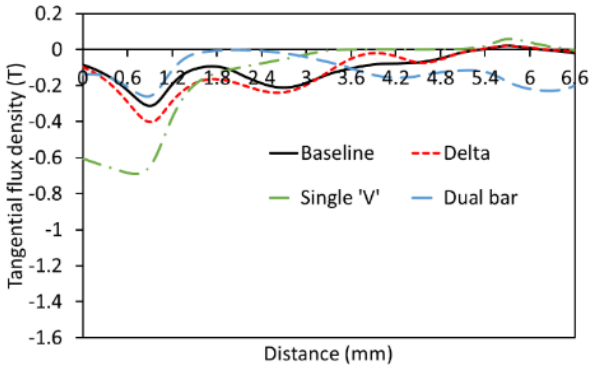

(b) Calculated tangential flux density.

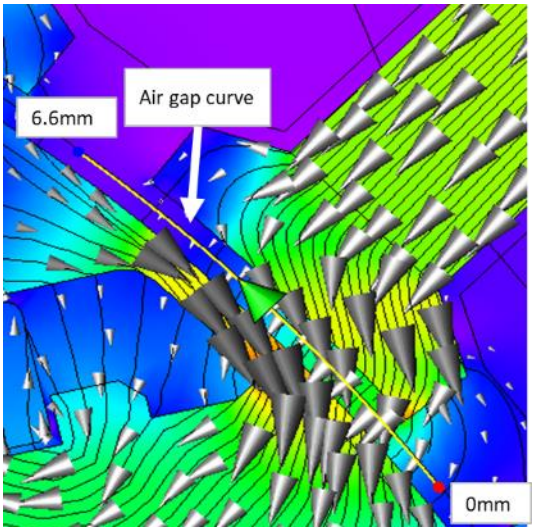

(c) Baseline machine, flux density and flux lines.

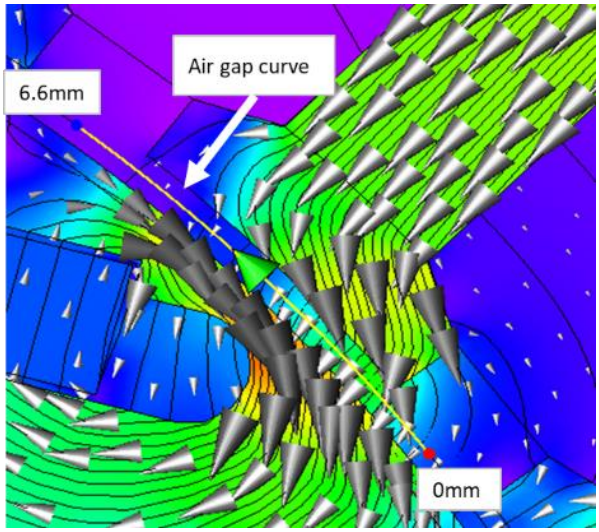

(d) Delta machine, flux density and flux lines.

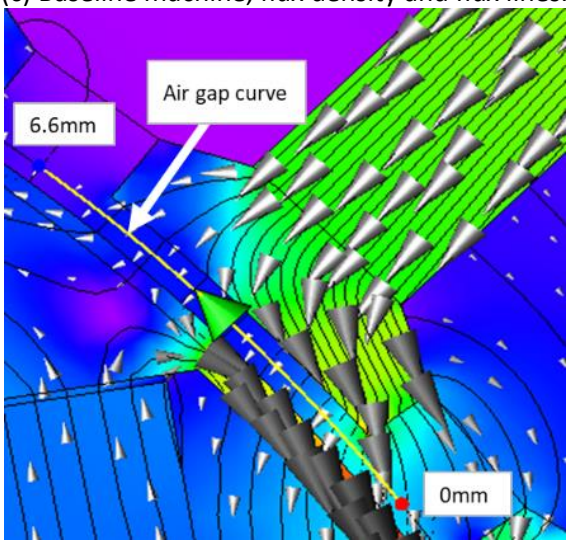

(e) Single layer 'V' machine, flux density and flux.

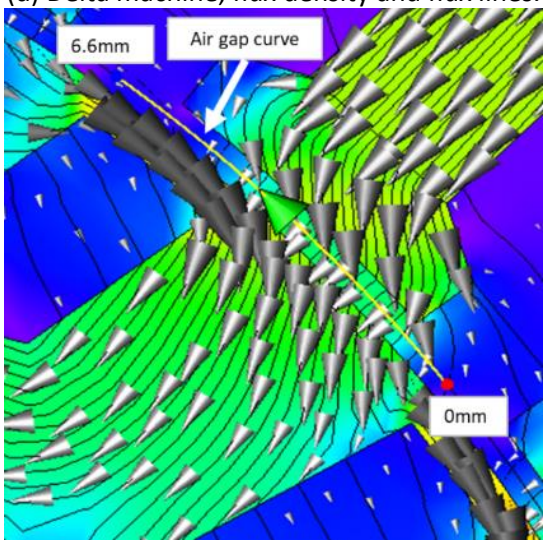

(f) Dual bar machine, flux density and flux lines.

Fig. 7.4.19 Calculated flux densities on the mid-air gap curve and distributions for each machine with rotor at 30° and machine operating at 1500rpm, I_{rms} = 26.7A, β = 45°.

From Fig. 7.4.19 it can be seen that the most significant difference between operating the machine at β = 45° and β = 0° lies in the tangential flux component which has been pulled almost entirely in one direction, with only a small amount positive flux density towards the upper side of the curve where the flux densities can be seen to drop in Fig. 7.4.19 (c) to (f). This trend is best observed on the single layer 'V' machine. Fig. 7.4.20 shows the change in radial and tangential flux on the topology at the 30° rotor position in the no-load, full current with β = 0° and full current with β = 45°.

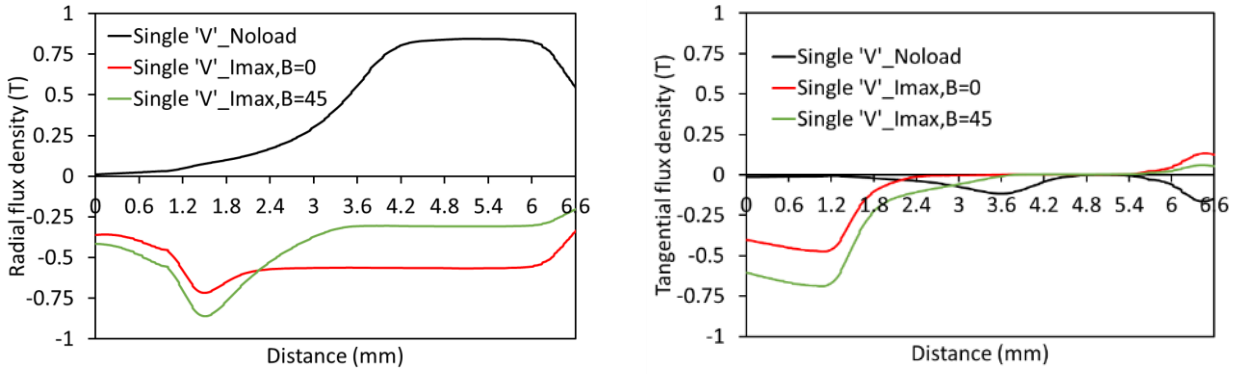

(a) Radial flux density distribution (b) Tangential flux density distribution

Fig. 7.4.20 Radial and tangential flux densities in single layer 'V' machine along air gap curve with rotor at 30° position and machine under no-load, I_{rms} = 26.7A, β = 0° and I_{rms} = 26.7A, β = 45° conditions.

The difference between the load and no-load conditions was explored in chapter 3 but the aspect of greater interest is the effect of the current angle on the radial and tangential flux. It can be seen in Fig. 7.4.19(e) that there is a much larger contrast in the flux distribution across the tooth compared to the β = 0° position leading to a significant rise in the tangential flux density, effectively pulling the entire waveform downwards in Fig. 7.4.20(b) and doubling the tangential force versus the β = 0° condition. The very high flux density at the saturated region creates a larger peak of radial flux density at around ~1.5mm in Fig. 7.4.20(a) but the rest of the tooth lies over a region of very low flux meaning the net radial force is much lower. For the other topologies:

- Between the delta and the baseline, the delta shows a lower radial component which can be explained by the higher leakage flux in the rotor core above the flux barrier in Fig. 7.4.19(d).
- Much of the tooth on the Dual bar is aligned with the low reluctance inter-layer steel which from Fig 7.4.19(f) can be seen to have a very high flux density for much of the surface of the curve until the upper area where the alignment with flux barrier means the flux tapers off. This explains the high radial force calculated.

Again, the general observation at this rotor position with β = 45°is a significant change in the tangential flux density calculated along the resulting in large changes to both the tangential and radial force components. With the tooth aligned to the rotor having moved 45° from the start position the radial and tangential flux densities are once again compared along with the flux distribution at the measured tooth, the results are shown in Fig. 7.4.21.

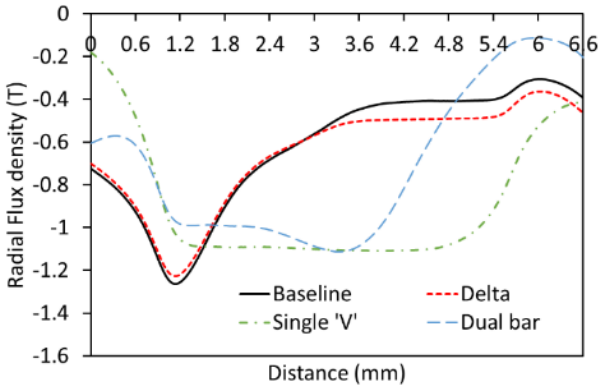

(a) Calculated radial flux density.

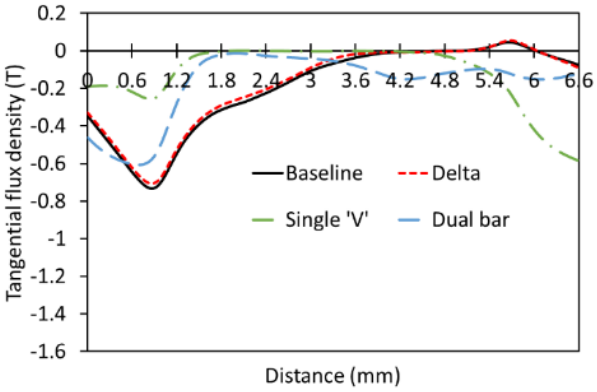

(b) Calculated tangential flux density.

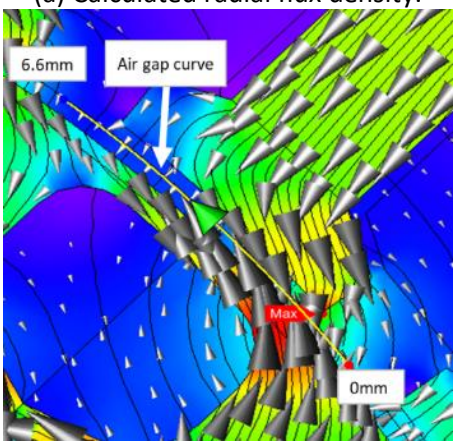

(c) Baseline machine, flux density and flux lines.

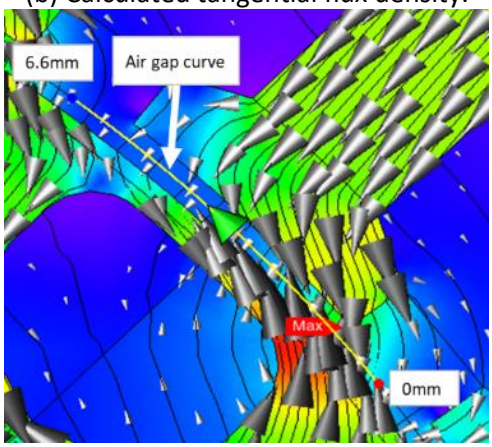

(d) Delta machine, flux density and flux lines.

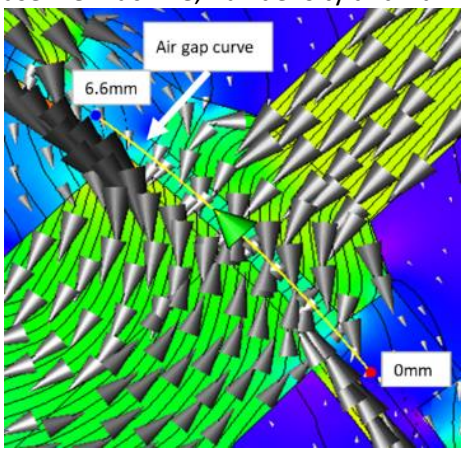

(e) Single layer 'V' machine, flux density and flux lines.

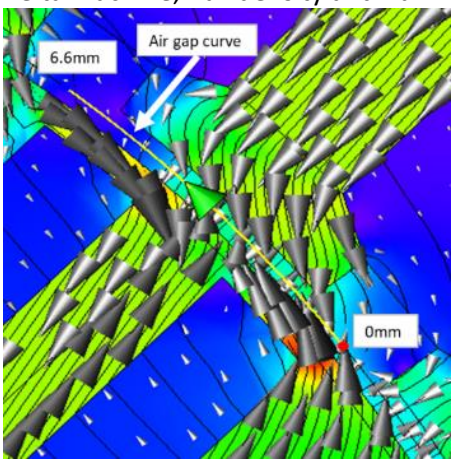

(f) Dual Bar machine, flux density and flux lines.

Fig. 7.4.21 Calculated flux densities on the mid-air gap curve and flux distributions for each machine with rotor at 45° and machine operating at 1500rpm, I_{rms} = 26.7A, β = 45°.

With the rotor position at 45° the tooth is once again aligned with the q-axis of the rotor. However, the general trend shows significantly higher tangential flux densities for all machines with the waveforms in Fig. 7.4.21(b) being pulled almost entirely below 0T, and only the peaks caused by the fringing at the tooth end (~5.6mm) does the flux density become positive for the delta and baseline. The trend of the radial flux density across the curve is much the same as the β =0° condition. The single 'V' and dual bar show the same difference

in behaviour than the delta and baseline which as previously highlighted share the same rotor geometry at this position.

- The delta and baseline topologies share identical geometry around the q-axis flux barrier at this point; and the tangential flux in Fig. 7.4.21(b) is identical.
    - Differences do lie in the radial flux distribution around the upper edge of the tooth, just past the mid-point (~3.25mm) where the delta topology appears to have a slightly higher flux density, again indicating a slightly higher leakage in the delta topology in this region.
    - This phenomenon is observed in the β =0° condition, but the higher flux density on the tooth means it is more apparent.
- The single 'V' shows a near identical radial flux density profile as the tooth is almost entirely over the inter-pole iron region, so the density is high. Compared to the β = 0° condition the tangential flux is pulled a bit higher at the extreme edge of the curve, but this only has marginal impact on the forces.
- The increase in tangential force and drop in radial force on the dual bar topology is more significant than the single 'V' but falls below the baseline and delta, again due to the inter pole iron allowing for a radial path for the flux to bridge the air gap.

The final aspect is the calculated radial and tangential flux densities along the mid-air gap curve when the rotor has rotated 60° from the start position can be seen in Fig. 7.4.22.

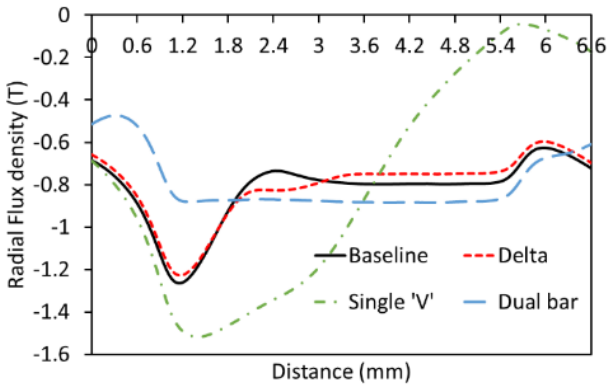

(a) Calculated radial flux density.

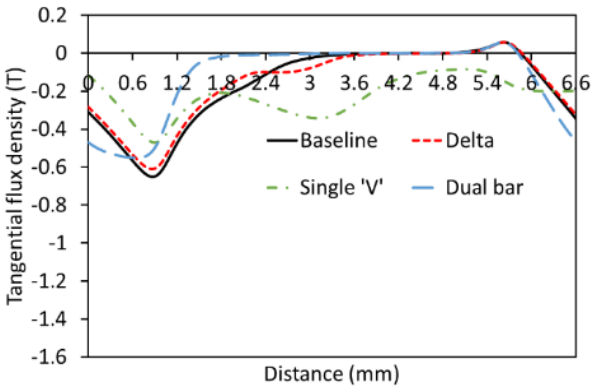

(b) Calculated tangential flux density.

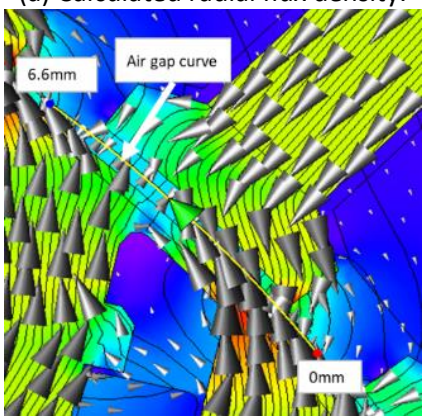

(c) Baseline machine, flux density and flux lines.

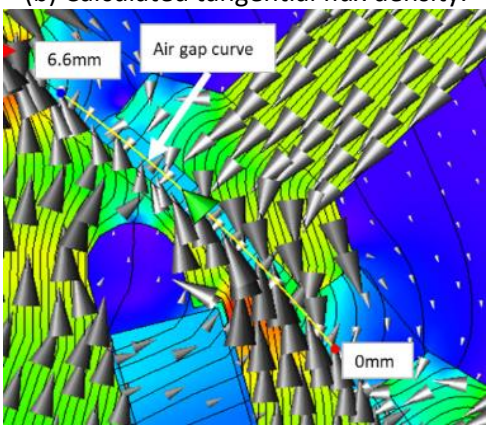

(d) Delta machine, flux density and flux lines.

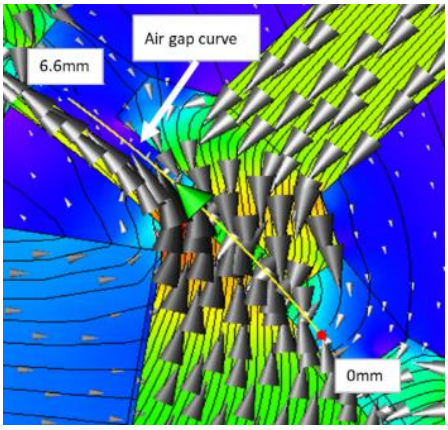

(e) Single layer 'V' machine, flux density and flux lines.

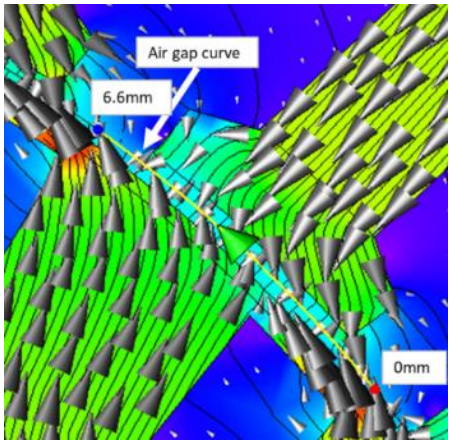

(f) Dual Bar machine, flux density and flux lines.

Fig. 7.4.22 Calculated flux densities on the mid-air gap curves and flux distributions for each machine with rotor at 60° and machine operating at 1500rpm, I_{rms} = 26.7A, β = 45°

The trend is much the same as the β = 0° condition as for the delta and baseline topologies the upper magnet layer flux barriers are aligned with much of the tooth giving a high peak at the lower edge of the tooth (again, around the 1mm point) then the saturated iron along the top of the flux barrier gives a pretty constant radial flux density across the tooth face. The higher flux density on the lower edge of the curve means the tangential forces are higher but the net radial forces have dropped.

Similar to the β = 0° condition the single layer 'V' has a very high peak at this position.

- The tooth is in alignment with the maximum flux density point on the rotor, which as previously observed, with the current angle at 45° means the bulk of the flux in the rotor core has traversed the iron tangentially to this point. This gives the very high flux densities observed in Fig. 7.4.22(a) which is very high up until around the mid-curve point where the flux barrier blocks the flux path.
- The tangential flux for the single 'V' also differs from the other topologies by not rising above 0T, from Fig. 7.4.22 (e) it can be seen that the upper side of the tooth has very low flux density.
- These characteristics act to boost the tangential force in particular to the highest tangential force of any of the analysed points.

Past 60° the tooth begins to align with the d-axis once more and the overall forces drop steeply until the final point, 90, which represents the end of one force cycle. After this point the process will repeat for the next pole passing the tooth.

7.4.5 Conclusion of tooth force investigation

The effect of different load conditions on the tooth forces for all 4 topologies has been analysed using the methodologies developed in chapter 3. All machines follow the same major trends as the analysis of the baseline machine:

Whilst the major trends from the base machine apply to all rotor topologies there are variations between the characteristics of each machine which causes differences in loading on the stator teeth as the rotor spins.

- Given the delta topology is derived from the same geometry as the baseline machine it shares much of the same characteristics, in particular around the q-axis position. At both the force probe and tooth force calculation positions the differences between the machines become clearer as the upper layer comes into alignment
    - More iron at the upper edge of the delta upper layer magnet leads to less saturation and more leakage at the magnet edge giving rise to slightly higher forces observed over this region as more flux bridges the air gap.
    - The reduced area of iron directly above the bar magnet on the delta upper layer gives higher flux densities in this region compared to the baseline, reflected in a slightly higher radial flux density on teeth aligned to the rotor d-axis than the baseline.
- The single layer on the 'V' topology has a unique force profile compared to the dual-layer topologies reflecting the more trapezoidal shape of the flux waveform having only 1 magnet layer produces.
    - The high flux density at the top of the magnet flux barrier closest to the rotor outer diameter has a clear influence on the distribution of the flux density across any tooth in alignment with this region producing sharp changes in flux density, observed as high peaks or "horns" as the flux seeks to bridge the air gap rather than the highly saturated steel at the magnet edge.
    - The highly saturated region combined with the flux barrier creates imbalances across the tooth aligned with the region; when the rotor is moved 30° from start position high levels of radial force but low tangential force vs. the other 3 topologies is observed, conversely very high tangential but relatively low radial forces at the 60° position.
- The dual layer bar topology is more in line with the delta and baseline topologies in the force characteristic recorded using the force probe. However, notable differences can be observed.
    - The peaks at the magnet tips of the 2 layers are out of phase with the delta and baseline reflecting the different magnet pitches the layers have compared to the other machines.
    - The saliency of the machine due to the q-axis flux paths at $\beta = 45°$ produce strong tangential flux densities, in particular in the force calculations at when the rotor is the 30° and 45° from the start position but lower radial flux densities.

Overall, it can be seen that the rotor geometry creates variations in the tooth forces and in particular features within the rotor core sat closest to the air gap have a strong influence on the forces the tooth experiences as the rotor spins across the air gap from it.

7.5 Comparison of vibratory and ERP performance

The final aspect of the topologies is a comparison of the vibratory performance. This utilises the model shown in Chapter 6 with the EM forces from the different machines applied to the 3D mechanical model. As was discussed in Chapter 6 the machines can be represented as quarter models but require the stators to be rotated half a slot pitch to avoid issues with the symmetry multiplier. Fig. 7.5.1 shows the 4 topologies set up and ready for simulating.

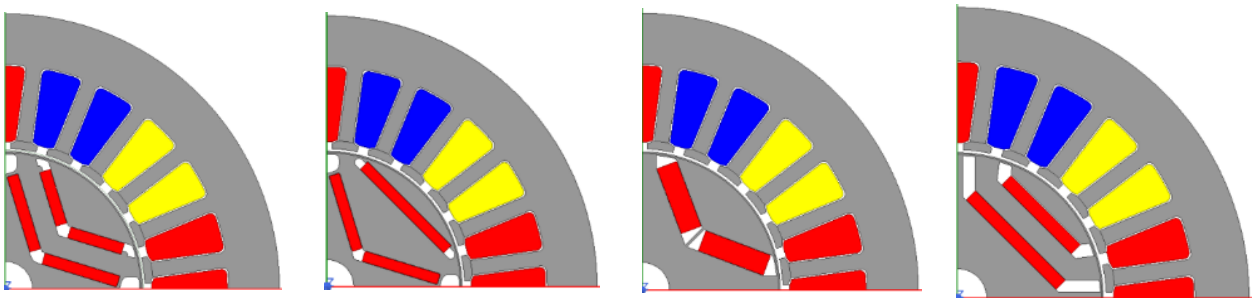

(a) Baseline (b) Delta (c) Single layer 'V' (d) Dual bar

Fig. 7.5.1 ¼ models of each topology correctly orientated for harmonic force calculation.

The topologies are applied to the mechanical model developed in Chapter 5 in the same method as described in Chapter 6. The major difference here is that this comparison is between different FE models, rather than case where the developed model was being compared with the experimental results. There are no physical limits to the machine like the imposed speed limit - meaning the machines can be operated to much higher speeds. Two aspects will be studied:

- Vibratory performance.
- Equivalent radiated power (ERP).

The vibratory performance uses the same setup as shown in Chapter 6, and the acceleration "probe" location is shown in Fig. 7.5.2 (a). The ERP tool within ANSYS® estimates the radiated noise from each machine and requires that the external faces of the motor are selected, as shown in Fig. 7.5.2 (b).



(a) Acceleration probe location (b) Exterior faces for ERP calculation

Fig. 7.5.2 Set up of 3D model for calculated vibratory and ERP comparison.

Whilst there are no real limitations to the machine speeds or loads there is a significant limitation with the PC running the simulations; the FE models required are extremely large in size (<50GB), taking very large amounts of processing time and quickly filling a hard drive leading to errors. To compare 4 machines at the

same resolution as the comparison between the baseline and measured data would require a very high level of storage and computational time so to mitigate this the resolution was limited. Given the objective is to compare the relative performance of each machine against the baseline line then provided each model uses the same settings then this is a fair compromise.

7.5.1 Vibratory performance comparison

3 speeds are compared, one in the constant torque region (3000rpm), one in the flux weakening region (6000rpm) and one in the very high-speed region (9000rpm). The machines are operated at full load and the results can be seen in Fig. 7.5.3.

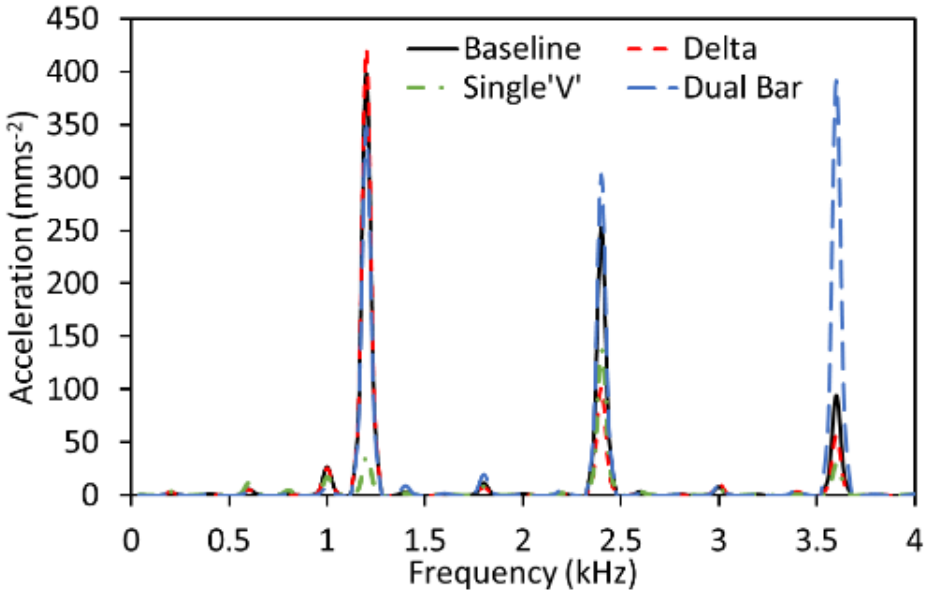

(a) 3000rpm, full load

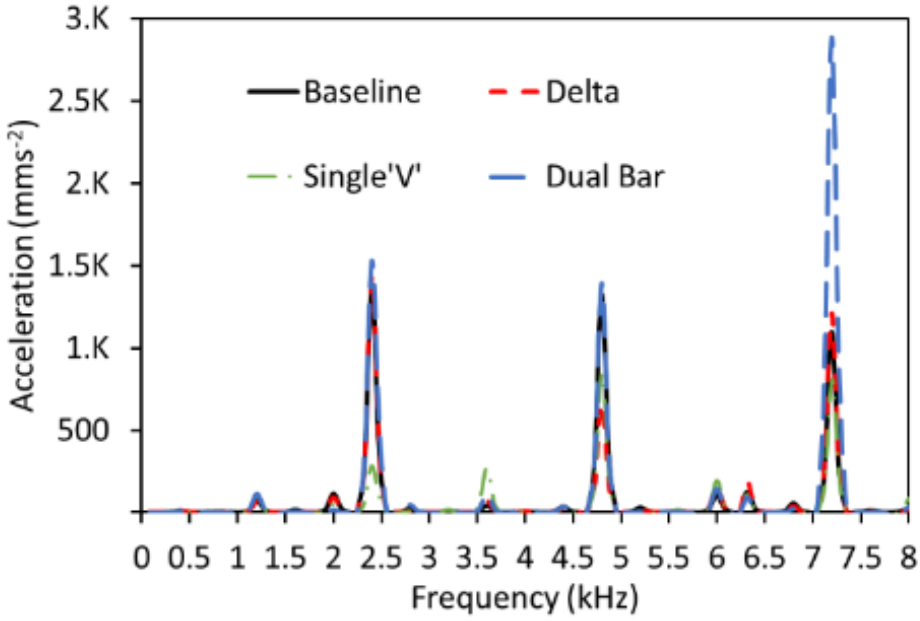

(b) 6000rpm, full load

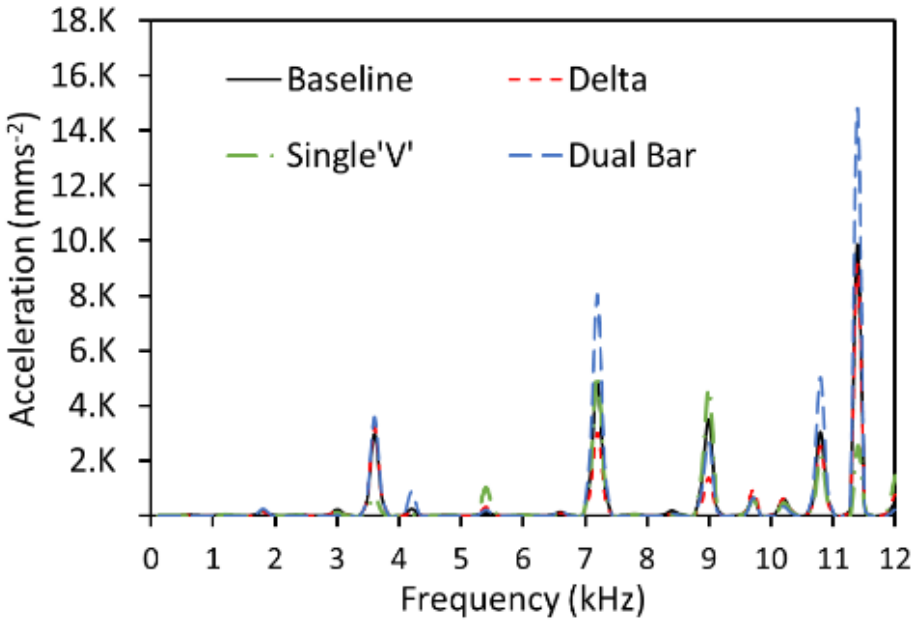

(c) 9000rpm, full load

Fig. 7.5.3. Comparison of the vibratory performance of the 4 machines at full load and 3000rpm, 6000rpm and 9000rpm.

Table 7.5.1 compares the amplitudes in Fig. 7.5.3.

Table 7.5.1 Key frequencies and amplitudes of vibratory performance comparison.

Speed (rpm)	Baseline		Delta		Single 'V'		Dual Bar	
	Freq (Hz)	Acc (mms-2)	Freq (Hz)	Acc (mms-2)	Freq (Hz)	Acc (mms-2)	Freq (Hz)	Acc (mms-2)
3000	1200	398.8	1200	422.32	1200	37.1	1200	348.1
	2400	253.3	2400	102.2	2400	137.1	2400	302.9
	3600	94.5	3600	56.5	3600	30.0	3600	391.65
6000	2400	1364.1	2400	1427.2	2400	285.7	2400	1531.7
	4800	1325	4800	665.79	4800	844.9	4800	1393.1
	7200	1096.8	7200	1211.1	7200	806.8	7200	2888
9000	3600	2967.2	3600	3240.2	3600	724.7	3600	3607.7
	7200	4862.2	7200	3018.4	7200	5161	7200	8061.5
	9000	3482.2	9000	1378.1	9000	4651.9	9000	2686.4
	10800	3034.4	10800	2589.3	10800	2195.4	10800	5048.3
	11400	9856.5	11400	9146.2	11400	2550	11400	14835

From the results the general trend of the baseline and the Delta following each other that has been observed through the entire study continues with the vibratory performance although the baseline appears to show higher amplitudes at the $24f_e$ frequency at 3000rpm and 600rpm. The dual bar shows similar amplitudes at the main ripple frequency ($12f_e$) for all speeds; however, it shows the highest peaks at the 2nd and 3rd ripple harmonics at 3000rpm and 6000rpm and at the 4th harmonics at 9000rpm. Clearly, a calculated machine mode sits at around 11400Hz with all 4 machines providing high amplitudes.

The single layer 'V' machine shows very low vibration amplitudes relative to the other machines only exceeding the other machines at the 3rd harmonic of the ripple frequency at the high speed 9000rpm.

From these results, it can be seen the single layer 'V' has the best vibratory performance compared to the other topologies.

7.5.2 Comparison using ERP level waterfall diagrams

An effective way of comparing the relative machine performance is to use an equivalent radiated power waterfall diagram. This tool estimates the radiated structure sound power versus the rotor RPM from the calculated surface vibrations of the machine structure [ANS19]. ANSYS® calculates the ERP as follows [ANS19].

$$ERP = \frac{1}{2}\rho_0 c \sigma_{rf}(f) \iint_s |v_n|^2 ds \tag{7.1}$$

where *c* is the speed of sound (34.325ms^{-1}), ρ_0 is the mass density (1.2041kg/m^3), σ_{rf} is the radiation factor (set to 1) and v_n is the normal velocity of the vibrating structure.

The equivalent radiated power level is expressed as [ASN19]:

$$ERPL = 10 \log\left(\frac{ERP}{W_{ref}}\right) \tag{7.2}$$

Where W_{ref} is the reference sound power (equal to 10 -12W)

This comparison was not possible with the experimental data. However, in this section the comparison is against the FE model of the baseline so the relative performance of each rotor design versus the baseline machine can be compared. To work properly a wide speed band is best so speeds from 1500 to 10500pm stepped in 1500rpm intervals are applied. The resultant waterfall diagrams are shown in Fig. 7.5.3.

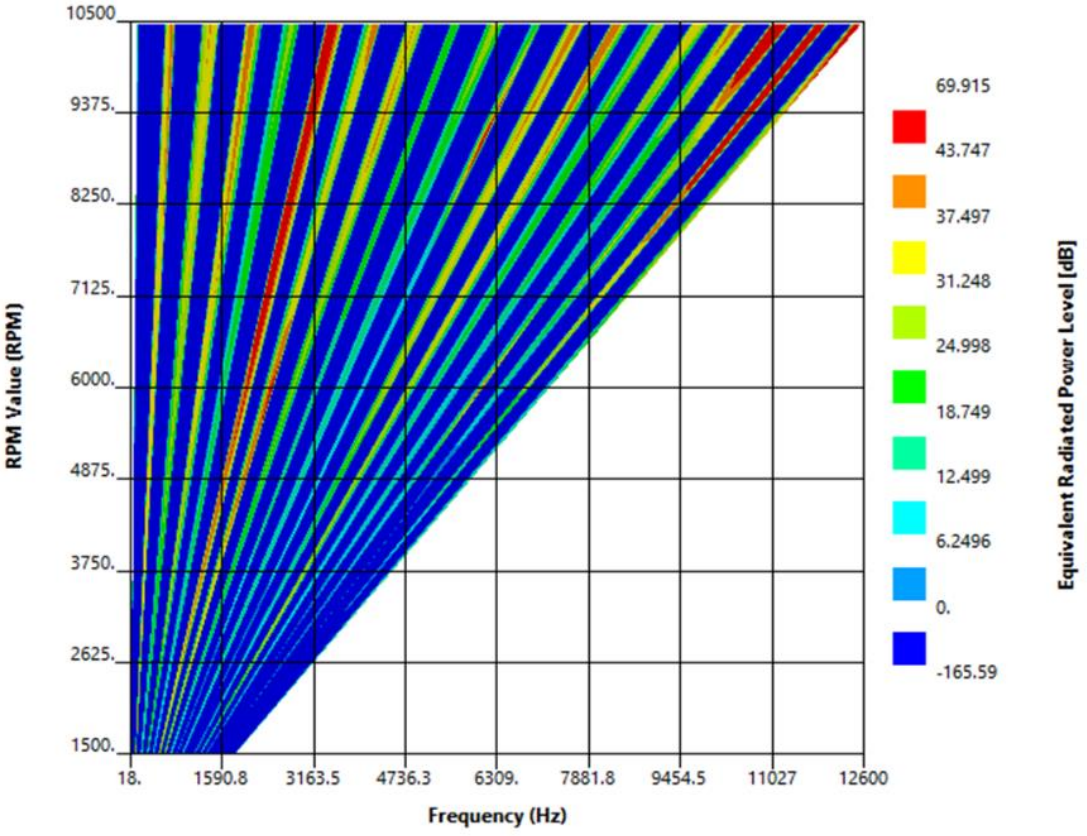

(a) Baseline machine

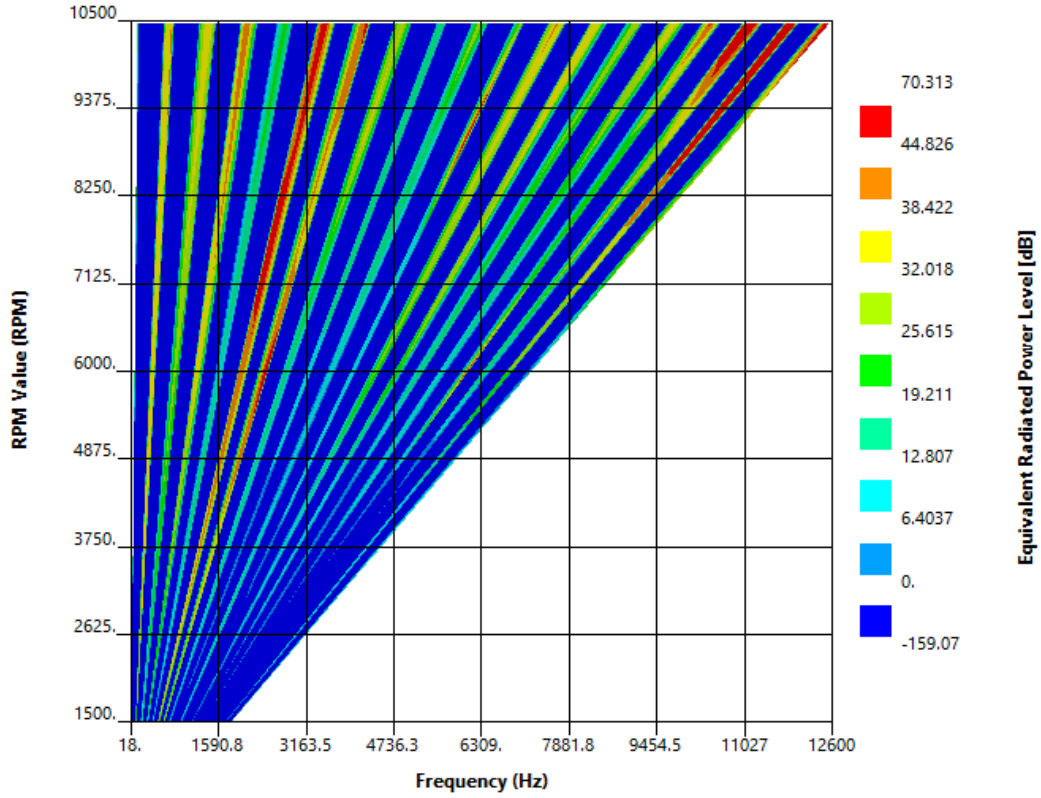

(b) Delta topology

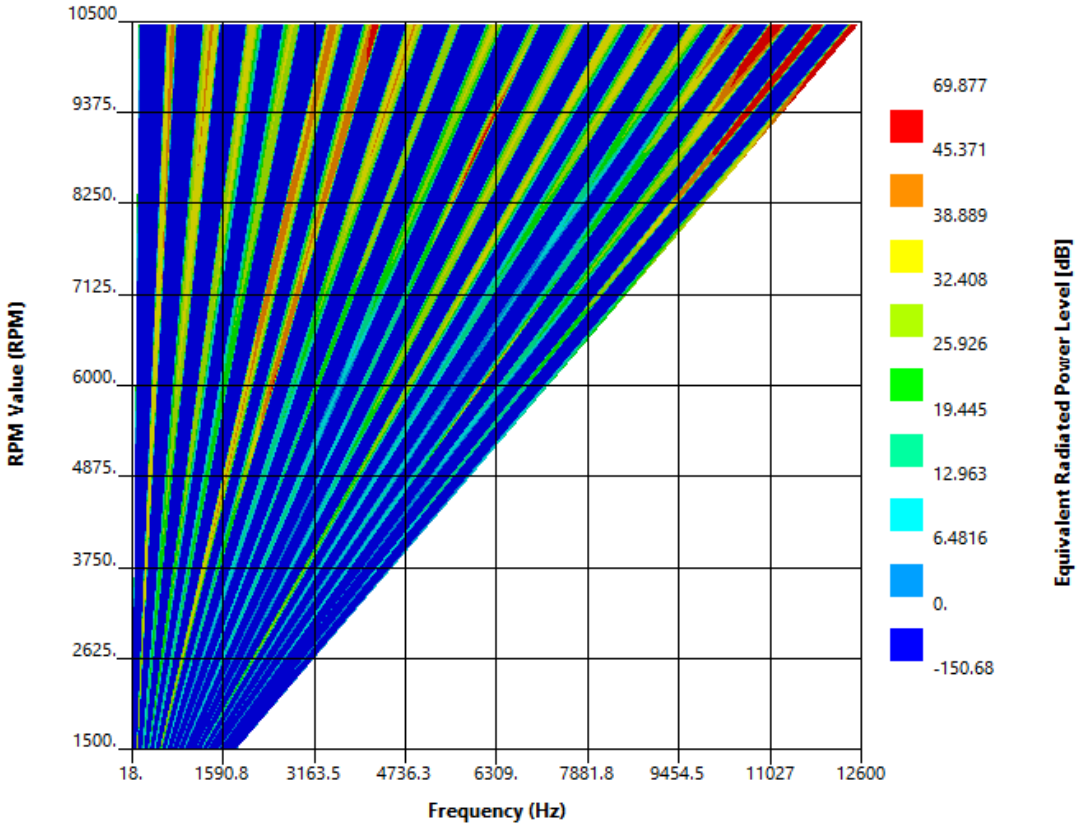

(c) Single 'V' topology

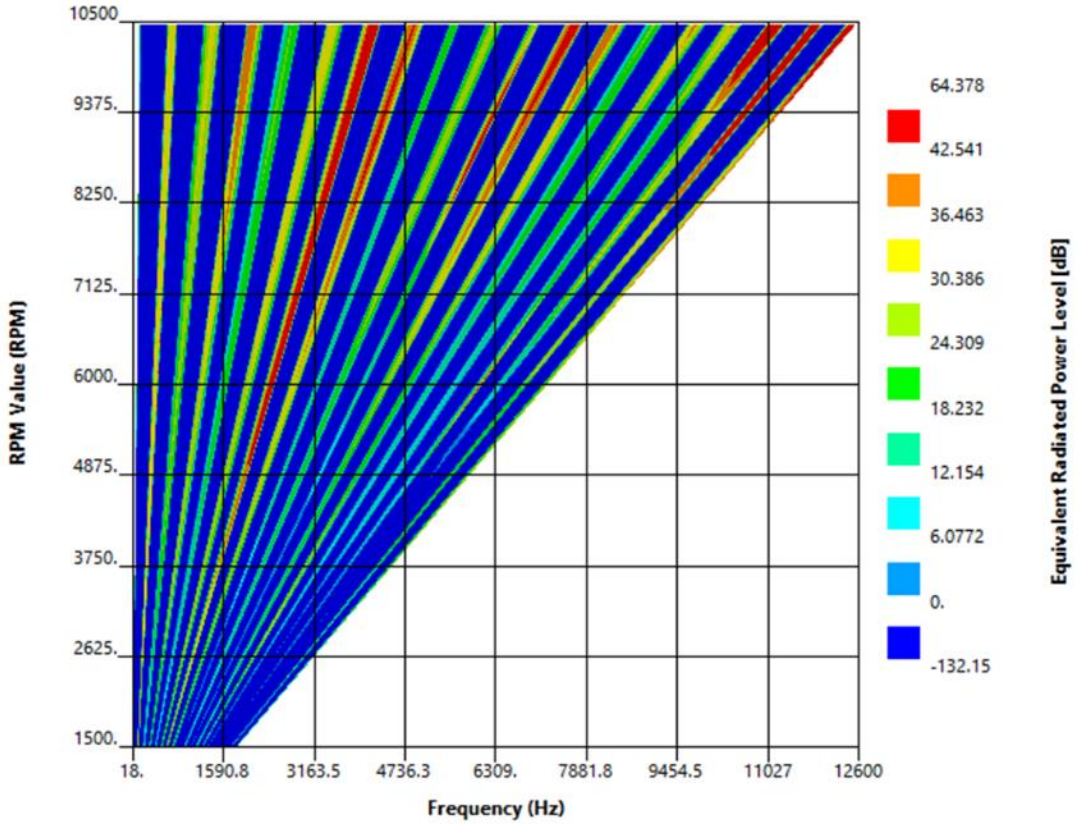

(d) Dual bar topology

Fig. 7.5.3 ERPL waterfall diagrams for the 4 machines designs.

Care should be taken with the results for the Dual bar topology, ANSYS® automatically sets the scale for the results and the maximum ERPL for the Dual bar is 64.378 dB compared to ~70dB for the other machines.

All machines see high noise bands from around 10kHz to 12.6kHz in the very high-speed region with the dual bar seeing a slightly lower maximum. The Delta and the Baseline once again match very closely with little to differentiate between the machines. Whilst the Dual bar has the lowest maximum it shows a number of higher noise bands in the mid-frequency range at higher speed, between 4.7kHz to 7.8kHz at speeds exceeding 3000rpm., reflecting the high vibratory harmonics observed in the previous vibration calculations. The single layer 'V' follows the trend from the vibratory results by displaying a starkly different trace to the other machines with only the concern region at the top right of the waterfall diagram showing similar levels to the other machines, highlighted as a machine mode in the vibration testing. All the calculated frequency bands show much lower decibel levels than the other machines. This perhaps reflects the significantly lower ripple torque calculated during the FE analysis.

7.6 Summary of topology study

Four electric machine topologies common to EV traction motor applications were studied and designed such that they matched the baseline machine as closely as possible in all aspects except for the rotor topology design; this enables a fair comparison of the machines and ensures any differences are due to the rotor design.

Once developed the four topologies were run through a comprehensive series of FE analysis from magnetostatic flux distribution through to multi-physics modelling of the vibration and ERP performance of each machine, using the mechanical model developed previously in this thesis. The general conclusions of the study are:

- The delta type topology matches the dual layer 'V' topology very closely with only minor differences in a few aspects such as slightly lower cogging fundamental and small differences in radial forces on the teeth.
- The Dual bar type topology showed initial promise with competitive performance in terms of lower magnet volume and lower cogging torque, however it exhibits a high ripple rate at increased current angle levels which is reflected in higher vibratory harmonic components and calculated noise, in particular at high speeds (>6000rpm).
- The single layer 'V' initially showed some concerns with high EMF harmonics however very low cogging and ripple torque results in the lowest vibratory and noise results out of the four machines by a good margin.

It can therefore be seen that with finer design optimisation of the magnets and magnet end barriers of the single layer 'V' to mitigate the high region of flux saturation at the magnet tips the topology would be the best-balanced design for this machine.

8 General conclusions

In this thesis, an electromagnetic and mechanical model of a 20kW IPMSM machine has been developed using empiric data from detailed static and dynamic measurements of a prototype baseline machine. The developed model shows good alignment to the empiric data from the prototype machine allowing the model to act as a baseline or datum from which to compare the effects of different rotor designs on the overall performance of the machine providing good confidence in the results.

As was covered in detail in chapter 1 the development of these models requires a multi-physics approach to the development and having to deal with all aspects from how to efficiently represent the orthotropic core materials to the effects of changing the PWM frequency on the machine. During this process, 4 common themes that interlinked the work came to light:

1. Effect of control and strategy switching strategy on vibration.
2. Influence of the machine structure and representation of the materials on the modal performance of the machine.
3. Issues with linking the electromagnetic and mechanical finite element packages.
4. Influence of common rotor topologies used in EV drivetrain applications on both electromagnetic performance and vibration.

This chapter will briefly summarise each of the above themes, followed by future work raised by the study.

8.1 Effect of control and switching strategy on vibratory performance

8.1.1 Influence of switching strategy and frequency

During the measurement of the dynamic vibratory performance of the machine, it was quickly observed that the PWM was a large contributor to the vibratory performance. In addition to the contribution from the switching frequency, f_c, two side bands at f_c +/- $3f_e$ were observed, as highlighted in Fig. 8.1.1.

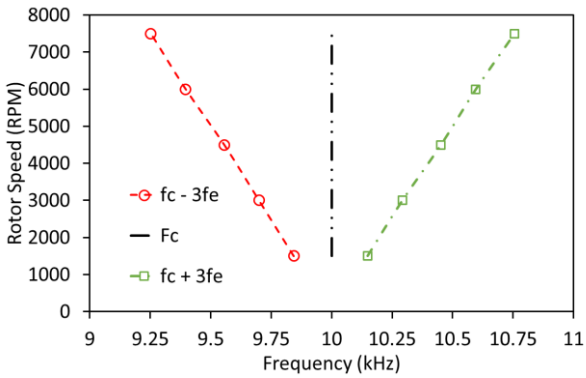

Fig. 8.1.1 Upper and lower PWM frequency bands detected at different speeds.

The characteristics of the side bands were initially difficult to understand. Below 3000rpm, the side bands are insignificant, they can be found if looked for but do not present any real issue. Beyond 3000rpm, the

upper side band (f_c+3f_e) begins to interact with one or more machine modes until reaching a peak at 6000rpm when the sideband is ~10.6kHz. Increasing the speed to 7500rpm, the amplitude begins to drop, a good indication that the band has passed beyond the mode.

The source of the side bands was found to be due to a 3rd harmonic of the electrical frequency that is deliberately added to the machine due to the space vector PWM (SVPWM) control used. This control technique was shown to be popular for EV drivetrain applications as adding the 3rd harmonic "flattens" the sinusoidal waveform from the drive effectively giving additional overhead on the voltage limit. This additional voltage overhead effectively increases the base speed of the machine, reducing the required flux weakening current and increasing efficiency. The cost of this is the resultant air gap flux harmonics which in this machine interacts with a high frequency mode of the machine.

The PWM frequency was adjusted to 8kHz and 12kHz and the machine operated at a range of speeds and torques to see what effect this had on the machine. It was found that:

- When F_c = 8kHz, much of the high peaks around the PWM frequency disappeared, indicating a lower number of machine modes sit in this frequency band.
- When F_c = 12kHz, some of the highest peaks measured in the testing was found. It appears that the upper band at this switching frequency is close to a breathing mode (mode 0) as all sensors showed very high amplitudes.

The study highlights the importance of carefully selecting the PWM switching frequency according to both the need to reduce switching loss and mitigate vibratory issues.

8.1.2 Influence of flux weakening control.

During the measurement, it was shown that at all speeds and loads as the current angle increased from 0° towards the MTPA point the amplitudes of the measured accelerations dropped, as illustrated in Fig. 8.1.2.

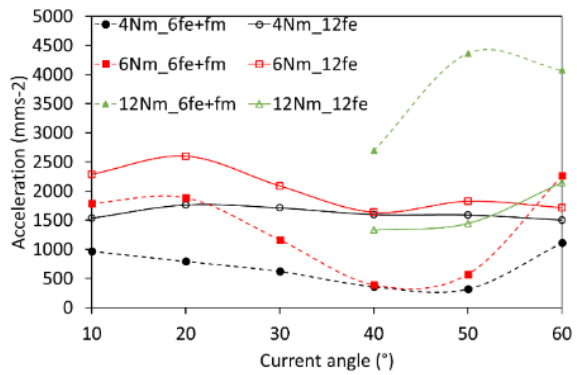

Fig. 8.1.2 Acceleration of key harmonics at different torques and current angles at 1500rpm.

The trend is stark at higher torques as the higher current means higher forces are encountered but in all cases the acceleration reaches a minimum at a current angle of 40°. The reasoning for the drop is seen during the tooth force analysis in chapter 3. Shifting the current angle to the optimum angle for the reluctance component causes the flux in the rotor core to move in a more tangential direction towards the q-axis,

following the low reluctance paths of the inter-magnet layer and upper steel region, as illustrated in Fig. 8.1.3 which compares the flux distributions in the machine with current angles of zero and 45°.

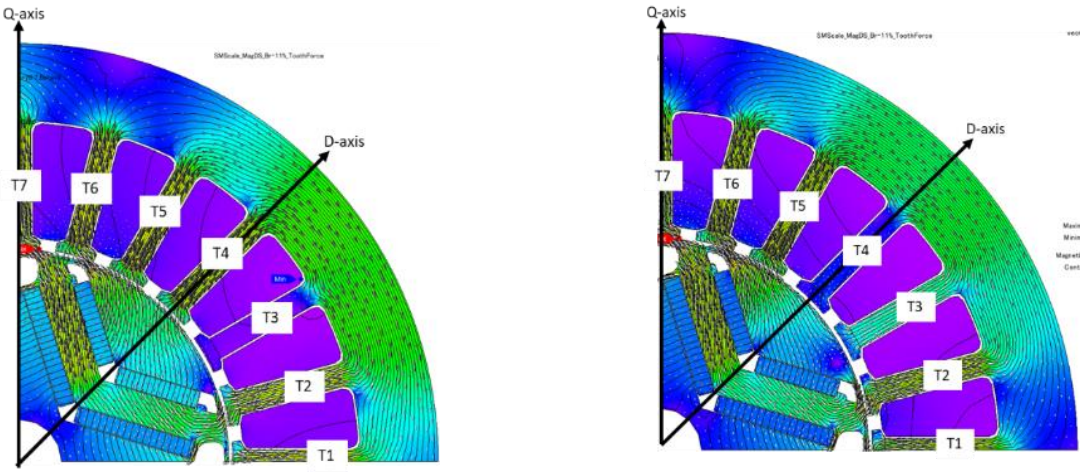

(a) β = 0°. (b) β = 45°.

Fig. 8.1.3 Comparison of flux distributions at initial position (rotor = 0°) with a rotor speed of 1500rpm and maximum current (I= 26.7A_{rms}), β = 0° and β = 45°.

This creates a net boost in the tangential flux component (higher torque) but also a drop in the radial flux component. This analysis is confirmed in the physical measurement of the machine. Pushing the current angle beyond the optimum however sees a sharp increase in radial forces, as observed in the testing however also increases the risk of demagnetising the PMs. The matching of the measured behaviour with that of the FE model gives good confidence in the model performance.

8.2 Modelling the machine structure

The machine structure was shown to be asymmetric along the longitudinal axis of the machine, primarily due to the design of the cooling system. Fig. 8.2.1 shows an exploded view of the prototype machine.

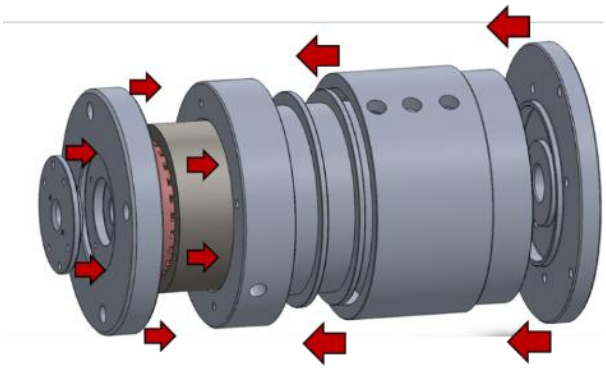

Fig. 8.2.1 Y-Z baseline machine structure (exploded view).

Whilst this approach represents a good solution for fabricating a prototype machine, the structural complexity necessitates a 3D FE model to replicate. Not only that, but the complexity also means that modelling the structure is difficult; to simply import a 3D shape of the machine into an FE package would result in large errors and the large number of variables that influence, and this means it would be difficult to trust the resultant model.

8.2.1 Impact hammer test results

Given the availability of the prototype machine and a spare stator from the original project, it was decided that the machine would be measured using an impact hammer test at different stages of assembly, the results of which could be used to build the complex 3D model in various stages. The hammer test results are shown in Fig. 8.2.2.

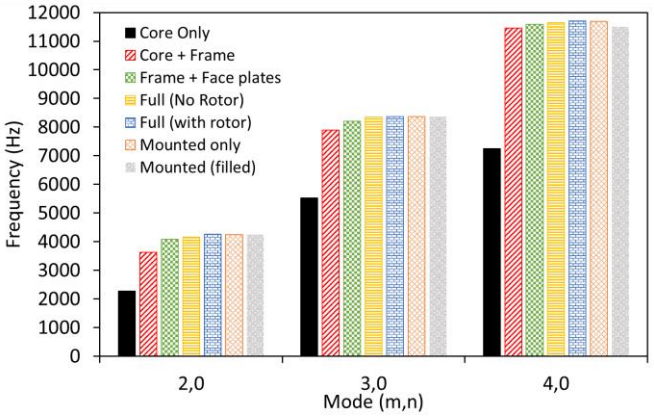

Fig. 8.2.2 Results of impact hammer tests on the machine at increasing levels of assembly.

It can be seen that the machine was measured from the stator core all the way through to being mounted and setup ready for dynamic testing.

- Moving from the core only to the wound core in the frame shows a very large increase in modal frequencies, reflecting the large increase in stiffness.
    - Unfortunately, the scenarios of the wound core and unwound core in the frame could not be tested although they would be very useful.
- Adding the face plates proved a further increase step in stiffness, although not as large as moving from the stator only to the wound stator in frame.
- Assembling the rotor in the machine added a small increase in stiffness, but the rotor does not provide much contribution.
- Mounting the machine has minimal impact on the radial modes. However, the addition of the coolant fluid does see a perceptible drop in frequency, indicating the mass has some influence.

8.2.2 Modelling the lamination materials

The stator and rotor cores are both formed of laminated magnetic steel plates separated by very thin layers of material of a very high electrical resistance to reduce the effects of eddy currents on the machine. This means mechanical attributes such as the Young's modulus or Poisson's ratio are very different in the radial plane (X-Y) than the longitudinal plane (Y-Z) which makes modelling the mechanical attributes of the core particularly challenging. The solution found was to utilise a method of representing composite materials used in mechanical engineering applications. The primary benefit is that the orthotropic material properties can be calculated and inputted into the FE tool, and the resultant material applied to a simple 3D shape for the

stator. Key to the calculation is obtaining the mass density, Young's modulus, and Poisson's ratio of the material from the lamination supplier and the stack factor of the core to understand what the ratio of lamination steel to epoxy is. The material parameters were obtained from the supplier, but the stack factor was given as an estimate. This presented a problem as stack factor is a critical component in the calculation of the composite properties, in particular the longitudinal stiffness which is non-linear as illustrated in Fig. 8.2.3.

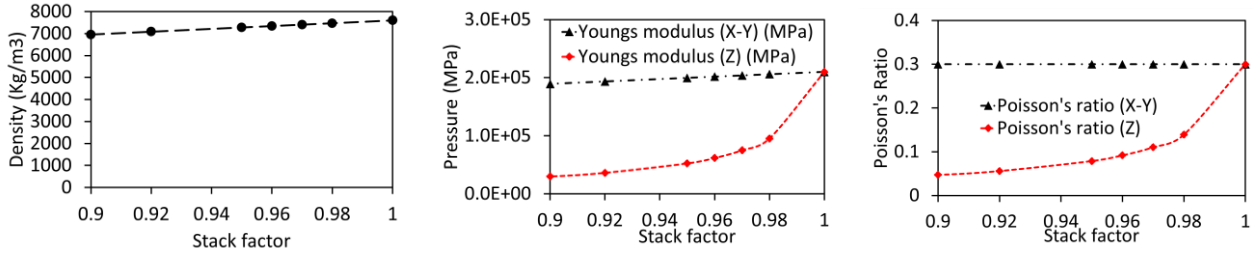

(a) Mass density (b) Young's modulus (c) Poisson's ratio

Fig. 8.2.3 Influence of stack factor on the mechanical properties of the orthotropic composite.

A 3D FE model of the stator was made and composite materials representing stack factors of between 0.9 and 0.98 were calculated and added to the FE tool allowing a parametric sweep to be run, the results of which can be compared with the measured data. This is shown in Fig. 8.2.4.

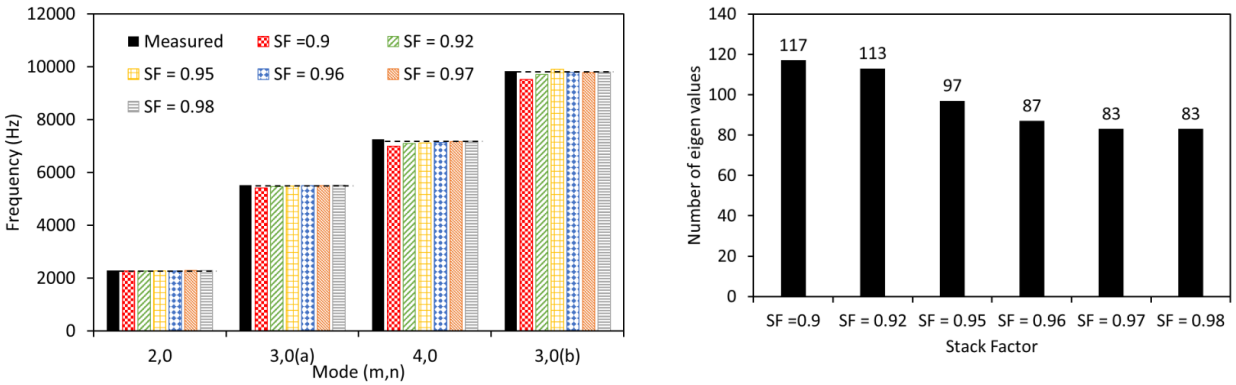

(a) Modal frequencies (b) Number of eigenvalues (12kHz sweep).

Fig. 8.2.4 Comparison of the FE stack factor parametric sweep and the measured results.

From the results it can be seen that a stack factor of 0.97 or 0.98 aligns well with the measured data. In addition, the FE tool encountered a higher number of eigenvalues at the lower stack factors owing primarily to a far higher number of tooth modes due to the lower longitudinal stiffness of the part. A stack factor of 0.98 was the final chosen value which gives the orthotropic properties shown in Table 8.2.1.

Table 8.2.1 Orthotropic properties of composite representation of stator lamination stack.

Stack factor	Mass density (kg/m^3)	E_{xy} (MPa)	E_z (MPa)	Poisson ratio (X-Y)	Poisson ratio (Z)	G_{xy} (MPa)	Gz (MPa)
0.98	7471	$2.06x10^5$	$9.54x10^4$	0.3	0.139	$7.92x10^4$	$3.67x10^4$

8.2.3 Modelling the windings

The windings share the same concern with the lamination cores in that they are have non-homogeneous material properties. The baseline machine is a distributed wound machine so has the added issue of having large end windings which are a very complex shape and further complicated by the hand-wound nature of the winding process and the method of binding and potting the end windings. As with the laminations this is a problem almost as old as the machines themselves and so a good solution was found in the literature [KI02]. Within the paper it was shown that a best fit curve using the slot fill factor could be used to determine the Young's modulus of the winding. The mass density was calculated as a composite using the same method as the lamination core, based on the assumption that the potting material filled 100% of the slot not occupied by windings. The derived material properties are shown in Table 8.2.2.

Table 8.2.2 Calculated material properties for winding equivalent composite.

Mass density (kg/m^3)	Young's modulus (MPa)	Poisson's ratio
4668.5	0.628	0.343

The next key point is how to represent the windings. 4 scenarios were proposed, as illustrated in Fig. 8.2.5.

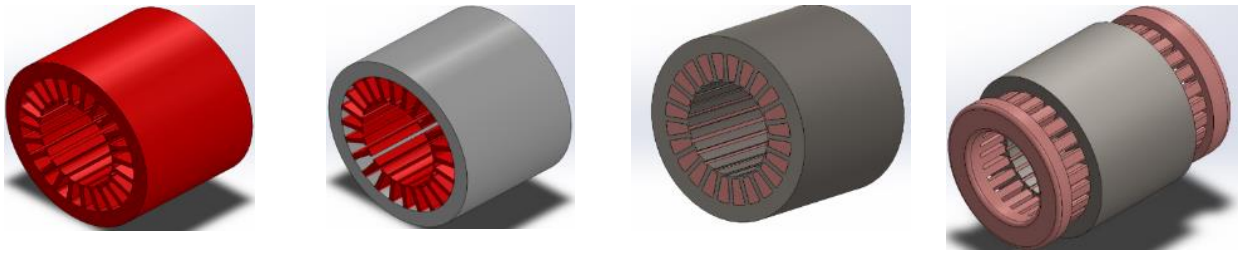

(a) Mass of windings added to stator core

(b) Mass of windings added to stator teeth

(c) Windings modelled in slot only

(d) End winding (simplified model)

Fig. 8.2.5 Methods of representing the windings.

The end winding model in Fig. 8.2.5(d) is based on the measurements of the prototype machine taken when the machine was dissembled for the impact hammer test. Attempts at a more accurate model proved unwieldy and overly complex for the FE so a simplified winding model resembling a squirrel cage from an induction machine rotor was developed. The calculated performance of each model is shown in Fig. 8.2.6 and shows that the scenarios of the windings in-slot and the end winding model both show good alignment to the measured modes.

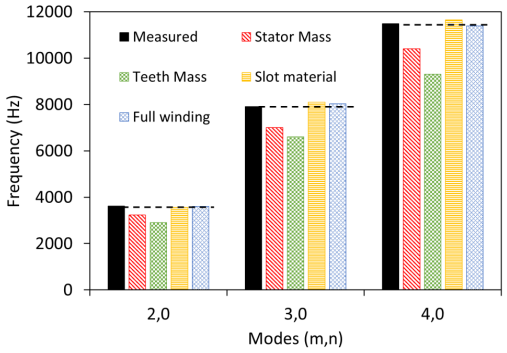

(a) Comparison of key circumferential nodes

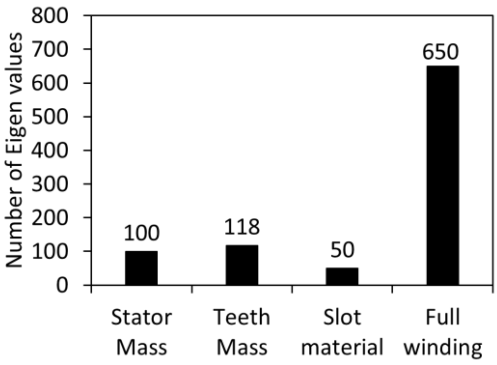

(b) Calculated number of eigen values (12kHz sweep)

Fig. 8.2.6 Comparison of modal characteristics of the four representations of the windings.

From Fig. 8.2.6(b) it can be seen that for the full winding model the alignment to the measured results is good but the number of eigen values generated during a 12kHz sweep is extremely high reflecting the number modes the end windings encounter. Given the similar performance versus the measured and the lower processing overheads the windings in slot only model (Fig. 8.2.5(c)) was selected.

8.2.4 Building the full assembly model

With the laminations and windings fixed and showing good alignment with the measured results the 3D model could be developed, following the same sequence as the measured test. Before this could begin, the excessive processing times made it clear that the 3D model had to be simplified to reduce the processing overhead of the model. Non-essential complex geometry and mesh optimisation was undertaken to find the best balance between speed and fidelity. To highlight the improvement the model of the machine with the wound stator in the case in its initial complex shape was compared with the simplified shape with and without optimised mesh, and the results can be seen in Fig. 8.2.7.

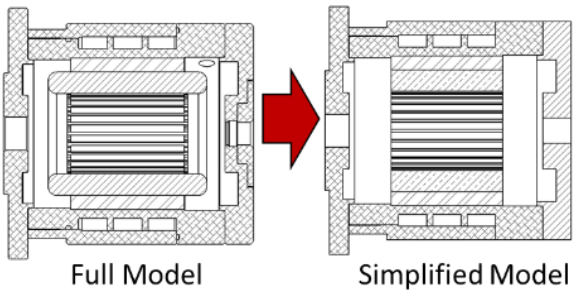

(a) Simplified 3D model of machine structure.

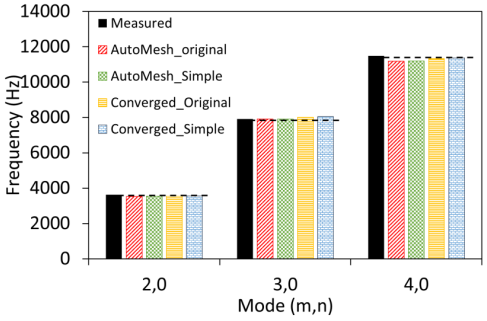

(b) Comparison of circumferential modes for the wound stator in case model.

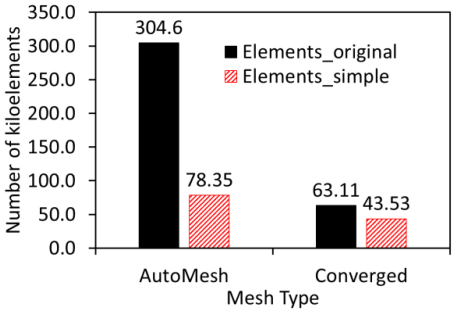

(c) Mesh elements in compared models.

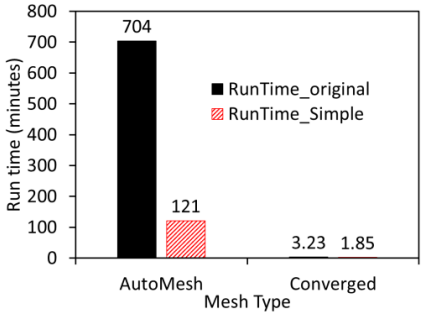

(d) FE calculation run time for compare models.

Fig. 8.2.7 Comparison of complex and simplified models with automatic and optimised meshes.

It can be seen that all the models tested showed good alignment with the measured data. However, when looking at the mesh elements and resultant run times the differences are stark. With the non-optimised mesh on the complex model the run time was in excess of 10 hours, simplifying the model led to a very large drop-in run time, around 2 hours. This run-time, whilst a marked improvement on the initial model, was shown to be very poor compared to the use of an optimised mesh, which saw a time of 3.23 minutes with the complex model and 1.85 minutes with the simple model, respectively.

The simplification of the model had some drawbacks, the primary one being that the bolt holes used to align and constrain the model had been removed making “attaching” the front and rear face plates more complicated. Three options were explored, as summarised in Table 8.2.3.

Table 8.2.3 Comparison of different contact methods for the front and rear face plates

Option	Description	Advantages	Disadvantages
Bonded	All mating surfaces linked as if welded or glued with strong epoxy.	✓ ANSYS® default. ✓ Simple to implement, no additional shapes etc.	× Effectively renders assembly as a single structure – too stiff.
Weld tool	Two points matching points on each mating surface picked and act like a spot weld.	✓ Strong, localised bond. ✓ Can be applied to multiple points on shape. ✓ No additional shapes or meshing required.	× Requires common connection point between parts (mesh node or geometry). × If using mesh, script required. × Single linkage point.
Bolt face	Bolt faces added to mating surfaces and bonded using bond tool to replicate action of bolt bonding face plate.	✓ Allows bonding method applied to specific area. ✓ Better representation of actual bolt interface.	× Extra geometry required for bolt faces. × Increased model complexity.

Bonding is the simplest method whereas both the weld tool and bolt face method required some modifications to the 3D shape.

- The weld tool worked best when the 3D was physically split to form an intersection at the location of each bolt hole on the main case and face plates.
- The bolt face method initially used 2D circles on the mating faces. However, the shape struggled to mesh; using 3D cylinders inside the shape of the same material solved the issue.

The results of the comparison of the different methods with the measured condition of the model with both face plates attached (no coolant shell or rotor) are shown in Fig. 8.2.8.

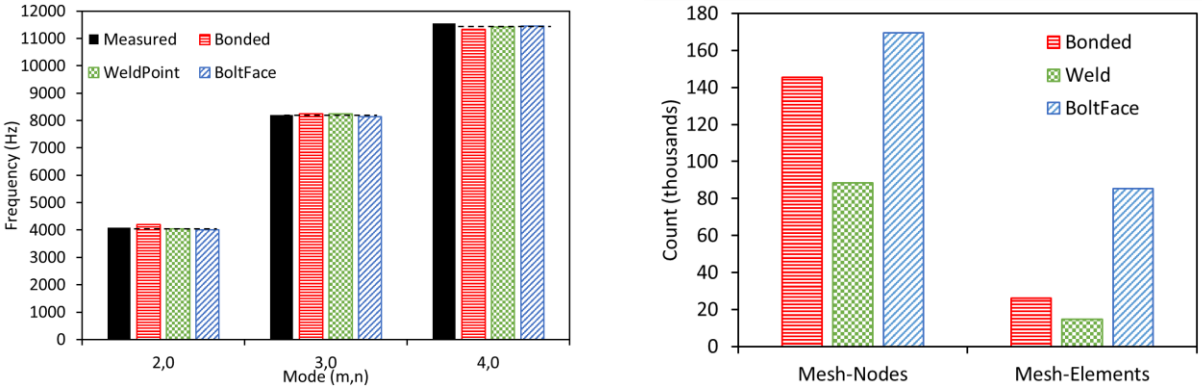

(a) Modal frequencies (b) Mesh complexity

Fig 8.2.8 Comparison of the different contact methods of the face plates and the resultant mesh.

It can be seen that the bonded method renders the structure marginally too stiff for the mode 2,0 and 3,0 and is slightly lower than the measured at mode 4,0. The bolt and weld point methods are closely matched. Looking at the mesh complexity it can be seen that the process of splitting the model to obtain a reliable weld point had the unexpected benefit of dropping the mesh density. Splitting the shape up clearly aided the meshing tool to form a more efficient mesh than the bonded method which did not modify the structure at all or the bolt face which required complex mesh geometry around the cylindrical structures used to provide the interface.

The final aspect to add is the coolant shell shown in Fig 8.2.9.

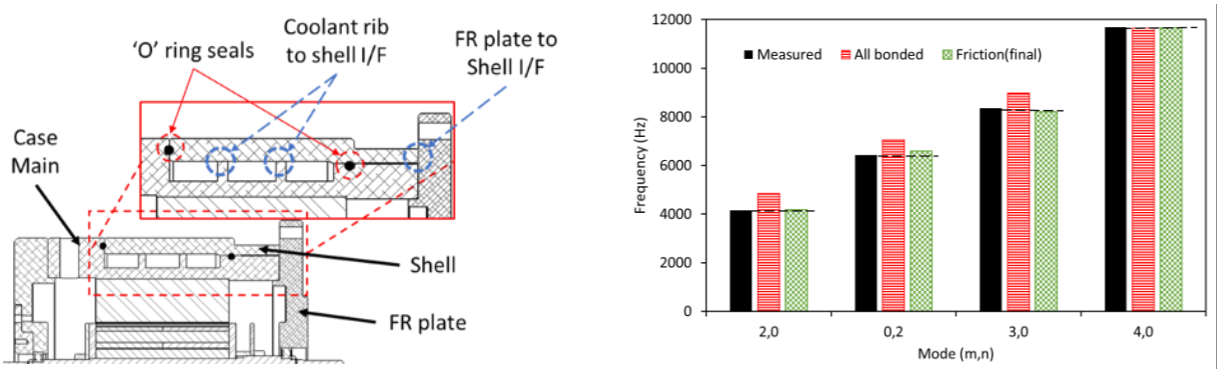

(a) Contact points between coolant shell and machine assembly

(b) Modal frequency vs. measured with all bonded contact type and tuned frictional type

Fig. 8.2.9 Contact points between the main machine structure, front face plate and the coolant shell.

On applying the shape, it was quickly found the bonding method applied by ANSYS® as default rendered the machine too stiff with the calculated modal frequencies significantly higher than the measured results. Manually applying the "Frictional" type of bond allowed the link between the contact points of the main case and the coolant shell to better replicate the fact that the shell is held in place by a friction fit between the 'o' on rings on the rear face of the shell and the front inner bore. The frictional fit allows the coefficient of friction, μ_s, between the parts to be adjusted. A coarse study found varying μ_s between the extremes of 0, 0.5, and 1 meant that the modal performance changed from too stiff ($\mu_s = 1$) to not stiff enough ($\mu_s = 0$). It was shown

that using an empirically derived range of μ_s between nitrile (the 'o' ring) and aluminium (the case) the optimisation tool within the ANSYS® could be utilised to find the optimal μ_s at each contact point. The results are shown in Fig. 8.2.9(b).

The final aspects looked at were the influence of the rotor, mounting the machine and the effects of coolant. Fig. 8.2.10 highlights the findings from each study.

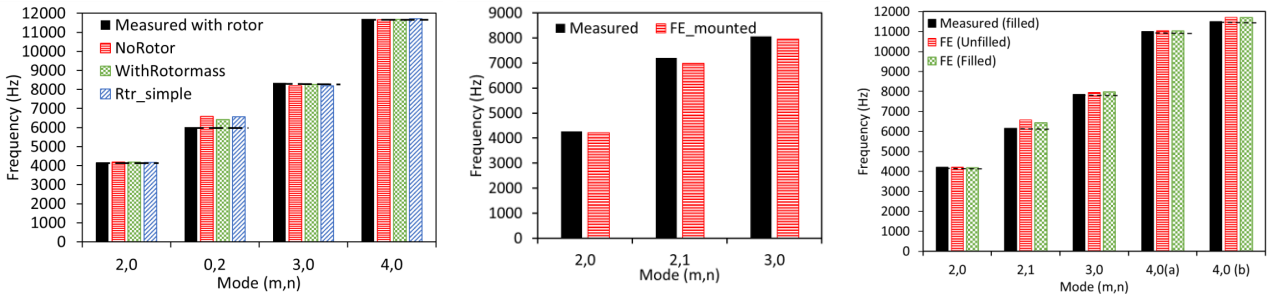

(a) Influence of rotor (b) Mounted machine (c) Influence of coolant as a mass

Fig. 8.2.10 Results of the final phase of the mechanical model development.

From Fig. 8.2.10, it was concluded:

- Adding the rotor as a mass applied to the end plates was found to be an effective method of representing the rotor, a simple model created extra complexity and a large number of eigen modes
- The fixed and cylindrical support methods of representing the link between the face plate of the machine and the mounting bracket for the dynamometer gives good alignment with the measured.
- Adding the coolant as a mass shows a marginal improvement over the model with no coolant so is included in the model; representing the fluid as a mass adds no additional complexity to the model in terms of additional shapes or mesh so is a good solution.

With the final model in place, the last step of the model is to obtain the mechanical transfer function. This is achieved using the Harmonic Response tool of the ANSYS® workbench tool suit. A force tool is applied to the outer casing and data captured from the impact hammer during the impact testing is inputted into the tool. From here the response can be measured, initially the system is undamped so the optimisation tool within ANSYS® is once again utilised, using the measured acceleration as a target (+/-2% error) and the damping factor of 1.47×10^{-2} was found; the resultant response for mode (2,0) is shown in Fig. 8.2.11.

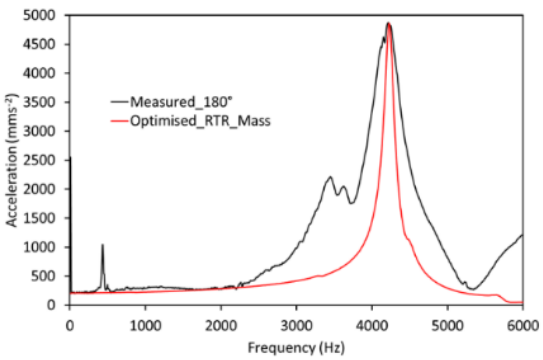

Fig. 8.2.11 Final tuned system response of FE model compared with measured results.

8.3 Linking the electromagnetic FE model to the mechanical model

As established, forces on the stator are due to the interaction of the magnetic flux density harmonics in the air gap from all the different facets of the machine design and operation whereas the reaction to the forces is dependent on the geometry, materials, and assembly of the machine structure. These problems are both solved using very different FE tools so how to link these very different tools is a core problem in this thesis. Three primary methods are employed and summarised in Table 8.3.1:

Table 8.3.1 Comparison of primary techniques of calculating tooth forces

Option	Description	Advantages	Disadvantages
Analytical	Air gap flux density is calculated analytically using equivalent magnetic circuit and forces calculated with Maxwell stress tensor.	✓ Quick method of establishing forces. ✓ No real requirement for expensive FE software or licenses.	× Models get complex when dealing with slotting or saturation etc. × Prone to errors due to calculation complexity. × Forces need to be manually applied to mechanical model.
Hybrid method	FE method used to calculate air flux density then forces analytically derived using Maxwell stress tensor.	✓ Uses more accurate FE calculations for flux density. ✓ Enables detailed analysis of force distribution on individual teeth.	× Additional effort required to generated force harmonics. × Forces need to be manually applied to mechanical model. × Prone to errors due to need to export calculated forces and apply to mechanical tool.
Full FE or Automated method	FE tool calculates forces, typically using virtual work method then exports force harmonics to mechanical FE tool.	✓ FE tool handles the calculation effort. ✓ Partial model can be used to speed up process time. ✓ Link to mechanical FE tool automated.	× Very expensive software required. × Force calculation methods unclear. × Nodal method sensitive to mesh density. × Difficult to account for design aspects such as skewing – 3D model may be required.

From Table 8.3.1, the hybrid and full FE methods were utilised; the hybrid method allows for more detailed analysis of the tooth forces acting on one or more teeth at different rotor positions and machine loads giving an insight into how the flux density distribution in the air gap and therefore the forces change due to aspects such as current advance angle in flux weakening control or design aspects such as the IPM rotor topology. The full FE method is utilised for the full vibratory simulations as although the calculation methods tend to be proprietary and masked the tool does the work of calculating the force harmonics and then directly exporting them to the mechanical FE tool increasing the efficiency and minimising errors created in the user either manually transferring the forces or writing scripts to achieve the same goal.

8.3.1 Hybrid method

The hybrid method involves drawing a curve in the air gap which is used as the surface onto which the Maxwell stress tensor can be calculated, as illustrated in Fig. 8.3.1.

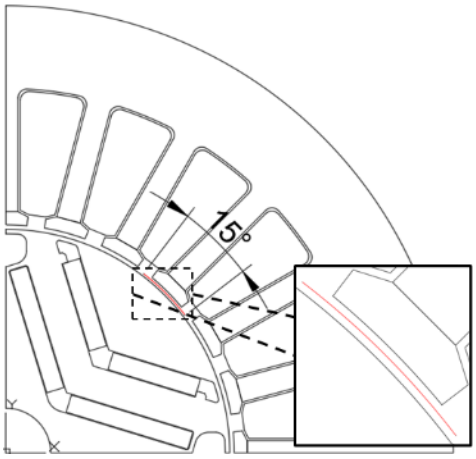

Fig. 8.3.1 Air gap curve location.

The key questions are the length of the curve and its radial position. An investigation into the literature and some experimentation in the FE tool revealed:

- The curve should cover one slot pitch, starting and ending in the mid-slot points either side of the tooth.
    - This ensures the fringe air gap flux which is attempting to avoid the low permeance of the slot gap to interact with the tooth edge is captured.
- The curve should be located in the mid-air gap as the best-balanced solution.
    - Locating the curve on the tooth surface results in concerns with accuracy due to non-linearities such as saturation as well as issues in variations of permanence due to the nature of the mesh at the air gap/tooth tip boundary creating large spikes in flux density.
    - Locating the curve near the rotor surface risks the same problems with the stator tooth surface, as well as the issue that sitting over the slide mesh that moves with the rotor (in a fractional model) means past a certain point the curve “falls off” the mesh so there is no flux density calculated and therefore the forces drop to zero.

8.3.2 Full FE method

For the full FE method, the method recommended by ANSYS® is to split the tooth tips from the main stator such that they form individual objects. The ANSYS® tool then automatically determines all the faces of the tooth that interfaces with the air gap and uses a form of the virtual work method to calculate the edge force density. Fig. 8.3.2(a) shows the tooth tips split for on the 2D FE model and Fig. 8.3.2 (b) shows the forces mapped to the 3D stator.

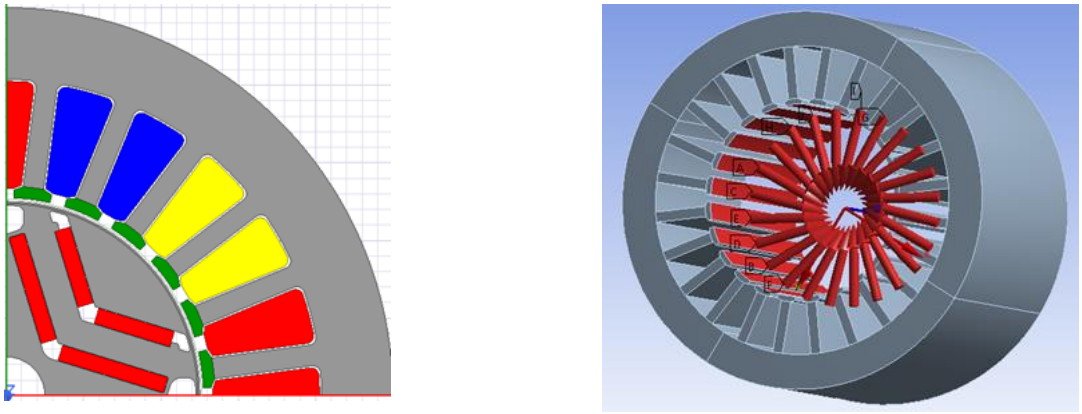

(a) 2D model with tooth tips split (b) Mapped forces on 3D mechanical model

Fig. 8.3.2 Modifications to 2D FE model to capture tooth forces and mapping the forces to the 3D mechanical model.

The symmetrical nature of the machine and the fact it is unskewed meant that the electromagnetic FE model could be represented as a ¼ model and the FE tool would do the job of converting the results to that of a full-sized model. This greatly reduced calculation time; however, care has to be taken with the orientation of the stator along the symmetric boundaries of the model to erroneous spurious force vectors being generated by the symmetry multiplier and also great care must be taken to ensure the co-ordinate systems of the 2D and 3D models match otherwise the tool will attempt to map the forces incorrectly leading to errors and lost time.

8.3.3 Results of full FE method

During the implementation of the full multi-physics model, time limitations meant that full coverage of the MTPA points or similar could not be achieved and thus 4 speed points were chosen: 2 in the constant speed region (1500rpm, 3000rpm) and 2 in the constant power region (6000rpm, 7500rpm). At each speed point the machine was simulated at no load and maximum load and the results compared to the experimental data. Fig. 8.3.3 shows the results for 3000rpm at max torque and 7500rpm at max torque.

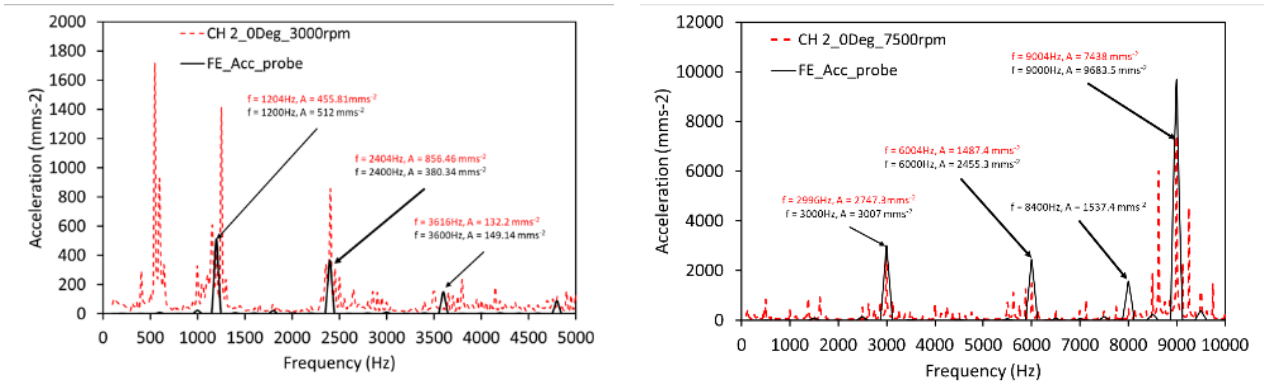

(a) 3000rpm @ 15.3Nm (b) 7500rpm @ 8.6Nm

Fig. 8.3.3 Comparison of low speed and high-speed FE and measured results with machine at full load.

The results show very reasonable alignment at high speed with the key frequencies from the measured results matching well and the amplitudes in reasonable alignment, in particular at the 3kHz ($12f_e$) and 6kHz ($24f_e$) points. The low speed shows more mixed results. The frequencies match well but as discussed in the

chapter the test rig showed high amplitude frequencies at ~580Hz across much of the speed range tested and was picked up in the impact hammer test only when the machine was mounted, indicating some aspect of the test stand or wider rig was excited at this frequency and being picked up by the acceleration sensors. At 1200rpm the model aligns well with the 1204hz component identified in measurement, but both these amplitudes are low compared to the high peak identified at 1254Hz ($12f_e + f_m$) which was a unique characteristic at this speed. The source of this peak was not identified due to the complexity of the setup, but the likely candidates are interactions with a dynamic mode on the rotor or other aspects such as the fluid dynamics of coolant fluid flowing within the casing at full load along with the induced motion on the pipes providing supply and return paths of the fluid. More investigations into this would be useful and is discussed in the next steps later in this chapter.

8.4 Influence of rotor topology on vibratory behaviour

8.4.1 Selecting and matching the different rotor topologies

Given the very large number of variations of rotor topologies available the decision was quickly taken to limit the scope to the most common automotive topologies, which after a review of available data was shown to be four key rotor topologies which are shown in Fig. 8.4.1.

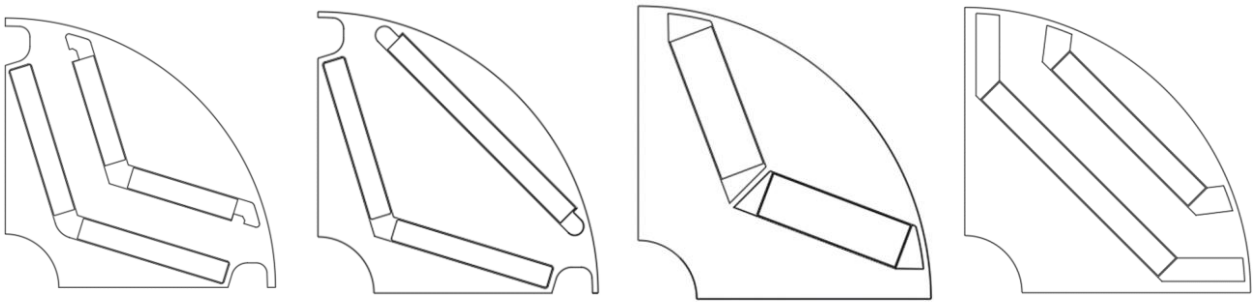

(a) Dual layer ‘V’ (b) Delta (c) Single layer ‘V’ (d) Dual layer bar

Fig. 8.4.1 IPM rotor topologies selected for comparison.

Each of the topologies identified were from a large variety of vehicles; from small city EVs (e.g., BMW i3) to large hybrid SUVs (Lexus LS600). Given the large differences in machine size and design to simply draw each topology and compare the performance is unreasonable as there are simply too many variables to allow a fair comparison. It was decided that the key parameters of the baseline machine including the slot pole combination, stator design and winding design, rotor outer diameter and active length and materials would all be held constant. In addition, the voltage and current limits of the baseline machine are held constant as is the T-N curve envelope. All these aspects ensure that any variation in performance is down to the rotor topologies.

A basic outlay of each topology was derived; the baseline is already a dual layer ‘V’ and the other rotor topologies developed using the baseline as a template and utilising the literature and FE tools. From there a detailed series of optimisation procedures on the magnet geometry of each topology was undertaken which targeted two key performance parameters:

- Average torque of 15.3Nm with an error of +/- 2%
- Minimise torque ripple.

The top 4 designs that match the criteria were fed through a MATLAB based T-N mapping tool to establish which of the designs best aligned to the T-N curve of the machine. The resultant T-N curves are shown in Fig. 8.4.2 with the base speed and maximum torques listed in Table 8.4.1.

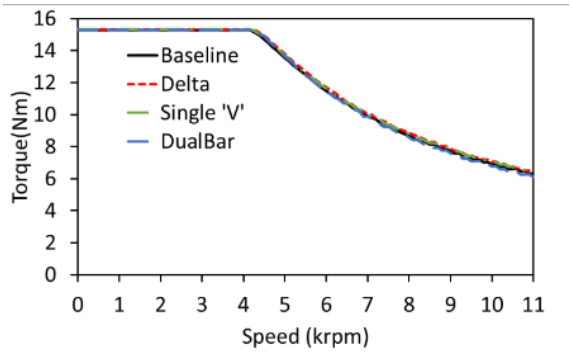

Fig. 8.4.2 Matched T-N curves for all 4 machines.

Table 8.4.1 Comparison of maximum average torque and base speed for the 4 topologies

	Baseline	Delta	Single layer 'V'	Dual Bar
Max average torque	15.3	15.33	15.32	15.28
Base speed	4200	4200	4200	4300

8.4.2 Performance comparison of the 4 topologies

The first aspect to compare is the magnet volume of each topology, being an automotive application cost tends to be a high priority and minimising the use of rare earth materials utilised is desirable both due to the cost and historic instabilities in supply. Fig. 8.4.3 compares the PM volumes of for each rotor topology.

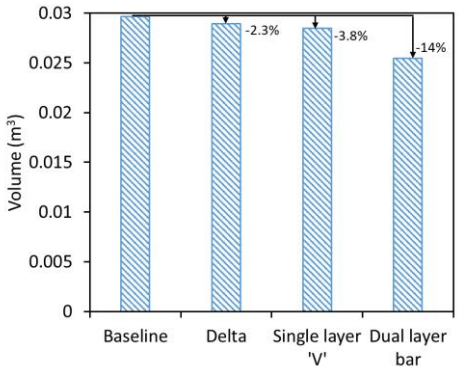

Fig. 8.4.3 Comparison of magnet volumes between the 4 topologies.

The dual layer 'V' of the baseline machine has the PMhighest volume, the Delta and single layer 'V' are lower but the Dual layer bar type has a significant drop in volume indicating it would offer the lowest cost option out of the 4 compared topologies.

Following the volume study, the next key performance aspect is the back EMF profile, shown in Fig. 8.4.4

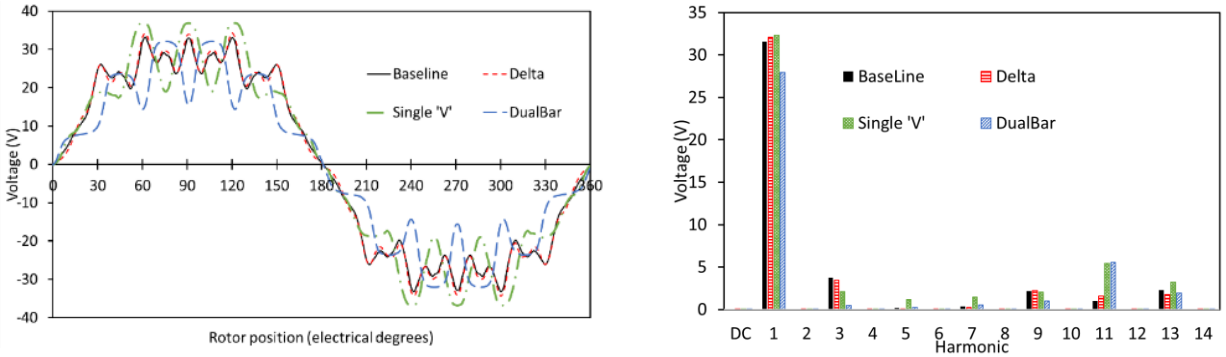

(a) Waveform (b) Harmonics

Fig. 8.4.4 Comparison of back EMF waveforms and harmonics of all 4 topologies at 1200rpm.

The single layer 'V' can be seen to have the least sinusoidal EMF profile. This is expected given the other topologies are multiple layered so have more control over the EMF profile. The concern for both the single layer 'V' and dual bar type is the high 11th harmonic which greatly exceeds that of the baseline and delta types.

Looking at the torque composition the average torque was derived using the d and q axis flux values calculated by the FE tool. The mutual torque value at each point is then estimated by determining the on-load PM linkage, ψ_m, when the current angle is 0° meaning the only torque component is the mutual component. The reluctance component is then determined by subtracting the mutual component from the total calculated torque for each subsequent current point. This method is crude as it does not account for non-linearities such as saturation but it provides an indication of torque composition. More accurate values could be obtained using techniques such as the frozen permeability method, but this was outside the remit of this project. Fig. 8.4.5 (a) shows the torque profile with each machine at maximum current and the current angle incremented between 0° and 90° steps whilst Fig. 8.4.5(b) shows the balance of mutual and reluctance torque for each machine with the current angle at 50°.

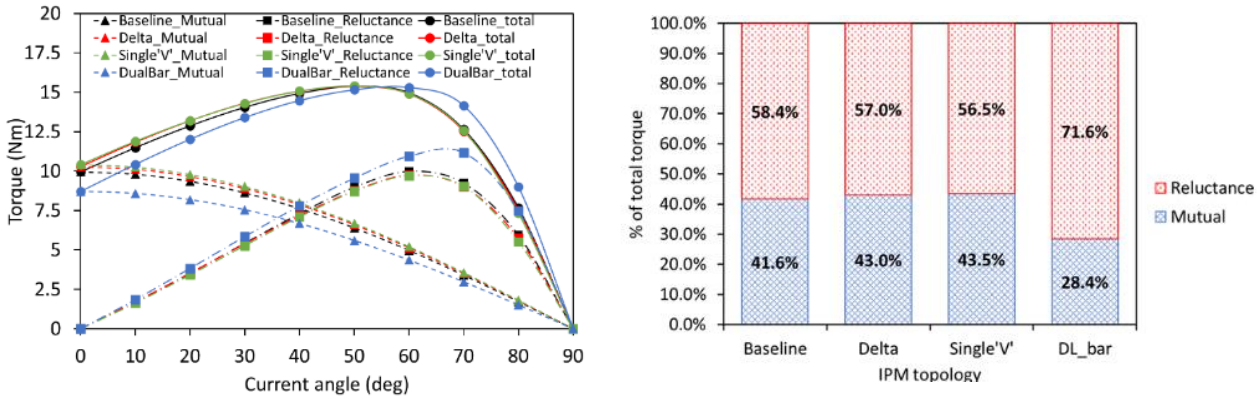

(a) Torque components at increasing current angle (b) Torque composition at Imax and β = 50°

Fig. 8.4.5 Comparison of torque composition of each topology at maximum current and increasing current angle.

The dual layer bar deviates the highest from the other 3 topologies in terms of its torque profile. Given the lower magnet volume it has to rely on a higher reluctance torque component to achieve the maximum torque. In terms of loss and efficiency the maximum efficiencies calculated are shown in Table 8.4.3.

Table 8.4.3 Comparison of maximum calculated efficiency for each machine.

	Baseline	Delta	Single 'V'	Dual layer bar
Max efficiency	92.96%	93.25%	93.26%	93.25%

It was shown that the reason the efficiencies are so closely aligned is the copper loss in the stator dominates all machine topologies, which is of little surprise given all the machines share identical stators. Fig. 8.4.6 shows the loss breakdown of each machine at (a) low speed high torque and (b) high speed low torque.

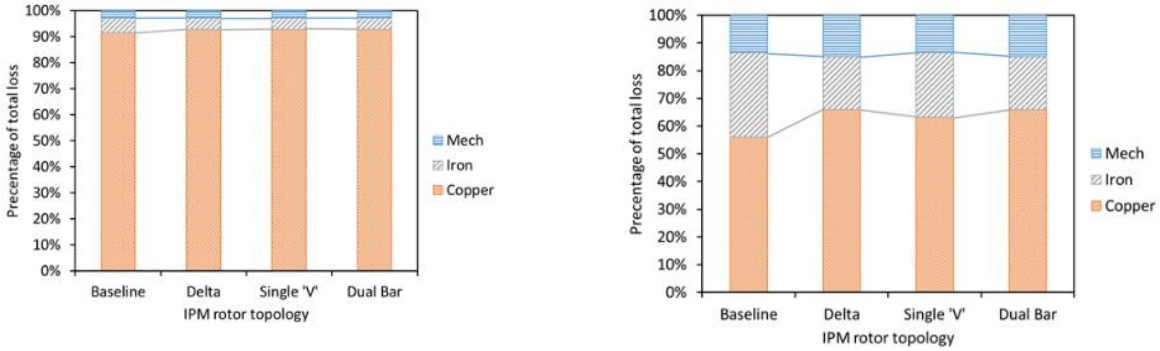

(a) Loss @ 9Nm, 3000rpm (b) Loss @ 3Nm, 7500rpm

Fig. 8.4.6 Loss distribution comparison at low speed high torque and high-speed low torque.

The copper loss is >50% of the total loss in all cases. It can be seen that in terms of the iron loss the baseline machine is the worst performer with the single layer 'V' next followed by the delta and the dual bar. However, the variations are not enough to significantly impact the overall efficiencies.

8.4.3 Torque pulsations - cogging and ripple torques

The torque pulsations, namely the cogging torque and ripple torque for each machine was calculated and compared. The cogging torque profile for one cogging cycle (15 degrees mechanical) and resultant harmonics are shown in Fig. 8.4.7.

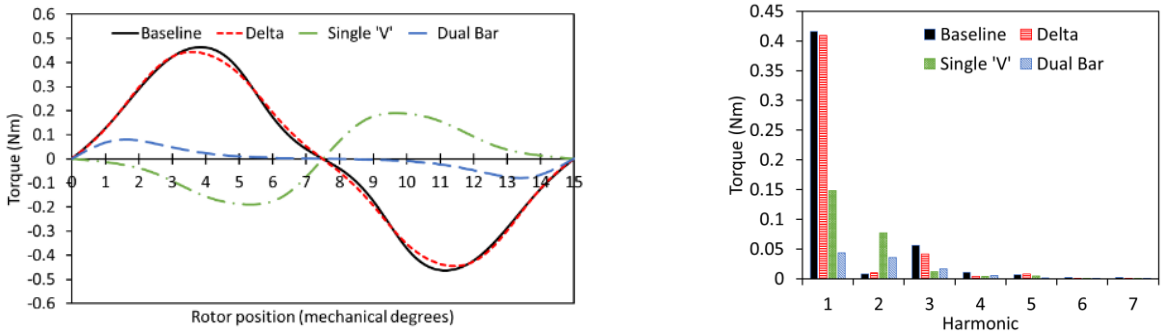

(a) Waveforms (b) Harmonics

Fig. 8.4.7 Comparison of cogging torques for the 4 rotor topologies.

From the results, it is clear that baseline and delta topologies are more or less the same; the delta is slightly lower in the fundamental and the 3rd harmonics. The single layer 'V' and dual layer bar type show very low cogging torque. The dual bar can be partially explained by the lower magnet content so the air gap flux

density and therefore the cogging forces are lower. For the single layer 'V' it was shown that both the low fundamental and high 2nd harmonic can be attributed to the low total magnet pole arc to pole-pitch ratio of the topology. The ratios of the 4 designs are shown in Table 8.4.4.

Table 7.3.13 Magnet pole arc to pole pitch ratios for four machines

	Baseline	Delta	Single layer 'V'	Dual layer Bar
Magnet pole arc to pole pitch ratio	0.86	0.86	0.67	0.84

The values in Table 7.3.13 for the dual layer topologies are based on the lower layers. The baseline and Delta have identical ratios as the magnet pole of lower layer 'V' in both machines are only 0.1° different owing to the slightly thinner magnets on the Delta. The single layer is significantly different than the dual layer machines.

Fig. 8.4.8 shows the ripple rate of each machine with the current at maximum and the current angle stepped from 0° to 80° in 10° steps.

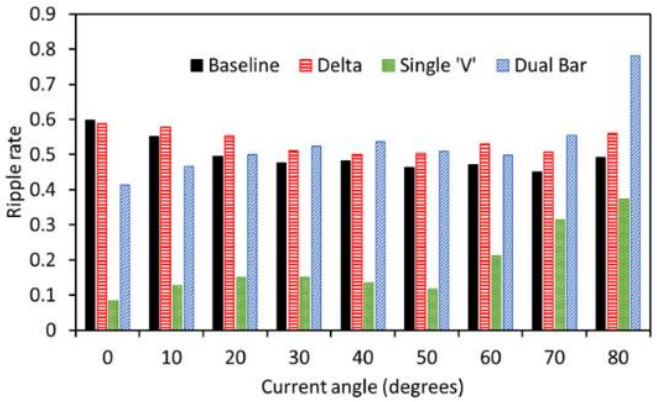

Fig. 8.4.8 Comparison of the ripple rate of the four rotors at Imax and increasing current angles.

The results of the ripple rate show a stark contrast between the single layer 'V' and the other topologies with the Single layer 'V' showing significantly less ripple across the swept current angles. The Dual bar topology on the other hand has gone from being the lowest in terms of cogging torque to showing the highest torque ripple around the MTPA point.

8.4.4 Tooth forces

Tooth forces on the topologies were evaluated using the hybrid method detailed earlier. The forces are calculated for the rotor positions at 15° increments under 3 different load conditions, no load, maximum current with β = 0° and maximum current with β = 45°. Fig. 8.4.9 shows the calculated results.

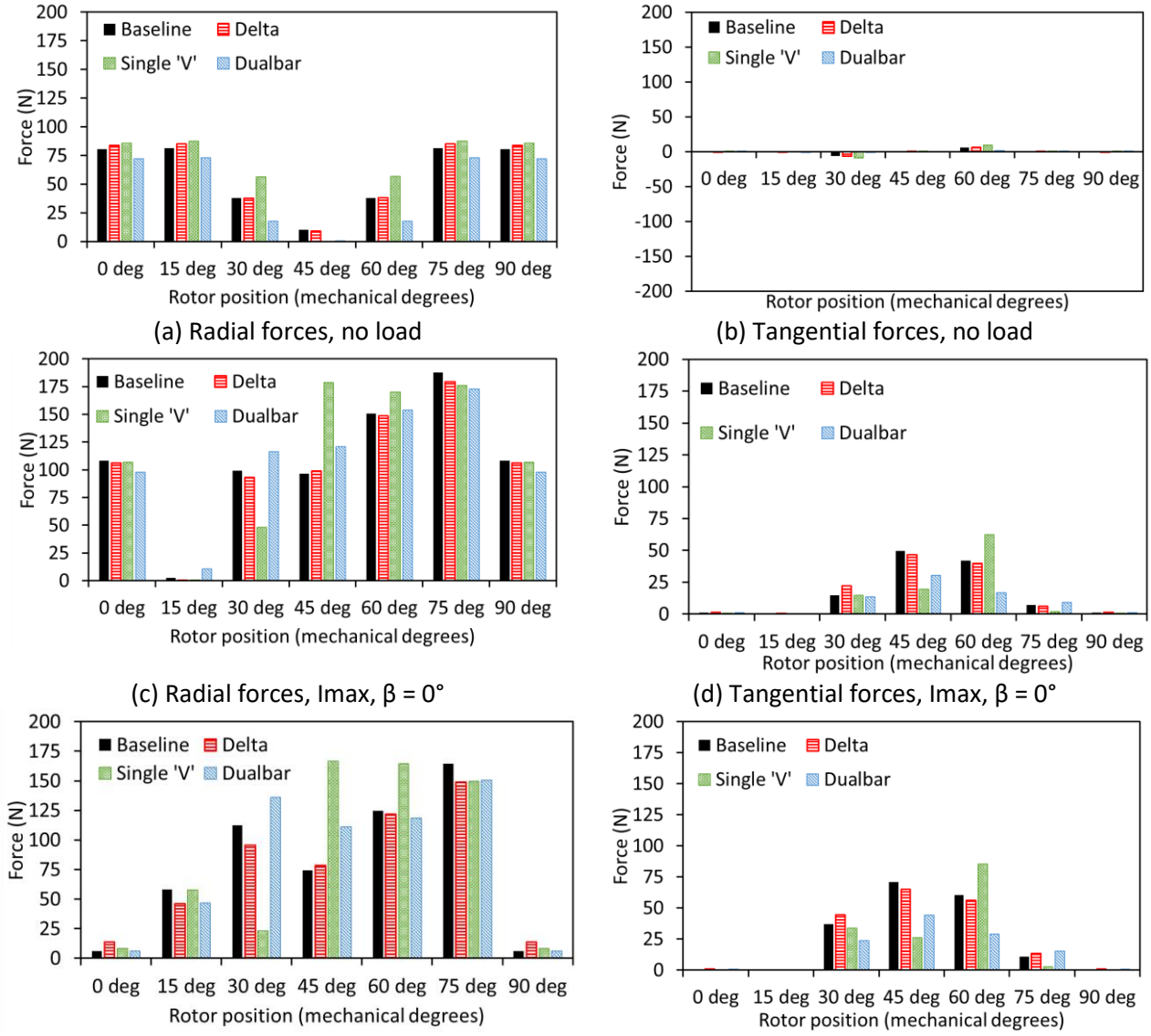

(a) Radial forces, no load

(b) Tangential forces, no load

(c) Radial forces, Imax, β = 0°

(d) Tangential forces, Imax, β = 0°

(e) Radial forces, Imax, β = 45°

(f) Tangential forces, Imax, β = 45°

Fig. 8.4.9 Comparison of calculated tooth forces for the 4 machines at different rotor positions under different load conditions.

In the no load conditions all 4 topologies show good symmetry around 45°, i.e., 45° to 90° is a mirror image of 0° to 45°. When maximum current is applied things are much different. The single layer 'V' shows the highest deviation from the other topologies, in particular at 30°, 45° and 60°.

- When the rotor has moved 30° from the start position, the air gap curve is sat almost entirely over the magnet end flux barrier, with only a small part of the curve interacting with the high flux density sat at the back end of the magnet.
    - This imbalance is strongest when the current angle is at 45° and the radial force is very low whist the tangential is relatively high.
- When the rotor has moved 45° the curve is aligned with the rotor q-axis and there is no flux barrier. The curve experiences a very high radial flux density due to a strong inter-pole flux density bridging the air gap.

- At 60° the curve aligns with the highly saturated region at the tip of the next magnet pole leading to a high flux density bridging the air gap and very high tooth forces.

The saturation caused by the magnet upper end flux barrier and lack of q-axis barrier on the single layer means the topology bucks the trend of lowering the radial force at β = 45° when the rotor is at the 45° (q-axis) and 60° position. This can also be observed on the dual layer bar at 45° which again has no barrier at this position.

In addition to the Maxwell stress tensor method the nodal force method in JMAG was used to allow the force profiles over one magnetic force cycle to be compared. The "probe" sat mid-tooth on the q-axis of each machine at the initial rotor position, Fig. 8.4.10(a), and traces the force acting on the "probe" as the rotor rotates underneath. The same load conditions as the Maxwell stress tensor method is used and the radial force profiles can be seen in Fig. 8.4.10 (b) to (d).

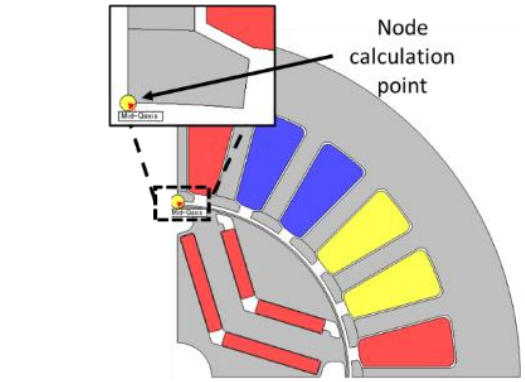

(a) Position of nodal force probe on stator

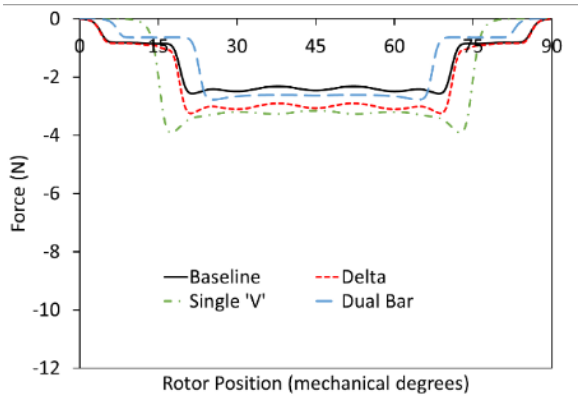

(b) No load radial forces

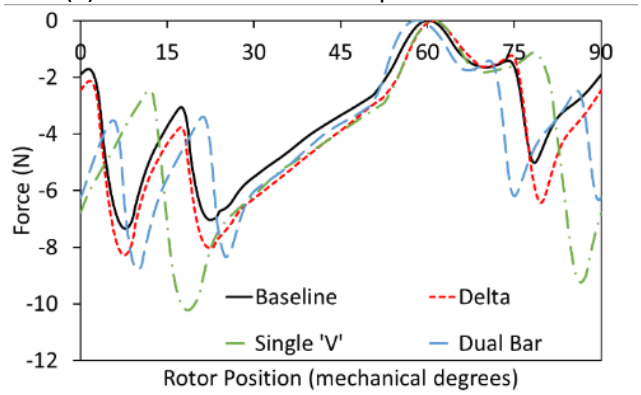

(c) Imax, β = 0° radial forces

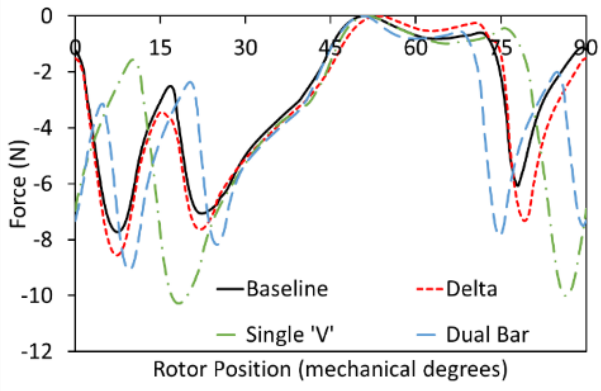

(d) Imax, β = 45° radial forces

Fig. 8.4.10 Comparison of radial forces from nodal force probe in FE tool.

The no load radial forces (Fig. 8.4.10 (b)) are all low in amplitude and symmetrical, the only source of flux in this condition is the PM flux. The no load trace serves to highlight the differences in the radial flux from the rotor for each topology with the starkest difference being the non-stepped profile of the single layer 'V' showing a sharp rise in force as the main flux from the PMs align to the nodal probe.

The full load looks highly distorted for all cases. This is due to the armature MMF pulling the rotor flux towards the q-axis. The Delta and baseline follow a very similar profile in both load cases (Fig. 8.4.10 (c) and (d)) owing

to the similarities in the design, in particular around the q-axis barrier and lower layer magnets which are almost identical. The differences become more apparent as the force probe aligns with the upper layer magnet, in particular around the magnet end flux barrier on the Delta topology where higher flux leakage in the region results in more flux traversing radially to the tooth and hence higher forces. Compared to the baseline, the single 'V' and dual bar the main force trends are similar to the above with some notable differences:

- The single layer and dual bar have no q-axis flux barriers so the flux density acting on the nodal force probe is considerably higher.
- The difference in pitch of the lower and upper-layer magnet flux barriers on the Dual bar means the forces profile appears slightly of phase with the Delta and baseline, which share the same barrier positions.
- The single layer topology sees a very sharp rise at the ~20° and ~80° positions where there are very high flux densities at the tips of the magnet upper flux barriers, indicating an issue with this design.

When the current angle is shifted to 45° it was shown that the flux in each rotor is being pulled more strongly in the direction of the q-axis meaning the region of low flux density on the rotor is shifted approximately 10° to around 50° which is why the profile seems a little different to the condition with no current angle applied. The above highlights how much the differences in topology can affect the forces. Even between the Delta and dual layer which share so much geometry higher radial forces can be seen on the delta around the region of the upper layer PM flux barrier indicating the difference in geometry means more flux is leaking from the region than the dual layer.

8.4.5 Vibratory and ERP performance

The final aspect to compare was the vibratory performance. This was achieved using the harmonic analysis tool and the techniques developed in Chapter 6. The 4 different topologies were initially simulated at 3000rpm, 6000rpm and 9000rpm at full load. The results for 3000rpm and 6000 rpm are shown in Fig. 8.4.11

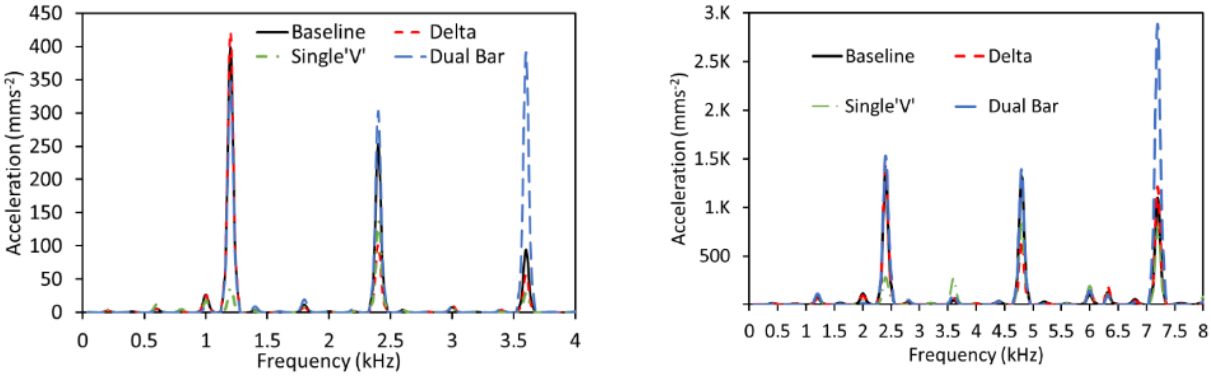

(a) 3000rpm, full load (b) 6000rpm, full load.

Fig. 8.4.11 Comparison of the vibratory performance of the 4 machines at full load and 3000rpm, 6000rpm and 9000rpm.

The general observations are:

- The Delta and baseline follow closely as observed throughout the study, and the only notable difference is at 4.8kHz at 6000rpm where the baseline exceeds the Delta.
- The Dual bar topology is slightly lower than the baseline at the ripple frequency but sees much larger amplitudes at the higher harmonics, in particular the 3rd harmonic.
- The single layer 'V' shows very low vibratory amplitudes compared to the other machines, a result that reflects the low ripple torque calculated previously in the study.

The FE tool also offered the ability to calculate the equivalent radiated power (ERP) of each machine. Whilst these cannot be compared to measured data they provide useful insights into the comparative difference of each machine from the baseline. The results of the calculation are shown in Fig.8.4.12.

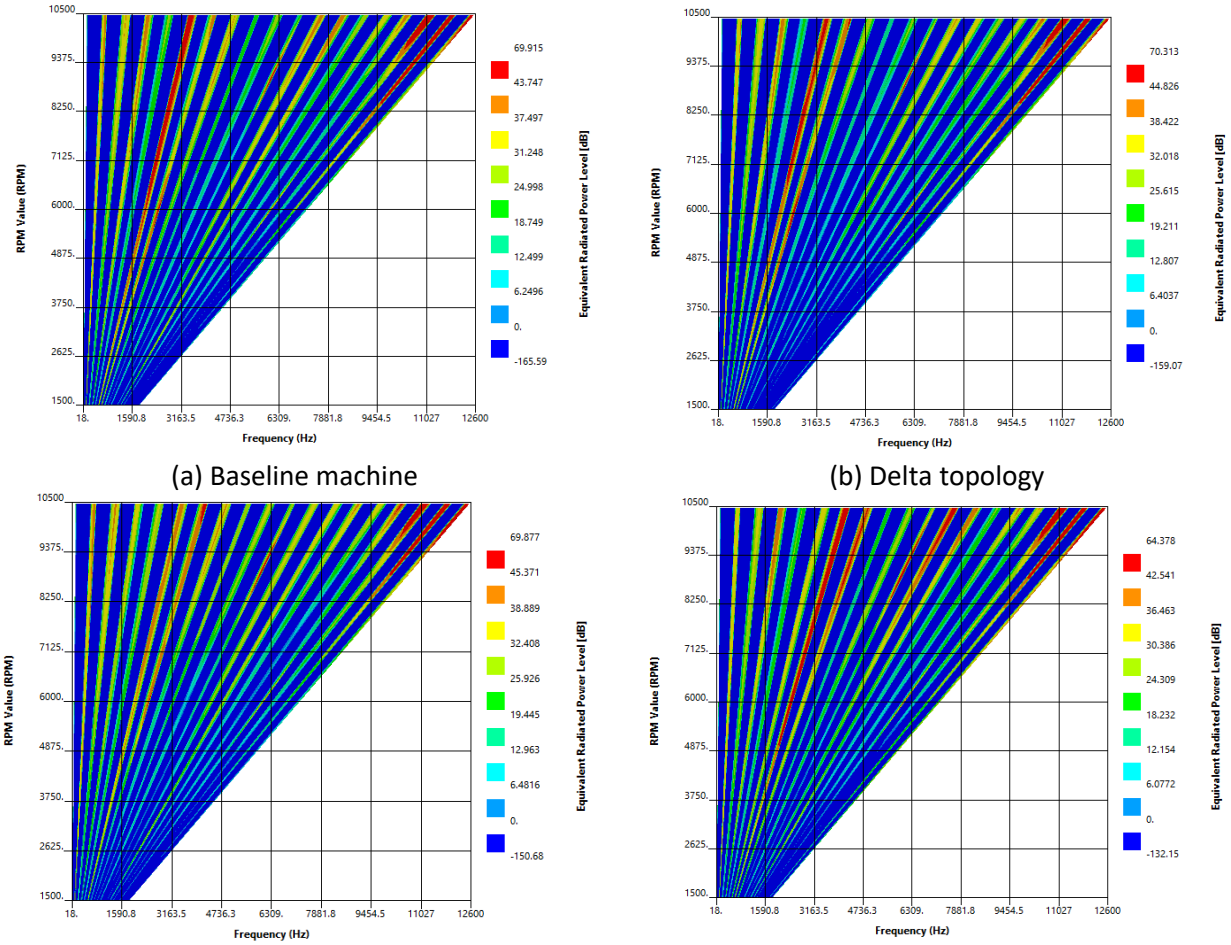

(a) Baseline machine

(b) Delta topology

(c) Single layer 'V' topology

(d) Dual bar topology

Fig. 8.4.12 Comparison of equivalent radiated power level waterfall diagrams for all machines.

The results show the general trend of the delta and baseline topologies matching in performance extends to this comparison. Despite having a lower maximum value, the dual bar topology exhibits higher noise levels across the bandwidth than the other machines, in particular at speeds above 7000rpm. The single layer 'V' topology has the lowest level of noise across the bandwidth and from these calculations at least has been shown to be the best performing machine in terms of vibratory performance.

8.5 Next steps and future work

The requirement to build such a complex model using empirically derived data has proven a large undertaking and necessitated covering a very wide scope of topics, from the influence of PWM switching and control techniques to the influence of the IPM rotor geometry on the tooth forces. With such a large scope there were a number of topics of interest that could not be tackled in the time available in addition to further work that can be achieved given the developed model and techniques. This section will briefly discuss some of these.

8.5.1 Acoustic measurement and modelling

The noise component of noise and vibration was omitted from this thesis. The simple reason for this is that the test facilities available were too noisy making capturing the noise prohibitively difficult. Whilst a semi-anechoic chamber was available the dynamometer and power supply the prototype machine required could not be moved to the chamber. Thus, future work would involve finding a method of adapting the test rig such that the noise could be measured to understand which aspects of the various vibratory traits found would influence the audible noise and what actions could be taken to remove it.

8.5.2 Scalability and modelling the skew

As discussed at the start of the thesis the baseline machine used in all the testing and modelling is a ¼ scale prototype of a full sized 80kW EV traction machine that was analogous to the 1st generation Nissan LEAF. This machine, shown in Fig 8.5.1, has exactly the same structure as the baseline machine used in this thesis; the way which the face plates, main case and shell interact and are attached is identical.

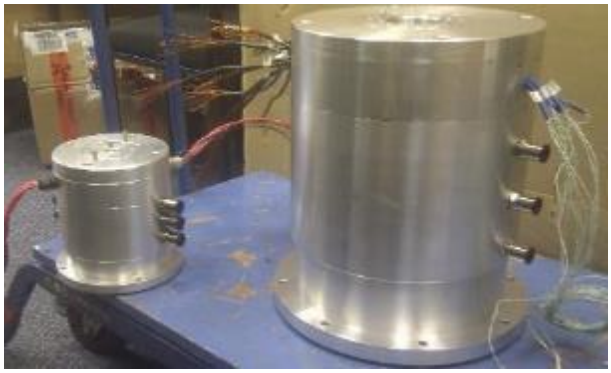

Fig. 8.5.1 Baseline (1/4 scale) and full-sized prototypes.

Applying all the techniques developed in this thesis, in particular the method of simplifying and building the 3D mechanical assembly would be an excellent method of testing the effectiveness of the methods on the same structure scaled up. From a vibratory standpoint understanding how two systems of similar structure but larger size compare would be of interest, in particular from a modal analysis standpoint. The machine is much larger, and the materials and fabrication methods are the same so the understanding the differences in modal frequencies and if any relationship between them could be drawn would be very useful.

In terms of dynamic testing the comparison would not be as straight forwards as aside from the much higher current and torque requirements from the test rig the full-scale machine has a single step skew, a necessity given potential the issues a high cogging torque would create on such large machine, but it would require modifications to the model to account for the skew, perhaps requiring a 3D electromagnetic FE model to account for the complexities a skew adds to the air gap flux.

8.5.3 Rotor model and expand the scope of the system model

The rotor is currently represented as a mass owing to the results of the hammer test. The rotor by its nature is a very dynamic part and is more than capable of causing damage and vibrations from its own modes and eccentricities, as was unfortunately experienced during the testing of the baseline machine. A detailed model of the rotor to understand these aspects would be useful and indeed the vibrations that the output shaft would experience for the different rotor topologies studied. These vibratory conditions can be used to input into larger mechanical models of the gear box and other downstream components on the driveline such as the differential to understand what effect the vibrations have on the driveline and the effects on aspects such as gear tooth fatigue etc. This information would prove very useful for improving the specifications and design of gearboxes to mitigate the effects of these vibrations on the driveline.

In a similar theme the existing model could be used to understand the vibration transmitted to the vehicle allowing the effects of different bushing materials and designs to be evaluated.

8.5.4 Influence of coolant and supply on dynamic vibratory performance

Similar to the rotor the static modal FE model represents the coolant as a mass. It was shown that this offered an acceptable compromise as it gave the FE model reasonable alignment with the experimental hammer test data. Comparing the dynamic experiment results and the FE model shows that whilst the frequencies align the amplitudes in the FE are much lower, in particular at lower speeds. It has been discussed that modes from the rotor or other aspects of the test rig are likely responsible for some of the peaks observed in the measurement that are not shown in the FE but the representation of the coolant and the influence of the coolant flowing around the stator core was not discussed. In terms of modelling the coolant this would require an additional CFD (computational fluid dynamics) aspect to be added to approximate the effect of the fluid which is a whole new topic in itself.

From an experimental point of view the influence of the coolant could be established by removing the shell altogether and attaching the acceleration sensors to the inside of the coolant channels, directly above the stator core. Whilst care would have to be taken to run in short bursts so as not to overheat the machine and/or sensors it would allow the effect of the coolant and the thin water jacket to be observed and compared with the existing results to understand the effects and allow deeper analysis.

8.5.5 Shape optimisation of the stator and rotor air gap faces and flux barriers

The literature is full of different methods of optimising the IPM topology with different features such as rotor profiling or flux barriers etc, as well as shape optimisation of the tooth tips. A selection of these would be used to explore a wide range of different options to understand which balance of rotor and stator designs work such the vibratory forces are mitigated as far as possible. The ideal solution would eliminate the need to skew the machine, as although effective, skewing results in reduced torque and introduces complexities in the air gap harmonics which are difficult to model. The applying these designs to the techniques developed in the thesis allows a more holistic view of each design to made, from the EMF and torque performance all the way to the vibratory performance, differentiating the study from much of the literature that focuses on only the losses or tooth forces.

Bibliography

[AB11] Anders Brandt, “Noise and Vibration Analysis: Signal analysis and experimental procedure“, John Wiley & sons Ltd, 2011.

[AB12] A. Boudouda, N. Boudjerda, M. Melit, B. Nekhoul, K. El Khamlichi Drissi, and K. Kerroum, "Optimized RPWM technique for a variable speed drive using induction motor," in Electromagnetic Compatibility (EMC EUROPE), 2012 International Symposium on, 2012, pp. 1-6.

[AC12] A. Cassat, C. Espanet, R. Coleman, L. Burdet, E. Leleu, D. Torregrossa, et al., "A practical solution to mitigate vibrations in industrial PM motors having concentric windings," IEEE Transactions on Industry Applications, vol. 48, pp. 1526-1538, 2012.

[AC15] A.Cue. "Volkswagen’s Diesel Emission Scandal “Dieselgate“." Opgehaald van The University of North Texas: http://www. ashleighcue. com/PDF/CueDieselgate. pdf (2015).

[AC19] Adam C, Vaucford, “Telsa Model 3”, [ONLINE], available: https://commons.wikimedia.org/w/index.php?curid=83930074

[AD15] A. Das, A. Konwar, A. Dalal, and P. Kumar, "Investigation of PMSM motor performance with different magnet configurations and rotor surface profiling," in 2015 IEEE International Transportation Electrification Conference (ITEC), 2015, pp. 1-6.

[AGJ96] A. G. Jack, B. C. Mecrow, and J. A. Haylock, "A comparative study of permanent magnet and switched reluctance motors for high-performance fault-tolerant applications," IEEE Transactions on Industry Applications, vol. 32, pp. 889-895, 1996.

[AKP16] A. K. Putri, M. Hombitzer, D. Franck, and K. Hameyer, "Cost-oriented design of high speed low power interior permanent magnet synchronous machines," in 2016 XXII International Conference on Electrical Machines (ICEM), 2016, pp. 1446-1452.

[AMT04] A. M. Trzynadlowski, K. Borisov, L. Yuan, Q. Ling, and W. Zhiqiang, "Mitigation of electromagnetic interference and acoustic noise in vehicular drives by random pulse width modulation," in Power Electronics in Transportation (IEEE Cat. No.04TH8756), 2004, pp. 67-71.

[ANS11] ANSYS inc, "Electormangetic Force Coupling in Electric Machines", Presentation, ANSYS Inc, 2011 [ONLINE] available: https://support.ansys.com/staticassets/ANSYS/Conference/Chicago/downloads/Electromagnetic%20Force%20Couplingin%20-%20ANSYS.pdf

[ANS15] ANSYS inc, "Workshop 13: Coupling of harmonic forces from Maxwell Transient to Structural Harmonic and Acoustics - 2D to 3D motor example", Acoutstics ACTx R170, tutorial, ANSYS Inc. Septermber 2015 [ONLINE] available:

[AS16] A. Saito, M. Kuroishi, and H. Nakai, "Empirical vibration synthesis method for electric machines by transfer functions and electromagnetic analysis," IEEE Transactions on Energy Conversion, vol. 31, pp. 1601-1609, 2016.

[AT00] Agilent Technologies Application note 243 -3, ‘The fundamentals of modal testing’, Agilent technologies, 2000.

[ATDA11] A. T. D. Almeida, F. J. T. E. T. E. Ferreira, and J. A. C. Fong, "Standards for efficiency of electric motors," IEEE Industry Applications Magazine, vol. 17, pp. 12-19, 2011.

[BB18] B. Bedkowski, P. Dukalski, T. Jarek, and T. Wolnik, "The efficiency analysis of various structural solutions of the wheel motor cooling systems," in 2018 XIII International Conference on Electrical Machines (ICEM), 2018, pp. 995-1000.

[BD09] B.Drury, "The Control Techniques Drives and Control Handbook", 2nd Edition, The Institution of Engineering and Technology

[BG06] G. Bo, Z. Yifan, and R. Yi, "Torque ripple minimization in interior PM machines using FEM and multiple reference frames," in Industrial Electronics and Applications, 2006 1ST IEEE Conference on, 2006, pp. 1-6.

[BH04] B.Haskins, J.Stecklein, B.Dick, G.Moroney, R.Lovell, J.Dabney.. (2004). 8.4.2 Error Cost Escalation Through the Project Life Cycle. INCOSE International Symposium. 14. 1723-1737.

[BK05] Brüel & Kjær, "Product data: Impact hammers – type 8206", Impact hammer datasheet, May 2005

[BK06] Brüel & Kjær, "Product data: Piezoelectric accelerometer, miniature DeltaTron Accelerometers type 4518", Accelerometer datasheet, March 2006.

[BK18] Brüel & Kjær, "Product data: 16-channel CCLD Conditioning Amplifiers types 2694-A/B/C/D", Conditioning amplifier datasheet, May 2018.

[BSR91] B. S. Rahman and D. K. Lieu, "The origin of permanent magnet induced vibration in electric machines," Journal of Vibration and Acoustics, vol. 113, pp. 476-481, 1991

[BYY06] B.-y. Yang, P. Hyun-kag, and K. Byung-il, "Design of flux barrier for reducing torque ripple and cogging torque in ipm type BLDC motor," in Electromagnetic Field Computation, 2006 12th Biennial IEEE Conference on, 2006, pp. 241-241.

[CB00] C. Breton, J. Bartolome, J. A. Benito, G. Tassinario, I. Flotats, C. W. Lu, et al., "Influence of machine symmetry on reduction of cogging torque in permanent-magnet brushless motors," IEEE Transactions on Magnetics, vol. 36, pp. 3819-3823, 2000.

[CB03] C. Breton, J. Bartolome, J. A. Benito, G. Tassinario, I. Flotats, C. W. Lu, et al., "Influence of machine symmetry on reduction of cogging torque in permanent-magnet brushless motors," IEEE Transactions on Magnetics, vol. 36, pp. 3819-3823, 2000.

[CC20] C. Cheetham, "Remembering the trail blazing original Toyota Prius", The official blog of Toyota UK, [Online], available: https://blog.toyota.co.uk/remembering-the-trail-blazing-original-toyota-prius

[CCC02] C. C. Chan, "The state of the art of electric and hybrid vehicles," Proceedings of the IEEE, vol. 90, pp. 247-275, 2002.

[CGV70] C. G. Veinott, "Fractional and sub-fractional horsepower electric motors" 3rd edition, McGraw-hill, 1970.

[CHS09] C. H. Simmons, D. E. Maguire, and N. Phelps, "Manual of Engineering Drawing", 3rd Edition, Newnes, 2009, pp 151-158.

[CL19] C. Liao, W. Jiang, and Z. Zhang, "Analysis of electromagnetic vibration characteristics of an interior permanent magnet synchronous motor," in 2019 22nd International Conference on Electrical Machines and Systems (ICEMS), 2019, pp. 1-5.

[CM14] C.Morris (2014), "Tesla D is more revolutionary than you think", Chargeddevs.com, [Online], available: https://chargedevs.com/newswire/tesla-d-is-more-revolutionary-than-you-think/

[CM20] Celera Motion Motor Technology, "Mounting design guide" Celera Motion Technical notes, TN-2101, Rev 160701, [Online], Available: https://www.celeramotion.com/wp-content/uploads/sites/6/2019/03/TN-2101-Celera-Motion-Frameless-Motor-Installation-and-Design-Guide.pdf

[CR18] C. Ruoff, "Tesla's top motor engineer talks about designing a permanent magnet machine for Model 3", Chargeddevs.com, February 27, 2018, [Online], https://chargedevs.com/features/teslas-top-motor-engineer-talks-about-designing-a-permanent-magnet-machine-for-model-3/ [Accessed Apr 2020]

[CP08] Cogent Power (Surahammars Burks AB), "Electrical Steel, Non-Orientated, fully processed", Lamination steel Datasheet, June 2008, [Online] https://cogent-power.com/downloads, Accessed June 2016

[CRF82] C. R. Fuller and F. J. Fahy. Characteristics of wave propagation and energy distributions in cylindrical elastic shells filled with fluid. J. Sound Vibration, pages 501–518, 1982.

[DE06] D.Eisenburg, W.Kauzmann, "The structure and Properties of Water", Oxford Classic Texts in the Physical Sciences, Clarendon Press, 2006, ISBN 0-19-857026-0.

[DGD09] D. G. Dorrell, H. Min-Fu, and G. Youguang, "Unbalanced magnet pull in large brushless rare-earth permanent magnet motors with rotor eccentricity," IEEE Transactions on Magnetics, vol. 45, pp. 4586-4589, 2009.

[DGD94] D. G. Dorrell and A. C. Smith, "Calculation of UMP in induction motors with series or parallel winding connections," IEEE Transactions on Energy Conversion, vol. 9, pp. 304-310, 1994.

[DH12] Duane Hanselman, "Brushless motors: magnetic design, performance, and control", E-Man Press LLC, 2012.

[DHL12] D. H. Lee, J. H. Lee, and J. W. Ahn, "Mechanical vibration reduction control of two-mass permanent magnet synchronous motor using adaptive notch filter with fast Fourier transform analysis," Electric Power Applications, IET, vol. 6, pp. 455-461, 2012.

[DI05] D. Ishak, Z. Q. Zhu, and D. Howe, "Unbalanced magnetic forces in permanent magnet brushless machines with diametrically asymmetric phase windings," in Industry Applications Conference, 2005. Fourtieth IAS Annual Meeting. Conference Record of the 2005, 2005, pp. 1037-1043 Vol. 2.

[DI06] D. Ishak, Z. Q. Zhu, and D. Howe, "Comparison of PM brushless motors, having either all teeth or alternate teeth wound," IEEE Transactions on Energy Conversion, vol. 21, pp. 95-103, 2006.

[DIK05] D. Iles-Klumpner, M. Risticevic, and I. Boldea, "Advanced optimization design techniques for automotive interior permanent magnet synchronous machines," in IEEE International Conference on Electric Machines and Drives, 2005., 2005, pp. 227-234.

[DM09] D. Miyagi, N. Maeda, Y. Ozeki, K. Miki, and N. Takahashi, "Estimation of iron loss in motor core with shrink fitting using FEM analysis," IEEE Transactions on Magnetics, vol. 45, pp. 1704-1707, 2009.

[DP97] Di Pietro, Carlo C., Sian S. Lie, and Nagwa Elkasabgy. "Electric vehicle motor." U.S. Patent No. 5,682,074. 28 Oct. 1997

[DSHL13] Daniel S.H.Lo. "Finitie Element Mesh Generation", CRC Press, Boca Raton, FL, 2013.

[DW10] D. Wu and E. Chen, "Stator design for a 1000 kW HTSC motor with air-gap winding," IEEE Transactions on Applied Superconductivity, vol. 21, pp. 1093-1096, 2011.

[DY17] D. Yu, X. Y. Huang, Y. T. Fang, and J. Zhang, "Design and comparison of interior permanent magnet synchronous traction motors for high speed railway applications," in 2017 IEEE Workshop on Electrical Machines Design, Control and Diagnosis (WEMDCD), 2017, pp. 58-62.

[DYK13a] D. Y. Kim, G. H. Jang, and J. K. Nam, "Magnetically induced vibrations in an IPM motor due to distorted magnetic forces arising from flux weakening control," IEEE Transactions on Magnetics, vol. 49, pp. 3929-3932, 2013.

[EA15] E. Aydin, L. Yingjie, I. Aydin, M. Timur Aydemir, and B. Sarlioglu, "Minimization of torque ripples of interior permanent magnet synchronous motors by particle swarm optimization technique," in Transportation Electrification Conference and Expo (ITEC), 2015 IEEE, 2015, pp. 1-6.

[EC15] E. Carraro, N. Bianchi, S. Zhang, and M. Koch, "Performance comparison of fractional slot concentrated winding spoke type synchronous motors with different slot-pole combinations," in Energy Conversion Congress and Exposition (ECCE), 2015 IEEE, 2015, pp. 6067-6074.

[EC19] Edward Carman, "ANSYS solutions for Electric machine NVH", ANSYS 2019 Innovation User Conference, May 2019, Coventry, UK [ONLINE] available at: https://www.ansys.com/-/media/ansys/en-gb/presentations/2019-innovation-conference-presentations/2019-inn-conf-day2-electric-machine-nvh.pdf [accessed January 2020]

[ECL04] E. C. Lovelace, T. M. Jahns, T. A. Keim, and J. H. Lang, "Mechanical design considerations for conventionally laminated, high-speed, interior PM synchronous machine rotors," IEEE Transactions on Industry Applications, vol. 40, pp. 806-812, 2004.

[ECTS93] E. C. T. So and S. J. Yang, "The effect of tooth shape on radial forces in step motors," IEEE Transactions on Magnetics, vol. 29, pp. 2413-2415, 1993.

[EE00] EngineersEDGE, "ISO Socket Head Screw Size Data Table Chart ISO4762", Engineers Edge, LLC, 2000, [online] Available at: https://www.engineersedge.com/iso_socket_head_screw.htm, Accessed March 2020.

[EF93] E. Favre, L. Cardoletti, and M. Jufer, "Permanent-magnet synchronous motors: a comprehensive approach to cogging torque suppression," IEEE Transactions on Industry Applications, vol. 29, pp. 1141-1149, 1993.

[EL18] Engineering Library, "Coefficient of friction", [Online] Available at: https://engineeringlibrary.org/reference/coefficient-of-friction {Accessed May 2018].

[EM20] Emetor AB, "Electric motor winding calculator", [Online] Available at: https://www.emetor.com/windings/ [Accessed October 2020].

[EMF62] E. M. Freeman, "The calculation of harmonics, due to slotting, in the flux-density waveform of a dynamo-electric machine," Proceedings of the IEE - Part C: Monographs, vol. 109, pp. 581-588, 1962.

[ERL65] E. R. Laithwaite, "Differences between series and parallel connection in machines with asymmetric magnetic circuits," Proceedings of the Institution of Electrical Engineers, vol. 112, pp. 2074-2082, 1965.

[ETB04] Engineering ToolBox, (2004). Friction and Friction Coefficients. [online] Available at: https://www.engineeringtoolbox.com/friction-coefficients-d_778.html [Accessed May 2018].

[FC15] F. Chauvicourt, C. Faria, A. Dziechciarz, and C. Martis, "Influence of rotor geometry on NVH behavior of synchronous reluctance machine," in Ecological Vehicles and Renewable Energies (EVER), 2015 Tenth International Conference on, 2015, pp. 1-6.

[FC19] F. Chauvicourt, C. Faria, W. Desmet, and J. J. C. Gyselinck, "Transversally asymmetric stiffness of laminated stator core: a solution for noise mitigation of electric machines," IEEE Transactions on Energy Conversion, vol. 34, pp. 613-619, 2019.

[FCN07] F.C. Nelson, "Rotor dynamics without equations." International Journal of COMADEM 10.3 (2007): 2

[FM03] F. Magnussen and C. Sadarangani, "Winding factors and Joule losses of permanent magnet machines with concentrated windings," in IEEE International Electric Machines and Drives Conference, 2003. IEMDC'03., 2003, pp. 333-339 vol.1.

[FM07] F. Magnussen and H. Lendenmann, "Parasitic effects in PM machines with concentrated windings," IEEE Transactions on Industry Applications, vol. 43, pp. 1223-1232, 2007.

[GDL15] G. D. Lee, G. T. Kim, H. K. Shin, and C. J. Kim, "The optimum design of interior permanent magnet synchronous motor for the vibration reduction," in 2015 18th International Conference on Electrical Machines and Systems (ICEMS), 2015, pp. 227-231.

[GJL16] G. J. Li, B. Ren, Z. Q. Zhu, Y. X. Li, and J. Ma, "Cogging torque mitigation of modular permanent magnet machines," IEEE Transactions on Magnetics, vol. 52, pp. 1-10, 2016.

[GO11] G. Ombach and J. Junak, "Torque ripple optimization of skewed IPM motor for field weakening operation," in Electrical Machines and Systems (ICEMS), 2011 International Conference on, 2011, pp. 1-7.

[GQ09] G. Qi, J. T. Chen, Z. Q. Zhu, D. Howe, L. B. Zhou, and C. L. Gu, "Influence of skew and cross-coupling on flux-weakening performance of permanent-magnet brushless AC machines," IEEE Transactions on Magnetics, vol. 45, pp. 2110-2117, 2009.

[GTP14a] G. T. d. Paula, J. R. B. d. A. Monteiro, T. E. P. d. Almeida, M. P. d. Santana, and W. C. A. Pereira, "Evaluation of surface mounted PM machine's parameters on load conditions using Frozen Permeability Method. Part. I," in 2014 IEEE 23rd International Symposium on Industrial Electronics (ISIE), 2014, pp. 806-811.

[GTP14b] G. T. d. Paula, J. R. B. d. A. Monteiro, T. E. P. d. Almeida, M. P. d. Santana, W. C. A. Pereira, and C. M. R. Oliveira, "Evaluation of surface mounted PM machine's parameters on load conditions using frozen permeability method. Part. II," in Electrical Machines (ICEM), 2014 International Conference on, 2014, pp. 156-161.

[GTP14c] G. T. d. Paula, J. R. B. d. A. Monteiro, T. E. P. d. Almeida, M. P. d. Santana, W. C. A. Pereira, and C. M. R. Oliveira, "Evaluation of surface mounted PM machine's parameters on load conditions using frozen permeability method. Part. III," in Industry Applications (INDUSCON), 2014 11th IEEE/IAS International Conference on, 2014, pp. 1-7.

[HJC13] H.J Chien, C.C Wang, and C.K Shih. "Structural improvement of a canned motor pump." U.S. Patent No. 8,597,000. 3 Dec. 2013.

[HJP02] H. Jung-Pyo, H. Kyung-Ho, and L. Ju, "Stator pole and yoke design for vibration reduction of switched reluctance motor," IEEE Transactions on Magnetics, vol. 38, pp. 929-932, 2002.

[HM17] Hitachi Metals, “Magnet Wire”, Winding material datasheet, April 2017.

[HSK04] K. Hong-Seok and K. Kwang-Joon, "Characterization of noise and vibration sources in interior permanent-magnet brushless DC motors," IEEE Transactions on Magnetics, vol. 40, pp. 3482-3489, 2004.

[HSK13] H. s. Kim, Y. M. You, and B. i. Kwon, "Rotor shape optimization of interior permanent magnet BLDC motor according to magnetization direction," IEEE Transactions on Magnetics, vol. 49, pp. 2193-2196, 2013.

[HYID13] H. Y. I. Du, H. Lei, and L. Hejie, "Modeling and analysis of electromagnetic vibrations in fractional slot PM machines for electric propulsion," in Energy Conversion Congress and Exposition (ECCE), 2013 IEEE, 2013, pp. 5077-5084.

[IEA20] IEA, Electric car deployment in selected countries, 2013-2018, IEA, Paris, [Online]. Available: https://www.iea.org/data-and-statistics/charts/electric-car-deployment-in-selected-countries-2013-2018

[IEC08] International Electrotechnical Commission. "Magnetic materials–part 2: Methods of measurement of the magnetic properties of electrical steel strip and sheet by means of an epstein frame." (2008).

[IY99] I. Yamakoshi, Y. Koike, and K. Takagi, "Motor casing and method of producing same." U.S. Patent No. 5,952,751. 14 Sep. 1999.

[JAH84] J. A. Houldsworth and D. A. Grant, "The use of harmonic distortion to increase the output voltage of a three-phase PWM inverter," IEEE Transactions on Industry Applications, vol. IA-20, pp. 1224-1228, 1984.

[JB14] J. Blum, J. Merwerth, and H. Herzog, "Investigation of the segment order in step-skewed synchronous machines on noise and vibration," in 2014 4th International Electric Drives Production Conference (EDPC), 2014, pp. 1-6.

[JC12] J.Cattelin, Mémoires de l’Académie des Sciences, Arts et Belles-Lettres de Touraine, tome 25, 2012, p. 67-92.

[JD15] J. Ding, P. Zhang, and J. Li, "Fatigue life prediction of IGBT module for metro vehicle traction converter based on traction calculation," in 2015 IEEE 11th International Conference on Power Electronics and Drive Systems, 2015, pp. 1116-1121.

[JDE02] J. D. Ede, K. Attalah, and D. Howe, “Design variants of modular permanent magnet brushless motor,” J. Appl. Phys., vol. 91, no. 10, pp. 6973– 6975, 2002.

[JEV68] J.E. Vranick, "Prediction of windage loss in alternators", National Aeronatics and Space Administration (NASA), NASA technical reports server, 1971, [Online], available: https://ntrs.nasa.gov/citations/19710000073

[JFE97] J. F. Eastham, D. M. Ionel, M. J. Balchin, T. Betzer and E. Demeter, "Finite element analysis of an interior-magnet brushless DC machine, with a step-skewed rotor," in *IEEE Transactions on Magnetics*, vol. 33, no. 2, pp. 2117-2119, March 1997

[JFG06] Jacek F.Gieras, Chong Wang, Joseph Ch Lai, “Noise of Polyphaser Electric Motors” , CRC Press, Taylor & Francis Group, LLC, 2006.

[JFG07] J. F. Gieras, W. Chong, C. S. L. Joseph, and N. Ertugrul, "Analytical prediction of noise of magnetic origin produced by permanent magnet brushless motors," in Electric Machines & Drives Conference, 2007. IEMDC '07. IEEE International, 2007, pp. 148-152.

[JFM09] J. F. May and C. L. Baldwin, "Driver fatigue: The importance of identifying causal factors of fatigue when considering detection and countermeasure technologies," Transportation Research Part F: Traffic Psychology and Behaviour, vol. 12, pp. 218-224, 5// 2009.

[JJ10] J. Junak and G. Ombach, "Performance optimisation of the brushless motor with IPM rotor for automotive applications," in The XIX International Conference on Electrical Machines - ICEM 2010, 2010, pp. 1-5.

[JKT09] J. K. Tangudu, T. M. Jahns, A. M. El-Refaie, and Z. Q. Zhu, "Segregation of torque components in fractional-slot concentrated-winding interior PM machines using frozen permeability," in 2009 IEEE Energy Conversion Congress and Exposition, 2009, pp. 3814-3821.

[JLC84] J. Coulomb and G. Meunier, "Finite element implementation of virtual work principle for magnetic or electric force and torque computation," IEEE Transactions on Magnetics, vol. 20, pp. 1894-1896, 1984.

[JM13] JMAG Application note, “Vibration analysis of an SR motor”, JAC138SRM, JSOL Corporation, 2013

[JM18] JMAG designer Version 18.0, help, “Nodal force method, force setting panel”, JSOL Corporation, 2019

[JM18b] JMAG designer Version 18.0, help, “Multi-objective genetic algorithm”, JSOL Corporation, 2019

[JM88] J. Mizia, K. Adamiak, A. R. Eastham, and G. E. Dawson, "Finite element force calculation: comparison of methods for electric machines," IEEE Transactions on Magnetics, vol. 24, pp. 447-450, 1988.

[JMP01] J.M Pijanowski. "Electric machine with structural spacer." U.S. Patent Application 09/757,928, filed Oct 18, 2001.

[JQZ15] J. Q. Zheng, W. X. Zhao, J. H. Ji, and G. H. Liu, "Design and comparison of interior permanent-magnet machines for hybrid electric vehicles," in 2015 IEEE International Conference on Applied Superconductivity and Electromagnetic Devices (ASEMD), 2015, pp. 234-235.

[JRH10] J.R Hendershot and T.J.E Miller, “Design of brushless permanent-magnet machines”, Motor design books LLC, 2010

[JS14] J. Sun, H. Feng, and C. Zhu, "Identification of laminated core and winding's physical parameters by stator's modal testings," in 2014 17th International Conference on Electrical Machines and Systems (ICEMS), 2014, pp. 1488-1492.

[JS16] J. Srinivasan, K. Selvaraj, J. Chitrarasu, and R. Resmi, "Design and analysis of squirrel cage induction motor in short pitch and full pitch winding configurations using FEA," in 2016 International Conference on Emerging Technological Trends (ICETT), 2016, pp. 1-10.

[JSP12] Joon Sung Park, Bon-Gwan Gu, Jin-Hong Kim, Jun-Hyuk Choi and In-Soung Jung, "Development of BLDC motor drive for automotive applications," 2012 Electrical Systems for Aircraft, Railway and Ship Propulsion, Bologna, 2012, pp. 1-6, doi: 10.1109/ESARS.2012.6387424

[JTB90] J. T. Boys and P. G. Handley, "Harmonic analysis of space vector modulated PWM waveforms," IEE Proceedings B - Electric Power Applications, vol. 137, pp. 197-204, 1990.

[JW06] J. Wang, Z. P. Xia, S. a. Long, and D. Howe, "Radial force density and vibration characteristics of modular permanent magnet brushless ac machine," IEE Proceedings - Electric Power Applications, vol. 153, pp. 793-801, 2006.

[JWJ16] J. W. Jiang, B. Bilgin, Y. Yang, A. Sathyan, H. Dadkhah, and A. Emadi, "Rotor skew pattern design and optimisation for cogging torque reduction," IET Electrical Systems in Transportation, vol. 6, pp. 126-135, 2016.

[JZ18] J. Zhao, Y. Liu, and X. Xu, "Comparisons of Concentrated and Distributed Winding PMSM in MV Power Generation," in 2018 XIII International Conference on Electrical Machines (ICEM), 2018, pp. 2437-2443.

[KC17] K. Culmer (2017). "Throwback Thursday: 1996 General motors EV1 first drive", [Online]: Available: https://www.autocar.co.uk/car-news/anything-goes-throwback-thursday/throwback-thursday-1996-general-motors-ev1-first-drive

[KD01] K. Dabala, "Analysis of mechanical losses in three-phase squirrel-cage induction motors," ICEMS'2001. Proceedings of the Fifth International Conference on Electrical Machines and Systems (IEEE Cat. No.01EX501), Shenyang, China, 2001, pp. 39-42 vol.1, doi: 10.1109/ICEMS.2001.970604.

[KD14] K. Doyeon, S. Jeongyong, and J. Gunhee, "Magnetic and structural finite element analysis of rotor vibrations due to magnetic forces in IPM motor," IEEE Transactions on Magnetics, vol. 50, pp. 753-756, 2014.

[KEKD03] K. E. K. Drissi, P. C. K. Luk, B. Wang, and J. Fontaine, "A novel dual-randomization PWM scheme for power converters," in IEEE 34th Annual Conference on Power Electronics Specialist, 2003. PESC '03., 2003, pp. 480-484 vol.2.

[KI02] K. Itori, S. Noda, F. Ishibashi, and H. Yamawaki, "Young's modulus of windings on finite element method for natural frequency analysis of stator core in induction motor," Transactions of the Japan Society of Mechanical Engineers Series C, vol. 68, pp. 1343-1348, 05/01 2002.

[KI08] K.Inaba, J.E.Shepherd, "Impact generated stress waves and coupled fluid-structure responses", In Proceedings of the SEM XI International Congress & Exposition on Experimental and Applied Mechanics, June 2-5 2008, Orlando, FL USA. Paper 136.

[KI09] K.Inaba, J.E.Shepherd, "Fluid interaction in liquid filled composite tubes under impulsive loading," SEM annual conference and Exposition on Experimental and applied Mechanics, Albuquerque, New Mexico USA, June 1-4, 2009, paper 413.

[KJ04] K. Jiao, Z. Li, M. Chen, C. Wang, and S. Qi, "Effect of different vibration frequencies on heart rate variability and driving fatigue in healthy drivers," International Archives of Occupational and Environmental Health, vol. 77, pp. 205-212, 2004.

[KJ10] K. Jeonghu, M. Seungjae, and H. Jung-Pyo, "Optimal stator design of interior permanent magnet motor to reduce torque ripple using the level set method," IEEE Transactions on Magnetics, vol. 46, pp. 2108-2111, 2010.

[KK14a] K. Kiyota, T. Kakishima, and A. Chiba, "Estimation and comparison of the windage loss of a 60 kW Switched Reluctance Motor for hybrid electric vehicles," in Power Electronics Conference (IPEC-Hiroshima 2014 - ECCE-ASIA), 2014 International, 2014, pp. 3513-3518.

[KK14b] K. Kiyota, T. Kakishima, and A. Chiba, "Cylindrical rotor design for acoustic noise and windage loss reduction in switched reluctance motor for HEV applications," in Energy Conversion Congress and Exposition (ECCE), 2014 IEEE, 2014, pp. 1814-1821.

[KPP18] K. P. Paduszyński and Z. Goryca, "Relationship between asymmetrical distribution of the magnets and cogging torque of BLDC motor with external rotor," in 2018 Conference on Electrotechnology: Processes, Models, Control and Computer Science (EPMCCS), 2018, pp. 1-4.

[KR13] K. Rajashekara, "Present status and future trends in electric vehicle propulsion technologies," IEEE Journal of Emerging and Selected Topics in Power Electronics, vol. 1, pp. 3-10, 2013.

[KSI05] K. Sung-Il, L. Ji-Young, K. Young-Kyoun, H. Jung-Pyo, Y. Hur, and J. Yeon-Hwan, "Optimization for reduction of torque ripple in interior permanent magnet motor by using the Taguchi method," IEEE Transactions on Magnetics, vol. 41, pp. 1796-1799, 2005.

[KSI06] K. Sung-Il, H. Jung-Pyo, K. Young-Kyoun, N. Hyuk, and C. Han-Ik, "Optimal design of slotless-type PMLSM considering multiple responses by response surface methodology," IEEE Transactions on Magnetics, vol. 42, pp. 1219-1222, 2006.

[KT17] Keysight Technologies, "35670A Dynamic Signal Analyzer", Signal analyser datasheet, December 2017.

[KTK01] K. Kyung-Tae, K. Kwang-Suk, H. Sang-Moon, T.-J. Kim, and J. Yoong-Ho, "Comparison of magnetic forces for IPM and SPM motor with rotor eccentricity," IEEE Transactions on Magnetics, vol. 37, pp. 3448-3451, 2001.

[KW12] K. Wang, Z. Q. Zhu, G. Ombach, and W. Chlebosz, "Optimal rotor shape with third harmonic for maximizing torque and minimizing torque ripple in IPM motors," in 2012 XXth International Conference on Electrical Machines, 2012, pp. 397-403.

[KW14] K. Wang, Z. Q. Zhu, G. Ombach, and W. Chlebosz, "Torque ripple and magnetic forces on teeth in IPM machines," COMPEL: The International Journal for computation and mathematics in Electrical and Electronic Engineering, vol. 33, pp. 1487-1501, 2014.

[KY15] K. Yamazaki and W. Fukushima, "Loss analysis of induction motors by considering shrink fitting of stator housings," IEEE Transactions on Magnetics, vol. 51, pp. 1-4, 2015.

[LC11] L. Chong, R. Dutta, and M. F. Rahman, "Performance comparison between concentrated and distributed wound IPM machines used for field weakening applications," in International Aegean Conference on Electrical Machines and Power Electronics and Electromotion, Joint Conference, 2011, pp. 616-619.

[LF10] L. Fang, S. O. Kwon, T. Sun, and J. P. Hong, "Optimal shape design of double-barriers in single-layer interior PM synchronous motor for reducing torque pulsation," in 2010 International Conference on Electrical Machines and Systems, 2010, pp. 1239-1241.

[LG09] L. Guo and L. Parsa, "Effects of magnet shape on torque characteristics of Interior Permanent Magnet machines," in 2009 IEEE Electric Ship Technologies Symposium, 2009, pp. 93-97.

[LPW20] L.P Williams, "Michael Faraday",Encyclopedia Britannica, September 2020, [Online], Available: https://www.britannica.com/biography/Michael-Faraday

[LSH09] L. Sang-Ho, H. Jung-Pyo, H. Sang-Moon, L. Woo-Taik, L. Ji-Young, and K. Young-Kyoun, "Optimal design for noise reduction in interior permanent-magnet motor," IEEE Transactions on Industry Applications, vol. 45, pp. 1954-1960, 2009.

[MB14] M. Boesing, A. Hofmann, and R. W. De Doncker, "Universal acoustic modeling framework for electrical drives," in Power Electronics, Machines and Drives (PEMD 2014), 7th IET International Conference on, 2014, pp. 1-6.

[MB98] M. Besbes, C. Picod, F. Camus, and M. Gabsi, "Influence of stator geometry upon vibratory behaviour and electromagnetic performances of switched reluctance motors," IEE Proceedings - Electric Power Applications, vol. 145, pp. 462-468, 1998.

[MC14] M. Conggan and Z. Shuguang, "Black-box method of identification and diagnosis of abnormal noise sources of permanent magnet synchronous machines for electric vehicles," EEE Transactions on Industrial Electronics, vol. 61, pp. 5538-5549, 2014.

[MC15] M. Caruso, A. O. D. Tommaso, S. Emma, and R. Miceli, "Analysis, characterization and minimization of IPMSMs cogging torque with different rotor structures," in 2015 Tenth International Conference on Ecological Vehicles and Renewable Energies (EVER), 2015, pp. 1-6.

[MEHG93] M. E. H. Benbouzid, G. Reyne, S. Derou, and A. Foggia, "Finite element modeling of a synchronous machine: electromagnetic forces and mode shapes," IEEE Transactions on Magnetics, vol. 29, pp. 2014-2018, 1993.

[MG12] M. Guarnieri, "Looking back to electric cars," in HISTory of ELectro-technology CONference (HISTELCON), 2012 Third IEEE, 2012, pp. 1-6.

[MS03] M. Sanada, K. Hiramoto, S. Morimoto, and Y. Takeda, "Torque ripple improvement for synchronous reluctance motor using asymmetric flux barrier arrangement," in 38th IAS Annual Meeting on Conference Record of the Industry Applications Conference, 2003., 2003, pp. 250-255 vol.1.

[MSI14] M. S. Islam, R. Islam, and T. Sebastian, "Noise and vibration characteristics of permanent-magnet synchronous motors using electromagnetic and structural analyses," IEEE Transactions on Industry Applications, vol. 50, pp. 3214-3222, 2014.

[MVD12] M. v. d. Giet, K. Kasper, R. W. D. Doncker, and K. Hameyer, "Material parameters for the structural dynamic simulation of electrical machines," in 2012 XXth International Conference on Electrical Machines, 2012, pp. 2994-3000.

[MW18] MatWeb, “Aluminium 6061-T4; 6061-T451”, MatWeb LLC, [Online]. Available: http://www.matweb.com/search/DataSheet.aspx?MatGUID=d5ea75577b1b49e8ad03caf007db5ba8, Accessed May 2018.

[NB12] N. Borchardt, R. Kasper, and W. Heinemann, "Design of a wheel-hub motor with air gap winding and simultaneous utilization of all magnetic poles," in 2012 IEEE International Electric Vehicle Conference, 2012, pp. 1-7.

[NG10] Nissan Global (2010), “Nissan LEAF”, Nissan Motor corporation, [Online], available: https://www.nissan-global.com/EN/NISSAN/LEAF/

[NG19] Nissan Global (2019), “e-Powertrain”, Nissan Motor Corporation, [Online], available: https://www.nissan-global.com/EN/TECHNOLOGY/OVERVIEW/e_powertrain.html

[NTN12] NTN Global (2012), " NTN Rolling bearings handbook", NTN Corporation, [Online], Available: https://www.ntnglobal.com/en/products/catalog/pdf/9012E.pdf

[OD88a] Ole Døssing, “Structural Testing Part 1, Mechanical Mobility Measurements”, Brüel & Kjær application note br0458, April 1988, https://www.bksv.com/media/doc/br0458.pdf, accessed February 2018

[OD88b] Ole Døssing, “Structural Testing Part 2, Modal analysis and simulation”, Brüel & Kjær application note br0507, April 1988, https://www.bksv.com/media/doc/br0507.pdf, accessed February 2018.

[PD14] P. Diouf and W. Herbert, "Understanding rotor balance for electric motors," in Pulp and Paper Industry Technical Conference, Conference Record of 2014 Annual, 2014, pp. 7-17.

[PPB96] PP Benham, RJ Crawford, and CG Armstrong, “Mechanics of Engineering Materials” Second Edition, Pearson Education Ltd, 1996.

[PV98] P. Vijayraghavan and R. Krishnan, "Noise in electric machines: a review," in Industry Applications Conference, 1998. Thirty-Third IAS Annual Meeting. The 1998 IEEE, 1998, pp. 251-258 vol.1.

[RI09] R. Islam and I. Husain, "Analytical model for predicting noise and vibration in permanent magnet synchronous motors," in Energy Conversion Congress and Exposition, 2009. ECCE 2009. IEEE, 2009, pp. 3461-3468.

[RM14] R. Mistry, B. Finley, S. Kreitzer, and R. Queen, "Influencing factors on motor vibration & rotor critical speed in design, test and field applications," in 2014 IEEE Petroleum and Chemical Industry Technical Conference (PCIC), 2014, pp. 227-236.

[RP16] R. Pupadubsin, A. Steven, J. D. Widmer, and B. C. Mecrow, "Mechanical material properties for structural simulation model of switched reluctance machines," in 2016 XXII International Conference on Electrical Machines (ICEM), 2016, pp. 2293-2299.

[RP20] R. Pile, G. Parent, E. Devillers, T. Henneron, Y. Le Menach, J. Le Besnerais, et al., "Application limits of the Airgap Maxwell tensor," 2020.

[RV79] R.Vernon "The product cycle hypothesis in a new international environment." Oxford bulletin of economics and statistics 41.4 (1979): 255-267.

[SAE10] S. A. Evans, "Salient pole shoe shapes of interior permanent magnet synchronous machines," in The XIX International Conference on Electrical Machines - ICEM 2010, 2010, pp. 1-6.

[SAL01a] S. A. Long, Z. Q. Zhu, and D. Howe, "Vibration behaviour of stators of switched reluctance motors," IEE Proceedings - Electric Power Applications, vol. 148, pp. 257-264, 2001.

[SAL01b] Stephen Andrew Long, “Acoustic noise and vibration of switched reluctance machines”. PhD Thesis, The University of Sheffield, Sheffield, UK, November 2001, Accessed May 2018, [Online] available: http://etheses.whiterose.ac.uk/14498/.

[SB12] S. Baldizzone, C. J. Novak, and N. C. Kar, "Experimental investigations of noise and vibration in electric machines," in 2012 IEEE Transportation Electrification Conference and Expo (ITEC), 2012, pp. 1-6.

[SC10] S. Chaithongsuk, N. Takorabet, B. Nahid-Mobarakeh, and F. Meibody-Tabar, "Optimal design of PM motors for quasi-sinusoidal air-gap flux density," in 45th International Universities Power Engineering Conference UPEC2010, 2010, pp. 1-6.

[SC16] C. Siwei, L. Huangda, J. Zhewu, and W. Dong, "Practical design considerations of stator lamination fixtures in permanent magnet machines," in 2016 IEEE 8th International Power Electronics and Motion Control Conference (IPEMC-ECCE Asia), 2016, pp. 2849-2853.

[SES07] S. E. Schulz and D. L. Kowalewski, "Implementation of variable-delay random PWM for automotive applications," IEEE Transactions on Vehicular Technology, vol. 56, pp. 1427-1433, 2007.

[SHH07] S. H. Han, T. M. Jahns, and W. L. Soong, "Torque ripple reduction in interior permanent magnet synchronous machines using the principle of mutual harmonics exclusion," in 2007 IEEE Industry Applications Annual Meeting, 2007, pp. 558-565.

[SJY78] S.J Yang, 'Finite element method in evaluating the stator natural frequencies of small machines', Proc. International Conference on Electrical machines, 1978, pp. G3-G8.

[SJY81] S.J Yang, "Low-noise electrical motors", Monographs in Electrical and Electronic Engineering, Oxford University Press, 1981.

[SKL12] L. Sun-Kwon, K. Gyu-Hong, and H. Jin, "Finite element computation of magnetic vibration sources in 100 kW two fractional-slot interior permanent magnet machines for ship," IEEE Transactions on Magnetics, vol. 48, pp. 867-870, 2012.

[SLC03] S.L. Capitaneanu, B. de Fomel, M. Fadel, and F. Jadot, "On the acoustic noise radiated by PWM AC motor drives," Automatika, vol. 44, pp. 137–145, 2003.

[SM00] S. Morimoto, M. Sanada, and Y. Takeda, "Performance of PM assisted synchronous reluctance motor for high efficiency and wide constant power operation," in Industry Applications Conference, 2000. Conference Record of the 2000 IEEE, 2000, pp. 509-514 vol.1.

[SM89] S. Morimoto, Y. Takeda, T. Hirasa, and K. Taniguchi, "Expansion of operating limits for permanent magnet motor by optimum flux-weakening," in Conference Record of the IEEE Industry Applications Society Annual Meeting, 1989, pp. 51-56 vol.1.

[SMH06] H. Sang-Moon, L. Hong-Joo, K. Tae-Soon, J. Yoong-Ho, and H. Jung-Pyo, "The influence of electromagnetic force upon the noise of an IPM motor used in a compressor," IEEE Transactions on Magnetics, vol. 42, pp. 3494-3496, 2006.

[SN87] S. Noda, S. Mori, F. Ishibashi, and K. Itomi, "Effect of coils on natural frequencies of stator cores in small induction motors," IEEE Transactions on Energy Conversion, vol. EC-2, pp. 93-99, 1987.

[SW95] S. Williamson, T. J. Flack, and A. F. Volschenk, "Representation of skew in time-stepped two-dimensional finite-element models of electrical machines," IEEE Transactions on Industry Applications, vol. 31, pp. 1009-1015, 1995.

[TEM04] T. E. McDevitt, R. L. Campbell and D. M. Jenkins, "An investigation of induction motor zeroth-order magnetic stresses, vibration, and sound radiation," IEEE Transactions on Magnetics, vol. 40, no. 2, pp. 774-777, March 2004.

[TGH91] T. G. Habetler and D. M. Divan, "Acoustic noise reduction in sinusoidal PWM drives using a randomly modulated carrier," IEEE Transactions on Power Electronics, vol. 6, pp. 356-363, 1991.

[TI15] T. Ishigami, Y. Tanaka, and H. Homma, "Motor stator with thick rectangular wire lap winding for HEVs," IEEE Transactions on Industry Applications, vol. 51, pp. 2917-2923, 2015.

[TJK01] T.-J. Kim, H. Sang-Moon, K. Kyung-Tae, W.-B. Jung, and U. K. Chul, "Comparison of dynamic responses for IPM and SPM motors by considering mechanical and magnetic coupling," IEEE Transactions on Magnetics, vol. 37, pp. 2818-2820, 2001.

[TM11] Roadster_2.5_windmills.jpg: Tesla Motors Inc.derivative work: Mariordo (talk) - Roadster_2.5_windmills.jpg, Copyrighted free use Tesla motors Inc., 2011 [ONLINE], available: https://commons.wikimedia.org/w/index.php?curid=14709997

[TMJ87] T. M. Jahns, "Flux-weakening regime operation of an interior permanent-magnet synchronous motor drive," IEEE Transactions on Industry Applications, vol. IA-23, pp. 681-689, 1987.

[TMJ96] T. M. Jahns and W. L. Soong, "Pulsating torque minimization techniques for permanent magnet AC motor drives-a review," IEEE Transactions on Industrial Electronics, vol. 43, pp. 321-330, 1996.

[TN14] T. Nakada, S. Ishikawa, and S. Oki, "Development of an electric motor for a newly developed electric vehicle," 2014.

[TZ04] T. Zhangjun, P. Pillay, A. M. Omekanda, L. Chen, and C. Cetinkaya, "Young's modulus for laminated machine structures with particular reference to switched reluctance motor vibrations," IEEE Transactions on Industry Applications, vol. 40, pp. 748-754, 2004.

[UJS11] U. J. Seo, Y. D. Chun, J. H. Choi, P. W. Han, D. H. Koo, and J. Lee, "A technique of torque ripple reduction in interior permanent magnet synchronous motor," IEEE Transactions on Magnetics, vol. 47, pp. 3240-3243, 2011.

[WC01] W. Cai and P. Pillay, "Resonant frequencies and mode shapes of switched reluctance motors," IEEE Transactions on Energy Conversion, vol. 16, pp. 43-48, 2001.

[WC02] C. Wei, P. Pillay, and T. Zhangjun, "Impact of stator windings and end-bells on resonant frequencies and mode shapes of switched reluctance motors," IEEE Transactions on Industry Applications, vol. 38, pp. 1027-1036, 2002.

[WF13] W. Fei and Z. Q. Zhu, "Comparison of cogging torque reduction in permanent magnet brushless machines by conventional and herringbone skewing techniques," IEEE Transactions on Energy Conversion, vol. 28, pp. 664-674, 2013.

[WL14] W. Liang, J. Wang, P. C. Luk, W. Fang, and W. Fei, "Analytical modeling of current harmonic components in PMSM drive with voltage-source inverter by SVPWM technique," IEEE Transactions on Energy Conversion, vol. 29, pp. 673-680, 2014.

[WL18] W. Liang, P. C. Luk, and W. Fei, "Investigation of Magnetic Field Interharmonics and Sideband Vibration in the FSCW IPMSM Drive With the SPWM Technique," IEEE Transactions on Power Electronics, vol. 33, pp. 3315-3324, 2018.

[WLS93] W. L. Soon, D. A. Staton, and T. J. E. Miller, "Design of a new axially-laminated interior permanent magnet motor," in Industry Applications Society Annual Meeting, 1993., Conference Record of the 1993 IEEE, 1993, pp. 27-36 vol.1.

[WLS94] W. L. Soong and T. J. E. Miller, "Field-weakening performance of brushless synchronous AC motor drives," IEE Proceedings - Electric Power Applications, vol. 141, pp. 331-340, 1994.

[WO05] O. Wen, A. El-Antably, H. Surong, and T. A. Lipo, "Analysis of optimal stator concentric winding patterns design," in 2005 International Conference on Electrical Machines and Systems, 2005, pp. 94-98 Vol. 1.

[WQC13a] W. Q. Chu and Z. Q. Zhu, "Average torque separation in permanent magnet synchronous machines using frozen permeability," IEEE Transactions on Magnetics, vol. 49, pp. 1202-1210, 2013.

[WR15] W. Ren, Q. Xu, and Q. Li, "Asymmetrical V-shape rotor configuration of an interior permanent magnet machine for improving torque characteristics," IEEE Transactions on Magnetics, vol. 51, pp. 1-4, 2015.

[XG17] X. Ge, Z. Q. Zhu, G. Kemp, D. Moule, and C. Williams, "Optimal step-skew methods for cogging torque reduction accounting for three-dimensional effect of interior permanent magnet machines," IEEE Transactions on Energy Conversion, vol. 32, pp. 222-232, 2017.

[XI05] L. Xiaodong and S. Nandi, "Analysis of a 3-phase induction machine with inclined static eccentricity," in Electric Machines and Drives, 2005 IEEE International Conference on, 2005, pp. 1606-1613.

[YFS06] Y. F. Shi, Z. Q. Zhu, and D. Howe, "Torque-speed characteristics of interior-magnet machines in brushless AC and DC modes, with particular reference to their flux-weakening performance," in 2006 CES/IEEE 5th International Power Electronics and Motion Control Conference, 2006, pp. 1-5.

[YH09] Y. Haodong, H. Zeyin, and C. Yangsheng, "Electromagnetic vibration of interior permanent magnet brushless motors under brushless DC and AC operation," in Electrical Machines and Systems, 2009. ICEMS 2009. International Conference on, 2009, pp. 1-6.

[YH97] Y. Honda, T. Nakamura, T. Higaki, and Y. Takeda, "Motor design considerations and test results of an interior permanent magnet synchronous motor for electric vehicles," in IAS '97. Conference Record of the 1997 IEEE Industry Applications Conference Thirty-Second IAS Annual Meeting, 1997, pp. 75-82 vol.1.

[YH98] Y. Honda, T. Higaki, S. Morimoto, and Y. Takeda, "Rotor design optimisation of a multi-layer interior permanent-magnet synchronous motor," IEE Proceedings - Electric Power Applications, vol. 145, pp. 119-124, 1998.

[YMIC14] Yokogawa Meters and Instruments Corporation, "WT3000 Precision Power Analyzer User's Manual (Vol 1/3)", Manual No: IM 760301-01E, 8th Edition, February 2014.

[YHJ12] Y. H. Jeong, K. Kim, Y. J. Kim, B. S. Park, and S. Y. Jung, "Design characteristics of PMa-SynRM and performance comparison with IPMSM based on numerical analysis," in 2012 XXth International Conference on Electrical Machines, 2012, pp. 164-170.

[YSC06] Y. S. Chen, Z. Q. Zhu, and D. Howe, "Vibration of PM brushless machines having a fractional number of slots per pole," IEEE Transactions on Magnetics, vol. 42, pp. 3395-3397, 2006.

[YX14] Y. Xiao and P. Zhou, "A general method to calculate harmonic response of teeth in electric machine," in 9th IET International Conference on Computation in Electromagnetics (CEM 2014), 2014, pp. 1-2.

[YY17] Y. Yang, S. M. Castano, R. Yang, M. Kasprzak, B. Bilgin, A. Sathyan, et al., "Design and comparison of interior permanent magnet motor topologies for traction applications," IEEE Transactions on Transportation Electrification, vol. 3, pp. 86-97, 2017.

[ZG18] Z. Gmyrek and A. Cavagnino, "Influence of punching, welding, and clamping on magnetic cores of fractional KiloWatt motors," IEEE Transactions on Industry Applications, vol. 54, pp. 4123-4132, 2018.

[ZQZ00] Z. Q. Zhu and D. Howe, "Influence of design parameters on cogging torque in permanent magnet machines," IEEE Transactions on Energy Conversion, vol. 15, pp. 407-412, 2000.

[ZQZ03] Z. Q. Zhu, S. Ruangsinchaiwanich, N. Schofield, and D. Howe, "Reduction of cogging torque in interior-magnet brushless machines," IEEE Transactions on Magnetics, vol. 39, pp. 3238-3240, 2003.

[ZQZ06] Z. Q. Zhu, J. X. Shen, and D. Howe, "Flux-weakening characteristics of trapezoidal back-emf machines in brushless DC and AC Modes," in 2006 CES/IEEE 5th International Power Electronics and Motion Control Conference, 2006, pp. 1-5.

[ZQZ07a] Z. Q. Zhu, D. Ishak, D. Howe, and C. Jintao, "Unbalanced magnetic forces in permanent-magnet brushless machines with diametrically asymmetric phase windings," IEEE Transactions on Industry Applications, vol. 43, pp. 1544-1553, 2007.

[ZQZ07b] Z. Q. Zhu and D. Howe, "Electrical machines and drives for electric, hybrid, and fuel cell vehicles," Proceedings of the IEEE, vol. 95, pp. 746-765, 2007.

[ZQZ09] Z. Q. Zhu, Z. P. Xia, L. J. Wu, and G. W. Jewell, "Influence of slot and pole number combination on radial force and vibration modes in fractional slot PM brushless machines having single- and double-layer windings," in 2009 IEEE Energy Conversion Congress and Exposition, 2009, pp. 3443-3450.

[ZQZ09b] Z. Q. Zhu, "A simple method for measuring cogging torque in permanent magnet machines," in 2009 IEEE Power & Energy Society General Meeting, 2009, pp. 1-4.

[ZQZ12] Z. Q. Zhu, K. Wang, and G. Ombach. (2012, Optimal magnet shaping with third order harmonic for maximum torque in brushless AC machines. IET Conference Proceedings, 81-81. Available: http://digital-library.theiet.org/content/conferences/10.1049/cp.2012.0275

[ZQZ14] Z. Q. Zhu, L. J. Wu, and M. L. M. Jamil, "Influence of Pole and Slot Number Combinations on Cogging Torque in Permanent-Magnet Machines With Static and Rotating Eccentricities," IEEE Transactions on Industry Applications, vol. 50, pp. 3265-3277, 2014.

[ZQZ92] Z. Q. Zhu and D. Howe, "Analytical prediction of the cogging torque in radial-field permanent magnet brushless motors," IEEE Transactions on Magnetics, vol. 28, pp. 1371-1374, 1992.

[ZQZ93] Z. Q. Zhu and D. Howe, "Instantaneous magnetic field distribution in brushless permanent magnet DC motors. III. Effect of stator slotting," IEEE Transactions on Magnetics, vol. 29, pp. 143-151, 1993.

[ZR94] Z. Ren, "Comparison of different force calculation methods in 3D finite element modelling," IEEE Transactions on Magnetics, vol. 30, pp. 3471-3474, 1994

[ZT04] T. Zhangjun, P. Pillay, A. M. Omekanda, L. Chen, and C. Cetinkaya, "Young's modulus for laminated machine structures with particular reference to switched reluctance motor vibrations," IEEE Transactions on Industry Applications, vol. 40, pp. 748-754, 2004.